8-2009

SYNTHESIS AND CHARACTERIZATION OF MAGNETIC SOLIDS CONTAINING PERIODIC ARRAYS OF TRANSITION METAL OXIDE NANOSTRUCTURES

Wendy Queen
Clemson University, wqueen@clemson.edu

SYNTHESIS AND CHARACTERIZATION OF MAGNETIC SOLIDS CONTAINING PERIODIC ARRAYS OF TRANSITION METAL OXIDE NANOSTRUCTURES

A Dissertation
Presented to
the Graduate School of
Clemson University

In Partial Fulfillment
of the Requirements for the Degree
Doctor of Philosophy
Chemistry

---

by
Wendy Lee Queen
August 2009

Accepted by:
Dr. Shiou-Jyh Hwu, Committee Chair
Dr. Murray Daw
Dr. Joe Kolis
Dr. Bill Pennington

ABSTRACT

The ultimate goal of the research presented in this dissertation was to explore new systems containing low-dimensional magnetic nanostructures in hopes of finding new extended solids exhibiting novel magnetic properties due to the confined magnetic lattices. The scope of this research is threefold: 1) to explore new solids containing low-dimensional magnetic nanostructures in the A-M-X-O system, where A = alkali and alkaline-earth metal cations, M = first-row transition metal cations, and X = P, As, or V, 2) to characterize these new materials and, through chemical substitution, fine tune (and optimize) magnetic and electronic properties of solids that exhibit confined magnetic nanostructures, and 3) to perform structure/property correlation studies to seek the origins of any unusual physical phenomena associated with the size, shape, and geometry of the magnetic nanostructures.

Throughout this study, diamagnetic oxyanions XO_m^{n-} were utilized to structurally insulate and electronically confine the transition metal oxide lattices. Typical reactions included various transition metal oxides, main group oxides such as P_4O_{10} or As_2O_5, and alkali/alkaline-earth metal oxides. Most of these starting materials have high melting points and low solubility. As a result, high-temperature solid state methods are utilized. In the solid state, single crystal growth sometimes suffers because of slow diffusion across the crystalline interface. In order to alleviate this problem, alkali and alkaline-earth metal halides are employed as a high-temperature flux. These salts have much lower melting points than covalent metal oxides and can aid in the synthesis and crystal growth of materials that cannot be achieved in other solvent media.

There are additional advantages to using molten halide fluxes, for they can also act as reactants in the synthetic systems. First, it was considered that, like the aforementioned diamagnetic oxyanions, ionic salt could also be utilized to reduce the dimensionality of the TM-oxide magnetic lattices. The difference between these two diamagnetic insulators is found in their bonding interactions with respect to the transition metal oxide nanostructures. The oxyanions are covalent in nature, while the salt is more ionic in nature and therefore is less likely to function as a pathway for superexchange. As a result, it was thought that this salt could further aid in the confinement of the magnetic TM-oxide lattices, hence, many of the reactions were carried out in a huge excess of salt. This was done not only to increase the reaction kinetics, but also in hopes of obtaining interesting phase formations such as metal oxide nanostructures engulfed in a sea of salt.

In this study, diamagnetic oxyanions XO_m^{n-} and/or salt, utilized to terminate the propagation of the transition metal oxide lattices, allowed the formation of structures with 2-D sheets, 1-D chains, and 0-D clusters. Exploratory synthesis in this mixed polyhedral system consisting of the tetrahedral oxyanions and the transition metal oxide with varying coordination environments, has proven to be extremely rich and has rendered many new compounds of magnetic and catalytic interest. The new discoveries are grouped into chapters according to their lattice types, where Chapter 3 and Chapter 5 present two extensive compound families that contain two dimensional metal oxide sheets, Chapter 6 presents a lattice with 1-D $[MO_4Cl]_\infty$ chains, and Chapters 4, 7, and 8 all present materials containing 0-D magnetic metal oxide clusters.

DEDICATION

This dissertation is dedicated to my father.

I would not take anything in the whole wide “hickey” for the times, the lessons, and the love.

ACKNOWLEDGMENTS

I would like to extend my deepest gratitude to the many people who have had major contributions to my success. First, I would like to give a special thanks to my research advisor, Dr. Shiou-Jyh Hwu for his guidance and support throughout my graduate studies. I would also like to thank Dr. Murray Daw, Dr. Joe Kolis, and Dr. Bill Pennington for serving as my committee members. I would like to thank the National Science Foundation which provided funding for my research and the many collaborators including, Dr. Joan Hudson and the Clemson Electron Microscopy Lab, Jesse Alonzo and Dr. Jim O'brien from Quantum Design, Dr. Craig Brown of NIST, and Dr. Jian He and Dr. Malcome Skove from the Clemson Physics Department. I would like to give a special thanks to Dr. Don Vanderveer for all of the time he spent teaching me X-ray crystallography.

I would like to thank all of the past and present members of the research group, especially Dr. Lei Wang, Dr. Sanjaya Ranmohotti, Dr. Greg Becht, Palmer West, Matt Williams, Adam Siegfried, Jaewoong Hur, and Duminda Sanjeewa for all the laughs and support. I also owe a special thanks to many wonderful undergraduate students including Palmer West, Chris Briere, Patrick Moore, Ryan Pavlick, Mike Gorka, Shane Reighard, and Mathew Dunlap, all of which have made a contribution to my research endeavors.

I would like to thank my family, especially my mom, for her undying support throughout my education. Last, but certainly not least, I would like to thank all of my friends, especially Kelli and Erin, for their love, support, and always believing in me, even when I did not.

TABLE OF CONTENTS

Page

TITLE PAGE i

ABSTRACT ii

DEDICATION iv

ACKNOWLEDGMENTS v

LIST OF TABLES ix

LIST OF FIGURES xiv

CHAPTER

I. INTRODUCTION 1

II. EXPERIMENTAL METHODS 31

Introduction 31
Reaction Procedures 32
Starting Materials 36
Characterization Techniques 39
Literature Cited 56

III SYNTHESIS AND CHARACTERIZATION OF A NEW FAMILY OF METAL (II) PHOSPHATES EXHIBITING A TRIANGULAR MAGNETIC LATTICE, $ANa_3M_7(PO_4)_6$ (A = Cs, Rb, K and M = Mn, Fe, Co) 59

Introduction 59
Synthetic Procedures 62
Characterization 64
Results and Discussion 86
Conclusion 110
Literature Cited 114

IV. SYNTHESIS AND CHARACTERIZATION OF EXTENDED SOLIDS CONTAINING EQUILATERAL TRIANGULAR $Fe_3(\mu_3\text{-}O)$ MAGNETIC NANOSTRUCTURES 117

Introduction 117
Synthetic Procedures 120
Characterization 130
Results and Discussion 139
Conclusion 160
Literature Cited 162

V. STRUCTURALLY RELATED COMPOUNDS CONTAINING EXTENDED $[M_3O_{12}]_\infty$ MAGNETIC SHEETS 165

Introduction 165
Synthetic Procedures 169
Characterization 171
Results and Discussion 183
Conclusion 212
Literature Cited 215

VI. SYNTHESIS AND CHARACTERIZATION OF NOVEL SALT-INCLUSION VANADATES, $(CsCl)M(VO_3)_2$ where M = Mn, Co, Ni, Cu, or Zn 217

Introduction 217
Synthetic Procedures 219
Characterization 225
Results and Discussion 234
Conclusion 248
Literature Cited 250

VII. SYNTHESIS AND CHARACTERIZATION OF HIGH NUCLEARITY CLUSTER-BASED SALT-INCLUSION COMPOUNDS 252

Introduction 252
V_{15} 255
Synthetic Procedures 255
Characterization 256
Results and Discussion 258
V_{14} 272

Synthetic Procedures 272
Characterization 274
Results and Discussion 278
Cu_{14} 301
Synthetic Procedures 301
Characterization 304
Results and Discussion 312
Conclusion 328
Literature Cited 332

VIII. SYNTHESIS AND CHARACTERIZATION A SALT-INCLUSION POROUS SOLID CONTAINING ISOLATED POLYOXOMETALATE CORES, (SALT)•$Cs_{2.5}(V_5O_9)(AsO_4)_2$ AND (SALT)•$Cs_2(V_4O_8)(AsO_4)_2$ COMPOUNDS 336

Introduction 336
Synthetic Procedures 339
Characterization 349
Results and Discussion 360
Conclusion 389
Literature Cited 391

IX. CONCLUSIONS 395

APPENDICES 414

I: NEW MIXED POLYHEDRAL FRAMEWORKS 414

LIST OF TABLES

Table Page

2.1 Starting materials used in high-temperature solid state reactions 38

3.1 Crystallographic data for compounds **1-9** 68

3.2 Atomic parameters for compounds **1-9** 70

3.3 Anisotropic thermal parameters ($Å^2$) for compounds **1-9** 75

3.4 Selected bond distances and bond angles for compounds **1-9** 80

3.5 Comparison of unit cells from various colored single crystals of compounds **1-3** 88

3.6 Parameters obtained from Curie-Weiss fit of the high temperature χ^{-1} data for **1-9** 96

3.7 Crystallographic data for $Na_4Co_7(AsO_4)_6$ and $Na_4Ni_7(AsO_4)_6$ 108

4.1 Unit cell refinements performed on the Ga^{3+}- and Mn^{3+}- doped derivative 129

4.2 Crystallographic data for compounds **1-3** 131

4.3 Atomic parameters for compounds **1-3** 132

4.4 Anisotropic thermal parameters ($Å^2$) for compounds **1-3** 133

4.5 Selected bond distances and angles for compounds **1-3** 135

5.1 Crystallographic data and magnetic properties of structurally related compounds 168

5.2 Crystallographic data for compounds **1-6**. 173

5.3 Atomic parameters for **1-6** 176

5.4 Anisotropic thermal parameters for compounds **1-6**. 178

5.5 Selected bond distances and angles for Compounds **1-6**. 180

List of Tables (Continued)

Table Page

6.1 Crystallographic data for compounds **1-6**. 226

6.2 Atomic parameters for **1-6**. 228

6.3 Anisotropic thermal parameters for compounds **1-6**.. 230

6.4 Selected bond distances and angles for Compounds **1-6**. 232

6.5 Results from the Curie-Weiss fitting of the χ^{-1} data for compounds **1-4**. .. 247

7.1 Crystallographic data for $Cs_{11}Na_3(V_{15}O_{36})Cl_6$ (**1**). 259

7.2 Atomic parameters for $Cs_{11}Na_3(V_{15}O_{36})Cl_6$ (**1**). 260

7.3 Anisotropic thermal parameters for $Cs_{11}Na_3(V_{15}O_{36})Cl_6$ (**1**). 260

7.4 Selected bond distances and bond angles for $Cs_{11}Na_3(V_{15}O_{36})Cl_6$ (**1**)..... 261

7.5 Bond valence sum calculations for $Cs_{11}Na_3(V_{15}O_{36})Cl_6$ (**1**). 261

7.6 Crystallographic data **2** and **3** 277

7.7 Atomic parameters for **2** and **3**..... 279

7.8 Anisotropic thermal parameters for **2** and **3**. 281

7.9 Selected bond distances and angles for **2** and **3**. 284

7.10 Bond valence sum calculations for **2** and **3**. 288

7.11 Crystallographic data for Cu_{14} (**4-6**). 307

7.12 Atomic parameters for Cu_{14} (**4-6**)..... 308

7.13 Anisotropic thermal parameters ($Å^2$) for Cu_{14} (**4-6**)..... 309

7.14 Selected bond distances and angles for Cu_{14} (**4-6**) 312

7.15 Bond valence sum calculations for **4-6**. 315

List of Tables (Continued)

Table Page

8.1 Unit cell refinements of various powder samples 353

8.2 Single crystal structure solutions from seven (salt)•$Cs_{(6-n)}(V_5O_9)^{n+}(AsO_4)_2$ crystals 354

8.3 Crystallographic data for V_5 and V_4. 355

8.4 Atomic parameters for V_5 and V_4. 356

8.5 Anisotropic Thermal Parameters ($Å^2$) for V_5 and V_4. 357

8.6 Selected bond distances and bond angles for V_5 and V_4. 358

8.7 Bond valence sum calculations for $Cs_{3.5}Na_{1.46}(V_5O_9)(AsO_4)_2Cl_{2.33,}$ V_5, and $Cs_{3.64}Na_{1.40}(V_4O_8)(AsO_4)_2Cl_{3.04}$, V_4. 359

8.8 Surface area analysis for multiple reactions. 371

I.1 Crystallographic data for $Rb_3ClMn(VO_3)_4$. 416

I.2 Atomic parameters for $Rb_3ClMn(VO_3)_4$. 416

I.3 Refined unit cell parameters of the stoichiometric synthesis of $Ba_3M(V_2O_7)_2$ where M = Mn or Co. 422

I.4 Crystallographic data of $Ba_3M(V_2O_7)_2$ where M = Mn or Co. 423

I.5 Atomic parameters of $Ba_3M(V_2O_7)_2$ where M = Mn or Co 424

I.6 Curie-Weiss fitting parameters obtained from $Ba_3M(V_2O_7)_2$ where M = Mn or Co. 430

I.7 Crystallographic data of $Ba_5Cl_4Co_3(V_2O_7)_3$_ 434

I.8 Atomic parameters of $Ba_5Cl_4Co_3(V_2O_7)_3$. 434

I.9 Crystallographic data of $BaClMV_2O_7$, M = Mn or Fe. 439

I.10 Atomic parameters of $BaClM(V_2O_7)$, M = Mn or Fe. 440

List of Tables (Continued)

Table Page

I.11 Crystallographic data of $Ba_7Cl_4M(V_2O_7)_3$, M = Mn, Co, Cu. 443

I.12 Atomic parameters of $Ba_7Cl_4M(V_2O_7)_3$, M = Mn, Co, Cu.. 444

I.13 Crystallographic data of $Ba_5MCl_6M(V_2O_7)_2$ M = Mn or Co. 448

I.14 Atomic parameters of $Ba_5MCl_6M(V_2O_7)_2$ M = Mn or Co.. 449

I.15 Crystallographic data of $(AX)Cu_5O_2(VO_4)_2$ A/X = Rb/Cl, Cs/Cl, and Cs/Br 455

I.16 Atomic parameters of $(AX)Cu_5O_2(VO_4)_2$ A/X = Rb/Cl, Cs/Cl, and Cs/Br 456

I.17 Crystallographic data of $A_5MCl_6VO_{1-x}Cl_x(VO_3)_4$ A/M = Rb/Fe or Cs/Fe or Cs/V and $Cs_{4.75}V_2O_2(VO_3)_8$. Atomic parameters of $BaClM(V_2O_7)$, M = Mn or Fe.....461

I.18 Atomic parameters of $A_5MCl_6VO_{1-x}Cl_x(VO_3)_4$ A/M = Rb/Fe or Cs/Fe or Cs/V and $Cs_{4.75}V_2O_2(VO_3)_4$. 462

I.19 Crystallographic data of $Rb_2Na_2V_4O_4(PO_4)_4$.....469

I.20 Atomic parameters of $Rb_2Na_2V_4O_4(PO_4)_4$. 470

I.21 Crystallographic data of $KCo_4(AsO_4)_3$ and $NaMn_4(VO_4)_3$. 472

I.22 Atomic parameters $KCo_4(AsO_4)_3$ and $NaMn_4(VO_4)_3$. 473

I.23 Crystallographic data of $Ba_2Na_{13}Co_4(AsO_4)_8Cl$. 480

I.24 Atomic parameters $Ba_2Na_{13}Co_4(AsO_4)_8Cl$. 481

I.25 Crystallographic data of $CsKCo_2(AsO_4)_2$. 484

I.26 Atomic parameters $Cs_2K_2Co_4(AsO_4)_4$.....485

I.27 Crystallographic data of $BaNa_2Co(PO_4)_2$. 489

I.28 Atomic parameters $BaNa_2Co(PO_4)_2$. 489

List of Tables (Continued)

Table Page

I.29 Crystallographic data of $Cs_3ClCo_3(P_2O_7)_2$. 492

I.30 Atomic parameters $Cs_3ClCo_3(P_2O_7)_2$. 493

I.31 Crystallographic data of $CsNaM(P_2O_7)$ where M = Fe, Co, or Cu. 496

I.32 Atomic parameters $CsNaM(P_2O_7)$, where M = Fe, Co, or Cu. 497

I.33 Crystallographic data of $Sr_2Fe(AsO_4)_2Cl$. 503

I.34 Atomic parameters $Sr_2Fe(AsO_4)_2Cl$. 504

I.35 Crystallographic data of $Ba_{1.25}Na_{3.25}Cu_3(AsO_4)_4$. 507

I.36 Atomic parameters $Ba_{1.25}Na_{3.25}Cu_3(AsO_4)_4$. 508

I.37 Crystallographic data of $BaNa_8Cu_6O_2(PO_4)_6$. 511

I.38 Atomic parameters $BaNa_8Cu_6O_2(PO_4)_6$. 512

LIST OF FIGURES

Figure Page

1.1 Diagram showing the temperature-dependent magnetic susceptibility for various types of magnetic materials....4

1.2 Schematic representations of (A) paramagnetism, (B) ferromagnetism, (C) antiferromagnetism, and (D) ferrimagnetism 4

1.3 Energy barrier to magnetization reversal. Upon reduction of particle volume, the energy barrier is also reduced 8

1.4 Structure of $Mn_{12}OAc$. This material is depicted as having a large spin ground state S = 10. The inner core Mn^{4+} ions are shown in green and the outer core Mn^{3+} ions are shown in orange. AFM coupling between the inner and outer core leads to a large spin ground state S=10....11

1.5 Hysteresis loop of $Mn_{12}OAc$ (blue) compared to a classical loop (red). The stepped variations are attributed to quantum tunneling of magnetization, QTM....13

1.6 Schematic drawings of different types of low-dimensional magnetic nanostructures (blue) of 0- (oligomer), 1- (wire) and 2- (sheet) dimensions formed *via* electronic insulation from surrounding oxyanions (red) that restrict the propagation of the magnetic components 17

1.7 Structure (top) and schematic drawing (bottom) of 2-dimensional $La_4Ti(Si_2O_7)_2(TiO_2)_{4m}$ where the double TiO_2 rutile slabs (m = 2) are insulated from one another by the nonmagnetic oxyanions....18

1.8 Octahedral connectivity in three different situations, corner-sharing, edge-sharing, and face-sharing. Around the edges show various connectivities between metal polyhedra (dark grey) and the oxyanion (white). 23

2.1 Schematic view of the fully computer-controlled Sieverts apparatus used in the hydrogen adsorption study. 51

3.1 Calculated powder pattern of $RbNa_3Fe_7(PO_4)_6$ compared to the PXRD pattern obtained from the high-yield synthesis of the powder. The extra peaks, not observed in the calculated PXRD pattern, are marked with asterisks
....65

List of Figures (Continued)

Figure Page

3.2 Plot of the cell volume of $ANa_3M_7(PO_4)_6$ as a function of atomic number of the A-site cation, A = K, Rb, or Cs. 87

3.3 Partial structure of the Fe-O network. The solid lines represent Fe-O bonds with distances ranging from 2.01-2.26 Å. The dotted lines are 2.48 Å for Fe(2) and 2.60 Å for Fe(5). The bond valence sum (BVS) calculations show the contributions of long bonds to the overall valence of these iron sites 90

3.4 Partial structure of the Fe-O network showing fused triangular magnetic lattices (highlighted in cyan). Parallel iron(II) oxide chains are interlinked through sharing vertex oxygen atoms of the $Fe(5)O_{4+2}$ polyhedra *via* long bonds of Fe(2)-O(11) 92

3.5 Connectivity of FeO_n polyhedra (n = 4~6) within the *ab* (top) and *bc* (bottom left) plane and with phosphate groups (bottom right) 93

3.6 Inverse molar magnetic susceptibility, χ^{-1}, vs *T* plots of the $RbNa_3M_7(PO_4)_6$ series (M = Mn, Fe, Co) at H = 100 Oe on ground powder of selected single crystals. The inset shows the χT plots 95

3.7 M vs *T* plots of $RbNa_3Fe_7(PO_4)_6$ and the low-temperature region (inset) of the $ANa_3Fe_7(PO_4)_6$ series (A = K, Rb, Cs) at H = 100 Oe on ground powder of selected single crystals showing a ferromagnetic transition at T_1 98

3.8 Hysteresis loops of magnetization (M) vs. applied magnetic field on an oriented single crystal (0.3mg) of $RbNa_3Fe_7(PO_4)_6$ showing Normalized magnetization (M/Ms) is plotted against the saturation value (Ms) at H = 5T 100

3.9 Hysteresis loops showing evidence of magnetic anisotropy. Magnetization (M) vs. applied magnetic at 2K with field applied along the easy axis, *a*, and perpendicular to *a*. When the field is applied perpendicular to *a* the hysteresis is diminished 100

3.10 Hysteresis loops of magnetization (M) vs. applied magnetic field on an oriented single crystal (1.0 mg) of $KNa_3Fe_7(PO_4)_6$ approximately along the crystallographic *a* axis 102

List of Figures (Continued)

Figure Page

3.11 Hysteresis loops of magnetization (M) vs. applied magnetic field on a powder of ground single crystals (7.7 mg) of $CsNa_3Co_7(PO_4)_6$, **9**. Broad steps appear in the 5K and 2K data. The inset shows stepped variations in the 5K field dependent powder data of $RbNa_3Fe_7(PO_4)_6$, **5** 102

3.12 FC/ZFC temperature dependent plots of $RbNa_3Fe_7(PO_4)_6$ single crystal with various fields applied along the *a* axis 104

3.13 *AC* magnetic susceptibility, χ', along with the out-of-phase component, χ'' (inset), on a single crystal of $RbNa_3Fe_7(PO_4)_6$. The oscillating field was applied with varying frequencies along the *a* axis with zero applied *dc* field 104

3.14 Heat capacity data in magnetic fields, 0, 1, and 3T, applied parallel and perpendicular to the *a* axis on a single crystal for $RbNa_3Fe_7(PO_4)_6$, **5** 106

3.15 M-O framework of $Na_4Ni_7(AsO_4)_6$, showing similar structural features to the title compound family, $ANa_3M_7(PO_4)_6$. (right) The M-O framework is insulated *via* surrounding $(AsO_4)^{3-}$ oxyanions 109

3.16 M-O framework of $RbNa_3Fe_7(PO_4)_6$ showing triangular magnetic lattices highlighted in dark green. The right image shows the M-O lattice insulated *via* surround $(PO_4)^{3-}$ oxyanions 109

3.17 Molar magnetic susceptibility, χ (●), and inverse molar magnetic susceptibility data, χ^{-1} (○), for $Na_4Ni_7(AsO_4)_6$ at 0.5T. This data shows a decrease in the susceptibility due to antiferromagnetic coupling 111

4.1 PXRD pattern of ground single crystals of $Ba_{10}Na_5Fe_7(\mu_3\text{-}O)_2(PO_4)_{14}$ compared to the calculated patterns of the trigonal and monoclinic phases of **1**. The single crystals appear to be a mixture of both phases 121

4.2 PXRD pattern showing a100% yield synthesis of **2** at 850°C using various conditions vs. the calculated powder pattern of **2**, $Ba_{10}Na_5Fe_7(\mu_3\text{-}O)_2(AsO_4)_{12}(AsO_3)_2$ 123

Figure Page

4.3 PXRD patterns showing a comparison between the observed pattern from a stoichiometric yield of compound **1** *vs.* the calculated powder patterns of the trigonal and monoclinic phases of $Ba_{10}Na_5Fe_7(\mu_3\text{-}O)_2(PO_4)_{14}$ 126

4.4 PXRD pattern showing the high-yield synthesis of compound **3** vs. the calculated powder pattern of $Sr_{14}NaFe_{10}(\mu_3\text{-}O)_2(PO_4)_{17}Cl$, obtained from the single crystal structure solution..... 126

4.5 PXRD patterns showing the attempted high-yield synthesis of **3** at various temperatures ranging from 650-950°C. These powder patterns are compared to the calculated powder patterns of both the trigonal and monoclinic phases of **1** and the calculated powder pattern of **3**. It should be noted that regardless of the isotherm temperature, there is no sign of the formation of a material having the same structure as **1** 128

4.6 Powder patterns for Ga^{3+}- and Mn^{3+}- doped reactions for compound **1**. These reactions were stoichiometric with respect to the targeted compounds, $Ba_{10}Na_5MFe_6(\mu_3\text{-}O)_2(PO_4)_6$. Post-synthesis regrind and reheat, at 850°C for 10 days, was carried out to create a purer product 129

4.7 Variable temperature PXRD patterns obtained form a 100% yield synthesis of **1**, $Ba_{10}Na_5Fe_7(\mu_3\text{-}O)_2(PO_4)_{14}$ vs. the calculated powder patterns obtained from the trigonal and monoclinic phases of **1**. There is no significant change upon heating and cooling the sample, indicating that there is no structural transition occurring under these conditions. 137

4.8 Perspective view of **1** (top) showing the layers along the crystallographic *c* axis and the projected view of a single Fe-P-O slab found within the *ab* plane 140

4.9 Projected view of the Fe(1) cation that is surrounded by 6 $Fe_3\mu_3\text{-}O(PO_4)_6$ units (3 have been removed for clarity) in compound **1**. The equilateral triangles are outlined in yellow 142

Figure Page

4.10 Projected view showing $3Fe_3\mu_3$-O units in **2** (left). The projected view shows the three-fold disorder of the As(3) and O(9) atoms (right). Both As(3) and O(9) are 1/3 occupied while O(8) is 2/3 occupied, giving rise to $As(3)O_3$ polyhedra that are found loosely coordinated to surrounding $Fe_3\mu_3$-$O(AsO_4)_6$ units, the long Fe(2)-O(8) distance is equal to 2.81(4)Å. It should be noted that the lone pair of electrons in As^{3+} would have to point toward one of the Fe^{3+} atoms in one of the 3 surrounding $Fe_3\mu_3$-$O(AsO_4)_6$ units, based on the 2/3 occupancy of O(8 144

4.11 Perspective view of compound **3** illustrating the Fe-O-P connectivity along the crystallographic *c* axis. The bottom figure shows the connectivity within the $[Fe^{III}_7(\mu_3\text{-}O_2)(PO_4)_{14}]$ slab, which contains Fe(1) and Fe(2) sites within the *ab* plane. This slab is common to all compounds **1-3**..... 146

4.12 Perspective view of the non-layered $Sr_{14}NaFe_{10}O_2(PO_4)_{17}Cl$, **3**. $[Fe^{III}_7(\mu_3\text{-}O_2)(PO_4)_{14}]$ slabs that are common to all three compounds (**1-3**) are bridged in **3** *via* the Fe(3)-containing slab (bottom). The bottom image shows the connectivity and coordination of the Fe(3) site within the *ab* plane of **2**. This view shows a slab consisting of alternating corner-sharing Fe_3Cl and Fe_3O_3 equilateral triangles, highlighted in yellow 147

4.13 Magnetic susceptibility (○), χ, and inverse magnetic susceptibility (●), χ^{-1} for compound **1** at applied fields 0.01 (blue) and 0.5 T (red). The inset shows the χT plot of **1**. There is a steep increase at approximately 250K, indicative of ferro(i)magnetic exchange 151

4.14 Inverse molar magnetic susceptibility data, χ^{-1}, collected on a single crystal of **1**, 3.5 mg, in various applied fields, 0, 0.5T. The high-temperature portion of the curve, 270-400K was fit using Curie-Weiss law. 151

4.15 Field-dependent magnetization data collected on a single crystal of **1** (3.5mg) at 300K (red) and 350K (blue). The field was applied parallel to the *c* axis. The hysteresis is diminished at temperatures below 250K. The inset shows the field-dependent data at 120K 153

4.16 Heat capacity data collected on a single crystal of **1**, 6.6mg, in various applied fields, 0, 0.01, and 1 T. The transition seen above 250K coincides with the transitions observed in the magnetic susceptibility data..... 153

Figure Page

4.17 Perspective view showing the trigonal version of **1**. The phosphate group is centered between 3 equilateral triangular Fe_3O nanostructures. The dotted lines represent long Fe-O distances of 2.685(1) Å. The unit cell constants for the trigonal version of $Ba_{10}Na_5Fe_7O_2(PO_4)_{14}$ are highlighted in green 156

4.18 Projected view showing the thermal ellipsoids (50% probability factor) of the monoclinic phase of **1**. The phosphate group has shifted closer to one of the Fe_3O trimers, causing a loss of the 3-fold symmetry, and giving rise to a lower symmetry phase of compound **1**. The dotted lines represent long Fe-O bonds. The unit cell dimensions for the monoclinic version of $Ba_{10}Na_5Fe_7O_2(PO_4)_{14}$ and the new bond distances and angles are highlighted in green 156

4.19 Molar magnetic susceptibility (○) and inverse molar magnetic susceptibility (●) of $Ba_{10}Na_5Fe_7O_2(AsO_4)_{12}(AsO_3)_2$, **2** measured at an applied field of 0.01T 158

4.20 Molar magnetic susceptibility (○) and inverse molar magnetic susceptibility (●) of $Sr14NaFe_{10}O_2(PO_4)_{17}$, **3** measured at an applied field of 0.01T 158

5.1 Partial structure of $[M_3O_{12}]_\infty$ (M = Fe, Co, Ni) sheet made of corner-shared MO_6 octahedra, a feature commonly adopted by **I-III** structure types, see text 167

5.2 Ball-and-stick representation showing a perspective view of $BaNaCo_3(AsO_4)_3$, **1**, structure type **I**, along the channels 184

5.3 Projected view of the Co-O connectivity within the *ac* plane of $BaNaCo_3(AsO_4)_3$, **1** (left). The $Co(1)O_6$ polyhedra share two corner oxygen atoms with $Co(2)O_6$ polyhedra *via* O(4) atoms and each $Co(2)O_6$ polyhedron shares 4 equatorial O(2) atoms with neighboring Co(1) polyhedra. Looking at the projected view of the Co-O connectivity within the *ab* plane (right), it can be seen that the Co(1) polyhedra also share an additional edge with other Co(1)O6 octahedra, forming a 3-D Co-O lattice 186

Figure Page

5.4 Polyhedral view of the connectivity between Co(1) and neighboring Co(2), As(1), and As(2) atoms in $BaNaCo_3(AsO_4)_3$, **1**. Co(1) shares O(1) with two As(2) atoms, O(3) with two As(1) atoms, and an additional edge with As(1) *via* O(2) 187

5.5 Polyhedral view of the connectivity between Co(2) and neighboring Co(1), As(1), and As(2) atoms in $BaNaCo_3(AsO_4)_3$, **1**. As(1) shares the four equatorial O(2) atoms with Co(2), while As(2) shares the two axial O(4) atoms with Co(2) 187

5.6 Projected view of the *ac* plane of $Ba_2NaCo_3(AsO_4)_3$, **1**, structure type **I**. Na and Ba cations are located within 6-membered ring windows. For the Co-O framework, see Fig. 5.1 188

5.7 Close-up view of the 6-membered ring windows observed when viewing $Ba_2NaCo_3(AsO_4)_3$, **1**, structure type **I,** along the crystallographic *a* (left) and *b* (right) directions. 188

5.8 Projected view of $Na_8Co_{6.25}O_{0.25}(AsO_4)_4(As_2O_7)_4$, **3**, structure type **II**, within the *ab* plane. Co-O-As layers are separated from one another by Na cations 190

5.9 Projected view of the $Co_3(AsO_4)_4$ layer within the *bc* plane of $Na_8Co_{6.25}O_{0.25}(AsO_4)_4(As_2O_7)_4$, **3**, structure type **II** (left). The $Co(1)O_6$ polyhedra share two corner oxygen atoms with $Co(2)O_6$ polyhedra via O(7,8) atoms (right). Each $Co(2)O_6$ polyhedra shares 4 equatorial O(7,8) atoms with neighboring Co(1) polyhedra 190

5.10 Ball-and-stick representation of the metal oxide lattices in structure types **I** (top) and **II** (bottom). The 3-D Co-O lattice observed in **1** can be broken down into Co_3O_{12} slabs that are interconnected *via* edge-sharing $Co(1)O_6$ polyhedra. Compound **3,** structure type **II,** has the same Co_3O_{12} slabs that are isolated from one another *via* interslab Na cations and As(3) polyhedra, leading to the formation of a layered-type structure. The layers in **3** are stacked directly on top of one another. As a result, the $Co(1)O_6$ polyhedra, which are edge-shared in **1** (highlighted in green), are shifted with respect to one another between the slabs in **3** 192

List of Figures (Continued)

Figure Page

5.11 Projected view of $Sr_2NaFe_3(AsO_4)_4Cl$, **5**, structure type **III**, within the *ab* plane. Fe-O-As layers are separated from one another by Sr, Na, and Cl ions 195

5.12 Projected view of the $[Fe_3(AsO_4)_4]^{4-}$ layer within the *ac* plane of $Sr_2NaFe_3(AsO_4)_4Cl$, **5**, structure type **III** (left)**.** As observed for **I** and **II, III** also has 6-membered ring windows. The $Fe(1)O_6$ polyhedra share two corner oxygen atoms with $Fe(2)O_6$ polyhedra *via* O(4) atoms (right). Each $Fe(2)O_6$ polyhedra shares 4 equatorial O(4) atoms with neighboring Fe(1) polyhedra 197

5.13 Ball-and-stick representation of the Co-O lattice in (top left) $Ba_2NaCo_3(AsO_4)_3$, **1**, (structure type **I**) compared to the Co-O lattice in (middle right) $Na_8Co_{6.25}O_{0.25}(AsO_4)_4(As_2O_7)_4$, **3**, (structure type **II)**, and the (bottom left) Fe-O lattice observed in $Sr_2NaFe_3(AsO_4)_4Cl$, **5** (structure type **III**). All structures have a common M_3O_{12} slab. These slabs are interconnected in **1** *via* Co(1) edge-sharing polyhedra. The M_3O_{12} slabs are stacked directly on top of one another in **II**, while they are stacked in an ABA fashion in **III** 198

5.14 Ball-and-stick representation illustrating the bridging As(2) cations observed in **1**, $Ba_2NaCo_3(AsO_4)_3$, vs. the nonbridging As(2) cations found in **5**, $Sr_2NaFe_3(AsO_4)_4Cl$. The multiplicity of the As(2) site is increased from 4 to 8 due to the nonlayered structure formation in **5** 200

5.15 Ball-and-stick representation showing the Fe-O lattice in $Sr_2Na_{0.66}Fe_{3.34}(PO_4)_4Cl_{0.8}$, **4**, (structure type **III**). The observed layers are partially linked by $Fe(3)O_4Cl_2$ polyhedra. The site was partially occupied with 34% Fe(3) and 66% Na(1) 202

5.16 Ball-and-stick representation showing the mixed Fe(3)/Na(1) site (observed in **4**) and the Cl(1) and O(1) ligands surrounding it. The bond distances for this same site in compounds **4**-**6** are compared (highlighted in green). Compound **4** has much closer Fe(3)/Na(1)-O distances, a direct result of smaller interslab distances, making it more accommodating for a transition metal. The Cl(1) site is partially occupied at 0.40 due to short inter Cl(1) distances 204

Figure Page

5.17 Molar magnetic susceptibility, χ (●), and the inverse molar magnetic susceptibility, χ^{-1} (○), of a ground powder of single crystals of $Ba_2NaCo_3(AsO_4)_4$, **1**, at 0.5T 206

5.18 Molar magnetic susceptibility, χ (●), and the inverse molar magnetic susceptibility, χ^{-1} (○), of ground single crystals of $Sr_2NaFe_3(AsO_4)_4Cl$, **5** at 0.5T. The inset shows the χT at applied fields of (○) 0.01 and (●) 0.5T 208

5.19 Molar magnetic susceptibility, χ (●), and the inverse molar, χ^{-1} (○), magnetic susceptibility of ground single crystals of $Ba_{1.88}Na_{0.75}Fe_3(AsO_4)_4Cl$, **6** at 0.01T. The inset shows the χT at applied fields of (○) 0.01 and (●) 0.5T 208

5.20 FC molar magnetic susceptibility, χ (red), and ZFC molar magnetic susceptibility (blue) of ground single crystals of $Sr_2NaFe_3(AsO_4)_4Cl$, **5**, at applied fields of 0.01T (squares) and 0.5T (circles) 210

5.21 FC molar magnetic susceptibility, χ, (red) and ZFC molar magnetic susceptibility (blue) of ground single crystals of $Ba_{1.88}Na_{0.75}Fe_3(AsO_4)_4Cl$, **6**, at applied fields of 0.01T(squares) and 0.5T (circles) 210

5.22 Isothermal magnetization data of a ground powder of single crystals of $Sr_2NaFe_3(AsO_4)_4Cl$, **5**, at 5, 12, and 25K 211

5.23 Isothermal magnetization data of a ground powder of single crystals of $Ba_{1.88}Na_{0.75}Fe_3(AsO_4)_4Cl$, **6**, collected at 5 and 40K. There may be an error in the 40K data, and it needs to be recollected. See text for details 211

6.1 Calculated powder pattern of (CsCl)$Mn(VO_3)_2$ (**1**) compared to the 100% yield synthesis. Impurity peaks are marked with asterisks 222

6.2 Calculated powder pattern of (CsCl)$Co(VO_3)_2$ (**2**) compared to the 100% yield synthesis. Impurity peaks are marked with asterisks 222

6.3 Calculated powder pattern of (CsCl)$Ni(VO_3)_2$ (**3**) compared to the 100% yield synthesis. Impurity peaks are marked with asterisks 223

Figure Page

6.4 Calculated powder pattern of (CsCl)Cu(VO_3)$_2$ (**4**) compared to the 100% yield synthesis. Impurity peaks are marked with asterisks 223

6.5 Calculated powder pattern of (CsCl)Zn(VO_3)$_2$ (**6**) compared to the 100% yield synthesis. Impurity peaks are marked with asterisks 224

6.6 Extended structure of compound (CsCl)Co(VO_3)$_2$, **2**. The Co octahedra share an apical Cl^- anion to form $[CoO_4Cl]_\infty$ chains. Each magnetic chain is electronically confined by metavandate chains, $(VO_3)_\infty$. A close-up, right, shows the connectivity between the CoO_4Cl_2 octahedra and VO_5 polyhedra revealing 6-membered ring windows..... 235

6.7 Projected view of (CsCl)Co(VO_3)$_2$, **2**, showing the $[CoO_4Cl]_\infty$ chains which are nearly orthogonal to the $[VO_3]_\infty$ metavanadate chains..... 237

6.8 Perspective view showing Cs coordination environments observed for (CsCl)Co(VO_3)$_2$, **2** 237

6.9 Projected view showing the layered, extended structure of (CsCl)Co(VO_3)$_2$, **5**. The apical Cl^- anions point into the space between layers, where the Cs^+ cations are located. 239

6.10 Projected view of the layers separated by Cs^+ cations in **5**. The CoCl(VO_3)$_2$ sheets found within the *ab* plane stack along the crystallographic *c* direction in an ABA type fashion 240

6.11 Ball-and-stick representation showing the Cs coordination environments observed for (CsCl)Co(VO_3)$_2$, **5.** Each Cs^+ cation has a coordination number of 12, with $8O^{2-}$ and $4Cl^-$ anions 240

6.12 Molar magnetic susceptibility, χ, of the compounds having structure type **I**, **1-4**..... 243

6.13 χT of the series of compounds having structure type **I**, **1-4,** 0.5T. The χT plot of **2** shows a peak indicating that there may be some interesting change in the spin dynamics at that temperature. The inset shows χ data of **2**. There is an observed field- dependence in the transition upon changing the applied field from 0.5(□) to 0.01T(■) 245

Figure Page

6.14 Inverse molar magnetic susceptibility, at 0.5T, for compounds having structure type **I**, **1**-**4**. The Cu containing compound, **4**, has a high temperature anomaly seen as a slight decrease in the χ^{-1} data. As a result of this, the Curie-Weiss fit gave unrealistic parameters 245

7.1 PXRD patterns showing the 100% yield synthesis of $Cs_{11}Na_3(V_{15}O_{36})Cl_6$. The PXRD pattern of the polycrystalline product is compared to the calculated pattern of **1** based on the single crystal X-ray diffraction solution..... 257

7.2 Ball and stick drawing showing a perspective view of the structure of **1** with discrete Cl-centered $[V_{15}O_{36}]^{8-}$ clusters embedded in a Cs/NaCl salt matrix 263

7.3 Close-up view of the Cl-centered $[V_{15}O_{36}]^{8-}$ cluster. The cluster has a 3-fold rotation symmetry approximately perpendicular to the plane of the page 263

7.4 Partial structures of the $[V_{15}O_{36}]^{8-}$ showing the three crystallographically distinct vanadium sites. (left) V(1) and V(3) form bowl-like caps on the top and bottom of the $[V_{15}O_{36}]^{8-}$ cluster. (right) V(2) share edges with the three V(3) to link the bowls. All of the short V=O bonds have been removed for clarity..... 265

7.5 View of $Cs_4Na_2V_{10}O_{28}\bullet 10H_2O$. The compound contains a $[V_{10}O_{28}]^{6-}$ core surrounded by Cs and Na cations and water molecules..... 267

7.6 View of $Cs_{4.25}V_{11}O_{28}\bullet 5H_2OCl_{0.75}$. The $[V_{10}O_{28}]^{6-}$ cores are isolated by surrounding Cs^+ cations and $VCl_{0.75}(H_2O)_5$ polyhedra 267

7.7 HRTEM image of the crystalline products obtained from the green solution after the dissolution of **1.** The top is the [101] view of the $Cs_4Na_2V_{10}O_{28}\bullet 10H_2O$ structure. and the bottom shows the [100] view of **1**..... 269

7.8 Molar magnetic susceptibility, χ (○), and the inverse molar magnetic susceptibility, χ^{-1} (●) collected with an applied field of 0.01T. The inset shows the magnetic moment, μ_{eff}, plotted as a function of temperature 271

Figure Page

7.9 Field-dependent magnetization plot for $Cs_{11}Na_3V_{15}O_{36}Cl_6$ at various temperatures ranging from 2-10K.....273

7.10 PXRD pattern of the 100% yield attempt for $Cs_5(V_{14}O_{22})(As_2O_5)_4Cl$, $Cs_5(V_{14}O_{22})(As_2O_5)_4Br$, and $Cs_5(V_{14}O_{22})(As_2O_5)_4I$ compared to the calculated PXRD pattern of $Cs_5(V_{14}O_{22})(As_2O_5)_4Cl$. The table below shows the unit cell refinement of the three powder patterns 275

7.11 Perspective view showing extended structure of $Cs_5(V_{14}O_{16})(AsO_3)_8Cl$. Each $[V_{14}As_8O_{42}Cl]^{5-}$ cluster is surrounded by Cs^+ cations 289

7.12 Polyhedral view of the Cl-centered $[V_{14}As_8O_{42}]^{4-}$,V_{14}, cluster. The cluster is capped with eight AsO_3 polyhedra.....289

7.13 Polyhedral view showing eight edge-sharing square pyramids that form a ring around the center of each $[V_{14}As_8O_{42}Cl]^{5-}$ core 290

7.14 Partial structure of the $[V_{14}As_8O_{42}Cl]^{5-}$ core. The polyhedral view shows two capping V_3O_{11} units found above and below the 8-membered ring....290

7.15 Perspective view of the extended structure of $Cs_5(V_{14}O_{34})(AsO_3)_2Cl•2.6H_2O$, along the crystallographic a and c axes. The discrete $[V_{14}As_2O_{40}Cl]^{5-}$ clusters are surrounded by Cs cations.....293

7.16 Close-up polyhedral view of an individual $[V_{14}As_2O_{40}Cl]^{5-}$cluster 293

7.17 Polyhedral view of two V_3O_{11} units interlinked *via* two corner-sharing AsO_3 trigonal prisms. This connectivity forms a $V_6As_2O_{24}$ belt that goes around the center of cluster in **3**.....295

7.18 Polyhedral view showing a single V_4O_{16} capping unit from above(left). The image on the right shows two V_4O_{16} units that sit above and below the plane of the $V_6As_2O_{24}$ belt. The units are shifted 45° with respect to one another.....295

7.19 Projected view of $Cs_5(V_{14}As_8O_{42}Br)•1.5\ H_2O$. The clusters are surrounded by Cs^+ cations and water molecules.....299

Figure Page

7.20 Views of the $[V_{14}As_8O_{42}Br]^{5-}$ core. The Br-centered core has eight crystallographically distinct V sites which are found in a square pyramidal geometry. The V-Br distances are highlighted in green 299

7.21 Molar magnetic susceptibility and inverse molar magnetic susceptibility for compound **2** at an applied field of 0.01T 300

7.22 Field-dependent magnetization plot for compound **2** at 2K 302

7.23 Powder pattern of the high yield synthesis of **4** and **6** vs. their resective calculated powder patterns. It appears that when targeting **4** or **6** through a stoichiometric syntheses, the predominate phase is the targeted one, but the other phase still forms 305

7.24 Powder pattern of the high-yield synthesis of Cu_{14} with excess salt compared to the calculated PXRD patterns of **4** (tetragonal) and **6** (cubic). It appears that the predominant phase may be the tetragonal compound, **4**. Using excess salt allowed the most pure product 305

7.25 Perspective view showing extended structure of $Na_{35.5}Cu_{27.75}O_8(AsO_4)_8Cl_{11}$ with Cu clusters embedded in a salt matrix 316

7.26 SEM images of crystals found in the high-yield synthesis of **4** and **5**. The morphology of the crystals reflects the symmetry of the unit cell..... 316

7.27 Cubo-octahedron made of the twelve external Cu atoms found in the $[Cu_{14}(\mu_4O_8)(AsO_4)_8]^{12-}$ core 318

7.28 Perspective view of the $[Cu_{14}(\mu_4O_8)(AsO_4)_8]^{12-}$ core (left). Each cluster has two $Cu_5O_4(AsO_4)_4$ caps that are interlinked by corner-sharing $Cu(1)O_4$ polyhedra (right). 318

7.29 Perspective view showing the disordered center of the Cu_{14} clusters observed in $Na_{35.5}Cu_{27.75}O_8(AsO_4)_8Cl_{11}$. There are three partially-occupied Cu sites within the cluster 320

7.30 Thermal ellipsoids of Cu(3-5) with a 50% probability factor. The Cu(5) site is elongated along the crystallographic *c* axis 322

Figure Page

7.31 Perspective view showing two possible clusters found in $Na_{35.5}Cu_{27.75}O_8(AsO_4)_8Cl_{11}$. (top) This cluster shows a core having fourteen copper atoms in the cluster with the two Cu(3) sites occupied. (bottom) This cluster shows a cluster with only thirteen copper atoms due to the occupied Cu(5) site. Notice the elongated thermal parameters which mean that Cu(5) likely is closer to a 4-coordinate distorted square planar copper.....324

7.32 Perspective view of the cubic derivative, **6**, of the Cu_{14} clusters that pack in an ABCDA arrangement.....325

7.33 Perspective view of the clusters packing arrangement in an ABA fashion observed in the tetragonal derivative, **4**, of the Cu_{14} cluster 325

7.34 Molar magnetic susceptibility and inverse molar magnetic susceptibility for a mixture of **4** and **6**.....327

7.35 Field-dependent magnetization plot for a mixture of compounds **4** and **6** at 2K and applied fields ranging from ±5T. The powder was obtained from a high- yield synthesis showing a mixture of **4** and **6**.....329

8.1 Calculated powder X-ray diffraction pattern obtained from the crystal structure solution of $Cs_{3.5}Na_{1.46}(V_5O_9)(AsO_4)_2Cl_{2.33}$, V_5, *vs*. a powder pattern from a high yield synthesis targeting (salt)•$Cs_{2.5}(V_5O_9)(AsO_4)_2$. The high yield product was heated in H_2O for 5 hours for salt removal. There is a shift of diffraction pattern to the right (higher 2θ angle) after heating, signifying a reduction in the unit cell volume attributed to the salt in the channel being washed out, see inset 342

8.2 Calculated powder X-ray diffraction patterns of $Cs_{3.5}Na_{1.46}(V_5O_9)(AsO_4)_2Cl_{2.33}$, V_5, with the central V(3) removed and $Cs_{3.64}Na_{1.40}(V_4O_8)(AsO_4)_2Cl_{3.04}$, V_4, *vs*. a powder pattern from a 100% yield synthesis targeting the fully oxidized V_4 cluster with the composition (salt)•$Cs_2(V_4O_8)(AsO_4)_2$.....342

Figure Page

8.3 Calculated powder pattern obtained from the crystal structure solution of $Cs_{3.5}Na_{1.46}(V_5O_9)(AsO_4)_2Cl_{2.33}$, V_5, *vs*. a powder pattern for a high yield synthesis targeting (salt)•$Cs_{2.5}(V_5O_9)(AsO_4)_2$. The high yield product was sonicated in H_2O for various periods of time. There is a shift to higher 2θ values after longer sonication times, indicating a reduction in the unit cell volume due to the removal of salt. The elemental analysis of the 100% yield synthesis (bottom) before and after the 8-hour sonication is also shown. Initially, there is a significant amount of Cs and Cl, however, after the 8-hour sonication, the amount of Cs is reduced and the Cl is gone. These results strongly support the loss of salt in the structure upon washing 343

8.4 Calculated powder pattern for $Cs_{3.5}Na_{1.46}(V_5O_9)(AsO_4)_2Cl_{2.33}$, V_5, compared to experimental powder patterns of (salt)•$Cs_{6-n}(V_5O_9)^{n+}(AsO_4)_2$ for n = 4, 4.5, and 6. It should be noted that if n = 6, a neutral framework should be obtained..... 346

8.5 Calculated powder pattern for $Cs_{3.5}Na_{1.46}(V_5O_9)(AsO_4)_2Cl_{2.33}$,$V_5$, compared to experimental powder patterns of (salt)•$Cs_{6-n}(V_5O_9)^{n+}(AsO_4)_2$ for n = 2, 2.5, and 3..... 346

8.6 Calculated powder pattern of $Cs_{3.5}Na_{1.46}(V_5O_9)(AsO_4)_2Cl_{2.33}$, V_5, compared to the post-synthesis oxidation products from the I_2 and H_2O_2 reactions and the Li^+ ion exchange attempt. The images in the bottom right hand corner show the color change in the material upon H_2O_2 oxidation. The 100% yield powder goes from dark blue-green to red..... 348

8.7 Calculated powder pattern for $Cs_{3.5}Na_{1.46}(V_5O_9)(AsO_4)_2Cl_{2.33}$, V_5, and $Cs_{3.64}Na_{1.40}(V_4O_8)(AsO_4)_2Cl_{3.04}$, V_4, *vs*. powder patterns from high yield syntheses targeting the neutral frameworks (salt)•$(V_4CuO_8)(AsO_4)_2$ and (salt)•$(V_4NiO_8)(AsO_4)_2$. The goal was to put Cu^{2+}/Ni^{2+} in the square planar V(3) site 350

Figure Page

8.8 Calculated powder pattern of $Cs_{3.5}Na_{1.46}(V_5O_9)(AsO_4)_2Cl_{2.33}$ and the powder patterns of the reactions targeting $(CsX)Cs_{2.5}(V_5O_9)(AsO_4)_2$ where x = Br^- or I^-. The powder patterns closely resemble the calculated PXRD pattern of the CsCl derivative, V_5. Shifts to lower 2θ values indicate an increase in the unit cell volume. Refined unit cell parameters obtained for the CsBr derivative (refined in the *Fd*-3*m* spacegroup (no.227)) were a = 33.33(2) and V = 37034(60). A unit cell refinement of the CsI derivative could not be obtained, presumably because of the poor quality of the powder pattern 350

8.9 Perspective view of the framework along the crystallographic *c*-axis. Small salt-containing channels can be seen along this direction 362

8.10 Perspective view of the $[V_5O_{17}]$ core. There are 4 basal V atoms, two V(1) and two V(2) and there is one apical V(3) site. V(3) shares all 4 edges with V(1) and V(2) square pyramids. The apical oxygen atom of V(3) cannot be seen as it is pointed away from the bowl-like aggregate..... 364

8.11 Perspective view of the framework along the [110] direction showing large salt-containing channels consisting of $6AsO_4$ and $6VO_5$ polyhedra... 364

8.12 Perspective view showing channeled structure formed by the V_5 clusters 366

8.13 Perspective view of the V_5 cage consisting of 6 $[V_5O_{17}]$ clusters. The black sphere in the center represents the solvent-free void found in the single crystal structure, calculated to be approximately 326 $Å^3$ of free space 368

8.14 Perspective view of the salt cage that forms inside of the cavity. The salt cage is capped on 6 sides by $[V_5O_9]$ aggregates, and within the sphere is a solvent-free void with a volume of 326$Å^3$ 369

8.15 A single slab cut from the *ac* plane of the structure. The slabs stack in an ABCDA fashion. The clusters undergo a 4_1 screw axis as they propagate along the *a*, *b*, or *c* axis. Within the slab, the $[V_5O_{17}]$ cores are interconnected *via* AsO_4 polyhedra to form the rim around the void containing the cage, shown on the right..... 369

Figure Page

8.16 TGA curve of a 100% yield sample of V_5, $Cs_{2.5}(V_5O_9)(AsO_4)_2 \cdot nH_2O$ after soaking to remove the salt. The curve shows an approximate weight loss of 10.5%. This weight loss is equivalent to 6.6 water molecules per formula unit, $Cs_{2.5}(V_5O_9)(AsO_4)_2 \cdot 6.6H_2O$ 372

8.17 View of the V_5 and the fully-oxidized V_4 cluster with the center V(3) site empty. The V-O and V-V distances show a significant decrease upon oxidation 376

8.18 V-O and V-V distances observed for the $V_{4/5}$-containing compound observed in the n = 4.5 reaction, see text. When compared to the V_4 and V_5 clusters, this one shows intermediate distances as expected..... 376

8.19 H_2 adsorption isotherm collected on the soaked sample (S.A. = 150(2) m^2/g), $Cs_{2.5}(V_5O_9)(AsO_4)_2$, at 77 and 87K in pressures up to 47 bar 382

8.20 H_2 adsorption isotherm collected on the sample (S.A. = 242(4) m^2/g), that was oxidized via H_2O_2 382

8.21 Comparison of the partial structures of the V_5 and the V_{10} cluster. Upon doubling the V to As ratio in the single crystal reaction, there is evidence found of a $[V_{10}O_{18}]$ core..... 384

8.22 Molar magnetic susceptibility (□) and inverse magnetic susceptibility (■) performed on 100% yield synthesis of (salt)•$Cs_{2.5}(V_2O_5)(AsO_4)_2$ at an applied field of 0.01T. The inset shows the μ_{eff} plotted as a function of temperature 386

8.23 Field-dependent magnetization plot performed on 100% yield synthesis of (salt)•$Cs_{2.5}(V_2O_5)(AsO_4)_2$ at T = 2K. The inset shows the comparison of these field- dependent plots at T = 2, 3.5, 5, and 10K. At T = 10 K, the plot becomes linear 388

I.1 Perspective view of $Rb_3ClMn(VO_3)_4$, **8**. Looking at the *ab* plane there are 5- and 6-membered ring windows containing the Rb^+ cations 417

I.2 Perspective view of the *bc* plane of $Rb_3ClMn(VO_3)_4$ showing layers separated by Rb cations (left). The image on the right shows the Cl-centered acentric unit. The Cl is off-center in the distorted octahedral coordination of 2Mn+4Rb found in $Rb_3ClMn(VO_3)_4$..... 419

Figure Page

I.3 PXRD patterns showing the products of the stoichiometric synthesis of $Ba_3M(V_2O_7)_2$, where M = Mn and Co. Obvious impurity peaks are marked with asterisks. The calculated PXRD pattern of **1** is included for comparison 422

I.4 Perspective view of the $Ba_3Mn(V_2O_7)_2$ structure showing the covalent $[MnV_4O_{14}]_\infty^{6-}$ chains isolated *via* surrounding Ba^{2+} cations 426

I.5 Projected view along *c* showing the packing arrangement of parallel manganese vanadate chains. $[Mn_2O_{10}]$ dimers are shaded in blue. The color codes are the same throughout the structure presentations 426

I.6 Partial structure of a single $[MnV_4O_{14}]_\infty$ chain extending infinitely along the crystallographic *a* direction. The chain contains Mn_2O_{11} dimers made of edge-sharing MnO_6 octahedra. The manganese oxide dimers are isolated by two sets of crystallographically independent $[V_2O_7]$ pyrovandates but interlinked by one, $V(1,3)_2O_7$ resulting in a relatively short O(6)···O(13) distance of 2.83(1) Å, see text 428

I.7 Molar magnetic susceptibility, χ (○), and inverse molar magnetic susceptibility, χ^{-1} (▲), collected in an applied field of 0.5T. The data was obtained from a ground sample of selected single crystals of $Ba_3Mn(V_2O_7)_2$ (**1**) 430

I.8 Molar magnetic susceptibility, χ (○), and inverse molar magnetic susceptibility, χ^{-1} (▲), collected in an applied field of 0.5T. The data was obtained from a ground sample of selected single crystals of $Ba_3Co(V_2O_7)_2$ (**2**). The inset shows the χT data 432

I.9 Perspective view of $Ba_5Cl_4Co_3(V_2O_7)_3$. The material consists of structurally confined equilateral triangular units (highlighted in yellow). Looking along *c* a three-fold axis can be seen as three of the six highlighted triangles are coplanar 435

I.10 Perspective view of $Ba_5Cl_4Co_3(V_2O_7)_3$ along *c* showing a single slab of coplanar Co_3 μ_3-Cl units. From this view it is seen that there is no direct covalent linkage between coplanar equilateral triangular units (highlighted in yellow) 435

Figure Page

I.11 Perspective view of $Ba_5Cl_4Co_3(V_2O_7)_3$ along *a*. From this view it is seen that the highlighted equilateral triangular units, are structurally confined by VO_4^{3-} polyhedra. The coplanar Co3μ_3-Cl slabs are stacked in an ABC type arrangement along the *c* axis.....437

I.12 Molar magnetic susceptibility, χ (○), and inverse molar magnetic susceptibility, χ^{-1} (▲), collected in an applied field of 0.01T. The data was obtained from a ground sample of selected single crystals of $Ba_5Cl_4Co_3(V_2O_7)_3$. The inset shows the χT data.....437

I.13 Projected view showing the channeled structure of $BaClMnV_2O_7$.....441

I.14 Projected view showing a close-up view of the large channel that extends along the crystallographic *b* axis.....441

I.15 Projected view showing the structure of $Ba_7Cl_4Co(V_2O_7)_3$ along the crystallographic *c* axis (top). The structure consists of 1-D $CoCl_2(V_2O_7)_2$ chains that extend infinitely along the *c* direction (bottom). The chains are surrounded by Ba, Na, and Cl ions There are also individual $(V_2O_7)^{4-}$ units found within the structure 446

'I.16 Perspective view showing the extended structure of $Ba_5CoCl_6Co(V_2O_7)_2$ (top). The left image shows $[CoCl_6]_\infty$ chains and the bottom one shows $[Co(V_2O_7)_2]_\infty$ sheets 450

I.17 Molar magnetic susceptibility, χ (○), and inverse molar magnetic susceptibility, χ^{-1} (▲), collected in an applied field of 0.5T. The data was obtained from a ground sample of selected single crystals of $Ba_5CoCl_6Co(V_2O_7)_2$.....451

I.18 PXRD pattern showing the stoichiometric synthesis of $CsClCu_5O_2(VO_4)_2$ 454

I.19 PXRD pattern showing the stoichiometric synthesis of $RbClCu_5O_2(VO_4)_2$ 454

I.20 Projected view of the $(CsCl)Cu_5O_2(VO_4)_2$ framework. The structure has 6-membered ring windows that contain the Cs and Cl ions.....458

Figure Page

I.21 Projected view showing the connectivity between the $Cu(1)O_5$ trigonal bipyramidal and $Cu(2)O_4$ square planar polyhedra in $(CsCl)Cu_5O_2(VO_4)_2$ 459

I.22 Projected view of the Cu-O framework in $(CsCl)Cu_5O_2(VO_4)_2$. The Cu-O framework forms 2-D sheets. The sheets are interlinked by the fully oxidized $(VO_4)^{3-}$ tetrahedra 459

I.23 Perspective view of $Cs_5VCl_6VO(VO_3)_4$. Looking at the *ac* plane the layered structure is revealed. The structure consists of $[VO(VO_3)_4]_\infty$ sheets that extend infinitely within the *ab* plane. The layers are separated from one another by Cs^+ cations and VCl_6 polyhedra shown on the right 464

I.24 Projected view of $Cs_{4.75}V_2O_2(VO_3)_8$ (left). The structure is made up of the same $VO(VO_3)_4$ sheets that extend infinitely within the *ab* plane..... 466

I.25 Projected view showing the channeled structure of $Rb_2Na_2V_4O_4(PO_4)_4$. The structure has two channels. The smaller one contains only Rb^+ cations, while the larger one contains both Rb^+ and Na^+ cations..... 468

I.26 Polyhedral view showing the coordination around the V(2) and V(3) polyhedra. The long V(3)-O(18) distance gives rise to a pseudo-octahedral geometry and corner sharing between the $V(3)O_6$ and $V(2)O_5$ polyhedra..... 468

I.27 PXRD pattern obtained from a high yield synthesis of $NaMn_4(VO_4)_3$ is compared to the calculated powder pattern. Obvious impurity peaks are marked with asterisks..... 473

I.28 Projected view showing the channeled structure of $KCo_4(AsO_4)_3$ and the 3-D Co-O-As framework 474

I.29 Polyhedral view showing the channels in $KCo_4(AsO_4)_3$ (left). The polyhedral view on the right shows the connectivity between neighboring CoO_x polyhedra..... 474

I.30 Projected view of the extended structure of $NaMn_4(VO_4)_3$ along the crystallographic *b* axis (left). The condensed structure forms Mn-V-O cages (right) around the Na^+ cations 476

Figure Page

I.31 Close-up view of the $Mn(1)O_6$ (left) and $Mn(2)O_6$ (right) connectivity. Both polyhedra share two edges and two corners with nearest neighbors ... 476

I.32 Molar magnetic susceptibility, χ (○), and inverse molar magnetic susceptibility, χ^{-1} (▲), collected in an applied field of 0.01T. The data was obtained from a ground sample of selected single crystals of $NaMn_4(VO_4)_3$. The inset shows the χT data. ... 478

I.33 Projected view showing the extended structure of $Ba_2Na_{13}Co_4(AsO_4)_8Cl$ ... 482

I.34 Polyhedral view showing the coordination around the two crystallographically distinct Co^{2+} cations ... 482

I.35 Projected view showing the extended structure of $CsKCo_2(AsO_4)_2$ ... 486

I.36 Polyhedral view showing a close-up view of the two channels found in $CsKCo_2(AsO_4)_2$ ... 486

I.37 Projected view showing the extended structure of $CsKCo_2(AsO_4)_2$ along *c* ... 487

I.38 Polyhedral view showing a close-up view of the 6-membered channel that runs along the *c* axis ... 487

I.39 Projected view showing the extended structure of $BaNa_2Co(PO_4)_2$ along *b* ... 490

I.40 View of the $[Co(PO_4)_2]_\infty$ slab ... 490

I.41 Projected view showing the extended structure of $Cs_3ClCo_3(P_2O_7)_2$ along *c* ... 494

I.45 Projected view showing the extended structure of $CsNaCo(P_2O_7)$ along *a* (right) and *b* (left) ... 501

I.46 Polyhedral view showing the connectivity of CoO_4 polyhedra ... 501

I.47 Projected view showing the extended structure of $Sr_2Fe(AsO_4)_2Cl$. Sr^{2+} and Cl^- ions are found in the space between the slabs ... 505

Figure Page

I.48 Projected view showing the $[Fe(AsO_4)_2]_\infty$ slabs (left). The polyhedral view on the right shows the connectivity of the FeO_6 polyhedra, which share an edge forming dimers that are structurally isolated *via* AsO_4 polyhedra 505

I.49 Projected view showing the extended structure of $Ba_{1.25}Na_{3.25}Cu_3(AsO_4)_4$. Ba^{2+} and Na^{+}ions are found in the space between the slabs 509

I.50 Polyhedral view showing the connectivity of $[Cu_3(AsO_4)_4]_\infty$ slabs. The CuO_x polyhedra share corners forming trimers, which are structurally isolated *via* AsO_4 polyhedra..... 509

I.51 Projected view showing the extended structure of $BaNa_8Cu_6O_2(PO_4)_6$ (top). The extended structure consists of 1-D chains made of edge sharing $Cu(1)O_5$ and $Cu(1)O_4$ polyhedra (left). The $Cu(3)O_5$ trigonal pyramids are structurally confined *via* AsO_4 polyhedra 513

CHAPTER ONE

INTRODUCTION

Solid state chemistry deals with the synthesis, structure, and properties of solid materials. These materials can be molecular or nonmolecular and crystalline or noncrystalline (amorphous) in nature. The term molecular solid refers to solids made of molecules that are held together through intermolecular forces such as H-bonding, dipole-dipole, induced-dipole, van der waals interactions, etc. Nonmolecular solids, often referred to as extended solids due to the extended nature of their bonding, exhibit covalent and ionic bonding interactions, which are considerably stronger than the aforementioned intermolecular counterparts. Extended solids consist of three-dimensional arrays of atoms or ions, and their properties are solely determined by how the atoms pack in three dimensions. For a full appreciation of solid state chemistry, one must possess a sound understanding of the structure of solids and the nature of bonding, especially in view of the fact that structure dictates function.

The directions of the solid state chemistry field have been influenced by many factors ranging from great discoveries to environmental issues. Since the development of X-ray crystallography in the early 1900's by William Lawrence Bragg, the field of solid state chemistry has been driven by the development of many technologically advanced materials including ferroelectric perovskites in the 1940's[1], zeolite and platinum-based catalysts discovered in the 1950's[2], high purity silicon used in the electronics industry in the 1960's[3], high T_c superconductors in the 1980's[4], and the colossal magnetoresistant manganese perovskites in the 1990's[5]. Recently, several environmental issues such as the

need for alternative energy sources and a reduction in the evolution of greenhouse gases have also begun to govern the current and future directions of the field, thereby driving the development of new materials for solid state devices such as lithium ion batteries, fuel cells, hydrogen storage materials, and solar panels. Due to the broad range of topics and materials classified within the realm of solid state chemistry, it often encompasses many other areas of study, such as solid state physics, materials science, mineralogy, metallurgy, electronics, and ceramics. It is within this broad range of active topics in solid state science that the synthetic solid state chemist finds a playground for exploration. The main objective of any solid state chemist involves searching for correlations between the structures of solids and the broad range of properties they exhibit, such as electronic, magnetic, dielectric, optical, and superconducting.

The focus of this dissertation is on the synthesis and characterization of new extended solids containing low-dimensional magnetic nanostructures. Within this work, many new magnetic materials have been discovered. For the reader's sake, some basic fundamentals of magnetism are presented in the following paragraphs. Also, systems that give us some inspiration for this work will be discussed in order to set the stage for the investigation presented in the following chapters.

Fundamentals of Magnetism

Solid state materials are often classified by how they behave in the presence of an applied magnetic field. When a material is placed in a magnetic field, it develops magnetization. The magnetization, M, and applied field, H, are related to one another by

magnetic susceptibility, χ, which is a material's degree of magnetization with respect to an applied magnetic field, as $M = \chi H$.[6] Materials that exhibit magnetic susceptibilities that are small and negative are classified as diamagnetic. Diamagnetism arises from paired electrons, and all materials have some diamagnetic character due to the presence of core electrons. Diamagnetic materials tend to repel a magnetic field, giving rise to a slightly negative susceptibility, shown in Figure 1.1. Materials that exhibit positive magnetic susceptibilities are labeled as paramagnetic, and this phenomenon, which is commonly observed in materials containing magnetically dilute transition metal elements, arises from the presence of unpaired electrons, Figure 1.2(A). Paramagnetic materials show a slight increase in the susceptibility, Figure 1.1, as a function of decreasing temperature. As the material is cooled, less thermally activated randomization leads to slightly higher susceptibility, which results from an increase in the number of aligned magnetic moments in the presence of an applied magnetic field.

In 1895, Pierre Curie derived an equation that stated that the molar magnetic susceptibility is inversely proportional to temperature, $\chi = C/T$, where C is the Curie constant.[7] This equation holds true for paramagnetic materials, which are magnetically dilute, meaning that each paramagnetic ion acts independently of the others. In undiluted magnetic solids, it is often observed that there is direct interaction, or exchange, between magnetic centers. For these materials, the molar magnetic susceptibility, χ_m, is described by Curie-Weiss law which states that $\chi_m = C/(T-\theta)$, where θ is the Weiss constant.

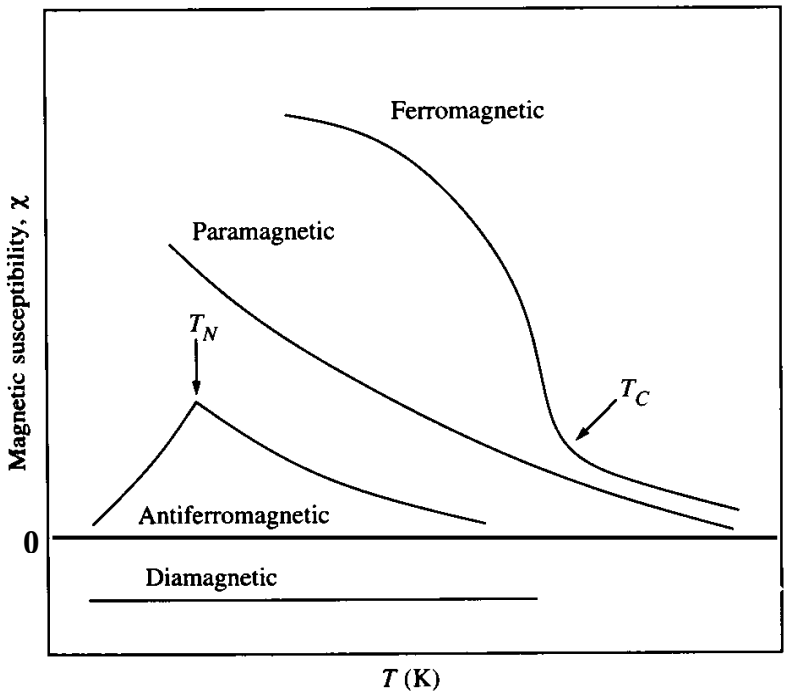

Figure 1.1: Diagram showing the temperature-dependent magnetic susceptibility for various types of magnetic materials.

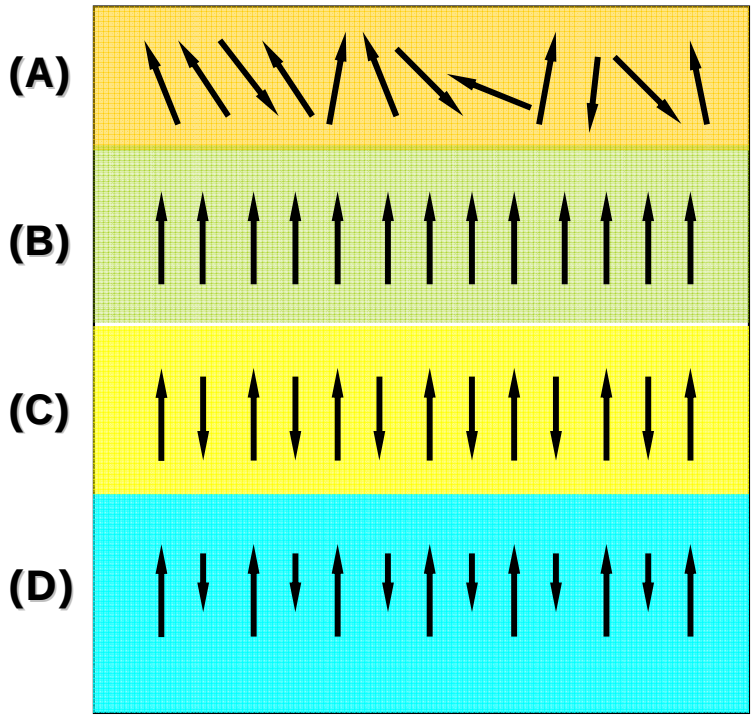

Figure 1.2: Schematic representations of (A) paramagnetism, (B) ferromagnetism, (C) antiferromagnetism, and (D) ferrimagnetism.

Other types of magnetic interactions are associated with localized electrons and are observed in undiluted paramagnetic materials. In fact, when magnetic ions are brought within close proximity, magnetic exchange can occur. This exchange is classified as direct, where moments between atoms are close enough to have significant overlap of their wave functions, or indirect, where the moments couple over relatively large distances *via* an intermediate diamagnetic ion or through itinerant (delocalized) electrons according to Ruderman-Kittel-Kasuya-Yosida (RKKY) theory.[8] In this work, the focus is on an indirect type of exchange, superexchange, which is defined as an interaction between moments through the orbital of a nonmagnetic (or diamagnetic) ion. There are rules developed by Goodenough[9] and Kanamori[10] to help determine the sign and magnitude of the superexchange between ions. If the sign is positive, usually observed for M-O-M angles near or below 90°, the material is ferromagnetic, indicating the magnetic moments on neighboring ions prefer a parallel alignment, Figure 1.2(B). These materials show a sudden increase at the Curie temperature, T_C, where the material begins to show magnetic order, shown in Figure 1.1. If the sign is negative, usually observed for M-O-M angles up to 180°, the material is antiferromagnetic, indicating the moments prefer an antiparallel alignment, Figure 1.2(C). These have a characteristic decrease in their susceptibility, at the Néel temperature, T_N, due to the cancelation of magnetic moments, shown in Figure 1.1. In instances where there is antiparallel alignment but one magnetic moment is larger than the other, it is called ferrimagnetism, Figure 1.2(D). This is observed in many materials, the most famous of which are spinels and inverse spinels. There is one other type of magnetic interaction, referred to as Pauli

paramagnetism. In metallic materials, which have itinerant electrons, only the conduction electrons near the Fermi level contribute to the susceptibility. This type of material shows a weak, temperature-independent paramagnetism.

Top Down vs. Bottom Up Approach to Magnetic Materials

The oldest known magnetic material is magnetite, Fe_3O_4, which is thought to be the first material exploited by man for its magnetic properties. It is believed that this material was first utilized by the ancient Chinese to make compasses.[11] Today this mineral is still used in many applications such as a toner in electrophotography, a micronutrient in fertilizers, a pigment in paints, and an aggregate in high-density concrete.[12] Currently, magnetite is the most investigated material in nanoapplications such as drug delivery and in magnetic resonance imaging contrast agents.[13]

Since the discovery of magnetite and its exploitation, much research has been geared towards the investigation of magnetic materials as these have many applications and offer new fundamental knowledge pertaining to structure and function. One active area of magnetic research is in magnetic data storage, which has been known since 1878.[14] Current magnetic data storage is utilized in both hard disk drives in computers and in popular MP3 players. IBM introduced the first commercial hard drive in 1956 with an initial storage capacity of 5MB and areal densities of approximately 2kbit/in^2.[15] In order to keep up with public demands to increase the storage capacities of existing materials, particle sizes have been constantly reduced. Once reduced below a critical size, usually 10 - 100nm, the materials become single domain magnetic particles. It is

known that domains form in order to reduce magnetostatic energy. At some point, as the particle volume is decreased, the reduction in magnetostatic energy becomes smaller than the energy required for domain formation. Upon the formation of single domain magnetic particles (which usually occurs when the diameter is less than 100nm), the materials begin to show magnetic behavior different from their bulk counterparts. This occurrence is referred to as superparamagnetism, and is defined as a phenomenon by which magnetic materials may exhibit a behavior similar to paramagnetism at temperatures below the Curie or the Néel temperature.[16] These superparamagnetic particles have a greatly reduced energy barrier to magnetization reversal, shown in Figure 1.3.

In 1948, Stoner and Wohlfarth derived an equation allowing one to predict the energy barrier to magnetization reversal, $E_A = KV\sin^2\theta$, where K is the magnetic anisotropy of the particle of interest, V is the particle volume, and θ is the angle between the easy axis of magnetization and the magnetic moment.[17] As can be seen in the aforementioned equation, the energy barrier, E_A, is proportional to particle volume, V. As the volume is decreased, the energy barrier to magnetization reversal is also decreased and, at some point, becomes equivalent to thermal energy. As a result, the magnetic moment begins to coherently flip back and forth over the top of the energy barrier. This onset is referred to as the superparamagnetic limit and will diminish the ability of material to store information and in turn, limit its future in magnetic data storage technology.

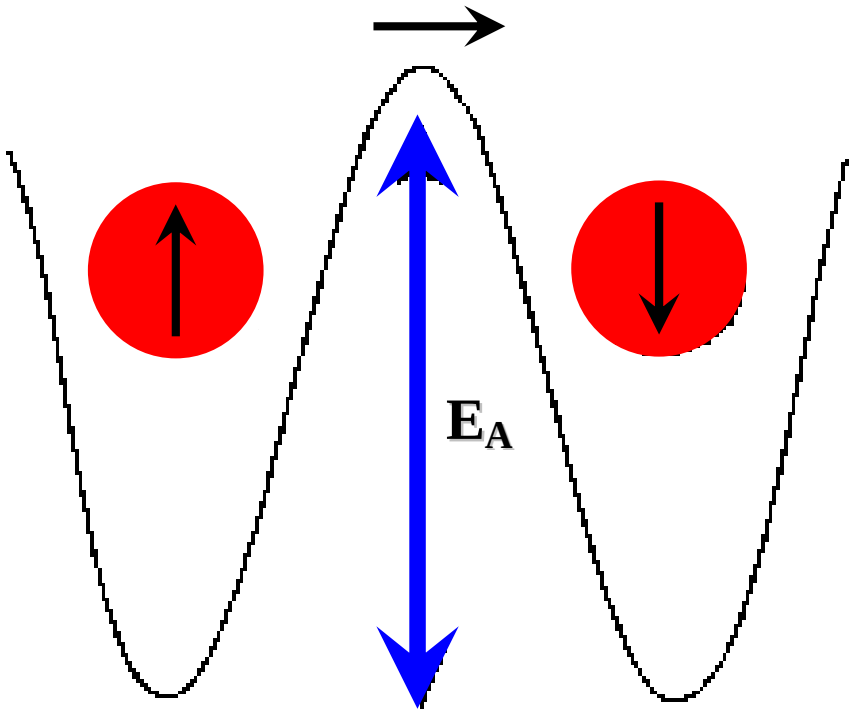

Figure 1.3: Energy barrier to magnetization reversal. Upon reduction of particle volume, the energy barrier is also reduced.

As a result of the onset of superparamagnetism, some researchers choose to take a bottom up approach to magnetic materials, where they construct molecules with high-nuclearity magnetic cores that are electronically insulated by large bulky organic ligands. In fact, many molecular chemists have used Mother Nature's synthetic strategies as a model for their own. Christou's group received inspiration from the oxygen-evolving manganese-based complexes observed in Photosystem II. In their effort to synthesize a model complex for the highest oxidation state of the biological cycle, they attempted to oxidize manganese acetate *via* permanganate. The group successfully synthesized a $Mn^{3+/4+}$ containing complex, $[Mn_{12}O_{12}(O_2CPh)_{16}(H_2O)_4]$, $Mn_{12}OAc$.[18] This new discovery of $Mn_{12}OAc$ sparked much attention from the physics community, and Gatteschi *et al*. began investigating the magnetic properties of a similar material whose structure was reported in 1980, $[Mn_{12}O_{12}(O_2CMe)_{16}(H_2O)_4]$.[19] From the presence of an out of phase peak in the ac susceptibility, it was deduced that this metal oxide cluster could be magnetized for extended periods of time without the formation of long-range magnetic order.[20] This phenomenon resulted from a large energy barrier to magnetization reversal, giving rise to a very slow relaxation process in $Mn_{12}OAc$ and, in turn, hysteresis. As a result of this discovery, the phrase Single Molecule Magnet (SMM) was coined and defined as discrete molecules that, below a certain temperature referred to as the blocking temperature, T_B, function as a single magnetic domain of nanoscale dimensions.[21]

Although this slow relaxation process occurred at very low temperatures, it sparked much interest because the presence of magnetic hysteresis, a phenomenon

normally associated with bulk magnetic materials, suggested that these materials could be employed as bits for information storage technology. Each molecule can serve as one bit, where information is stored in terms of binary digits, 1's and 0's. SMMs could be used to store information where binary digits are represented by the magnetization orientation of the material.[22] Based on the size of these potential bits, aerial densities of 30 terabits / cm^2 could be reached using SMMs, while current technology using magnetic nanoparticles will only allow densities of 3 gigabits / cm^2. SMMs, often referred to as the bottom up approach to high density data storage, could allow an increase in storage density by approximately 10^4.[23] Even though these materials offer a variety of advantages over the current materials used in information storage, they have very low magnetic critical temperatures, making it impractical for use in current computing systems.

For a material to show slow relaxation, and hence be classified as a SMM, there are two major criteria. The first is a large ground spin state S, where all metal ions in the molecule participate in a cooperative way. Figure 1.4 shows an image of $Mn_{12}OAc$. The molecule has an internal core consisting of four Mn^{4+} (shown in green) cations and an outer core of eight Mn^{3+} ions (shown in orange). The outer core of Mn has ferromangnetic coupling, S = 16, and the inner core of Mn exhibits ferromagnetic coupling, S = 6. As rationalized from an S=10 ground state, the exchange between the two cores is antiferromagnetic. The second criterion is that a SMM must also possess significant magnetoanisotropy of the easy axis, which refers to preferred orientation of magnetic moments along one direction. The magnetic anisotropy in $Mn_{12}OAc$ acetate

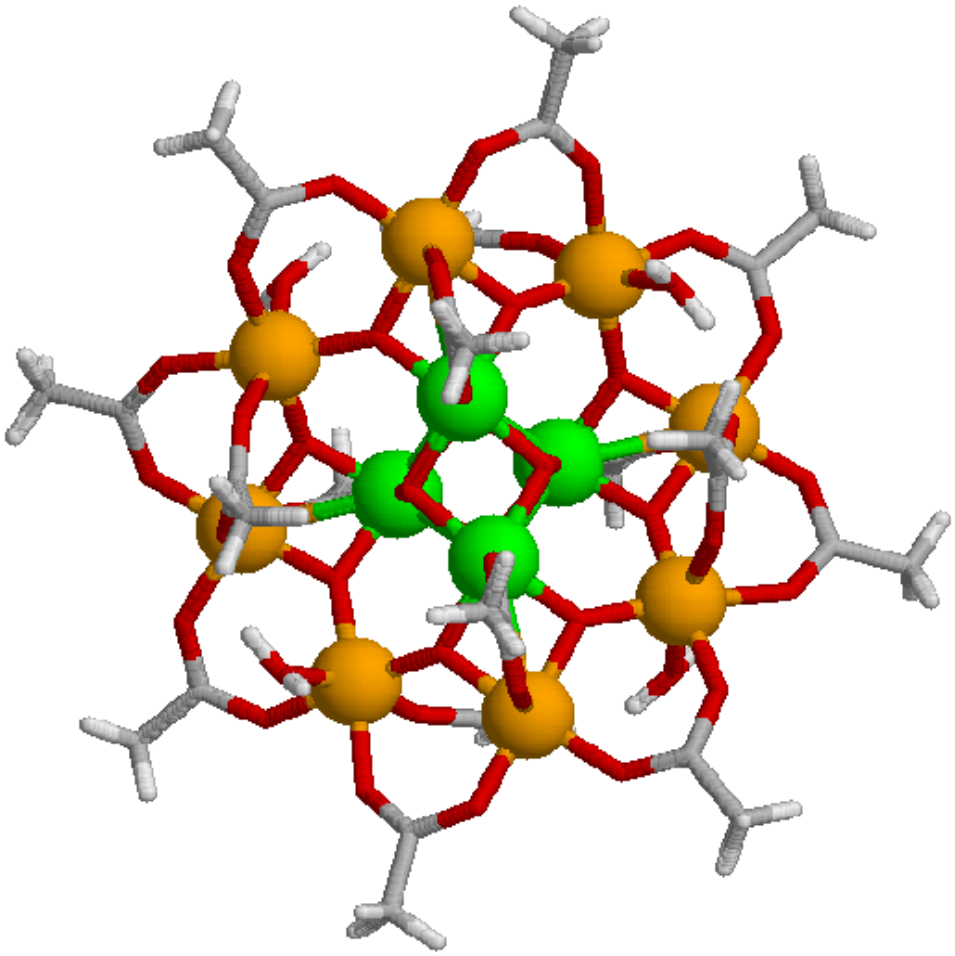

Figure 1.4: Structure of $Mn_{12}OAc$. This material is depicted as having a large spin ground state S = 10. The inner core Mn^{4+} ions are shown in green and the outer core Mn^{3+} ions are shown in orange. AFM coupling between the inner and outer core leads to a large spin ground state S=10.

results from the *Jahn-Teller* elongations which all occur approximately parallel to the crystallographic *c*-axis. The combinations of these two criteria lead to an energy barrier to magnetization reversal and in turn can lead to slow relaxation of the magnetization.

In 1996, while collecting orientation dependent isothermal magnetization data, Friedman *et al*. observed stepped variations in the hysteresis plot of $Mn_{12}OAc$.[24] Later these steps, shown in Figure 1.5, were determined to be the result of another relaxation mechanism, known as quantum tunneling of the magnetization (QTM). Instead of spin reversal through thermal relaxation over the barrier, QTM occurs when the magnetic moment reverses its spin *via* tunneling through the barrier. QTM can occur from a thermally excited state, which is referred to as phonon assisted quantum tunneling or it can occur from the ground state, which is a completely temperature-independent mechanism. Due to quantum tunneling, it has been stated that SMMs could be utilized as a qubit (or quantum bit) for quantum computing applications. SMMs have exhibited slow thermal relaxation over the barrier that gives rise to hysteresis, a phenomenon associated with bulk magnets. On the other hand, quantum tunneling of magnetization that occurs through the barrier is associated with finite or quantum objects. As a result of the combined relaxation processes, SMMs are often described as a bridge between the classical and quantum worlds of physics.[25]

Although proposed by Glauber in 1963,[26] the first one-dimensional system showing slow relaxation was not revealed until nearly 40 years later. This material was discovered in 2001, by Gatteschi *et al*. This new class of nanomagnets, called Single Chain Magnets (SCMs), was found to contain single chains that could be individually

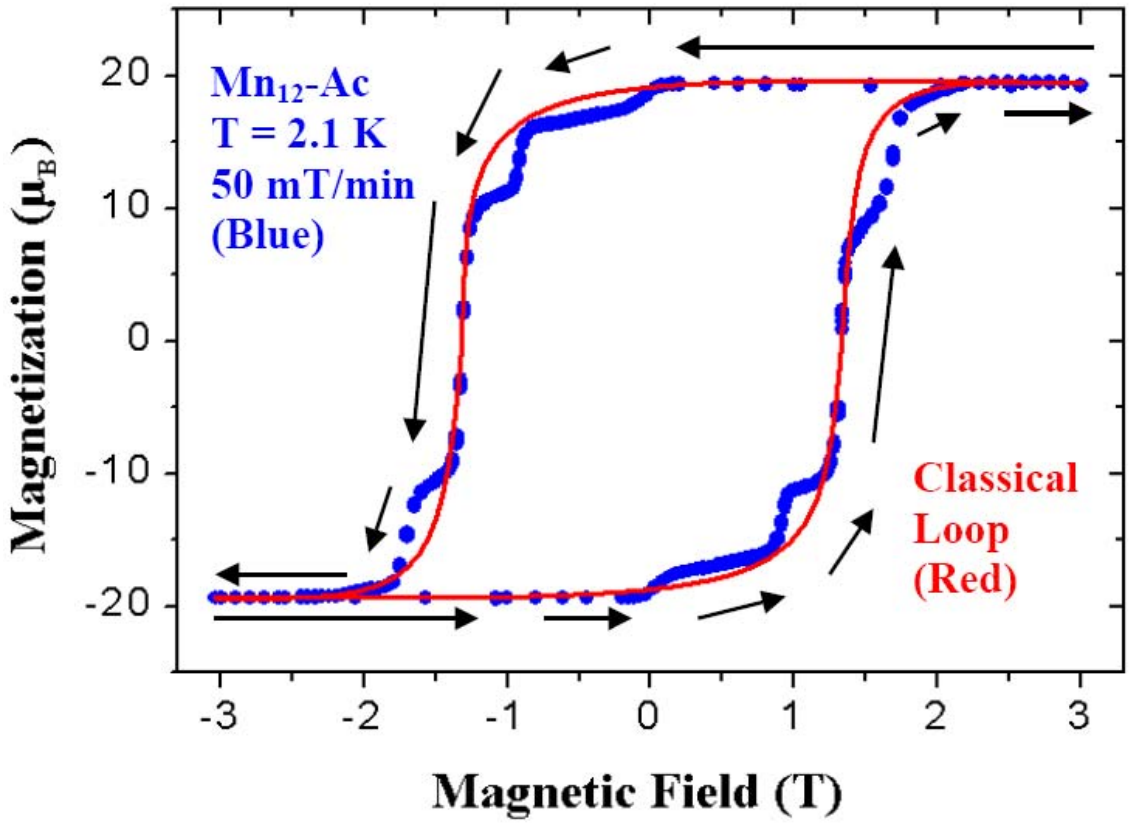

Figure 1.5: Hysteresis loop of $Mn_{12}OAc$ (blue) compared to a classical loop (red). The stepped variations are attributed to quantum tunneling of magnetization, QTM.[24b]

magnetized. This SCM, Co(hfac)2[NITPhOMe] (where hfac = hexaflouroacetylacetonate and NITPhOMe = 4'-methoxy-phenyl-4,4,5,5-tetramethylimidazoline-1-oxyl-3-oxide), is made up of $Co(hfac)_2$ moieties that alternate with the NITPhOMe radical, forming a helical structure resulting from the trigonal crystal symmetry. The material has antiferromagnetic exchange between low spin Co^{2+} and the radical, giving rise to a net ferrimagnetic exchange due to the uncompensated magnetic moment of the Co ion.[27] Like SMMs, these SCMs remain in their paramagnetic state, but due to uniaxial magnetic anisotropy and strong intrachain magnetic interactions, these materials have extremely long relaxation times at low temperatures, allowing them to exhibit hysteresis. Although these materials also exhibit slow relaxation at very low temperatures, < 10K, it is stated that the restrictions to produce samples that will be compatible with industrial applications are much less severe,[28] because, as a whole, these materials reveal higher energy barriers to magnetization reversal compared to the current SMM systems. There are a few requirements for SCMs. First, the material must behave as a one-dimensional ising type ferro or ferri magnet. Second, it must exhibit intrachain coupling significantly stronger, by 10^4 times, than interchain coupling.

In 2004, an extended solid, $Ca_3Co_2O_6$, was found to show slow relaxation and signals of QTM.[29] This material is described as a spin chain compound that has strong ising-like character. The material consists of 1-D chains made of alternating face sharing Co^{3+} octahedra and trigonal pyramids that run along the *c* axis of a hexagonal unit cell.[30] The chains, which are set on a triangular arrangement, are isolated *via* surrounding Ca^{2+}

cations. The material reportedly has intrachain ferromagnetic coupling and interchain antiferromagnetic coupling, and, owing to the triangular lattice, the interchain interactions are frustrated, inhibiting this material from forming long-range magnetic order.[31] Similar quantum behaviors have been observed in the "spin-ice" pyrochlores such as $Dy_2Ti_2O_7$ and $Ho_2Ti_2O_7$.[32]

Proposed Research

Research in molecular magnetism is moving very rapidly. Since the discovery of slow relaxation in $Mn_{12}OAc$ in 1991, hundreds of papers have been published describing new SMM and SCM systems. Despite the fast progress, their future prospects of becoming next-generation storage materials are still hampered by very low transition temperatures, <10K. The extended solid systems are not showing much more promise, as it is apparently very hard to create nonmolecular solids containing truly confined magnetic lattices. Recently reported extended solids exhibiting quantum effects have relied on geometrically frustrated magnetic lattices (kagomé and kagomé-like; see later discussions in Chapter 4) as these can inhibit the formation of long range magnetic order. Based on the recent findings, it is likely that there are many more existing extended solids that exhibit quantum effects from these types of lattice arrangements, but they are still undiscovered because of the lack of general knowledge about characterization methods in condensed matter communities.

Despite the inherent disadvantages of extended solids, we have decided to pursue quantum magnetic solids with extended frameworks, as the study of newly synthesized

magnetic materials is interesting in its own right. They have much to offer in terms of new knowledge about how structure dictates function. We have proposed to synthesize new magnetic materials while paying special attention to chemical systems that can lead to targeted low-dimensional magnetic solids. In order to improve on the past and current research in the area of SMMs and SCMs, we have proposed to take a unique approach by replacing organic ligands with inorganic species. Our goal is to build extended frameworks containing magnetic nanostructures that are encapsulated and, in turn, insulated by rigid inorganic ligands. If true magnetic confinement can be achieved in extended solids, it is thought that by replacing the bulky organic ligands with more rigid inorganic ones, we can decrease the degree of phonon interactions and hopefully increase magnetic critical temperatures.

In order to create these low-dimensional magnetic lattices, nonmagnetic oxyanions such as $(SiO_4)^{4-}$, $(PO_4)^{3-}$, and $(AsO_4)^{3-}$ can be utilized to terminate the propagation of the transition metal oxide lattice. The confined magnetic lattices can have various dimensionalities including 0-D clusters, 1-D chains, and 2-D sheets[33], shown in Figure 1.6. This idea has been demonstrated in many previously reported systems such as $La_4Ti(Si_2O_7)_2(TiO_2)_{4m}$[34], shown in Figure 1.7. This metal silicate has a layered structure that contains two-dimensional rutile-like titanium oxide slabs that are separated from one another *via* silicate slabs, $[La_4Ti(Si_2O_7)_2]$. As observed in $La_4Ti(Si_2O_7)_2(TiO_2)_{4m}$, magnetic nanostructures often adopt structural features similar to bulk materials, allowing us to study spin-spin and spin-lattice interactions in electronically simplified systems.

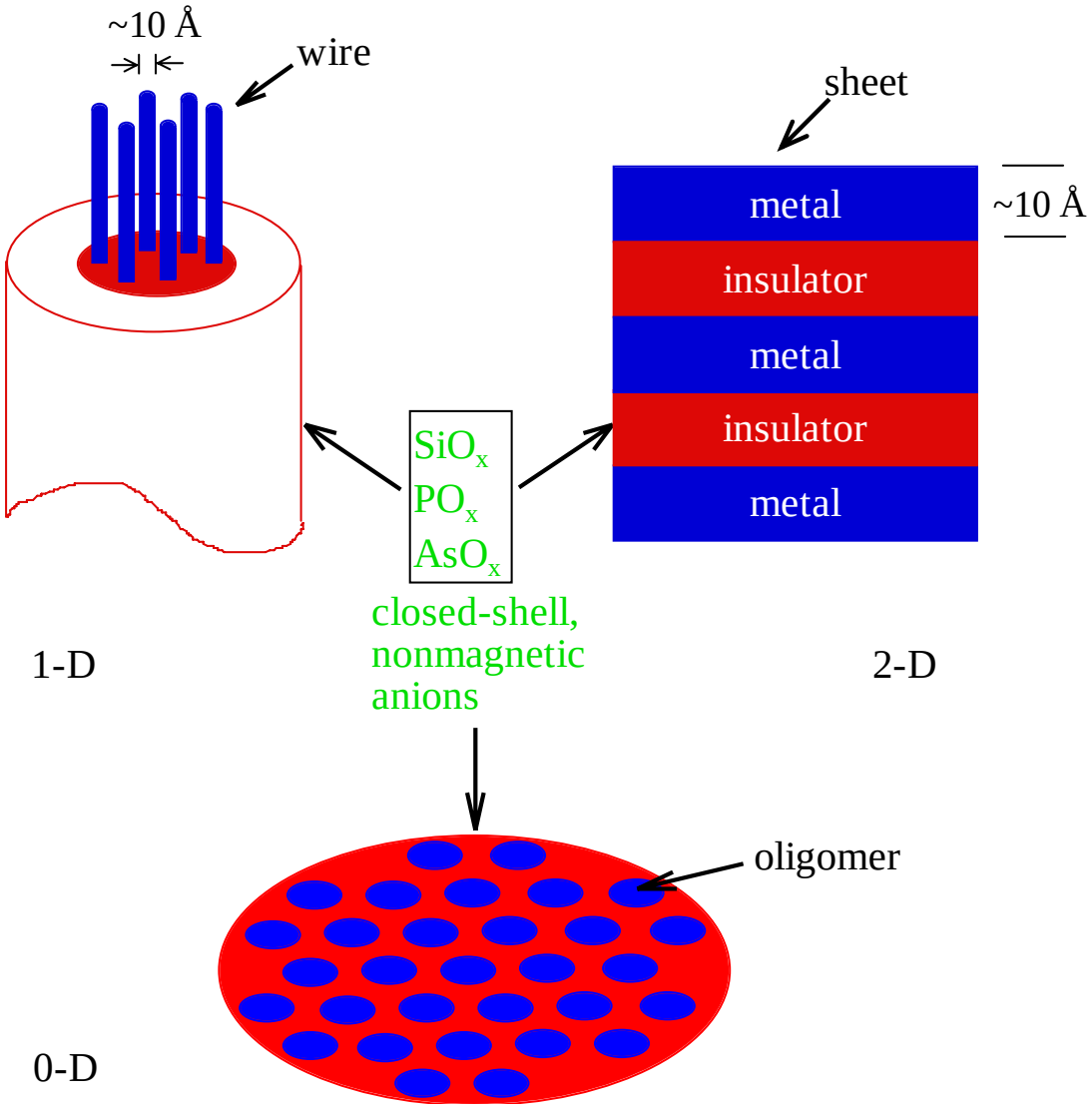

Figure 1.6: Schematic drawings of different types of low-dimensional magnetic nanostructures (blue) of 0- (oligomer), 1- (wire) and 2- (sheet) dimensions formed *via* electronic insulation from surrounding oxyanions (red) that restrict the propagation of the magnetic components.

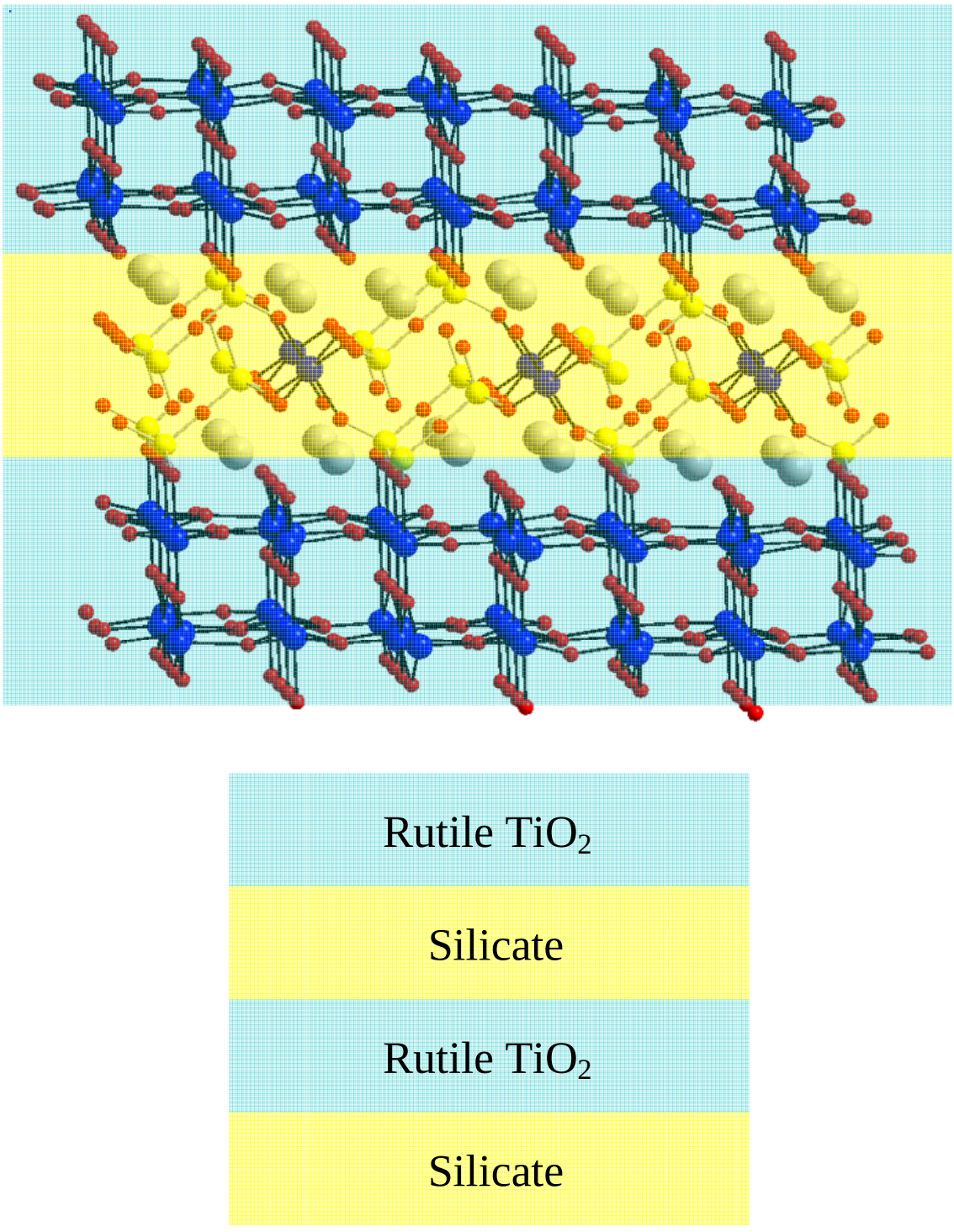

Figure 1.7: Structure (top) and schematic drawing (bottom) of 2-dimensional $La_4Ti(Si_2O_7)_2(TiO_2)_{4m}$ where the double TiO_2 rutile slabs (m = 2) are insulated from one another by the nonmagnetic oxyanions.

To seek additional diversity in structure formation, it was proposed that substituting the $(XO_4)^{3-}$ oxyanions (X = P, As) with a fully oxidized early transition metal such as $(VO_4)^{3-}$ would allow new structural chemistry to be unveiled. This chemistry is attractive for many reasons. Structurally, like their silicate counterparts, fully oxidized vanadium(V) compounds could achieve more diversity due to their ability to form vanadate units of varying size, shape, and geometry such as dimers, trimers, chains, and rings. Unlike Si, P, and As however, V can adopt several different coordination environments and can therefore achieve even greater structural versatility. Vanadium also has an additional characteristic that later transition metals do not. In its highest oxidation states, 4+ or 5+, vanadium often exhibits short vanadyl type, V=O, bonds. These vanadyl bonds can serve as a terminating group which will naturally restrict the propagation of the metal oxide lattice and increase our likelihood of forming low-dimensional magnetic structures. This idea is taken from what has already been demonstrated in polyoxometallate chemistry as many vanadium clusters have been observed with cage-like cores.[35] Most of these cage-like aggregates consist of VO_5 square pyramidal polyhedra with short apical vanadyl bonds that point away from the cage. Some examples of these include the following compositions: $[V_{12}O_{32}]^{4-}$, $[V_{15}O_{36}]^{5-}$, $[V_{18}O_{42}]^{12-}$, $[V_{19}O_{49}]^{9-}$, and $[V_{34}O_{82}]^{10-}$.[36]

Furthermore, mixing vanadium with a second TM is particularly attractive as the resulting compounds could have potential applications in areas linked to catalysis, batteries, and magnetism due to the variable crystal chemistry of the added transition

metals. Once new vanadate frameworks are formed, they could chemically be further reduced to enhance the magnetic interactions in the system.

So we proposed to study the phase formation in the A-M-X-O system, where A = alkali and alkaline-earth metal cations, M = first-row transition metal cations, X = P, As, V. Typical reactions carried out in this study include various transition metal oxides, main group oxides such as P_4O_{10} or As_2O_5, and alkali/alkaline-earth metal oxides. Most of these starting materials have high melting points and low solubility. As a result, high-temperature solid state methods are utilized. In the solid state, single crystal growth of refractory oxides sometimes suffers because of slow diffusion across the crystalline interface. In order to alleviate this problem, alkali and alkaline-earth metal halides are employed as a high-temperature flux. These salts have much lower melting points than covalent metal oxides and can aid in the synthesis and crystal growth of materials that cannot be achieved in other solvent media.

There are additional advantages to using molten halide fluxes, for they can also act as reactants in the synthetic systems. First, it was considered that, like the aforementioned diamagnetic oxyanions, ionic salt could also be utilized to reduce the dimensionality of the TM-oxide magnetic lattices. The difference between these two diamagnetic insulators is found in their bonding interactions with respect to the transition metal oxide nanostructures. The oxyanions are covalent in nature, while the salt is ionic and therefore does not function as a pathway for superexchange. As a result, it was thought that this salt could further aid in the confinement of the magnetic TM-oxide lattices, hence, many of the reactions were carried out in a huge excess of salt. This was

done not only to increase the reaction kinetics, but also in hopes of obtaining interesting phase formations such as metal oxide nanostructures engulfed in a sea of salt.

Second, the salt can add even more structural versatility, as it can provide a Cl-anion as a ligand to coordinate the metal cation. The relatively weak M-Cl bond does not always provide enough energy to promote the *s* electrons for orbital hybridization, thus, unlike the O^{2-} anion, which forms many different M-O-M angles, the M-Cl-M angle is more likely to adopt a linear geometry. The O^{2-} bonds tend to be more covalent in character and can promote magnetic exchange. Weaker M-Cl bonds, on the other hand, render the electrons more localized on the Cl-anion and less likely to become involved in exchange interactions. Due to the nature of the Cl-anion, it is thought that its incorporation into the magnetic lattice can alter magnetic properties and offer structure-property correlation studies of fundamental importance.

Our group has done much work in the area of salt-inclusion chemistry to develop hybrid solids based on transition metal phosphates, arsenates, and silicates.[37] Exploratory synthesis has resulted in a large number of novel solids that exhibit fascinating nanostructures of magnetic,[38] electronic,[39] and catalytic interest.[40] This synthetic approach has also allowed the isolation of several novel porous noncentrosymmetric (NCS) solids where the salt lattices reveal a templating effect for the formation of special frameworks. These include honeycomb-like channels in $[BaCl]CuPO_4$ (CU-1),[41] irregular channel structures in two members of the $Cu_{2n-1}(P_2O_7)_n^{2-}$ series $Cs_2Cu_7(P_2O_7)_4 \cdot 6CsCl$ (CU-9, n = 4) and $Cs_2Cu_5(P_2O_7)_3 \cdot 3CsCl$ (CU-11, n = 3),[42] fresnoite-type polar framework of $Ba_2Mn(Si_2O_7)Cl$ (CU-13),[43] and non-bonding-electron-directed

channels in $(Ba_6Cl_3)M_{4+x}Si_{12-x}O_{34}$ (CU-14, where M = Mn, x = 0; M = Fe, x = 1).[44] In all cases, the Cl-centered acentric salt units have been identified as playing an essential role in the formation of NCS solids. It is our continued interest to explore new NCS materials for their potential applications in nonlinear optics, chiral catalysis, or ferroelectrics.[45]

The scope of this research is threefold. The first step is to explore new solids containing low-dimensional magnetic nanostructures in the MO_n/XO_m system (where M = first-row transition metal cations; X = V, P, or As). Exploratory synthesis using mixed polyhedra, consisting of the tetrahedral oxyanions and the transition metal oxide with varying coordination environments, has proven to be extremely rich and has rendered many new compounds of magnetic and catalytic interest. Consider for a moment the versatility of the metal oxides. They have various coordination environments, oxidation states, and can link in a variety of different ways. To illustrate this versatility, Figure 1.8 shows metal octahedra with various connectivity including corner-sharing, edge-sharing, and face-sharing. As the number of bridging oxygen is increased, the M-M distance is decreased. In fact, the M-M distance observed between two face-sharing polyhedra is so short that they are less likely to form due to repulsion between the two positive cations. Next, consider the added versatility due to the M-O-X linkages. Some examples of these are also shown in Figure 1.8. These oxyanions, although restricted in their coordination environments, add much to the resulting structure formation, as they too can form multiple types of linkages.

The second step is to characterize newly synthesized materials and, through chemical substitution, fine tune (and optimize) magnetic and electronic properties of

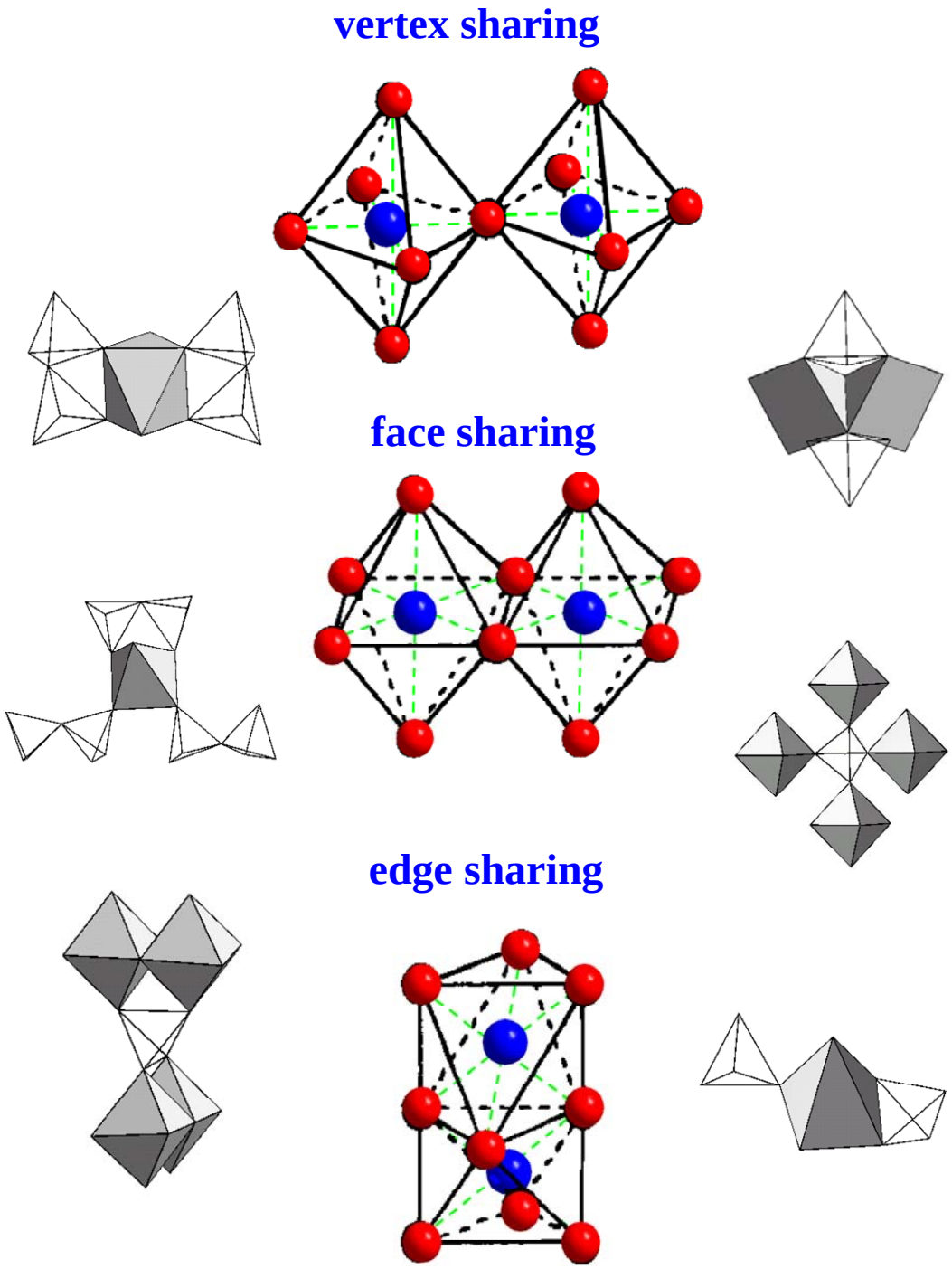

Figure 1.8: Octahedral connectivity in three different situations, corner-sharing, edge-sharing, and face-sharing. Around the edges show various connectivities between metal polyhedra (dark grey) and the oxyanion (white).

solids that exhibit confined magnetic nanostructures. Once a new chemical system is found to be versatile, various transition metals can be added in order to see how different magnetic ions affect the properties of the materials. For example, depending on the structure of the material, exchanging high spin d^5 ions with d^6 or d^7 will greatly alter the magnetic response of the material, as the orbital contribution of the latter two is unquenched in certain ligand field environments. It is already known that magnetic behavior in condensed phases is sensitive to the local structure where magnetic spins are coupled; therefore, incremental changes like the one described can offer much information about the magnetic properties of new systems. Chemical alteration of a material may not always entail adding new magnetic components. In fact, diamagnetic ions can also be doped into these metal oxide lattices in order to alter or decrease the dimensionality of the nanostructures. Cation substitutions, especially in the A-site, can also be performed in order to alter the volumes of unit cells to try to enhance or decrease the magnetic interactions. Incremental changes made to chemical composition can sometimes test the stability of certain structure types and lead to the formation of phases that have features that are structurally related, but different from the original material.

The last step is to characterize the chemically altered materials so that structure/property correlation studies can be performed in order to seek the origins of any unusual physical phenomena associated with the size, shape, and geometry of the magnetic nanostructures.

The following chapters will present several different compound families synthesized using the methods described in the previous paragraphs. Unless otherwise

noted within the individual chapters, the general synthesis and characterization are reported in Chapter 2. These synthetic methods have rendered the formation of many materials with varying dimensionalities ranging from 2-D metal oxide sheets (Chapters 3 and 5) to 1-D metal chloride chains (Chapter 6) to O-D metal oxide clusters (Chapters 4, 7, and 8). Chapters 3-5 highlight the structural versatility inherent in the mixed polyhedral system, consisting of tetrahedral oxyanions and the transition metal oxide with varying coordination environments. These chapters report three new oxyanion-based families and their interesting magnetic phenomena. Chapters 6-8 highlight the utility of molten salt synthesis and its role as a structure directing agent aiding in the formation of special frameworks such as magnetic metal oxide nanoclusters and channeled structures. These chapters will also highlight the structural versatility inherent in the newly explored vanadium system. All of these materials will be discussed in light of their structures and magnetic properties in individual chapters as well as in the conclusion chapter (Chapter 9) where some future work is also highlighted.

Literature Cited

1. Cross, L.E., Newnham, R.E. *Ceramics and Civilization: History of Ferroelectrics*; The American Ceramic Society Inc. **1987**, *111*. 290-291.

2. Rabo, J.A, Schoonover, M.W. *Appl. Catal., A* **2001**, *222*, 261–275.

3. Safa, O., Kasap, P.C. *Springer Handbook of Electronic and Photonic Materials* Springer. **2006**, Chapter 13.

4. (a) Bednorz, J.G., Müller, K.A., *Z. Phys.* B, **1986**, *64*, 189-193.

   (b) Wu, M. K, Ashburn, J.R., Torng, C.J., Hor, P.H., Meng, R.L., Gao, L., Huang, Z.J., Wang, Y.Q., Chu, C.W. *Phys. Rev. Lett.* **1987**, *58*, 908-910.

   (c) Beno, M.A., Soderholm, L., Capone II, D.W., Hinks, D.G., Jorgensen, J.D., Grace, J.D., Shculler, I.K., Segre, C.U., Zhang, K., *Appl. Phys. Lett.* **1987**, *51*, 57-59.

5. Jin, S., Tiefel, T.H., McCormack, M., Fastnacht, R.A., Ramesh, R., Chen,L.H. *Science* 1994, **264**, 413-415.

6. Huheey, J.E., Keiter, E.A., Keiter, R.L., *Inorganic Chemistry: Principles of Structure and Reactivity* Harper Collins, **1993**.

7. Huebener, R.P., Luebbig, H. *A Focus of Discoveries, World Scientific*: London **2008**.

8. Rao, C.N.R., Gopalakrishnan, J. *New Directions in Solid State Chemistry*, Cambridge University Press: Cambridge, **1997**.

9. (a) Goodenough, J. B. *Phys. Rev*. **1955**, 100, 564-573.

   (b) Goodenough, J. B. *J. Phys.Chem. Solids* **1958**, 6, 287-297.

10. Kanamori, J. *Trans*. *Magn*. *Soc*. *Japan*. **2001**, *1*, 1-10.

11. Livingston, J.D., *Driving Force: The Natural Magic of Magnets*; Harvard University Press: Cambridge **1996**.

12. http://geology.com/minerals/magnetite.shtml (accessed May 1, 2009).

13. (a) Pankhurst, Q.A., Connolly, J., Jones, S.K., Dobson, *J. J Phys. D.: Appl.*

Phys. **2003**, *36*, R167-R181.

(b). Brähler, M., Georgieva, R., Buske, N., Müller, A., Müller, S., Pinkernelle, J., Teichgräber, U., Voigt, A., Bäumler, H. *Nano Lett.*, **2006**, *6* (11), 2505-2509.

(c) Suwa, T., Ozawa, S., Ueda, M., Ando, N., Kitajima, M. *Int. J. Cancer* **1998**, *75*, 626-634.

(d) Guo, S., Li, D., Zhang, L., Li, J., Wang, E. *Biomat.* , **2009**, *30*(10) 1881-1889.

(e) Son, S.J., Reichel, J., He, B., Schuchman, M., Lee, S.B. *J. Am. Chem. Soc.* **2005**, *127*, 7316-7317.

14. Engel, F., Hammar, P. *A Selected History of Magnetic Recording* **2006**, 1-10.

15. Daniel, D., Mee, C.D., Clark, M.H., *Magnetic Recording: The First 100 Years* **1999**.

16. Bean, C.P. *J. Appl. Phys*. **1955**, *26*, 1381-1383.

17 Stoner, E., Wolfarth, P. *Philos. Trans. R. Soc. London, Ser. A* **1948**, *240*, 599-642.

18. Christou, G. *Acc.Chem. Res*.**1989**, *22*, 328-335.

19. Lis, T. *Acta Crys. B.* **1980**, *36*, 2042-2046.

20. Caneschi, A., Gatteschi, D., Sessoli, R., Barra, A.-L., Brunel, L.C., Guillot, M. *J. Am. Chem. Soc.* **1991**, *113*, 5873-5874.

21. Sessoli, R., Tsai, H.L., Schake, A.R., Wang, S., Vincent, J.B., Folting, K., Gatteschi, D., Christou, G., Hendrickson, D.N., *J. Am. Chem. Soc*., **1993**, *115*, 1804-1816.

22. Leuenberger, M.N., Loss, D. *Nature* **2001**, *410*, 789-793.

23. Ritter, S. *C & E News*, **2004**, 82, 29-32.

24. (a) Friedman, J., Sarachik, M., Tejada, J., Maciejewski, J., Ziolo, R. *Phys. Rev. Lett.* **1996**, *76*, 3820-3833.

(b) Thomas, L., Lionti, F., Ballou, R., Gatteschi, D., Sessoli, R., Barbara, B. *Nature* **1996**, *383*, 145-147.

25. Christou, G., Gatteschi, D., Hendrickson, D.N., Sessoli, R. *MRS Bulletin*, **2000**, *25*, 66-71.

26. Glauber, R.J. *J. Math. Physics* **1963**, *4*, 294-307.

27. Caneschi, A., Gatteschi, D., Lalioti, N., Sangregorio, C., Sessoli, R., Venturi, G., Vindigni, A., Rettori, A., Pini, M.G., Novak, M.A *Angew. Chem. Int. Ed*. **2001**, *40*, 1760-1763.

28. Coulon, C., Miyasaka, H., Clérac, R. Single-Chain Magnets: Theoretical Approach and Experimental Systems,. *In Single-Molecule Mangets and Related Phenomena*; Mingos, D.M.P, Winpenny, R.; Springer: Berlin, **2006**; p. 163-206.

29. Hardy V., Flahaut D. *Phys. Rev. B* **2004**, *70*, 214439-1-214439-7

30. Fjellvag, H., Gulbrandsen, E., Aasland, S., Olsen, A., Hauback, B. *J. Solid State Chem.* **1996**, *124*, 190-194.

31. (a) Kageyama, H., Yoshimura, K., Kosuge, K., Mitamura, H., Goto, T. *J. Phys. Soc. Jpn.* **1997**, *66*, 1607-1610.

(b) Niitaka, S., Yoshimura, K., Kosuge, K., Nishi, M., Kakurai, K., *Phys. Rev. Lett.* **2001**, *87*, 177202-1-177202-4.

32. (a) Snyder, J., Ueland, B.G., Slusky, J.S., Karunadasa, H., Cava, R.J., Mizel, A., Schiffer, P. *Phys. Rev. Lett*. **2003**, *91*, 107201-1-107201-4.

(b) Ehlers, G., Cornelius, A.L., Orendac, M., Kajnakova, M., Fennell, T., Bramwell, S.T., Gardner, J.S. *J. Phys. Condens. Matter* **2003**, *15*, L9–L15.

33. Hwu, S.-J. *Chem. Mater* .**1998**, *10, 2846-2859*.

34. (a) Liao, C.H., Chang, P.-C., Kao, H.M., Lii K.-H. *Inorg. Chem.*, **2005**, *44*, 9335-9339.

(b) Hwu, S.-J., Ulutagay, M.K., Clayhold, J.A., Mackay, R., Wardojo, T.A., O'Connor, C.J., Krawiec, M. *J Am Chem. Soc*., **2002**, *124*, 12404-12405.

35. (a) Müller, A., Penk, M., Rolfng, R., Krickemeyer, E., Döring, J. *Angew. Chem. Int. Ed. Engl*., **1990**, *29*, 926-927.

(b) Dong, B., Gómez-García, C.J., Peng J., Benmansour, S.; Ma, J. Po*lyhedron*, **2007**, *26*, 1310–1316.

36. (a) Day, V.W., Klemper, W.G., Yaghi, O.M., *J. Am. Chem. Soc*., **1989**, *111*, 5959-5961.

(b) Müller, A., Krickemeyer, E., Penk, M., Wallberg, H.-J., Bögge, H. *Angew*. *Chem*. *Int*. *Ed*. *Engl*., **1987**, *26*, 1045-1046.

(c) Müller, A, Sessoli, R., Krickemeyer, E., Bögge, H., Meyer, J., Gatteschi, D., Pardi, L., Westphal, J.; Hovemeier, K., Rolfing, R., Doring, J., Hellweg, F., Beugholt, C., Schmidtmann, M. *Inorg*. *Chem*., **1997**, *36*, 5239-5250.

(d) Johnson, G.K., Schlemper, E. O. *J*. *Am*. *Chem*. *Soc*., **1978**, *100*, 3645-3646.

(e) Suber, L., Bonamico, M., Fares, V. *Inorg*. *Chem*., **1997**, *36*, 2030-2033.

(f) Müller, A., Penk, M., Krickemeyer, E., Bögge, H., Wallberg, H.-J, *Angew*. *Chem*. *Int*. *Ed*. *Engl*., **1988**, *27*, 1719-1721.

(g) Müller, A, Rolfng, R, Döring, J, and Penk, M, *Angew*. *Chem*. *Int*. *Ed*., **1991**, *30*, 588-590.

37. Ulutagay, M.-K., Hwu, S.-J., Clayhold, J.A. *Inorg. Chem.*, **2003**, *42*, 2405-2409.

38. Roland, B.K., Flora, W.H., Selby, H.D., Armstrong, N.R., Zheng, Z. *J. Am. Chem. Soc*., **2006**, *128*, 6620-6625.

39. (a) Hung, Y., Hwu, S.-J. *Inorg. Chem*, **1993**, *32*, 5427-5428.

(b) Patil, D.S., Venkatramani, N., Rohatagi, V.K. *J. Mater. Sci*. **1988**, *23*, 3367-3374.

40. Wang, S.; Hwu, S.-J.; Paradis, J. A.; Whangbo, M-H. *J*. *Am*. *Chem*. *Soc*. **1995**, *117*, 5515-5522.

41. Etheridge, K.M.S., Hwu, S.-J. *Inorg. Chem*. **1995**, *34*, 3123-3125.

42. Huang, Q., Hwu, S.-J. *Inorg. Chem*. **2003**, *42*, 655-657.

43. Mo, X., Hwu, S.-J. *Inorg. Chem.* **2003**, *42*, 3978-3980.

44. Mo, X., Ferguson, E., Hwu, S.-J. *Inorg. Chem.* **2005**, *44*, 3121-3126.

45. (a) Bein,T. *Curr. Opin. Solid State Mater. Sci.* **1999**, *4*, 85-96.

(b) Keszler, D.A. *Curr. Opin. Solid State Mater. Sci.* **1999**, *4*, 155-162.

(c) Yaghi, O.M., Li, H., Davis, C., Richardson, D., Groy, T.L. *Acc. Chem. Res.* **1998**, *31*, 474-484.

(d) Marder, S.R., Sohn, J.E., Stucky, G.D. *Materials for Nonlinear Optics: Chemical Perspective*; ACS Symposium Series 455; American Chemical Society: Washington, DC, **1991.**

CHAPTER TWO

EXPERIMENTAL METHODS

There have been many discoveries in the last several decades that have lent inspiration to the synthesis of new solid-state materials with novel properties. One such discovery occurred in 1986, when a research group led by Bednorz and Müller reported high-temperature superconductivity in several ceramic oxides, $La_{2-x}Ba_xCuO_{4-x}$ and $YBa_2Cu_3O_7$.[1] This discovery, along with many others, sparked a renewed interest in the properties of solids. As a result, many scientists began thinking of clever untraditional methods, such as sol-gel, electrochemical, and microwave methods[2] that could lead to the discovery of new materials.

The most commonly used process for the synthesis of new solid-state materials is through traditional high-temperature methods where components are mixed in specific molar ratios and then heated to high temperatures (usually > 500°C). These high temperature methods, often referred to as ceramic methods, typically take place in the solid state and must be very precise due to the lack of ability to purify the products through recrystallization, a direct result of low solubility. High temperature is required in order to increase the reaction kinetics, allowing faster diffusion of the particles across the crystalline interface. In order to improve the speed of diffusion and generate more intimately mixed starting materials, traditional grinding processes are utilized. These help reduce particle size, and in turn increase surface area, allowing an increase in the rate of diffusion across the interface. Many synthetic methods, such as hydrothermal,

solvothermal, precursor, and flux techniques have been developed to overcome the slow diffusion processes and more intimately mix the starting materials.[3]

Once a new solid-state material is made, it is an essential part of any investigation to fully characterize the material to determine its chemical, as well as physical properties. If it is crystalline, the investigation usually begins with the structure characterization *via* single crystal and/or powder X-ray diffraction, as these techniques provide a precise method for determining the positions of atoms. It is known that structure dictates function, and from structure alone many interesting characteristics can be determined about a new material. The structural features of a new material can aid the chemist in determining the proper path for future characterization as solids are known to exhibit a wide range of physical properties, such as magnetic, optical, or electrical properties.

Chapter 2 is focused on the synthetic methods used in the formation of the new solids presented in the following chapters and the techniques used in their characterization.

Reaction Procedures

Because most extended solids cannot be purified once they are made, it is important for the reactants used to be stoichiometric and pure. A common source of non-stoichiometry as well as impurities (contamination) is the moisture and oxygen in air, which may cause irreversible damage to the starting materials, causing uncontrollable reaction conditions. For this reason, most of the reactants used in the reactions described in the following chapters were all stored and ground in a nitrogen-purged drybox manufactured by MBraun Incorporated. To minimize the exposure of the drybox and its

contents to the atmosphere, additional materials required in the synthesis such as mortars, pestles, and funnels, were dried and pumped in through an antechamber. Depending on the size of the items being brought into the drybox, they were either pumped in through a small or large antechamber. If pumped in through the small antechamber, the procedures require evacuation for 15 minutes, backfilling with N_2, followed by evacuation for an additional 15 minutes. The chamber was then backfilled again with N_2 and the materials were pulled into the drybox. In instances where the large antechamber was used, evacuation was performed in 30 minute intervals. When transferring paper or aluminum foil into the box, the materials were first dried in an oven, placed in one of the antechambers, and then evacuated overnight. All reactants were weighed using an OHAUS analytical microbalance and then ground together using an agate mortar and pestle. The well-mixed reactants were placed in a fused silica ampoule, approximately 6 inches in length. It should be noted that in some cases the reactive molten-salt can chew up the silica ampoules, causing silicon incorporation into the products or causing the tubes to explode. In order to avoid this, carbon-coating was employed. The carbon coats serve as barriers between the salt and glass. To create the carbon coat, 3-4 mL of acetone were poured into the ampoules. Then the acetone was poured out and the bottom 2 inches of the ampoule were run back and forth through an open flame to create a dark black coat. Once the ampoule cooled, the carbon coat was checked for thin areas. In instances where thin coats were observed, the procedures would be repeated again until the tube had a uniform coat with no exposed glass.

Once loaded into the fused silica ampoules, reactions were typically sealed under vacuum using a propane torch, wrapped in an insulation made of glass fibers, and placed upright inside of a high-temperature box furnace with a programmable controller. To avoid eruption of the fused silica ampoule and to facilitate crystal growth, slow heating and cooling were employed. The reactions were heated at a rate of 1°C/min to a target temperature, usually 150°C above the melting point of the eutectic flux, and then held there for various time periods ranging from 12 hours to 4 days. The heating programs used are specified in each chapter. Reactions were either furnace cooled directly to room temperature or slowly cooled to around 450°C at 0.1°C/min to enhance crystal growth, followed by furnace cooling to room temperature.

In a few instances, 100% yield reactions were heated in open air instead of being sealed under vacuum. This procedure was specifically utilized when precursors that have gaseous decomposition products, such as CO_2 in Cs_2CO_3, were used. Precursors have decomposition temperatures where gas is evolved, and as a result the reactions were heated in open silica ampoules and gaseous products were vented out of the top of the high-temperature box furnace into the hood. The precursor method offered two advantages in high-temperature synthesis. First, it offered an alternative to the traditional stoichiometric synthesis. For example, due to the unavailability of certain reactants such as Cs_2O or Rb_2O, their carbonate counterparts can be used instead. Once the materials decompose, the needed stoichiometric reaction is accomplished. Second, as the precursors decompose, they break into even smaller particles than can be achieved with physical grinding. The decomposition creates starting materials with smaller particle sizes / higher surface areas,

which aids the reaction kinetics. Unfortunately, however, most of these reactions lead to the formation of polycrystalline materials. This lack of crystal growth is likely due to the absence of the melt and fast cooling.

Typical reactions included various metal oxides, main group oxides such as P_4O_{10} or As_2O_5, and alkali/alkaline-earth metal oxides. Most of these starting materials, as shown in Table 2.1, are intrinsically refractory and high melting. Unless extremely high temperatures are utilized, the diffusion process across grain boundaries is very slow, severely hindering the reaction rate. In order to alleviate this problem and promote crystal growth, alkali/alkaline-earth metal halides and eutectic combinations of these salts were employed. In the molten state, the salts are highly corrosive to the metal oxide reactants and act as high temperature "solvents". They have relatively lower melting points than most of the oxide reactants, and their melts are utilized to increase diffusion and thus promote quicker chemical reactions within the desired systems. Eutectic fluxes help to decrease reaction temperatures as low as 600°C and greatly enhance crystal growth. They also allow easy retrieval of the reaction products, as the salts can be washed away with deionized water. Once the reaction products were washed, acetone was used to dry them, and removal of the water and acetone was performed via vacuum filtration. It should be noted that only half of each reaction was washed with water to prevent the dissolution/decomposition of any water-soluble/sensitive materials present in the reaction products.

On several occasions, the salt not only served as a reaction medium, but a reactant as well. Selected combinations of salt can serve to facilitate new structure formation. As

illustrated in the following chapters, there were multiple extended solids formed whose structures were dictated by the presence of salt. Three major structure types were observed during this work. The first type consists of extended solids containing nanostructured metal oxide lattices insulated by surrounding salt. In this structure type, the salt's main function is to terminate the infinite propagation of the covalent lattices forming low-dimensional metal oxide lattices. The second structure type is the open framework structure where the covalent lattices form around the salt. Upon washing the material with water, the neutral salt is removed and a porous material remains. The third type is the layered structure where covalent slabs, which extend infinitely in two directions, are sandwiched on top and bottom by a salt-like lattice.

Last, the salt can also be utilized *in situ* as a source of unavailable alkali oxides. For example, Cs_2O and Rb_2O are commercially unavailable, and the evolution of gases from their carbonate and nitrate precursors, when utilized in a sealed system, can often cause the silica ampoule to blow. Instead, metathesis reactions can be utilized to generate the unavailable oxide. An example of this is shown in the following reaction:

$$2n\ ACl + 2\ MO_{n/2} \rightarrow n\ A_2O + 2\ MCl_n,$$

where A represents monovalent alkali metal cations (such as Cs or Rb) and M can be either a transition metal or small alkaline-earth metal cation.

Starting Materials

The emphasis of this project was in the synthesis of new transition metal phosphates, arsenates, and vanadates *via* high-temperature solid-state methods. Table 2.1

lists the sources, molecular weight, purity, and melting points for the starting materials used in the synthesis of the compounds discussed in this dissertation.

Table 2.1: Starting materials used in high-temperature solid state reactions

Compounds	Chemical Formula	Source, purity	g/mol	Melting points (˚C)
Ammonium Arsenate, monobasic	$(NH_4)H_2AsO_4$	Alfa Aesar, 99.9%	158.97	300 dec.
Ammonium Phosphate, monobasic	$(NH_4)H_2PO_4$	Aldrich, 99.9%	115.03	190
Arsenic Pentoxide	As_2O_5	Aldrich, 98%	229.84	315
Barium Chloride	$BaCl_2$	Aldrich, 99.9%	208.25	963
Barium Nitrate	$Ba(NO_3)_2$	Aldrick 99%	261.34	592
Barium Oxide	BaO	Aldrich, 97%	153.34	1920
Cesium Carbonate	Cs_2CO_3	Alfa Aesar, 99.9%	325.82	610
Cesium Chloride	CsCl	Alfa Aesar, 99.99%	168.36	646
Cesium Nitrate	$CsNO_3$	Alfa Aesar, 99%	194.91	414
Cesium Metavanadate	$CsVO_3$	Alfa Aesar 99.9%	231.84	-------
Cesium Orthovanadate	Cs_3VO_4	Alfa Aesar 99.9%	513.65	-------
Cobalt (II) Oxide	CoO	Alfa Aesar, 95%	74.93	1935
Copper (II) Oxide	CuO	Alfa Aesar 99.7%	79.55	1326
Iron (II) Oxide	FeO	Aldrich, 99.99%	71.85	1420
Iron (III) Oxide	Fe_2O_3	Alfa Aesar, 99.945%	159.69	1565
Manganese (II) Oxide	MnO	Alfa Aesar, 99.5%	70.94	------
Manganese (III) Oxide	Mn_2O_3	Aldrich, 99%	157.86	1080 dec.
Manganese (IV) Oxide	MnO_2	Alfa Aesar, 99.9%	86.94	535 dec.
Phosphorus Pentoxide	P_2O_5	Aldrich, 98%	141.94	580
Nickel (II) Oxide	NiO	Alfa Aesar 99%	74.71	1984
Potassium Chloride	KCl	Alfa Aesar, 99.9%	74.55	776
Potassium Superoxide	KO_2	Alfa Aesar, 96.5%	71.1	380
Rubidium Chloride	RbCl	Alfa Aesar, 99.8%	120.92	718
Sodium Oxide	Na_2O	Alfa Aesar, 85%	61.98	1275
Sodium Peroxide	Na_2O_2	Aldrich, 97%	77.98	460
Sodium Carbonate	Na_2CO_3	Alfa Aesar, 99.95%	105.99	851
Sodium Chloride	NaCl	Alfa Aesar, 99.9%	58.44	801
Sodium Nitrate	$NaNO_3$	GFS Chemicals, 99.9%	84.99	308
Strontium Nitrate	$Sr(NO_3)_2$	Aldrich, 98%	211.64	570
Vanadium (II) Oxide	VO	Alfa Aesar, 99%	66.94	950
Vanadium (III) Oxide	V_2O_3	Alfa Aesar, 99.7%	149.88	1970
Vanadium (IV) Oxide	VO_2	Alfa Aesar, 99%	82.94	1967
Vanadium (V) Oxide	V_2O_5	Alfa Aesar, 99.6%	181.88	690
Zinc (II) Oxide	ZnO	Alfa Aesar 99.9%	81.37	1975

dec: decomposition

Characterization Techniques

The complete characterization of a new compound is an integral part of exploratory synthesis in materials science research. The materials discussed in the following chapters were subject to various types of characterization including single crystal and powder X-ray diffraction, thermal analysis, surface area analysis, ac/dc magnetic susceptibility, UV/Vis spectroscopy, and elemental analysis, all of which were performed in house. Other characterization methods were performed through collaboration, including heat capacity measurements with Dr. Jian He and Dr. Malcome Skove of the Clemson Physics Department, and hydrogen adsorption studies, with Dr. Craig Brown of NIST, transmission electron microscopy, performed by Dr. JoAn Hudson of the Clemson University Electron Microscopy Lab, and ac susceptibility with Dr. Jim O'Brien of Quantum Design. The following paragraphs include methods of characterization and instrumentation details used for compound characterization presented in this dissertation.

Single crystal X-ray diffraction (SXRD): Crystalline materials are homogenous solids with an ordered internal arrangement of atoms. SXRD is the most important technique used to probe the internal structure of crystals, as it precisely reveals the positions of atoms within solid crystalline materials. The properties of extended solids are determined by how the atoms pack in three dimensions. As a result, the structure determination of the materials presented within this study was an important step in determining the utility of a new material and the future steps required for its characterization. For an experienced solid-state chemist, the structure of a new material

can sometimes give an indication about what chemical modifications need to be made before any further characterization is done.

SXRD is a multi-step process including sample preparation, data collection, and structure refinement. Single crystals were selected under an optical microscope equipped with a polarized light attachment and mounted on quartz fibers with epoxy. The glass fibers were then embedded in modeling clay and mounted inside of a tension pin. Typically high quality single crystals were identified as having well-defined faces and homogenous color with ideal sizes ranging from 0.1-0.3 mm across. For data collection, the crystals were centered on a four-circle AFC8 diffractometer equipped with a Mercury CCD area detector. Data were typically collected at room temperature (~300K unless otherwise specified) using Mo Kα radiation (λ = 0.71073Å) produced by a graphite monochromator. Unless the first four frames revealed a reduced unit cell with dimensions larger than 30Å, the crystal-to-detector distance was approximately 27.6 mm. In instances where large unit cell dimensions were revealed, the detector was moved back to either 32.6 or 37.6 mm. The structures were solved by direct methods using the *SHELXTL 6.1*[4] program and refined on F^2 by least-squares, full-matrix techniques. The unit cell dimensions and orientation matrices were determined from a set of four frames with ω ranging from 0º-90º with intervals of 30°. The exposure time of each frame was dependent on the diffraction intensity of the single crystal. For most data collections, 480 frames were obtained typically over 3-6 hours. In data sets lacking intensity at angles close to 50º, longer scan times were used. An empirical multi-scan absorption correction was applied using a multi-scan technique, the *REQABS*[5] routine in the *CrystalClear*[6]

software package. The *CrystalClear* software also corrects for Lorentz-polarization effects. The data was then integrated, merged and averaged to create a data file (intensity and *hkl*) for structure solution determination. Structure refinement using the software package *SHEXTL* involves the determination of a trial structure, refinement of that structure using a Fourier difference map to identify new atoms, and repeating this process until a feasible structure is in good agreement with the data. All atoms except hydrogen were refined anisotropically if possible. Once a crystal structure was solved, *PLATON*[7], a crystallography software, was utilized to check the crystal structures for higher symmetry. In instances where higher symmetry was found, the software allowed for the conversion from one space group to the other and then the data was refined again using the *SHEXTL* software package. Once a crystal structure was solved, a cif, crystallographic information file, was created and *checkCIF* (a service set up by the International Union of Crystallography that checks cif files for potential errors) was performed. When errors were found, efforts were made to correct them. On some occasions *checkCIF* reported, as a warning message, frameworks with large internal voids. In these cases, *PLATON* was used to obtain the atomic coordinates of the solvent free space and calculate the electron count per void to prove that it was in fact free of solvent. Small electron counts for large volumes of space indicate solvent-free voids. All of the structure pictures seen throughout the following chapters were generated using the *Diamond 2.1*[8] program.

SXRD was also utilized to orient single crystals for orientation-related property studies such as field-dependent magnetization or heat capacity. The single crystals were

mounted on the glass fiber along one crystal axis. After the first four frames of data were obtained, the unit cell dimensions were determined. The diffractometer was then utilized to take axial photos along the crystallographic axis of interest. The direction of interest could be determined, as it was oriented perpendicular to the x-ray beam. The identification of the axis could be further confirmed by measuring the distances between parallel rows of diffraction spots on the computer screen. These spots represented parallel planes of atoms within the structure.

Powder X-ray diffraction (PXRD): PXRD is a finger-printing technique used in the structure characterization of newly synthesized solid-state materials. In fact, when single crystals are not available, it is almost the only method for the identification of reaction products and is considered to be the most powerful method for the determination of phase purity (within ca. 5% of error) for stoichiometric reactions. PXRD patterns in this work were obtained using a SCINTAG XDS 2000 θ/θ powder diffractometer (SCINTAG Inc., Sunnyvale, CA) employing Cu Kα radiation (λ = 1.5406Å), a graphite monochromator, and a liquid-nitrogen-cooled germanium detector. The diffractometer was operated by the DMSNT[9] software package running on a PC. Reaction products were ground in an agate mortar and placed on a zero-background sample holder. Each sample's diffraction pattern was collected using step-wise 2θ scans with step sizes ranging from 0.02 - 0.03° at room temperature in the typical range $5° < 2\theta < 65°$ with various scan rates. The experimental powder patterns were compared to calculated powder patterns generated via the programs *PCW23* and *Mercury 1.4.2*[10]. To generate calculated powder patterns, these two programs utilize crystallographic information files

(cif), some of which, if previously published, were obtained from the data stored in the ICSD (Inorganic Crystal Structure Database, NIST). On occasion, profile refinements of selected powder patterns were also obtained using the *GSAS/EXPGUI*[11] and *Full-Prof*[12] programs.

Variable temperature PXRD was also used to investigate possible structural transitions in newly synthesized materials. The multi-sample holder was replaced with a variable temperature (VT) chamber. A standard quartz sample was utilized to adjust the height of the VT attachment to eliminate shifts in the powder patterns. The sample was then placed in the pan and a cap containing a Germanium window, transparent to incoming X-rays, was placed on top of the chamber. The vacuum pump was turned on, sealing the sample from the atmosphere, and liquid N_2 was allowed to flow through the sample chamber. Inside the VT chamber, a heater and thermocouple were utilized to control the sample temperature. Once the sample reached the target temperature, a powder x-ray pattern was obtained using the same parameters as listed above. See Chapter 3 for specific experimental conditions.

Bond Valence Sum Analysis: Transition metals provide rich structural chemistry due to various achievable oxidation states and coordination environments. Often, oxidation states of metals are hard to determine, especially when examining structures with partial occupancies or mixed sites. Bond valence sum, BVS, calculations can be utilized to help further support the oxidation states of metal cations determined from the single crystal structure solutions. The following equation is used to describe the relationship between the bond valence, s, and the bond distance, r:

$$s=exp[(r_o-r)/B]$$

The bond distances, r, used were obtained from crystallographic information files. B is empirically determined to be 0.37 and this parameter is found to vary little from one atom pair to another. The last parameter, r_0, is the reference bond length and is specific to certain atom pairs and valence states. The bond valence was determined for each atom pair and then those values were added together to give the total oxidation state of the metal cations. In this study, the *Valence*[13a] program was utilized to perform BVS calculations. The bond-valence parameters, other than r_0, used in the program were based on the "Accumulated Table of Bond Valence Parameters" (latest updated version on May 2, 2006) in the file bvparm.cif provided by Prof. I. D. Brown.[13b]

Magnetic susceptibility: Magnetic susceptibility measurements were performed on single crystals and powder samples with sizes ranging from 1.5 – 25 mg using a Quantum Design MPMS-5S SQUID (Superconducting Quantum Interference Device) magnetometer. For the temperature-dependent studies, the measurements were performed over a 2-300 K temperature range in various applied DC-magnetic fields ranging from 100 – 5000 Oe. The samples were placed inside of a gelcap that was suspended inside of a drinking straw. The straw was attached to the end of the sample rod using Kapton tape. The magnetic susceptibility of the container was previously determined and its data was corrected for the diamagnetic effect of the drinking straw and gelatin capsule. The acquired magnetic data were also corrected for core diamagnetism resulting from core electrons.[14] When applicable, the inverse molar magnetic susceptibility, χ^{-1}, data were fit using the Curie-Weiss law. From the fit, the Weiss

constant, θ, and the effective magnetic moment, μ, were obtained. From these variables, important information such as the nature of the magnetic coupling between nearest neighbors and the spin state of the metals present in the sample can be deduced.

Zero-field-cooling / field-cooling (ZFC/FC) experiments were performed on spin-ordered phases and provided evidence of magnetic irreversibility in instances where a divergence was observed in the two collected data sets. The difference in these two measurements is the absence or presence of an applied magnetic field upon cooling the sample. For ZFC measurements, the samples were cooled from 300 - 2K in the absence of an applied field, and then data were collected from 2 - 300K in the presence of an applied dc field. For FC measurements, the samples were cooled from 300K-2K in the presence of an applied dc field, followed by a data collection from 2-300K also in the presence of a magnetic field. It should be noted that the field strength and number of collected data points were dependent on the system of interest and that cooling and heating rates were kept constant throughout all experiments. At temperatures below 30K samples were heated and cooled at rates of 2 or 5K/minute, while above 30K, samples were cooled and heated at 10K/minute. The point of magnetic irreversibility, T_{irr}, occurs where ZFC and FC curves diverge, often referred to as thermomagnetic irreversibility (TMI). TMI has been observed in magnetically unordered systems such as spin glass type materials[15] and in magnetically-ordered systems[16]. In magnetically-ordered phases, large TMI has been attributed to two major processes including pinning of domain walls and hindrance to domain rotation in superparamagnetic type particles having large magnetic anisotropy.[17] Domain walls move easily while cooling in the presence of an

applied field. This process increases the size of the domains with magnetic moments parallel to the field and the total magnetization of the sample. When a sample is cooled in the absence of an applied field, the random orientation of the magnetic domains can become frozen. When a magnetic field is applied at low temperatures, the energy may not be adequate to depin the domain wall, so that $M_{ZFC} < M_{FC}$. Increasing the magnitude of the applied field favors movement of the domain walls, making the difference between M_{ZFC} and M_{FC} smaller, and shifting T_{irr} to lower temperatures.

In materials showing ferri or ferromagnetic ordering determined by a sudden decrease in the inverse magnetic susceptibility, χ^{-1}, field-dependent studies were carried out at various temperatures below the onset of the magnetic ordering. Field sweeps were performed in the range of -5 to 5T. From these measurements, hysteresis curves were obtained and data such as the coercive field and the remnant magnetization were extracted from the curve. On some occasions, calculations were performed to convert from emu to μ_B, allowing the determination of the number of unpaired electron per formula unit.

Heat Capacity: Heat capacity is a useful measurement for many new chemical systems. This property can supply important information about a lattice including structural and electronic transitions and magnetic properties. Heat capacity is defined as the amount of heat required to change the temperature of a substance by one degree. Heat capacity was measured on a Quantum Design Physical Property Measurement System (PPMS) using a heat capacity puck. The PPMS has precise control of various parameters including the temperature (1.8 – 400 K), magnetic field (0-9 Tesla), and high

vacuum (near 0.01 μbar). The heat capacity puck has a small micro-calorimeter platform that the samples are mounted on. The sample, typically in sub-mm dimensions and 5-20 mg in mass, is mounted on the platform using a small amount of cryogenic Apiezon N grease. Good thermal contact between the sample and the platform needs to be maintained. The sample platform is suspended by eight thin wires that serve as the electrical leads for an embedded heater and thermometer. The wires also provide a well-defined thermal connection between the sample platform and the puck body. An additional thermometer embedded in the puck provides an accurate determination of the puck temperature. A thermal shield aids in maintaining stable sample temperature and uniformity.

The PPMS uses a comparison method to determine the heat capacity of the sample. First, the puck is run with the Apiezon N grease without the sample and the baseline data, called the addendum, is obtained. The sample is then mounted onto the puck and the measurement is run again. The heat capacity is measured using a relaxation technique. The Cernox heater on the sample platform increases the temperature and the thermometer measures the temperature of the sample as it cools. The addendum is subtracted from the raw heat capacity data allowing the determination of the sample's heat capacity. In instances where orientation-dependent heat capacity measurements were required, a special sample holder was used to maintain sample orientation with respect to the direction of the magnetic field. In these cases the fixture was included as part of the addendum.

Surface Area Analysis: Surface area and porosity are two important physical properties that determine the quality and utility of many materials. Differences in these properties of various particles within a material, which otherwise may have the same physical dimensions, can greatly influence their performance characteristics. A Micromeritics' Accelerated Surface Area and Porosimetry analyzer, ASAP 2020, was utilized to determine the surface area and porosity of several materials presented here. This instrument can provide single and multipoint BET (Brunauer, Emmett, and Teller) surface area, pore volume, and pore area distributions in the mesopore and macropore ranges through the BJH (Barrett, Joyner, and Halenda) method[18], micropore distribution by the MP method[19], and total micropore volume by the t-Plot and s-Plot methods[20]. The most important features of this instrument include two independent vacuum systems that allow degassing and analysis processes to occur simultaneously, an oil-free "dry" vacuum option to prevent oil contamination, a two-station intelligent degas system for fully automated degassing with controlled heating profiles, a long-duration cryogen system for unattended analyses, and twelve gas inlets that are automatically selectable to allow for automated selection of pretreatment, backfill, and analysis gases. There are multiple adsorptives available on this instrument including N_2, CO, CO_2, H_2, and He. In this work, physisorption experiments using a common adsorptive, N_2, were performed to determine the multipoint BET surface area of some of the materials presented. First, the material of interest was placed in a sample holder and weighed. It was then put on the degas station, heated to a target temperature (60-160°C) at a rate of 10°C/minute, degassed to a pressure of 10mmHg, and held at the target temperature for 2 additional

hours. Once cooled to room temperature, the materials were reweighed, and then transferred to the analysis station where the surface area, pore size, and pore volume were determined.

H_2 Adsorption: H_2 adsorption was performed *via* collaboration with Craig Brown of NIST on a fully computer-controlled Sieverts apparatus developed on the basis of the volumetric method. A schematic diagram is shown in Figure 2.1.[21] The instrument operates in a sample temperature range of 4 to 1500 K and a pressure range of 0 to 100 bar. In the volumetric method, gas is transferred from a dosing cell with known volume to the sample cell while the gas pressure and temperature are controlled and recorded. The instrument is equipped with four pressure gauges, all with different pressure ranges (100, 500, and 3000 psi), to allow a precise measurement of the pressure. For isotherm measurements below room temperature, the sample temperature is controlled using a closed cycle refrigerator (CCR). The cold volumes for the empty cell were determined using He gas as a function of pressure at every temperature used for the real sample measurements and were used to calculate the sample adsorption. Further details about the experiment and the calculations used in the experiment can be obtained in reference 17.

For each experiment, the sample space was evacuated and then a vacuum leak check was performed, followed by a high pressure He leak check. During the high-pressure leak, if no decrease in pressure is observed over an hour interval, the test is passed. Then at room temperature a helium adsorption experiment is performed to determine cell + sample volume. The sample was then cooled to 77 K where H_2 was

loaded into the sample cell. The sample was then heated to 150 K, held under vacuum for 1hr, cooled to 87K, and the steps were repeated. For each data point on the isotherm, the equilibrium in temperature and pressure was typically 150 or 300 seconds.

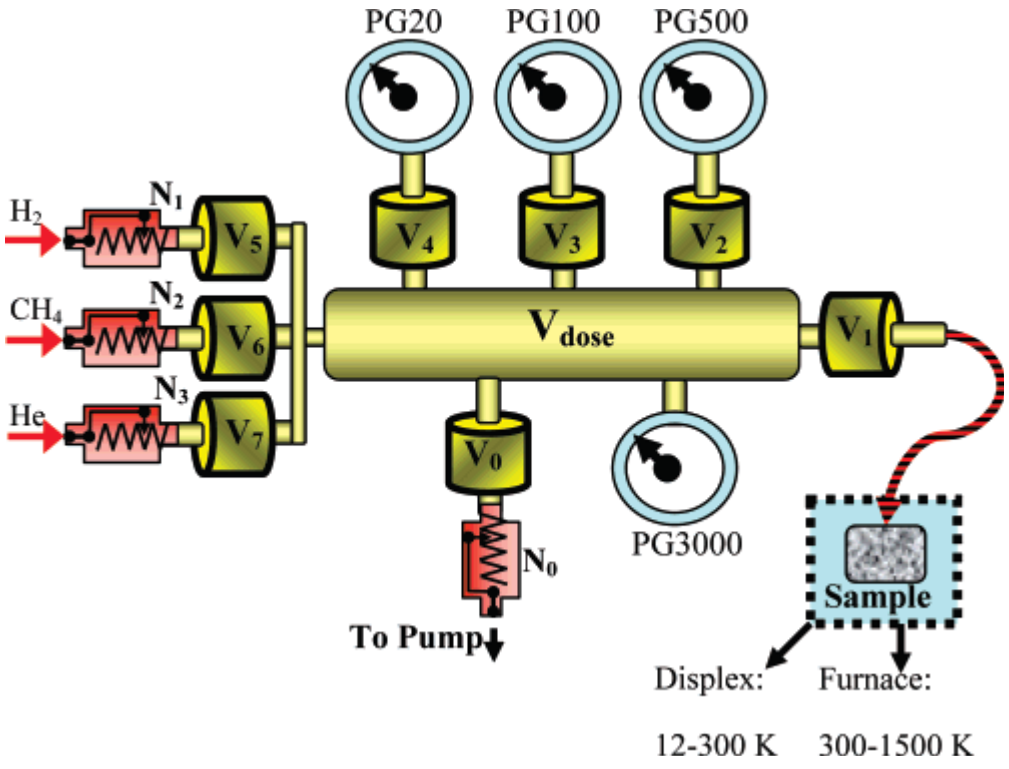

Figure 2.1: Schematic view of the fully computer-controlled Sieverts apparatus used in the hydrogen adsorption study.

Thermogravimetric Analysis: Thermograviametric analysis (TGA) is an analytical technique often used to determine a material's thermal stability and the percentage of volatile components by measuring a sample's weight change as it is heated. This technique was used in this study to determine the weight change due to chemical decomposition over various temperature ranges and weight loss due to the evaporation of water. TGA measurements were performed on a DuPont 951 Analyzer. The instrument came equipped with a horizontal microbalance, tube furnace, and thermocouple which was positioned directly under the sample pan. Samples were in powder form weighing from 10-30 mg. Each sample was placed in a tared platinum pan, placed inside of the tube furnace, and heated at a rate of 5°C/min under a nitrogen atmosphere. The weight change was then measured as a function of applied temperature with an upper limit of 1100°C.

Differential Scanning Calorimetry: The differential scanning calorimetry (DSC) technique monitors the energy required to maintain a zero temperature difference between a sample and an inert reference material. Essentially, it measures the enthalpy change between the sample and reference. This technique is especially useful to help monitor phase changes that are not accompanied by a change in weight such as melting, crystallization, or structural transitions. The DSC records the temperature difference between the sample and reference which is then plotted as a function of time or temperature. Any changes in the sample that result in the absorption or evolution of heat are detected, allowing one to determine whether the changes a material undergoes are endothermic or exothermic in nature. The measurements were performed using a DSC

820 from Mettler Toledo. The DSC 820 is based on the heat flux principles which means the sample and reference, enclosed inside a single furnace, are connected by a low-resistance heat path (a metal disc). Enthalpy changes in the sample cause a difference in its temperature relative to the reference. In this study, DTA was utilized to look for possible structural transitions. The measurements were performed on ground polycrystalline or single crystal samples. The samples, ranging from 10-15 mg, were weighed and then loaded into an aluminum sample pan that was sealed by applying force to the top of the pan lid with a press. The sample and reference pans were then placed inside of the furnace and then heated and cooled at various rates to a target temperature under a N_2 atmosphere.

Electron Microscopy (SEM and EDX): Scanning electron microscopy (SEM) is a technique that was used throughout this project to study the texture, topography, and surface features of newly synthesized solid materials. Semi-quantitative elemental analysis was performed on all newly synthesized materials via Energy Dispersive X-ray Spectroscopy (EDX). Elemental analysis provided further verification of the chemical compositions of newly synthesized materials. Both SEM and EDX were performed using a Hitachi S-3400 scanning electron microscope equipped with an OXFORD EDX microprobe. Single crystals or powder samples were selected using an optical microscope and placed on a piece of carbon tape applied directly to the carbon specimen disk. The tape helped to maintain the positions of the samples throughout the analysis and also acted as a conductor, allowing the dissipation of charged electrons. A piece of copper tape, used to calibrate the instrument, was also placed on the carbon disk just

above the carbon tape. After sample preparation, the sample holder was positioned inside of the sample chamber and then placed under vacuum. The scans were carried out using a 20 kV working voltage and 15 mm working distance.

High Resolution Transmission Electron Microscopy (HRTEM): High Resolution Transmission Electron Microscopy was carried out through collaboration with Dr. JoAn Hudson of the Clemson University Microscopy Lab. HRTEM is a technique used to obtain high resolution images (on the atomic scale) of thin specimens. HRTEM was performed using a Hitachi H-9500. The instrument operates under a 300kV accelerating voltage and high vacuum (10^{-7}torr or higher) and can reach magnifications of up to 1,500,000x. This technique was used to see the lattices in various crystalline samples in order to help determine the identity of various species in solution. The samples were either dissolved or suspended in deionized water and then added drop wise to a copper grid with a film support. The grid was allowed to dry and the process was repeated two additional times. Once the grid was dry, it was inserted into the instrument and placed under vacuum.

UV/Vis Diffuse Reflectance Measurements: In this study, UV-Vis spectroscopy, a useful tool for studying the absorption spectra of transition metal frameworks, was utilized to identify ligand to metal charge transfer (*LMCT*) bands and *d-d* transitions. In this region of the electromagnetic spectrum, materials undergo electronic transitions. This technique can allow a quantitative determination of bandgap size in semiconducting and insulating type materials. The UV-Vis spectra were recorded on a variable bandpass Shimadzu 3101PC UV/VIS/NIR spectrophotometer with a maximum

resolution of 0.1nm. The instrument comes equipped with two detectors. The first is a photomultiplier tube which detects photons with wavelengths ranging from 190-830 nm. The second is a PbS detector used to detect photons with wavelengths ranging from 830-2500 nm in length. The instrument also comes equipped with two light sources including a deuterium lamp that emits light within the 200-360 nm range and a tungsten halogen lamp that emits light within the 360-2500 nm range. The system has a six grating design used to separate light from the source into its component parts. For solid samples, an integrating sphere attachment is provided. First, a blank sample, $BaSO_4$, was used to collect the background. Then, ground polycrystalline or single crystal samples were smeared onto the surface of the $BaSO_4$ sample holder and secured inside the integrating sphere attachment. The spectra were acquired in the range of 0.5-6.5 eV (190-2400 nm) using the diffuse reflectance measurement. The absorption data (α/S) were converted to reflectance using the Kubelka-Munk function $\alpha/S = (1-R)_2/2R$, where R is the reflectance at a given energy, α is the absorption coefficient, and S is the scattering coefficient.[22]

Literature Cited

1. (a) Bednorz, J.G., Müller, K.A., *Z. Phys.* B, **1986**, *64*, 189-193.

   (b) Wu, M. K, Ashburn, J.R., Torng, C.J., Hor, P.H., Meng, R.L., Gao, L., Huang, Z.J., Wang, Y.Q., Chu, C.W. *Phys. Rev. Lett.* **1987**, *58*, 908-910.

   (c) Beno, M.A., Soderholm, L., Capone II, D.W., Hinks, D.G., Jorgensen, J.D., Grace, J.D., Shculler, I.K., Segre, C.U., Zhang, K., *Appl. Phys. Lett.* **1987**, *51*, 57-59.

2. Kenneth T., Harris, D.M., , Edwards, P.P. Turning Points in Solid-State, Materials and Surface Science: A Book in Celebration of the Life and Work of Sir John Meurig Thomas Royal Society of Chemistry: Great Britain, **2008**. Chapter 4.

3. Smart, L., Moore, E., *Solid State Chemistry: An Introduction;* CRC Press: New York, 1995, Chapter 3.

4. *SHELXTL:*

   (a) Sheldrick, G.M. In "Crystallographic Computing 3" (Sheldrick, G. M.; Kruger, C.; Goddard, R.; Eds), Oxford Univ. Press: London, **1985**, p 175-189.

   (b) Sheldrick, G. M. In "SHELXTL, Version 6.1 Structure Determination Software Programs" Bruker Analytical X-ray Systems Inc., Madison, WI, **2001**.

5. Jacobson, R. A.; *REQABS Empirical Absorption Correction*, v. 1.1-03101998; Molecular Structure Corporation: Research Forest, TX, **1996-1998**.

6. MSC; *CrystalClear*, Rigaku/MSC: The Woodlands, TX, USA, **1999**.

7. *PLATON:*

   (a) Spek, A. L. *Acta Cryst*. **1990**, *A46*, C34.

   (b) Spek, A. L. *A Multipurpose Crystallographic Tool* Utrecht University, Utrecht, The Northerlands, **2002**.

8. *Diamond*: v. 2.1, Brandeuburg, K. **1999**.

9. *DMSNT*: v. 1.37; Scintag, Inc. Sunnyvale CA 94086.

10. (a) *PCW*: v. 2.4, Kraus, W.; Nolze, G. **2000**, Federal Institute for Materials Research and Testing, Rudower Chaussee 5, 12489 Berlin, Germany.

(b) *MERCURY 1.4.2*: The Cambridge Crystallographic Data Centre, Cambridge, UK, **2004**.

11. B. H. Toby, EXPGUI, a graphical user interface for GSAS, *J. Appl. Cryst.* **2001**, *34*, 210-211.

12. *WinPLOTR/FullProf:*

(a) Roisnel, T., Rodríguez-Carvajal, J. *WinPLOTR*: a Windows tool for powder diffraction patterns analysis *Materials Science Forum, Proceedings of the Seventh European Powder Diffraction Conference* (EPDIC 7), **2000**, 118-123.

(b) Rodríguez-Carvajal, *J. Physica B*. **1993**, *192*, 55-69.

13. (a) *VALENCE* for DOS, Version 2.0, Brown, I. D. *J. Appl. Crystallogr.* **1996**, *29*, 479-480.

(b) Brown, I. D., Altermatt, D. *Acta Cryst.* **1985**, *B41*, 244-247.

14. C.J. O'Connor, *J. Prog. Inorg. Chem.* **1982**, *29*, 203-276.

15. Kaczorowski, D., Noel, H. J. Phys.: *Condens. Matter* **1993**, *5*, 9185-9195.

16. (a) Roy, S.B., Pradhan, A.K., Chaddah, P., *J. Phys.: Condens. Matter* **1994**, *6*, 5155-5160.

(b) Roy, S.B., Pradhan, A.K., Chaddah, P. *Phil. Mag.* **1995**, *71*, 97-104.

(c) Roy, S.B., Pradhan, A.K., Chaddah, P. *Physica B* **1996**, *223–224*, 198-200.

(d) Roy, S.B., Pradhan, A.K., Chaddah, P. *Phil. Mag.* **1997**, *75*, 303-310.

(e) Roy, S.B., Pradhan, A.K., Chaddah, P. *J. Alloys Compounds* **2001**, *326*, 112-116.

17. Gopalakrishnan, I.K., Bagkar, N., Ganguly, R., Kulshreshtha, S.K. *J. Cryst. Growth* **2005**, *280*, 436-441.

18. Barrett, E.P., Joyner, L.G., Halenda, P.P. *J. Am. Chem. Soc*. **1951**, *73*, 373-380

19. Mikhail, R. S. H.; Brunauer, S.; Bodor, E. E. *J. Colloid Interface Sci*. **1968**, *26*, 45-53.

20. Lippens, B. C.; De Boer, J. H. *J. Catal*. **1965**, *4*, 319-323.

21. Zhou, W., Wu, H., Hartman, M.R., Yildirim T., *J. Phys. Chem. C* **2007**, *111*, 16131-16137.

22. Kubelka, P. J. *Opt. Soc. Am.* **1948**, 38, 448-457.

CHAPTER THREE

SYNTHESIS AND CHARACTERIZATION OF A NEW FAMILY OF METAL (II) PHOSPHATES EXHIBITING A TRIANGULAR MAGNETIC LATTICE: $ANa_3M_7(PO_4)_6$ (A = Cs, Rb, K and M = Mn, Fe, Co)

Introduction

Ferro- and ferri-magnetic materials are classically defined as materials that can display a spontaneous magnetization in the absence of an external magnetic field. When the magnetic ions are brought within close proximity of one another, that is, in a certain dimension or geometry, these materials often exhibit an enhanced magnetization response to an applied magnetic field. Through field-dependent magnetization studies, important parameters including saturation and remnant magnetization and coercive field are identified, allowing ferro(i)magnetic materials to be classified as "hard" or "soft" magnets. "Hard" magnets, often referred to as permanent magnets, have common characteristics including a high saturation magnetization, coercive field, and remnant magnetization in their corresponding hysteresis loops. Ferro(i)magnetic solids exhibiting nearly rectangular hysteresis loops with a relatively small coercive field are considered suitable for magnetic recording and information-storage applications in computing.

In the 1930's, Fenkel and Dorfman made the first prediction of the existence of single domain magnetic particles.[1] Since this prediction, public demands for higher storage densities in computing devices have driven scientists to reduce the size of ferro(i)magnetic particles, currently used in information storage, below the critical size

(less than 100 nm) at which they form single magnetic domains. In this regime, they can exhibit paramagnetic behavior below the Curie temperature (T_C), a phenomenon known as superparamagnetism. The onset of superparamagnetism places a limit on the storage capacity that can be achieved in future hard drives. For next-generation devices for quantum computing[2] and information storage[3], ferro- and ferrimagnetic solids with confined magnetic lattices are sought because of the inherent quantum-mechanical effects associated with confined spins.

We have begun exploring different systems of extended solids containing electronically confined transition metal oxide magnetic nanostructures.[4] Phosphates, arsenates, and silicates, XO_4^{n-}, are utilized in conjunction with transition metal oxides, MO_x, to create new mixed-framework solids. In the past, this research was driven by the desire for new porous zeolite-like materials. However, the research described in this dissertation is primarily focused on the discovery of new magnetic insulators. What we have learned from our previous studies of mixed-framework solids is that the oxyanions serve as a closed-shell, nonmagnetic ligand to electronically confine the magnetic lattices, capable of creating extended solids containing low-dimensional magnetic nanostructures. This work has led to a large number of framework solids containing interesting structural features, such as the triangular magnetic lattices discussed below, that create unexpectedly rich magnetochemistry.

Most existing mixed framework systems have the metal (M) to oxyanion (XO_4^{n-}) ratio, $M/X < 1$. The work discussed in this chapter was focused on exploring metal-rich areas of the phase diagram in hopes of enriching the interaction between magnetic ions.

The emphasis of Chapter 3 is on a large family of new magnetic insulators recently synthesized using high-temperature, solid-state techniques. This compound family, $ANa_3M_7(PO_4)_6$, has nine compositions where A/M = K/Mn, **1**, Rb/Mn, **2**, Cs/Mn, **3**, K/Fe, **4**, Rb/Fe, **5**, Cs/Fe, **6**, K/Co, **7**, Rb/Co, **8**, and Cs/Co, **9**. All of these can be synthesized in the forms of both single crystal and powder. In the case where large size of crystals are available, magnetic property studies were carried out including orientation-dependent analysis. In general, these new metal-rich phases have a 3-D structure and reveal interesting magnetochemistry. These include ferrimagnetic transitions (T_c < 16K) for all of the Fe^{2+}- and Co^{2+}-containing derivatives and stepped magnetization in the earlier reported $RbNa_3Fe_7(PO_4)_6$ **5**,[5] as well as later discovered $KNa_3Fe_7(PO_4)_6$, **4**, and $CsNa_3Co_7(PO_4)_6$, **9**.

Magnetization steps resulting from quantum tunneling of the magnetization have been reported for molecular magnets[6,7] and a few condensed solids, including the "spin-ice" pyrochlores (for example, $Dy_2Ti_2O_7$ and $Ho_2Ti_2O_7$)[8], and $Ca_3Co_2O_6$.[9] These compounds feature a large-spin ground state and significant magnetoanisotropy, which are essential properties for quantum-device applications. Most of these features can be attributed to geometrically frustrated magnetic lattices[10] and to ions with uniaxial magnetic properties[11] respectively. Other step-like anomalies in the magnetization of extended solids have been attributed to avalanches[12a], spin rearrangements[12b], and domain-wall depinning.[12c] In the following sections, the synthesis, characterization, and possible origins for magnetization steps observed in some of the members of the new compound family, $ANa_3M_7(PO_4)_6$, where A = K, Rb, Cs; M = Mn, Fe, Co, will be

discussed. For a structural comparison, two other derivatives have been included, $Na_4M_7(AsO_4)_6$, where M = Ni and Co in the discussion.

Synthesis

Single Crystal Synthesis of $ANa_3M_7(PO_4)_6$ (Compounds 1-9): All nine new phases contain divalent transition metal cations, M(II), and these metal(II) phosphates were synthesized using high-temperature molten-salt methods. For the synthesis of **1** and **4-6**, MO and P_4O_{10} were mixed in various ratios, where $MO:P_4O_{10}$ = 7:1.5 (M = Mn, Fe). For **7-9**, unless the $CoO:P_4O_{10}$ ratio was adjusted to 5:0.5, no targeted compound will form. In the case of Cs/Co synthesis, the 7:1.5 ratio resulted in the formation of a different phase all together, $Cs_2Na_6Co_7O_2(PO_4)_6$.[13] Therefore, I employed the 5:0.5 ratio for the synthesis of all three Co derivatives, **7-9**. For the synthesis of **2**, $Mn_2O_3:Na_2O_2:P_4O_{10}$ were mixed in a 2:1:1 mol ratio while compound **3** was made using $Mn_2O_3:P_4O_{10}$ in a 1:4 mol ratio.[14] It should be noted that it is likely that the synthesis of **2** and **3** can be achieved using the MnO and P_4O_{10} 7:1.5 ratios, but it has not yet been attempted.

To facilitate crystal growth, all nine reactions were carried out in molten-salt media. The reactions were mixed with an ACl/NaCl eutectic flux equal to three times the mass of the oxide reactants. The reactants and salts were then ground together for 15 minutes in a nitrogen-purged drybox and placed in a carbon-coated quartz ampoule. They were then sealed under vacuum and heated, at a rate of 1°C/min, to 150°C above the melting point of the eutectic flux used, held for 4 days, and then slowly cooled, at a

rate of 0.1°C/min, to 450°C, followed by furnace-cooling. Single crystals of $ANa_3M_7(PO_4)_6$ were obtained in various yields (≈10-60%). It should be noted that for most of the above listed reactions, the only source of the A^+ and Na^+ cations was salt, and as a result, many water soluble chloride-rich by-products formed. An example is $CsCoCl_3$ found in the reaction targeting compound **9**. The new phases were retrieved by washing the reaction products with deionized water to remove the salt. Single crystals of $ANa_3Mn_7(PO_4)_6$[13] derivatives were yellow-orange or red in color, while the $ANa_3Fe_7(PO_4)_6$ derivatives were brown or yellowish-brown, and the $ANa_3Co_7(PO_4)_6$ derivatives appeared dark purple in color

100% Yield Synthesis of $RbNa_3Fe_7(PO_4)_6$: 100% yield synthesis of $RbNa_3Fe_7(PO_4)_6$, **5**, was attempted using stoichiometric combinations of a wide range of reactants. Multiple reactions were attempted varying many parameters including heating programs, starting materials, and atmosphere. The reaction giving the highest yield of this material consisted of FeO, Fe, P_4O_{10}, Rb_2CO_3, and Na_2O mixed in a 6.79:0.21:1.5:0.5:1.5 mol ratio (ca. 0.3g). The small amount of Fe was used to offset the 14% Na_2O_2 impurity in the Na_2O material because the reaction was carried out in a sealed ampoule under vacuum. The reactants were ground together for 15 minutes in a nitrogen-purged drybox, place in a silica ampoule, and sealed under vacuum. The reactions were heated to 800°C, held there for 2 days, and then furnace-cooled to room temperature. Rb_2CO_3 was used as a source of Rb_2O, as this oxide is not readily available. It is expected that the carbonate will decompose *in situ* to create a stoichiometric reaction. Due to the evolution of CO_2 gas during the decomposition of Rb_2CO_3, the silica

ampoules are prone to explosion. To avoid this, the total mass of reactants was reduced (0.4g) and larger ampoules were used in order to give the gas more room to expand without blowing the tube. Efforts were also made to synthesize Rb-containing precursors, and although the phase formation could be seen in almost all reactions, 100% yield was never successful. It should be noted that these reactions were not successful in open air conditions either. The powder pattern of the 100% yield attempt in a sealed tube is shown in Figure 3.1. There are several impurity peaks resulting from one or multiple unidentified phases. It is not yet known, but intermittent grinding may aid in the creation of a purer product. Since the aforementioned salt flux reactions led to the production of large single crystals suitable for characterization, efforts were not made to synthesize high yields of any compositions other than **5**. It should be noted that precursor reactions also were not successful.

Characterization

Elemental Analysis: Qualitative elemental analysis was performed on compounds **1-9**. Elemental analysis was performed on the single crystals used in the structure determination. The results showed the presence of the respective elements in the chemical formula.

Heat Capacity: Heat capacity was measured on a Quantum Design Physical Property Measurement System (PPMS Model). This measurement was performed on an

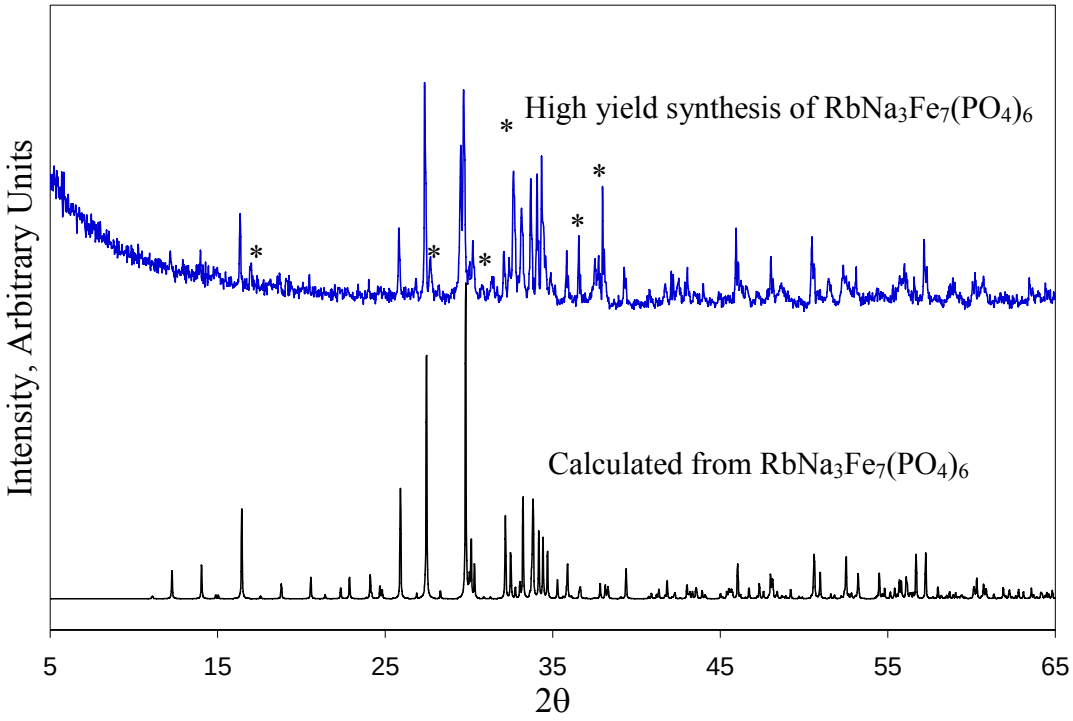

Figure 3.1: Calculated powder pattern of $RbNa_3Fe_7(PO_4)_6$ compared to the PXRD pattern obtained from the high-yield synthesis of the powder. The extra peaks, not observed in the calculated PXRD pattern, are marked with asterisks.

aligned single crystal (9.9 mg) in the absence of a field and then in applied fields of 1 and 3 Tesla. A special sample holder and Apiezon N grease were utilized to help maintain sample orientation with respect to the direction of the magnetic field. Heat capacity data was collected while the samples were heated from 2-30 K with magnetic fields applied along the *a* axis and perpendicular to the *a* axis.

Magnetic Properties: Magnetic susceptibility was measured with a Quantum Design SQUID (Superconducting Quantum Interference Device) MPMS-5S magnetometer. The ground powder samples of selected single crystals of **1-9** were employed for the initial temperature-dependent studies, as well as FC and ZFC experiments in applied fields of 100 and 5000 Oe and temperatures ranging from 2-300K. Sample sizes ranged from 2-10 mg. Field-dependent measurements were performed with magnetic field, H, ranging from -50000 Oe to 50000 Oe at various temperatures. Field-dependent measurements were performed on powders as well as an aligned single crystal of compounds **4-9**. AC susceptibility measurements were performed with zero applied dc field, a driving field of 3 Oe, and frequencies ranging from 0.2-1000Hz. These measurements were performed on an aligned single crystal (0.3mg) of $RbNa_3Fe_7(PO_4)_6$.

Powder X-ray Diffraction: PXRD was used to confirm the presence of each phase in the respective 100% yield reactions. The powder diffraction patterns for compound **5** is shown in Figure 3.1. The powder X-ray diffraction data were collected at room temperature using Cu Kα radiation in the 2θ range of 5–65°, a step size of 0.02, and a scan rate of 0.002°/s.

Single Crystal X-ray Diffraction: Data were collected on optically selected single crystals at room temperature (~300K) using Mo Kα radiation (λ = 0.71073Å) produced by a graphite monochromator. The crystal-to-detector distance was approximately 27.6 mm and exposure times ranged from 5 - 40 seconds. The crystallographic data for compounds **1-9** are summarized in Table 3.1 The atomic coordinates, thermal parameters, and selected bond distances and angles are listed in Tables 3.2-3.4. The secondary extinction parameter was refined for **1** and **5-9**, but remained unrefined for **2-4**. For these three compounds, the parameters were insignificant and were, therefore, removed from the refinement. SXRD was also utilized to perform orientation-dependent characterization, including magnetic susceptibility, field-dependent magnetic measurements, and heat capacity, on various single crystals ranging from 0.3 - 9.9 mg.

Table 3.1: Crystallographic data for compounds **1-9**

empirical formula, Compound	$KNa_3Mn_7(PO_4)_6$, **1**	$RbNa_3Mn_7(PO_4)_6$, **2**[a]	$CsNa_3Mn_7(PO_4)_6$, **3**	$KNa_3Fe_7(PO_4)_6$, **4**	$RbNa_3Fe_7(PO_4)_6$, **5**
Color/shape	dark red/ multifaceted	dark red/ multifaceted	dark red/ multifaceted	brown/ multifaceted	brown/multifaceted
crystal size (mm)	0.43 x 0.27 x 0.18	0.08 x 0.05 x 0.03	0.23 x 0.19 x 0.15	0.43 x 0.27 x 0.18	0.18x 0.12x 0.12
formula weight (amu)	1062.47	1108.83	1156.28	1068.84	1115.21
space group, *Z*	*C*2/*c* (no. 15), 4				
T, °C	25				
a, Å	13.153(3)	13.130(3)	13.168(3)	13.003(3)	12.981(3)
b, Å	10.887(2	10.877(2)	10.915(2)	10.762(2)	10.777(2)
c, Å	15.973(3)	15.978(3)	16.027(3)	15.708(3)	15.732(3)
β, degree	113.24(3)	113.02(3)	113.11(3)	113.64(3)	113.62(3)
V, Å^3	2101.6(7)	2100.1(7)	2118.8(7)	2013(2)	2016(3)
linear abs. coeff., mm^{-1}	4.906	7.015	6.364	5.774	7.958
F_{000}	2036	2108	2180	2064	2136
d_{calc}, g cm^{-3}	3.358	3.507	3.625	3.526	3.673
data/restraints/parameters	1863/0/191	1853 / 0 / 190	1871 / 0 / 190	1781/0/191	1761/0/191
secondary extinction	0.0022(2)	---	---	---	0.0053(3)
reflections collected / unique/R_{int}[b]	8860/1863/0.0326	8705 / 1853/0.0552	8622 / 1871/0.0687	8239 / 1781/0.0294	8376 / 1761/0.0265
final R1/wR2 [c] [$I > 2\ \sigma(I)$]	0.0400/0.1164	0.0497/ 0.1263	0.0566/0.1406	0.031/0.086	0.027/0.081
R1/wR2 (all data)	0.0426/ 0.1190	0.0646/ 0.1402	0.0773/0.1544	0.0333/ 0.0873	0.0276/ 0.0824
GOF	1.041	1.072	1.10	1.07	0.99
Largest difference peak/hole (e$^-$/Å^3)	2.336/2.649	1.968/-1.922	2.115/-2.012	1.519/-1.241	1.179/ -1.058

[a] The observed volume of **2** is larger than **1**. This is further discussed in the text. [b] $R_{int} = \Sigma \mid Fo^2 - Fo^2\ (mean) \mid / \Sigma[\ Fo^2]$; [c] **1** R1 = $\Sigma\ ||F_o| - |F_c|| / \Sigma|F_o|$; *w*R2 = $\{[\Sigma[w(F_o^2-F_c^2)^2] / [\Sigma w(F_o)^2)^2]\}^{(1/2)}$; w=1/[\s^2^(Fo^2^)+(0.0619P)^2^+10.7220P] where P=(Fo^2^+2Fc^2^)/3; **2** R1 = $\Sigma\ ||F_o| - |F_c|| / \Sigma|F_o|$; *w*R2 = $\{[\Sigma[w(F_o^2-F_c^2)^2] / [\Sigma w(F_o)^2)^2]\}^{(1/2)}$; w=1/[\s^2^(Fo^2^)+(0.0773P)^2^+23.7354P] where P=(Fo^2^+2Fc^2^)/3; **3** R1 = $\Sigma\ ||F_o| - |F_c|| / \Sigma|F_o|$; *w*R2 = $\{[\Sigma[w(F_o^2-F_c^2)^2] / [\Sigma w(F_o)^2)^2]\}^{(1/2)}$; w=1/[\s^2^(Fo^2^)+(0.0775P)^2^+17.7985P] where P=(Fo^2^+2Fc^2^)/3; **4** *R* 1= $\Sigma(||F_o| - |F_c||)/\Sigma|F_o|$; *wR* = $\{\Sigma w[(|F_o| - |F_c|)^2]/\Sigma w[(|F_o|)^2]\}^{(1/2)}$; *w^-1 = σ^2(F)*); **5** R1 = $\Sigma\ ||F_o| - |F_c|| / \Sigma|F_o|$; *w*R2 = $\{[\Sigma[w(F_o^2-F_c^2)^2] / [\Sigma w(F_o)^2)^2]\}^{(1/2)}$; w=1/[\s^2^(Fo^2^)+(0.0584P)^2^+9.3170P] where P=(Fo^2^+2Fc^2^)/3

Table 3.1: Crystallographic data for compounds **1-9** cont…

empirical formula	$CsNa_3Fe_7(PO_4)_6$, **6**	$KNa_3Co_7(PO_4)_6$, **7**	$RbNa_3Co_7(PO_4)_6$, **8**	$CsNa_3Co_7(PO_4)_6$, **9**
Color / shape	brown/ multifaceted	purple/ multifaceted	purple/ multifaceted	purple/ multifaceted
crystal size (mm)	0.32 x 0.20 x 0.18	0.21 x 0.15 x 0.12	0.33 x 0.24 x 0.14	0.40 x 0.18 x 0.16
formula weight (amu)	1162.65	1090.40	1136.77	1184.21
space group, *Z*	*C*2/*c* (no. 15), 4			
T, °C	25			
a, Å	13.0036(3)	12.8301(3)	12.8383(3)	12.8438(3)
b, Å	10.7900(2)	10.6979(2)	10.7214(2)	10.7637(2)
c, Å	15.8298(3)	15.5338(3)	15.5770(3)	15.6301(3)
β, degree	113.60(3)	113.50(3)	113.47(3)	113.54(3)
V, $Å^3$	2035.25(3)	1955.23(3)	1966.77(2)	1980.96(3)
μ (Mo Kα), mm^{-1}	7.271	6.691	8.899	8.206
F_{000}	2208	2092	2164	2236
d_{calc}, g cm^{-3}	3.794	3.704	3.839	3.970
data/restraints/parameters	1797/0/191	1999/0/191	1728/0/191	1749/0/191
secondary extinction	0.0021(2)	0.0011(1)	0.0011(1)	.00025(7)
reflections collected / unique/ R_{int} [b]	8464 / 1795/ 0.0492	9113 / 1999/ 0.0325	8162 / 1728/ 0.0354	8330 / 1749/ 0.0640
final R1/wR2 [c] [$I > 2\ \sigma(I)$]	0.037/0.108	0.028/0.079	0.028/0.079	0.045/0.0955
R1/wR2 (all data)	0.0378/0.1084	0.0337/ 0.0786	0.0311/ 0.0794	0.0600/ 0.1013
GOF	1.08	1.03	1.04	1.11
Largest difference peak / hole (e^- / $Å^3$)	1.749/ -2.101	1.269/ -1.045	1.293/-1.106	1.598/-1.078

[b] $R_{int} = \Sigma \mid Fo^2 - Fo^2\ (mean) \mid / \Sigma[Fo^2]$; [c] **6** R1 = $\Sigma \mid\mid F_o \mid - \mid F_c \mid\mid / \Sigma \mid F_o \mid$; *w*R2 = {[$\Sigma[w(F_o^2-F_c^2)^2] / [\Sigma w(F_o)^2)^2]$}^(1/2); w=1/[\s^2^(Fo^2^)+(0.0714P)^2^+19.3855P] where P=(Fo^2^+2Fc^2^)/3; ; **7** R1 = $\Sigma \mid\mid F_o \mid - \mid F_c \mid\mid / \Sigma \mid F_o \mid$; *w*R2 = {[$\Sigma[w(F_o^2-F_c^2)^2] / [\Sigma w(F_o)^2)^2]$}^(1/2); w=1/[\s^2^(Fo^2^)+(0.0519P)^2^+6.2683P] where P=(Fo^2^+2Fc^2^)/3; **8** R1 = $\Sigma \mid\mid F_o \mid - \mid F_c \mid\mid / \Sigma \mid F_o \mid$; *w*R2 = {[$\Sigma[w(F_o^2-F_c^2)^2] / [\Sigma w(F_o)^2)^2]$}^(1/2); w=1/[\s^2^(Fo^2^)+(0.0451P)^2^+26.1195P] where P=(Fo^2^+2Fc^2^)/3; **9** R1 = $\Sigma \mid\mid F_o \mid - \mid F_c \mid\mid / \Sigma \mid F_o \mid$; *w*R2 = {[$\Sigma[w(F_o^2-F_c^2)^2] / [\Sigma w(F_o)^2)^2]$}^(1/2); w=1/[\s^2^(Fo^2^)+(0.0584P)^2^+9.3170P] where P=(Fo^2^+2Fc^2^)/3;

Table 3.2: Atomic parameters for compounds **1-9**

Atom	Wycoff position	sof	x	y	z
			$KNa_3Mn_7(PO_4)_6$, **1**		
K	4*e*	1.0	0	-0.2628(3)	1/4
Na1	8*f*	1.0	0.0189(2)	0.2604(2)	0.0172(2)
Na2	4*d*	1.0	1/4	1/4	1/2
Mn1	4*e*	1.0	0	0.0822(1)	1/4
Mn2	8*f*	1.0	0.18276(6)	0.03946(7)	0.62531(5)
Mn3	4*e*	1.0	1/2	0.12124(9)	3/4
Mn4	8*f*	1.0	0.31077(6)	-0.00042(7)	0.85983(5)
Mn5	4*c*	1.0	1/4	-1/4	1/2
P1	8*f*	1.0	0.4123(1)	0.0001(1)	0.57947(8)
P2	8*f*	1.0	0.0934(1)	-0.0007(1)	0.42838(8)
P3	8*f*	1.0	0.2112(1)	-0.2292(1)	0.73027(9)
O1	8*f*	1.0	0.5339(3)	0.0140(3)	0.6488(2)
O2	8*f*	1.0	0.2455(3)	-0.0940(3)	0.7285(2)
O3	8*f*	1.0	0.1057(3)	0.1130(3)	0.4878(2)
O4	8*f*	1.0	0.3468(3)	0.0599(3)	0.6301(2)
O5	8*f*	1.0	0.3911(3)	0.0725(3)	0.4923(2)
O6	8*f*	1.0	-0.0269(3)	-0.0224(4)	0.3617(2)
O7	8*f*	1.0	0.3872(3)	-0.1360(3)	0.5601(3)
O8	8*f*	1.0	0.2115(3)	-0.2991(4)	0.6461(3)
O9	8*f*	1.0	0.0919(3)	-0.2319(3)	0.7268(3)
O10	8*f*	1.0	0.1538(3)	0.0211(4)	0.3648(2)
O11	8*f*	1.0	0.1393(3)	-0.1088(3)	0.4933(3)
O12	8*f*	1.0	0.2942(3)	-0.2846(4)	0.8174(3)
			$RbNa_3Mn_7(PO_4)_6$, **2**		
Rb	4*e*	1.0	0	-0.2581(1)	1/4
Na1	8*f*	1.0	0.0188(3)	0.2591(3)	0.0198(3)
Na2	4*d*	1.0	1/4	1/4	1/2
Mn1	4*e*	1.0	0	0.0838(2)	1/4
Mn2	8*f*	1.0	0.18351(9)	0.0384(1)	0.62554(7)
Mn3	4*e*	1.0	1/2	0.1205(1)	3/4
Mn4	8*f*	1.0	0.31053(9)	-0.0006(1)	0.86054(7)
Mn5	4*c*	1.0	1/4	-1/4	1/2
P1	8*f*	1.0	0.4115(2)	0.0015(2)	0.5782(1)
P2	8*f*	1.0	0.0936(1)	0.0004(2)	0.4290(1)
P3	8*f*	1.0	0.2116(2)	-0.2297(2)	0.7299(1)
O1	8*f*	1.0	0.5331(4)	0.0162(5)	0.6466(3)
O2	8*f*	1.0	0.2464(4)	-0.0940(5)	0.7293(3)
O3	8*f*	1.0	0.1095(4)	0.1139(5)	0.4886(3)
O4	8*f*	1.0	0.3464(4)	0.0584(5)	0.6307(3)
O5	8*f*	1.0	0.3884(5)	0.0760(5)	0.4924(4)
O6	8*f*	1.0	-0.0283(4)	-0.0173(5)	0.3644(4)
O7	8*f*	1.0	0.3874(4)	-0.1346(5)	0.5568(4)
O8	8*f*	1.0	0.2113(5)	-0.2977(5)	0.6442(4)
O9	8*f*	1.0	0.0928(4)	-0.2332(5)	0.7269(4)
O10	8*f*	1.0	0.1521(4)	0.0178(6)	0.3633(4)
O11	8*f*	1.0	0.1382(4)	-0.1095(5)	0.4933(4)
O12	8*f*	1.0	0.2946(5)	-0.2860(6)	0.8161(4)

Table 3.2: Atomic parameters for compounds **1-9** cont…

Atom	Wycoff position	sof	x	y	z
			$CsNa_3Mn_7(PO_4)_6$, **3**		
Cs	4*e*	1.0	0	-0.25764(9)	1/4
Na1	8*f*	1.0	0.0187(4)	0.2577(4)	0.0208(4)
Na2	4*d*	1.0	1/4	1/4	1/2
Mn1	4*e*	1.0	0	0.0854(2)	1/4
Mn2	8*f*	1.0	0.1847(1)	0.0370(1)	0.62637(9)
Mn3	4*e*	1.0	1/2	0.1176(2)	3/4
Mn4	8*f*	1.0	0.3101(1)	-0.0007(1)	0.8619(1)
Mn5	4*c*	1.0	1/4	-1/4	1/2
P1	8*f*	1.0	0.4113(2)	0.0034(2)	0.5763(2)
P2	8*f*	1.0	0.0931(2)	0.0004(2)	0.4284(2)
P3	8*f*	1.0	0.2109(2)	-0.2307(2)	0.7313(2)
O1	8*f*	1.0	0.5332(6)	0.0165(6)	0.6438(5)
O2	8*f*	1.0	0.2469(6)	-0.0953(6)	0.7316(5)
O3	8*f*	1.0	0.1128(5)	0.1112(6)	0.4901(4)
O4	8*f*	1.0	0.3485(6)	0.0544(7)	0.6329(5)
O5	8*f*	1.0	0.3859(6)	0.0832(6)	0.4920(5)
O6	8*f*	1.0	-0.0281(6)	-0.0144(6)	0.3641(4)
O7	8*f*	1.0	0.3857(6)	-0.1308(6)	0.5522(5)
O8	8*f*	1.0	0.2110(6)	-0.2974(6)	0.6453(5)
O9	8*f*	1.0	0.0912(6)	-0.2340(6)	0.7273(5)
O10	8*f*	1.0	0.1503(6)	0.0167(7)	0.3614(4)
O11	8*f*	1.0	0.1354(6)	-0.1120(6)	0.4903(5)
O12	8*f*	1.0	0.2929(6)	-0.2873(7)	0.8176(5)
			$KNa_3Fe_7(PO_4)_6$, **4**		
K	4*e*	1.0	0	-0.2545(2)	1/4
Na1	8*f*	1.0	0.0191(2)	0.2619(2)	0.0186(2)
Na2	4*d*	1.0	1/4	1/4	1/2
Fe1	4*e*	1.0	0	0.08279(7)	1/4
Fe2	8*f*	1.0	0.18382(4)	0.04007(5)	0.62565(4)
Fe3	4*e*	1.0	1/2	0.11902(7)	3/4
Fe4	8*f*	1.0	0.30859(4)	-0.00089(5)	0.85739(4)
Fe5	4*c*	1.0	1/4	-1/4	½
P1	8*f*	1.0	0.41237(8)	-0.00295(8)	0.58015(7)
P2	8*f*	1.0	0.09300(8)	-0.00059(8)	0.42838(7)
P3	8*f*	1.0	0.20950(9)	-0.22932(9)	0.73004(7)
O1	8*f*	1.0	0.5359(2)	0.0122(3)	0.6510(2)
O2	8*f*	1.0	0.2439(2)	-0.0921(2)	0.7272(2)
O3	8*f*	1.0	0.1069(2)	0.1155(3)	0.4885(2)
O4	8*f*	1.0	0.3475(2)	0.0620(3)	0.6310(2)
O5	8*f*	1.0	0.3901(2)	0.0662(3)	0.4897(2)
O6	8*f*	1.0	-0.0292(2)	-0.0248(3)	0.3610(2)
O7	8*f*	1.0	0.3861(2)	-0.1412(3)	0.5640(2)
O8	8*f*	1.0	0.2123(2)	-0.3027(3)	0.6464(2)
O9	8*f*	1.0	0.0873(2)	-0.2313(2)	0.7231(2)
O10	8*f*	1.0	0.1510(2)	0.0208(3)	0.3610(2)
O11	8*f*	1.0	0.1423(2)	-0.1082(3)	0.4968(2)
O12	8*f*	1.0	0.2933(3)	-0.2813(3)	0.8209(2)

Table 3.2: Atomic parameters for compounds **1-9** cont…

Atom	Wycoff position	sof	x	y	z
			$RbNa_3Fe_7(PO_4)_6$, **5**		
Rb	4*e*	1.0	0	-0.25313(6)	1/4
Na1	8*f*	1.0	0.0192(2)	0.2606(2)	0.0198(2)
Na2	4*d*	1.0	1/4	1/4	1/2
Fe1	4*e*	1.0	0	0.08397(7)	1/4
Fe2	8*f*	1.0	0.18464(4)	0.03897(5)	0.62594(3)
Fe3	4*e*	1.0	1/2	0.11772(7)	3/4
Fe4	8*f*	1.0	0.30840(4)	-0.00018(5)	0.85807(3)
Fe5	4*c*	1.0	1/4	-1/4	1/2
P1	8*f*	1.0	0.41178(7)	-0.00115(8)	0.57884(6)
P2	8*f*	1.0	0.09324(7)	0.00038(8)	0.42865(6)
P3	8*f*	1.0	0.21003(8)	-0.22996(8)	0.73040(7)
O1	8*f*	1.0	0.5353(2)	0.0135(2)	0.6491(2)
O2	8*f*	1.0	0.2447(2)	-0.0927(2)	0.7280(2)
O3	8*f*	1.0	0.1098(2)	0.1159(2)	0.4891(2)
O4	8*f*	1.0	0.3477(2)	0.0607(3)	0.6314(2)
O5	8*f*	1.0	0.3888(2)	0.0706(2)	0.4892(2)
O6	8*f*	1.0	-0.0299(2)	-0.0203(3)	0.3624(2)
O7	8*f*	1.0	0.3845(2)	-0.1387(2)	0.5596(2)
O8	8*f*	1.0	0.2128(2)	-0.3019(3)	0.6466(2)
O9	8*f*	1.0	0.0875(2)	-0.2325(2)	0.7238(2)
O10	8*f*	1.0	0.1500(2)	0.0197(3)	0.3604(2)
O11	8*f*	1.0	0.1413(2)	-0.1085(2)	0.4955(2)
O12	8*f*	1.0	0.2939(2)	-0.2829(3)	0.8210(2)
			$CsNa_3Fe_7(PO_4)_6$, **6**		
Cs	4*e*	1.0	0	-0.25316(4)	1/4
Na1	8*f*	1.0	0.0196(2)	0.2586(2)	0.0216(2)
Na2	4*d*	1.0	1/4	1/4	1/2
Fe1	4*e*	1.0	0	0.0858(1)	1/4
Fe2	8*f*	1.0	0.18617(5)	0.03655(7)	0.62737(5)
Fe3	4*e*	1.0	1/2	0.11538(9)	3/4
Fe4	8*f*	1.0	0.30826(6)	0.00017(8)	0.86043(5)
Fe5	4*c*	1.0	3/4	-1/4	1/2
P1	8*f*	1.0	0.4109(1)	0.0008(1)	0.57686(8)
P2	8*f*	1.0	0.0929(1)	0.0009(1)	0.42994(8)
P3	8*f*	1.0	0.2094(1)	-0.2315(1)	0.73072(9)
O1	8*f*	1.0	0.5341(3)	0.0143(4)	0.6460(2)
O2	8*f*	1.0	0.2449(3)	-0.0944(3)	0.7301(2)
O3	8*f*	1.0	0.1132(3)	0.1139(3)	0.4922(2)
O4	8*f*	1.0	0.3479(3)	0.0556(4)	0.6328(2)
O5	8*f*	1.0	0.3862(3)	0.0784(4)	0.4902(2)
O6	8*f*	1.0	-0.0307(3)	-0.0149(4)	0.3657(3)
O7	8*f*	1.0	0.3825(3)	-0.1347(3)	0.5528(2)
O8	8*f*	1.0	0.2134(3)	-0.3013(4)	0.6473(3)
O9	8*f*	1.0	0.0868(3)	-0.2349(3)	0.7240(3)
O10	8*f*	1.0	0.1482(3)	0.0197(4)	0.3610(2)
O11	8*f*	1.0	0.1392(3)	-0.1105(4)	0.4935(3)
O12	8*f*	1.0	0.2931(3)	-0.2865(4)	0.8209(3)

Table 3.2: Atomic parameters for compounds **1-9** cont…

Atom	Wycoff position	sof	x	y	z
			$KNa_3Co_7(PO_4)_6$, **7**		
K	4*e*	1.0	0	-0.2501(2)	1/4
Na1	8*f*	1.0	0.0182(2)	0.2642(2)	0.0175(2)
Na2	4*d*	1.0	1/4	1/4	1/2
Co1	4*e*	1.0	0	0.08671(6)	1/4
Co2	8*f*	1.0	0.18467(4)	0.03964(5)	0.62450(3)
Co3	4*e*	1.0	1/2	0.12232(6)	3/4
Co4	8*f*	1.0	0.30757(4)	0.00043(5)	0.85640(3)
Co5	4*c*	1.0	1/4	-1/4	1/2
P1	8*f*	1.0	0.41313(7)	-0.00293(8)	0.58167(6)
P2	8*f*	1.0	0.09285(7)	0.00023(8)	0.42760(6)
P3	8*f*	1.0	0.21059(8)	-0.22959(8)	0.72733(7)
O1	8*f*	1.0	0.5385(2)	0.0156(2)	0.6522(2)
O2	8*f*	1.0	0.2466(2)	-0.0918(2)	0.7268(2)
O3	8*f*	1.0	0.1072(2)	0.1157(2)	0.4892(2)
O4	8*f*	1.0	0.3474(2)	0.0642(2)	0.6328(2)
O5	8*f*	1.0	0.3878(2)	0.0641(2)	0.4886(2)
O6	8*f*	1.0	-0.0312(2)	-0.0237(3)	0.3607(2)
O7	8*f*	1.0	0.3887(2)	-0.1423(2)	0.5681(2)
O8	8*f*	1.0	0.2130(2)	-0.3024(3)	0.6423(2)
O9	8*f*	1.0	0.0855(2)	-0.2313(2)	0.7192(2)
O10	8*f*	1.0	0.1494(2)	0.0235(3)	0.3578(2)
O11	8*f*	1.0	0.1446(2)	-0.1084(2)	0.4952(2)
O12	8*f*	1.0	0.2941(2)	-0.2851(3)	0.8179(2)
			$RbNa_3Co_7(PO_4)_6$, **8**		
Rb	4*e*	1.0	0	-0.24971(6)	1/4
Na1	8*f*	1.0	0.0183(2)	0.2624(2)	0.0187(2)
Na2	4*d*	1.0	1/4	1/4	1/2
Co1	4*e*	1.0	0	0.08824(7)	1/4
Co2	8*f*	1.0	0.18532(5)	0.03804(6)	0.62501(4)
Co3	4*e*	1.0	1/2	0.12056(8)	3/4
Co4	8*f*	1.0	0.30741(5)	0.00030(6)	0.85709(4)
Co5	4*c*	1.0	1/4	-1/4	1/2
P1	8*f*	1.0	0.41261(9)	-0.0014(1)	0.58026(7)
P2	8*f*	1.0	0.09259(9)	0.0007(1)	0.42747(7)
P3	8*f*	1.0	0.21077(9)	-0.2305(1)	0.72784(8)
O1	8*f*	1.0	0.5380(2)	0.0164(3)	0.6505(2)
O2	8*f*	1.0	0.2474(2)	-0.0929(3)	0.7281(2)
O3	8*f*	1.0	0.1102(2)	0.1149(3)	0.4907(2)
O4	8*f*	1.0	0.3477(2)	0.0615(3)	0.6333(2)
O5	8*f*	1.0	0.3869(3)	0.0688(3)	0.4889(2)
O6	8*f*	1.0	-0.0321(2)	-0.0194(3)	0.3618(2)
O7	8*f*	1.0	0.3870(2)	-0.1401(3)	0.5634(2)
O8	8*f*	1.0	0.2126(3)	-0.3020(3)	0.6424(2)
O9	8*f*	1.0	0.0857(3)	-0.2320(3)	0.7202(2)
O10	8*f*	1.0	0.1485(3)	0.0227(3)	0.3571(2)
O11	8*f*	1.0	0.1428(3)	-0.1099(3)	0.4936(2)
O12	8*f*	1.0	0.2940(3)	-0.2871(3)	0.8183(2)

Table 3.2: Atomic parameters for compounds **1-9** cont…

Atom	Wycoff position	sof	x	y	z
			$CsNa_3Co_7(PO_4)_6$, **9**		
Cs	4*e*	1.0	0	-0.25131(7)	1/4
Na1	8*f*	1.0	0.0177(3)	0.2601(3)	0.0195(3)
Na2	4*d*	1.0	1/4	1/4	1/2
Co1	4*e*	1.0	0	0.0900(1)	1/4
Co2	8*f*	1.0	0.18650(9)	0.0357(1)	0.62598(7)
Co3	4*e*	1.0	1/2	0.1184(1)	3/4
Co4	8*f*	1.0	0.30702(9)	0.0006(1)	0.85852(7)
Co5	4*c*	1.0	1/4	-1/4	1/2
P1	8*f*	1.0	0.4123(2)	0.0005(2)	0.5782(1)
P2	8*f*	1.0	0.0924(2)	0.0005(2)	0.4276(1)
P3	8*f*	1.0	0.2104(2)	-0.2314(2)	0.7294(1)
O1	8*f*	1.0	0.5379(5)	0.0172(5)	0.6480(4)
O2	8*f*	1.0	0.2475(5)	-0.0938(5)	0.7303(4)
O3	8*f*	1.0	0.1133(5)	0.1125(5)	0.4918(4)
O4	8*f*	1.0	0.3500(5)	0.0579(5)	0.6355(4)
O5	8*f*	1.0	0.3847(5)	0.0758(5)	0.4886(4)
O6	8*f*	1.0	-0.0327(5)	-0.0149(5)	0.3627(4)
O7	8*f*	1.0	0.3843(5)	-0.1363(5)	0.5565(4)
O8	8*f*	1.0	0.2121(5)	-0.3019(5)	0.6433(4)
O9	8*f*	1.0	0.0845(5)	-0.2338(5)	0.7210(4)
O10	8*f*	1.0	0.1468(5)	0.0211(5)	0.3570(4)
O11	8*f*	1.0	0.1407(5)	-0.1125(5)	0.4911(4)
O12	8*f*	1.0	0.2932(5)	-0.2893(5)	0.8193(4)

Table 3.3: Anisotropic thermal parameters (Å^2) for compounds **1-9**

Atom	U_{11}	U_{22}	U_{33}	U_{12}	U_{13}	U_{23}
			$KNa_3Mn_7(PO_4)_6$, **1**			
K	0.147(4)	0.042(2)	0.043(2)	0.00000	0.014(2)	0.00000
Na1	0.035(1)	0.018(1)	0.071(2)	0.002(1)	0.034(1)	0.005(1)
Na2	0.018(2)	0.016(2)	0.163(6)	-0.000(1)	0.035(3)	0.023(2)
Mn1	0.0134(5)	0.0130(6)	0.0128(5)	0.00000	0.0039(4)	0.00000
Mn2	0.0092(4)	0.0129(5)	0.0112(4)	-0.0003(3)	0.0039(3)	0.0008(3)
Mn3	0.0108(5)	0.0103(5)	0.0110(5)	0.00000	0.0048(4)	0.00000
Mn4	0.0089(4)	0.0161(5)	0.0116(4)	-0.0006(3)	0.0046(3)	0.0009(3)
Mn5	0.0079(7)	0.0111(7)	0.139(2)	0.0000(5)	-0.0007(9)	-0.0181(8)
P1	0.0080(6)	0.0117(7)	0.0094(6)	-0.0014(4)	0.0042(5)	-0.0029(4)
P2	0.0081(6)	0.0114(7)	0.0096(6)	0.0008(4)	0.0040(5)	0.0004(4)
P3	0.0112(7)	0.0081(6)	0.0175(7)	-0.0002(4)	0.0061(5)	0.0005(5)
O1	0.008(2)	0.021(2)	0.016(2)	-0.002(1)	0.004(1)	-0.006(1)
O2	0.011(2)	0.010(2)	0.013(2)	-0.001(1)	0.004(1)	0.000(1)
O3	0.024(2)	0.016(2)	0.014(2)	0.003(2)	0.005(2)	-0.004(1)
O4	0.011(2)	0.020(2)	0.016(2)	-0.001(1)	0.009(1)	-0.005(1)
O5	0.020(2)	0.022(2)	0.014(2)	-0.001(2)	0.007(2)	0.002(2)
O6	0.009(2)	0.027(2)	0.016(2)	-0.002(1)	0.004(1)	0.003(2)
O7	0.015(2)	0.014(2)	0.029(2)	-0.005(1)	0.008(2)	-0.006(2)
O8	0.027(2)	0.013(2)	0.032(2)	-0.005(2)	0.018(2)	-0.007(2)
O9	0.013(2)	0.012(2)	0.029(2)	-0.000(1)	0.010(2)	0.001(2)
O10	0.012(2)	0.036(2)	0.016(2)	0.004(2)	0.010(2)	0.004(2)
O11	0.016(2)	0.015(2)	0.023(2)	0.004(1)	0.007(2)	0.008(2)
O12	0.019(2)	0.022(2)	0.036(2)	0.001(2)	0.006(2)	0.015(2)
			$RbNa_3Mn_7(PO_4)_6$, **2**			
Rb	0.0562(9)	0.0320(7)	0.0326(7)	0.00000	0.0159(7)	0.00000
Na1	0.027(2)	0.023(2)	0.064(3)	0.002(1)	0.027(2)	0.004(2)
Na2	0.022(3)	0.026(3)	0.244(13)	0.002(3)	0.045(5)	0.0030(5)
Mn1	0.0158(8)	0.0193(9)	0.0159(8)	0.00000	0.0054(7)	0.00000
Mn2	0.0094(6)	0.0147(6)	0.0124(6)	0.0000(4)	0.0043(4)	0.0006(4)
Mn3	0.0122(8)	0.0124(8)	0.0115(7)	0.00000	0.0048(6)	0.00000
Mn4	0.0107(6)	0.0186(6)	0.0128(6)	-0.0007(4)	0.0053(4)	0.0000(4)
Mn5	0.0086(9)	0.012(1)	0.117(2)	0.0005(7)	-0.000(1)	-0.016(1)
P1	0.0105(9)	0.0114(9)	0.0097(9)	-0.0014(7)	0.0047(7)	-0.0024(7)
P2	0.0076(9)	0.0125(9)	0.0089(8)	-0.0008(7)	0.0030(7)	-0.0002(7)
P3	0.0106(9)	0.0104(9)	0.018(1)	-0.0004(7)	0.0050(7)	0.0000(7)
O1	0.012(3)	0.019(3)	0.016(3)	-0.002(2)	0.004(2)	-0.005(2)
O2	0.015(3)	0.010(2)	0.019(3)	-0.002(2)	0.009(2)	0.001(2)
O3	0.018(3)	0.014(3)	0.016(3)	-0.002(2)	0.004(2)	-0.005(2)
O4	0.012(3)	0.026(3)	0.018(3)	0.001(2)	0.010(2)	-0.004(2)
O5	0.021(3)	0.023(3)	0.017(3)	-0.005(2)	0.009(2)	0.007(2)
O6	0.007(2)	0.027(3)	0.023(3)	-0.001(2)	0.004(2)	-0.002(2)
O7	0.017(3)	0.013(3)	0.029(3)	-0.007(2)	0.011(2)	-0.008(2)
O8	0.035(3)	0.018(3)	0.025(3)	-0.003(3)	0.022(3)	-0.008(2)
O9	0.012(3)	0.010(3)	0.033(3)	-0.003(2)	0.009(2)	0.003(2)
O10	0.011(3)	0.038(3)	0.016(3)	0.003(2)	0.009(2)	-0.001(2)
O11	0.016(3)	0.014(3)	0.028(3)	0.003(2)	0.009(2)	0.004(2)
O12	0.019(3)	0.028(3)	0.033(3)	-0.004(3)	0.004(3)	0.014(3)

Table 3.3: Anisotropic thermal parameters ($Å^2$) for compounds **1-9** cont..

Atom	U_{11}	U_{22}	U_{33}	U_{12}	U_{13}	U_{23}
			$CsNa_3Mn_7(PO_4)_6$, **3**			
Cs	0.0386(6)	0.0226(5)	0.0290(6)	0.00000	0.0133(4)	0.00000
Na1	0.035(3)	0.021(2)	0.055(3)	0.001(2)	0.029(2)	0.003(2)
Na2	0.033(4)	0.023(4)	0.227(14)	0.004(3)	0.051(7)	0.017(6)
Mn1	0.019(1)	0.018(1)	0.012(1)	0.00000	0.0052(8)	0.00000
Mn2	0.0137(8)	0.0172(8)	0.0147(7)	-0.0007(6)	0.0053(6)	-0.0008(6)
Mn3	0.016(1)	0.016(1)	0.012(1)	0.00000	0.0048(8)	0.00000
Mn4	0.0154(8)	0.0216(9)	0.0153(8)	-0.0017(6)	0.0059(6)	-0.0007(6)
Mn5	0.014(1)	0.012(1)	0.130(3)	-0.000(1)	-0.001(2)	-0.015(2)
P1	0.012(1)	0.014(1)	0.014(1)	-0.0019(9)	0.0049(9)	-0.0021(9)
P2	0.010(1)	0.013(1)	0.013(1)	0.0001(9)	0.0039(9)	-0.0002(9)
P3	0.013(1)	0.013(1)	0.022(1)	0.0009(9)	0.006(1)	0.000(1)
O1	0.015(4)	0.026(4)	0.021(4)	0.002(3)	0.004(3)	-0.010(3)
O2	0.018(4)	0.013(3)	0.021(4)	0.002(3)	0.010(3)	0.004(3)
O3	0.016(4)	0.020(4)	0.020(4)	-0.004(3)	0.004(3)	-0.007(3)
O4	0.014(4)	0.034(4)	0.019(4)	-0.005(3)	0.005(3)	-0.007(3)
O5	0.022(4)	0.024(4)	0.021(4)	-0.002(3)	0.009(3)	0.003(3)
O6	0.016(4)	0.025(4)	0.017(3)	0.003(3)	0.002(3)	-0.002(3)
O7	0.020(4)	0.012(4)	0.032(4)	-0.004(3)	0.008(3)	-0.007(3)
O8	0.040(4)	0.015(4)	0.030(4)	0.001(3)	0.024(3)	0.000(3)
O9	0.016(3)	0.012(3)	0.033(4)	-0.001(3)	0.007(3)	-0.003(3)
O10	0.016(4)	0.032(4)	0.019(3)	0.005(3)	0.009(3)	0.006(3)
O11	0.020(4)	0.013(3)	0.029(4)	0.003(3)	0.010(3)	0.009(3)
O12	0.018(4)	0.022(4)	0.033(4)	-0.006(3)	0.001(3)	0.012(3)
			$KNa_3Fe_7(PO_4)_6$, **4**			
K	0.100(2)	0.032(1)	0.030(1)	0.00000	0.006(1)	0.00000
Na1	0.031(1)	0.0167(9)	0.064(1)	0.0008(7)	0.031(1)	0.0035(9)
Na2	0.018(2)	0.022(2)	0.184(5)	0.000(1)	0.034(2)	0.034(2)
Fe1	0.0114(4)	0.0116(4)	0.0113(4)	0.00000	0.0037(3)	0.00000
Fe2	0.0098(3)	0.0109(3)	0.0122(3)	-0.0001(2)	0.0047(2)	0.0010(2)
Fe3	0.0120(4)	0.0094(4)	0.0095(4)	0.00000	0.0046(3)	0.00000
Fe4	0.0089(3)	0.0198(4)	0.0123(3)	-0.0011(2)	0.0046(2)	0.0004(2)
Fe5	0.0083(5)	0.0086(4)	0.0716(8)	-0.0001(3)	-0.0021(5)	-0.0092(4)
P1	0.0084(5)	0.0101(5)	0.0093(5)	-0.0013(4)	0.0036(4)	-0.0025(4)
P2	0.0082(5)	0.0097(5)	0.0095(5)	0.0009(4)	0.0032(4)	0.0007(4)
P3	0.0115(5)	0.0076(5)	0.0170(5)	0.0000(4)	0.0065(4)	0.0008(4)
O1	0.009(1)	0.021(2)	0.015(1)	-0.001(1)	0.004(1)	-0.005(1)
O2	0.014(1)	0.009(1)	0.015(1)	-0.002(1)	0.006(1)	0.001(1)
O3	0.023(2)	0.013(1)	0.015(1)	0.004(1)	0.006(1)	-0.002(1)
O4	0.012(1)	0.017(1)	0.015(1)	-0.000(1)	0.008(1)	-0.005(1)
O5	0.020(1)	0.020(2)	0.012(1)	-0.002(1)	0.007(1)	-0.001(1)
O6	0.009(1)	0.023(2)	0.016(1)	-0.002(1)	0.004(1)	0.001(1)
O7	0.017(1)	0.011(1)	0.024(2)	-0.001(1)	0.009(1)	-0.002(1)
O8	0.026(2)	0.012(1)	0.030(2)	-0.004(1)	0.018(1)	-0.007(1)
O9	0.013(1)	0.010(1)	0.025(2)	-0.001(1)	0.009(1)	0.0008(1)
O10	0.011(1)	0.033(2)	0.014(1)	0.006(1)	0.006(1)	0.007(1)
O11	0.018(1)	0.013(1)	0.019(1)	0.003(1)	0.006(1)	0.005(1)
O12	0.020(2)	0.020(2)	0.030(2)	0.000(1)	0.005(1)	0.013(1)

Table 3.3: Anisotropic thermal parameters (Å^2) for compounds **1-9** cont..

Atom	U_{11}	U_{22}	U_{33}	U_{12}	U_{13}	U_{23}
			$RbNa_3Fe_7(PO_4)_6$, **5**			
Rb	0.0430(4)	0.0222(3)	0.0203(4)	0.00000	0.0075(3)	0.00000
Na1	0.028(1)	0.0152(9)	0.057(1)	0.0010(7)	0.028(1)	0.0039(8)
Na2	0.023(2)	0.023(2)	0.242(7)	0.000(1)	0.043(3)	0.038(2)
Fe1	0.0090(4)	0.0107(4)	0.0081(4)	0.00000	0.0015(3)	0.00000
Fe2	0.0083(3)	0.0092(3)	0.0087(3)	-0.0002(2)	0.0031(2)	0.0012(2)
Fe3	0.0093(4)	0.0084(4)	0.0063(4)	0.00000	0.0026(3)	0.00000
Fe4	0.0078(3)	0.0194(4)	0.0088(3)	-0.0011(2)	0.0027(2)	0.0006(2)
Fe5	0.0070(5)	0.0071(4)	0.0652(8)	-0.0001(3)	-0.0031(4)	-0.0081(4)
P1	0.0070(5)	0.0087(5)	0.0062(5)	-0.0013(3)	0.0021(4)	-0.0021(3)
P2	0.0062(5)	0.0079(5)	0.0070(5)	0.0005(3)	0.0018(4)	0.0004(3)
P3	0.0091(5)	0.0060(5)	0.0137(5)	0.0002(3)	0.0040(4)	0.0008(3)
O1	0.007(1)	0.018(1)	0.012(1)	0.000(1)	0.003(1)	-0.005(1)
O2	0.011(1)	0.008(1)	0.013(1)	-0.001(1)	0.004(1)	0.000(1)
O3	0.015(1)	0.011(1)	0.010(1)	0.000(1)	0.002(1)	-0.002(1)
O4	0.012(1)	0.018(1)	0.012(1)	-0.000(1)	0.007(1)	-0.004(1)
O5	0.018(1)	0.016(1)	0.009(1)	-0.002(1)	0.004(1)	0.001(1)
O6	0.007(1)	0.018(1)	0.014(1)	-0.001(1)	0.001(1)	0.000(1)
O7	0.012(1)	0.011(1)	0.020(1)	-0.002(1)	0.006(1)	-0.004(1)
O8	0.023(1)	0.012(1)	0.025(2)	-0.004(1)	0.016(1)	-0.006(1)
O9	0.011(1)	0.009(1)	0.025(2)	0.000(1)	0.007(1)	0.002(1)
O10	0.011(1)	0.026(2)	0.012(1)	0.003(1)	0.006(1)	0.002(1)
O11	0.016(1)	0.012(1)	0.016(1)	0.004(1)	0.004(1)	0.006(1)
O12	0.016(1)	0.018(2)	0.025(2)	-0.000(1)	0.003(1)	0.013(1)
			$CsNa_3Fe_7(PO_4)_6$, **6**			
Cs	0.0213(3)	0.0161(3)	0.0165(3)	0.00000	0.0070(2)	0.00000
Na1	0.023(1)	0.016(1)	0.054(2)	0.0003(8)	0.024(1)	0.004(1)
Na2	0.024(3)	0.017(2)	0.29(1)	0.002(2)	0.060(5)	0.032(3)
Fe1	0.0105(5)	0.0149(6)	0.0108(5)	0.00000	0.0025(4)	0.00000
Fe2	0.0057(4)	0.0111(4)	0.0082(4)	-0.0008(3)	0.0033(3)	0.0003(3)
Fe3	0.0078(5)	0.0086(5)	0.0054(5)	0.00000	0.0023(4)	0.00000
Fe4	0.0075(4)	0.0248(5)	0.0101(4)	-0.0012(3)	0.0037(3)	0.0013(3)
Fe5	0.0048(6)	0.0070(7)	0.088(1)	0.0001(4)	-0.0030(7)	-0.0117(6)
P1	0.0056(6)	0.0094(7)	0.0057(6)	-0.0013(4)	0.0030(5)	-0.0022(4)
P2	0.0041(6)	0.0075(6)	0.0071(6)	0.0002(4)	0.0019(5)	-0.0002(4)
P3	0.0067(7)	0.0078(6)	0.0142(7)	0.0008(4)	0.0046(5)	0.0019(5)
O1	0.005(2)	0.021(2)	0.016(2)	-0.000(1)	0.003(1)	-0.006(2)
O2	0.010(2)	0.011(2)	0.016(2)	-0.002(1)	0.005(1)	0.000(1)
O3	0.012(2)	0.014(2)	0.008(2)	-0.001(1)	0.002(1)	-0.004(1)
O4	0.012(2)	0.020(2)	0.014(2)	-0.002(2)	0.010(2)	-0.006(2)
O5	0.016(2)	0.021(2)	0.010(2)	-0.000(2)	0.004(1)	0.004(2)
O6	0.001(2)	0.023(2)	0.018(2)	-0.002(1)	-0.001(1)	-0.003(2)
O7	0.011(2)	0.014(2)	0.017(2)	-0.003(1)	0.006(1)	-0.006(2)
O8	0.022(2)	0.014(2)	0.025(2)	-0.002(2)	0.015(2)	-0.004(2)
O9	0.007(2)	0.012(2)	0.029(2)	-0.000(1)	0.008(2)	0.002(2)
O10	0.012(2)	0.030(2)	0.014(2)	0.002(2)	0.009(2)	-0.001(2)
O11	0.014(2)	0.016(2)	0.029(2)	0.005(2)	0.008(2)	0.010(2)
O12	0.014(2)	0.024(2)	0.027(2)	0.001(2)	0.002(2)	0.015(2)

Table 3.3: Anisotropic thermal parameters (Å^2) for compounds **1-9** cont..

Atom	U_{11}	U_{22}	U_{33}	U_{12}	U_{13}	U_{23}
			$KNa_3Co_7(PO_4)_6$, **7**			
K	0.058(1)	0.0313(8)	0.0235(8)	0.00000	0.0044(8)	0.00000
Na1	0.0254(9)	0.0166(9)	0.054(1)	0.0017(7)	0.0252(9)	0.0047(8)
Na2	0.022(2)	0.025(2)	0.238(7)	0.001(1)	0.044(3)	0.042(3)
Co1	0.0089(3)	0.0098(3)	0.0095(3)	0.00000	0.0030(3)	0.00000
Co2	0.0094(3)	0.0100(3)	0.0098(3)	0.0001(2)	0.00352)	0.0010(2)
Co3	0.0093(3)	0.0088(3)	0.0091(3)	0.00000	0.0042(3)	0.00000
Co4	0.0097(3)	0.0138(3)	0.0090(3)	-0.0007(2)	0.0033(2)	-0.0005(2)
Co5	0.0088(4)	0.0081(4)	0.0376(5)	0.0003(3)	0.0000(3)	-0.0041(3)
P1	0.0076(4)	0.0098(4)	0.0079(4)	-0.0006(3)	0.0031(4)	-0.0017(3)
P2	0.0081(4)	0.0080(4)	0.0077(4)	0.0008(3)	0.0028(3)	0.0006(3)
P3	0.0090(4)	0.0071(4)	0.0129(5)	-0.0001(3)	0.0048(4)	0.0003(3)
O1	0.010(1)	0.017(1)	0.011(1)	-0.002(1)	0.003(1)	-0.005(1)
O2	0.012(1)	0.009(1)	0.013(1)	-0.002(1)	0.006(1)	0.0009(9)
O3	0.016(1)	0.011(1)	0.011(1)	0.001(1)	0.002(1)	-0.002(1)
O4	0.01(1)	0.015(1)	0.014(1)	-0.000(1)	0.006(1)	-0.005(1)
O5	0.017(1)	0.016(1)	0.013(1)	-0.000(1)	0.006(1)	-0.000(1)
O6	0.009(1)	0.020(1)	0.014(1)	-0.001(1)	0.002(1)	-0.001(1)
O7	0.014(1)	0.011(1)	0.019(1)	-0.002(1)	0.006(1)	-0.004(1)
O8	0.022(1)	0.012(1)	0.024(2)	-0.002(1)	0.015(1)	-0.005(1)
O9	0.008(1)	0.008(1)	0.017(1)	-0.0014(9)	0.005(1)	0.001(1)
O10	0.011(1)	0.024(1)	0.010(1)	0.003(1)	0.005(1)	0.003(1)
O11	0.014(1)	0.013(1)	0.016(1)	0.002(1)	0.006(1)	0.004(1)
O12	0.013(1)	0.019(1)	0.022(2)	0.000(1)	0.003(1)	0.009(1)
			$RbNa_3Co_7(PO_4)_6$, **8**			
Rb	0.0287(4)	0.0224(4)	0.0180(4)	0.00000	0.0058(3)	0.00000
Na1	0.023(1)	0.016(1)	0.051(1)	0.0002(8)	0.023(1)	0.0041(9)
Na2	0.023(2)	0.023(2)	0.270(9)	0.002(2)	0.055(4)	0.037(3)
Co1	0.0058(4)	0.0107(4)	0.0081(4)	0.00000	0.0018(3)	0.00000
Co2	0.0071(3)	0.0114(3)	0.0084(3)	-0.0003(2)	0.0027(2)	0.0008(2)
Co3	0.0069(4)	0.0099(4)	0.0078(4)	0.00000	0.0032(3)	0.00000
Co4	0.0073(3)	0.0151(3)	0.0080(3)	-0.0009(2)	0.0026(2)	-0.0003(2)
Co5	0.0068(5)	0.0084(4)	0.0389(6)	0.0009(3)	-0.0010(4)	-0.0040(4)
P1	0.0057(5)	0.0102(5)	0.0060(5)	-0.0007(4)	0.0020(4)	-0.0014(4)
P2	0.0061(5)	0.0087(5)	0.0057(5)	0.0005(4)	0.0017(4)	0.0004(4)
P3	0.0064(5)	0.0077(5)	0.0119(5)	0.0003(4)	0.0037(4)	0.0004(4)
O1	0.006(2)	0.017(2)	0.011(1)	-0.002(1)	0.002(1)	-0.005(1)
O2	0.009(1)	0.011(2)	0.013(2)	-0.001(1)	0.004(1)	0.001(1)
O3	0.013(2)	0.013(1)	0.01(2)	-0.000(1)	0.003(1)	-0.003(1)
O4	0.010(2)	0.016(3)	0.010(1)	-0.000(1)	0.005(1)	-0.003(1)
O5	0.015(2)	0.016(2)	0.008(1)	-0.001(1)	0.004(1)	0.001(1)
O6	0.005(2)	0.021(2)	0.010(2)	-0.002(1)	0.001(1)	-0.001(1)
O7	0.012(2)	0.011(2)	0.019(2)	-0.002(1)	0.003(1)	-0.002(1)
O8	0.020(2)	0.013(2)	0.021(2)	-0.001(1)	0.013(1)	-0.002(1)
O9	0.010(2)	0.009(2)	0.021(2)	0.000(1)	0.007(1)	0.002(1)
O10	0.011(2)	0.024(2)	0.009(1)	0.003(1)	0.005(1)	0.003(1)
O11	0.012(2)	0.013(2)	0.015(2)	0.004(1)	0.004(1)	0.006(1)
O12	0.012(2)	0.018(2)	0.020(2)	0.000(1)	0.002(1)	0.01(1)

Table 3.3: Anisotropic thermal parameters ($Å^2$) for compounds **1-9** cont..

Atom	U_{11}	U_{22}	U_{33}	U_{12}	U_{13}	U_{23}
			$CsNa_3Co_7(PO_4)_6$, **9**			
Cs	0.0210(4)	0.0181(4)	0.0173(4)	0.00000	0.0068(3)	0.00000
Na1	0.026(2)	0.015(2)	0.050(2)	0.000(2)	0.023(2)	0.003(2)
Na2	0.032(4)	0.018(3)	0.28(2)	0.001(3)	0.070(6)	0.023(5)
Co1	0.0080(8)	0.0138(8)	0.0101(7)	0.00000	0.0027(6)	0.00000
Co2	0.0098(6)	0.0127(6)	0.0111(5)	-0.0003(4)	0.0042(4)	0.0006(4)
Co3	0.0081(8)	0.0121(8)	0.0083(7)	0.00000	0.0032(6)	0.00000
Co4	0.0110(6)	0.0149(6)	0.0107(6)	-0.0010(4)	0.0041(4)	-0.0004(4)
Co5	0.0099(8)	0.0082(8)	0.049(1)	-0.0003(7)	0.0000(8)	-0.0041(7)
P1	0.01(1)	0.01(1)	0.006(1)	-0.0023(8)	0.0019(8)	-0.0027(7)
P2	0.007(1)	0.011(1)	0.010(1)	0.0011(8)	0.0035(8)	-0.0005(8)
P3	0.008(1)	0.01(1)	0.016(1)	0.0009(8)	0.0052(8)	0.0003(8)
O1	0.004(3)	0.020(3)	0.014(3)	0.001(2)	0.001(2)	-0.007(2)
O2	0.005(3)	0.011(3)	0.016(3)	0.000(2)	0.001(2)	0.001(2)
O3	0.020(3)	0.010(3)	0.013(3)	-0.003(2)	0.009(2)	-0.005(2)
O4	0.013(3)	0.024(3)	0.008(3)	-0.003(2)	0.004(2)	-0.005(2)
O5	0.014(3)	0.022(3)	0.015(3)	0.002(2)	0.007(2)	0.001(2)
O6	0.005(3)	0.022(3)	0.011(3)	-0.001(2)	0.000(2)	0.000(2)
O7	0.011(3)	0.014(3)	0.017(3)	-0.003(2)	-0.001(2)	-0.004(2)
O8	0.020(3)	0.013(3)	0.022(3)	-0.001(2)	0.013(3)	0.000(2)
O9	0.008(3)	0.014(3)	0.024(3)	-0.005(2)	0.007(2)	-0.001(2)
O10	0.011(3)	0.022(3)	0.012(3)	0.001(2)	0.007(2)	0.004(2)
O11	0.018(3)	0.018(3)	0.022(3)	0.006(3)	0.012(3)	0.008(2)
O12	0.014(3)	0.016(3)	0.018(3)	-0.005(2)	0.004(2)	0.010(2)

Table 3.4: Selected bond distances and bond angles for compounds **1**-**9**

Bond Distances		Bond Angles	
		$KNa_3Mn_7(PO_4)_6$, **1**	
Mn(1)-O(9) 2.147(4)*2	P(1)-O(7) 1.523(4)	O(9)-Mn(1)-O(9) 81.3(2)	O(1)-Mn(4)-O(2) 89.8(1)
Mn(1)-O(10) 2.230(4)*2	P(1)-O(5) 1.527(4)	O(9)-Mn(1)-O(10) 88.8(1)	O(10)-Mn(4)-O(2) 88.1(1)
Mn(1)-O(6) 2.260(4)*2	P(1)-O(4) 1.539(3)	O(9)-Mn(1)-O(10) 118.4(1)	O(5)-Mn(4)-O(2)130.0(1)
	P(1)-O(1) 1.552(4)	O(10)-Mn(1)-O(10) 145.2(2)	O(1)-Mn(4)-O(8) 92.2(1)
Mn(2)-O(12) 2.093(4)		O(9)-Mn(1)-O(6) 142.5(1)	O(10)-Mn(4)-O(8) 89.6(2)
Mn(2)-O(2) 2.106(3)	P(2)-O(11) 1.527(4)	O(9)-Mn(1)-O(6) 88.4(1)	O(5)-Mn(4)-O(8) 114.7(2)
Mn(2)-O(4) 2.140(3)	P(2)-O(3) 1.529(4)	O(10)-Mn(1)-O(6) 64.8(1)	O(2)-Mn(4)-O(8) 115.3(1)
Mn(2)-O(6) 2.148(3)	P(2)-O(10) 1.536(3)	O(10)-Mn(1)-O(6) 97.2(1)	
Mn(2)-O(3) 2.176(4)	P(2)-O(6) 1.537(4)	O(6)-Mn(1)-O(6) 119.5(2)	O(7)-Mn(5)-O(7) 180.0(3)
			O(7)-Mn(5)-O(11) 87.4(2)
Mn(3)-O(9) 2.124(4)*2	P(3)-O(12) 1.514(4)	O(12)-Mn(2)-O(2) 110.2(2)	O(7)-Mn(5)-O(11)92.6(2)
Mn(3)-O(1) 2.178(3)*2	P(3)-O(2) 1.543(3)	O(12)-Mn(2)-O(4) 85.4(2)	O(11)-Mn(5)-O(11) 180.0(2)
Mn(3)-O(4) 2.265(3)*2	P(3)-O(8) 1.545(4)	O(2)-Mn(2)-O(4) 88.0(1)	
	P(3)-O(9) 1.547(4)	O(12)-Mn(2)-O(6) 91.0(2)	O(7)-P(1)-O(5)]111.7(2)
Mn(4)-O(1) 2.107(3)		O(2)-Mn(2)-O(6) 87.6(1)	O(7)-P(1)-O(4) 113.4(2)
Mn(4)-O(10) 2.108(3)		O(4)-Mn(2)-O(6) 173.0(1)	O(5)-P(1)-O(4) 108.8(2)
Mn(4)-O(5) 2.108(4)		O(12)-Mn(2)-O(3) 91.9(2)	O(7)-P(1)-O(1) 108.6(2)
Mn(4)-O(2) 2.181(3)		O(2)-Mn(2)-O(3) 157.9(1)	O(5)-P(1)-O(1) 111.5(2)
Mn(4)-O(8) 2.209(4)		O(4)-Mn(2)-O(3) 93.4(1)	O(4)-P(1)-O(1) 102.5(2)
		O(6)-Mn(2)-O(3) 92.7(1)	
Mn(5)-O(7) 2.086(3)*2			O(11)-P(2)-O(3) 106.6(2)
Mn(5)- (11)2.091(4)*2		O(9)-Mn(3)-O(9) 82.3(2)	O(11)-P(2)-O(10) 113.5(2)
		O(9)-Mn(3)-O(17) 88.7(1)	O(3)-P(2)-O(10) 109.3(2)
		O(9)-Mn(3)-O(1) 146.2(1)	O(11)-P(2)-O(6) 112.0(2)
		O(1)-Mn(3)-O(1) 115.2(2)	O(3)-P(2)-O(6) 112.5(2)
		O(9)-Mn(3)-O(4) 116.9(1)	O(10)-P(2)-O(6) 103.0(2)
		O(9)-Mn(3)-O(4) 89.5(1)	
		O(1)-Mn(3)-O(4) 65.7(1)	O(12)-P(3)-O(2) 106.7(2)
		O(1)-Mn(3)-O(4) 95.5(1)	O(12)-P(3)-O(8) 110.8(2)
		O(4)-Mn(3)-O(4) 145.7(2)	O(2)-P(3)-O(8) 110.6(2)
			O(12)-P(3)-O(9) 112.2(2)
		O(1)-Mn(4)-O(10) 77.6(2)	O(2)-P(3)-O(9)108.4(2)
		O(1)-Mn(4)-O(5) 88.8(1)	O(8)-P(3)-O(9) 108.0(2)
		O(10)-Mn(4)-O(5) 91.9(1)	
		$RbNa_3Mn_7(PO_4)_6$, **2**	
Mn(1)-O(9) 2.149(6)*2	P(1)-O(5) 1.518(5)	O(9)-Mn(1)-O(9) 81.7(3)	O(10)-Mn(4)-O(2) 88.0(2)
Mn(1)-O(10) 2.225(5)*2	P(1)-O(7) 1.524(5)	O(9)-Mn(1)-O(10) 89.7(2)	O(1)-Mn(4)-O(2) 90.4(2)
Mn(1)-O(6) 2.285(6)*2	P(1)-O(4) 1.542(5)	O(9)-Mn(1)-O(10) 119.5(2)	O(5)-Mn(4)-O(2) 129.1(2)
	P(1)-O(1) 1.551(5)	O(10)-Mn(1)-O(10) 142.4(3)	O(10)-Mn(4)-O(8) 88.5(2)
Mn(2)-O(12) 2.096(6)		O(9)-Mn(1)-O(6) 86.9(2)	O(1)-Mn(4)-O(8) 91.6(2)
Mn(2)-O(2) 2.105(5)	P(2)-O(3) 1.523(5)	O(10)-Mn(1)-O(6) 64.4(2)	O(5)-Mn(4)-O(8) 115.2(2)
Mn(2)-O(6) 2.119(5)	P(2)-O(11) 1.535(5)	O(10)-Mn(1)-O(6) 97.0(2)	O(2)-Mn(4)-O(8) 115.7(2)
Mn(2)-O(4) 2.119(5)	P(2)-O(10) 1.535(5)	O(9)-Mn(1)-O(6) 141.5(2)	
Mn(2)-O(3) 2.178(5)	P(2)-O(6) 1.539(5)	O(6)-Mn(1)-O(6) 122.5(3)	O(7)-Mn(5)-O(7) 180.0
			O(7)-Mn(5)-O(11) 87.0(2)
Mn(3)-O(9) 2.123(5)*2	P(3)-O(12) 1.511(6)	O(12)-Mn(2)-O(2) 109.2(2)	O(7)-Mn(5)-O(11) 93.0(2)
Mn(3)-O(1) 2.184(5)*2	P(3)-O(9) 1.542(6)	O(12)-Mn(2)-O(6) 91.9(2)	O(11)-Mn(5)-O(11) 180.0(3)
Mn(3)-O(4) 2.270(5)*2	P(3)-O(2) 1.546(5)	O(2)-Mn(2)-O(6) 87.7(2)	
	P(3)-O(8) 1.554(5)	O(12)-Mn(2)-O(4) 85.9(2)	O(5)-P(1)-O(7) 111.4(3)
Mn(4)-O(10) 2.107(5)		O(2)-Mn(2)-O(4) 87.8(2)	O(5)-P(1)-O(4) 108.6(3)
Mn(4)-O(1) 2.108(5)		O(6)-Mn(2)-O(4) 174.0(2)	O(7)-P(1)-O(4) 113.7(3)
Mn(4)-O(5) 2.114(6)		O(12)-Mn(2)-O(3) 91.9(2)	O(5)-P(1)-O(1) 111.6(3)
Mn(4)-O(2) 2.181(5)		O(2)-Mn(2)-O(3) 158.8(2)	O(7)-P(1)-O(1) 108.9(3)

Table 3.4: Selected bond distances and bond angles for compounds **1**-**9** cont..

Bond Distances		Bond Angles	
$RbNa_3Mn_7(PO_4)_6$, **2** Cont.			
Mn(4)-O(8) 2.222(6)		O(6)-Mn(2)-O(3) 93.0(2)	O(4)-P(1)-O(1) 102.3(3)
		O(4)-Mn(2)-O(3) 92.7(2)	
Mn(5)-O(7) 2.091(5)*2			O(3)-P(2)-O(11) 106.8(3)
Mn(5)-O(11) 2.093(5)*2		O(9)-Mn(3)-O(9) 82.9(3)	O(3)-P(2)-O(10) 110.1(3)
		O(9)-Mn(3)-O(1) 145.0(2)	O(11)-P(2)-O(10) 113.0(3)
		O(9)-Mn(3)-O(1) 87.7(2)	O(3)-P(2)-O(6) 111.9(3)
		O(1)-Mn(3)-O(1) 117.4(3)	O(11)-P(2)-O(6) 112.1(3)
		O(9)-Mn(3)-O(4) 89.3(2)	O(10)-P(2)-O(6) 102.9(3)
		O(9)-Mn(3)-O(4) 117.3(2)	
		O(1)-Mn(3)-O(4) 65.4(2)	O(12)-P(3)-O(9) 112.2(3)
		O(1)-Mn(3)-O(4) 96.1(2)	O(12)-P(3)-O(2) 106.4(3)
		O(4)-Mn(3)-O(4) 145.4(3)	O(9)-P(3)-O(2) 108.7(3)
			O(12)-P(3)-O(8) 111.3(4)
		O(10)-Mn(4)-O(1) 178.3(2)	O(9)-P(3)-O(8) 107.9(3)
		O(10)-Mn(4)-O(5) 92.4(2)	O(2)-P(3)-O(8) 110.4(3)
		O(1)-Mn(4)-O(5) 89.2(2)	
$CsNa_3Mn_7(PO_4)_6$, **3**			
Mn(1)-O(9) 2.133(7)*2	P(1)-O(7) 1.519(7)	O(9)-Mn(1)-O(9) 80.9(4)	O(1)-Mn(4)-O(2) 90.8(3)
Mn(1)-O(10) 2.212(7)*2	P(1)-O(5) 1.530(7)	O(9)-Mn(1)-O(10) 90.6(3)	O(10)-Mn(4)-O(2) 87.2(3)
Mn(1)-O(6) 2.280(7)*2	P(1)-O(4) 1.550(8)	O(9)-Mn(1)-O(10) 120.4(3)	O(5)-Mn(4)-O(2) 126.5(3)
	P(1)-O(1) 1.551(7)	O(10)-Mn(1)-O(10) 140.4(4)	O(1)-Mn(4)-O(8) 90.8(3)
Mn(2)-O(12) 2.088(7)		O(9)-Mn(1)-O(6) 141.2(3)	O(10)-Mn(4)-O(8) 88.7(3)
Mn(2)-O(2) 2.125(7)	P(2)-O(3) 1.518(7)	O(9)-Mn(1)-O(6) 87.0(3)	O(5)-Mn(4)-O(8) 118.2(3)
Mn(2)-O(4) 2.127(7)	P(2)-O(6) 1.531(7)	O(10)-Mn(1)-O(6) 64.3(3)	O(2)-Mn(4)-O(8) 115.4(2)
Mn(2)-O(6) 2.142(7)	P(2)-O(11) 1.538(7)	O(10)-Mn(1)-O(6) 96.3(3)	
Mn(2)-O(3) 2.168(7)	P(2)-O(10) 1.546(7)	O(6)-Mn(1)-O(6) 123.0(4)	O(11)-Mn(5)-O(11) 180.0(4)
			O(11)-Mn(5)-O(7) 86.6(3)
Mn(3)-O(9) 2.131(7)*2	P(3)-O(12) 1.513(7)	O(12)-Mn(2)-O(2) 109.7(3)	O(11)-Mn(5)-O(7) 93.4(3)
Mn(3)-O(1) 2.211(7)*2	P(3)-O(2) 1.552(7)	O(12)-Mn(2)-O(4) 85.9(3)	O(7)-Mn(5)-O(7) 180.0(4)
Mn(3)-O(4) 2.245(7)*2	P(3)-O(9) 1.552(8)	O(2)-Mn(2)-O(4) 87.4(3)	
	P(3)-O(8) 1.559(7)	O(12)-Mn(2)-O(6) 93.0(3)	O(7)-P(1)-O(5) 112.0(4)
Mn(4)-O(1) 2.108(7)		O(2)-Mn(2)-O(6) 87.0(3)	O(7)-P(1)-O(4) 112.3(4)
Mn(4)-O(10) 2.110(7)		O(4)-Mn(2)-O(6) 173.5(3)	O(5)-P(1)-O(4) 109.2(4)
Mn(4)-O(5) 2.127(7)		O(12)-Mn(2)-O(3) 91.3(3)	O(7)-P(1)-O(1) 109.4(4)
Mn(4)-O(2) 2.180(7)		O(2)-Mn(2)-O(3) 159.0(3)	O(5)-P(1)-O(1) 111.8(4)
Mn(4)-O(8) 2.234(7)		O(4)-Mn(2)-O(3) 92.8(3)	O(4)-P(1)-O(1) 101.7(4)
		O(6)-Mn(2)-O(3) 93.6(3)	
Mn(5)-O(11) 2.094(7)*2			O(3)-P(2)-O(6) 112.9(4)
Mn(5)-O(7) 2.101(7)*2		O(9)-Mn(3)-O(9) 81.0(4)	O(3)-P(2)-O(11) 106.8(4)
		O(9)-Mn(3)-O(1) 143.7(3)	O(6)-P(2)-O(11) 111.6(4)
		O(9)-Mn(3)-O(1) 87.3(3)	O(3)-P(2)-O(10) 110.8(4)
		O(1)-Mn(3)-O(1) 120.2(4)	O(6)-P(2)-O(10) 102.0(4)
		O(9)-Mn(3)-O(4) 90.0(3)	O(11)-P(2)-O(10) 112.8(4)
		O(9)-Mn(3)-O(4) 117.8(3)	
		O(1)-Mn(3)-O(4) 65.3(3)	O(12)-P(3)-O(2) 106.1(4)
		O(1)-Mn(3)-O(4) 96.4(3)	O(12)-P(3)-O(9) 112.2(4)
		O(4)-Mn(3)-O(4) 144.2(4)	O(2)-P(3)-O(9) 109.0(4)
			O(12)-P(3)-O(8) 111.7(4)
		O(1)-Mn(4)-O(10) 177.5(3)	O(2)-P(3)-O(8) 109.9(4)
		O(1)-Mn(4)-O(5) 89.4(3)	O(9)-P(3)-O(8) 107.9(4)
		O(10)-Mn(4)-O(5) 93.0(3)	

Table 3.4: Selected bond distances and bond angles for compounds **1**-**9** cont..

Bond Distances		Bond Angles	
		$KNa_3Fe_7(PO_4)_6$, **4**	
Fe(1)-O(9) 2.099(3)*2	P(1)-O(7) 1.525(3)	O(9)-Fe(1)-O(9) 80.8(2)	O(5)-Fe(4)-O(2) 131.9(1)
Fe(1)-O(10) 2.144(3)*2	P(1)-O(5) 1.526(3)	O(9)-Fe(1)-O(10) 90.5(1)	O(1)-Fe(4)-O(2) 89.4(1)
Fe(1)-O(6) 2.248(3)*2	P(1)-O(4) 1.542(3)	O(9)-Fe(1)-O(10) 117.8(1)	O(10)-Fe(4)-O(2) 88.0(1)
	P(1)-O(1) 1.553(3)	O(10)-Fe(1)-O(10) 143.7(2)	O(5)-Fe(4)-O(8) 112.2(1)
Fe(2)-O(2) 2.044(3)		O(9)-Fe(1)-O(6) 145.2(1)	O(1)-Fe(4)-O(8) 92.7(1)
Fe(2)-O(12) 2.071(3)	P(2)-O(3) 1.533(3)	O(9)-Fe(1)-O(6) 87.9(1)	O(10)-Fe(4)-O(8) 89.3(1)
Fe(2)-O(4) 2.110(3)	P(2)-O(11) 1.535(3)	O(10)-Fe(1)-O(6) 66.0(1)	O(2)-Fe(4)-O(8) 115.9(1)
Fe(2)-O(6) 2.110(3)	P(2)-O(6) 1.537(3)	O(10)-Fe(1)-O(6) 95.0(1)	
Fe(2)-O(3) 2.139(3)	P(2)-O(10) 1.543(3)	O(6)-Fe(1)-O(6) 118.0(2)	O(7)-Fe(5)-O(7) 180.0(1)
			O(7)-Fe(5)-O(11) 92.0(1)
Fe(3)-O(9) 2.108(3)*2	P(3)-O(12) 1.514(3)	O(2)-Fe(2)-O(12) 112.5(1)	O(7)-Fe(5)-O(11) 88.0(1)
Fe(3)-O(1) 2.131(3)*2	P(3)-O(8) 1.546(3)	O(2)-Fe(2)-O(4) 89.0(1)	O(11)-Fe(5)-O(11)180.0(2)
Fe(3)-O(4) 2.198(3)*2	P(3)-O(2) 1.549(3)	O(12)-Fe(2)-O(4) 84.4(1)	
	P(3)-O(9) 1.549(3)	O(2)-Fe(2)-O(6) 87.1(1)	O(7)-P(1)-O(5) 112.0(2)
Fe(4)-O(5) 2.042(3)		O(12)-Fe(2)-O(6) 91.1(1)	O(7)-P(1)-O(4) 113.4(2)
Fe(4)-O(1) 2.083(3)		O(4)-Fe(2)-O(6) 172.4(1)	O(5)-P(1)-O(4) 108.8(2)
Fe(4)-O(10) 2.084(3)		O(2)-Fe(2)-O(3) 158.2(1)	O(7)-P(1)-O(1) 108.6(2)
Fe(4)-O(2) 2.116(3)		O(12)-Fe(2)-O(3) 89.4(1)	O(5)-P(1)-O(1) 111.8(2)
Fe(4)-O(8) 2.148(3)		O(4)-Fe(2)-O(3) 93.1(1)	O(4)-P(1)-O(1) 101.8(2)
		O(6)-Fe(2)-O(3) 92.9(1)	
Fe(5)-O(7) 2.022(3)*2			O(3)-P(2)-O(11) 105.7(2)
Fe(5)-O(11) 2.059(3) *2		O(9)-Fe(3)-O(9) 80.4(2)	O(3)-P(2)-O(6) 113.4(2)
		O(9)-Fe(3)-O(1) 88.4(1)	O(11)-P(2)-O(6) 112.4(2)
		O(9)-Fe(3)-O(1) 148.4(1)	O(3)-P(2)-O(10) 109.4(2)
		O(1)-Fe(3)-O(1) 114.7(2)	O(11)-P(2)-O(10) 14.3(2)
		O(9)-Fe(3)-O(4) 90.5(1)	O(6)-P(2)-O(10) 102.0(2)
		O(1)-Fe(3)-O(4) 94.8(1)	
		O(1)-Fe(3)-O(4) 67.4(1)	O(12)-P(3)-O(8) 111.0(2)
		O(9)-Fe(3)-O(4) 114.6(1)	O(12)-P(3)-O(2) 105.8(2)
		O(4)-Fe(3)-O(4) 147.6(2)	O(8)-P(3)-O(2) 110.9(2)
			O(12)-P(3)-O(9) 113.1(2)
		O(5)-Fe(4)-O(1) 88.1(1)	O(8)-P(3)-O(9) 107.8(2)
		O(5)-Fe(4)-O(10) 93.0(1)	O(2)-P(3)-O(9) 108.2(2)
		O(1)-Fe(4)-O(10)177.2(1)	
		$RbNa_3Fe_7(PO_4)_6$, **5**	
Fe(1)-O(9) 2.096(3)*2	P(1)-O(7) 1.526(3)	O(9)-Fe(1)-O(9) 80.5(2)	O(5)-Fe(4)-O(2) 129.9(1)
Fe(1)-O(10) 2.139(3)*2	P(1)-O(5) 1.529(3)	O(9)-Fe(1)-O(10) 118.4(1)	O(10)-Fe(4)-O(2) 87.9(1)
Fe(1)-O(6) 2.257(3)*2	P(1)-O(4) 1.539(3)	O(9)-Fe(1)-O(10) 91.0(1)	O(1)-Fe(4)-O(2) 89.6(1)
	P(1)-O(1) 1.548(3)	O(10)-Fe(1)-O(10) 142.2(2)	O(5)-Fe(4)-O(8) 114.1(1)
Fe(2)-O(2) 2.049(3)		O(9)-Fe(1)-O(6) 87.1(1)	O(10)-Fe(4)-O(8) 89.3(1)
Fe(2)-O(12) 2.067(3)	P(2)-O(3) 1.529(3)	O(9)-Fe(1)-O(6) 144.2(1)	O(1)-Fe(4)-O(8) 92.4(1)
Fe(2)-O(4) 2.097(3)	P(2)-O(11) 1.532(3)	O(10)-Fe(1)-O(6) 65.7(1)	O(2)-Fe(4)-O(8) 116.0(1)
Fe(2)-O(6) 2.098(3)	P(2)-O(6) 1.535(3)	O(10)-Fe(1)-O(6) 95.1(1)	
Fe(2)-O(3) 2.142(3)	P(2)-O(10) 1.540(3)	O(6)-Fe(1)-O(6) 120.2(1)	O(7)-Fe(5)-O(7) 180.0
			O(7)-Fe(5)-O(11) 88.3(1)
Fe(3)-O(9) 2.108(3)*2	P(3)-O(12) 1.516(3)	O(2)-Fe(2)-O(12) 112.30(1)	O(7)-Fe(5)-O(11) 91.7(1)
Fe(3)-O(1) 2.138(3)*2	P(3)-O(8) 1.543(3)	O(2)-Fe(2)-O(4) 89.1(1)	O(11)-Fe(5)-O(11) 180.0(2)
Fe(3)-O(4) 2.194(3)*2	P(3)-O(2) 1.551(3)	O(12)-Fe(2)-O(4) 84.8(1)	
	P(3)-O(9) 1.552(3)	O(2)-Fe(2)-O(6) 86.7(1)	O(7)-P(1)-O(5) 111.4(2)
Fe(4)-O(5) 2.048(3)		O(12)-Fe(2)-O(6) 91.9(1)	O(7)-P(1)-O(4) 113.2(2)
Fe(4)-O(10) 2.082(3)		O(4)-Fe(2)-O(6) 173.2(1)	O(5)-P(1)-O(4) 109.2(2)
Fe(4)-O(1) 2.082(3)		O(2)-Fe(2)-O(3) 158.9(1)	O(7)-P(1)-O(1) 109.4(2)
Fe(4)-O(2) 2.123(3)		O(12)-Fe(2)-O(3) 88.8(1)	O(5)-P(1)-O(1) 111.8(2)

Table 3.4: Selected bond distances and bond angles for compounds **1**-**9** cont..

Bond Distances		Bond Angles	
		$RbNa_3Fe_7(PO_4)_6$, **5** Cont.	
Fe(4)-O(8) 2.152(3)		O(4)-Fe(2)-O(3) 92.4(1)	O(4)-P(1)-O(1) 101.6(1)
		O(6)-Fe(2)-O(3) 93.4(1)	
Fe(5)-O(7) 2.014(3)*2			O(3)-P(2)-O(11) 106.2(2)
Fe(5)-O(11) 2.059(3)*2		O(9)-Fe(3)-O(9) 80.0(2)	O(3)-P(2)-O(6) 112.9(2)
		O(9)-Fe(3)-O(1) 88.0(1)	O(11)-P(2)-O(6) 112.4(2)
		O(9)-Fe(3)-O(1) 147.2(1)	O(3)-P(2)-O(10) 109.7(2)
		O(1)-Fe(3)-O(1) 116.6(2)	O(11)-P(2)-O(10) 113.9(2)
		O(9)-Fe(3)-O(4) 114.9(1)	O(6)-P(2)-O(10) 101.9(1)
		O(9)-Fe(3)-O(4)90.5(1)	
		O(1)-Fe(3)-O(4) 67.01(9)	O(12)-P(3)-O(8) 111.2(2)
		O(1)-Fe(3)-O(4) 95.5(1)	O(12)-P(3)-O(2) 106.0(2)
		O(4)-Fe(3)-O(4) 147.4(2)	O(8)-P(3)-O(2) 110.6(2)
			O(12)-P(3)-O(9) 112.8(2)
		O(5)-Fe(4)-O(10) 93.0(1)	O(8)-P(3)-O(9) 108.0(2)
		O(5)-Fe(4)-O(1) 88.1(1)	O(2)-P(3)-O(9) 108.3(1)
		O(10)-Fe(4)-O(1) 177.4(1)	
		$CsNa_3Fe_7(PO_4)_6$, **6**	
Fe(1)-O(9) 2.098(4)*2	P(1)-O(7) 1.519(4)	O(9)-Fe(1)-O(9) 79.9(2)	O(5)-Fe(4)-O(2) 127.2(2)
Fe(1)-O(10) 2.145(4)*2	P(1)-O(5) 1.527(4)	O(9)-Fe(1)-O(10) 92.2(2)	O(10)-Fe(4)-O(2) 87.5(1)
Fe(1)-O(6) 2.298(4)*2	P(1)-O(1) 1.543(4)	O(9)-Fe(1)-O(10) 118.2(2)	O(1)-Fe(4)-O(2) 89.6(1)
	P(1)-O(4) 1.545(4)	O(10)-Fe(1)-O(10) 141.2(2)	O(5)-Fe(4)-O(8) 117.6(2)
Fe(2)-O(12) 2.052(4)		O(9)-Fe(1)-O(6) 142.9(2)	O(10)-Fe(4)-O(8) 89.7(2)
Fe(2)-O(2) 2.056(4)	P(2)-O(3) 1.524(4)	O(9)-Fe(1)-O(6) 85.8(2)	O(1)-Fe(4)-O(8) 91.9(2)
Fe(2)-O(6) 2.081(4)	P(2)-O(11) 1.527(4)	O(10)-Fe(1)-O(6) 64.9(1)	O(2)-Fe(4)-O(8) 115.2(1)
Fe(2)-O(4) 2.080(4)	P(2)-O(6) 1.529(3)	O(10)-Fe(1)-O(6) 96.3(1)	
Fe(2)-O(3) 2.133(4)	P(2)-O(10) 1.542(4)	O(6)-Fe(1)-O(6) 123.6(2)	O(7)-Fe(5)-O(7) 180.0
			O(7)-Fe(5)-O(11) 92.0(2)
Fe(3)-O(9) 2.104(4)*2	P(3)-O(12) 1.527(4)	O(12)-Fe(2)-O(2) 112.1(1)	O(7)-Fe(5)-O(11) 88.0(2)
Fe(3)-O(1) 2.163(4)*2	P(3)-O(8) 1.539(4)	O(12)-Fe(2)-O(6) 93.4(2)	O(11)-Fe(5)-O(11) 180.00(1)
Fe(3)-O(4) 2.198(4)*2	P(3)-O(2) 1.550(4)	O(2)-Fe(2)-O(6) 86.7(1)	
	P(3)-O(9) 1.555(4)	O(12)-Fe(2)-O(4) 85.5(2)	O(7)-P(1)-O(5) 111.1(2)
Fe(4)-O(5) 2.074(4)		O(2)-Fe(2)-O(4) 89.2(1)	O(7)-P(1)-O(1) 110.4(2)
Fe(4)-O(10) 2.096(4)		O(6)-Fe(2)-O(4) 175.0(2)	O(5)-P(1)-O(1) 111.8(2)
Fe(4)-O(1) 2.098(4)		O(12)-Fe(2)-O(3) 88.3(2)	O(7)-P(1)-O(4) 112.4(2)
Fe(4)-O(2) 2.149(4)		O(2)-Fe(2)-O(3) 159.6(1)	O(5)-P(1)-O(4) 109.6(2)
Fe(4)-O(8) 2.158(4)		O(6)-Fe(2)-O(3) 92.6(1)	O(1)-P(1)-O(4) 101.3(2)
		O(4)-Fe(2)-O(3) 92.2(1)	
Fe(5)-O(7) 2.016(3)*2			O(3)-P(2)-O(11) 106.4(2)
Fe(5)-O(11) 2.058(4)*2		O(9)-Fe(3)-O(9) 79.6(2)	O(3)-P(2)-O(6) 112.5(2)
		O(9)-Fe(3)-O(1) 87.1(2)	O(11)-P(2)-O(6) 112.5(2)
		O(9)-Fe(3)-O(1) 145.6(2)	O(3)-P(2)-O(10) 110.1(2)
		O(1)-Fe(3)-O(1) 119.5(2)	O(11)-P(2)-O(10) 113.4(2)
		O(9)-Fe(3)-O(4) 115.6(2)	O(6)-P(2)-O(10) 102.0(2)
		O(9)-Fe(3)-O(4) 91.0(2)	
		O(1)-Fe(3)-O(4) 66.4(1)	O(12)-P(3)-O(8) 110.9(2)
		O(1)-Fe(3)-O(4) 96.0(1)	O(12)-P(3)-O(2) 105.9(2)
		O(4)-Fe(3)-O(4) 145.9(2)	O(8)-P(3)-O(2) 110.4(2)
			O(12)-P(3)-O(9) 112.4(2)
		O(5)-Fe(4)-O(10) 92.6(2)	O(8)-P(3)-O(9) 108.4(2)
		O(5)-Fe(4)-O(1) 88.8(1)	O(2)-P(3)-O(9) 108.8(2)
		O(10)-Fe(4)-O(1) 177.1(2)	

Table 3.4: Selected bond distances and bond angles for compounds **1**-**9** cont..

Bond Distances		Bond Angles	
		$KNa_3Co_7(PO_4)_6$, **7**	
Co(1)-O(9) 2.060(3)*2	P(1)-O(7) 1.521(3)	O(9)-Co(1)-O(9) 82.6(1)	O(5)-Co(4)-O(2) 131.4(1)
Co(1)-O(10) 2.092(3)*2	P(1)-O(5) 1.529(3)	O(9)-Co(1)-O(10) 117.4(1)	O(1)-Co(4)-O(2) 88.5(1)
Co(1)-O(6) 2.250(3)*2	P(1)-O(4) 1.546(3)	O(9)-Co(1)-O(10) 91.5(1)	O(10)-Co(4)-O(2) 87.7(1)
	P(1)-O(1) 1.556(3)	O(10)-Co(1)-O(10) 142.3(2)	O(5)-Co(4)-O(8) 110.2(1)
Co(2)-O(2) 2.032(3)		O(9)-Co(1)-O(6) 86.7(1)	O(1)-Co(4)-O(8) 92.8(1)
Co(2)-O(12) 2.048(3)	P(2)-O(3) 1.528(3)	O(9)-Co(1)-O(6) 147.7(1)	O(10)-Co(4)-O(8) 89.8(1)
Co(2)-O(4) 2.057(2)	P(2)-O(11) 1.529(3)	O(10)-Co(1)-O(6) 66.7(1)	O(2)-Co(4)-O(8) 118.5(1)
Co(2)-O(6) 2.078(3)	P(2)-O(6) 1.536(3)	O(10)-Co(1)-O(6) 93.2(1)	
Co(2)-O(3) 2.098(3)	P(2)-O(10) 1.547(3)	O(6)-Co(1)-O(6) 116.7(1)	O(11)-Co(5)-O(11) 180.0(2)
			O(11)-Co(5)-O(7) 88.4(1)
Co(3)-O(9) 2.074(2)*2	P(3)-O(12) 1.510(3)	O(2)-Co(2)-O(12) 110.5(1)	O(11)-Co(5)-O(7) 91.6(1)
Co(3)-O(1) 2.110(2)*2	P(3)-O(8) 1.545(3)	O(2)-Co(2)-O(4) 88.2(1)	O(7)-Co(5)-O(7) 180.0
Co(3)-O(4) 2.166(3)*2	P(3)-O(2) 1.546(3)	O(12)-Co(2)-O(4) 84.3(1)	
	P(3)-O(9) 1.559(3)	O(2)-Co(2)-O(6) 87.1(1)	O(7)-P(1)-O(5) 112.0(2)
Co(4)-O(5) 2.017(3)		O(12)-Co(2)-O(6) 89.6(1)	O(7)-P(1)-O(4) 113.7(2)
Co(4)-O(1) 2.039(3)		O(4)-Co(2)-O(6) 170.5(1)	O(5)-P(1)-O(4) 108.3(2)
Co(4)-O(10) 2.054(3)		O(2)-Co(2)-O(3) 159.0(1)	O(7)-P(1)-O(1) 108.7(2)
Co(4)-O(2) 2.093(3)		O(12)-Co(2)-O(3) 90.6(1)	O(5)-P(1)-O(1) 112.1(2)
Co(4)-O(8) 2.127(3)		O(4)-Co(2)-O(3) 94.4(1)	O(4)-P(1)-O(1) 101.6(1)
		O(6)-Co(2)-O(3) 92.94(1)	
Co(5)-O(11) 2.011(3)*2			O(3)-P(2)-O(11) 105.9(2)
Co(5)-O(7) 2.028(3)*2		O(9)-Co(3)-O(9) 82.0(1)	O(3)-P(2)-O(6) 113.1(2)
		O(9)-Co(3)-O(1) 86.9(1)	O(11)-P(2)-O(6) 112.8(2)
		O(9)-Co(3)-O(1) 150.7(1)	O(3)-P(2)-O(10) 109.6(2)
		O(1)-Co(3)-O(1) 114.5(1)	O(11)-P(2)-O(10) 114.0(2)
		O(9)-Co(3)-O(4) 114.0(1)	O(6)-P(2)-O(10) 101.7(1)
		O(9)-Co(3)-O(4) 91.6(1)	
		O(1)-Co(3)-O(4) 68.42(9)	O(12)-P(3)-O(8) 110.5(2)
		O(1)-Co(3)-O(4) 93.3(1)	O(12)-P(3)-O(2) 106.1(2)
		O(4)-Co(3)-O(4) 146.6(1)	O(8)-P(3)-O(2) 111.6(2)
			O(12)-P(3)-O(9) 113.3(2)
		O(5)-Co(4)-O(1) 88.8(1	O(8)-P(3)-O(9) 107.2(2)
		O(5)-Co(4)-O(10) 93.0(1)	O(2)-P(3)-O(9) 108.1(1)
		O(1)-Co(4)-O(10) 176.1(1)	
		$RbNa_3Co_7(PO_4)_6$, **8**	
Co(1)-O(9) 2.052(3)*2	P(1)-O(7) 1.523(3)	O(9)-Co(1)-O(9) 82.6(2)	O(5)-Co(4)-O(2) 129.7(1)
Co(1)-O(10) 2.093(3)*2	P(1)-O(5) 1.526(3)	O(9)-Co(1)-O(10) 118.2(1)	O(1)-Co(4)-O(2) 88.8(1)
Co(1)-O(6) 2.260(3)*2	P(1)-O(4) 1.543(3)	O(9)-Co(1)-O(10) 91.8(1)	O(10)-Co(4)-O(2) 87.6(1)
	P(1)-O(1) 1.556(3)	O(10)-Co(1)-O(10) 140.8(2)	O(5)-Co(4)-O(8) 111.8(1)
Co(2)-O(2) 2.041(3)		O(9)-Co(1)-O(6) 86.0(1)	O(1)-Co(4)-O(8) 92.1(1)
Co(2)-O(12) 2.044(3)	P(2)-O(3) 1.531(3)	O(9)-Co(1)-O(6) 146.8(1)	O(10)-Co(4)-O(8) 89.9(1)
Co(2)-O(4) 2.053(3)	P(2)-O(6) 1.533(3)	O(10)-Co(1)-O(6) 66.5(1)	O(2)-Co(4)-O(8) 118.5(1)
Co(2)-O(6) 2.067(3)	P(2)-O(11) 1.534(3)	O(10)-Co(1)-O(6)93.2(1)	
Co(2)-O(3) 2.092(3)	P(2)-O(10) 1.549(3)	O(6)-Co(1)-O(6) 118.6(2)	O(11)-Co(5)-O(11) 180.0(2)
			O(11)-Co(5)-O(7) 91.9(1)
Co(3)-O(9) 2.081(3)*2	P(3)-O(12) 1.516(3)	O(2)-Co(2)-O(12) 110.4(1)	O(11)-Co(5)-O(7) 88.1(1)
Co(3)-O(1) 2.119(3)*2	P(3)-O(8) 1.544(3)	O(2)-Co(2)-O(4) 88.1(1)	O(7)-Co(5)-O(7) 180.0
Co(3)-O(4) 2.167(3)*2	P(3)-O(2) 1.548(3)	O(12)-Co(2)-O(4) 84.6(1)	
	P(3)-O(9) 1.562(3)	O(2)-Co(2)-O(6) 86.8(1)	O(7)-P(1)-O(5) 111.6(2)
Co(4)-O(5) 2.034(3)		O(12)-Co(2)-O(6) 90.6(1)	O(7)-P(1)-O(4) 113.2(2)
Co(4)-O(1) 2.042(3)		O(4)-Co(2)-O(6) 171.4(1)	O(5)-P(1)-O(4)108.8(2)
Co(4)-O(10) 2.055(3)		O(2)-Co(2)-O(3) 159.7(1)	O(7)-P(1)-O(1) 109.4(2)
Co(4)-O(2) 2.097(3)		O(12)-Co(2)-O(3) 90.0(1)	O(5)-P(1)-O(1) 112.0(2)
		O(4)-Co(2)-O(3) 93.8(1)	O(4)-P(1)-O(1) 101.4(2)

Table 3.4: Selected bond distances and bond angles for compounds **1**-**9** cont..

Bond Distances		Bond Angles	
		$RbNa_3Co_7(PO_4)_6$, **8** Cont.	
Co(4)-O(8) 2.135(3)		O(6)-Co(2)-O(3) 93.4(1)	O(3)-P(2)-O(6) 112.9(2)
			O(3)-P(2)-O(11) 105.7(2)
Co(5)-O(11) 2.012(3)*2		O(9)-Co(3)-O(9) 81.2(2)	O(6)-P(2)-O(11) 112.8(2)
Co(5)-O(7) 2.019(3)*2		O(9)-Co(3)-O(1) 86.6(1)	O(3)-P(2)-O(10) 110.0(2)
		O(9)-Co(3)-O(1) 149.3(1)	O(6)-P(2)-O(10) 101.8(2)
		O(1)-Co(3)-O(1) 116.4(2)	O(11)-P(2)-O(10) 113.8(2)
		O(9)-Co(3)-O(4) 114.5(1)	
		O(9)-Co(3)-O(4) 91.6(1)	O(12)-P(3)-O(8) 110.8(2)
		O(1)-Co(3)-O(4) 68.0(1)	O(12)-P(3)-O(2) 106.1(2)
		O(1)-Co(3)-O(4) 93.8(1)	O(8)-P(3)-O(2) 111.5(2)
		O(4)-Co(3)-O(4) 146.0(2)	O(12)-P(3)-O(9) 112.9(2)
			O(8)-P(3)-O(9) 107.3(2)
		O(5)-Co(4)-O(1) 88.9(1)	O(2)-P(3)-O(9) 108.2(2)
		O(5)-Co(4)-O(10) 93.2(1)	
		O(1)-Co(4)-O(10)176.4(1)	
		$CsNa_3Co_7(PO_4)_6$, **9**	
Co(1)-O(9) 2.043(6)*2	P(1)-O(7) 1.522(6)	O(9)-Co(1)-O(9) 81.5(3)	O(1)-Co(4)-O(2) 89.2(2)
Co(1)-O(10) 2.094(6)*2	P(1)-O(5) 1.533(6)	O(9)-Co(1)-O(10) 118.7(2)	O(5)-Co(4)-O(2) 127.0(2)
Co(1)-O(6) 2.269(6)*2	P(1)-O(4) 1.547(6)	O(9)-Co(1)-O(10) 93.2(2)	O(10)-Co(4)-O(2) 87.3(2)
	P(1)-O(1) 1.555(6)	O(10)-Co(1)-O(10) 138.5(3)	O(1)-Co(4)-O(8) 91.2(2)
Co(2)-O(12) 2.042(6)		O(9)-Co(1)-O(6) 85.7(2)	O(5)-Co(4)-O(8) 114.9(2)
Co(2)-O(2) 2.048(5)	P(2)-O(3) 1.522(6)	O(9)-Co(1)-O(6) 146.0(2)	O(10)-Co(4)-O(8) 90.2(2)
Co(2)-O(4) 2.059(6)	P(2)-O(6) 1.528(6)	O(10)-Co(1)-O(6) 65.8(2)	O(2)-Co(4)-O(8) 118.2(2)
Co(2)-O(6) 2.064(6)	P(2)-O(11) 1.536(6)	O(10)-Co(1)-O(6) 93.2(2)	
Co(2)-O(3) 2.096(6)	P(2)-O(10) 1.541(6)	O(6)-Co(1)-O(6) 120.3(3)	O(11)-Co(5)-O(11) 180.0(4)
			O(11)-Co(5)-O(7) 88.0(2)
Co(3)-O(9) 2.076(5)*2	P(3)-O(12) 1.517(6)	O(12)-Co(2)-O(2) 110.5(2)	O(11)-Co(5)-O(7) 92.0(2)
Co(3)-O(4) 2.141(5)*2	P(3)-O(8) 1.552(6)	O(12)-Co(2)-O(4) 84.7(2)	O(7)-Co(5)-O(7) 180.0(3)
Co(3)-O(1) 2.141(5)*2	P(3)-O(2) 1.554(6)	O(2)-Co(2)-O(4) 88.1(2)	
	P(3)-O(9) 1.569(6)	O(12)-Co(2)-O(6) 91.7(2)	O(7)-P(1)-O(5) 111.1(3)
Co(4)-O(1) 2.043(6)		O(2)-Co(2)-O(6) 86.2(2)	O(7)-P(1)-O(4) 112.6(3)
Co(4)-O(5) 2.045(6)		O(4)-Co(2)-O(6) 171.7(2)	O(5)-P(1)-O(4) 109.5(3)
Co(4)-O(10) 2.061(6)		O(12)-Co(2)-O(3) 89.2(2)	O(7)-P(1)-O(1) 110.8(3)
Co(4)-O(2) 2.099(6)		O(2)-Co(2)-O(3) 160.3(2)	O(5)-P(1)-O(1) 112.1(3)
Co(4)-O(8) 2.139(6)		O(4)-Co(2)-O(3) 93.6(2)	O(4)-P(1)-O(1) 100.4(3)
		O(6)-Co(2)-O(3) 93.8(2)	
Co(5)-O(11) 2.006(6)*2			O(3)-P(2)-O(6) 112.7(3)
Co(5)-O(7) 2.009(6)*2		O(9)-Co(3)-O(9) 79.9(3)	O(3)-P(2)-O(11) 106.4(3)
		O(9)-Co(3)-O(4) 92.3(2)	O(6)-P(2)-O(11) 112.9(3)
		O(9)-Co(3)-O(4) 115.2(2)	O(3)-P(2)-O(10) 110.3(3)
		O(4)-Co(3)-O(4) 144.6(3)	O(6)-P(2)-O(10) 101.4(3)
		O(9)-Co(3)-O(1) 147.8(2)	O(11)-P(2)-O(10) 113.2(3)
		O(9)-Co(3)-O(1) 86.2(2)	
		O(4)-Co(3)-O(1) 67.6(2)	O(12)-P(3)-O(8) 110.8(3)
		O(4)-Co(3)-O(1) 94.1(2)	O(12)-P(3)-O(2) 106.5(3)
		O(1)-Co(3)-O(1) 118.9(3)	O(8)-P(3)-O(2) 111.3(3)
			O(12)-P(3)-O(9) 112.8(3)
		O(1)-Co(4)-O(5) 89.2(2)	O(8)-P(3)-O(9) 106.9(3)
		O(1)-Co(4)-O(10) 176.4(2)	O(2)-P(3)-O(9) 108.6(3)
		O(5)-Co(4)-O(10) 93.2(2)	

Results and Discussion

Nine new transition metal(II) phosphate compounds have been synthesized by conventional solid-state methods. Sizable single crystals of each phase were grown in molten-salt media. The title compounds, $ANa_3M_7(PO_4)_6$ (where A = K, Rb, Cs; M = Mn, Fe, Co), crystallize in a monoclinic spacegroup, *C2/c* (no. 15), Z = 4. The crystallographic data for these compounds, all of which are isostructural, is presented in Table 3.1.

Figure 3.2 shows the volumes of all nine derivatives plotted as a function of increasing atomic number. The cell volume follows the expected trend by decreasing with the substitution of first-row transition metals from left to right. As expected, the volumes increase as the size of the A-site cation is increased. This trend, however, is not observed for the volumes of $KNa_3Mn_7(PO_4)_6$, **1**, and $RbNa_3Mn_7(PO_4)_6$, **2**, which are 2101.6(7)Å^3 and 2100.1(7)Å^3 respectively. Evaluation of more single crystals of the Mn derivatives, **1**-**3**, has revealed slight variation in the unit cell volume, ±10Å^3. Comparisons between the unit cell parameters of various single crystals of **1**-**3** are shown in Table 3.5. Darker crystals of **1**-**3** (A/Mn) have consistently shown slightly smaller volumes than lighter ones. It is thought that the smaller volumes are resulting from possible defects related to cation non-stoichiometry (*e.g.*, $A_{1-\delta}Na_3Mn_7(PO_4)_6$ and $ANa_3Mn_{7-\delta}(PO_4)_6$), within the crystal structures, resulting in a small amount of Mn^{3+} in the Mn^{2+} sites. Higher valent metals are smaller, possibly causing a slight reduction in the total observed unit cell volume. The hypothesis is further supported by observed variations in crystal colors for both Mn and Fe derivatives. Their colors range from red

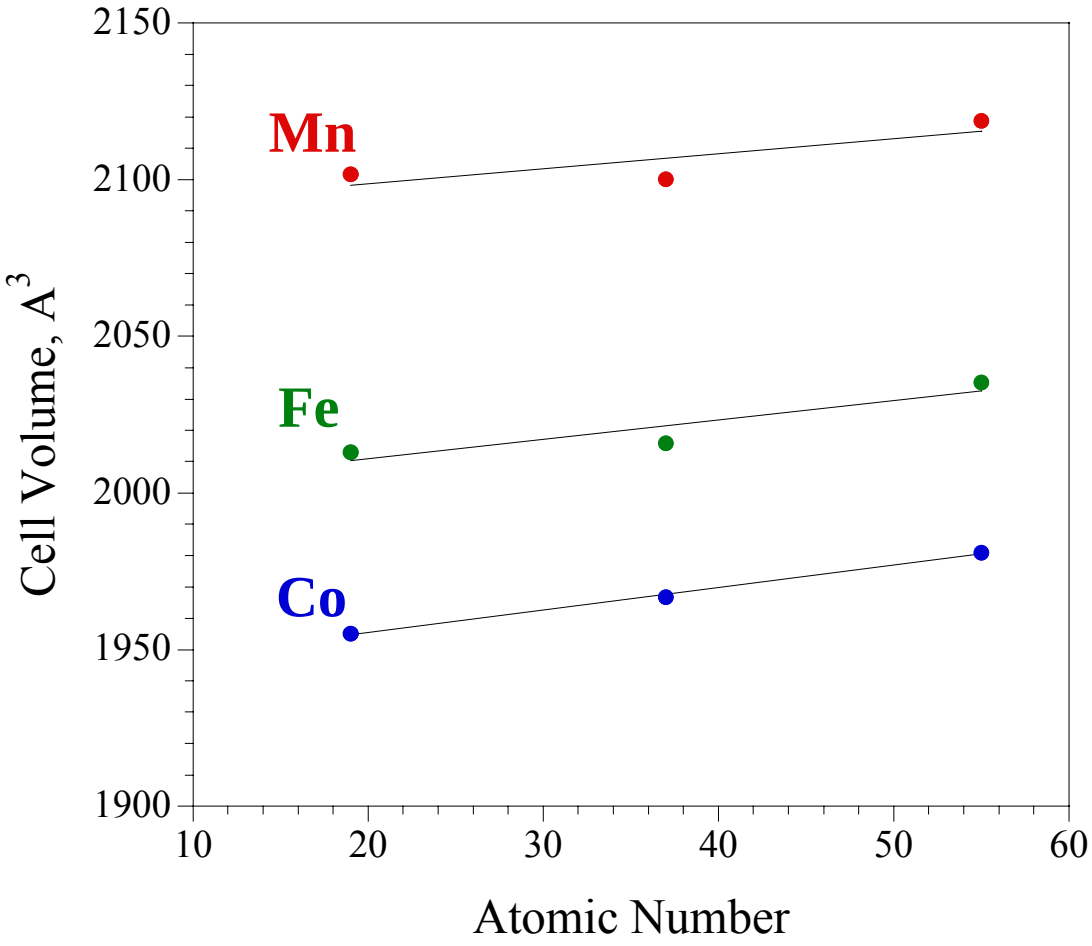

Figure 3.2: Plot of the cell volume of $ANa_3M_7(PO_4)_6$ as a function of atomic number of the A-site cation, A = K, Rb, or Cs.

Table 3.5: Comparison of unit cells from various colored single crystals of compounds **1-3**

empirical formula[a] compound	$KNa_3Mn_7(PO_4)_6$ **1**	$KNa_3Mn_7(PO_4)_6$ **1**	$RbNa_3Mn_7(PO_4)_6$ **2**	$RbNa_3Mn_7(PO_4)_6$ **2**	$CsNa_3Mn_7(PO_4)_6$ **3**	$CsNa_3Mn_7(PO_4)_6$ **3**
Color shape	dark red multifaceted	light red multifaceted	dark red multifaceted	light orange rectangular	dark red multifaceted	Orange, rectangular
crystal size (mm)	0.43 × 0.27 × 0.18	0.38 × 0.19 × 0.19	0.08 × 0.05 × 0.03	0.47 × 0.23 × 0.27	0.23 × 0.19 × 0.15	0.12 × 0.07 × 0.06
formula weight (amu)	1062.47	1062.47	1108.83	1108.83	1156.27	1156.27
space group, Z	*C*2/*c* (no. 15), 4					
T, °C	25					
a, Å	13.153(3)	13.182(1)	13.130(3)	13.163(3)	13.168(3)	13.185(2)
b, Å	10.887(2	10.892(1)	10.877(2)	10.883(3)	10.915(2)	10.922(1)
c, Å	15.973(3)	15.994(2)	15.978(3)	15.976(3)	16.027(3)	16.028(2)
β, degree	113.24(3)	113.170(6)	113.02(3)	113.05(2)	113.11(3)	113.111(8)
V, Å^3	2101.6(7)	2111.3(4)	2100.1(7)	2105.9(9)	2118.8(7)	2123.1(5)

(small volume) to yellowish-orange (large volume) and dark brown (small) to yellowish-brown (large) for Mn and Fe respectively. These consistent variations in color can help explain the observed overlap between the volumes of compounds **1** and **2**. High-spin octahedral Mn^{3+}, d^4, (also for Fe^{2+}, d^6) can have *d-d* transitions in the visible range, while high-spin octahedral Mn^{2+}, d^5, (also for Fe^{3+}) is expected to lack visible color, a result of spin-forbidden electronic transitions. It is thought that single crystals with small amounts of Mn^{3+} defects, or, by the same token, those lacking Fe^{3+} defects, could result in darker crystal color.

Variations in crystal color have been more frequently observed for the Mn compounds. This observation can be explained through the synthesis, as Mn^{3+} was used as a reactant for compounds **2** and **3**, while only Mn^{2+} was used for **1.** Compound **1** could have a larger volume than **2** due to the lack of Mn^{3+} resulting in fewer defects. In the Fe reactions, only Fe^{2+} was used and, combining high-temperature and carbon coating, both of which promote reduction, leaving little room for oxidation of the Fe derivatives, **4**-**6**, rendering more uniform color and volumes of the final products. To test this hypothesis, it might be worthwhile to run the reactions for **2** and **3** with only Mn^{2+} to see if a better correlation between unit cell volume is observed for **1**-**3**.

Since compounds **1**-**9** are isostructural, the structure of $RbNa_3Fe_7(PO_4)_6$ will be discussed from this point forward. The crystal structure reveals a three-dimensional framework consisting of five unique FeO_n polyhedra (n = 4+2, 5, 5+1, 6; the second numbers represent the number of long bonds, shown as dotted lines) in each asymmetric unit, Figure 3.3. The assymetric units are interlinked at each end by PO_4 tetrahedra.

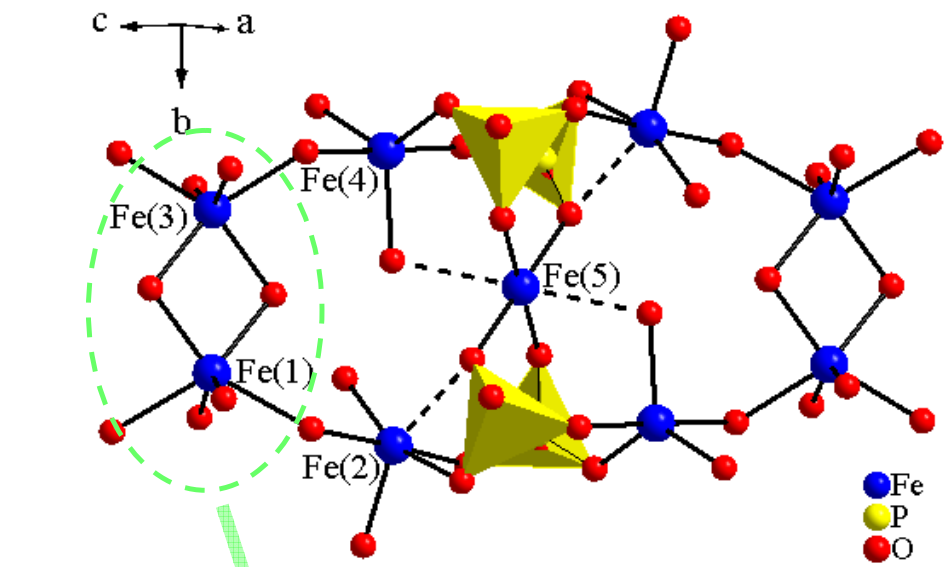

∠Fe(1)-O-Fe(3)	99.76(1)°
d_{Fe-O}	2.10~2.26 Å
$d_{Fe(1)-Fe(3)}$	3.22(3) Å

	d_{Fe-O}, Å	BVS
$Fe(1)O_6$	2.10~2.26	1.91
$Fe(2)O_5$	2.05~2.14	1.89
$Fe(3)O_6$	2.11~2.19	1.98
$Fe(4)O_5$	2.05~2.15	1.88
$Fe(5)O_4$	2.01~2.06	1.77

	d_{Fe-O}, Å	BVS
Fe(2)-O	2.48 (1x)	2.03
Fe(5)-O	2.60 (2x)	1.96

Figure 3.3: Partial structure of the Fe-O network. The solid lines represent Fe-O bonds with distances ranging from 2.01-2.26 Å. The dotted lines are 2.48 Å for Fe(2) and 2.60 Å for Fe(5). The bond valence sum (BVS) calculations show the contributions of long bonds to the overall valence of these iron sites.

When considering the long bonds of 2.48(1) Å and 2.60(1) Å, all of the Fe-O polyhedra are psuedo-ocatahedral, with the exception of Fe(4) which forms a slightly distorted trigonal bipyramid whose axial oxygen run approximately parallel with the crystallographic axis. For simplicity, the metal–oxygen network is shown as iron–oxygen chains, which are interconnected by the $Fe(5)O_4$ polyhedra and the PO_4 units. The nearest-neighbor magnetic couplings between iron(II) centers are arranged in triangular fashion, Figure 3.4, bridged by oxygen atoms. Electronically, the PO_4 groups serve to space and possibly to insulate the magnetic iron–oxygen chains.

In the overall structure, the chains of vertex-sharing FeO_n polyhedra, which run along the *a* direction, are interconnected, *via* edge sharing Fe(1) and Fe(3) polyhedra to form slabs parallel to the *ab* plane, Figure 3.5 (top). These slabs are insulated from one another *via* surrounding $(PO_4)^{3-}$ units, Figure 3.5 (bottom right). The only interslab connectivity is through long Fe(5)---O bonds, 2.60(1) Å, Figure 3.5 (bottom left). The chains consist of trinuclear units of Fe(1)/Fe(2)/Fe(4) or Fe(2)/Fe(3)/Fe(4) that can be seen in Figure 3.4 (highlighted in blue). The shorter Fe-O distances range from 2.01–2.26 Å and are comparable to the sum of the Shannon crystal radii of Fe^{2+} (0.92 A) and O^{2-} (1.21 A) of 2.13 A.[15] The Fe-O-Fe bond angles range from 108.0–128.18 and are comparable to the values commonly reported for iron phosphates.[16] Bond valence sum (BVS) calculations[17] have further supported the Fe^{2+} oxidation state as shown in Figure 3.3. As expected, the Fe···Fe distance between the edge-sharing Fe(1)O6 and Fe(3)O6 polyhedra (3.215(1)A) is shorter than those between the vertex-sharing polyhedra (3.38–3.88 A). The Fe(1)-O-Fe(3) angle found in the shared edge (99.76(1)) is also smaller

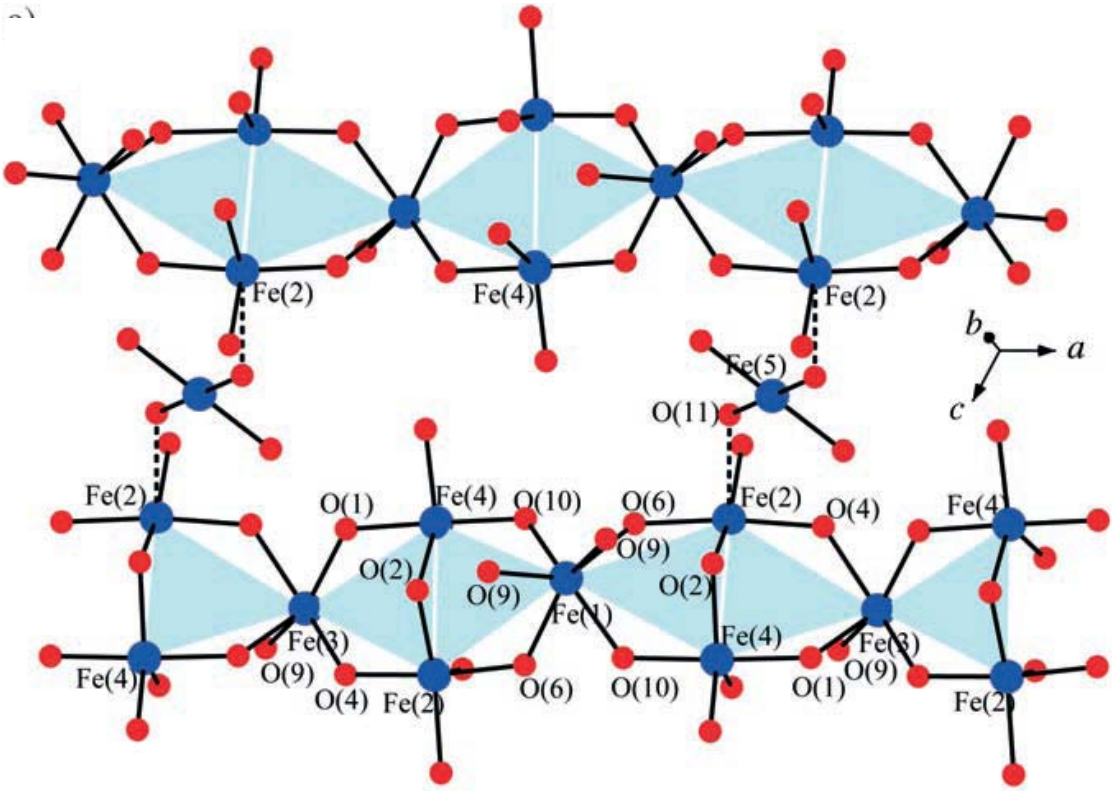

Figure 3.4: Partial structure of the Fe-O network showing fused triangular magnetic lattices (highlighted in cyan). Parallel iron(II) oxide chains are interlinked through sharing vertex oxygen atoms of the $Fe(5)O_{4+2}$ polyhedra *via* long bonds of Fe(2)-O(11).

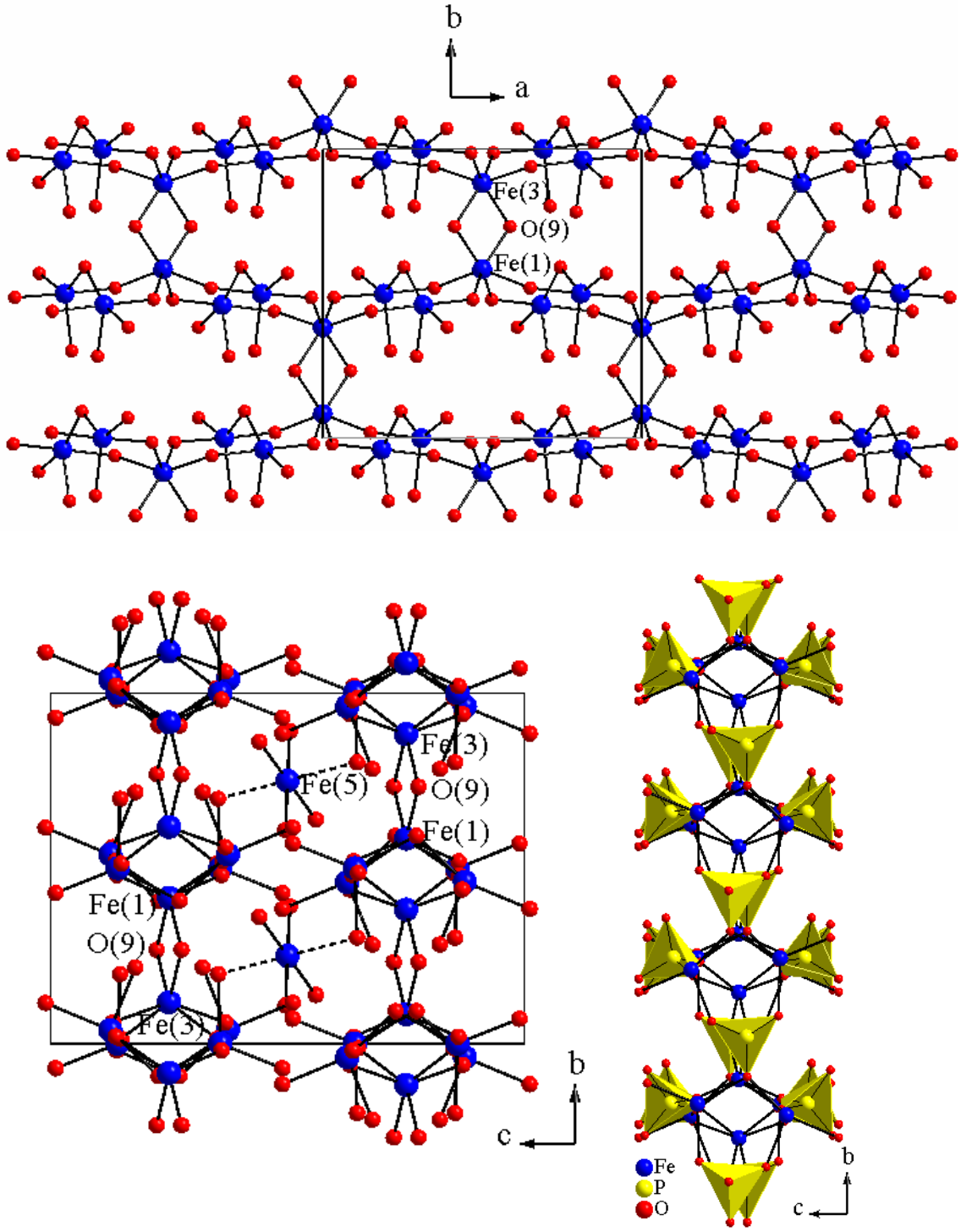

Figure 3.5: Connectivity of FeO_n polyhedra (n = 4~6) within the *ab* (top) and *bc* (bottom left) plane and with phosphate groups (bottom right).

than those through the shared vertices. Given the diversity of bond distances and angles and the multiple superexchange pathways, complex magnetic interactions are expected. The DC magnetic susceptibility of a ground powder of selected crystals of **1**-**9** was measured as a function of temperature at an applied magnetic field (H) of 100 Oe. The molar magnetic susceptibility data reveals ferrimagnetic transitions for all of the Fe^{2+} and Co^{2+} derivatives, **4**-**9**, whereas the Mn^{2+} derivatives, **1**-**3**, show only antiferromagnetic transitions at low temperature. For simplicity, Figure 3.6 shows a comparison of the inverse molar magnetic susceptibility, χ^{-1}, for only the Rb/M derivatives, **2**, **5**, and **8**. Both **5** and **8** have a characteristic decrease in the χ^{-1} indicating ferrimagnetic ordering, while the χ^{-1} for **2** shows an increase at ≈ 10 K, indicating antiferromagnetic exchange. The inset of Figure 3.6 shows the χT plotted for the Rb/M derivatives and reveals an expected decrease in the magnitude of χT as the spin state decreases from Fe^{2+}, d^6 with an S = 2, to Co^{2+}, d^7 with an S = 3/2.

The inverse of the molar magnetic susceptibilities of the Rb/M analogs, **2**, **5**, and **8** are linear over the temperature range 40–300 K. A Curie-Weiss fit to the linear portion of theses curve indicates effective magnetic moments of (μ_{eff}) of 5.91(1), 5.60(1), and 4.29(1) μ_B for compounds **2**, **5**, and **8** respectively, see Table 3.6. The μ_{eff} for the Mn derivative is proportional to the expected spin-only value equal to 5.9μ_B, whereas the μ_{eff} for both the Co and Fe derivatives are much higher than the expected spin-only values, 4.9 μ_B for a high-spin Fe^{2+} (d^6) ion and 3.9 for a high-spin Co^{2+} (d^7) ion. As found for other highly correlated high-spin Fe^{2+} and Co^{2+} systems, we expect that the orbital contributions of the ligand field play a significant role,[18] causing the difference in the

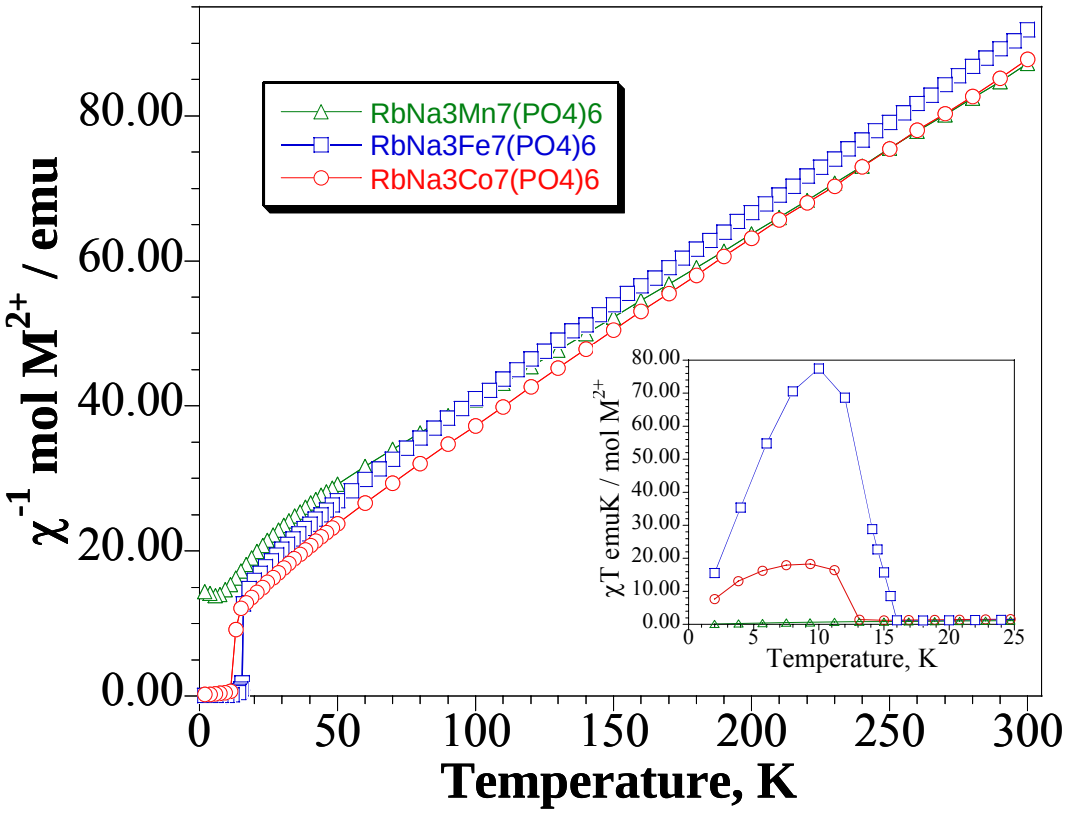

Figure 3.6: Inverse molar magnetic susceptibility, χ^{-1}, vs T plots of the $RbNa_3M_7(PO_4)_6$ series (M = Mn, Fe, Co) at H = 100 Oe on ground powder of selected single crystals. The inset shows the χT plots.

Table 3.6: Parameters obtained from Curie-Weiss fit of the high temperature χ^{-1} data for **1-9**.

$ANa_3M_7(PO_4)_6$	μ_{eff} (μ_B)	μ_{cal} (μ_B) $\sqrt{4S(S+1)}$	μ_{cal} (μ_B) $\sqrt{4S(S+1) + L(L+1)}$	θ	*T*c (K)
$KNa_3M_7(PO_4)_6$					
Mn^{2+}, d^5, S=5/2	5.76(6)	5.9	L=0	-66(2)	---
Fe^{2+}, d^6, S=2	5.5(1)	4.9	5.48	-46(1)	16
Co^{2+}, d^7, S=3/2	5.18(9)	3.9	5.20	-43(2)	13.5
$RbNa_3M_7(PO_4)_6$					
Mn^{2+}, d^5, S=5/2	5.91(1)	5.9	L=0	-76.6(3)	---
Fe^{2+}, d^6, S=2	5.60(1)	4.9	5.48	-58.3(6)	15.5
Co^{2+}, d^7, S=3/2	4.29(1)	3.9	5.20	-48.6(5)	15
$CsNa_3M_7(PO_4)_6$					
Mn^{2+}, d^5, S=5/2	6.23(5)	5.9	L=0	-73(1)	---
Fe^{2+}, d^6, S=2	5.49(1)	4.9	5.48	-47.9(5)	14
Co^{2+}, d^7, S=3/2	4.99(1)	3.9	5.20	-47(4)	12

measured and expected values of the effective magnetic moments. Taking the orbital contribution into account, the magnetic moments of Fe^{2+} and Co^{2+} are 5.48μ_B and 5.20μ_B respectively. The negative Weiss constants, θ, calculated to be -76.6(3), -58.3(6), and -45.4(9)K, for **2**, **5**, and **8** respectively indicates an antiferromagnetic coupling between nearest neighbors at high temperature, which is consistent with the geometrically frustrated magnetic lattice highlighted in Figure 3.4. For comparison, Table 3.6 shows results on the Curie Weiss fit for compounds **1**-**9**.

The general features of the magnetization (M) versus temperature (T) curve of **5**, Figure 3.7, at 100 Oe suggests a ferrimagnetic transition at ≈ 14.6 K (T_1) followed by an additional antiferromagnetic component at 6 K (T_2). The M vs. T curves of the $ANa_3Fe_7(PO_4)_6$ series show a systematic decrease in the magnitude of the magnetization below T_1 with increasing size of the A-site cation. The large ferrimagnetic moment of the compounds is due to the exchange field (Weiss field) of the closely-spaced magnetic Fe^{2+} ions.[19] The magnetization values near T_2 increase when the magnetic ions are brought closer together upon replacement of the Rb^+ ions with smaller K^+ ions. The general profile of the magnetization versus temperature curves suggests predominately antiferromagnetic coupling above T_1. Between T_1 and T_2, ferrimagnetic interactions dominate, overcoming the decrease in the magnetic moment. The drop in the moment below T_2 could signal an additional antiferromagnetic coupling or zero-field splitting.

The field-dependent magnetization measurements confirm ferrimagnetic ordering in compounds **4**-**9** as hysteresis curves have been obtained on powders of ground single crystals for all Co and Fe derivatives at temperatures below T_1 ≈ 15K. For

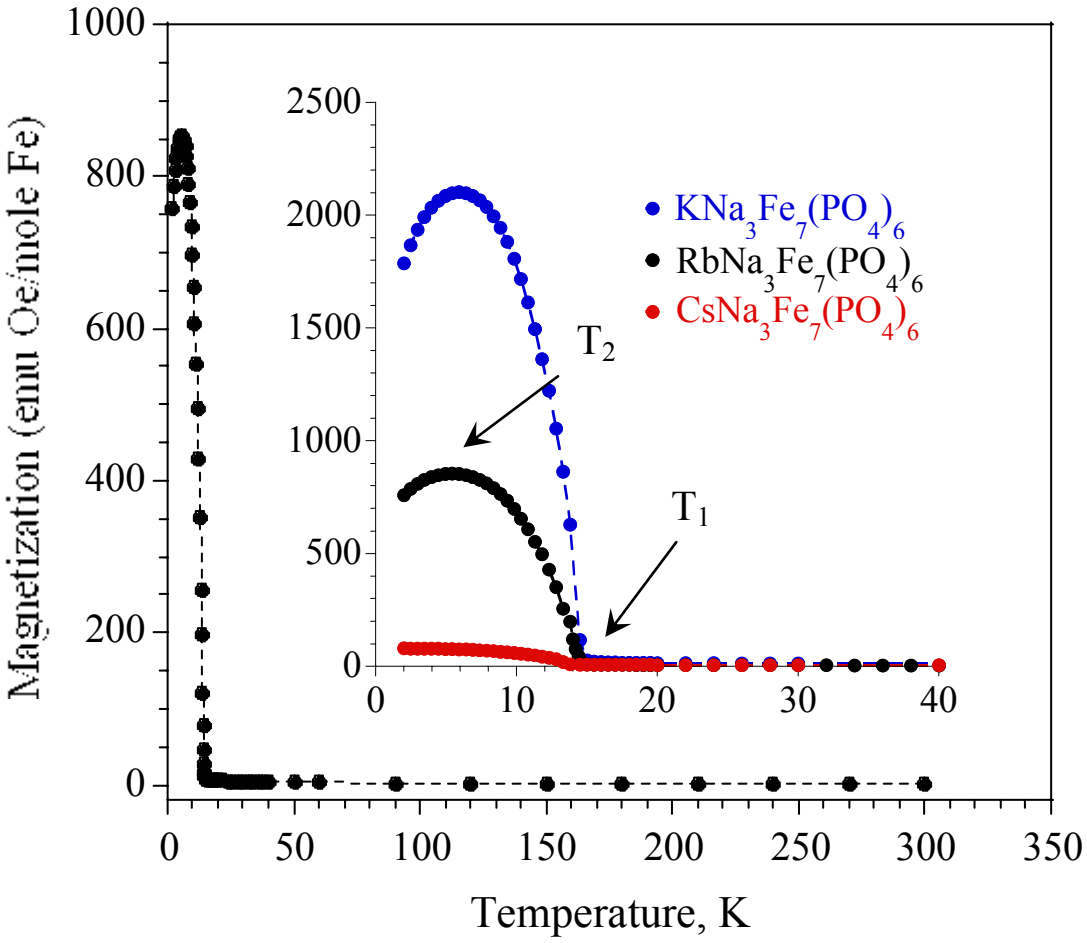

Figure 3.7: M vs *T* plots of $RbNa_3Fe_7(PO_4)_6$ and the low-temperature region (inset) of the $ANa_3Fe_7(PO_4)_6$ series (A = K, Rb, Cs) at H = 100 Oe on ground powder of selected single crystals showing a ferromagnetic transition at T_1.

$RbNa_3Fe_7(PO_4)_6$, **5**, (0.3 mg), as well as $KNa_3Fe_7(PO_4)_6$, **4**, (1.0 mg), orientation-dependent magnetization studies were also carried out on oriented single crystals. The hysteresis curves for compound **5**, seen in Figure 3.8, show the relative magnetization (M/Ms; Ms is the saturation magnetization at 5 T versus field).[5] This data was acquired with the magnetic field applied along the crystallographic *a* axis (Figure 3.8), which is approximately parallel to the pseudo-threefold rotation axes of the distorted $Fe(2)O_5$ and $Fe(4)O_5$ trigonal bipyramids (Figure 3.3). These magnetization *vs*. field curves were measured immediately below T_1, at 10 and 12 K, and show remnant magnetization, confirming the existence of ferrimagnetic coupling. As the temperature is decreased, the coercive field is expectedly increased. At temperatures below T_2, sudden jumps in the magnetization resulting from a cascade of spins changing direction, is observed in the hysteresis loops. These field-induced transitions could possibly be attributed to one of the following structural characteristics or combinations thereof: geometrically frustrated triangles in the magnetic lattice (Figure 3.4, left), the short Fe···Fe distance between the edge-sharing $Fe(1)O_6$ and $Fe(3)O_6$ polyhedra, or the uniaxial properties of the Fe^{2+} moments of the $Fe(2)O_5$ and $Fe(4)O_5$ trigonal bipyramids. Note that these stepped transitions are much sharper for the single crystal than for the polycrystalline sample first investigated, indicating a large magnetic anisotropy. Furthermore, the orientation-dependent magnetization studies have also revealed the presence of uniaxial magnetic properties. When the field was applied to a direction orthogonal to the *a* axis, the hysteresis was diminished, Figure 3.9.

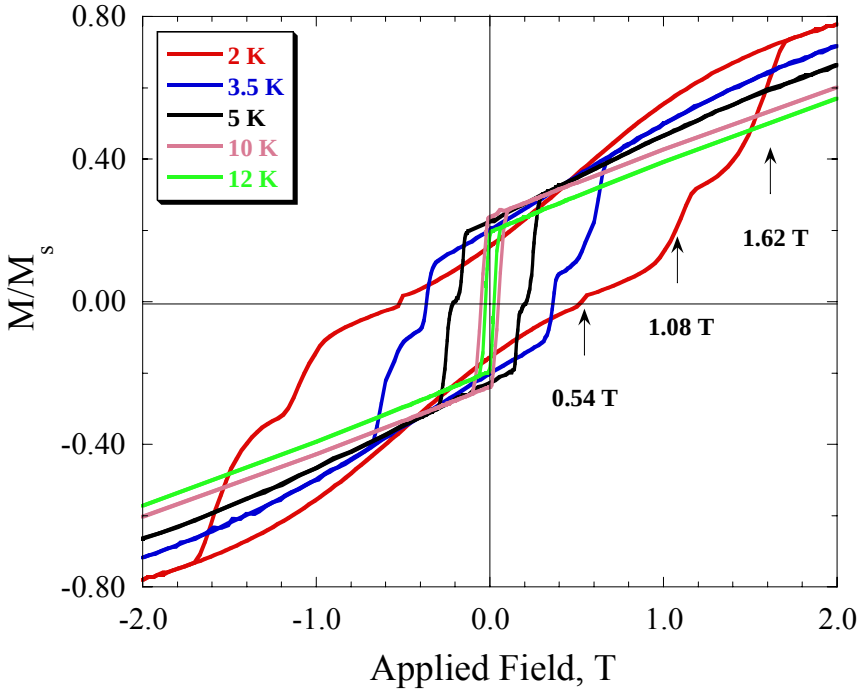

Figure 3.8: Hysteresis loops of magnetization (M) vs. applied magnetic field on an oriented single crystal (0.3mg) of $RbNa_3Fe_7(PO_4)_6$ showing Normalized magnetization (M/Ms) is plotted against the saturation value (Ms) at H = 5T.

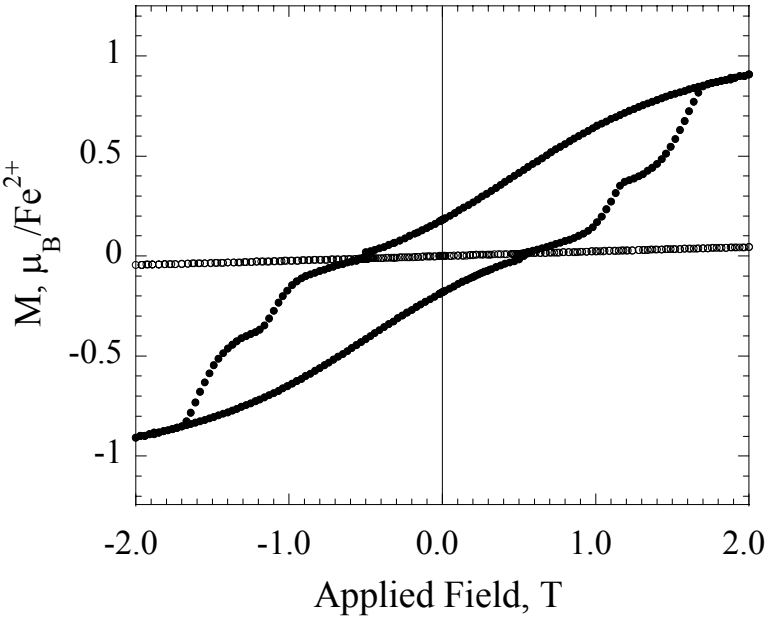

Figure 3.9: Hysteresis loops showing evidence of magnetic anisotropy. Magnetization (M) vs. applied magnetic at 2K with field applied along the easy axis, *a*, and perpendicular to *a*. When the field is applied perpendicular to *a* the hysteresis is diminished.

After the observation of magnetization steps in **5**, we also followed up on the structure-property correlation studies by looking at the field-dependent magnetization data for a single crystal of the K/Fe analog, **4**, as shown in Figure 3.10. In this measurement, the field was applied along the crystallographic *a* axis. As observed for **5**, theses data also show stepped variations in the hysteresis, however, these phenomena are not nearly as pronounced as the steps observed in Figure 3.7. In neither instance were steps observed with fields applied perpendicular to the crystallographic *a* axis. As a result, it is thought that these magnetization steps are likely not the result of domain wall depinning and are directly related to the triangular magnetic lattice. Also, the steps seen in the hysteresis curve of **4** are very small and do not occur at regular repeating intervals. The crystal used in the orientation-dependent studies of **4** was much larger and not as good in quality as the crystal used for the same studies of **5**. Some twinning observed in the crystal of **4** could have resulted in less pronounced magnetization steps. The twinning could cause the crystal to shift on the sample platform, as the material has strong magnetic anisotropy. It should be noted that crystal shifting was observed when doing the orientation-dependent studies of **5** and, therefore, a smaller, better quality crystal was selected for the study. It should also be noted that the only other analog to give evidence of magnetization steps was the Cs/Co derivative, **9**. Even though magnetization data has not been collected on oriented single crystals, due to the lack of large enough single crystals, the hysteresis, Figure 3.11, obtained from ground single crystals shows a broad step in the 2K data, similarly observed for **4** and **5**.

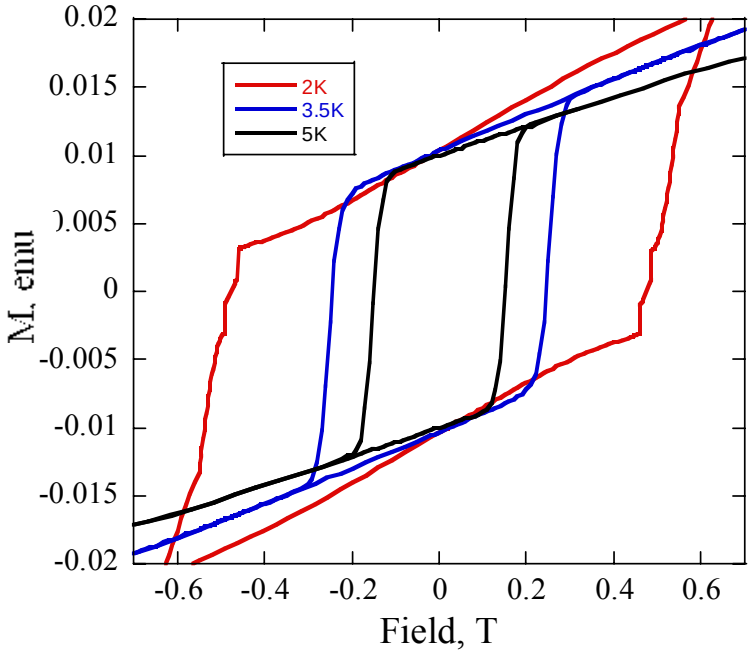

Figure 3.10: Hysteresis loops of magnetization (M) vs. applied magnetic field on an oriented single crystal (1.0 mg) of $KNa_3Fe_7(PO_4)_6$ approximately along the crystallographic *a* axis.

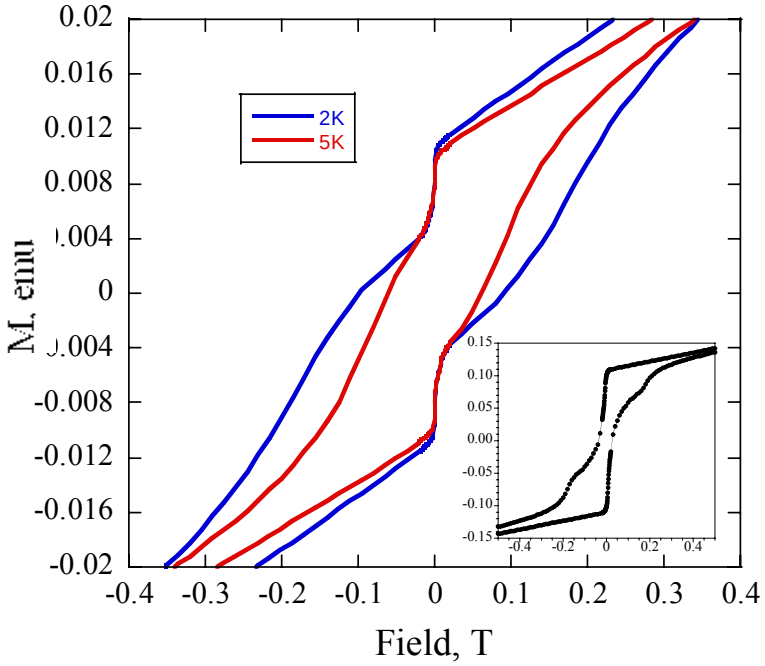

Figure 3.11: Hysteresis loops of magnetization (M) vs. applied magnetic field on a powder of ground single crystals (7.7 mg) of $CsNa_3Co_7(PO_4)_6$, **9**. Broad steps appear in the 5K and 2K data. The inset shows stepped variations in the 5K field dependent powder data of $RbNa_3Fe_7(PO_4)_6$, **5**.

Zero-field-cooled (ZFC) and field-cooled (FC) measurements of the magnetic moment were carried out on the oriented single crystal of **5** from 2-30K at applied fields of 1, 50, 250, and 1000 Oe, as shown in Figure 3.12. A strong easy-axis anisotropy was quantified ($M_a/M_\perp \approx 1330$ at 2 K and 1 Oe, Fig. 3.12 where Ma = field applied parallel to *a* and $M_\perp$ = field applied perpendicular to *a*), and the second transition was found to occur below the merging temperature of the ZFC and FC curves. This divergence is often referred to as thermomagnetic irreversibility (TMI) and has been observed in magnetically unordered systems such as spin glass type materials[21] and in magnetically ordered systems[22]. The temperature at which the plots merge decreases as the applied field increases, which is consistent with the notion of a field-induced transition or spin flipping due to magnetic frustration, while T_2 conceivably remains unchanged in the FC curves. The magnetic tail in the ZFC curves suggests that these transitions are the result of field-induced spin coupling. Further evidence provided by AC susceptibility measurements also suggests an intriguing change in the spin dynamics around T_1. Figure 3.13 shows the temperature dependence of the real component of the AC magnetic susceptibility (χ') of a single crystal of **5** at five different frequencies at zero field. A double-peak feature is detected, which corresponds to the shoulder near T_1. As the frequency is increased, the susceptibility decreases. For temperatures below T_1, hysteresis appears in the magnetization versus field curves, see Figure 3.8; the curve at 2 K exhibits a succession of magnetization steps with a roughly constant field spacing of approximately 0.54 T. Also, there is a non-zero out of phase, χ'' (Figure 3.13 inset), component in the ac susceptibility peak relating to some type of slow relaxation process.

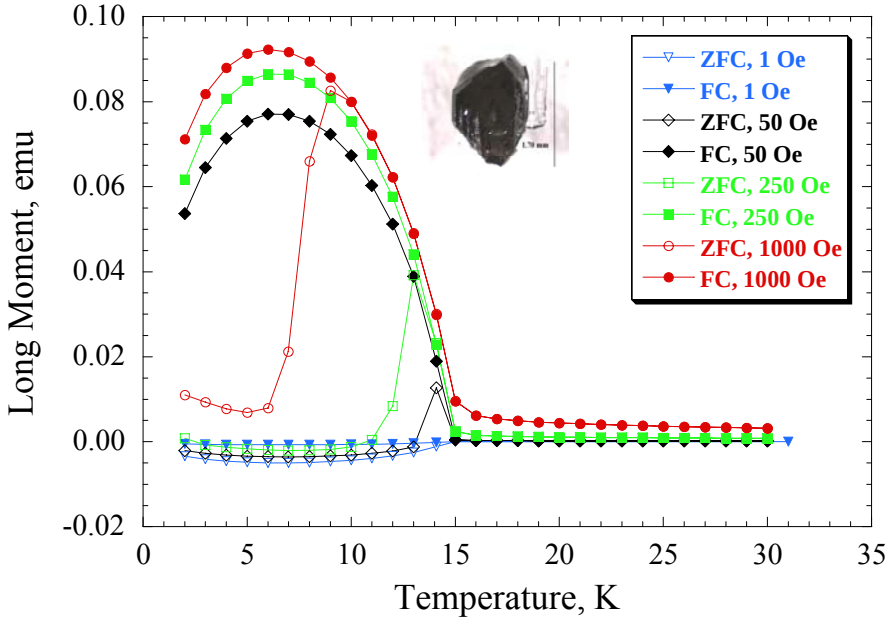

Figure 3.12: FC/ZFC temperature dependent plots of $RbNa_3Fe_7(PO_4)_6$ single crystal with various fields applied along the *a* axis.

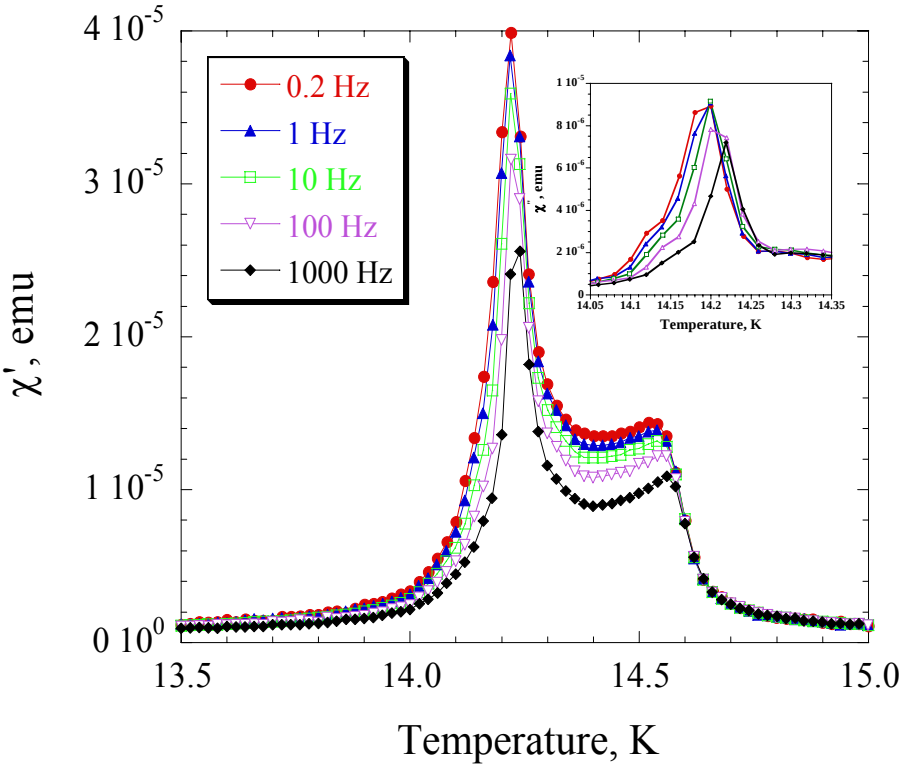

Figure 3.13: *AC* magnetic susceptibility, χ', along with the out-of-phase component, χ'' (inset), on a single crystal of $RbNa_3Fe_7(PO_4)_6$. The oscillating field was applied with varying frequencies along the *a* axis with zero applied *dc* field.

The AC susceptibility measurements, however, do not show a large enough frequency-dependence necessary for quantum tunneling of magnetization. Instead the shifts are closer to what has been previously observed for spin glass type materials.[22] Thus, we feel that spin frustration probably underpins the field-dependent jumps in the stepped magnetization shown in Figure 3.8.

Preliminary heat-capacity studies for **5**, shown in Figure 3.14, reveal a small change in the latent heat at T_1, which is indicative of a transition that is electronic in nature. The measurements were performed on a single crystal (9.9 mg) with magnetic fields of 0, 1, and 2 T applied along *a* and perpendicular to *a*. The measurements show no difference with respect to the direction of the applied field. This unexpected result is likely due to one or more combinations of several factors. From SXRD it was discerned that the crystal used for heat capacity measurements was not as high quality as the crystals used in the magnetic measurements, likely the result of twinning. Also, the sample shows an extremely strong response to an applied field sometimes causing the crystals to dismount from the sample holder or simply change directions, causing the loss of the orientation-dependence already observed in the field-dependent magnetization studies. To shed new light on the origin of the magnetic anomalies further heat capacity measurements performed on smaller, high quality single crystals will be required.

It should be noted that the A-site cation in the series presented here, $ANa_3M_7(PO_4)_6$, can be substituted with any alkali metal cation with the exception of Na. Upon replacement of the A-site cation with Na, a different structure type forms. This

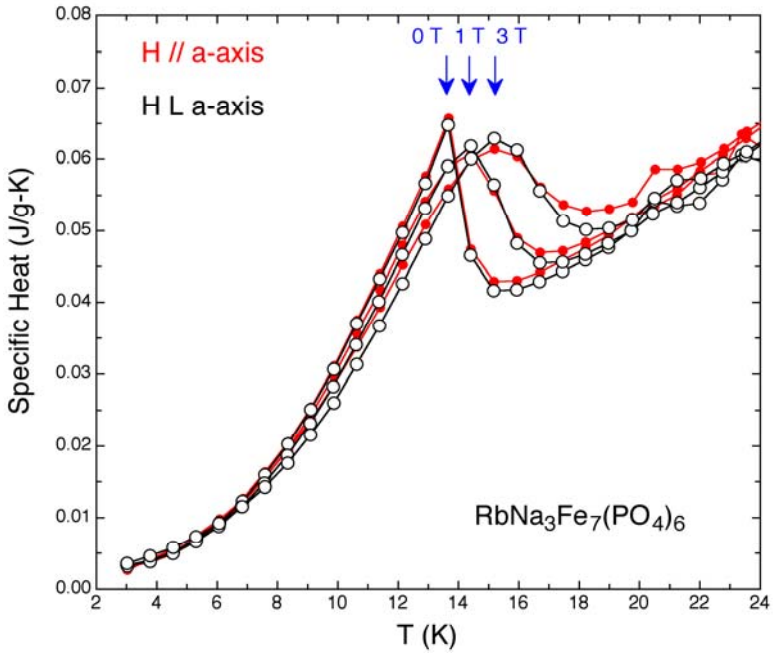

Figure 3.14: Heat capacity data in magnetic fields, 0, 1, and 3T, applied parallel and perpendicular to the *a* axis on a single crystal for $RbNa_3Fe_7(PO_4)_6$, **5**.

structure has been reported for $Na_4Co_7(PO_4)_6$ and $Na_4Ni_7(PO_4)_6$.[23] In this study, the $Na_4Co_7(AsO_4)_6$ and $Na_4Ni_7(AsO_4)_6$ derivatives were synthesized while trying to make arsenate analogs of title compounds. Both of these compounds crystallize in the *C*2/*m* (no. 12) spacegroup. The unit cell dimensions for $Na_4Co_7(AsO_4)_6$ are a = 10.720(2), b = 14.789(3)Å, c = 6.682(1)Å, β = 105.60(3)°, and V= 1019(8)Å^3, while the unit cell dimensions for $Na_4Ni_7(AsO_4)_6$ are a = 10.904(2)Å, b = 14.355(3)Å, c = 6.667(1)Å, β = 104.56(3)°, and V=1010(8)Å^3. The crystallographic data can be seen in Table 3.7.

Figures 3.15 and 3.16 show a comparison between the structures of compound **5** and the $Na_4Ni_7(AsO_4)_6$ analog. Due to the fact that both the Ni/As and Co/As derivatives are isostructural, the structure of the Ni derivative will be discussed from this point forward. In this compound, there are three crystallographically distinct Ni^{2+} cations, all of which are octahedrally coordinated by O^{2-}. These polyhedra share edges and corners to form a triangular magnetic lattice similarly observed in the title compound family, $ANa_3M_7(PO_4)_6$. These Ni-O triangular ribbons are interconnected *via* two edge-sharing $Ni(1)O_6$ polyhedra and two corner-sharing $Ni(2)O_6$ and $Ni(3)O_6$ polyhedra. Within the ribbons, the $Ni(3)O_6$ polyhedra share an edge with one another and then two corners with neighboring $Ni(1)O_6$ octahedra, allowing the propagation of the triangular ribbons along the crystallographic *a* axis. Figure 3.16(left) shows a similar Fe-O lattice observed in compound **5**. The major difference in the observed structures is seen in the coordination environments of the M^{2+} cations. Compound **5** has five crystallographically distinct Fe sites, all of which are pseudo-octahedral with the exception of Fe(4), which is

Table 3.7: Crystallographic data for $Na_4Co_7(AsO_4)_6$ and $Na_4Ni_7(AsO_4)_6$

empirical formula	$Na_4Co_7(AsO_4)_6$[1]	$Na_4Ni_7(AsO_4)_6$[2]
Color / shape	purple/ multifaceted	green / multifaceted
crystal size (mm)	0.15 × 0.08 × 0.05	0.1 × 0.04 × 0.07
formula weight (amu)	1337.99	1336.45
space group, *Z*	*C*2/*m* (no. 12), 2	
T, °C	25	
a, Å	10.710(2)	10.904(2)
b, Å	14.789(3)	14.355(3)
c, Å	6.682(1)	6.667(1)
β, degree	105.60(3)	104.56(3)
V, Å^3	1019.4(3)	1010.1(3)
μ (Mo Kα), mm^{-1}	15.428	16.345
F_{000}	1246	1260
d_{calc}, g cm^{-3}	4.359	4.394
data/restraints/parameters	937 / 0 / 112	928 / 0 / 113
secondary extinction	---------	0.0035(5)
reflections collected / unique / R_{int}[a]	4097 / 937 / 0.0368	3737 / 928 / 0.0518
final R1/wR2[b] [$I > 2\ \sigma(I)$]	0.0267 / 0.0692	0.0492 / 0.1439
R1/wR2 (all data)	0.0292 / 0.0713	0.0521 / 0.1458
GOF	1.109	1.115
Largest difference peak / hole (e$^-$ / Å^3)	0.723 / -0.900	1.198 / -1.356

[a] R_{int} = Σ | *Fo*^2- *Fo*^2 (mean) | / Σ[*Fo*^2]; [1b] R1 = Σ ||F_o| - |F_c|| / Σ|F_o|; *w*R2 = {[Σ[*w*(F_o^2-F_c^2)^2] / [Σw(F_o)^2)^2]}^(1/2); w=1/[\s^2^(Fo^2^)+(0.0470P)^2^+1.1122P] where P=(Fo^2^+2Fc^2^)/3; ; [2b] R1 = Σ ||F_o| - |F_c|| / Σ|F_o|; *w*R2 = {[Σ[*w*(F_o^2-F_c^2)^2] / [Σw(F_o)^2)^2]}^(1/2); w=1/[\s^2^(Fo^2^)+(0.0617P)^2^+105.6428P] where P=(Fo^2^+2Fc^2^)/3

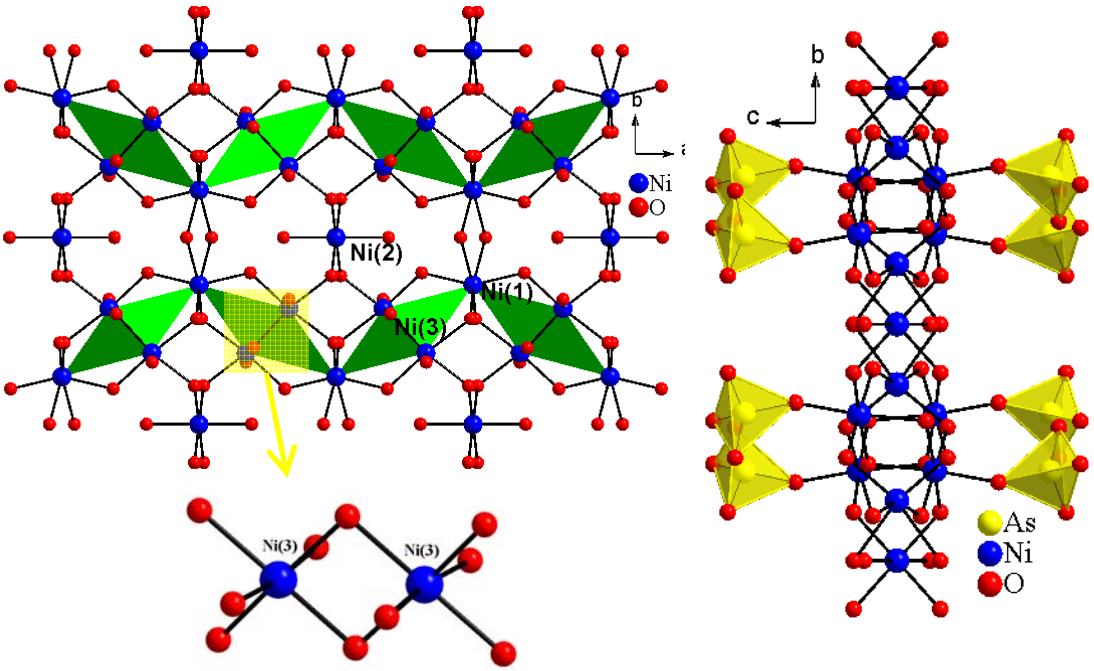

Figure 3.15: (left) M-O framework of $Na_4Ni_7(AsO_4)_6$, showing similar structural features to the title compound family, $ANa_3M_7(PO_4)_6$. (right) The M-O framework is insulated *via* surrounding $(AsO_4)^{3-}$ oxyanions.

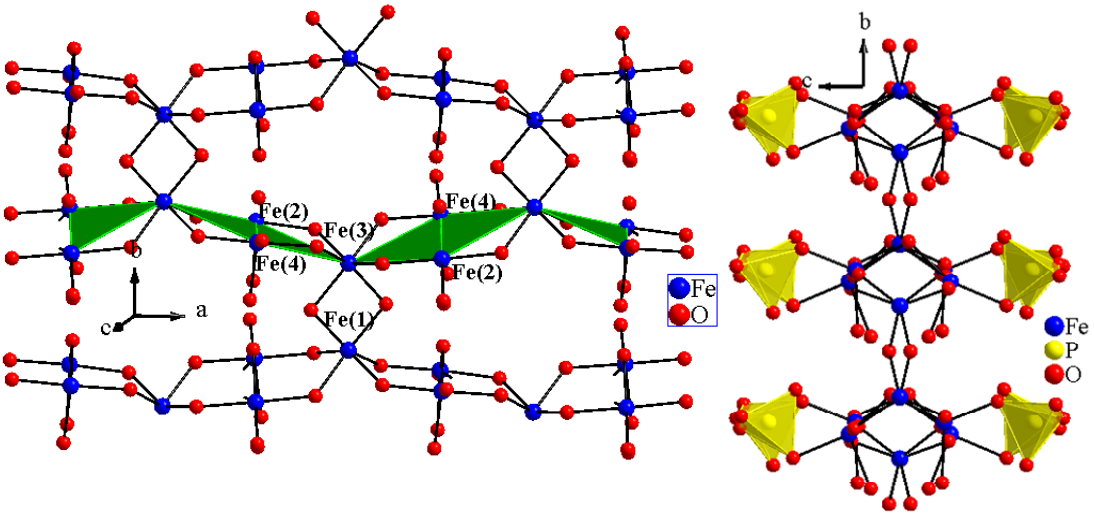

Figure 3.16: (left) M-O framework of $RbNa_3Fe_7(PO_4)_6$ showing triangular magnetic lattices highlighted in dark green. The right image shows the M-O lattice insulated *via* surround $(PO_4)^{3-}$ oxyanions.

trigonal bipyramidal. Also, the triangular ribbons in compound **5** only have corner-sharing polyhedra along the chain axis, whereas the Ni compound shows edge-sharing between $Ni(3)O_6$ octahedra (highlighted in yellow in Figure 3.15 (left)) across one triangular edge in the chain. The triangular ribbons in both compounds are interconnected *via* edge- sharing polyhedra forming 2-D M-O sheets, Figures 3.15(right) and 3.16(right).

The molar magnetic susceptibility, χ, and inverse molar magnetic susceptibility, χ^{-1}, data were collected on a ground sample of single crystals of $Na_4Ni_7(AsO_4)_6$ (2.3mg) at 0.5T, Figure 3.17. Upon decreasing temperature, the susceptibility shows a gradual increase, followed by a sudden decrease at approximately 20K, attributed to antiferromagnetic coupling. A Curie - Weiss fit was performed on the data in temperatures ranging from 200-300K. The parameters obtained from the fit include a magnetic moment, μ_{calc} equal to $3.2(3)\mu_B$, a Weiss constant, θ, equal to -24(10)K, and a temperature-independent parameter, χ_0, equal to 0.0022(2) emu/mol Ni^{2+}. The calculated magnetic moment is comparable to the expected spin-only value, μ_{eff}, equal to 2.83. The negative Weiss constant indicates antiferromagnetic exchange between nearest neighbors. It should be noted that the single crystal reaction of $Na_4Co_7(AsO_4)_6$ did not render a high enough yield for magnetic measurements.

Conclusions

Finally, a new family of metal(II) phosphates has been synthesized using high-temperature molten-salt methods. The magnetic behavior in condensed phases is

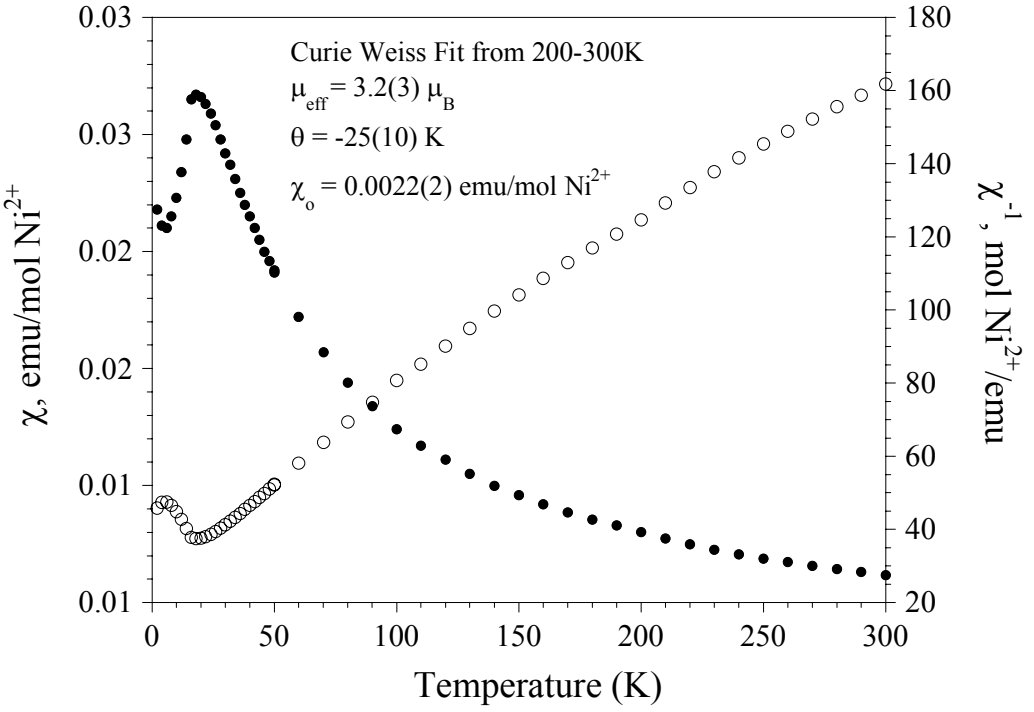

Figure 3.17: Molar magnetic susceptibility, χ (●), and inverse molar magnetic susceptibility data, χ^{-1} (○), for $Na_4Ni_7(AsO_4)_6$ at 0.5T. This data shows a decrease in the susceptibility due to antiferromagnetic coupling.

sensitive to the local structure where magnetic spins are coupled, and this extensive family presents a rare opportunity for an in-depth study of electronic interactions within the differing spin systems. Despite large M–O–M bridge angles and short M–M distances within the metal oxide chain normally expected to propagate antiferromagnetic exchange interactions, the inverse molar magnetic susceptibility and field-dependent magnetization data reveals ferrimagnetic transitions for all of the Fe^{2+} and Co^{2+} derivatives. The Mn^{2+} derivatives show only antiferromagentic transitions at low temperature. It is thought that this difference in magnetic response could be related to the orbital contribution observed from the Fe^{2+}- and Co^{2+}-containing derivatives. All of the metal polyhedra, with the exception of M(4), form distorted pseudo-octahedral geometries. M(4) forms a trigonal bipyramid geometry whose axial oxygen runs approximately parallel with the crystallographic *a* axis. It is known that heavily distorted octahedral geometries and the trigonal bipyramidal geometries will lead to orbital splitting diagrams that are very different from the ligand field splitting observed for a traditional octahedral environment, which demonstrates two sets of degenerate orbitals, t_2g and eg. Therefore, it is suspected that slight differences in the distribution of orbital energies could lead to quenching of the orbital component in some of these ions. This would lead to M cations with varying magnetic moments and, hence, a net ferrimagnetic exchange between neighboring ions. Compounds **4**, **5**, and **9** have also revealed step-like anomalies in the magnetization data, which are likely field-induced transitions resulting from the triangular magnetic lattice.

It might be interesting to compare the magnetic properties of the $Na_4M_7(AsO_4)_6$ series with those of **1-9**. The MO_6 polyhedra in the $Na_4M_7(AsO_4)_6$ derivatives are more symmetric and are only found in an octahedral geometry. It has been proposed that heavily distorted octahedral geometries and/or the trigonal bipyramidal geometries in **4-9** quench the orbital component of some of the ions within the framework, creating a ferrimagnetic exchange. If this argument is valid, then magnetic studies on $Na_4M_7(PO_4)_6$ (with M equal to magnetic ions having unquenched orbital contribution such as high spin Fe^{2+} and Co^{2+}) might lead to pure antiferromagnetic exchange.

To shed new light on the origin of the observed magnetic behavior of the $ANa_3M_7(PO_4)_6$ series, neutron-scattering studies by experts in the field will be required, hopefully allowing a determination of the magnetic structure of this complicated system. Geometrically-induced magnetic frustration, as stated above, can lead to non-zero magnetic spin and magnetic anomalies in field- and temperature-dependent magnetization processes.[2c] It is anticipated that through continued exploration of this system, more fascinating compounds containing magnetic nanostructures, especially compounds possessing large numbers of magnetic spins, are yet to be discovered. Understanding of the magnetic phenomena observed within this extensive family could be improved *via* comparative studies across different systems.

Literature Cited

1. Kittel, C. *Phys. Rev*., **1946**, 70, 965-971.

2. (a) Leuenberger, M. N., Loss, D. *Nature* **2001**, *410*, 789-793.

   (b) Meier, F., Levy, J., Loss, D. *Phys. Rev. B* **2003**, *68*, 134417-1-134417-15.

3. Sessoli, R., Gatteschi, D., Caneschi, A., Novak, M. A. *Nature* **1993**, *365*, 141–143.

4. (a) Hwu, S.-J. *Chem. Mater*. **1998**, *10*, 2846–2859

   (b) Ulutagay-Kartin, M., Etheredge, K. M. S., Schimek, G. L., Hwu, S.-J. *J. Alloys Compd*. **2002**, *338*, 80– 86.

   (c) Hwu, S.-J., Ulutagay-Kartin, M., Clayhold, J. A., Mackay, R., Wardojo, T. A., OMConnor, C. J., Krawiec, M. *J. Am. Chem. Soc*. **2002**, *124*, 12404–12405.

   (d) Ulutagay-Kartin, M., Hwu, S.-J., Clayhold, J. A. *Inorg. Chem*. **2003**, *42*, 2405-2409.

   (e) Mo, X., Etheredge, K. M. S., Hwu, S.-J., Huang, Q. *Inorg. Chem*. **2006**, *45*, 3478-3480.

   (f) Ranmohotti, K. G. S., Mo, X., Smith, M. K., Hwu, S.-J. *Inorg. Chem.* **2006**, *45*, 3665-3670.

5. Queen, W.L., Hwu, S.-J, Wang L., *Angew. Chem. Int. Ed*., **2007**,*46*, 5344-5347.

6. (a) Murugesu, M., Raftery, J., Wernsdorfer, W., Christou, G., Brechin, E. K. *Inorg. Chem*. **2004**, *43*, 4203-4209; and references therein.

   (b) Thompson, L. K., Waldmann, O., Xu, Z. *Coord. Chem. Rev*. **2005**, *249*, 2677-2690.

7. Ritter, S. K. *Chem. Eng. News* **2004**, *82*(50), 29-32.

8. (a) Snyder, J., Ueland, B. G., Slusky, J. S., Karunadasa, H., Cava, R. J., Mizel, A., Schiffer, P., *Phys. Rev. Lett.* **2003**, *91*, 107201-1-107201-4.

(b) Ehlers, G., Cornelius, A. L., Orendac, M., Kajnakova, M., Fennell, T. S., Bramwell, T., Gardner, J. S. *J. Phys. Condens. Matter* **2003**, *15*, L9-L15.

9. (a) Maignan, A., Hardy, V., HQbert, S., Drillon, M., Lees, M. R., Petrenko, O., Paul, D. M., Khomskii, D. *J. Mater. Chem.* **2004**, *14*, 1231-1236.

(b) Hardy, V., Lees, M. R., Petrenko, O. A., Paul, D. M., Flahaut, D., HQbert, S., Maignan, A. *Phys. Rev. B* **2004**, *70*, 064424-1-064424-7.

10. (a) Greedan, J. E. *J. Mater. Chem*. **2001**, *11*, 37-53.

(b) Greedan, J. E. *J. Alloys Compd*. **2006**, *408–412*, 444-455.

11. (a) Rosenkranz, S ., Ramirez, A. P., Hayashi, A., Cava, R. J., Siddharthan, R., Shastry, B. S. *J. Appl. Phys*. **2000**, *87*, 5914-5916.

(b) Dai, D., Whangbo, M.-H. *Inorg. Chem*. **2005**, *44*, 4407-4414.

12. (a) Rana, D. S., Malik, S. K. *Phys. Rev. B* **2006**, *74*, 052407-1-052407-4.

(b) Fernandes, J. C., Sarrat, F. S., Guimares, R. B., Freitas, R. S., Continentino, M. A., Doriguetto, A. C., Mascarenhas, Y. P., Ellena, J., Castellano, E. E., Tholence, J.-L., Dumas, J., Ghivelder, L. *Phys. Rev. B* **2003**, *67*, 104413-1-104413-7.

(c) Oiwa, A., Endo, A., Katsumoto, S., Iye, Y., Munekata, H., *Phys. Condens. Matter* **2000**, *284–288*, 1173-1174.

13. Queen, W.L., Hwu, S.-J. Unpublished results.

14. Huang, Q., Maloney, J., Hwu, S.-J., Unpublished results.

15. Shannon, R. D. *Acta Crystallogr. Sect. A.* **1976**, *32*, 751-767.

16. Becht, G., Hwu, S.-J. *Chem. Mater.* **2006**, *18*, 4221-4223.

17. (a) *VALENCE* for DOS, Version 2.0, Brown, I. D. *J. Appl. Crystallogr.* **1996**, *29*, 479-480.

(b) Brown, I. D. and Altermatt, D. *Acta Cryst.* **1985**, *B41*, 244-247.

18. Mabbs, F. E., Machin, D. J. *Magnetism and Transition Metal Complexes*, Halsted Press, New York, **1973**.

19. Drago, R. S. *Physical Methods in Chemistry*, Saunders, W. B. Philadelphia, **1977**.

20. Kaczorowski, D., Noel, H. J. Phys.: *Condens. Matter* **1993**, *5*, 9185-9195.

21. (a) Roy, S.B., Pradhan, A.K., Chaddah, P., *J. Phys.: Condens. Matter* **1994**, *6*, 5155-5160.

(b) Roy, S.B., Pradhan, A.K., Chaddah, P. *Phil. Mag.* **1995**, *71*, 97-104.

(c) Roy, S.B., Pradhan, A.K., Chaddah, P. *Physica B* **1996**, *223–224*, 198-200.

(d) Roy, S.B., Pradhan, A.K., Chaddah, P. *Phil. Mag.* **1997**, *75*, 303-310.

(e) Roy, S.B., Pradhan, A.K., Chaddah, P. *J. Alloys Compounds* **2001**, *326*, 112-116.

22. Hardy, V., Flahaut, D., Lees, M. R., Petrenko, Q. A. *Phys. Rev. B* **2004**, *70*, 214439-1-214439-7.

23. (a) Moring, J., Kostiner, E. *J. Solid State Chem.* **1986**, *62*(1), 105-11.

(b) Kobashi, D., Kohara, S., Yamakawa, J., Kawahara, A.. *Acta Crystallogr., Sect. C: Cryst. Struct. Commun.* **1998**, *C54*(1), 7-9.

CHAPTER FOUR

SYNTHESIS AND CHARACTERIZATION OF EXTENDED SOLIDS CONTAINING EQUILATERAL TRIANGULAR $Fe_3(\mu_3\text{-}O)$ MAGNETIC NANOSTRUCTURES

Introduction

Triangular-based metal-oxide nanostructures are a fundamental building block observed in both extended solid-state materials and biologically relevant materials such as ferritins and Mn-based catalysts used in the oxidation of water during photosynthesis.[1] As triangular-based systems are interesting in their own right, much research has been focused on these trinuclear units, and when compared to their higher nuclearity counterparts, they can provide a more straightforward interpretation of magnetic and electronic interactions between transition metal cations.

For extended solid-state materials, triangular-based lattices have drawn much interest due to the presence of magnetic frustration. This results from competing exchange interactions that are similar in magnitude, preventing antiparallel alignment observed in traditional antiferromagnets. At very low temperatures < 2K, where order is expected to be inevitable, these materials instead form multiple degenerate ground states, ultimately preventing the formation of long-range order. Alternatively, frustrated materials form exotic ground states such as spin glasses, spin liquids, or spin ice.[2] Although many triangular and tetrahedrally-based lattices were reported, little is still understood about this phenomenon. The Kagomé lattice is derived from two separate Japanese words, meaning the pattern of holes ("*me*", literally "eyes") in a basket ("*kago*").

The most famous magnetically frustrated system reported to date is a two-dimensional array of corner-sharing triangles with antiferromagnetically coupled magnetic ions at each vertex. This lattice is considered to be the origin of many other magnetically frustrated systems such as the layered $SrGa_4Cr_8O_{19}$ (SCGO) and $BaSn_2ZnGa_4Cr_6O_{22}$[3], the kagomé-staircases, $Ni_3V_2O_8$ and $Co_3V_2O_8$,[4] and three-dimensionally frustrated materials such as the spinels and the pyrochlores[5].

The research within this dissertation is focused on isolating magnetic nanostructures separated from one another by rigid inorganic oxyanion ligands, XO_n, (where X can be a fully oxidized early transition metal, such as V^{5+}, or a neighboring main group element such as P, Si, or As). The goal is to build extended solids containing singly oriented magnetic nanostructures or quantum dots. In compounds where finite numbers of paramagnetic centers are coupled, unusual quantum behavior can be observed. In addition to having a diverse number of coordination environments, transition metal oxides can link through a variety of different bridging modes (μ_2, μ_3, μ_4, etc.), giving rise to extended solids having very complex and unique magnetic properties. Structural versatility found within this system has led to a large number of interesting framework formations including oxyanion-based compounds containing triangular-based magnetic lattices discussed in this dissertation.

Chapter 4 is focused on the synthesis, structure analysis, and properties of three new extended solids containing trinuclear iron-oxide units, $Ba_{10}Na_5Fe_7(\mu_3\text{-}O)_2(PO_4)_{14}$, **1**, $Ba_{10}Na_5Fe_7(\mu_3\text{-}O)_2(AsO_4)_{12}(AsO_3)_2$, **2**, and $Sr_{14}NaFe_{10}(\mu_3\text{-}O)_2(PO_4)_{17}Cl$, **3**. These compounds contain $Fe_3(\mu_3\text{-}O)$ equilateral triangles that are structurally confined from one

another by the nonmagnetic oxyanions, $(PO_4)^{3-}$ or $(AsO_4)^{3-}$. The triangular $Fe_3(\mu_3\text{-O})$ nanostructure is similar to those observed in the trinuclear oxo-centered Fe complexes of what were referred to as "basic carboxylates". These complexes have the general formula $[M_3(\mu_3\text{-O})(O_2CR)_6L_3]^{n+}$ and have been extensively studied for the last 50 years.[6] In these materials, the $Fe_3(\mu_3\text{-O})$ nanostructures are usually planar and equilateral, resulting in trigonal symmetry. However, slight deviations in these structural properties have been observed and cause considerable variations in their physical properties.[7]

Like the "basic carboxylates" described above, compounds **2** and **3** show antiferromagnetic exchange between nearest neighbors; however, the temperature-dependent magnetic measurements of compound **1** have revealed that this solid has a ferrimagnetic anomaly at high temperatures (Tc > 300K), and the subsequent field-dependent studies at temperatures near Tc (T = 300°C) have shown magnetic hysteresis. It has been established that, in the Fe(III) μ_3-oxo bridged complexes, the triangles exhibit antiferromagnetic coupling between nearest neighbours. In instances where Fe-Fe or Fe-O distances or Fe-O-Fe bond angles are different, this leads to differences in magnetic coupling constants.[8] In this chapter, I will report the correlation parameters that warrant the difference in magnetic ordering among these otherwise $Fe_3(\mu_3\text{-O})$ units containing solids.

Due to the novel magnetic properties of **1**, efforts were made to synthesize derivatives for structure property correlation studies. Questions were raised in regard to chemical substitution, such as how reducing the size of the A-site cation or changing the nonmagnetic oxyanion would affect the magnetic properties of the materials. As a result,

two additional derivatives, **2** and **3**, were synthesized. First P was replaced with As in a stoichiometric reaction resulting in the formation of **2**, $Ba_{10}Na_5Fe_7(\mu_3\text{-}O)_2(AsO_4)_{12}(AsO_3)_2$ and, upon substitution of Ba with Sr, a new structurally-related compound was formed, $Sr_{14}NaFe_{10}(\mu_3\text{-}O)_2\ (PO_4)_{17}Cl$, **3**. Efforts were also made to achieve chemical substitution of other diamagnetic (Ga^{3+}) or paramagnetic ions (Mn^{3+}), in the Fe(III) sites in **1**. Here, these newly synthesized materials will be presented in light of their structural similarities and magnetic properties.

Synthesis

Single Crystal Growth of 1-3: Single crystals of $Ba_{10}Na_5Fe_7(\mu_3\text{-}O)_2(PO_4)_{14}$ were grown using high-temperature, molten-salt methods. FeO, P_4O_{10}, Na_2O_2, and BaO in a 6:1.5:4:1 mol ratio (ca. 0.3 g) were mixed with a $BaCl_2$/NaCl eutectic flux equal to five times the mass of the oxide reactants. The reaction was loaded in a nitrogen-purged drybox and reactants were placed in a carbon-coated quartz ampoule that was sealed under vacuum. The reaction was heated to 800°C where it was held for 4 days, slowly cooled to 450°C, and finally furnace-cooled to room temperature. The reaction was washed with deionized water revealing green hexagonally-shaped crystals (≈ 30 % yield) up to 2 mm in size. Within this reaction, there were unidentified black and colorless polycrystalline phases that account for the remaining 70% of the reaction products. A powder pattern of selected ground single crystals obtained from the above reaction, shown in Figure 4.1, indicates the existence of both a monoclinic and trigonal phase of the compound **1**. See further discussion below.

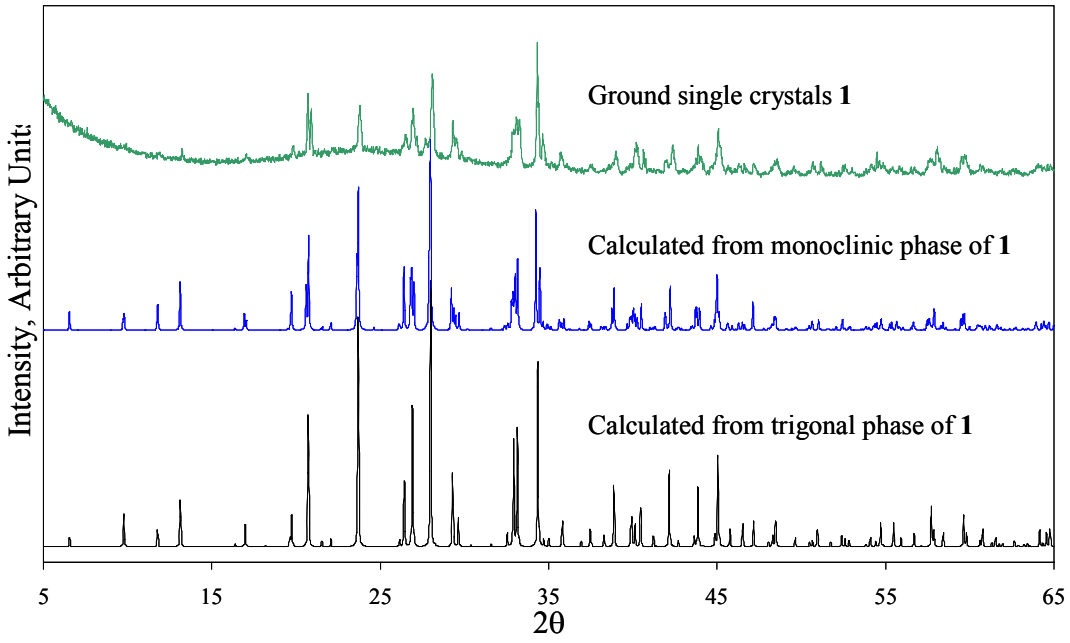

Figure 4.1: PXRD pattern of ground single crystals of $Ba_{10}Na_5Fe_7(\mu_3\text{-}O)_2(PO_4)_{14}$ compared to the calculated patterns of the trigonal and monoclinic phases of **1**. The single crystals appear to be a mixture of both phases.

For structure / property correlation studies, efforts were made to grow single crystals of an As derivative of **1**, $Ba_{10}Na_5Fe_7(\mu_3\text{-}O)_2(AsO_4)_{14}$. BaO, Na_2O, Fe_2O_3, FeO, and As_2O_5 were mixed in a 10:2.5:3.3:0.4:7 mol ratio (ca. 0.3g) and then added to a CsCl/NaCl or a $BaCl_2$/NaCl eutectic flux equal to three times the mass of the oxide reactants (0.9g). Once again, FeO was utilized to account for the 14 mol % Na_2O_2 impurity in Na_2O. Once ground and sealed under vacuum, the reactions were heated at 3°C/minute to 150°C above the eutectic melt of the added flux, held there for 4 days, slowly cooled to 450 at 0.1°C/ minute, and then furnace-cooled to room temperature. Red cubic single crystals obtained from the CsCl/NaCl reaction were analyzed and identified to be $Na_3Fe_2(AsO_4)_3$[9] (≈ 20%). The other phases included unidentified black and red polycrystalline powders. The $BaCl_2$/NaCl reaction yielded two crystalline phases including a large yield of brown single crystals of $Ba_{1.88}Na_{0.75}Fe_3(AsO_4)_4Cl$[10] (≈ 30%, refer to Chapter 5), a low yield of lime green crystals (< 5%), $Ba_2Fe_3(AsO_4)_4Cl$[10], and an unidentified colorless polycrystalline material. Both of these salt flux reactions yielded crystalline phases, none of which were the target compound, $Ba_{10}Na_5Fe_7(\mu_3\text{-}O)_2(AsO_4)_{14}$. As a result, efforts were made to derive a 100% yield of the targeted compound using a stoichiometric reaction. BaO, Na_2O, Fe_2O_3, FeO, and As_2O_5 were again mixed in a 10:2.5:3.3:0.4:7 mol ratio. The reactants were ground in a nitrogen-purged drybox, sealed under vacuum, and then heated to 850°C at 1°C/min, held there for four days, and then furnace-cooled to room temperature, yielding a lime green polycrystalline powder. The PXRD pattern is shown in Figure 4.2. The observed PXRD pattern of the product revealed evidence that the phase was present; so the product was sealed under vacuum again, reheated to 950°C

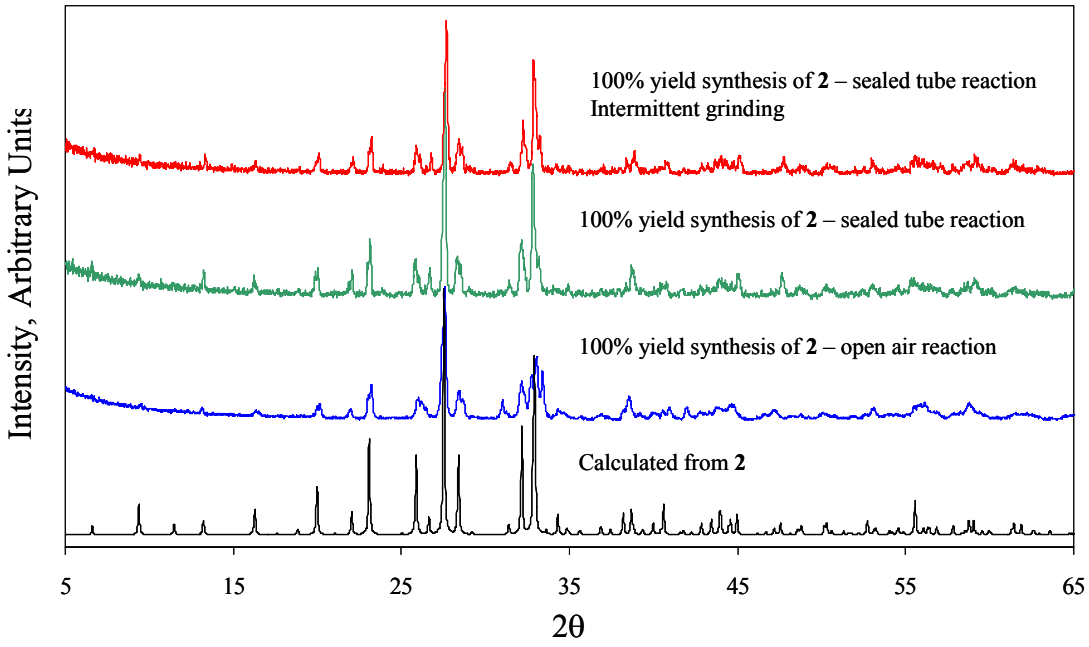

Figure 4.2: PXRD pattern showing a 100% yield synthesis of **2** at 850°C using various conditions vs. the calculated powder pattern of **2**, $Ba_{10}Na_5Fe_7(\mu_3\text{-}O)_2\ (AsO_4)_{12}(AsO_3)_2$.

at 3°C/minute, held there for 6 days, slowly cooled to 450°C to enhance crystal growth, and then furnace-cooled to room temperature. The reaction yielded, due to partial reduction of $As^{5+} \rightarrow As^{3+}$, single crystals of the title compound **2**, $Ba_{10}Na_5Fe_7(\mu_3\text{-}O)_2(AsO_4)_{12}(AsO_3)_2$, in an approximate 100% yield, as no other phases were observed in the PXRD pattern of the reaction product. It should be noted that none of the salt flux reactions were successful in growing single crystals of **2**. Lower temperature < 950°C always yielded **2**, but in a polycrystalline form. Therefore, higher temperatures had to be utilized to promote single crystal growth of this phase.

Multiple efforts were made to synthesize single crystals of a Sr derivative of **1**, $Sr_{10}Na_5Fe_7(\mu_3\text{-}O)_2(PO_4)_{14}$. SrO, Na_2O, Fe_2O_3, FeO, and P_4O_{10} were again mixed in a 10:2.5:3.3:0.4:3.5 mol ratio (ca. 0.3g) and then added to a $BaCl_2$/NaCl or a CsCl/NaCl eutectic flux equal to three times the mass of the oxide reactants (ca. 0.9g). The reaction was heated to 150°C above the melting point of the added flux, held there for 4 days, slowly cooled to 450°C, and then furnace-cooled to room temperature. The $BaCl_2$/NaCl reaction rendered a small yield of black single crystals of $Sr_2Na_{0.66}Fe_{3.34}(PO_4)_4Cl_{0.8}$[10] (< 10% refer to Chapter 5), yellow- green single crystals of $Ba_2SrFe_2(PO_4)_4$[10] (≈ 30%), and unidentified green and red polycrystalline material. The CsCl/NaCl reaction rendered a high yield of single crystals of the title compound (≈40%), **3**, a red polycrystalline phase (≈30%), and an unidentified colorless polycrystalline powder. It should be noted that a $SrCl_2$/NaCl flux was also utilized for the above reaction; however, the salt chewed up the silica ampoule in the furnace. Due to the successful growth of single crystals of the title

compound in the CsCl/NaCl reaction, no efforts were attempted to rerun the reaction in a $SrCl_2$/NaCl.

High-Yield Synthesis of Compounds 1-3: Efforts were made to synthesize 100% yield of compounds **1** and **2** first using open air reactions. $Ba(NO)_3$, $NaNO_3$, Fe_2O_3, and $(NH_4)H_2AsO_4$/$(NH_4)_2HPO_4$ were ground together in a 10:5:3.5:14 mol ratio and then placed in silica ampoules. These reactions were heated to 850°C, held there for 2 days, and then furnace-cooled to room temperature. The open air reaction targeting compound **2** is shown in Figure 4.1. It should be noted that neither open air reaction led to a 100% yield of the targeted compound. It was suspected that open air reactions could allow a partial reduction of the added Fe^{3+} or As^{5+}; hence, sealed tubes were utilized in the high- yield synthesis of compounds **1-3**. BaO/SrO, Na_2O, Fe_2O_3, FeO, and P_4O_{10} (or As_2O_5) were mixed in a 10:2.5:3.3:0.4:3.5(or 7) mol ratio. The reactants were ground in a nitrogen-purged drybox, placed in a silica ampoule, and then sealed under vacuum. The reactions were heated to 300°C, held there for 12 hours, and then furnace-cooled to room temperature. The silica ampoules were cracked open and the reaction contents were reground in open air. The reactants were then again placed in silica ampoules and resealed under vacuum for reheating. The reactions were heated to 850°C, held there for 2 days, and then furnace-cooled to room temperature. The powder patterns for the high-yield reactions can be seen in Figures 4.2-4.4. It should be noted that these reactions, for **1** and **2,** were also performed without intermittent grinding, and especially in the case of compound **1**, intermittent grinding led to the formation of a more pure product.

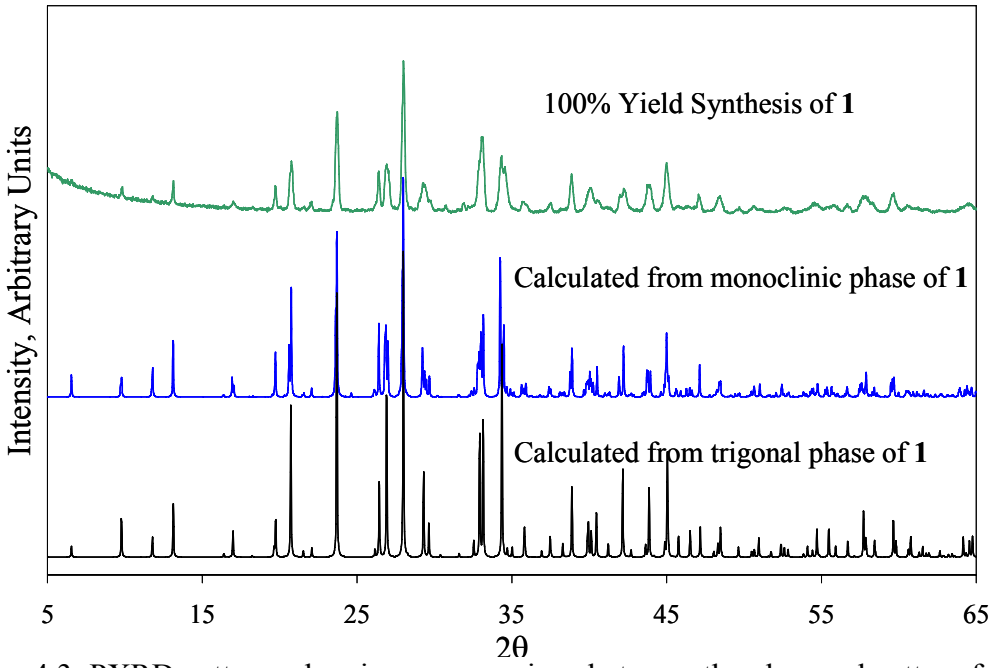

Figure 4.3: PXRD patterns showing a comparison between the observed pattern from a stoichiometric yield of compound **1** *vs.* the calculated powder patterns of the trigonal and monoclinic phases of $Ba_{10}Na_5Fe_7(\mu_3\text{-}O)_2(PO_4)_{14}$.

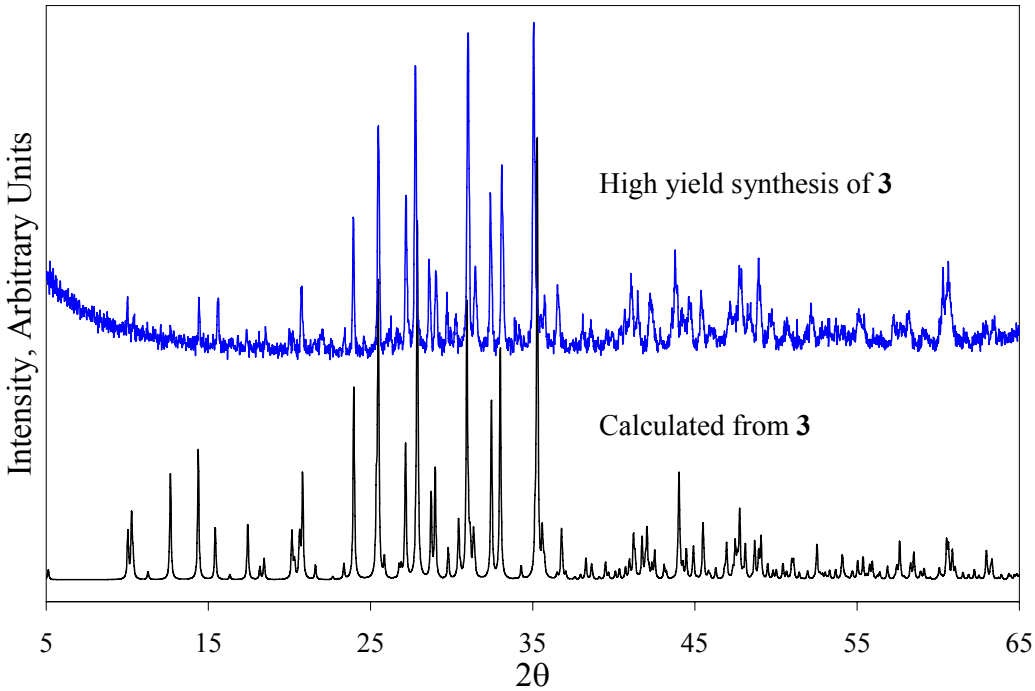

Figure 4.4: PXRD pattern showing the high-yield synthesis of compound **3** vs. the calculated powder pattern of $Sr_{14}NaFe_{10}(\mu_3\text{-}O)_2(PO_4)_{17}Cl$, obtained from the single crystal structure solution.

It should be noted that even though the three title compounds have different atomic ratios in their chemical formulas, all high-yield reactions were targeting compounds with the atomic ratios observed for **1**, $A_{10}Na_5Fe_7(\mu_3\text{-}O)_2(XO_4)_{14}$ (A/X = Ba/P, Ba/As, or Sr/P). Compound **3** contains a Cl^- anion. Since the wrong stoichiometry was used for the high-yield synthesis of **3**, it is no surprise that Figure 4.4, showing the PXRD pattern of this reaction, has several impurity peaks. Figure 4.5 shows multiple reactions targeting the Cl-free "$Sr_{10}Na_5Fe_7(\mu_3\text{-}O)_2(PO_4)_{14}$" in hopes that a Sr analog of **1** would form. Various temperatures ranging from 650-950°C were utilized for the sealed tube reactions; however, no sign of $Sr_{10}Na_5Fe_7(\mu_3\text{-}O)_2(PO_4)_{14}$ was ever observed. Efforts to synthesize high yields of $Sr_{14}NaFe_{10}(\mu_3\text{-}O)_2(PO_4)_{17}Cl$, **3,** using stoichiometric reactions were also unsuccessful. Although the phase formed, it did not form in high yields.

Through manipulation of the stoichiometric synthesis described above, attempts were also made to make other derivatives of compound **1**. Chemical substitutions were made in the aforementioned reaction to form $Ca_{10}Na_5Fe_7(\mu_3\text{-}O)_2(PO_4)_{14}$, $Sr_{10}Na_5Fe_7(\mu_3\text{-}O)_2(AsO_4)_{14}$, $Ba_{10}Na_5Mn_7(\mu_3\text{-}O)_2(PO_4)_{14}$, and $Ba_{10}Na_5MFe_6(\mu_3\text{-}O)_2(PO_4)_{14}$ where M = Ga^{3+} or Mn^{3+}. It should be noted that the Ca/P, Sr/As, and Ba/Mn derivatives were not observed in their respective powder patterns; however, when doping Ga or Mn into one of the Fe^{3+} sites, the phase formation is still observed. The PXRD patterns of the Mn- and Ga-doped reactions can be seen in Figure 4.6. From the PXRD pattern it appears that the Ga-doped material has a structure that is similar to compound **1**; however, the Mn-doped material, although shifted, appears to have a similar peak profile to compound **3**. It should be noted that Table 4.1 shows the refined unit cell parameters of the Ga^{3+}- and

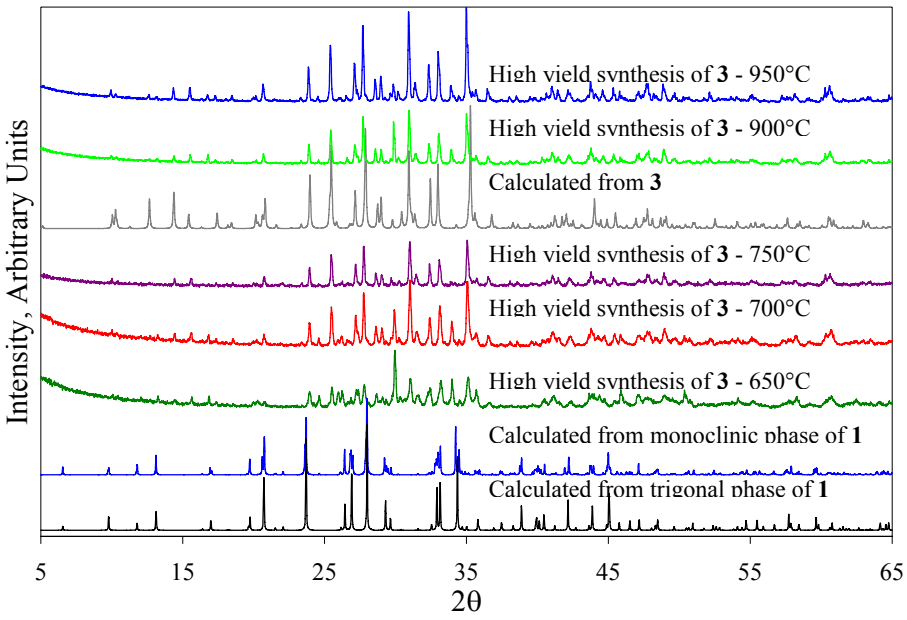

Figure 4.5: Attempted high-yield synthesis of **3** at various temperatures ranging from 650-950°C. These powder patterns are compared to the calculated powder patterns of both the trigonal and monoclinic phases of **1** and the calculated powder pattern of **3**. It should be noted that regardless of the isotherm temperature, there is no sign of the formation of a material having the same structure as **1**.

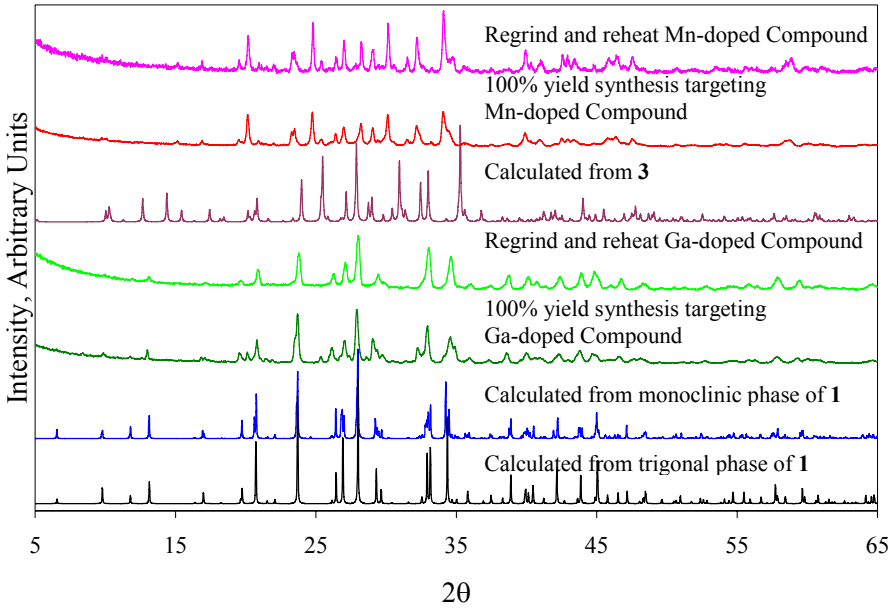

Figure 4.6: Powder patterns for Ga^{3+}- and Mn^{3+}- doped reactions for compound **1**. These reactions were stoichiometric with respect to the targeted compounds, $Ba_{10}Na_5MFe_6(\mu_3\text{-}O)_2(PO_4)_6$. Post-synthesis regrind and reheat, at 850°C for 10 days, was carried out to create a purer product. The powder patterns of the 10 day reactions were refined to obtain unit cell parameters (see Table 4.1 below)

Table 4.1: Unit cell refinements performed on the Ga^{3+}- and Mn^{3+}- doped derivatives

Sample	Sample type	unit cell parameters	Source of unit cell parameters	Figure # corresponding to powder pattern
$Ba_{10}Na_5\ Fe_7O_2(PO_4)_{14}$ Compound **1**	Single crystal	a = 10.432(2)Å c = 13.477(3) Å V = 1270.1(4) Å^3	SXRD	None
Ga-doped derivative Unit cell refined based on **1**	Powder	a =10.3866(6) Å c = 13.6158(1) Å V = 1272.1(1) Å^3	PXRD/Fullprof	Figure 4.6
$Sr_{14}NaFe_{10}O_2(PO_4)_{17}Cl$ Compound **3**	Single crystal	a = 10.212(2) Å c = 34.202(7) Å V = 3089(1) Å^3	SXRD	None
Mn-doped derivative Unit cell refined based on **3**	Powder	a = 10.271(2) Å c = 34.19(1) Å V = 3124(1) Å^3	PXRD/Fullprof	Figure 4.6

and Mn^{3+}-doped derivatives can be seen in Table 4.1, which were obtained using the Fullprof[11] program.

Characterization

Single Crystal X-ray Diffraction: Data were collected at room temperature (~300 K) and 160 K. The crystal-to-detector distance was approximately 27.6 mm for compound **1** and **2** and 37.6mm for compound **3** and scan times were 5, 15, and 60 seconds for **1-3** respectively. The crystallographic data for compounds **1-3** are summarized in Table 4.2. The atomic coordinates, thermal parameters, and selected bond distances and angles are listed in Tables 4.3- 4.5. It should be noted that the standard deviations for the sof of partially-occupied sites are not reported because SHELXTL[12] was first used to refine the occupancies and then they were fixed at the refined value or close to the refined value. Once the values are fixed, the standard deviations are no longer reported in the structure refinement files. It should also be noted that compound **2** has six restraints. These originate from the refinements of As(3) and O(9). These atoms had oddly shaped thermal ellipsoids that indicated disorder about the three-fold rotation axis. As a result the atoms were restrained in the z direction. The x and y coordinates were then slightly changed to move the atoms off of their special position and SHELXTL[12] was utilized to refine the coordinates generating three new atoms. The new x and y coordinates can be seen in Table 4.3.

Powder X-ray Diffraction: PXRD was used to confirm the presence of each phase in the respective high-yield reactions. The powder diffraction patterns for

Table 4.2: Crystallographic data for compounds **1-3**

empirical formula[a]	$Ba_{10}Na_5Fe_7O_2(PO_4)_{14}$	$Ba_{10}Na_5Fe_7O_2(AsO_4)_{12}(AsO_3)_2$	$Sr_{14}NaFe_{10}O_2(PO_4)_{17}Cl$
Compound	(**1**)	(**2**)	(**3**)
color / shape	Green/hexagonal plate	Green/thick hexagonal plate	Green/hexagonal plate
crystal size (mm)	0.2 × 0.2 × 0.08	0.05 × 0.04 × 0.04	0.08 × 0.08 × 0.04
formula weight (amu)	3240.78	3824.08	3490.11
space group, Z	*P*-3*m*1 (no. 164), 1	*P*-3*m*1 (no. 164), 1	$P6_3/mmc$ (no. 194), 2
T, °C		25	
a, Å	10.432(2)	10.871(4)	10.212(2)
c, Å	13.477(3)	13.373(3)	34.202(7)
V, Å^3	1270.1(4)	1368.7(8)	3089(1)
linear abs. coeff., mm^{-1}	10.167	17.419	14.876
F_{000}	1471	1707	3269
d_{calc}, g / cm^{-3}	4.237	4.640	3.753
data / restraints / parameters	890 / 0 / 102	955 / 6 [c] / 112	1091 / 0 / 130
secondary extinction	0.0031(5)	---------	---------
reflections collected / unique / R_{int}[a]	10728 / 890 / 0.1190	11478 / 955 / 0.1100	14050 / 1091 / 0.0785
final R1/wR2 [b] [$I > 2\sigma(I)$]	0.0617/ 0.1706	0.0857/ 0.2191/	0.0912 / 0.2247
R1/wR2 (all data)	0.0617/ 0.1706	0.0945/ 0.2289	0.0947/ 0.2268
GOF	1.105	1.151	1.107
Largest difference peak / hole (e$^-$ / Å^3)	2.274 / -1.935	2.941 / -3.581	2.071/ -1.911

[a] $R_{int} = \Sigma \mid Fo^2 - Fo^2 \text{ (mean)} \mid / \Sigma[Fo^2]$; [b] **1** R1 = $\Sigma \, ||F_o| - |F_c|| / \Sigma|F_o|$; *w*R2 = $\{[\Sigma[w(F_o^2-F_c^2)^2] / [\Sigma w(F_o)^2)^2]\}^{1/2}$; Rw = 1 / $[\sigma^2(Fo^2) + (0.0674P)^2+99.6543P]$ where P = $(Fo^2+2Fc^2) / 3$; **2** R1 = $\Sigma \, ||F_o| - |F_c|| / \Sigma|F_o|$; *w*R2 = $\{[\Sigma[w(F_o^2-F_c^2)^2] / [\Sigma w(F_o)^2)^2]\}^{1/2}$; Rw = 1 / $[\sigma^2(Fo^2) + (0.1132P)^2+86.3357P]$ where P = $(Fo^2+2Fc^2) / 3$; **3** R1 = $\Sigma \, ||F_o| - |F_c|| / \Sigma|F_o|$; *w*R2 = $\{[\Sigma[w(F_o^2-F_c^2)^2] / [\Sigma w(F_o)^2)^2]\}^{1/2}$; Rw = 1 / $[\sigma^2(Fo^2) + (0.0741P)^2+185.5417P]$ where P = $(Fo^2+2Fc^2) / 3$; [c] The restraints are described in the characterization section.

Table 4.3: Atomic parameters for compounds **1-3**

Atom	Wycoff position	sof	x	y	z
		$Ba_{10}Na_5Fe_7O_2(PO_4)_{14}$, **1**			
Ba1	6*i*	0.5	0.5228(2)	0.0457(4)	0.0161(2)
Ba2	6*i*	1.0	0.2943(2)	0.14715(7)	0.27944(9)
Ba3	1*a*	1.0	0	0	0
Na1	6*i*	0.67	0.531(2)	0.469(2)	0.476(2)
Na2	2*d*	0.5	2/3	1/3	0.427(2)
Fe1	1*b*	1.0	0	0	1/2
Fe2	6*i*	1.0	0.1220(4)	0.5610(2)	0.2670(2)
P1	6*i*	1.0	0.1759(3)	0.3519(6)	0.4227(3)
P2	6*i*	1.0	0.1690(3)	0.3381(6)	0.1232(4)
P3	2*d*	1.0	2/3	1/3	0.216(1)
O1	2*d*	1.0	1/3	2/3	0.269(2)
O2	12*j*	1.0	0.087(1)	0.417(1)	0.1631(7)
O3	12*j*	1.0	0.084(1)	0.410(1)	0.3683(7)
O4	6*i*	1.0	0.0904(8)	0.181(2)	0.4112(9)
O5	6*i*	1.0	0.2031(8)	0.406(2)	0.527(1)
O6	6*i*	1.0	0.0891(8)	0.178(2)	0.165(1)
O7	6*i*	1.0	0.1752(9)	0.350(2)	0.012(1)
O8	6*i*	1.0	0.586(1)	0.171(2)	0.252(2)
O9	2*d*	1.0	2/3	1/3	0.105(3)
		$Ba_{10}Na_5Fe_7O_2(AsO_4)_{12}(AsO_3)_2$, **2**			
Ba1	6*i*	0.5	0.5297(3)	0.0596(5)	0.0221(3)
Ba2	6*i*	1.0	0.2916(2)	0.14584(12)	0.2739(1)
Ba3	1*a*	1.0	0	0	0
Na1	6*i*	0.33	0.477(3)	0.523(3)	0.515(4)
Na2	6*i*	0.39	0.553(3)	0.447(3)	0.442(3)
Na3	2*d*	0.33	2/3	1/3	0.419(5)
Fe1	1*b*	1.0	0	0	1/2
Fe2	6*i*	1.0	0.1286(7)	0.5643(4)	0.2620(3)
As1	6*i*	1.0	0.1769(2)	0.3538(3)	0.4224(2)
As2	6*i*	1.0	0.1683(2)	0.3365(3)	0.1152(2)
As3	2*d*	0.33	0.7059(9)	0.3530(5)	0.2046(6)
O1	2*d*	1.0	1/3	2/3	0.269(3)
O2	12*j*	1.0	0.086(2)	0.424(2)	0.157(1)
O3	12*j*	1.0	0.080(2)	0.412(2)	0.363(1)
O4	6*i*	1.0	0.089(1)	0.179(2)	0.401(1)
O5	6*i*	1.0	0.206(1)	0.412(2)	0.540(2)
O6	6*i*	1.0	0.089(1)	0.178(2)	0.1642(16)
O7	6*i*	1.0	0.168(2)	0.337(3)	-0.007(2)
O8	6*i*	0.67	0.831(4)	0.416(2)	0.05(1)
O9	6*i*	0.33	0.641(3)	0.359(3)	0.0951
		$Sr_{14}NaFe_{10}O_2(PO_4)_{17}Cl$, **3**			
Sr1	4*e*	1.0	0	0	0.18730(9)
Sr2	12*k*	1.0	0.3002(3)	0.1501(1)	0.07918(6)
Sr3	12*k*	0.83	0.5289(3)	0.0578(6)	0.1879(1)
Sr4	6*g*	0.33	½	½	0
Na	4*f*	0.5	1/3	2/3	-0.028(1)
Fe1	2*a*	1.0	0	0	0
Fe2	12*k*	1.0	0.4420(2)	0.5580(2)	0.09482(8)

Table 4.3: Atomic parameters for compounds **1-3** cont…

Atom	Wycoff position	sof	x	y	z
$Sr_{14}NaFe_{10}O_2(PO_4)_{17}Cl$, **3** cont...					
Fe3	6*h*	1.0	0.1656(4)	0.3311(9)	1/4
P1	12*k*	1.0	0.1764(3)	0.3529(6)	0.0328(1)
P2	12*k*	1.0	0.1630(3)	0.3260(7)	0.1473(2)
P3	4*f*	1.0	2/3	1/3	0.1106(3)
P4	6*h*	1.0	0.352(1)	0.1762(7)	1/4
Cl	2*c*	1.0	1/3	2/3	1/4
O1	12*k*	1.0	0.0894(7)	0.179(1)	0.0354(3)
O2	24*l*	1.0	0.326(1)	0.406(1)	0.0548(3)
O3	4*f*	1.0	1/3	2/3	0.0919(7)
O4	12*k*	1.0	0.2049(9)	0.410(2)	-0.0087(4)
O5	12*k*	1.0	0.147(1)	0.293(2)	0.1900(5)
O6	12*k*	1.0	0.585(1)	0.171(3)	0.0949(7)
O7	6*h*	1.0	0.183(4)	0.091(2)	1/4
O8	24*l*	1.0	0.326(2)	0.415(2)	0.1361(4)
O9	12*k*	1.0	0.432(5)	0.216(2)	0.212(1)
O10	24*l*	0.5	0.135(3)	0.179(3)	0.1274(7)
O11	12*j*	0.5	0.389(4)	0.352(5)	1/4
O12	4*f*	1.0	2/3	1/3	0.1539(9)

Table 4.4: Anisotropic thermal parameters ($Å^2$) for compounds **1-3**

Atom	U_{11}	U_{22}	U_{33}	U_{12}	U_{13}	U_{23}
$Ba_{10}Na_5Fe_7O_2(PO_4)_{14}$, **1**						
Ba1	0.027(1)	0.056(3)	0.021(2)	0.028(1)	0.0102(8)	0.020(2)
Ba2	0.0253(9)	0.0167(6)	0.0149(7)	0.0127(4)	-0.0027(5)	-0.0013(2)
Ba3	0.015(1)	0.015(1)	0.008(1)	0.0077(5)	0.00000	0.00000
Na1	0.06(1)	0.06(1)	0.10(2)	-0.00(1)	-0.03(1)	0.03(1)
Na2	0.06(2)	0.06(2)	0.02(2)	0.028(8)	0.00000	0.00000
Fe1	0.012(2)	0.012(2)	0.009(3)	0.006(1)	0.00000	0.00000
Fe2	0.048(2)	0.021(1)	0.010(1)	0.024(1)	0.000(1)	0.0001(7)
P1	0.011(2)	0.016(3)	0.008(2)	0.008(1)	0.0013(9)	0.003(2)
P2	0.011(2)	0.008(2)	0.015(2)	0.004(1)	-0.000(1)	-0.001(2)
P3	0.055(6)	0.055(6)	0.038(7)	0.027(3)	0.00000	0.00000
O1	0.03(1)	0.03(1)	0.00(1)	0.017(5)	0.00000	0.00000
O2	0.020(5)	0.019(5)	0.015(4)	0.013(4)	0.002(4)	-0.005(4)
O3	0.010(5)	0.018(5)	0.023(5)	0.007(4)	-0.001(4)	0.003(4)
O4	0.021(6)	0.019(8)	0.010(6)	0.010(4)	0.004(3)	0.008(6)
O5	0.025(6)	0.008(7)	0.014(6)	0.004(3)	-0.003(3)	-0.006(6)
O6	0.023(6)	0.015(8)	0.025(7)	0.007(4)	0.000(3)	0.001(6)
O7	0.024(6)	0.016(8)	0.023(8)	0.008(4)	-0.001(3)	-0.002(6)
O8	0.043(9)	0.03(1)	0.08(1)	0.016(6)	-0.005(5)	-0.01(1)
O9	0.17(4)	0.17(4)	0.01(2)	0.09(2)	0.00000	0.00000
$Ba_{10}Na_5Fe_7O_2(AsO_4)_{12}(AsO_3)_2$, **2**						
Ba1	0.051(2)	0.079(3)	0.026(2)	0.039(2)	0.0136(9)	0.027(2)
Ba2	0.047(1)	0.0332(8)	0.0235(9)	0.0233(6)	-0.0056(8)	-0.0028(4)
Ba3	0.031(1)	0.031(1)	0.012(2)	0.0156(7)	0.00000	0.00000
Na1	0.07(4)	0.07(4)	0.08(9)	0.01(4)	-0.02(4)	0.02(4)
Na2	0.05(2)	0.05(2)	0.13(7)	0.02(2)	-0.02(2)	0.02(2)
Fe1	0.027(3)	0.027(3)	0.014(4)	0.013(2)	0.00000	0.00000

Table 4.4: Anisotropic thermal parameters (Å^2) for compounds **1-3** cont…

Atom	U_{11}	U_{22}	U_{33}	U_{12}	U_{13}	U_{23}
$Ba_{10}Na_5Fe_7O_2(AsO_4)_{12}(AsO_3)_2$, **2** cont...						
Fe2	0.103(5)	0.044(2)	0.018(2)	0.052(2)	-0.008(2)	-0.004(1)
As1	0.027(1)	0.028(2)	0.014(1)	0.0139(8)	0.0013(5)	0.002(1)
As2	0.032(1)	0.025(2)	0.020(1)	0.0127(8)	-0.0021(6)	-0.004(1)
As3	0.05(1)	0.031(5)	0.030(3)	0.025(6)	-0.009(4)	-0.004(2)
O1	0.04(1)	0.04(1)	0.03(2)	0.019(6)	0.00000	0.00000
O2	0.06(1)	0.045(9)	0.040(8)	0.032(9)	-0.021(8)	-0.024(7)
O3	0.035(9)	0.05(1)	0.041(9)	0.017(8)	0.000(7)	0.020(8)
O4	0.032(8)	0.02(1)	0.03(1)	0.012(5)	-0.003(4)	-0.006(8)
O5	0.07(1)	0.03(1)	0.013(8)	0.016(6)	0.001(4)	0.003(8)
O6	0.019(6)	0.015(9)	0.04(1)	0.007(4)	-0.005(4)	-0.009(8)
O7	0.09(2)	0.06(2)	0.02(1)	0.028(8)	-0.006(5)	-0.01(1)
O8	0.03(2)	0.05(2)	0.07(2)	0.02(1)	0.02(2)	0.012(9)
O9	0.05(3)	0.05(3)	0.08(4)	0.04(3)	0.01(1)	-0.01(1)
$Sr_{14}NaFe_{10}O_2(PO_4)_{17}Cl$, **3**						
Sr1	0.033(1)	0.033(1)	0.020(2)	0.0167(6)	0.00000	0.00000
Sr2	0.049(1)	0.0340(9)	0.028(1)	0.0244(7)	-0.0031(9)	-0.0016(5)
Sr3	0.125(3)	0.091(3)	0.040(2)	0.046(2)	-0.015(1)	-0.029(2)
Sr4	0.17(2)	0.17(2)	0.24(3)	-0.08(2)	0.15(2)	-0.15(2)
Na	0.04(1)	0.04(1)	0.05(2)	0.021(6)	0.00000	0.00000
Fe1	0.019(2)	0.019(2)	0.016(3)	0.009(1)	0.00000	0.00000
Fe2	0.031(1)	0.031(1)	0.021(1)	0.004(1)	0.0009(7)	-0.0009(7)
Fe3	0.070(3)	0.084(5)	0.045(3)	0.042(2)	0.00000	0.00000
P1	0.022(2)	0.022(3)	0.014(2)	0.011(1)	-0.0009(9)	-0.002(2)
P2	0.040(2)	0.030(3)	0.021(2)	0.015(2)	0.003(1)	0.006(2)
P3	0.059(5)	0.059(5)	0.017(5)	0.030(2)	0.00000	0.00000
P4	0.047(7)	0.054(5)	0.10(1)	0.023(3)	0.00000	0.00000
Cl	0.044(6)	0.044(6)	0.07(1)	0.022(3)	0.00000	0.00000
O1	0.020(5)	0.019(7)	0.014(6)	0.010(3)	0.000(2)	-0.001(5)
O2	0.027(5)	0.023(5)	0.042(6)	0.012(4)	-0.014(5)	-0.012(4)
O3	0.027(8)	0.027(8)	0.03(1)	0.013(4)	0.00000	0.00000
O4	0.066(9)	0.028(8)	0.021(7)	0.014(4)	0.005(3)	0.010(6)
O5	0.07(1)	0.07(1)	0.028(9)	0.035(7)	0.007(4)	0.014(8)
O6	0.07(1)	0.06(2)	0.08(2)	0.032(8)	0.000(6)	0.00(1)
O7	0.04(2)	0.19(4)	0.04(2)	0.022(9)	0.00000	0.00000
O8	0.055(9)	0.13(2)	0.08\(1)	0.06(1)	0.038(8)	0.07(1)
O9	0.18(4)	0.20(3)	0.19(4)	0.09(2)	0.16(3)	0.08(2)
O10	0.07(2)	0.04(1)	0.06(1)	0.03(1)	0.03(1)	0.02(1)
O11	0.06(2)	0.11(3)	0.01(1)	0.03(2)	0.00000	0.00000
O12	0.26(5)	0.26(5)	0.00(2)	0.13(3)	0.00000	0.00000

Table 4.5: Selected bond distances and angles for compounds **1**-**3**

Bond Distances		Bond Angles	
$Ba_{10}Na_5Fe_7O_2(PO_4)_{14}$, **1**			
Fe(1)-O(4) 2.02(1)*6	P(2)-O(7) 1.51(2)	O(4)- Fe(1)-O(4) 180.0(7)	O(5)-P(1)-O(3) 109.5(5)
Fe(2)-O(1) 1.909(4)	P(2)-O(6) 1.55(2)	O(4)-Fe(1)-O(4) 88.6(6)	O(3)-P(1)-O(3) 109.0(8)
Fe(2)-O(2) 1.951(9)*2	P(2)-O(2) 1.55(1)*2	O(4)-Fe(1)-O(4) 91.4(6)	O(5)-P(1)-O(4) 115.0(8)
Fe(2)-O(3) 1.97(1)*2	P(3)-O(9) 1.50(4)	O(1)-Fe(2)-O(2) 100.1(6)	O(3)-P(1)-O(4) 106.8(5)
Fe(2)-O(8) 2.65(2)	P(3)-O(8) 1.54(2)*3	O(2)- Fe(2)-O(2) 85.1(6)	O(7)-P(2)-O(6) 115.5(9)
P(1)-O(5) 1.49(1)	Fe(2)- Fe(2) 3.307(7)	O(2)-Fe(2)-O(3) 160.4(5)	O(7)-P(2)-O(2) 108.2(5)
P(1)-O(3) 1.55(1)		O(1)-Fe(2)-O(3) 99.4(6)	O(6)-P(2)-O(2) 107.6(5)
P(1)-O(3) 1.55(1)		O(2)-Fe(2)-O(3) 89.8(4)	O(2)-P(2)-O(2) 109.8(8)
P(1)-O(4) 1.55(2)		O(2)-Fe(2)-O(3) 160.4(5)	O(9)-P(3)- O(8) 108(1)
		O(3)-Fe(2)-O(3) 88.7(6)	O(8)-P(3)-O(8) 110.9(9)
		Fe(2)-O(1)-Fe(2) 119.97(4)	
$Ba_{10}Na_5Fe_7O_2(AsO_4)_{12}(AsO_3)_2$, **2**			
Fe(1)-O(4) 2.09(2)*6	As(2)-O(6) 1.62(2)	O(4)-Fe(1)-O(4) 180(1)	O(4)-As(1)-O(3) 105.6(7)
Fe(2)-O(1) 1.930(7)	As(2)-O(7) 1.63(2)	O(4)-Fe(1)-O(4) 88.3(7)	O(5)-As(1)-O(3) 109.8(7)
Fe(2)-O(2) 1.95(2)*2	As(2)-O(2) 1.70(2)*2	O(4)-Fe(1)-O(4) 91.7(7)	O(3)-As(1)-O(3) 110(1)
Fe(2)-O(3) 1.99(2)*2	As(3)-O(9) 1.64(2)	O(1)-Fe(2)-O(2)104.1(9)	O(6)-As(2)-O(7) 114(1)
Fe(2)-O(8) 2.81(4)	As(3)-O(8) 1.86(4)	O(2)-Fe(2)-O(2) 83(1)	O(6)-As(2)-O(2) 108.0(7)
As(1)-O(4) 1.66(2)	As(3)-O(8) 1.86(4)	O(1)-Fe(2)-O(3) 101.2(9)	O(7)-As(2)-O(2) 109.4(7)
As(1)-O(5) 1.67(2)	Fe(2)-Fe(2) 3.34(1)	O(2)-Fe(2)-O(3) 88.7(7)	O(2)-As(2)-O(2) 108(1)
As(1)-O(3) 1.68(2)*2		O(2)-Fe(2)-O(3) 154.6(8)	
		O(3)-Fe(2)-O(3) 88(1)	O(8)-As(3)-O(8) 114(2)
		Fe(2)-O(1)-Fe(2) 119.8(2)	O(9)-As(3)-O(8) 111(2)
			O(9)-As(3)-O(8) 104(1)
		O(4)-As(1)-O(5) 116(1)	O(9)-As(3)-O(8) 82(2)
			O(8)-As(3)-O(8) 92(1)
$Sr_{14}NaFe_{10}O_2(PO_4)_{17}Cl$, **3**			
Fe(1)-O(1) 1.99(1)*6	P(1)-O(4) 1.50(1)	O(1)-Fe(1)-O(1) 180.0(5)	O(11)-Fe(3)-O(11) 170(3)
Fe(2)-O(3) 1.924(4)	P(1)-O(2) 1.536(9)*2	O(1)-Fe(1)-O(1) 86.8(5)	
Fe(2)-O(8) 1.95(1)*2	P(1)-O(1) 1.54(1)	O(1)-Fe(1)-O(1) 93.2(5)	O(4)-P(1)-O(2) 111.1(5)
Fe(2)-O(2) 1.96(1)*2	P(2)-O(5) 1.49(2)*2	O(1)-Fe(1)-O(1)180.0(7)	O(2)-P(1)-O(2) 109.4(8)
Fe(2)-O(6) 2.54(2)	P(2)-O(8) 1.49(1)	O(1)-Fe(1)-O(1)180.0(8)	O(4)-P(1)-O(1) 112.9(8)
Fe(3)-O(5) 2.08(2)*2	P(2)-O(10)1.54(2)*2	O(3)-Fe(2)-O(8) 99.2(7)	O(2)-P(1)-O(1) 106.0(5)
Fe(3)-O(11) 2.19(4)	P(3)-O(12) 1.48(3)*3	O(8)-Fe(2)-O(8) 86(1)	O(5)-P(2)-O(8) 110.8(8)
Fe(3)-O(7) 2.540(7)*2	P(4)-O(9) 1.47(3)*2	O(3)-Fe(2)-O(2) 97.2(6)	O(8)-P(2)-O(8) 108(1)
Fe(3)-Cl(1) 2.968(8)	P(4)-O(7) 1.50(3)	O(8)-Fe(2)-O(2) 163.5(5)	O(5)-P(2)-O(10) 106(1)
	P(4)-O(11) 1.64(5)*2	O(8)-Fe(2)-O(2) 90.6(7)	O(8)-P(2)-O(10) 125(1)
	Fe(2)-Fe(2) 3.328(6)	O(2)-Fe(2)-O(2) 88.6(6)	O(8)-P(2)-O(10) 95(1)
		O(3)-Fe(2)-O(6) 177.1(9)	O(12)-P(3)-O(6) 110.5(9)
		O(8)-Fe(2)-O(6) 82.9(6)	O(6)-P(3)-O(6) 108.4(9)
		O(2)-Fe(2)-O(6) 80.8(5)	O(9)-P(4)-O(9) 123(4)
		O(5)-Fe(3)-O(5) 161(1)	O(9)-P(4)-O(7) 118(2)
		O(5)-Fe(3)-O(11) 90.8(2)	O(9)-P(4)-O(11) 84.5(8)
		O(5)-Fe(3)-O(7) 82.3(5)	O(7)-P(4)-O(11) 102(1)
		O(11)-Fe(3)-O(7)128(2)	Fe(2)-O(3)-Fe(2) 119.7(1)

compounds **1-3** and other derivatives are shown in Figures 4.1-4.6 above. With the exception of the PXRD pattern shown in Figure 4.7, the X-ray powder diffraction data were collected at room temperature in the 2θ range of 5–65° with a step size of .02 and a scan rate of 0.0025°/s. As for Figure 4.7, variable temperature PXRD, ranging from -90 to 90°C, was utilized to investigate the existence of possible structural transitions that occur upon heating or cooling **1** above and below the magnetic transition. The 2θ range for this sample was 10-50° with a step size of 0.0120°/sec.

Differential Scanning Calorimetry: DSC was performed to look for possible structural transitions in compound **1**. The measurements were performed using a DSC 820 from Mettler Toledo. In this study, several measurements were performed on a ground powder of selected single crystals and as prepared polycrystalline samples obtained from stoichiometric reactions. The samples, ranging from 10-15 mg, were weighed and then loaded into an aluminum sample pan that was sealed by applying force to the top of the pan lid with a press. The sample and reference pans were then placed inside of the furnace and then heated and cooled at various rates ranging from 0.5 to 10°C/minute under a N_2 atmosphere. The measurements were performed on various samples including 100% yield or a ground powder of selected single crystals. The sample and reference pans were then placed inside of the furnace and heated and/or cooled to a target temperature under a N_2 atmosphere, -150 to 150°C. Conditions were varied to investigate whether a structural transition could be dependent on the experimental conditions used.

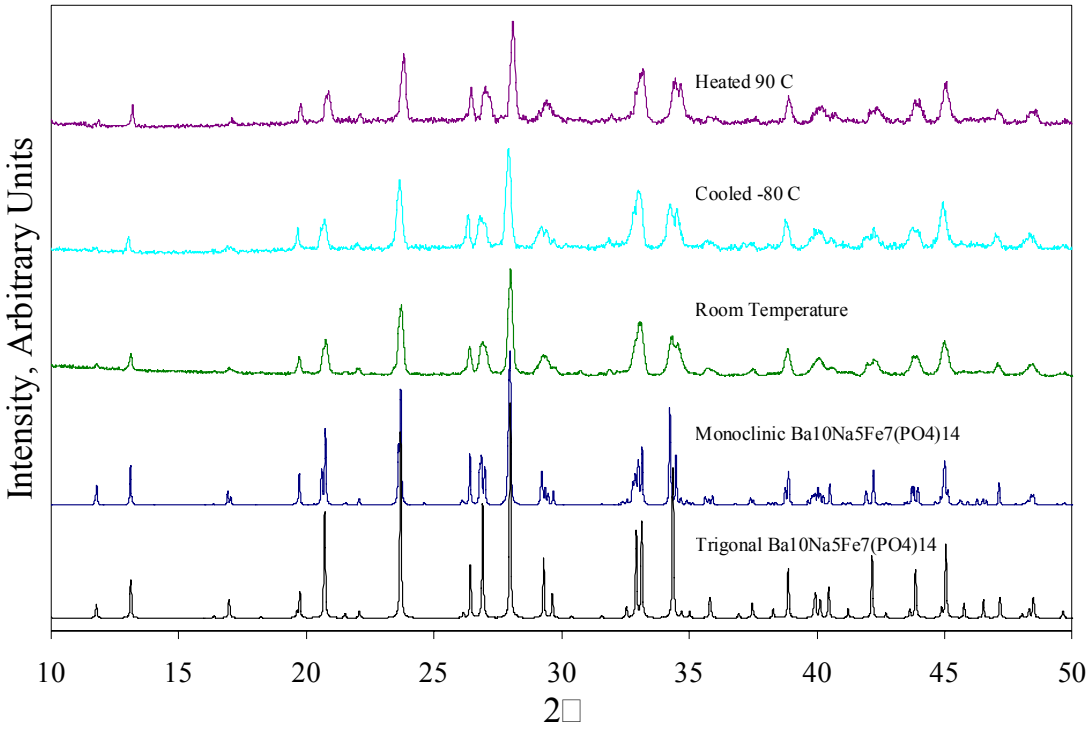

Figure 4.7: Variable temperature PXRD patterns obtained form a 100% yield synthesis of **1**, $Ba_{10}Na_5Fe_7(\mu_3\text{-}O)_2(PO_4)_{14}$ vs. the calculated powder patterns obtained from the trigonal and monoclinic phases of **1**. There is no significant change upon heating and cooling the sample, indicating that there is no structural transition occurring under these conditions.

Differential Thermal Analysis: DTA was performed on a 100% yield sample of compound **1**, 9.9 mg. The sample was heated at a rate of 10°C/minute to 1100°C then cooled at a rate of 10°C/min to room temperature. DTA was utilized to identify any phase transitions such as decomposition or melt.

Thermal Gravimetric Analysis: TGA was performed on a 100% yield sample (13.3mg) of compound **1**. The sample was placed in an alumina sample pan. The material was heated to 1100°C at 10°C/minute, held there for 10 minutes, and the cooled to room temperature at 10°C/minute. There was no observed change in the mass of the sample.

Magnetic properties: Magnetic susceptibility was measured with a Quantum Design SQUID MPMS-5S magnetometer. Temperature-dependent magnetic studies were performed on a ground powder of selected single crystals (6.6 mg) and a single crystal (3.5 mg) with fields applied along *c*. The initial temperature-dependent studies were performed over 2– 360 K in applied fields of 100 and 5000 Oe. The samples were placed in a gel capsule. The magnetic susceptibility was corrected for the contribution of the gel capsule and for the core diamagnetism (using Pascal Ms constants). Field-dependent measurements were performed with magnetic field ranging from 5T to -5T on powder as well as a single crystal (3.5 mg).

Heat Capacity: Measurements were performed on a Quantum Design PPMS. The studies were carried out on a single crystal (7.0mg) with 0 and 1T magnetic fields applied along the crystallographic *c* axis. The samples were placed in a special sample holder, and Apiezon N grease was used to maintain the crystal orientation.

Results and Discussion

Green hexagonally-shaped single crystals of $Ba_{10}Na_5Fe_7(\mu_3\text{-}O)_2(PO_4)_{14,}$ (**1**) $Ba_{10}Na_5Fe_7(\mu_3\text{-}O)_2(AsO_4)_{12}(AsO_3)_2$ (**2**), and $Sr_{14}NaFe_{10}(\mu_3\text{-}O)_2(PO_4)_{17}Cl$ (**3**) were grown using conventional high-temperature, solid-state methods. Large single crystals of **1** and **3** with sizes up to 2 mm were obtained using molten-salt methods. Unlike the compounds presented in chapter 3, **1**-**3** are slightly metal-deprived with respect to the Fe/X < 1 (X = a maingroup element such as P or As). These compounds are not isostructural but have similar structural features including Fe-O-X (X = As or P) slabs that contain $Fe_3(\mu_3\text{-}O)$ units that will be further described in the following paragraphs. Compounds **1** and **2** crystallize in a trigonal space group, *P*-3*m*1 (no. 164), while **3** crystallizes in a hexagonal space group, $P6_3/mmc$ (no. 194). The crystallographic data for these three compounds is listed in Table 4.2.

$Ba_{10}Na_5Fe_7(\mu_3\text{-}O)_2(PO_4)_{14}$ and $Ba_{10}Na_5Fe_7(\mu_3\text{-}O)_2(AsO_4)_{12}(AsO_3)_2$ are layered solids, shown in Figure 4.8. Despite the slight differences that will be discussed later, their structures are for the most part isostructural. Due to their similarities, unless otherwise stated, the structure of **1** will be discussed from this point forward. It contains two crystallographically distinct Fe(III) sites that are octahedrally coordinated by oxygen. The octahedral Fe(1) has a Fe-O bond distance of 2.02(1)Å and is isolated from other metal polyhedra *via* corner-sharing oxygen with 6 $(PO_4)^{3-}$ oxyanions. Fe(2), found in a distorted octahedral geometry, has one axial Fe(2)-O(1) bond distance of 1.909(4) Å, a second axial Fe(2)-O(8) distance of 2.65(2)Å, and 4 equatorial bonds consisting of 2 Fe(2)-O(2), 1.951(9) Å, and 2 Fe(2) O(3), 1.97(1) Å. Both Fe(1) and Fe(2) are found in

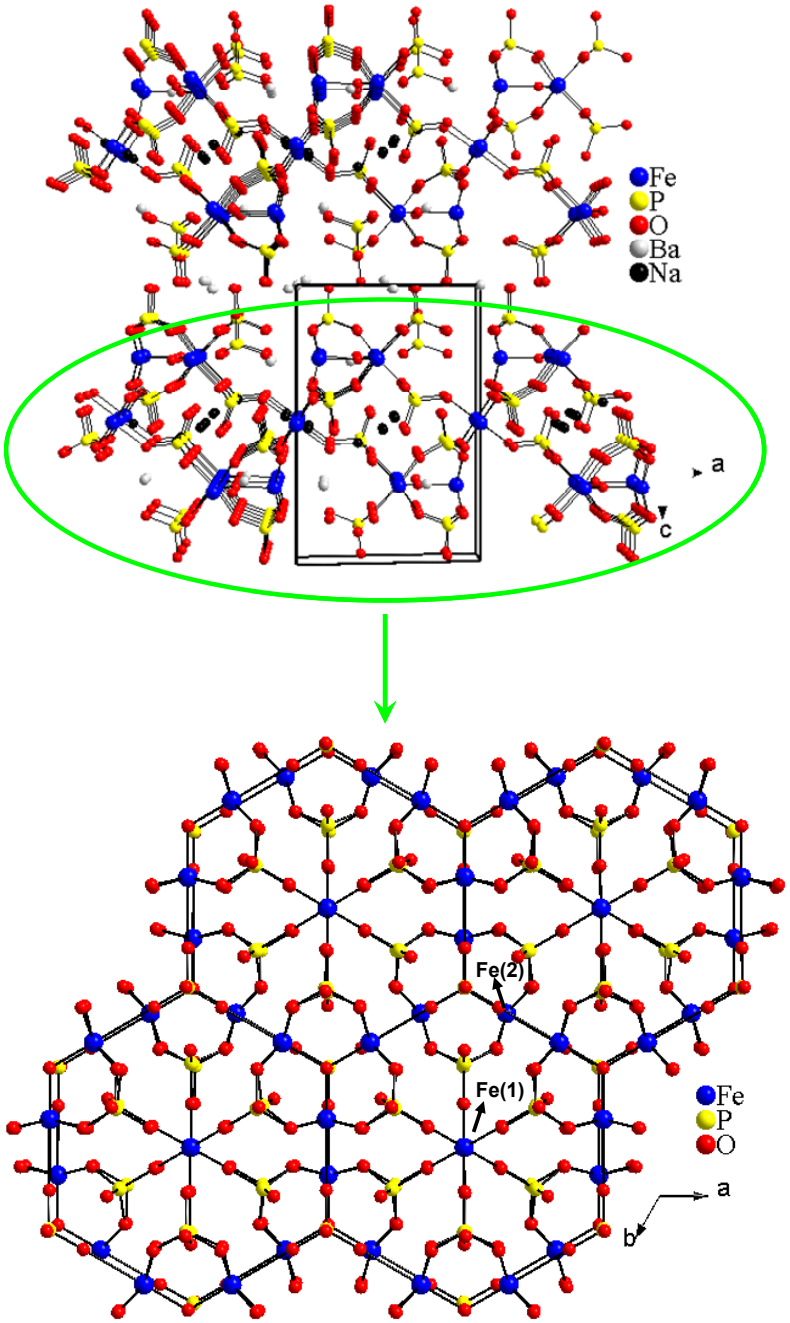

Figure 4.8: Perspective view of **1** (top) showing the layers along the crystallographic *c* axis and the projected view of a single Fe-P-O slab found within the *ab* plane.

a 3+ oxidation state which is similar to the value obtained from bond valence sum calculations[13] 2.96 and 2.99 for Fe(1) and Fe(2) respectively. Three distorted $Fe(2)O_6$ octahedra share a single axial oxygen to form an Fe_3O equilateral triangular nanostructure containing a μ_3 bridging mode, Figure 4.9. The long Fe(2)-Fe(2) distances, equal to 3.307(7)Å, preclude any possible significant metal-metal bonding and, therefore, it is expected that the Fe-O distances will determine the magnitude of the antiferromagnetic super exchange.[14] Each Fe(2) octahedron shares 4 corner equatorial oxygen atoms with surrounding $(PO_4)^{3-}$ units, electronically isolating the triangular $Fe_3(\mu_3\text{-}O)$ units from other metal polyhedra. Due to this connectivity, it is expected that magnetic coupling within the $Fe_3(\mu_3\text{-}O)$ nanostructure, occurring *via* super exchange, will be much stronger than the magnetic interactions occurring between the nanostructures. Each Fe(1) is surrounded by 6 $Fe_3(\mu_3\text{-}O)(PO_4)_6$ units and the Fe-O-P-O-Fe connectivity extends infinitely within the *ab* plane. When looking along *c*, the Fe-O-P layers, separated from one another *via* Ba ions, are revealed. The Ba cations are located both within and between the covalent layers, while Na is found within channels which run along the *a* and *b* axes.

When comparing the structures of $Ba_{10}Na_5Fe_7(\mu_3\text{-}O)_2(PO_4)_{14}$ and $Ba_{10}Na_5Fe_7(\mu_3\text{-}O)_2(AsO_4)_{12}(AsO_3)_2$, one major difference is observed. This difference becomes apparent when considering the empirical formulas of the two derivatives. Compound **2** has two less O atoms due to the presence of two three-coordinate As^{3+} cations in the structure, As(3). It, along with one oxygen atom, O(9), has three-fold disorder. Irregular thermal

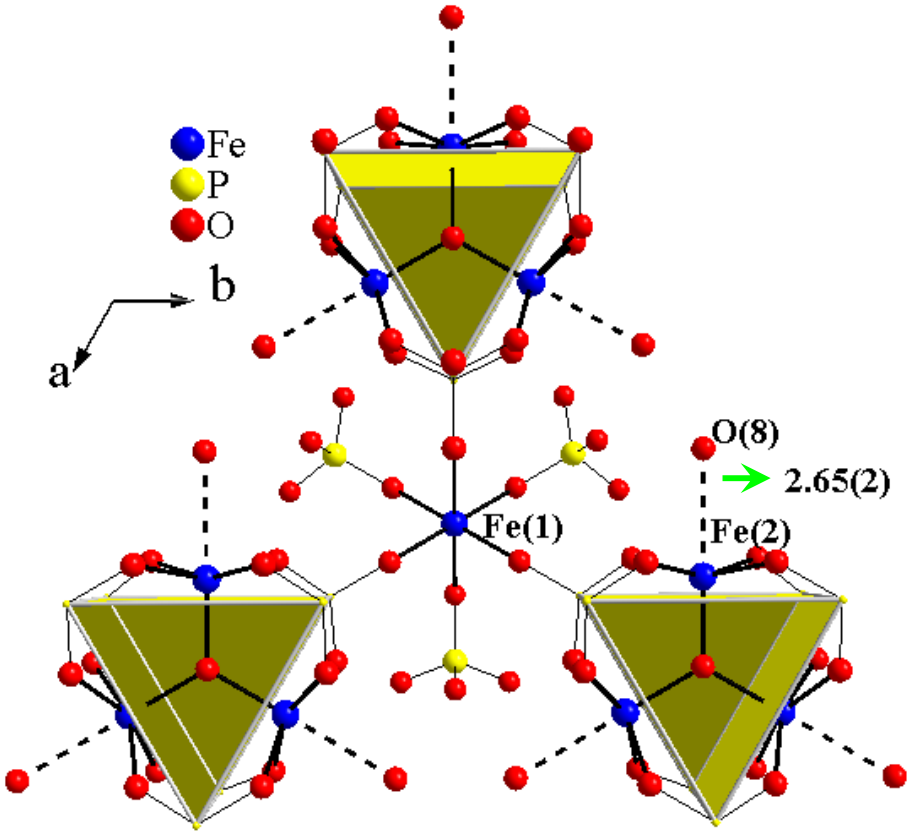

Figure 4.9: Projected view of the Fe(1) cation that is surrounded by 6 $Fe_3\mu_3$-$O(PO_4)_6$ units (3 have been removed for clarity) in compound **1**. The equilateral triangles are outlined in yellow.

parameters and As-O distances were observed for the two atoms. So in the structure refinement, the two atoms were bumped off of their three-fold symmetry sites and the atomic coordinates were refined by SHLXTL[12]. This act generated three As(3) atoms and three O(9) atoms, Figure 4.10. As a result, both sites are set at 1/3 occupancy. As(3) is also coordinated to O(8), and as a result of the large thermal parameters and the short As(3)-O(8) distances, the occupancy of O(8) was refined by SHELXTL[12] to 2/3. It should also be noted that despite the slight differences in the compositions of **1** and **2,** high yields of both materials were synthesized using stoichiometries targeting the composition of compound **1,** $Ba_{10}Na_5Fe_7O_2(XO_4)_{14}$ where X = P or As. This is not surprising as the single crystals of **2** were synthesized at 950°C, and it is known that at high temperature As^{5+} can easily be reduced to its 3+ form. Figure 4.10 shows that the $As(3)O_3$ polyhedron is weakly coordinated to the surrounding framework. This is deduced from long Fe(2)-O(8) distances of 2.81(4)Å. The weak coordination of the As(3) oxyanion, relative to the other As atoms in the framework, could increase the likelihood that the As(3) site will preferentially become reduced at high temperatures. Also, since the substitution of AsO_3 with AsO_4 has no effect on the overall charge balance of the structure, and the $As(3)O_3$ polyhedron has minimal connectivity to the surrounding framework, it would be no surprise if, when synthesized at lower temperature, the As(3) could actually be 4-coordinate and 5+. Further experimentation, such as annealing the reduced compound in oxygen may lead to the formation of an As analog, $Ba_{10}Na_5Fe_7O_2(AsO_4)_{14}$ having the same oxygen content as **1.** It should also be noted that both structures **1** and **2** possess partially occupied Ba and Na sites, which

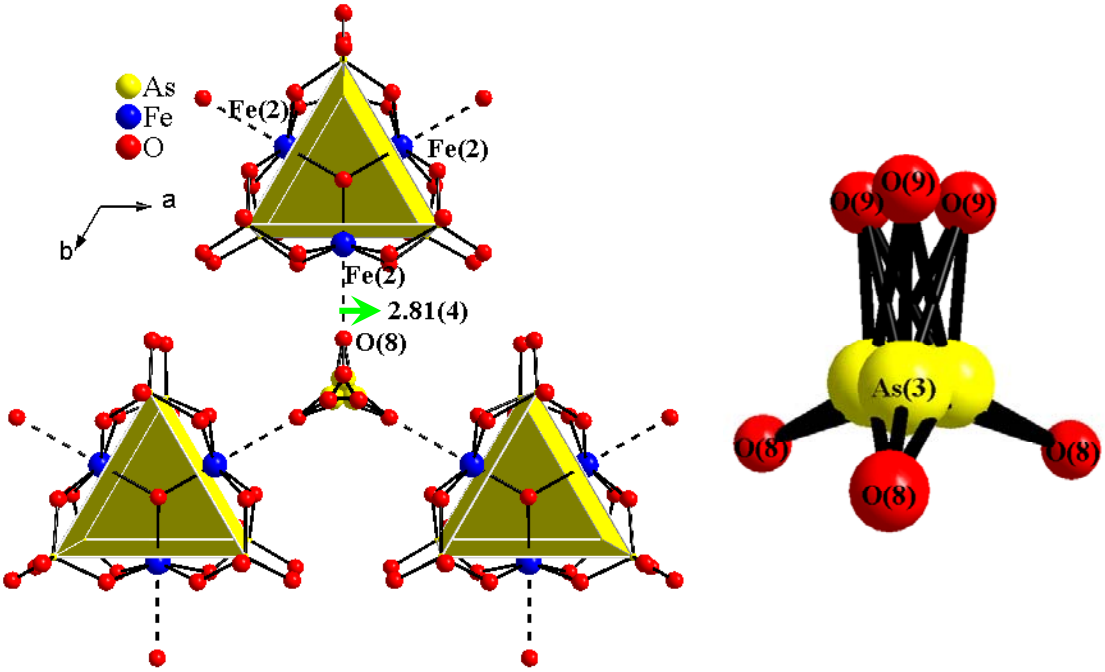

Figure 4.10: Projected view showing $3Fe_3\mu_3$-O units in **2** (left). The projected view shows the three-fold disorder of the As(3) and O(9) atoms (right). Both As(3) and O(9) are 1/3 occupied while O(8) is 2/3 occupied, giving rise to $As(3)O_3$ polyhedra that are found loosely coordinated to surrounding $Fe_3\mu_3$-$O(AsO_4)_6$ units, the long Fe(2)-O(8) distance is equal to 2.81(4)Å. It should be noted that the lone pair of electrons in As^{3+} would have to point toward one of the Fe^{3+} atoms in one of the 3 surrounding $Fe_3\mu_3$-$O(AsO_4)_6$ units, based on the 2/3 occupancy of O(8).

would otherwise give rise to short cation-cation distances within the structures. For **1**, Ba(1), Na(1), and Na(2) were refined to 0.5, 0.67, and 0.5 respectively. For **2**, Ba(1), Na(1), Na(2), and Na(3) were refined to 0.5, 0.33, 0.39, and 0.33 respectively.

When comparing the structures of $Ba_{10}Na_5Fe_7(\mu_3\text{-}O)_2(PO_4)_{14}$**,** **1**, and $Sr_{14}NaFe_{10}(\mu_3\text{-}O)_2(PO_4)_{17}Cl$, **3**, similar features are observed**.** These similarities are illustrated in Figures 4.8 and 4.11. Both materials have the same Fe(1)/Fe(2)-containing slabs denoted as $[Fe^{III}_7(\mu_3\text{-}O_2)(PO_4)_{14}]$. Fe(1) and Fe(2) in $Sr_{14}NaFe_{10}(\mu_3\text{-}O)_2(PO_4)_{17}Cl$ have the same connectivity and coordination environments as the Fe(1) and Fe(2) cations observed in **1**. Octahedral Fe(1) has six Fe-O(1) distances of 1.99(1)Å. The distorted octahedral Fe(2) has two axial bonds consisting of Fe(2)-O(3), 1.924(4)Å, and Fe(2)-O(6), 2.54(2)Å, and four equatorial bonds consisting of two Fe(2)-O(2), 1.96(1) Å, and two Fe(2)-O(8), 1.95(1) Å. As observed for **1**, the $Fe(2)O_6$ octahedra in **2** also share a single axial oxygen to form an Fe_3O equilateral triangular cluster containing a μ_3-oxygen bridge. Both Fe(1) and Fe(2) are in a 3+ oxidation state which is further supported by bond valence sum calculations.[13] The bond valence sum calculations rendered values equal to 3.21 and 3.12 for Fe(1) and Fe(2) respectively. The differences in **1** and **3** become evident went looking along the crystallographic *c* axis. In order to accommodate the smaller Sr^{2+} cation in **3**, the structure forms a non-layered solid. $Sr_{14}NaFe_{10}O_2(PO_4)_{17}Cl$ ($\equiv Sr_{14}Na[Fe^{II}_3(PO_4)_3Cl][Fe^{III}_7(\mu_3\text{-}O_2)(PO_4)_{14}]$) has an additional crystallographically distinct iron and phosphorous site, Fe(3) and P(4), that form a covalent slab bridging the $[Fe^{III}_7(\mu_3\text{-}O_2)(PO_4)_{14}]$ slabs, via P(2)-O(5)-Fe(3)-O(5)-P(2) linkages, as shown in Figure 4.12. The Fe(1)/Fe(2)-containing slabs are also slightly

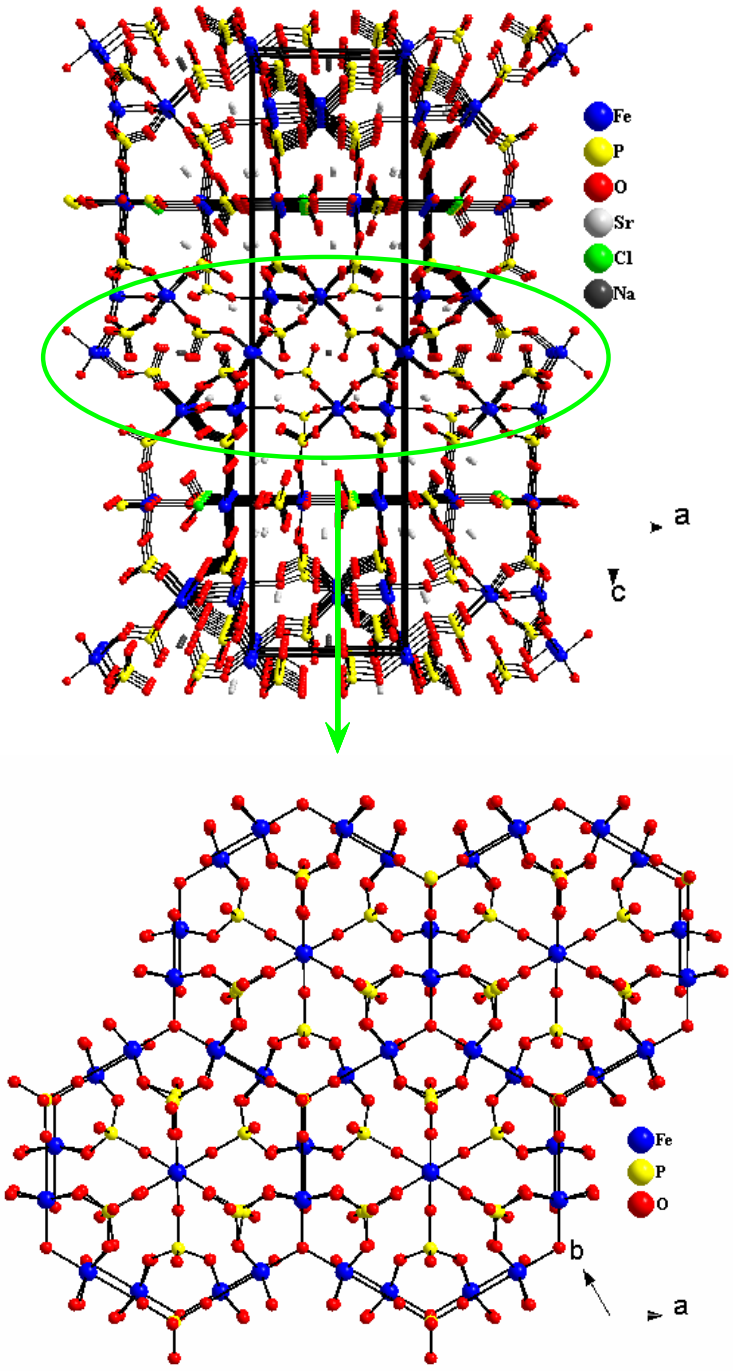

Figure 4.11: Perspective view of compound **3** illustrating the Fe-O-P connectivity along the crystallographic *c* axis. The bottom figure shows the connectivity within the $[Fe^{III}_7(\mu_3\text{-}O_2)(PO_4)_{14}]$ slab, which contains Fe(1) and Fe(2) sites within the *ab* plane. This slab is common to all compounds **1**-**3**.

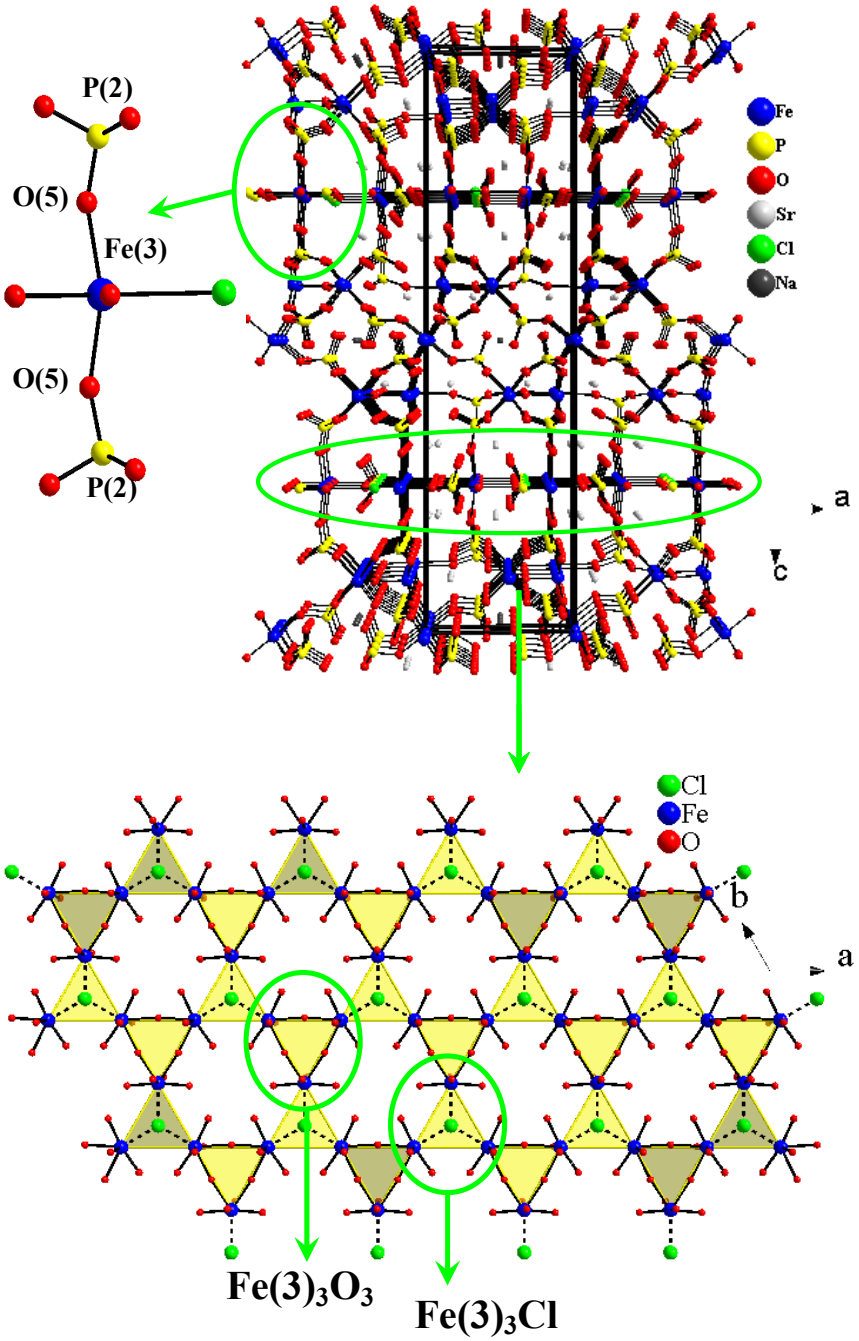

Figure 4.12: Perspective view of the non-layered $Sr_{14}NaFe_{10}O_2(PO_4)_{17}Cl$, **3**. $[Fe^{III}_7(\mu_3\text{-}O_2)(PO_4)_{14}]$ slabs that are common to all three compounds (**1**-**3**) are bridged in **3** *via* the Fe(3)-containing slab (bottom). The bottom image shows the connectivity and coordination of the Fe(3) site within the *ab* plane of **2**. This view shows a slab consisting of alternating corner-sharing Fe_3Cl and Fe_3O_3 equilateral triangles, highlighted in yellow.

shifted with respect to one another in **3** causing the *c* axis to be doubled, and, with the insertion of $[Fe^{II}_3(PO_4)_3]$ linker units (see Fig.4.12), approximately three times longer than observed in **1**. It should be noted that neither structure type has been found to coexist for either composition. Stoichiometric reactions, with various soak temperatures ranging from 650-950°C, targeting $Sr_{10}Na_5Fe_7O_2(PO_4)_{14}$, were run to see if an isostructural Sr analog of **1** would form; however, the PXRD data shown in Figure 4.5 shows no evidence of the phase formation. Therefore, it is assumed that the observed difference in the two "homologous" compounds is directly related to the size of the A site cation.

The covalent slab formed by Fe(3) serves as a bridge between the layers observed in **1,** shown in Figure 4.12. Fe(3) is in a 2+ oxidation state, and is coordinated to 5×O and 1×Cl atom, forming a highly distorted octahedral coordination with bonds including 2×Fe(3)-O(5), Fe(3)-O(11), 2×Fe(3)O(7), and Fe(3)Cl(1) equal to 2.08(2), 2.19(4), 2.540(7), and 2.968(8)Å in length respectively. The Fe(3) polyhedra share two corners with P(4) and 2 corners with P(2). It should be noted that the O(11) site is partially occupied, otherwise Fe(3) and P(4) would be 7-coordinate and 5-coordinate respectively. The occupancy parameter was refined to approximately 50% using the SHELXTL[12] software. O(7) is shared between neighboring Fe(3) polyhedra forming an equilateral triangular $Fe(3)_3O_3$ cluster. Each Fe(3) is loosely coordinated to Cl(1), forming a μ_3-chloro-bridging mode and a second $Fe(3)_3Cl$ equilateral triangular cluster. As shown in Figure 4.12, each Fe_3O_3 triangular cluster shares its vertex with three neighboring Fe_3Cl units, and vice versa, to form a 2-D slab similar to the 2-D kagomé-type lattice.

The single crystal structure solution of **3** has Cl^- present. This composition, further supported by EDX, is strange as the high yield synthesis of the material has been obtained without chlorine. This can easily be explained when looking at the coordination around the Cl anion. Each Cl is loosely coordinated to three Fe(3) atoms at 2.968(8)Å forming a μ_3-bridging mode between Fe(3) cations. This distance is long when compared to the Shannon crystal radii, 2.455Å, for 6-coordinate Fe and Cl. Due to the weak interaction between the two atoms, it is thought that the Cl may not be a necessity in the formation of the compound. The next nearest neighbors for Cl are O with distances of 3.53(2)Å and 3.89(1)Å and Sr with distances of 4.059(5)Å. When the site is refined as O, the thermal parameters go negative, indicating more electron density is needed. It should also be noted that the high-yield synthesis was targeting a compound with the composition $Sr_{10}Na_5Fe_7(\mu_3\text{-}O)_2(PO_4)_{14}$. This composition is significantly different from that of **3** (P/Fe = 2 *vs.* 1.4 respectively) which could account for the observed impurity peaks in the powder pattern in Figure 4.3. Stoichiometric reactions with P/Fe = 1.4 targeting the composition of compound **3** were all unsuccessful.

Besides the disorder already discussed above, there are a few issues with the structure solution of **3** that need to be addressed. O(10), like O(11), is partially occupied at approximately 50%, otherwise P(2) would be 5 coordinate. There is disorder in other cation sites including Na(1), Sr(3), and Sr(4) which were refined using SHELXTL to 0.5, 0.83, and 0.33 respectively. Na(1) and Sr(4) were found to be too close to one another, approximately 3.10(1)Å apart, indicating that the sites must be partially occupied. The occupancy of Sr(3) was refined because the thermal parameters were a little large, also

indicative of a partial occupancy or the co-inhabitance of a smaller atom like Na. Sr(3) and Sr(4) were refined also as a mixed Sr/Na site, however, no improvement in the refinement was observed. There are also several atoms with oddly-shaped thermal ellipsoids likely indicating disorder or a large amount of thermal motion. To eliminate some of the thermal motion, a low-temperature structure solution collected at 160 K was attempted for **3**; however, the oddly-shaped thermal ellipsoids remained a problem. There were also multiple room-temperature single crystal structure solutions attempted for compound **3**. The refinements for most of these crystals were not good and this is likely the result of some structural instability. The structure solution shown in Table 4.2 was chosen for comparison as this single crystal gave the best overall refinement.

As previously mentioned, all of the title compounds contain structurally isolated $Fe_3(\mu_3\text{-O})$ units. It is expected, based on the long Fe-Fe, equal to 3.307(7), 3.34(1), and 3.328(6)Å for compounds **1**-**3**, respectively, that the magnetic coupling will occur *via* super exchange through nonmagnetic μ_3-oxo site. Temperature-dependent magnetic measurements were performed on a ground sample of single crystals (6.6mg) of $Ba_{10}Na_5Fe_7(\mu_3\text{-O})_2(PO_4)_{14}$ in applied fields of 0.01 and 0.5 T seen in Figure 4.13. There is clearly a field-dependence as the susceptibility of the 0.5T data is noticeably smaller than that of the 0.01T data. There is a high-temperature anomaly seen in the $1/\chi$ for both fields. The transition occurring at approximately 250K, T_1, for H = 0.01T is shifted to slightly higher temperatures in the H = 0.5 T data and is suppressed. Further cooling the materials leads to an antiferromagnetic component, T_2, at approximately 5K. These data could not be fit using the Curie-Weiss law as a result of the nonlinear nature of the plots

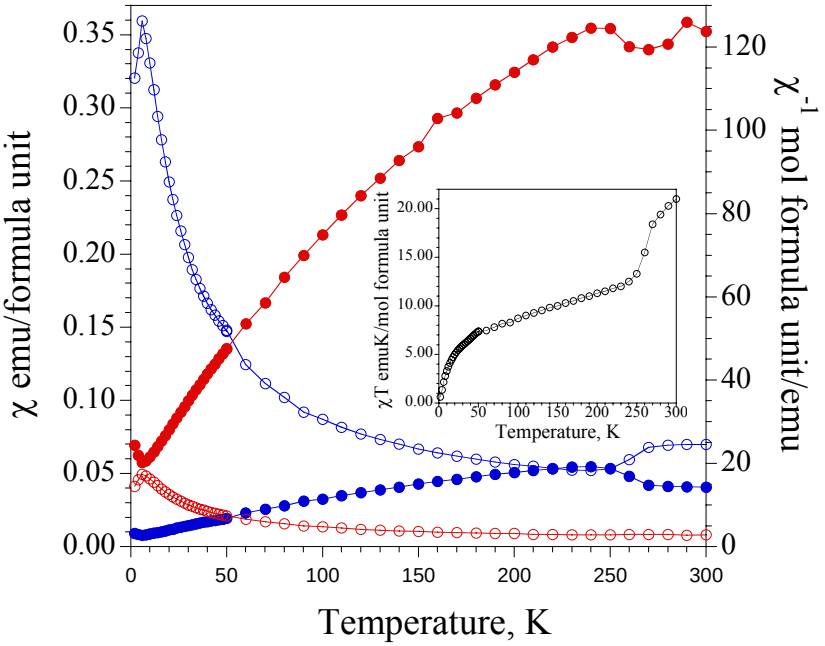

Figure 4.13: Magnetic susceptibility (○), χ, and inverse magnetic susceptibility (●), χ^{-1} for compound **1** at applied fields 0.01 (blue) and 0.5 T (red). The inset shows the χT plot of **1**. There is a steep increase at approximately 250K, indicative of ferro(i)magnetic exchange.

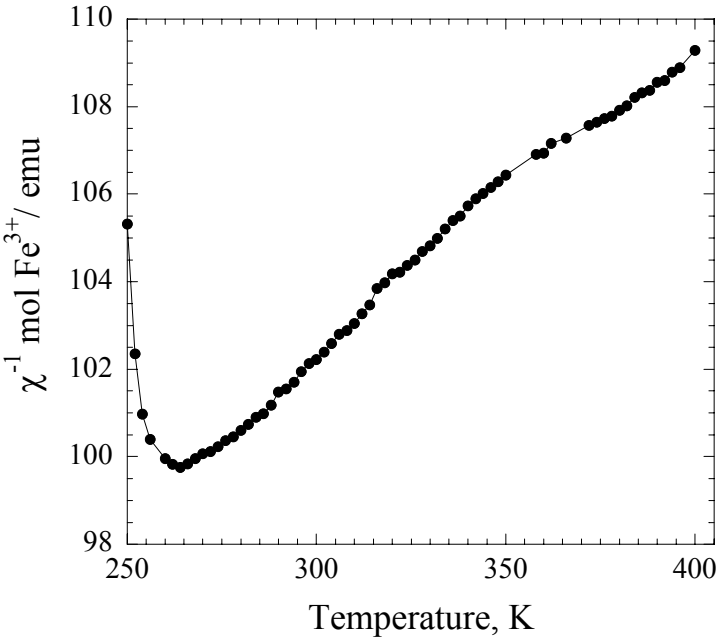

Figure 4.14: Inverse molar magnetic susceptibility data, χ^{-1}, collected on a single crystal of **1**, 3.5 mg, in various applied fields, 0, 0.5T. The high-temperature portion of the curve, 270-400K was fit using Curie-Weiss law.

at high temperature. However, higher temperature data (shown in Figure 4.14) ranging form 270 – 400K, was obtained using single crystal with an applied field (0.5T) along the crystallographic *c* axis. A Curie-Weiss fit of the data ranging from 270K- 400K rendered a χ_o = 0.0536(7) emu/mole Fe^{2+}, μ_{eff} = 5.4(6) μ_B, and θ = 51(16) K. The μ_{eff} is within the standard deviation of the expected spin-only value, 5.91 μ_B, for Fe^{3+}, d^5. The positive θ value is indicative of ferromagnetic exchange.

Field-dependent magnetization data collected on a single crystal of **1** (3.5mg) at 300 and 350 K confirm the presence of ferromagnetic-type ordering (Figure 4.15). The field was applied along the crystallographic *c* axis. The hysteresis observed at these temperatures shows a coercive field of 0.2T, which is approximately twice that observed for a ground powder of selected single crystals. This indicates that there is some magnetic anisotropy present in the system. At temperatures below T_1, ≈ 250 K, field-dependent measurements have revealed that the material no longer exhibits remnant magnetization. The isothermal magnetization data collected at 120K, shown in the inset of Figure 4.14, shows no hysteresis.

Heat capacity data was performed on a selected single crystal (3.5 mg) in the absence and presence of a magnetic field, 1 T, applied along the crystallographic *c* axis. This data, Figure 4.16, shows a small change in latent heat around T_1 coinciding with the observations from the magnetic data. It should be noted that the mass of the measured crystal is ≈ 3.5 mg, while the molar mass is large, resulting in a low signal-to-noise ratio. As a result of a large amount of noise, the presented data has undergone two

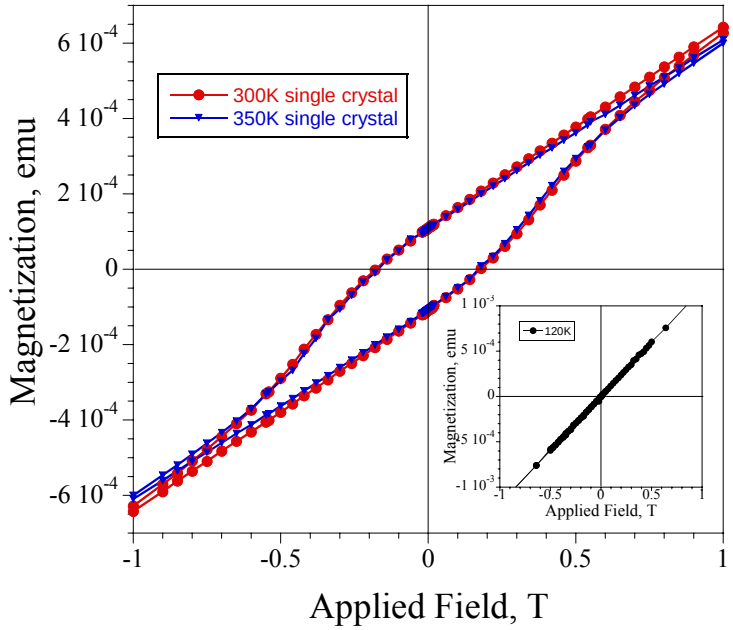

Figure 4.15: Field-dependent magnetization data collected on a single crystal of **1** (3.5mg) at 300K (red) and 350K (blue). The field was applied parallel to the *c* axis. The hysteresis is diminished at temperatures below 250K. The inset shows the field-dependent data at 120K.

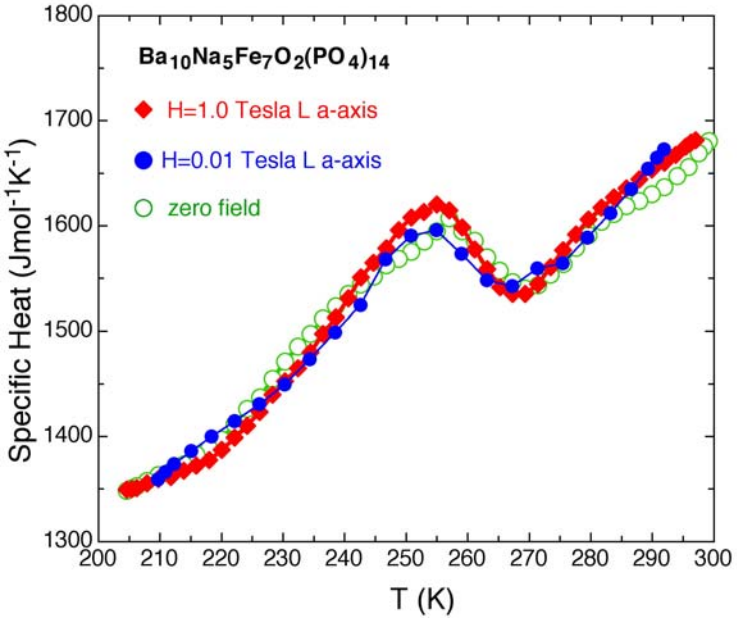

Figure 4.16: Heat capacity data collected on a single crystal of **1**, 6.6mg, in various applied fields, 0, 0.01, and 1 T. The transition seen above 250K coincides with the transitions observed in the magnetic susceptibility data.

consecutive 5-point smoothing processes. The error bar is approximately ± 3% in the y direction and is negligible in the x direction; however, the expected shift to higher *T* with higher field is not observed.

Based on the single crystal structure of **1**, the observed high-temperature ferromagnetic interactions were surprising. The μ_3-oxo bridge has been known to promote antiferromagnetic exchange *via* super exchange interactions. Magnetic centers set on the vertices of equilateral triangles usually lead to magnetic frustration which in turn results in multiple degenerate ground states and hence slow fluctuations between those. The result is that magnetic frustration leads to a paramagnetic-like behavior and no long-range magnetic order. It was originally thought that the remnant magnetization could be ferrimagnetic in nature and due to uncompensated spins resulting from the magnetic frustration. However, this is very unusual at high temperatures.

Once a Curie-Weiss fit of the data revealed a positive Weiss constant, other circumstances were considered to account for the high-temperature ferromagnetic response of **1**, including a ferromagnetic impurity or possibly a structural transition which could lead to some ferromagnetic exchange within this material. Multiple single crystals were analyzed to look for the existence of multiple phases. It has been proposed, especially in molecular materials, that spin frustration can lead to geometrical distortions.[15] In 2001, inelastic incoherent neutron scattering was utilized to uncover a spin frustration-induced asymmetry in $[Fe_3O(O_2CPh)_6(py)_3]ClO_4py$ that could not be detected by X-ray due to distortions concealed either by rotational disorder in the crystal structure or by pseudorotation occurring at rates greater than the timescale of the

experiment.[16] One single crystal was found with the same composition, but showed a reduction in cell symmetry when compared to **1**. Although a good refinement of this crystal was not obtained, the structural cause of the difference in symmetry was easily deduced. For **1**, the unit cell parameters are a = 10.431(2) Å, c= 13.477(3) Å, V = 1270.1(4) Å^3 in a trigonal spacegroup, P-3m1 (no. 164), while the new phase shows the following unit cell parameters: a = 32.491(7) Å, b = 10.396(2) Å, c = 18.169(4)Å, β = 123.88(3)°, and V = 5095(1) Å^3. The new phase has no 3-fold symmetry and crystallizes in a monoclinic space group $C2/c$ (no. 15). Figures 4.17 and 4.18 highlight the structural difference that leads to the reduction in symmetry. Figure 4.17 shows the trigonal compound **1** with the $(P(3)O_4)^{3-}$ oxyanion whose corner O(8) is weakly coordinated to three surrounding Fe(2) ions with a bond distance of 2.685(1)Å, represented by dotted lines. In the monoclinic phase, this oxyanion shifts closer to one of the surrounding Fe(2) cations, releasing the three-fold symmetry observed for **1**. The once-equivalent Fe(2) cations are no longer equivalent and form a scalene-type triangular cluster with three angles not equal to 60°. Figure 4.18 shows the new Fe(2,3,4)-O bond distances and new Fe(2)-Fe(3)-Fe(4) angles generated with the shift in the oxyanions. A calculated powder pattern was obtained from the single crystal structure solution of the monoclinic phase and compared to the ground single crystal samples utilized in the magnetic measurements. Evidence of both phases can be seen in the powder pattern shown in Figure 4.1. Multiple experiments were performed to look for a possible structural transition between the monoclinic and trigonal versions of compound **1**. DSC was performed on a sample of ground single crystals and a powder obtained from a 100%

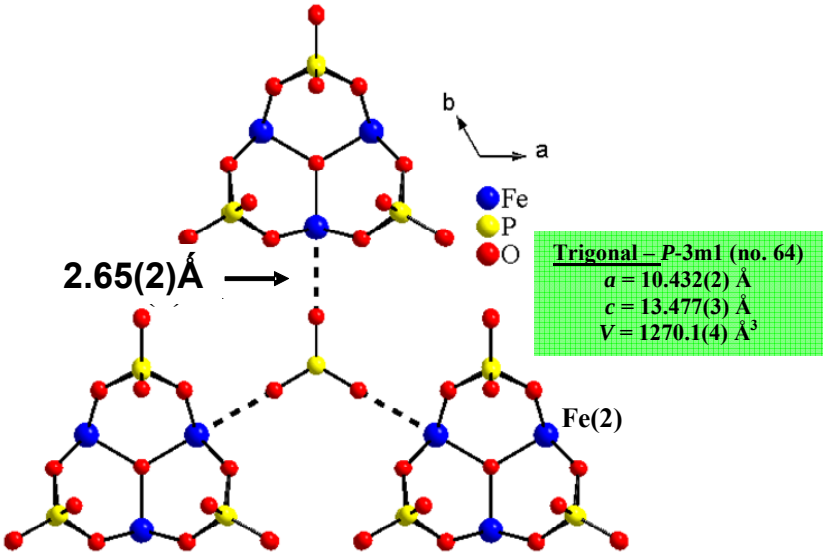

Figure 4.17: Perspective view showing the trigonal version of **1**. The phosphate group is centered between 3 equilateral triangular Fe_3O nanostructures. The dotted lines represent long Fe-O distances of 2.685(1) Å. The unit cell constants for the trigonal version of $Ba_{10}Na_5Fe_7O_2(PO_4)_{14}$ are highlighted in green.

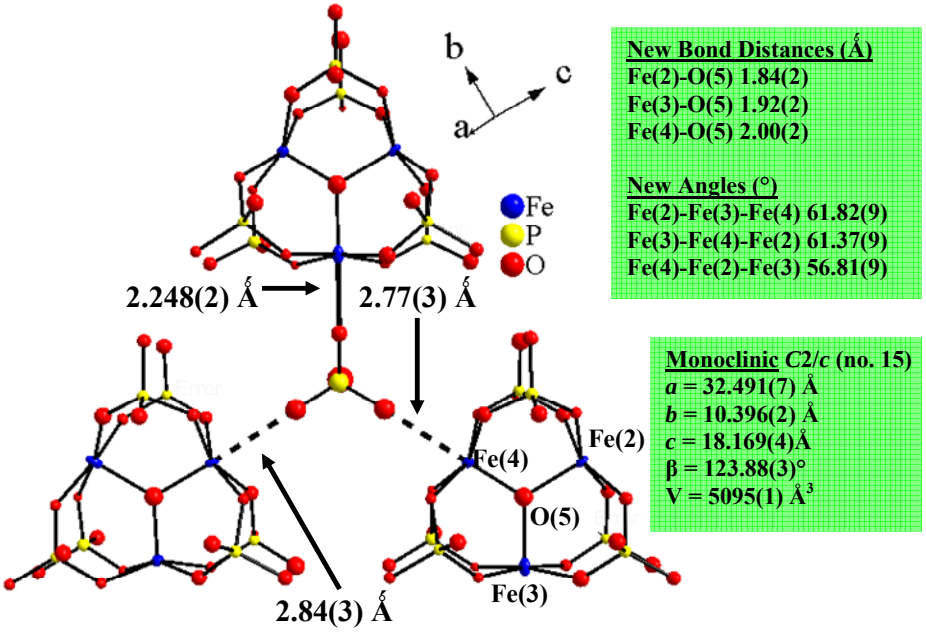

Figure 4.18: Projected view showing the thermal ellipsoids (50% probability factor) of the monoclinic phase of **1**. The phosphate group has shifted closer to one of the Fe_3O trimers, causing a loss of the 3-fold symmetry, and giving rise to a lower symmetry phase of compound **1**. The dotted lines represent long Fe-O bonds. The unit cell dimensions for the monoclinic version of $Ba_{10}Na_5Fe_7O_2(PO_4)_{14}$ and the new bond distances and angles are highlighted in green.

yield synthesis. The temperature was swept from 25 to -150 to 150 to 25°C again, however nothing was observed in the DSC plot. Variable temperature PXRD was also utilized to detect any possible structural transitions. X-ray powder patterns were obtained from the 100% yield synthesis of **1** at various temperatures including 25, -90, and 90°C. As shown in Figure 4.7, there is no significant change in the powder patterns, so it was concluded that the trigonal and monoclinic phases seem to coexist. Reaction conditions were also varied to see if the phase formation could be manipulated. Some reactions were heated for very long time periods (to promote the formation of the higher symmetry, trigonal compound), while others were quenched (to promote the formation of the lower symmetry, monoclinic phase). No further conclusions could be made from these experiments as the product formation did not appear to change.

Due to the interesting high-temperature ferromagnetic properties observed for **1**, extra efforts were made to synthesize other derivatives of the material in hopes that structure / property correlation studies would lead to the origin of the ferromagnetic properties. Temperature-dependent magnetic measurements were performed on a high-yield synthesis of compound **2**, $Ba_{10}Na_5Fe_7(\mu_3\text{-}O)_2(AsO_4)_{12}(AsO_3)_2$, and ground single crystals of compound **3**, $Sr_{14}NaFe_{10}O_2(PO_4)_{17}Cl$ in an applied field of 0.01T seen in Figures 4.19 and 4.20. A Curie-Weiss fit was performed on the high-temperature data ranging from 220-370 K. From the fit, the magnetic moment, μ, was determined to be 5.15(7) μ_B, which is slightly lower than the expected spin-only magnetic moment, 5.91. The Weiss constant, θ, was calculated to be -197(7) K, indicating antiferromagnetic coupling between nearest neighbors. A Curie-Weiss fit was performed on the

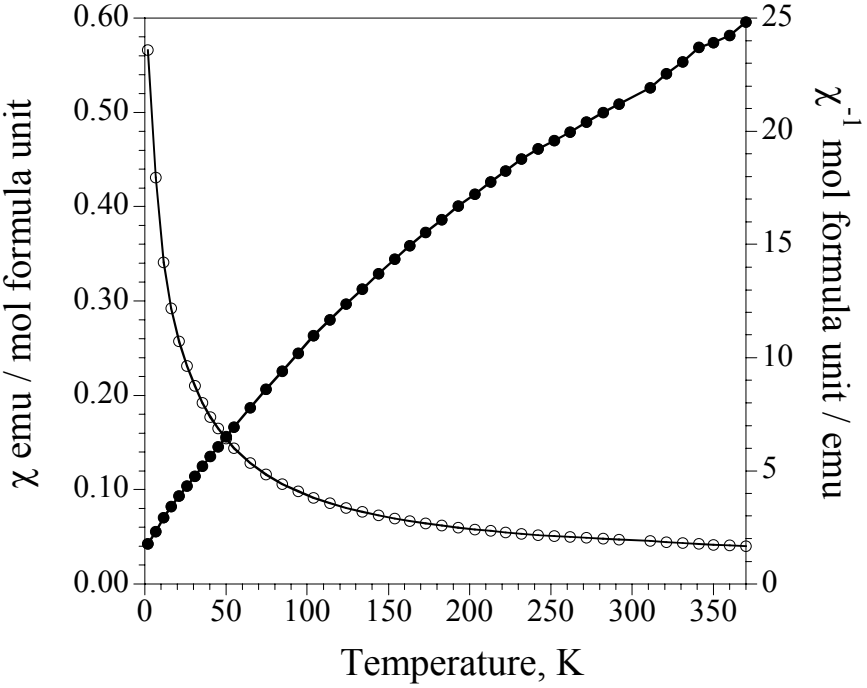

Figure 4.19: Molar magnetic susceptibility (○) and inverse molar magnetic susceptibility (●) of $Ba_{10}Na_5Fe_7O_2(AsO_4)_{12}(AsO_3)_2$, **2** measured at an applied field of 0.01T.

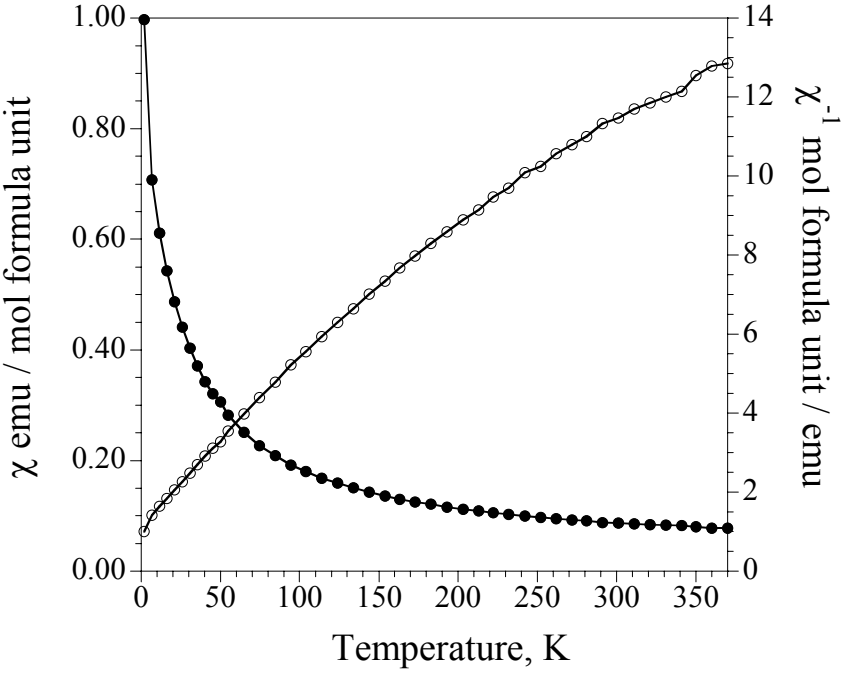

Figure 4.20: Molar magnetic susceptibility (○) and inverse molar magnetic susceptibility (●) of $Sr14NaFe_{10}O_2(PO_4)_{17}$, **3** measured at an applied field of 0.01T.

temperature-dependent data ranging from 150-370 K. From the fit, the calculated magnetic moment of **3** was determined to be 17.7(4)μ_B. This is comparable to the spin-only magnetic moment expected for seven Fe^{3+} ions, d^5, and three Fe^{2+}, d^6, 17.8μ_B. As observed for **2**, the negative Weiss constant, -146(8)K, indicates antiferromagnetic intracluster coupling. Both magnetic susceptibility plots for **2** and **3** show a paramagnetic-type behavior with no evidence of the development of long-range magnetic order.

Efforts were also made to dope other ions into compound **1**. It was thought that Ga^{3+}, a diamagnetic ion, may go into the octahedral Fe(1) site allowing one to see only the magnetic response from the $Fe_3\mu_3$-O units. Efforts were also made to dope Mn^{3+} into compound **1** to see how a different paramagnetic ion would affect the magnetic response of the material. The powder patterns from the high-yield reactions are shown in Figure 4.6, and the refined unit cell parameters for the Ga^{3+}- and Mn^{3+}-doped derivatives can be seen in Table 4.1. Interestingly enough, it appears that the Ga-doped compound forms the same structure as **1**; however, the powder pattern of the Mn-doped compound appears to have similar features to the calculated PXRD pattern of compound **3**. It was previously mentioned that it is thought that the formation of **3** was directly affected by the smaller A-site cation. Mn^{3+} is slightly larger than Fe^{3+}, and it is believed that maybe the longer Mn-O bond distances could serve to bridge the Fe(1)/Fe(2)-containing slabs forming the nonlayered structure observed in **3**. However, this is just speculation, as no single crystal structure has yet been obtained for the Mn-doped analog. Both the Ga and Mn-doped analogs have additional peaks in their powder patterns when compared to the

calculated patterns of **1** and **3**; however, it is not yet known whether these few extra peaks are the result of other phases or are additional peaks resulting from the doped product. It should also be noted that efforts to make a full Mn^{3+} derivative of **1** were also attempted, but were unsuccessful.

Conclusions

In summary, a new family of extended solids containing equilateral $Fe_3(\mu_3\text{-}O)$ triangular nanostructures has been synthesized using high-temperature, solid-state methods. The newly synthesized materials exhibit two different structure types and have the following chemical formulas: $Ba_{10}Na_5Fe_7(\mu_3\text{-}O)_2(PO_4)_{14}$, **1**, $Ba_{10}Na_5Fe_7(\mu_3\text{-}O)_2(AsO_4)_{12}(AsO_3)_2$, **2**, and $Sr_{14}NaFe_{10}(\mu_3\text{-}O)_2(PO_4)_{17}Cl$, **3**. Efforts were also made to alter the composition of **1** through chemical doping. The targeted compositions for these materials include $Ba_{10}Na_5MnFe_6(\mu_3\text{-}O)_2(PO_4)_{14}$ and $Ba_{10}Na_5GaFe_6(\mu_3\text{-}O)_2(PO_4)_{14}$. From the PXRD patterns of the high yield syntheses it appears that the formation of the Ga-containing compound was successful, but the formation of the Mn-derivative is still unclear, as the PXRD pattern more closely resembles the calculated PXRD pattern of 3. All of these materials were expected to show antiferromagnetic exchange between nearest neighbors, as was confirmed for compounds **2** and **3**. However, compound **1** shows ferromagnetic properties at high temperature that were verified *via* field-dependent magnetic measurements showing remnant magnetization at room temperature. The interesting properties observed for **1** have led to a close analysis of single crystals obtained from the molten-salt reaction. After close examination, evidence was found of

the existence of a trigonal and monoclinic phase. It was thought that a structural transition could be an explanation for the observed magnetic properties above 250K. However, multiple experiments including DTA, DSC, and variable temperature PXRD, revealed no evidence of a structural transition. Therefore, it is thought that the two phases, monoclinic and trigonal, coexist, as observed from the powder pattern of the single crystals, Figure 4.1. It is still unclear whether the high-temperature ferromagnetic properties observed for **1** are directly related to the existence of these two phases. It should also be considered that both a monoclinic and trigonal / hexagonal phase may exist for **2** and **3,** as these two derivatives, like **1**, also have loosely-coordinated oxyanions that could shift off of the 3-fold axis. The O atoms within these loosely coordinated oxyanions have long Fe-O distances of 2.65(2), 2.81(4), and 2.54(2) Å for compounds **1**-**3** respectively. In fact, in compound **2**, the As(3) site has already been refined as having 3-fold disorder, which could be directly related to its weak coordination to the framework (Figure 4.10). Also, when looking at the powder pattern obtained from a 100% yield synthesis of **2**, the peaks are broad relative to the calculated one, Figure 4.2, which could be the result of additional peaks from a lower symmetry species or due to nonstoichiometry, resulting from the reduction of the As^{3+} cation.

Literature Cited

1. (a) Högbom M., Nordlund P. *FEBS Lett.* **2004**, *567*, 79–182.

   (b) Mullins, C.S., Pecoraro, V.L., *Coord. Chem. Rev.* **2008,** *252*, 416-443.

   (c) Isobe, H., Shoji, M., Koizumi, K., Kitagawa, Y., Yamanaka, S., Kuramitsu, S. Yamaguchi, K. *Polyhedron* **2005**, 24, 2767-2777.

2. (a) Rotaru, G.-M., Roessli, B., Amato, A., Gvasaliya, S. N., Lushnikov, S. G., Shaplygina, T. A. *Condensed Matter* **2009**,1-5.

   (b) Cao, H., Gukasov, A., Mirebeau, I., Bonville, P., Dhalenne., G. *Phys. Rev. Lett.* **2008**, *101*, 196402/1-196402/4.

   (c) Zhou, H. D., Vogt, B. W., Janik, J. A., Jo, Y.-J., Balicas, L., Qiu, Y., Copley, J. R. D., Gardner, J. S., Wiebe, C. R. *Phys. Rev. Lett.* **2007**, *99*, 236401/1-236401/4.

   (d) Bramwell S. T., Gingras M. J. *Science* **2001**, *294*, 495-501.

3. (a) Obradors, X., Labarta, A., Isalgue´, A., Tejada, J., Rodriguez, J., Pernet, M. *Solid State Commun*. **1988**, *65*, 189-192

   (b) Ramirez, A.P., Espinosa, G.P., Cooper, A.S., *Phys. Rev. B*, **1992**, *45*, 2505-2508.

   (c) Ramirez, A.P., Espinosa, G.P., Cooper, A. S. Phys. Rev. Lett. **1990**, *64* 2070-2073.

   (d) Hagemann, I.S., Huang, Q., Giao, X.P.A., Ramirez, A.P., Cava, R.J. *Phys. Rev. Lett.* **2001**, *86*, 894-897.

4. Rogado, N., Lawes, G., Huse, D.A., Ramirez, A.P., Cava R.J. *Solid State Commun.* **2002**, *124*, 229–233.

5. (a) Ramirez, A.P., Hayashi, A., Cava, R.J., Siddharthan, R., Shastry, B.S. *Nature* **1999**, *399*, 333-335.

   (b) Bramwell, S.T., Gingras, M.J.P. *Science* **2001**, *294*, 1495-1501.

   (c) Lee, S.-H., Broholm, C., Ratcliff, W., Gasparovic, G., Huang, Q., Kim, T.H., Cheong, S.-W. *Nature* **2002**, *418*, 856-858.

(d) Greedan, J.E., Wiebe, C.R., Wills, A.S., Stewart, J.R., *Phys. Rev. B* **2002**, *65*, 184424-184431.

(e) Lee, S.-H., Qiu, Y., Broholm, C., Ueda, Y., Rush, J.J. *Phys. Rev. Lett.* **2001**, **86**, 5554-5557

6. Cannon, R. D., White, R. P. *Prog. Inorg. Chem.* **1988**, *36*, 195-298.

7. (a) Raptopoulou, C.P., Tangoulis, V., Psycharis V. *Inorg. Chem.* **2000**, *39,* 4452-4459.

8. (a) Anson, C. E., Bourke, J. P., Cannon, R. D., Jayasooriya, U. A., Molinier, M.; Powell, A. K. *Inorg. Chem.* **1997**, *36*, 1265 and references therein.

(b) Cano, J., Cauchy, T., Ruiz, E., Milios, C.J., Stoumpos, C. C., Stamatatos, T.C., Perlepes, S.P., Christou G., Brechin, E.K, *Dalton Trans.*, **2008**, 234-240.

9. Ouerfelli, N., Guesmi, A., Mazza, D.;Zid, M.F., Driss, A. *Acta Crystallographica C* **2008**, *64*(5), i41-i44.

10. Queen, W.L, S.-J. Hwu, Unpublised data, **2008**.

11. (a) Roisnel, T., Rodríguez-Carvajal, J. *WinPLOTR*: a Windows tool for powder diffraction patterns analysis *Materials Science Forum, Proceedings of the Seventh European Powder Diffraction Conference* (EPDIC 7), **2000**, 118-123.

(b) Rodríguez-Carvajal, *J. Physica B*. **1993**, *192*, 55-69.

12. (a) Sheldrick, G.M. In "Crystallographic Computing 3" (Sheldrick, G. M.; Kruger, C.; Goddard, R.; Eds), Oxford Univ. Press: London, **1985**, p 175-189.

(b) Sheldrick, G. M. In "SHELXTL, Version 6.1 Structure Determination Software Programs" Bruker Analytical X-ray Systems Inc., Madison, WI, **2001**.

13. (a) *VALENCE* for DOS, Version 2.0, Brown, I. D. *J. Appl. Crystallogr.* **1996**, *29*, 479-480.

(b) Brown, I. D. and Altermatt, D. *Acta Cryst.* **1985**, *B41*, 244-247.

14. Gorun SM, Lippard S. J. *Inorg. Chem* **1991**, *30*:1625-1630.

15. Murao T. *Phys. Lett.*, **1974**, *49A*, 33-35.

16. Sowrey, Frank E., Tilford *C.* Wocadlo, S.,Anson, C.E., Powell, A.K., Bennington, S.M., Montfrooij, W., Jayasooriya, U.A., Cannon, R.D., *J. Chem. Soc*., *Dalton Trans*., **2001**, 862-866.

CHAPTER FIVE

STRUCTURALLY RELATED COMPOUNDS CONTAINING EXTENDED $[M_3O_{12}]_\infty$ MAGNETIC SHEETS

Introduction

Serendipity often plays an important role in the discovery of new materials. In fact, much effort directed towards the synthesis of new materials is exploratory in nature, where the most a synthetic chemist can do is add the components required to achieve the desired product, and then vary the reaction conditions in hopes that luck is on his / her side. The most important part of exploratory synthesis is the ability to recognize what is unique and what can be done chemically to improve any newly explored systems. The research in this dissertation is focused on the synthesis of low-dimensional magnetic solids, where the transition metal oxide constituents are electronically confined by nonmagnetic oxyanions.[1] Oftentimes, mixed polyhedra, including the tetrahedral oxyanions and the transition metal oxide with varying coordination, can lead to many interesting frameworks. In fact, this chemistry, employed in our group to target low-dimensional magnetic solids, is often utilized in the synthesis of new zeolite-like porous frameworks[2] as well. These porous materials are multifunctional in that they can have zeolite-like properties such as shape-selective adsorption of small molecules as well as properties associated with the transition metals such as thermal stability, catalytic activity, and electronic and magnetic properties. Combining the porous nature of the

mixed polyhedral frameworks and the redox chemistry of the transition metal can lead to materials important in many fields such as ion exchange, separations, and catalysis.[3]

Chapter 5 is focused on the synthesis and characterization of an extensive series of structurally related compounds. These are transition metal phosphates and arsenates that have the following chemical compositions: $BaNaCo_3(AsO_4)_3$**, 1,** $Sr_{0.90}Na_{1.2}Ni_3(AsO_4)_3$, **2,** $Na_{16}Co_{6.25}O_{0.25}(AsO_4)_4(As_2O_7)_4$, **3**, $Sr_2Na_{0.66}Fe_{3.34}(PO_4)_4Cl_{0.8}$, **4**, $Sr_2NaFe_3(AsO_4)_4Cl$, **5**, and $Ba_{1.88}Na_{0.75}Fe_3(AsO_4)_4Cl$, **6**. These new phases crystallize with three different structure types denoted as **I** (**1**-**2**), **II** (**3**), and **III**(**4**-**6**). The structures contain common magnetic $[M_3O_{12}]_\infty$ sheets (shown in Figure 5.1) that are either interconnected *via* edge-sharing MO_6 polyhedra to form a 3-D M-O lattice, as observed in **I**, or separated *via* alkali/alkaline earth metal cations or alkali/alkaline-earth metal chloride salts to form layered-type lattices, as observed in **II** and **III**. These materials have interesting magnetic properties, and due to the nature of their channeled and layered structures where electropositive cations reside, it is thought that they could also be a prototype material for battery-related studies. Thus far, multiple reported solids exhibiting structures related to the title compounds have shown a wide range of chemical compositions.[4-11] The crystallographic data for these previously reported materials and the title compounds is compared in Table 5.1. Looking at the table, it is easily concluded that there is much opportunity for chemical substitution, especially within structure types **I** and **III**, as multiple derivatives of these have been synthesized with varying A-site cations, metal cations, and oxyanions. This compositional variation could offer a rare opportunity for an in-depth structure/property correlation study and possibly allow one to

chemically fine tune any observed interesting physical phenomena. Most of the compounds in Table 5.1 have Fe incorporation, with the exception of five compounds containing other scattered first-row transition metals, including Cr, Co, or Ni. This observation could indicate that there is still much chemistry to be unveiled in this extensive compound family. Upon chemical substitution, this system has a wide range of magnetic properties including ferro, ferri, and antiferromagnetic interactions.[4-7] Easy ion exchange and Li^+-reduction insertion processes, also reported in several of theses materials[4,6] may indicate high ionic conductivity, a requirement for applications in battery-related devices. It should be noted that, to the best of our knowledge, structure type **II** has never before been observed. Furthermore, this is the first report that describes an observed relationship between the structure types **I** and **III**. All three structure types will be described in light of their similarities.

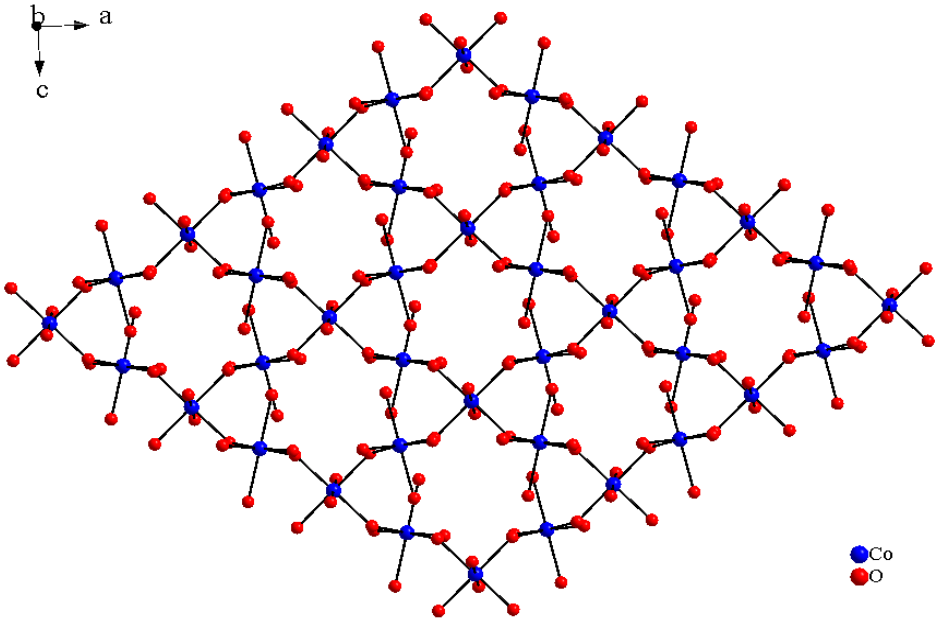

Figure 5.1: Partial structure of $[M_3O_{12}]_\infty$ (M = Fe, Co, Ni) sheet made of corner-shared MO_6 octahedra, a feature commonly adopted by **I-III** structure types, see text.

Table 5.1 Crystallographic data and magnetic properties of structurally related compounds

empirical formula[ref]	Related Structure	space group, *Z*	Unit cell dimensions	Magnetic Properties	reference
$SrFe_3(PO_4)_3$	**I**	*Imma*,4	*a*=10.413(4), *b*=13.406(4), *c*=6.5404(3)Å, *V*=916.1(1) Å^3	FM, Tc ≈ 55K	4
$NaV_3(PO_4)_3$	**I**	*Imma*,4	*a* =10.488(2), *b*=13.213(3), *c*=6.455(l) Å, V=894.5(1) Å^3	AFM	5
$KFe_3(AsO_4)_3$	**I**	*Imma*,4	*a*=10.807(2), *b*=13.612(3), *c*=6.676(1), Å *V*=982.0(3)Å^3	AFM, Tc ≈ 80K	6
α-$CrP0_4$	**I**	*Imma*,4	*a* =10.3797 (1), *b*=12.8452(2), *c*=6.2797(1)Å V =837.27(2) Å^3	AFM, T_N ≈ 9.1K	7
α-$CrAs0_4$	**I**	*Imma*,4	a=10.5466(1), b=13.2424(1), c=6.4612(1)Å V=902.36(1) Å^3	AFM, T_N ≈ 7.7K	7
$BaNaCo_3(AsO_4)_3$	**I**	*Imma*,4	*a*=10.719(2), *b*=14.091(3), *c*=6.789(1)Å, *V*=1025.4(4) Å^3	AFM, T_N ≈ 12K	this study
$Sr_{0.90}Na_{1.2}Ni_3(AsO_4)_3$	**I**	*Imma*,4	*a*=10.551(2), *b*=13.737(3), *c*=6.690(1)Å, *V*=969.6(3) Å^3	unknown	this study
$Na_{16}Co_{6.25}O_{0.25}(AsO_4)_4(As_2O_7)_4$	**II**	$P2_1/c$, 1	*a*=13.866(3), *b*=6.750(1), *c*=11.072(2)Å, β=100.90(3)° V=1017.7(4)Å^3	unknown	this study
$Sr_2Na_{0.66}Fe_{3.34}(PO_4)_4Cl_{0.8}$	**III**	*Cccm*,4	*a*= 6.556(1), *b*=20.320(4), *c*=10.543(2)Å, *V*=1404.6(5) Å^3	unknown	this study
$Sr_2NaFe_3(AsO_4)_4Cl$	**III**	*Cccm*,4	*a*=6.694(1), *b*=20.738(4), *c*=10.827(2)Å, *V*=1503.0(5)Å^3	AFM, T_c≈ 45K	this study
$Ba_{1.88}Na_{0.75}Fe_3(AsO_4)_4Cl$	**III**	*Cccm*,4	*a*= 6.827(1), *b*=21.408(4), *c*=10.830(2)Å, *V*= 1582.7(6)Å^3	AFM, T_c≈ 55K	this study
$Na_3Fe_3(PO_4)_4$	**III**	*C*2/*c*, 4	*a*= 19.601(8), *b*=6.387(1), *c*=10.575(6)Å, *β*=91.81(4)°, V=1323.2(4) Å^3	unknown	8
$Na_3Fe_3(PO_4)_4$	**III**	*Cccm*,4	*a*= 10.697(2), *b*=20.170(4), *c*=6.379(1)Å, *V*=1376.4(5)Å^3	unknown	6
$Cs_{0.85}K_{2.15}Fe_3(AsO_4)_4$	**III**	*Cccm*,4	*a*=11.005(2), *b*=21.517(4), *c*=6.379(1)Å, *V*=4730(2)Å^3	AFM, T_N ≈ 30K	6
$K_3Fe_3(AsO_4)_4$	**III**	*Cmca*, 4	*a*= 10.898(2), *b*=21.521(5), *c*=6.623(2)Å, *V*=1553.3(7) Å^3	unknown	9
$K_3Cr_3(PO_4)_4$	**III**	*Cmca*, 4	*a*=10.524(4), *b*=20.466(6), *c*=6.374(2)Å, *V*=1372.9(8)Å^3	unknown	10
$K_3Cr_3(AsO_4)_4$	**III**	*Cmca*, 4	*a*=10.671(1), *b*=20.911(5), *c*=6.500(3) Å, *V*=1450.4(8) Å^3	unknown	11

Synthesis

Single Crystal Synthesis of Compounds 1-6: All 6 new phases were synthesized using high temperature molten-salt methods. For the synthesis of **1-3,** BaO, Na_2O_2, CoO/NiO, and As_2O_5 were mixed in a 2:4:6:3 mol ratio and ground in a RbCl/NaCl eutectic flux equal to three times the mass of the oxide reactants. These two reactions were targeting $Na_{36}(Co/Ni)_{28}O_{16}(AsO_4)_{16}Cl_{12}$, derivatives of a cluster compound to be presented in Chapter 7. Instead of the targeted phase formation, the first reaction, containing CoO, led to the formation of burgundy multi-faceted single crystals of $BaNaCo^{II}_3(AsO_4)_3$ (≈20% yield)**, 1,** pink plate-like single crystals of $Na_{16}Co^{II}_{6.25}O_{0.25}(AsO_4)_4(As_2O_7)_4$, **3**, (<5% yield), colorless single crystals of $Ba_5(AsO_4)_3Cl$[12] (≈30% yield), dark purple single crystals of $NaCo^{II}AsO_4$[13](≈15% yield), and an unidentified green polycrystalline material (≈30% yield). For the synthesis of **2,** the same reaction was utilized, substituting NiO for CoO. The reaction resulted in the formation of green plate-like crystals of $Sr_{0.90}Na_{1.2}Ni^{II}_3(AsO_4)_3$ (<10% yield), **2**, colorless single crystals of $Ba_5(AsO_4)_3Cl$[12] (≈20% yield), and multiple green and yellow unidentified polycrystalline phases.

For the synthesis of **4**, Na_2O_2, SrO, FeO, Fe_2O_3, and P_4O_{10} were mixed in a 2.5:10:0.4:3.3:3.5 mol ratio and ground in a $BaCl_2$/NaCl eutectic flux equal to three times the mass of the oxide reactants. The targeted compound for this reaction was $Sr_{10}Na_5Fe^{III}_7O_2(PO_4)_{14}$, a derivative of the materials presented in Chapter 4. This reaction proved to be unsuccessful and instead led to the formation of multiple other phases including dark brown plate-like crystals of $Sr_2Na_{0.66}Fe^{II/III}_{3.34}(PO_4)_4Cl_{0.8}$ (≈ 10% yield), **4**,

yellow single crystals of $Ba_2SrFe^{III}_2(PO_4)_4$[14] (≈ 50% yield) and an unidentified green polycrystalline material (≈ 40% yield).

For the single crystal synthesis of **5**, Na_2O, SrO, FeO, Fe_2O_3, and As_2O_5 were mixed in a 2.5:10:0.4:3.3: 7 mol ratio (ca. 0.3g) and ground in a $BaCl_2$/NaCl flux equal to three times the mass of the oxide reactants. In this reaction, FeO was utilized to offset extra oxygen due to a 16 mol % "impurity" of Na_2O_2 in Na_2O ($2\ FeO + Na_2O_2 \rightarrow Fe_2O_3 + Na_2O$). The reaction was loaded in order to synthesize an additional derivative of the compounds presented in Chapter 4, $Sr_{10}Na_5Fe^{III}_7O_2(AsO_4)_{14}$. However, this reaction proved unsuccessful and instead led to the formation of several other phases, including light brown plate-like crystals of $Sr_2NaFe^{II/III}_3(AsO_4)_4Cl$, **5**, (≈10% yield), colorless single crystals of $Ba_5(AsO_4)_3Cl$[13] (≈50% yield), brown transparent crystals of $Sr_2Fe^{III}(AsO_4)_2Cl$[14] (≈ 30%), and unidentified black and colorless polycrystalline materials (≈ 10%).

For the single crystal synthesis of **6**, Na_2O, BaO, FeO, Fe_2O_3, and As_2O_5 were mixed in a 2.5:10:0.4:3.3:7 mol ratio (ca. 0.3g) and ground in a $BaCl_2$/NaCl flux equal to three times the mass of the oxide reactants. Again, FeO was utilized to account for a 16 mol% impurity of Na_2O_2 in Na_2O. The reaction was loaded in order to synthesize an additional derivative of the compounds presented in Chapter 4, $Ba_{10}Na_5Fe^{III}_7O_2(AsO_4)_{14}$. However, this reaction proved unsuccessful and instead led to the formation of several other phases including dark brown plate-like crystals of $Ba_{1.88}Na_{0.75}Fe^{II/III}_3(AsO_4)_4Cl$, **6**, (≈ 30%), lime green crystals of $Ba_2Fe^{III}_3(AsO_4)_4Cl$[14] (< 5%), and unidentified colorless and green polycrystalline material (≈ 65%).

To facilitate crystal growth, all six reactions were run in molten-salt media. The reactions were mixed with an ACl/NaCl eutectic flux equal to three times the mass of the oxide reactants. The reactants and salts were then ground together for 15 minutes in a nitrogen-purged dry box and placed in silica ampoules. The reactions were then sealed under vacuum and heated, at a rate of 1°C/min, to 150°C above the melting point of the eutectic flux used, held for 4 days, and then slowly cooled, at a rate of 0.1°C/min, to 450°C, followed by furnace cooling.

Characterization

Elemental Analysis: Qualitative elemental analysis was performed by EDAX on the single crystals used in the structure determination. The results showed the presence of the respective elements in the chemical formula.

Magnetic Properties Measurements: Magnetic measurements were carried out on a SQUID MPMS-5S magnetometer produced by Quantum Design. The zero field cooling and field cooling magnetic susceptibility were carried out in an applied magnetic field of H=0.01T or 0.5T in the temperature range of 2-300K or 2-400K for compounds **1** and **5**-**6**. The samples consisted of a ground powder obtained from selected single crystals. The sample masses were 5.4, 2.1, and 0.9 mg for compounds **1**, **5**, and **6** respectively. Field-dependent magnetization studies were also carried out on **5** and **6** at multiple temperatures below their respective transitions (T_c) in applied fields ranging from -5T to 5T.

Single Crystal X-ray Diffraction: Single crystals of the title compounds, **1-6,** were selected under an optical microscope. Data were collected at room temperature (~300K) using Mo Kα radiation (λ = 0.71073Å) produced by a graphite monochromator. The crystal-to-detector distance was approximately 27.6 mm, and the exposure times for the data sets ranged from 5-30 seconds. The crystallographic data for **1-6** are summarized in Table 5.2. The secondary extinction parameter is reported only for compounds **3**, **5**, and **6** as the parameter proved to be insignificant once refined for the other three derivatives. The atomic coordinates, thermal parameters, and selected bond distances and angles are listed in Tables 5.3, 5.4, and 5.6, respectively. It should be noted that the standard deviations for the sof of partially occupied sites are not reported because SHELXTL[15] was first used to refine the occupancies and then they were fixed at the refined value or close to the refined value. Once the values are fixed, the standard deviations are no longer reported in the structure refinement files.

Table 5.2 Crystallographic data for compounds **1**-**6**.

empirical formula, compound	$BaNaCo_3(AsO_4)_3$, **1**	$Sr_{0.90}Na_{1.2}Ni_3(AsO_4)_3$, **2**	$Na_{16}Co_{6.25}O_{0.25}(AsO_4)_4(As_2O_7)_4$, **3**
structure type	**I**	**I**	**II**
color / shape	red, multifaceted	green, multifaceted	pink, plate
crystal size (mm)	0.20 × 0.05 × 0.05	0.07 × 0.03 × 0.03	0.10 × 0.10 × 0.02
formula weight (amu)	753.88	699.34	2343.19
T, °C		25	
space group, *Z*	*Imma* (no. 74), 4	*Imma* (no. 74), 4	$P2_1/c$ (no. 14), 1
a, Å	10.719(2) A	10.551(2)	13.866(3)
b, Å	14.091(3) A	13.737(3)	6.750(1)
c, Å	6.789(1) A	6.6898(13)	11.072(2)
β, °	---------	---------	100.90(3)
V, $Å^3$	1025.4(4)	969.6(3)	1017.7(4)
linear abs. coeff., mm^{-1}	18.274	20.947	12.479
F_{000}	1372	1306	1095
d_{calc}, g / cm^{-3}	4.883	4.791	3.823
data / restraints / parameters	506 / 0 / 57	469 / 0 / 62	1787 / 0 / 188
secondary extinction	---------	---------	0.0029(7)
reflections collected / unique/ R_{int} [a]	4151 / 506 / 0.0480	3781 / 469 / 0.0493	8039 / 1787 / 0.0429
final R1/wR2 [b] [$I > 2\sigma(I)$]	0.0383/ 0.0968	0.0235/ 0.0525	0.0514/ 0.1501
R1/wR2 (all data)	0.0422/ 0.0979	0.0272/ 0.0540	0.0533/ 0.1515
GOF	1.248	1.127	0.838
largest difference peak / hole (e^- / $Å^3$)	1.130 /-1.887	0.888 / -0.808	1.575 / -1.293

Table 5.2 Crystallographic data for compounds **1-6** cont…

empirical formula	$Sr_2Na_{0.66}Fe_{3.34}(PO_4)_4Cl_{0.8}$, **4**	$Sr_2NaFe_3(AsO_4)_4Cl$, **5**	$Ba_{1.88}Na_{0.75}Fe_3(AsO_4)_4Cl$, **6**
structure type	**III**	**III**	**III**
color / shape	dark brown, plate	dark brown, plate	dark brown, plate
crystal size (mm)	0.10 × 0.09 × 0.04	0.08 × 0.07 × 0.03	0.12 × 0.09 × 0.06
formula weight (amu)	785.27	956.91	1056.35
T, °C		25	
space group, *Z*	*Cccm* (no. 66), 4	*Cccm* (no. 66), 4	*Cccm* (no. 66), 4
a, Å	6.556(1)	6.694(1)	6.827(1)
b, Å	20.320(4)	20.738(4)	21.408(4)
c, Å	10.543(2)	10.827(2)	10.830(2)
V, $Å^3$	1404.6(5)	1503.0(5)	1582.7(6)
linear abs. coeff., mm^{-1}	11.632	18.913	16.166
F_{000}	1487	1768	1912
d_{calc}, g / cm^{-3}	3.713	4.229	4.433
data / restraints / parameters	660 / 0 / 75	699 / 0 / 77	750 / 0 / 75
secondary extinction	---------	0.0008(2)	0.0004(1)
reflections collected / unique/ R_{int} [a]	4773 / 660 / 0.1103	5962 / 699 / 0.0700	6320 / 750 / 0.0640
final R1/wR2 [b] [$I > 2\ \sigma(I)$]	0.0496/ 0.1030	0.0462/ 0.1289	0.0434 / 0.1193
R1/wR2 (all data)	0.0795/ 0.1165	0.0502/ 0.1349	0.0446/ 0.1208
GOF	0.818	1.032	1.080
largest difference peak / hole (e^- / $Å^3$)	1.552 / -1.519	1.067 / -1.516	2.711 / -1.823

[a]R_{int} = Σ | *Fo*^2- *Fo*^2 (mean) | / Σ[*Fo*^2]; [b]**1** R1 = Σ ||F_o| - |F_c|| / Σ|F_o|; *w*R2 = {[Σ[*w*(F_o^2-F_c^2)^2] / [Σw(F_o)^2)^2]}^(1/2); w=1/[\s^2^(Fo^2^)+(0.0277P)^2^+10.3332P] where P=(Fo^2^+2Fc^2^)/3; **2** *R* 1= Σ(||F_o| - |F_c||)/Σ|F_o|; *wR* = {Σ*w*[(|F_o| - |F_c|)^2]/Σ*w*[(|F_o|)^2]}^(1/2); w=*1/[\s^2^(Fo^2^)+(0.0264P)^2^+6.0840P] where P=(Fo^2^+2Fc^2^)/3*); **3** *R* 1= Σ(||F_o| - |F_c||)/Σ|F_o|; *wR2* = {Σ*w*[(|F_o| - |F_c|)^2]/Σ*w*[(|F_o|)^2]}^(1/2); w=*1/[\s^2^(Fo^2^)+(0.0809P)^2^+79.5697P] where P=(Fo^2^+2Fc^2^)/3'*; **4** R1 = Σ ||F_o| - |F_c|| / Σ|F_o|; *w*R2 = {[Σ[*w*(F_o^2-F_c^2)^2] / [Σw(F_o)^2)^2]}^(1/2); w=1/[\s^2^(Fo^2^)+(0.0288P)^2^+0.0000P] where P=(Fo^2^+2Fc^2^)/3; **5** R1 = Σ ||F_o| - |F_c|| / Σ|F_o|; *w*R2 = {[Σ[*w*(F_o^2-F_c^2)^2] / [Σw(F_o)^2)^2]}^(1/2); w=1/[\s^2^(Fo^2^)+(0.0442P)^2^+6.6736P] where P=(Fo^2^+2Fc^2^)/3; **6** R1 = Σ ||F_o| - |F_c|| / Σ|F_o|; *w*R2 = {[Σ[*w*(F_o^2-F_c^2)^2] / [Σw(F_o)^2)^2]}^(1/2); w=1/[\s^2^(Fo^2^)+(0.0871P)^2^+25.3896P] where P=(Fo^2^+2Fc^2^)/3

Table 5.3 Atomic parameters for **1-6**

Atom	Wycoff position	sof	x	y	z
		$BaNaCo_3(AsO_4)_3$, **1**			
Ba	4*e*	1.0	0	3/4	0.0878(2)
Na	4*a*	1.0	1/2	1/2	½
Co1	8*g*	1.0	-1/4	0.8645(1)	-1/4
Co2	4*b*	1.0	1/2	1/2	0
As1	8*g*	1.0	1/4	0.5661(1)	¼
As2	4*e*	1.0	0	¾	0.5735(3)
O1	8*i*	1.0	-0.1249(8)	3/4	0.730(1)
O2	16*j*	1.0	0.3666(6)	0.4849(5)	0.2098(9)
O3	16*j*	1.0	0.2034(6)	0.6309(4)	0.0572(9)
O4	8*h*	1.0	0	0.8460(6)	0.431(1)
		$Sr_{0.90}Na_{1.2}Ni_3(AsO_4)_3$, **2**			
Sr	4*e*	0.9	0	3/4	0.0803(2)
Na1	4*a*	1.0	1/2	1/2	1/2
Na2	4*d*	0.2	1/4	3/4	1/4
Ni1	8*g*	1.0	-1/4	0.86362(6)	-1/4
Ni2	4*b*	1.0	1/2	1/2	0
As1	8*g*	1.0	1/4	0.56794(5)	1/4
As2	4*e*	1.0	0	3/4	0.5647(2)
O1	8*i*	1.0	-0.1245(5)	3/4	0.7260(7)
O2	16*j*	1.0	0.3663(3)	0.4832(2)	0.2084(5)
O3	16*j*	1.0	0.1983(4)	0.6342(2)	0.0564(5)
O4	8*h*	1.0	0	0.8483(3)	0.4173(8)
		$Na_{16}Co_{6.25}O_{0.25}(AsO_4)_4(As_2O_7)_4$, **3**			
Na1	4*e*	1.0	0.6769(4)	0.0256(8)	0.6992(5)
Na2	4*e*	1.0	0.5479(4)	0.2626(7)	0.4203(5)
Na3	4*e*	1.0	0.6837(4)	0.4976(9)	0.6331(5)
Na4	4*e*	0.56	1.1695(7)	0.445(2)	0.5420(9)
Na5	4*e*	0.38	1.098(1)	0.458(2)	0.523(1)
Na6	2*a*	0.12	1.00000	1/2	1/2
Co1	4*e*	1.0	0.8688(1)	0.2567(2)	0.7166(1)
Co2	2*c*	1.0	1.00000	1/2	1.00000
Co3	4*e*	0.06	1.239(2)	0.581(4)	0.568(2)
As1	4*e*	1.0	0.76033(8)	0.0761(2)	0.4410(1)
As2	4*e*	1.0	1.07432(8)	0.2574(2)	0.7673(1)
As3	4*e*	0.93	0.58159(9)	-0.2394(2)	0.3596(1)
As4	4*e*	0.07	0.5810(13)	-0.248(2)	0.433(2)
O1	4*e*	1.0	0.7610(5)	0.232(1)	0.5597(7)
O2	4*e*	1.0	0.8461(6)	-0.093(1)	0.4619(7)
O3	4*e*	1.0	0.6435(6)	-0.035(1)	0.4376(8)
O4	4*e*	1.0	0.7503(6)	0.205(1)	0.3105(7)
O5	4*e*	1.0	1.1439(6)	0.064(1)	0.8224(8)
O6	4*e*	1.0	1.1447(5)	0.450(1)	0.7485(7)
O7	4*e*	1.0	0.9898(5)	0.293(1)	0.8614(7)
O8	4*e*	1.0	0.9928(6)	0.224(1)	0.6322(7)
O9	4*e*	1.0	0.6355(7)	-0.440(1)	0.4239(8)
O10	4*e*	1.0	0.5964(7)	-0.223(1)	0.2145(7)
O11	4*e*	1.0	0.4672(6)	-0.211(1)	0.3773(9)
O12	4*e*	0.06	1.098(1)	0.458(2)	0.523(1)

Table 5.3 Atomic parameter for **1-6** cont…

Atom	Wycoff position	sof	x	y	z
		$Sr_2Na_{0.66}Fe_{3.34}(PO_4)_4Cl_{0.8}$, **4**			
Sr	8*l*	1.0	0.3658(2)	-0.08715(7)	1/2
Na	4*a*	0.66	0	0	1/4
Fe1	8*h*	1.0	0	0.1612(1)	1/4
Fe2	4*f*	1.0	1/4	1/4	1/2
Fe3	4*a*	0.34	0	0	1/4
P1	8*l*	1.0	0.1418(6)	0.0893(2)	1/2
P2	8*h*	1.0	1/2	0.2021(2)	3/4
Cl	8*g*	0.4	0.393(1)	0	3/4
O1	16*m*	1.0	0.000(1)	0.0882(4)	0.3842(9)
O2	8*l*	1.0	0.279(2)	0.0305(7)	1/2
O3	8*l*	1.0	0.274(2)	0.1512(6)	1/2
O5	16*m*	1.0	0.317(1)	0.1605(4)	0.7834(9)
O4	16*m*	1.0	0.045(1)	0.2482(4)	0.3613(8)
		$Sr_2NaFe_3(AsO_4)_4Cl$, **5**			
Sr	8*l*	1.0	0.3458(2)	-0.08609(6)	1/2
Na1	4*a*	0.9	0	0	1/4
Na2	4*e*	0.1	-1/4	1/4	1/2
Fe1	8*h*	1.0	0	0.15946(9)	1/4
Fe2	4*f*	1.0	1/4	1/4	1/2
As1	8*l*	1.0	0.1622(2)	0.09108(5)	1/2
As2	8*h*	1.0	1/2	0.20376(5)	3/4
Cl	4*b*	1.0	1/2	0	1/4
O1	16*m*	1.0	0.0034(9)	0.0927(3)	0.3795(6)
O2	8*l*	1.0	0.308(2)	0.0287(5)	1/2
O3	8*l*	1.0	0.316(1)	0.1553(4)	1/2
O4	16*m*	1.0	0.0475(9)	0.2404(3)	0.3624(5)
O5	16*m*	1.0	0.3050(9)	0.1586(3)	0.7922(7)
		$Ba_{1.88}Na_{0.75}Fe_3(AsO_4)_4Cl$, **6**			
Ba	8*l*	0.94	0.34989(9)	-0.08391(3)	1/2
Na	4*a*	0.75	0	0	1/4
Fe1	8*h*	1.0	0	0.16217(6)	1/4
Fe2	4*f*	1.0	1/4	1/4	1/2
As1	8*l*	1.0	0.1574(1)	0.09671(5)	1/2
As2	8*h*	1.0	1/2	0.20484(4)	3/4
Cl	8*g*	0.5	0.423(1)	0	3/4
O1	16*m*	1.0	0.0046(7)	0.0993(3)	0.3793(5)
O2	8*l*	1.0	0.290(1)	0.0355(4)	1/2
O3	8*l*	1.0	0.308(1)	0.1595(3)	1/2
O4	16*m*	1.0	0.0495(7)	0.2405(2)	0.3623(4)
O5	16*m*	1.0	0.3066(7)	0.1621(2)	0.7876(5)

Table 5.4 Anisotropic thermal parameters for compounds **1**-**6**.

Atom	U_{11}	U_{22}	U_{33}	U_{12}	U_{13}	U_{23}
			$BaNaCo_3(AsO_4)_3$, **1**			
Ba	0.0169(7)	0.0157(7)	0.0116(7)	0.00000	0.00000	0.00000
Na	0.019(4)	0.041(6)	0.015(5)	0.00000	0.00000	-0.001(4)
Co1	0.0054(9)	0.0048(9)	0.0062(9)	0.00000	0.0003(6)	0.00000
Co2	0.004(1)	0.006(1)	0.003(1)	0.00000	0.00000	0.0006(9)
As1	0.0043(7)	0.0064(7)	0.0026(7)	0.00000	-0.0001(5)	0.00000
As2	0.0029(9)	0.005(1)	0.005(1)	0.00000	0.00000	0.00000
O1	0.003(4)	0.008(5)	0.007(5)	0.00000	0.001(4)	0.00000
O2	0.007(3)	0.009(3)	0.008(3)	0.003(3)	0.001(2)	0.002(3)
O3	0.016(3)	0.012(3)	0.003(3)	0.007(3)	0.000(2)	0.004(3)
O4	0.011(5)	0.005(5)	0.008(5)	0.00000	0.00000	0.005(4)
			$Sr_{0.90}Na_{1.2}Ni_3(AsO_4)_3$, **2**			
Sr	0.0151(6)	0.0116(5)	0.0102(6)	0.00000	0.00000	0.00000
Na1	0.014(2)	0.055(3)	0.010(2)	0.00000	0.00000	-0.003(2)
Na2	0.05(2)	0.10(3)	0.03(2)	0.00000	-0.02(1)	0.0000
Ni1	0.0070(5)	0.0064(5)	0.0095(5)	0.00000	0.0004(3)	0.00000
Ni2	0.0087(7)	0.0107(7)	0.0099(7)	0.00000	0.00000	0.0000(5)
As1	0.0083(4)	0.0078(4)	0.0066(4)	0.00000	-0.0004(3)	0.00000
As2	0.0062(5)	0.0062(5)	0.0108(5)	0.00000	0.00000	0.00000
O1	0.010(3)	0.010(2)	0.013(3)	0.00000	-0.001(2)	0.00000
O2	0.009(2)	0.008(2)	0.012(2)	0.002(1)	0.002(1)	0.003(1)
O3	0.016(2)	0.013(2)	0.010(2)	0.004(1)	-0.003(2)	0.003(2)
O4	0.015(3)	0.005(2)	0.015(3)	0.00000	0.00000	0.004(2)
			$Na_{16}Co_{6.25}O_{0.25}(AsO_4)_4(As_2O_7)_4$, **3**			
Na1	0.020(3)	0.019(3)	0.034(3)	-0.003(2)	0.011(2)	-0.003(2)
Na2	0.023(3)	0.020(3)	0.029(3)	0.004(2)	0.000(2)	0.002(2)
Na3	0.030(3)	0.033(3)	0.021(3)	0.020(2)	-0.008(2)	-0.009(2)
Co1	0.013(1)	0.010(1)	0.007(1)	0.0005(8)	0.0014(8)	0.0000(8)
Co2	0.0073(7)	0.0080(8)	0.0081(7)	-0.0002(5)	0.0009(6)	-0.0008(5)
As1	0.0107(6)	0.0102(6)	0.0092(6)	0.0001(4)	0.0024(4)	-0.0006(4)
As2	0.0063(6)	0.0059(6)	0.0093(6)	0.0000(4)	0.0023(4)	-0.0007(4)
As3	0.0104(7)	0.0090(6)	0.0091(8)	-0.0001(4)	0.0018(5)	-0.0004(4)
O1	0.005(4)	0.019(4)	0.007(4)	0.002(3)	-0.004(3)	-0.005(3)
O9	0.029(5)	0.011(4)	0.022(4)	0.006(4)	-0.001(4)	0.006(3)
O5	0.020(4)	0.007(4)	0.027(5)	0.004(3)	0.003(4)	0.000(3)
O2	0.010(4)	0.020(4)	0.012(4)	-0.002(3)	0.005(3)	-0.004(3)
O3	0.018(4)	0.015(4)	0.028(5)	-0.009(3)	0.012(4)	-0.004(4)
O6	0.011(4)	0.012(4)	0.015(4)	0.001(3)	0.008(3)	-0.002(3)
O7	0.003(4)	0.022(4)	0.013(4)	0.001(3)	0.002(3)	-0.005(3)
O8	0.009(4)	0.015(4)	0.008(4)	0.001(3)	0.002(3)	-0.002(3)
O4	0.017(4)	0.017(4)	0.016(4)	0.005(3)	0.004(3)	0.006(3)
O10	0.034(5)	0.019(4)	0.007(4)	-0.003(4)	0.003(4)	0.001(3)
O11	0.008(4)	0.040(6)	0.028(5)	0.001(4)	0.001(4)	0.002(4)

Table 5.4 Anisotropic thermal parameters for compounds **1**-**6** cont…

Atom	U_{11}	U_{22}	U_{33}	U_{12}	U_{13}	U_{23}
			$Sr_2Na_{0.66}Fe_{3.34}(PO_4)_4Cl_{0.8}$, **4**			
Sr	0.0094(8)	0.0151(8)	0.025(1)	-0.0004(7)	0.00000	0.00000
Na	0.061(5)	0.015(4)	0.010(4)	0.00000	0.00000	0.00000
Fe1	0.015(1)	0.020(1)	0.021(2)	0.00000	0.003(1)	0.00000
Fe2	0.022(2)	0.019(2)	0.018(2)	0.001(2)	0.00000	0.00000
Fe3	0.061(5)	0.015(4)	0.010(4)	0.00000	0.00000	0.00000
P1	0.014(2)	0.013(2)	0.012(2)	0.001(2)	0.00000	0.00000
P2	0.012(2)	0.023(2)	0.014(3)	0.00000	-0.000(2)	0.00000
Cl	0.013(5)	0.015(5)	0.008(5)	0.00000	0.00000	0.000(4)
O1	0.027(5)	0.050(6)	0.023(6)	-0.013(5)	-0.004(4)	0.014(5)
O2	0.025(8)	0.019(8)	0.16(2)	0.007(6)	0.00000	0.00000
O3	0.019(6)	0.019(6)	0.025(8)	0.000(5)	0.00000	0.00000
O4	0.020(5)	0.024(5)	0.015(5)	0.002(3)	-0.008(4)	0.004(4)
O5	0.016(5)	0.007(4)	0.042(7)	-0.002(3)	0.010(4)	-0.001(4)
			$Sr_2NaFe_3(AsO_4)_4Cl$, **5**			
Sr	0.0130(8)	0.0112(7)	0.073(1)	0.0008(4)	0.00000	0.00000
Na1	0.35(3)	0.028(7)	0.031(6)	0.00000	0.00000	0.00000
Na2	0.03(4)	0.06(5)	0.01(3)	0.01(4)	0.00000	0.0000
Fe1	0.025(1)	0.017(1)	0.040(1)	0.00000	-0.0001(8)	0.00000
Fe2	0.021(1)	0.016(1)	0.036(1)	0.002(1)	0.00000	0.00000
As1	0.0106(7)	0.0076(7)	0.0267(7)	0.0006(4)	0.00000	0.00000
As2	0.0100(7)	0.0074(7)	0.0336(8)	0.00000	-0.0005(4)	0.00000
Cl1	0.39(3)	0.066(7)	0.058(5)	0.00000	0.00000	0.00000
O1	0.017(3)	0.027(3)	0.025(3)	-0.009(2)	-0.004(2)	0.003(3)
O2	0.019(5)	0.014(5)	0.15(1)	0.002(4)	0.00000	0.00000
O3	0.013(4)	0.009(4)	0.027(4)	-0.001(3)	0.00000	0.00000
O4	0.015(3)	0.010(3)	0.028(3)	-0.003(2)	-0.001(2)	-0.001(2)
O5	0.012(3)	0.016(3)	0.044(4)	-0.003(2)	0.004(3)	-0.005(3)
			$Ba_{1.88}Na_{0.75}Fe_3(AsO_4)_4Cl$, **6**			
Ba	0.0126(4)	0.0162(4)	0.0341(5)	0.0003(2)	0.00000	0.00000
Na	0.11(1)	0.040(6)	0.034(5)	0.00000	0.00000	0.00000
Fe1	0.0174(8)	0.0172(8)	0.0178(8)	0.00000	-0.0007(6)	0.00000
Fe2	0.0141(9)	0.015(1)	0.0191(9)	0.0011(7)	0.00000	0.00000
As1	0.0120(6)	0.0130(5)	0.0177(6)	0.0014(3)	0.00000	0.00000
As2	0.0105(5)	0.0113(5)	0.0171(6)	0.00000	0.0008(3)	0.00000
Cl	0.061(4)	0.070(5)	0.043(4)	0.00000	0.00000	-0.019(4)
O1	0.023(2)	0.038(3)	0.018(3)	-0.011(2)	-0.005(2)	0.001(2)
O2	0.024(4)	0.010(4)	0.15(1)	0.007(4)	0.00000	0.00000
O3	0.014(3)	0.009(3)	0.025(4)	-0.003(2)	0.00000	0.00000
O4	0.015(2)	0.011(2)	0.016(2)	-0.002(2)	-0.001(2)	-0.002(2)
O5	0.012(2)	0.017(3)	0.027(3)	-0.008(2)	-0.001(2)	0.003(2)

Table 5.5 Selected bond distances and angles for Compounds **1**-**6**.

Bond Distances	Bond Angles	
$BaNaCo_3(AsO_4)_3$, **1**		
Co(1)-O(1) 2.103(6)*2	O(1)0-Co(1)-O(1) 79.8(4)	O(2)-Co(2)-O(2) 180.000(1)
Co(1)-O(2) 2.125(7)*2	O(1)0-Co(1)-O(2) 175.0(3)	O(2)-Co(2)-O(4) 92.6(2)
Co(1)-O(3) 2.145(6)*2	O(1)-Co(1)-O(2) 103.2(2)	O(2)-Co(2)-O(4) 87.4(2)
	O(1)-Co(1)-O(2) 175.0(3)	O(4)-Co(2)-O(4) 180.0(1)
Co(2)-O(2) 2.029(6)*4	O(2)-Co(1)-O(2) 74.1(3)	
Co(2)-O(4) 2.220(9)*2	O(1)-Co(1)-O(3) 96.3(3)	O(3)-As(1)-O(3) 113.8(4)
	O(1)-Co(1)-O(3) 86.4(3)	O(3)-As(1)-O(2) 105.7(3)
As(1)-O(3) 1.672(6)*2	O(2)-Co(1)-O(3) 87.9(3)	O(3)- As(1)-O(2) 117.2(3)
As(1)-O(2) 1.716(6)*2	O(2)-Co(1)-O(3) 89.3(2)	O(2)-As(1)-O(2) 96.4(4)
	O(3)-Co(1)-O(3) 176.6(4)	
As(2)-O(4) 1.664(9)*2		O(4)-As(2)-O(4) 108.8(7)
As(2)-O(1) 1.708(9)*2	O(2)-Co(2)-O(2) 180.0(4)	O(4)-As(2)-O(1) 111.2(2)
	O(2)-Co(2)-O(2) 89.6(3)	O(1)- As(2)-O(1) 103.2(6)
	O(2)-Co(2)-O(2) 90.4(4)	
$Sr_{0.90}Na_{1.2}Ni_3(AsO_4)_3$, **2**		
Ni(1)-O(1) 2.053(3)*2	O(1)-Ni(1)-O(1) 81.0(2)	O(2)-Ni(2)-O(2) 180.0(2)
Ni(1)-O(2) 2.069(3)*2	O(1)-Ni(1)-O(2) 175.2(2)	O(2)-Ni(2)-O(4) 93.9(1)
Ni(1)-O(3) 2.121(3)*2	O(1)-Ni(1)-O(2) 102.2(2)	O(2)-Ni(2)-O(4) 86.1(1)
	O(2)-Ni(1)-O(2) 74.9(2)	O(4)-Ni(2)-O(4) 180.0(3)
Ni(2)-O(2) 1.997(3)*4	O(1)-Ni(1)-O(3) 95.8(2)	
Ni(2)-O(4) 2.156(4)*2	O(1)-Ni(1)-O(3) 85.4(2)	O(3)-As(1)-O(3) 114.1(2)
	O(2)-Ni(1)-O(3) 88.1(1)	O(3)-As(1)-O(2) 118.5(2)
As(1)-O(3) 1.675(3)*2	O(2)-Ni(1)-O(3) 90.6(1)	O(3)-As(1)-O(2) 105.2(2)
As(1)-O(2) 1.714(3)*2	O(3)-Ni(1)-O(3) 178.4(2)	O(2)-As(1)-O(2) 94.5(2)
As(2)-O(4) 1.672(4)*2	O(2)-Ni(2) O(2) 180.0	O(4)-As(2)-O(4) 107.7(3)
As(2)-O(1) 1.700(5)*2	O(2)-Ni(2)-O(2) 89.9(2)	O(4)-As(2)-O(1) 112.0(1)
	O(2)-Ni(2)-O(2) 90.1(2)	O(1)-As(2)-O(1) 101.2(3)
$Na_{16}Co_{6.25}O_{0.25}(AsO_4)_4(As_2O_7)_4$, **3**		
Co(1)-O(1) 2.074(7)	O(1)-Co(1)-O(7) 172.9(3)	O(8)-Co(2)-O(8) 180.000(1)
Co(1)-O(7) 2.104(8)	O(1)-Co(1)-O(8) 97.9(3)	O(7)-Co(2)-O(2) 82.9(3)
Co(1)-O(8) 2.118(8)	O(7)-Co(1)-O(8) 75.6(3)	O(7)-Co(2)-O(2) 97.1(3)
Co(1)-O(5) 2.119(8)	O(1)-Co(1)-O(5) 83.6(3)	O(8)-Co(2)-O(2) 99.6(3)
Co(1)-O(6) 2.120(8)	O(7)-Co(1)-O(5) 93.7(3)	O(8)-Co(2)-O(2) 80.4(3)
Co(1)-O(4) 2.121(8)	O(8)-Co(1)-O(5) 93.3(3)	O(2)-Co(2)-O(2) 180.000(2)
	O(1)-Co(1)-O(6) 90.0(3)	
Co(2)-O(7) 2.061(8)*2	O(7)-Co(1)-O(6) 93.4(3)	O(1)-Co(3)-O(4) 91(1)
Co(2)-O(8) 2.118(8)*2	O(8)-Co(1)-O(6) 94.9(3)	O(1)-Co(3)-O(9) 103(1)
Co(2)-O(2) 2.187(8)*2	O(5)-Co(1)-O(6) 170.3(3)	O(4)-Co(3)-O(9) 112(1)
	O(1)-Co(1)-O(4) 85.3(3)	O(1)-Co(3)-O(12) 103(1)
Co(3)-O(1) 1.89(3)	O(7)-Co(1)-O(4) 101.1(3)	O(4)-Co(3)-O(12) 114(1)
Co(3)-O(4) 1.96(3)	O(8)-Co(1)-O(4) 176.7(3)	O(9)Co(3)-O(12) 127(2)
Co(3)-O(9) 1.97(3)	O(5) -Co(1)-O(4) 86.4(3)	
Co(3)-O(12) 2.10(3)	O(6) -Co(1)-O(4) 85.8(3)	O(2)-As(1)-O(4) 115.2(4)
		O(2)-As(1)-O(1) 115.5(4)
As(1)-O(2) 1.633(8)	O(7)-Co(2)-O(7)180.000(1)	O(4)-As(1)-O(1) 109.7(4)
As(1)-O(4) 1.669(8)	O(7)-Co(2)-O(8) 88.5(3)	O(2)-As(1)-O(3) 110.1(4)
As(1)-O(1) 1.682(7)	O(7)-Co(2)-O(8) 91.5(3)	O(4)-As(1)-O(3) 105.9(4)

Table 5.5 Selected bond distances and angles for compounds **1-6** cont…

Bond Distances	Bond Angles	
$Na_{16}Co_{6.25}O_{0.25}(AsO_4)_4(As_2O_7)_4$, **3** cont...		
As(1)-O(3) 1.779(8)	O(1)-As(1)-O(3) 98.7(4)	O(9)-As(4)-O(11) 125(1)
		O(9)-As(4)-O(3) 118(1)
As(2)-O(6) 1.663(8)	O(6)-As(2)-O(5) 110.2(4)	O(11)-As(4)-O(3) 110(1)
As(2)-O(5) 1.669(8)	O(6)-As(2)-O(8) 107.5(4)	
As(2)-O(8) 1.711(8)	O(5)-As(2)-O(8) 117.1(4)	
As(2)-O(7) 1.725(7)	O(6)-As(2)-O(7) 116.6(4)	
	O(5)-As(2)-O(7) 107.5(4)	
As(3)-O(9) 1.642(8)	O(8)-As(2)-O(7) 97.7(4)	
As(3)-O(11) 1.646(9)		
As(3)-O(10) 1.661(8)	O(9)-As(3)-O(11) 114.5(5)	
As(3)-O(3) 1.762(8)	O(9)-As(3)-O(10) 110.1(4)	
	O(11)-As(3)-O(10) 113.9(5)	
As(4)-O(9) 1.51(2)	O(9)-As(3)-O(3) 107.0(4)	
As(4)-O(3) 1.68(2)	O(11)-As(3)-O(3) 104.1(4)	
As(4)-O(11) 1.60(2)	O(10)-As(3)-O(3) 106.5(4)	
$Sr_2Na_{0.66}Fe_{3.34}(PO_4)_4Cl_{0.8}$, **4**		
Fe(1)-O(1) 2.050(9)*2	O(1)-Fe(1)-O(1) 87.3(5)	O(3)-Fe(2)-O(3) 180.000(1)
Fe(1)-O(5) 2.105(7)*2	O(1)-Fe(1)-O(5) 96.3(3)	
Fe(1)-O(4) 2.141(8)*2	O(1)-Fe(1)-O(5) 83.2(3)	O(1)-Fe(3)-O(1) 179.9(5)
	O(5)-Fe(1)-O(5) 179.2(4)	O(1)-Fe(3)-O(1) 76.5(4)
Fe(2)-O(4) 1.988(8)*4	O(1)-Fe(1)-O(4) 167.3(4)	O(1)-Fe(3)O(1) 103.5(4)
Fe(2)-O(3) 2.01(1)*2	O(1)-Fe(1)-O(4) 102.7(3)	O(1)-Fe(3)Cl 89.9(2)
	O(5)-Fe(1)-O(4) 92.8(3)	O(1)-Fe(3)Cl 90.1(2)
Fe(3)-O(1) 2.283(9)*4	O(5)-Fe()- O(4) 87.9(3)	Cl-Fe(3)-Cl 180.0
Fe(3)-Cl(1) 2.579(9)*2	O(4)-Fe(1)-O(4) 68.8(4)	
		O(2)-P(1)-O(3) 108.3(7)
P(1)-O(2) 1.50(1)	O(4)-Fe(2)-O(4) 180.000(1)	O(2)-P(1)-O(1) 110.7(5)
P(1)-O(3) 1.53(1)	O(4)-Fe(2)-O(4) 94.7(5)	O(3)-P(1)-O(1) 110.8(4)
P(1)-O(1) 1.533(9)*2	O(4)-Fe(2)-O(4) 85.3(5)	O(1)-P(1)-O(1) 105.6(7)
	O(4)-Fe(2)-O(4) 85.3(5)	
P2 O5 1.512(7)*2	O(4)-Fe(2)-O(4) 180.000(1)	O(5)-P(2)-O(5) 112.1(6)
P2 O4 1.575(8)*2	O(4)-Fe(2)-O(3) 92.1(3)	O(5)-P(2)-O(4) 109.4(4)
	O(4)-Fe(2)-O(3) 87.9(3)	O(5)-P(2)-O(4) 112.6(4)
		O(4)-P(2)-O(4) 100.3(6)
$Sr_2NaFe_3(AsO_4)_4Cl$, **5**		
Fe(1)-O(1) 1.971(6)*2	O(1)-Fe(1)-O(1)90.7(4)	O(4)-Fe(2)-O(4) 180.000(1)
Fe(1)-O(5) 2.092(6)*2	O(1)-Fe(1)-O(5) 98.0(2)	O(4)-Fe(2)-O(4) 94.8(3)
Fe(1)-O(4) 2.098(6)*2	O(1)-Fe(1)-O(5) 81.4(2)	O(4)-Fe(2)-O(4) 85.2(3)
	O(5)-Fe(1)-O(5) 179.0(3)	
Fe(2)-O(3) 2.013(8)*2	O(1)-Fe(1)-O(4) 167.6(2)	O(2)-As(1)-O(1) 113.3(3)
Fe(2)-O(4)2.024(6)*4	O(1)-Fe(1)-O(4) 98.5(2)	O(1)-As(1)-O(1) 101.6(4)
	O(5)-Fe(1)-O(4) 91.6(2)	O(2)-As(1)-O(3)105.3(5)
As(1)-O(2) 1.62(1)	O(5)-Fe(1)-O(4) 89.2(2)	O(1)-As(1)-O(3) 111.7(3)
As(1)-O(1) 1.683(6)*2	O(4)-Fe(1)-O(4) 73.7(3)	
As(1)-O(3) 1.684(8)		O(5)-As(2)-O(5) 111.8(4)
	O(3)-Fe(2)-O(3) 180.000(2)	O(5)-As(2)-O(4) 115.4(3)
As(2)-O(5) 1.670(6)*2	O(3)-Fe(2)-O(4) 92.9(2)	O(5)-As(2)-O(4) 109.3(3)
As(2)-O(4) 1.710(6)*2	O(3)-Fe(2)-O(4) 87.1(2)	O(4)-As(2)-O(4) 94.8(4)

Table 5.5 Selected bond distances and angles for compounds **1**-**6** cont…

Bond Distances	Bond Angles	
$Ba_{1.88}Na_{0.75}Fe_3(AsO_4)_4Cl$, **6**		
Fe(1)-O(1) 1.942(5)*2	O(1)-Fe(1)-O(1) 92.3(3)	O(3)-Fe(2)-O(4) 92.0(2)
Fe(1)-O(4) 2.098(4)*2	O(1)-Fe(1)-O(4) 166.9(2)	O(4)-Fe(2)-O(4) 180.000(1)
Fe(1)-O(5) 2.132(5)*2	O(1)-Fe(1)-O(4) 97.6(2	
	O(4)-Fe(1)-O(4) 74.0(2)	
Fe(2)-O(3) 1.978(6)*2	O(1)-Fe(1)-O(5) 97.0(2)	O(2)-As(1)-O(1) 112.5(3)
Fe(2)-O(4) 2.034(4)*4	O(1)-Fe(1)-O(5) 83.0(2)	O(1)-As(1)-O(1) 102.7(4)
	O(5)-Fe(1)-O(4) 87.3(2)	O(2)-As(1)-O(3) 107.9(4)
As(1)-O(2) 1.593(8)	O(5)-Fe(1)-O(4) 92.7(2)	O(1)-As(1)-O(3) 110.6(2)
As(1)-O(1) 1.673(5)*2	O(5)-Fe(1)-O(5) 179.9(2)	
As(1)-O(3)1.689(6)		O(5)-As(2)-O(5) 113.3(4)
	O(3)-Fe(2)-O(3) 180.000(1)	O(5)-As(2)-O(4) 111.1(3)
As(2)-O(5)1.657(4)*2	O(4)-Fe(2)-O(4) 85.7(3)	O(5)-As(2)-O(4) 112.8(3)
As(2)-O(4)1.722(4)*2	O(4)-Fe(2)-O(4) 94.3(3)	O(4)-As(2)-O(4) 94.2(3)
	O(3)-Fe(2)-O(4) 88.0(2)	

Results and Discussion

Six new mixed-polyhedral-framework compounds have been synthesized by conventional solid state methods. Sizeable single crystals of these refractory oxides were grown in molten-salt media. The title compounds have various compositions including $BaNaCo^{II}_3(AsO_4)_3$, **1,** $Sr_{0.90}Na_{1.2}Ni^{II}_3(AsO_4)_3$, **2,** $Na_{16}Co^{II}_{6.25}O_{0.25}(AsO_4)_4(As_2O_7)_4$, **3,** $Sr_2Na_{0.66}Fe^{II/III}_{3.34}(PO_4)_4Cl_{0.8}$, **4**, $Sr_2NaFe^{II/III}_3(AsO_4)_4Cl$, **5**, $Ba_{1.88}Na_{0.75}Fe^{II/III}_3(AsO_4)_4Cl$, **6**. Although all of these complex oxides are not isostructural, they have strong structural relationships that will be presented in the following paragraphs. These materials form three different structure types denoted as **I** (**1**-**2**), **II** (**3**), and **III** (**4**-**6**). The materials crystallize in three different space groups including *Imma* (no. 74), *C*2/*c* (no. 14), and *Cmmc* (no.66) for structure types **I**, **II**, and **III**, respectively. The crystallographic data for these compounds can be found in Table 5.2.

Structure type **I** has been observed for $BaNaCo_3(AsO_4)_3$, **1**, and $Sr_{0.90}Na_{1.2}Ni_3(AsO_4)_3$, **2**. The only observed difference in these two compounds is that **2** has a bit of disorder in the Na and Sr atomic sites. An additional crystallographically distinct Na(2) site is also observed for **2**. The occupancies of the Sr and Na(2) sites were refined using SHELXTL[15] and found to be partially occupied at approximately 90% and 20%, respectively (refer to Table 5.3). Due to the similarities in these two compounds, the structure of **1** will be described from this point forward.

Compound **1** has a 3-dimensional Co-O-As framework, Figure 5.2, which consists of two crystallographically distinct Co^{2+} sites, both of which are octahedrally coordinated by oxygen. The 2+ oxidation states are further supported by bond valence sum

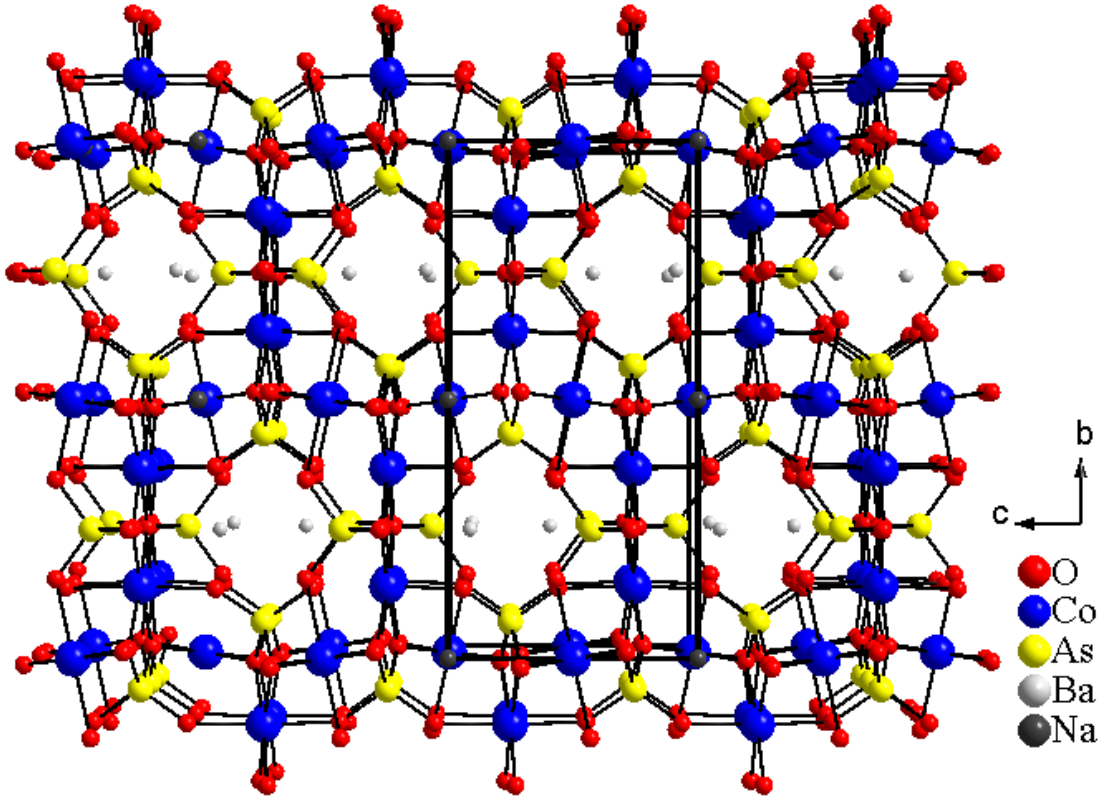

Figure 5.2: Ball-and-stick representation showing a perspective view of $BaNaCo_3(AsO_4)_3$, **1**, structure type **I**, along the channels.

calculations[16], 1.87 for Co(1) and 1.85 for Co(2). The Co(1) octahedron consists of 2×Co(1)-O(1), 2×Co(1)-O(2), and 2×Co(1)-O(3) bonds with lengths of 2.103(6) Å, 2.125(7) Å, and 2.145(6) Å, respectively. This octahedron shares two corner O(2) atoms with two Co(2) polyhedra, Figure 5.3 (left), and one edge with a neighboring Co(1) polyhedron *via* O(1), Figure 5.3 (right). This edge-sharing connectivity gives rise to the shortest Co-Co distance of 3.227(2) Å and a Co(1)-O(1)-Co(1) angle of 100.25(1)°. The distance between the corner-sharing Co(1) and Co(2) polyhedra is approximately 3.702(1)Å. The octahedral Co(2) has four Co(2)-O(2) bonds and two Co(2)-O(4) bonds equal to 2.029(6) Å and 2.220(9) Å for O(2) and O(4), respectively. The $Co(2)O_6$ octahedron shares four equatorial corner O(2) atoms with four surrounding $Co(1)O_6$ octahedra, Figure 5.3 (left). Both Co(1) and Co(2) also share all six surrounnding O atoms with neighboring AsO_4 tetrahedra. The As atoms are found in a 5+ oxidation state which is further supported by bond valence sum calculations[16], which gave values equal to 4.88 for As(1) and 4.99 for As(2). Figure 5.4 shows a polyhedral view of the connectivity between the Co(1) and As(1,2) polyhedra. Co(1) shares two corner O(3) atoms with As(1), two corner O(1) atoms with As(2), and an edge with As(1) *via* O(2). The polyhedral connectivity of Co(2) and surrounding As(1,2) atoms can be seen in Figure 5.5. Co(2) shares four equatorial O(2) atoms with As(1) and two axial O(4) atoms with As(2), Figure 5.5. Compound **1** also has intersecting channels that run along the crystallographic *a* and *b* axes that contain both Ba and Na cations, Figures 5.1 and 5.6. Looking along the crystallographic *a* axis, Figure 5.7 (left), six-membered ring windows, consisting of four $Co(1)O_6$ polyhedra and two $As(1)O_4$ polyhedra are seen, while along *b*,

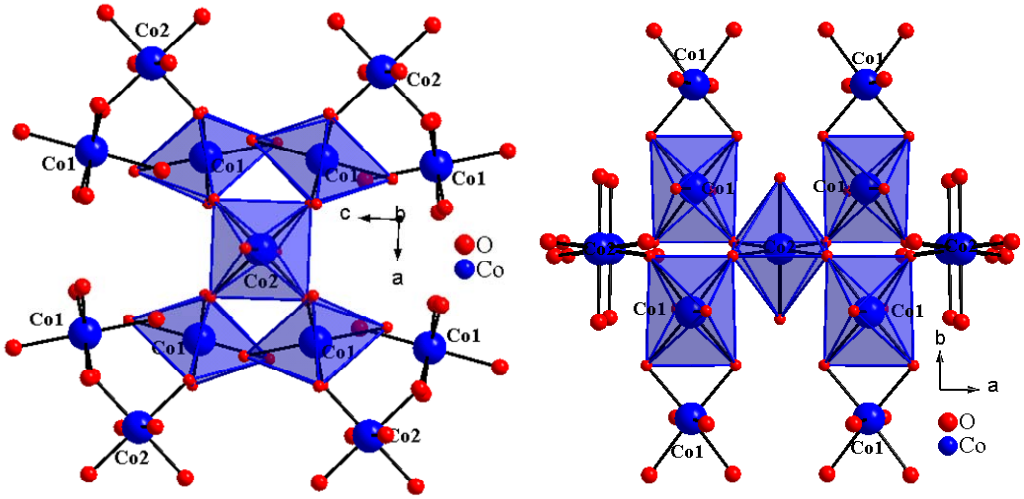

Figure 5.3: Projected view of the Co-O connectivity within the *ac* plane of $BaNaCo_3(AsO_4)_3$, **1** (left). The $Co(1)O_6$ polyhedra share two corner oxygen atoms with $Co(2)O_6$ polyhedra *via* O(4) atoms and each $Co(2)O_6$ polyhedron shares 4 equatorial O(2) atoms with neighboring Co(1) polyhedra. Looking at the projected view of the Co-O connectivity within the *ab* plane (right), it can be seen that the Co(1) polyhedra also share an additional edge with other Co(1)O6 octahedra, forming a 3-D Co-O lattice.

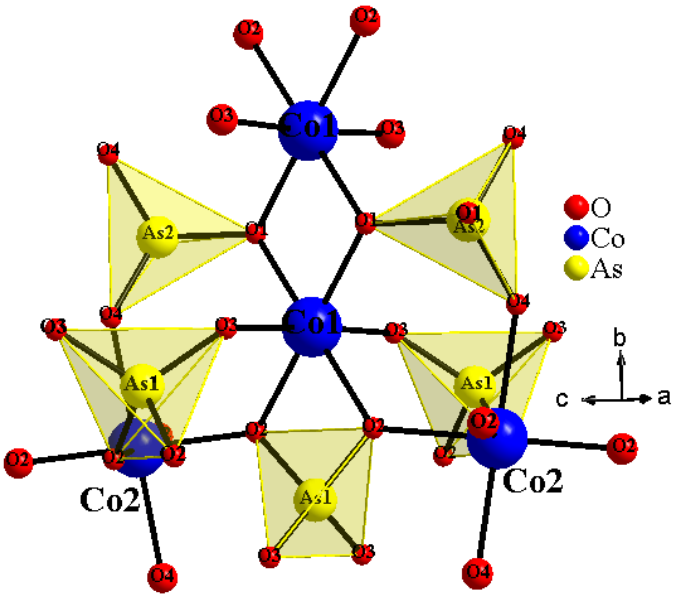

Figure 5.4: Polyhedral view of the connectivity between Co(1) and neighboring Co(2), As(1), and As(2) atoms in $BaNaCo_3(AsO_4)_3$, **1**. Co(1) shares O(1) with two As(2) atoms, O(3) with two As(1) atoms, and an additional edge with As(1) *via* O(2).

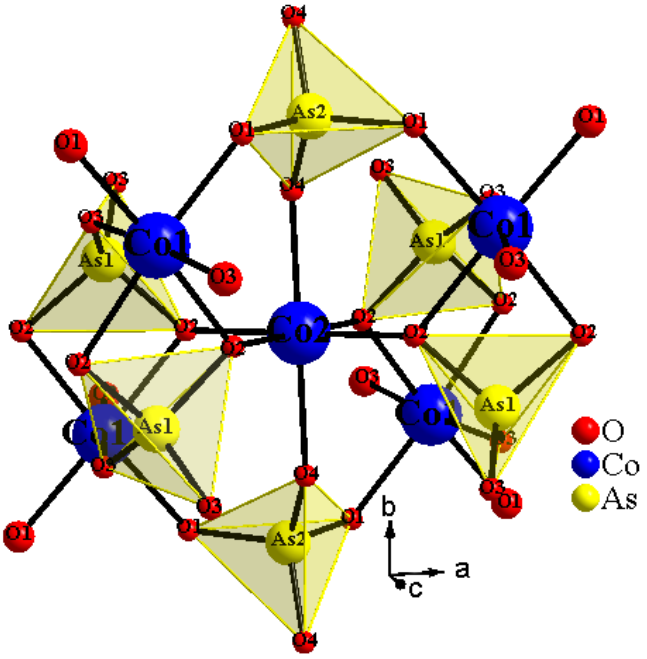

Figure 5.5: Polyhedral view of the connectivity between Co(2) and neighboring Co(1), As(1), and As(2) atoms in $BaNaCo_3(AsO_4)_3$, **1**. As(1) shares the four equatorial O(2) atoms with Co(2), while As(2) shares the two axial O(4) atoms with Co(2).

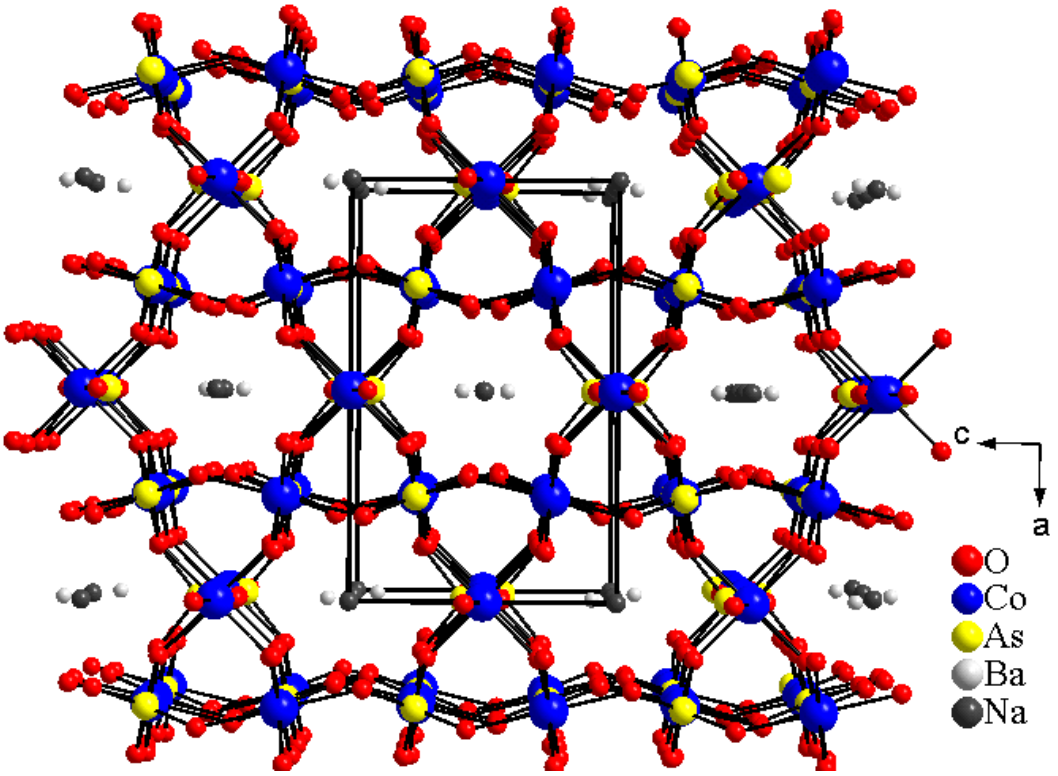

Figure 5.6: Projected view of the *ac* plane of $Ba_2NaCo_3(AsO_4)_3$, **1**, structure type **I**. Na and Ba cations are located within 6-membered ring windows. For the Co-O framework, see Fig. 5.1.

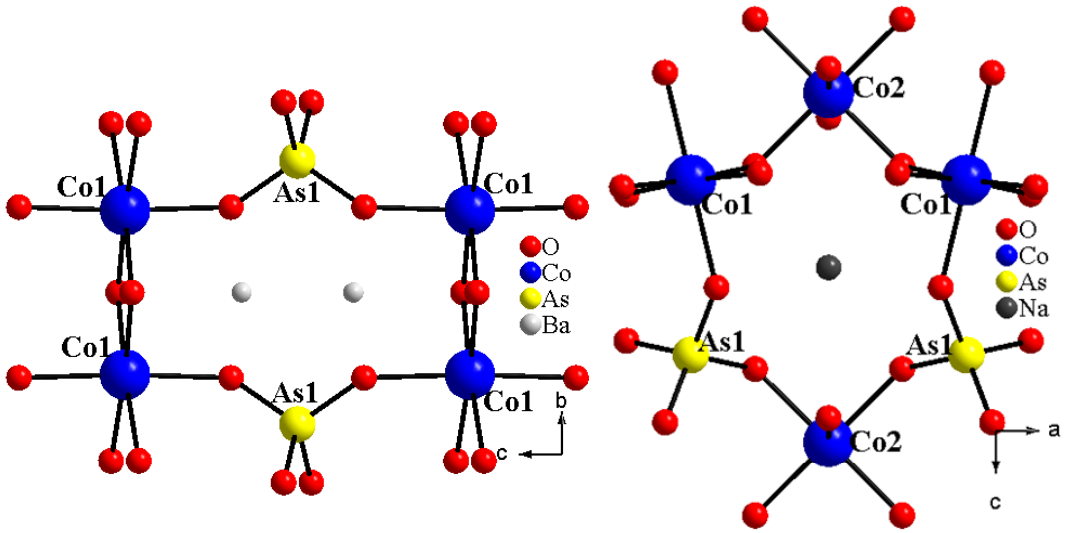

Figure 5.7: Close-up view of the 6-membered ring windows observed when viewing $Ba_2NaCo_3(AsO_4)_3$, **1**, structure type **I,** along the crystallographic *a* (left) and *b* (right) directions.

the observed 6-membered ring windows consist of two $Co(1)O_6$ polyhedra, two $Co(2)O_6$ polyhedra, and two $As(1)O_4$ polyhedra, Figure 5.7 (right).

$Na_{16}Co_{6.25}O_{0.25}(AsO_4)_4(As_2O_7)_4$, **3,** forms a different structure type, referred to as type **II**, and crystallizes in a monoclinic crystal system in the space group $P2_1/c$. A projected view of this compound is shown in Figure 5.8. When looking along the crystallographic *c* direction, a layered-type structure is revealed. Relative to **1,** **c**ompound **3** has a reduction in the dimensionality of the Co-O-As lattice, which is now 2-D. In fact, when comparing Figure 5.8 to 5.2, this difference becomes immediately evident as the 2-D Co-O-As slabs, $[Co_{3.125}O_{0.125}(AsO_4)_2(As_2O_7)_2]^{4-}$, are clearly isolated from one another in **3** *via* interslab Na^+ cations. It is noted that, due to fused neighboring $[Co_3O_{12}]_\infty$ sheets, the 3-D Co-O-As lattice in **1** contains channels. A single $[Co_{3.125}O_{0.125}(AsO_4)_2(As_2O_7)_2]^{4-}$ slab is shown approximately along the crystallographic *a* in Figure 5.9 (left). When comparing this to the projected view of **1** along the crystallographic *b* axis, the same 6-membered ring windows (highlighted in Figure 5.9) consisting of two $Co(1)O_6$ polyhedra, two $Co(2)O_6$ polyhedra, and two $As(1)O_4$ polyhedra, are observed in both structures.

Other similarities between **1** and **3** can be seen when taking a look within the 2-D slab. For instance, **3** also has two $Co(1,2)^{2+}$ cations that have the same connectivity and octahedral coordination environments as the Co(1) and Co(2) cations previously described in **1**. The local connectivity of the Co(1) and Co(2) cations in **1** and **3** can be compared in Figure 5.3 and Figure 5.9 (right), respectively. Compound **3** has $Co(1)O_6$ polyhedra that share two corner oxygen atoms with $Co(2)O_6$ polyhedra *via* O(7,8) atoms.

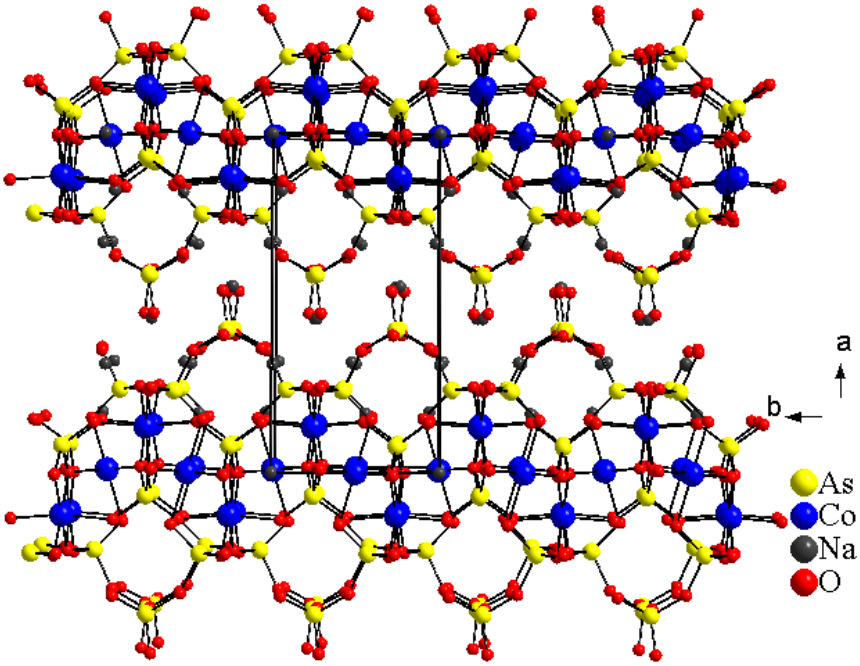

Figure 5.8: Projected view of $Na_8Co_{6.25}O_{0.25}(AsO_4)_4(As_2O_7)_4$, **3**, structure type **II**, within the *ab* plane. Co-O-As layers are separated from one another by Na cations.

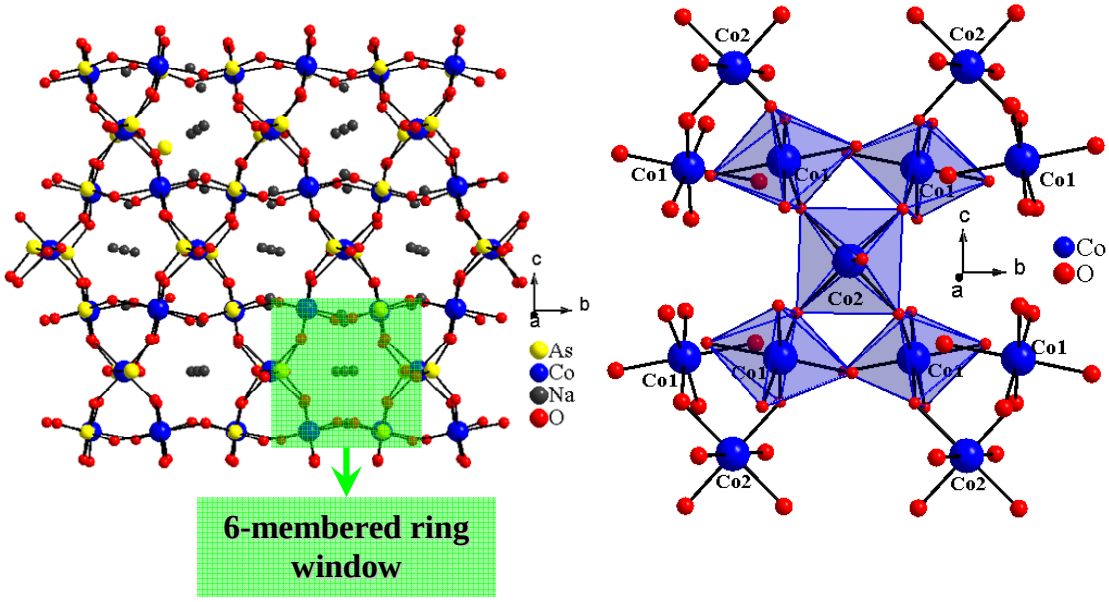

Figure 5.9: Projected view of the $Co_3(AsO_4)_4$ layer within the *bc* plane of $Na_8Co_{6.25}O_{0.25}(AsO_4)_4(As_2O_7)_4$, **3**, structure type **II** (left). The Co(1)O_6 polyhedra share two corner oxygen atoms with Co(2)O_6 polyhedra via O(7,8) atoms (right). Each Co(2)O_6 polyhedra shares 4 equatorial O(7,8) atoms with neighboring Co(1) polyhedra.

Each $Co(2)O_6$ polyhedron shares 4 equatorial O(7,8) atoms with four neighboring Co(1) polyhedra. Relative to **1**, the CoO_6 octahedra in **3,** which range from 2.07(4)-2.121(8)Å for Co(1)-O and from 2.061(8)-2.18(7) Å for Co(2)-O, are less symmetric. Although the distances are slightly different and the Co polyhedra are less symmetric, the average bond distances are very similar to those observed in **1**. Figure 5.10 shows a comparison between the 3-D Co-O lattice observed in **1** and the 2-D $[Co_3O_{12}]_\infty$ sheets observed in **3**. This figure reveals that the 3-D Co-O lattice for **1** can be broken down into $[Co_3O_{12}]_\infty$ sheets that are interconnected *via* edge-sharing $Co(1)O_6$ polyhedra. Compound **3** has the same $[Co_3O_{12}]_\infty$ sheets that are isolated from one another *via* Na cations and additional AsO_4 polyhedra, giving rise to the layered-type structure. The $[Co_3O_{12}]_\infty$ layers in **3** are stacked directly on top of one another making the $Co(1)O_6$ polyhedra, which are edge-shared in **1** (highlighted in green), to be shifted (depicted by green arrows) with respect to one another between the slabs. The $[Co_3O_{12}]_\infty$ slabs in **1** are stacked in an ABA type fashion along *b* (stacking direction), allowing the Co(1) polyhedra to line up and form an edge-sharing linkage (highlighted in green) and hence the 3-D Co-O structure.

There are multiple differences between **I** and **II** that need to be addressed. As a result of the layered nature of **II,** there are no intersecting channels as observed for compound **1**. There are several differences that also become immediately evident when comparing the chemical formulas of $Na_{16}Co_{6.25}O_{0.25}(AsO_4)_4(As_2O_7)_4$ and $BaNaCo_3(AsO_4)_3$. For example, compound **3** has pyroarsenate, As_2O_7, units in the chemical formula and a Co/As ratio < 1. The extra As oxyanion per $[Co_3O_{12}]_\infty$ slab is from the As(3)/As(4) sites which are partially occupied sites of approximately 93% and

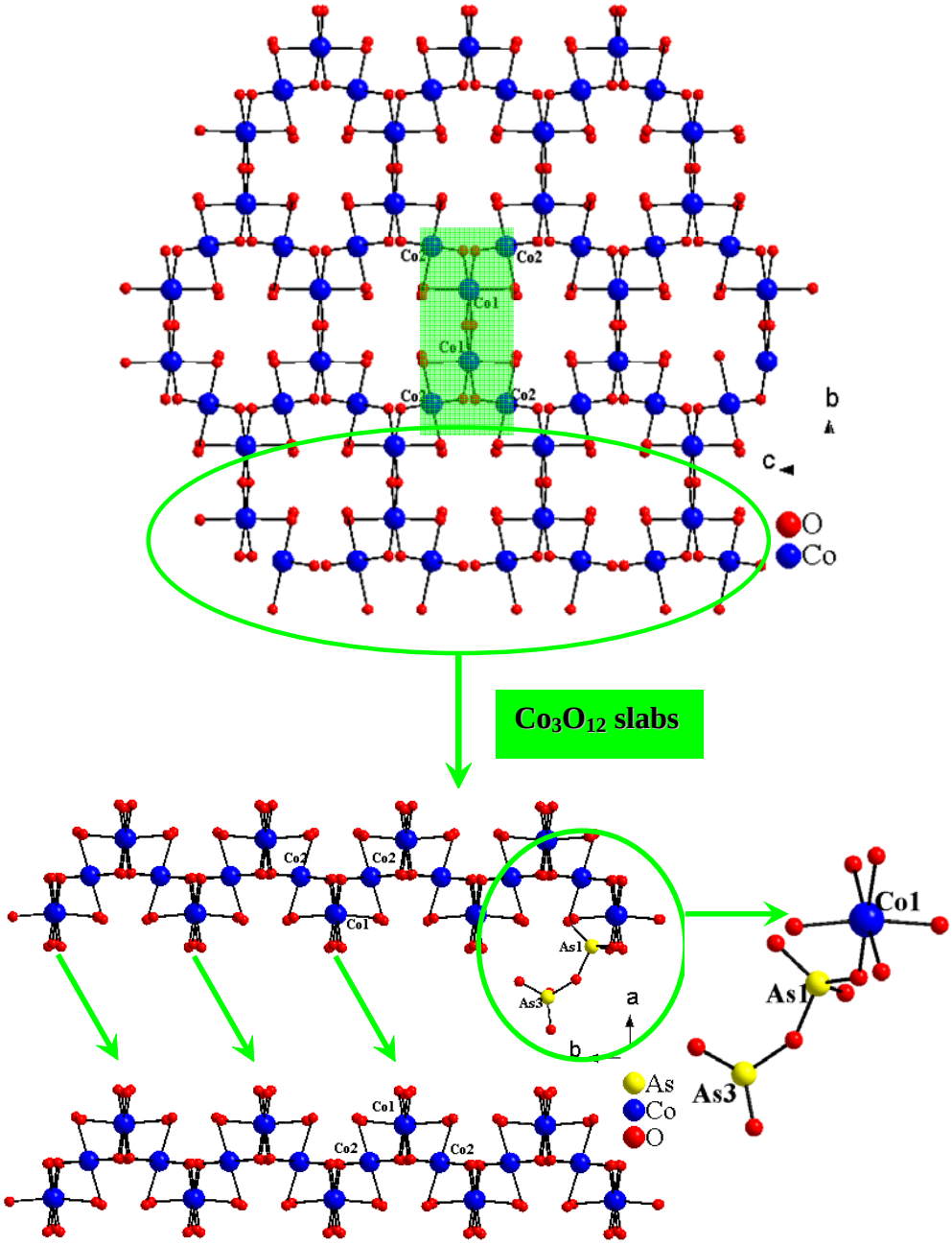

Figure 5.10: Ball-and-stick representation of the metal oxide lattices in structure types **I** (top) and **II** (bottom). The 3-D Co-O lattice observed in **1** can be broken down into Co_3O_{12} slabs that are interconnected *via* edge-sharing $Co(1)O_6$ polyhedra. Compound **3,** structure type **II,** has the same Co_3O_{12} slabs that are isolated from one another *via* interslab Na cations and As(3) polyhedra, leading to the formation of a layered-type structure. The layers in **3** are stacked directly on top of one another. As a result, the $Co(1)O_6$ polyhedra, which are edge-shared in **1** (highlighted in green), are shifted with respect to one another between the slabs in **3**.

7% respectively. These two As cations are in a 5+ oxidation state. This is further supported by bond valence sum calculations[16] which rendered values of 5.13 and 4.84 for As(3) and As(4) respectively. The As(4) site was revealed during the structure refinement as a large q peak, approximately 4 electrons/Å^3, indicating a large amount of residual electron density. The peak was refined as As, and then SHELXTL[15] was used to refine the occupancies of the As(3,4) atoms as they are very close to one another, approximately 0.82(2)Å apart. These As(3,4) atoms share a corner with neighboring As(1) tetrahedra, and point into the space between Co_3O_{12} slabs. This connectivity is illustrated in Figure 5.10. It should also be noted that there is much disorder present in the crystal structure of **3**. The chemical formula exhibits some disorder found within the Co_3O_{12} slabs resulting in a Co composition of approximately 6.25 rather than the expected value of 6. This additional Co(3) site was identified during the structure refinement *via* a large q peak, approximately 6 electrons/Å^3, again indicating a significant amount of residual electron density. It was refined as a partially occupied Co(3) site as it is too close to the Na(4) and Na(5) cations. Co(3) is found in a slightly distorted tetrahedral coordination *via* surrounding oxygen that have distances of 1.89(3), 1.96(3), 1.97(3), and 2.10(3)Å, for Co(3)-O(1), Co(3)-O(4), Co(3)-O(9), and Co(3)-O(12), respectively. O(12) is a nonbridging oxygen, and as a result is only present when Co(3) is present. Co(3) is connected to two neighboring Co(2) polyhedra *via* corner-sharing O(3) and O(1) atoms. Along with the aforementioned partially occupied sites, the occupancy of Na(4-6) was also refined due to close distances with other ions found within the structure. The occupancies, refined using SHELXTL[15] , were determined to be

0.56, 0.38, and 0.12, for Na(4-6) respectively. As a result of the severe disorder found within the crystal structure, most of the disordered atoms, including Co(3), O(12), Na(4), Na(5) and Na(6) were refined isotropically. The source of the disorder is not known, however, the structure refinement of several crystals has shown similar problems. Due to a large amount of twinning within these plate-like crystals, the structure refinements were rather poor; therefore, the solution with the best structure refinement was chosen to be presented here.

The last structure type to be described is the type **III** structure observed for compounds $Sr_2Na_{0.66}Fe_{3.34}(PO_4)_4Cl_{0.8}$, **4**, $Sr_2NaFe_3(AsO_4)_4Cl$, **5**, $Ba_{1.88}Na_{0.75}Fe_3(AsO_4)_4Cl$, **6**. The compounds crystallize in an orthorhombic crystal system, in the space group *Cccm* (no. 66). Due to the similarities in their structures, unless otherwise stated, **5** will be described from this point forward. According to the empirical formula, compound **5** must have two Fe^{3+} cations and one Fe^{2+} cation. Bond valence sum calculations[16] were performed on these Fe cations and it was determined that the Fe(1) site, which has a multiplicity of eight, is mixed 50% Fe^{2+}/Fe^{3+}, while Fe(2), which has a multiplicity of four, is all Fe^{3+}. The bond valence sum calculations rendered values of 2.57 and 3.16 for Fe(1) and Fe(2) respectively. It should be noted that, due to salt inclusion, the type **III** structure contains the Cl^- anion, which resides between $[Fe_3O_{12}]_\infty$ sheets. (see the discussions below).

A projected view of the *ab* plane of **5,** shown in Figure 5.11, reveals that the material has Fe-O-As slabs. Relative to **I**, structure type **III** also reveals a reduction in the dimensionality of the M-O-As lattice, from the 3-D, as observed in **I**, to 2-D, as

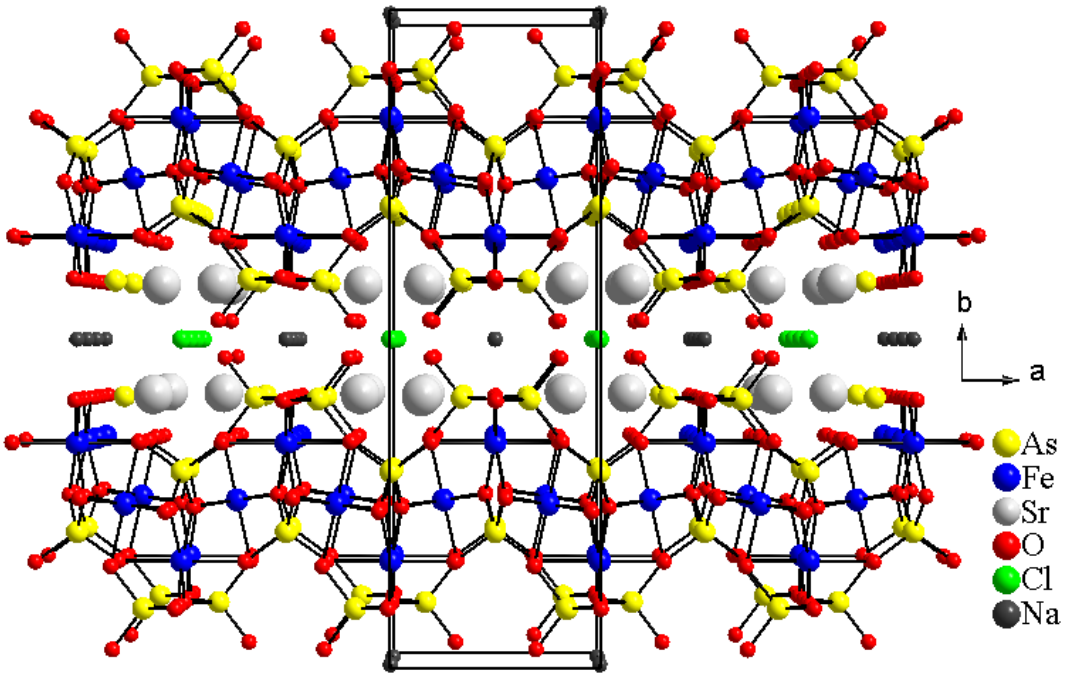

Figure 5.11: Projected view of $Sr_2NaFe_3(AsO_4)_4Cl$, **5**, structure type **III**, within the *ab* plane. Fe-O-As layers are separated from one another by Sr, Na, and Cl ions.

observed in both **II** and **III**. In fact, when comparing Figure 5.11 to 5.2, this difference becomes immediately evident as the 2-D Fe-O-As slabs, $[Fe_3(AsO_4)_4]^{4-}$, are clearly isolated from one another in **5** *via* interslab Sr, Na, and Cl ions. A projected view of a single $[Fe_3(AsO_4)_4]^{4-}$ slab is shown in Figure 5.12 (left). As observed for **I** and **II, III** also has the same 6-membered ring windows consisting of two $Fe(1)O_6$ polyhedra, two $Fe(2)O_6$ polyhedra, and two $As(2)O_4$ polyhedra. As discussed when comparing structure types **I** and **II**, **III** also has similarities to these structures when looking within the 2-D slab. For instance, **5** also has 2 $Fe(1,2)^{2+/3+}$ cations that have the same connectivity and octahedral coordination environments as the $Co(1)^{2+}$ and $Co(2)^{2+}$ cations previously described in **1** and **3**. Compound **5** has $Fe(1)O_6$ polyhedra that share two corner oxygen atoms with $Fe(2)O_6$ polyhedra *via* O(4) atoms, while each $Fe(2)O_6$ polyhedron shares 4 equatorial O(4) atoms with neighboring Fe(1) polyhedra. The local connectivity of the Fe(1) and Fe(2) cations in **5** is shown in Figure 5.12 (right). The Fe(1) octahedra consist of two Fe(1)-O(1) 1.971(6), two Fe(1)-O(4) 2.098(6), and two Fe(1)-O(5) 2.092(6), equal to 1.971(6), 2.098(6), and 2.092(6)Å respectively, and the Fe(2) octahedra consist of two Fe(2)-O(3) and four Fe(2)-O(4) equal to 2.013(8) and 2.024(6)Å respectively. The similarities in the local connectivities can be seen when comparing Figures 5.3 (left), **1**, and 5.12 (right), **5**. Figure 5.13 shows a view of the 3-D Co-O lattice in (top left) $Ba_2NaCo_3(AsO_4)_3$, **1**, (structure type **I**) compared to the 2-D Co-O lattice in (middle left) $Na_{16}Co_{6.25}O_{0.25}(AsO_4)_4(As_2O_7)_4$, **3** (structure type **II)**, and the 2-D Fe-O lattice observed in (bottom left) $Sr_2NaFe_3(AsO_4)_4Cl$, **5** (structure type **III**). All structures have a common M_3O_{12} sheet. These sheets are interconnected in **1** *via* Co(1) edge-sharing polyhedra,

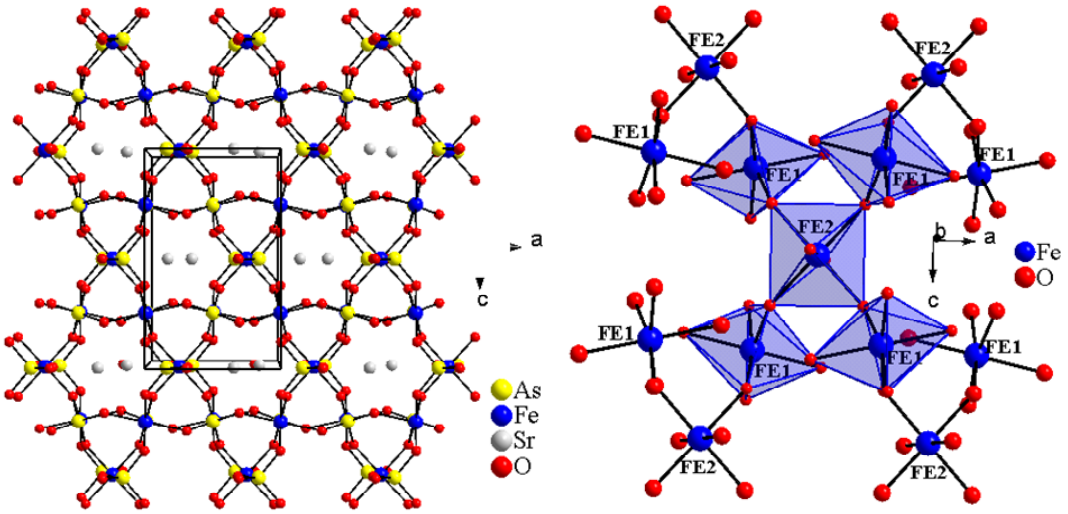

Figure 5.12: Projected view of the $[Fe_3(AsO_4)_4]^{4-}$ layer within the *ac* plane of $Sr_2NaFe_3(AsO_4)_4Cl$, **5**, structure type **III** (left)**.** As observed for **I** and **II, III** also has 6-membered ring windows. The $Fe(1)O_6$ polyhedra share two corner oxygen atoms with $Fe(2)O_6$ polyhedra *via* O(4) atoms (right). Each $Fe(2)O_6$ polyhedra shares 4 equatorial O(4) atoms with neighboring Fe(1) polyhedra.

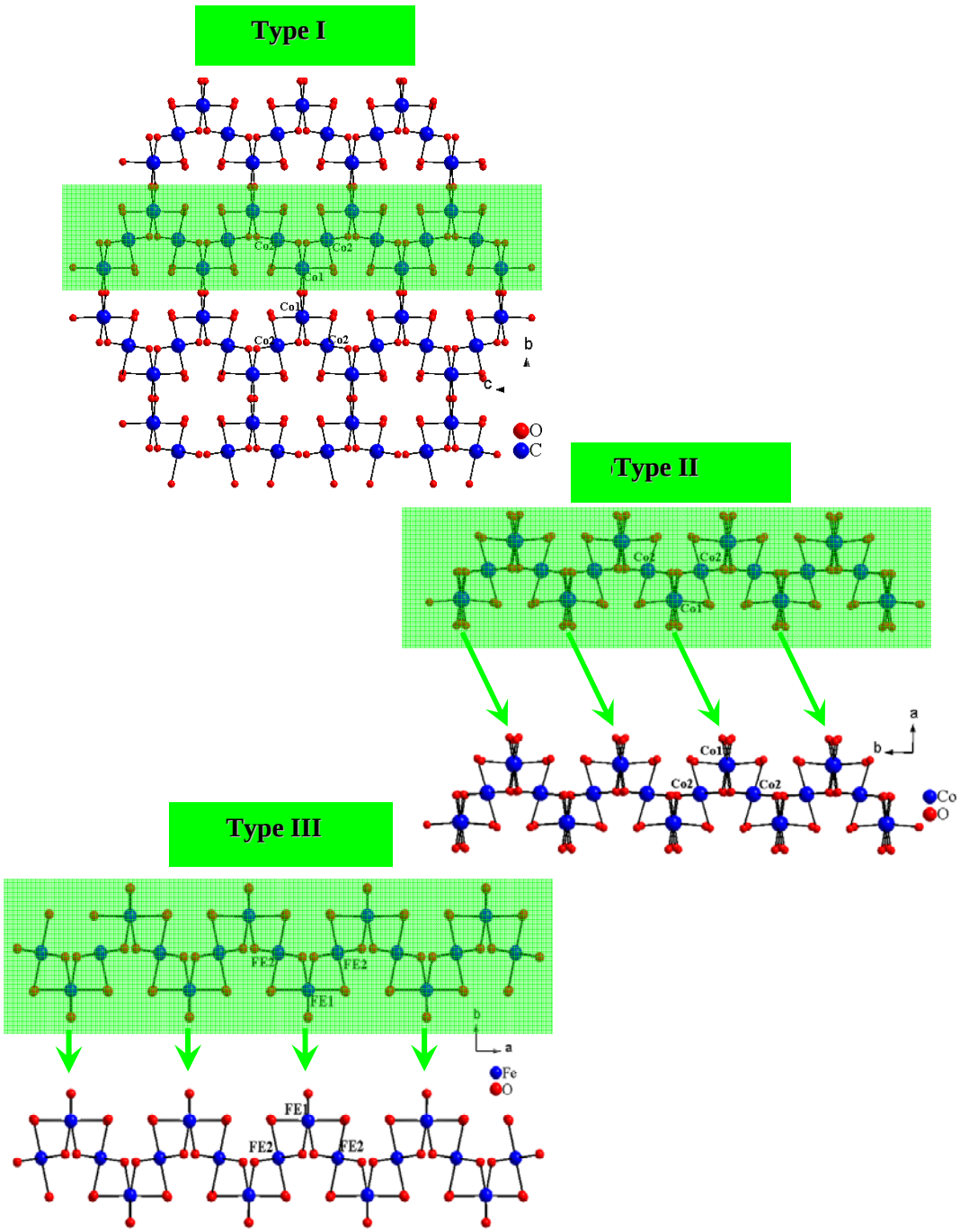

Figure 5.13: Ball-and-stick representation of the Co-O lattice in (top left) $Ba_2NaCo_3(AsO_4)_3$, **1**, (structure type **I**) compared to the Co-O lattice in (middle right) $Na_8Co_{6.25}O_{0.25}(AsO_4)_4(As_2O_7)_4$, **3**, (structure type **II)**, and the (bottom left) Fe-O lattice observed in $Sr_2NaFe_3(AsO_4)_4Cl$, **5** (structure type **III**). All structures have a common M_3O_{12} slab. These slabs are interconnected in **1** *via* Co(1) edge-sharing polyhedra. The M_3O_{12} slabs are stacked directly on top of one another in **II**, while they are stacked in an ABA fashion in **III**.

highlighted in green. In **3**, the $[Co_3O_{12}]_\infty$ slabs are stacked directly on top of one another, causing the $Co(1)O_6$ polyhedra to be staggered from one sheet to the next, while the $[Fe_3O_{12}]_\infty$ sheets in **5** are stacked in an ABA fashion, allowing the $Fe(1)O_6$ polyhedra to line up between neighboring planes.

Even though there are clearly multiple observed similarities when comparing structure type **III** with **I** and **II,** there are also many differences. For example, looking at the chemical formulas of **1,** $Ba_2NaCo_3(AsO_4)_3$, and **5**, $Sr_2NaFe_3(AsO_4)_4Cl$, one immediately notices that the M/As ratio is smaller in compound **5.** The reason for this is seen when looking at As(2), which bridges the Co(2) polyhedra between neighboring Co_3O_{12} layers in **1**. Since the Fe_3O_{12} slabs in **5** are separated, the number of these As atoms that no longer serve to bridge the layers, is doubled; therefore, the multiplicity of the As atoms increases from four in **1** to eight in **5,** refer to Figure 5.14. All three compounds showing structure type **III** have salt incorporation between the $[M_3O_{12}]\infty$ sheets, whereas those reported having structure type **I** and **II** do not. Looking at Table 5.1, it can be concluded that salt-inclusion is not a requirement for the formation of **III,** as multiple materials have been previously reported having the same structure with no salt-inclusion. In the previously reported materials, the $[M_3O_{12}]_\infty$ slabs are separated soley by A-site cations.

There are some structural issues that need to be addressed for the other two derivatives having structure type **III**, $Sr_2Na_{0.66}Fe_{3.34}(PO_4)_4Cl_{0.8}$, **4,** and $Ba_{1.88}Na_{0.75}Fe_3(AsO_4)_4Cl$, **6.** First looking at **6**, there are some partial occupancies for Ba, Na, and Cl. SHELXTL[15] was utilized to refine the occupancies due to large thermal

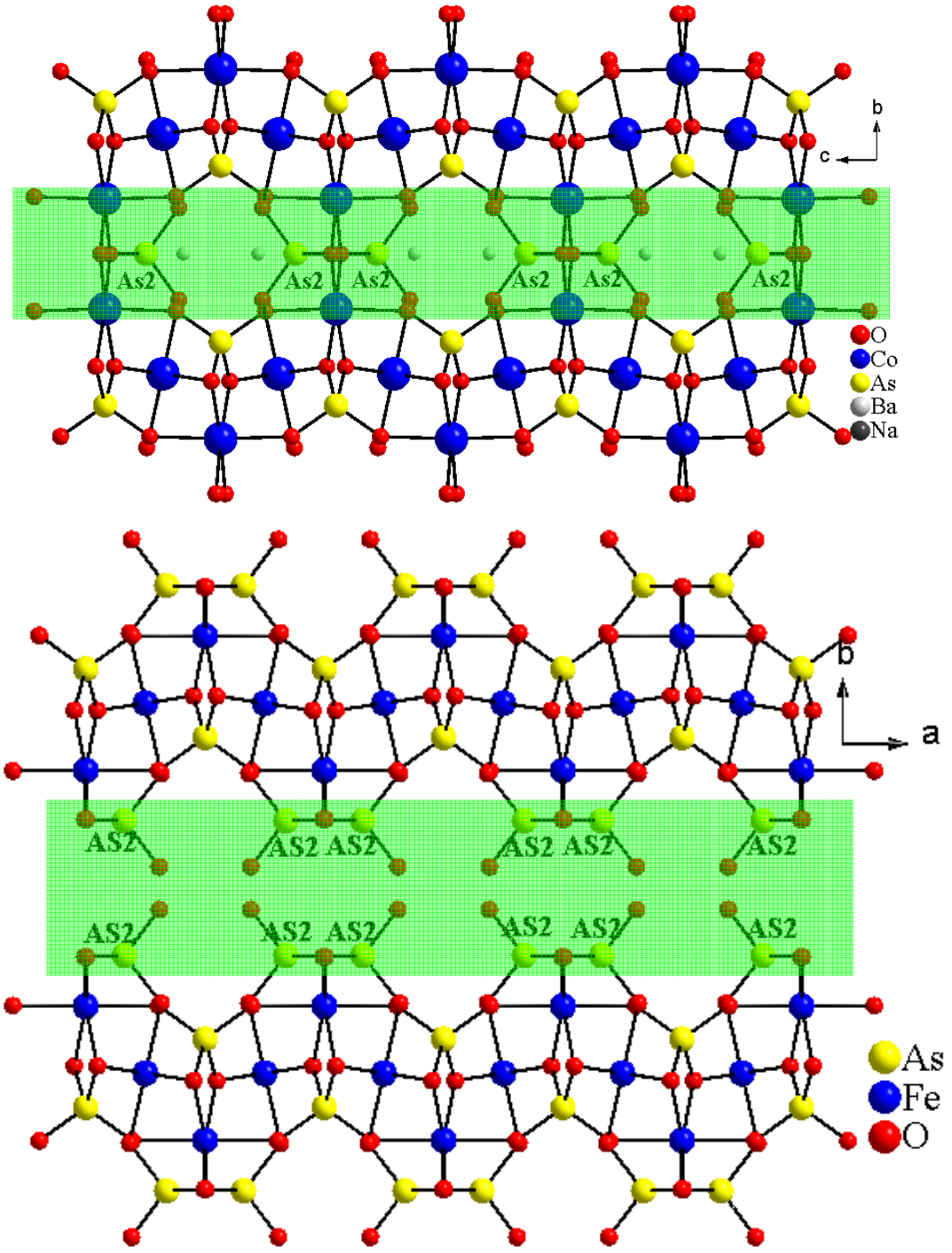

Figure 5.14: Ball-and-stick representation illustrating the bridging As(2) cations observed in **1**, $Ba_2NaCo_3(AsO_4)_3$, vs. the nonbridging As(2) cations found in **5**, $Sr_2NaFe_3(AsO_4)_4Cl$. The multiplicity of the As(2) site is increased from 4 to 8 due to the nonlavered structure formation in **5**.

parameters, and the Cl anion is refined at 50% because it is too close to itself. First looking at the chemical formula of **4,** there is a slightly larger Fe/P ratio compared to the Fe/As ratio observed in **5** and **6**. In fact, **4** has an octahedral site, shown between the $Fe_3(PO_4)_4$ layers in Figure 5.15, that was refined as both Fe(3) and Na. The site occupancies were refined by SHELXTL[15] to approximately 0.34/0.66 for Fe(3) and Na respectively. There were several reasons why the site was refined with both atoms. First, when refined purely as Na, the thermal parameters reflected that this atom did not have enough electron density, indicating that a larger atom was required. The surrounding anions had distances that were too short to be Sr, so the site was refined with Fe. When refined purely as Fe, the thermal parameters indicated that this atom had too much electron density and bond valence sum calculations[16] performed using the distances of surrounding atoms, which are 2.283(9) Å and 2.579(9) Å for four Fe(3)-O(1) and two Fe(3)-Cl(1) respectively, showed a value of approximately 1.5, indicating that the site is a bit large for an Fe^{2+} cation. However, bond valence sum calculations[16] using the same distances with Na in the site gave a value of 2.0, indicating the site was too small for Na. During this time it was determined that the Cl(1) site must be partially occupied due to its close dstances to itself, approximately 1.40(1) Å apart, and the occupancy was refined to approximately 0.40. This occupancy is close to that of the refined occupancy of Fe, so it is thought that Cl for the most part is only present when Fe is present. This means that the Fe(3)-Cl(1) distances could be 2.579(9) Å, while disorder in the system can allow the Na(1)-Cl(1) distance to be 3.977(9) Å, allowing the bond valence sum calculations[15] for Na to come out to approximately 1. After taking all of these scenarios into account, it

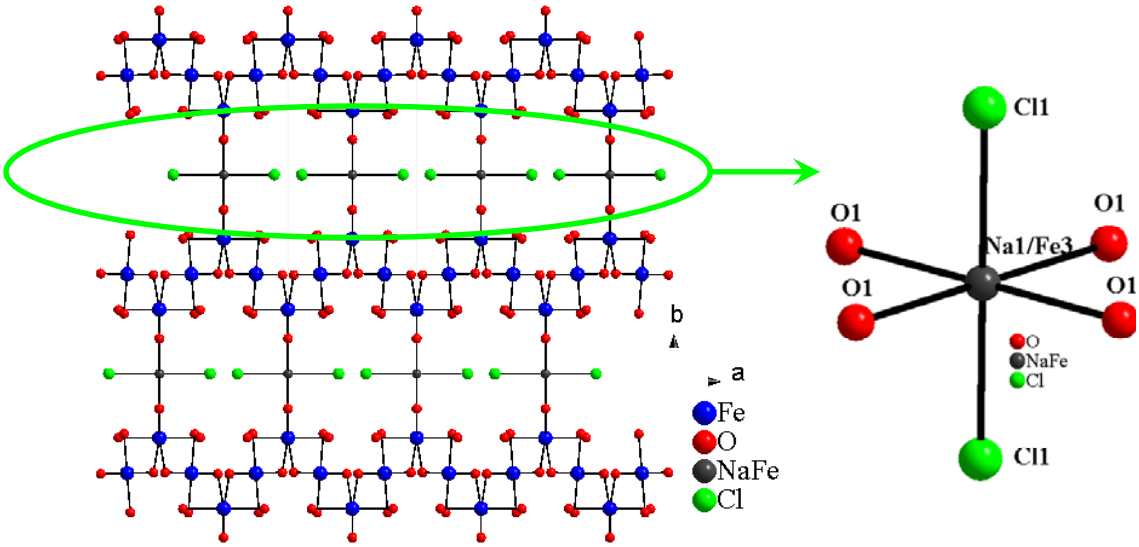

Figure 5.15: Ball-and-stick representation showing the Fe-O lattice in $Sr_2Na_{0.66}Fe_{3.34}(PO_4)_4Cl_{0.8}$, **4**, (structure type **III**). The observed layers are partially linked by $Fe(3)O_4Cl_2$ polyhedra. The site was partially occupied with 34% Fe(3) and 66% Na(1).

was decided that the site is most likely mixed with both Fe and Na. This decision is also supported by the oddly-shaped thermal parameters of this mixed site. There are observed elongations along the crystallographic *a* axis for both the Fe(3)/Na(1) and Cl(1) atoms, further supporting the presence of a disorder.

The Na/Fe(3) site in **4** is also seen in **5** and **6;** however, the site is refined purely as Na in both of these structures. Figure 5.16 shows a comparison of the distances between these sites and the surrounding anions, O(1) and Cl(1). The sites observed in both **5** and **6** show significantly longer Na(1)-O(1) and Na(1)-Cl(1) distances than those observed in **4**. It is thought that the incorporation of the smaller intraslab P^{5+} atoms and small interslab Sr^{2+} cations leads to a smaller overall interslab distance. As a result, the the O(1) atoms are closer, creating a more accomodating environment for the transtion metal cation. The interslab distances are 3.58(1) Å, 3.895(1) Å, and 4.247(1) Å for compounds **4**-**6** respectively. It is thought that compound **4** is revealing a glimpse of the formation of another 3-D structure type. It is suspected that if a slightly larger reduction in the interslab distances observed in **4** could be created through further chemical substitution, it is possible to obtain full transition metal substitution into the mixed Fe(3)/Na(1) site.

All of the title compounds contain M-O-M bridges. It is expected, due to the long M-M distances (greater than 3 Å), that the magnetic coupling will occur *via* super exchange through nonmagnetic (diamagnetic) oxide bridges. Temperature-dependent magnetic measurements were performed on ground single crystals of compounds **1**, **5,** and **6.** The masses were 4.6, 2.1, and 0.9mg for **1**, **5**, and **6** respectively, and the

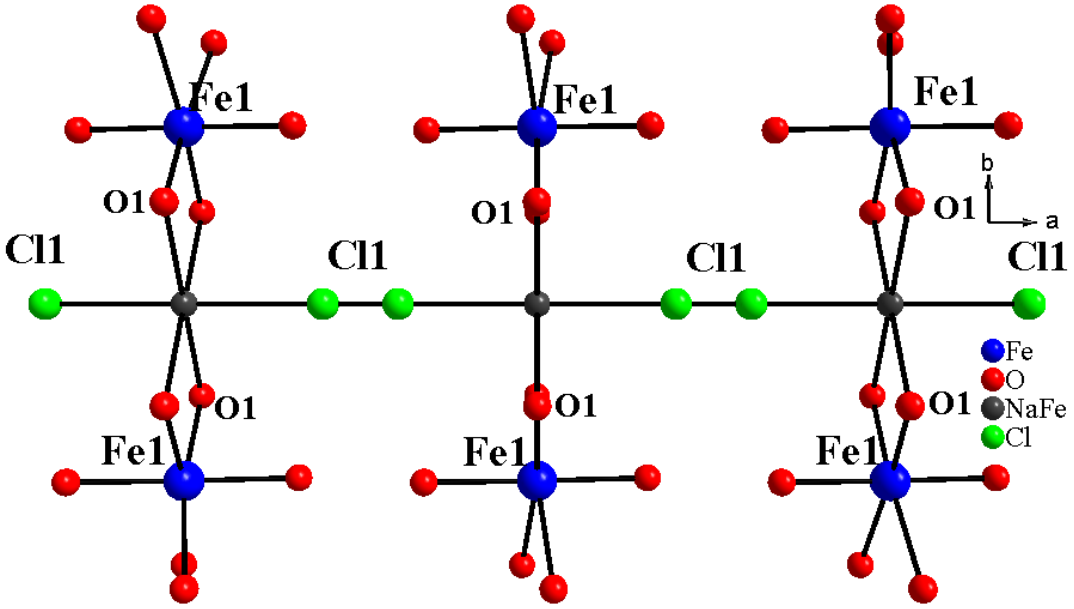

Compound 4	Compound 5	Compound 6
Na/Fe(3)-O(1) 2.283(9)	Na(1)-O(1)-2.385(1)	Na(1)-O(1)-2.385(1)
Na/Fe(3)-Cl(1) 2.579(9)	Na(1)-Cl(1)- 3.347(1)	Na(1)-Cl(1)- 2.887(1)
Na/Fe(3)-Cl(1)3.977(9)	O(1)-O(1) 3.895(1)	Na(1)-Cl(1)- 3.394(1)
O(1)-O(1) 3.58(1)		O(1)-O(1)-4.247(1)

Figure 5.16: Ball-and-stick representation showing the mixed Fe(3)/Na(1) site (observed in **4**) and the Cl(1) and O(1) ligands surrounding it. The bond distances for this same site in compounds **4-6** are compared (highlighted in green). Compound **4** has much closer Fe(3)/Na(1)-O distances, a direct result of smaller interslab distances, making it more accomodating for a transition metal. The Cl(1) site is partially occupied at 0.40 due to short inter Cl(1) distances.

measurements were performed in applied magnetic fields of 0.01 and 0.5 T. The molar magnetic susceptibility, χ, and inverse molar magnetic susceptibility, χ^{-1}, of **1** are shown in Figure 5.17. The susceptibility shows a steady increase up to approximately 12K followed by a sudden decrease, which is likely due to the appearance of long-range antiferromagnetic order. The inverse molar magnetic susceptibility shows a linear dependence at high temperatures. A Curie-Weiss fit to the linear portion of the curve, ranging from 100-300K, indicates an effective magnetic moment of (μ_{eff}) of 4.8(1)μ_B, which is slightly higher than the expected spin-only magnetic moment, 3.87μB, of a high-spin Co^{2+}, d^7, S=3/2. As found for other highly correlated high-spin Co^{2+} systems, it is expected that the orbital contributions of the ligand field play a significant role,[17] causing the difference in the measured and expected values of the effective magnetic moments. Taking the orbital contribution into account for a high-spin Co^{2+} (d^7) ion leads to a calculated magnetic moment of approximately 5.20μ_B. The temperature-independent parameter, χ_0, was determined to be 0.0014(1)μ_B, and a negative Weiss constant, θ, calculated to be -33(2) K, indicates antiferromagnetic exchange between nearest neighbors.

It was suspected, based on the long-range antiferromagnetic order observed in **1**, that the compounds containing mixed $Fe^{3+/2+}$ sites could lead to the development of a ferrimagnetic-type interaction due to a difference in the magnitude of the Fe^{2+} and Fe^{3+} magnetic moment. The reactions utilized in the synthesis of compounds **5** and **6** were the only two that produced a high enough yield of single crystals for magnetic characterization. Field cooling temperature-dependent molar magnetic susceptibility, χ,

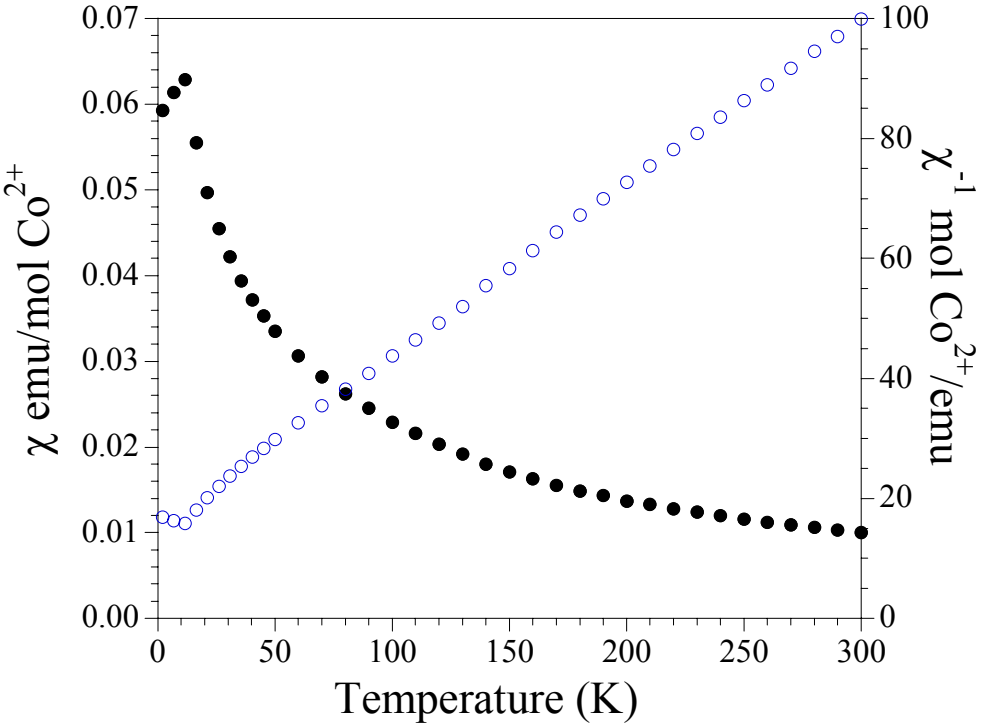

Figure 5.17: Molar magnetic susceptibility, χ (●), and the inverse molar magnetic susceptibility, χ^{-1} (○), of a ground powder of single crystals of $Ba_2NaCo_3(AsO_4)_4$, **1**, at 0.5T.

was collected for both materials in applied fields of 0.01 and 0.5T at temperatures ranging from 2-300K. The molar magnetic susceptibility, χ, and the inverse molar magnetic susceptibility, χ^{-1}, (at 0.5T) of compounds **5** and **6** are shown in Figures 5.18 and 5.19. Both susceptibility plots show a similar response. Upon decreasing temperature, the susceptibility gradually increases and then there is a sharp increase in χ at a T_c of approximately 25K for **5** and 50K for **6**. This sudden increase is likely the result of uncompensated antiferromagnetic exchange resulting from a difference in the magnitude of the magnetic moments of Fe^{3+} and Fe^{2+}. It should be noted that at 0.01T both materials show a decrease in the susceptibility at temperatures below T_c, likely indicating the development of interslab antiferromagnetic coupling; however, this additional antiferromagnetic component is suppressed at higher fields (0.5T). The χT plots of **4** and **5** are shown as the insets in Figures 5.18 and 5.19. It should also be noted that the ferrimagnetic transition in both materials is also suppressed at higher fields, indicating field dependence. The linear portion of the inverse molar magnetic susceptibility data of **5**, ranging from 170-300K, (at 0.5T) was fit using Curie-Weiss law. The fit rendered an effective magnetic moment, $\mu_{eff,}$ equal to $8.7(5)\mu_{B,}$ which is slightly lower than the expected spin-only magnetic moment for two Fe^{3+} and one Fe^{2+}, $9.69\mu_{B.}$ The temperature-independent term, $\chi_{0,}$ was found to be $0.0114(8)\ \mu_B$ and the θ was determined to be -126K, indicating antiferromagnetic coupling between nearest neighbors. It should be noted that no Curie-Weiss fit could be obtained from compound **6** as the high temperature data is not linear in nature. Higher temperature magnetic susceptibility data, collected up to 400K at 0.5T, showed curvature in the high

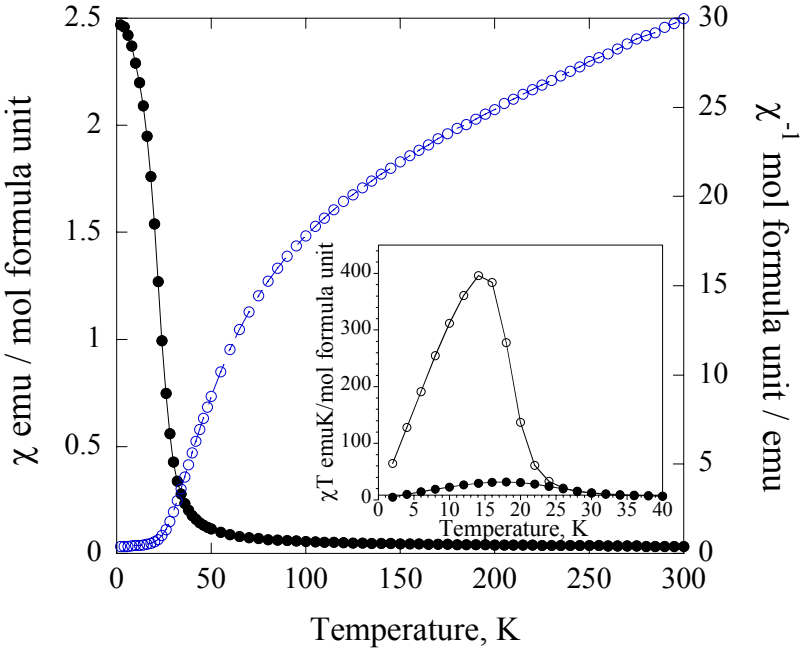

Figure 5.18: Molar magnetic susceptibility, χ (●), and the inverse molar magnetic susceptibility, χ^{-1} (○), of ground single crystals of $Sr_2NaFe_3(AsO_4)_4Cl$, **5** at 0.5T. The inset shows the χT at applied fields of (○) 0.01 and (●) 0.5T.

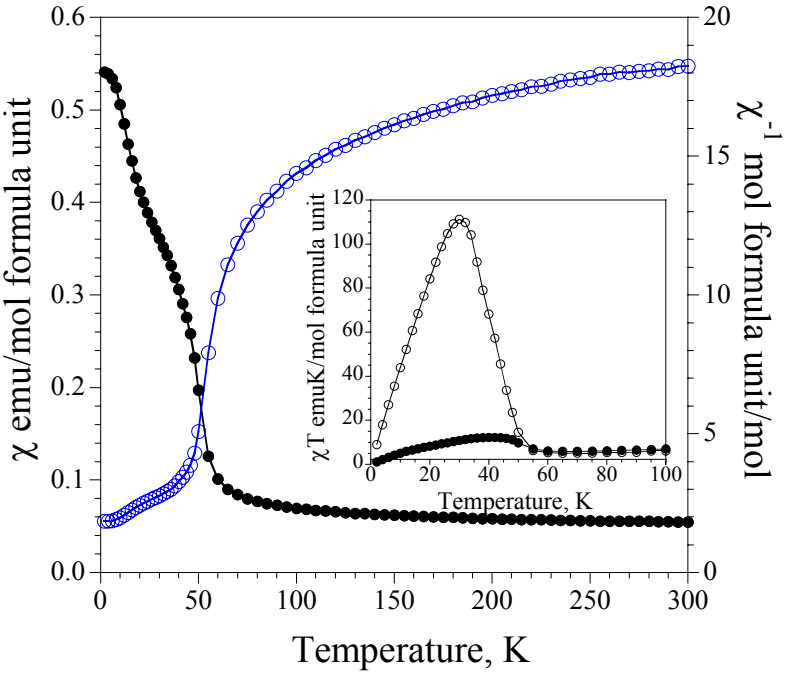

Figure 5.19: Molar magnetic susceptibility, χ (●), and the inverse molar, χ^{-1} (○), magnetic susceptibility of ground single crystals of $Ba_{1.88}Na_{0.75}Fe_3(AsO_4)_4Cl$, **6** at 0.01T. The inset shows the χT at applied fields of (○) 0.01 and (●) 0.5T.

temperature data, which also gave rise to unrealistic fitting parameters. It is likely that if higher temperatures could be achieved, a Curie-Weiss fit could be obtained.

Zero-field-cooled (ZFC) and field-cooled (FC) measurements of the magnetic moment were carried out on ground single crystals. Figures 5.20 and 5.21 show ZFC/FC plots at 0.01 and 0.5T with temperatures ranging from 2-30K for **5** and 2-60K for **6.** As observed for the materials presented in Chapter 3, these measurements show a divergence, which is often referred to as thermomagnetic irreversibility (TMI) and has been observed in many magnetically ordered systems[18]. This magnetic irreversibility is often visible at fields below the coercive field and is sometimes attributed to irreversibility in domain walls. The temperature at which the plots merge decreases as the applied field increases. In fact, at 0.5T the divergence can hardly be seen with the exception of a single point at approximately 2K for both **5** and **6**.

The field-dependent magnetization measurements confirm ferrimagnetic ordering of **5** and **6,** as hysteresis curves have been obtained on powders of ground single crystals for both derivatives. The isothermal magnetization curves for compounds **5** and **6** are shown in Figures 5.22 and 5.23 respectively. For **5**, the data were measured at temperatures below T_c, at 25, 12, and 5K. This plot reveals a very small coercive field at 5K, 0.015T, and negligible coercive fields at higher temperatures. Upon decreasing the temperature, the remnant magnetization observed for **5** increases due to the decrease in thermal energy, which allows less randomization of the magnetic moments. The hysteresis curves for **6** were collected also at temperatures below T_c, 5 and 40K. The coercive fields are approximately 0.0065T for the 40K data and 0.003T for the 5K data.

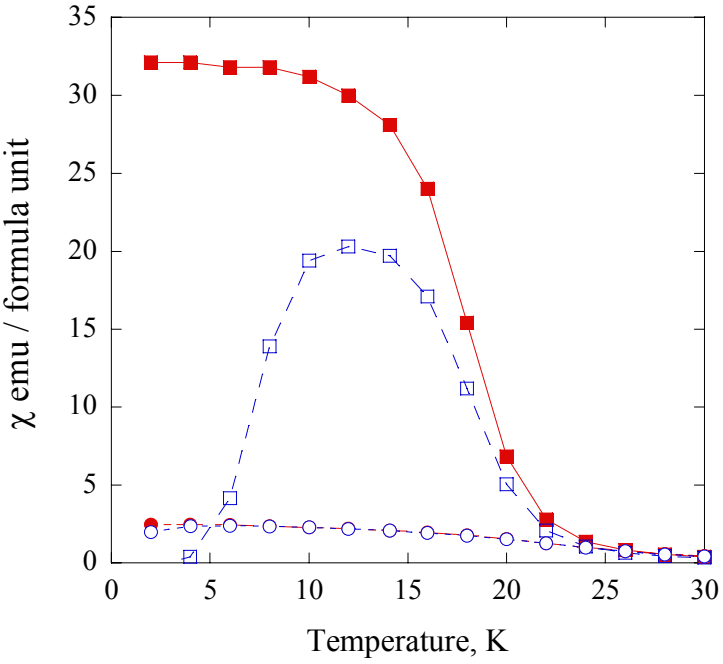

Figure 5.20: FC molar magnetic susceptibility, χ (red), and ZFC molar magnetic susceptibility (blue) of ground single crystals of $Sr_2NaFe_3(AsO_4)_4Cl$, **5**, at applied fields of 0.01T (squares) and 0.5T (circles).

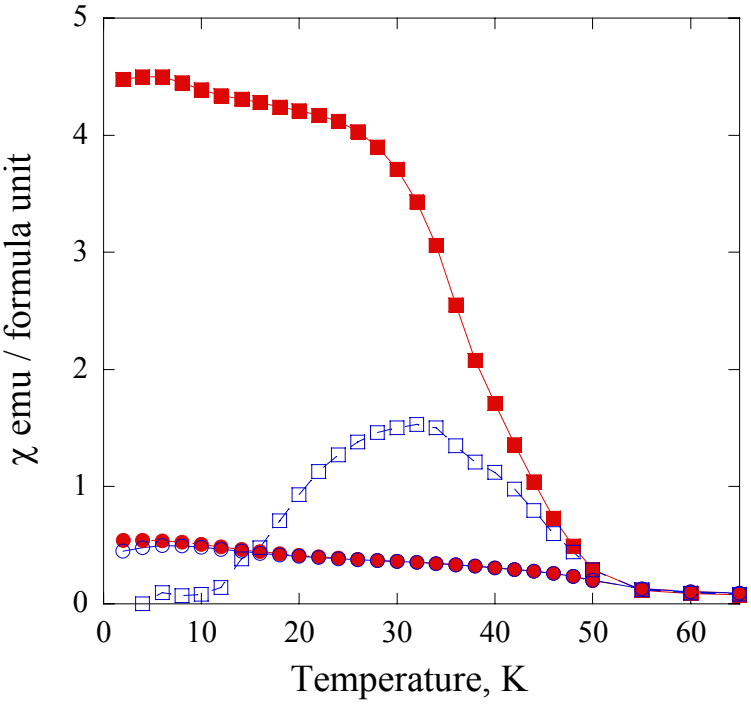

Figure 5.21: FC molar magnetic susceptibility, χ, (red) and ZFC molar magnetic susceptibility (blue) of ground single crystals of $Ba_{1.88}Na_{0.75}Fe_3(AsO_4)_4Cl$, **6**, at applied fields of 0.01T(squares) and 0.5T (circles).

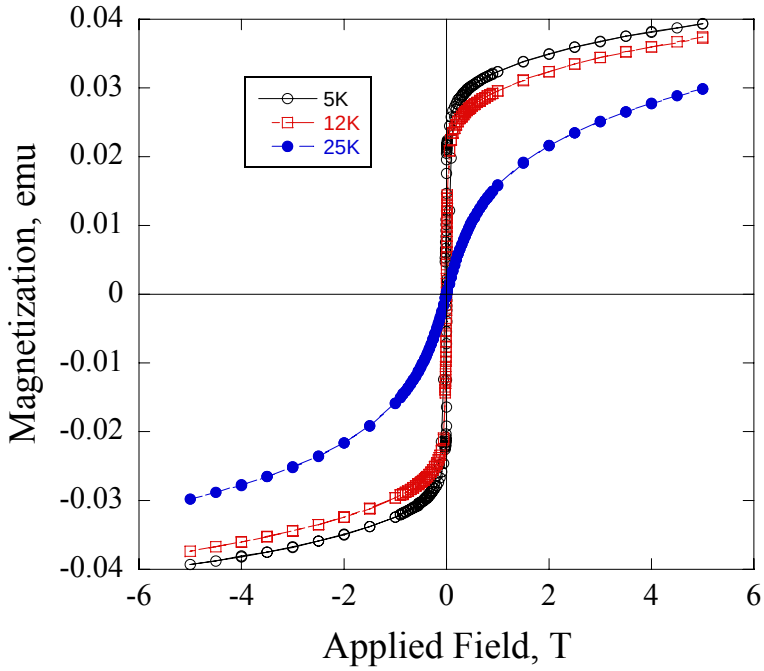

Figure 5.22: Isothermal magnetization data of a ground powder of single crystals of $Sr_2NaFe_3(AsO_4)_4Cl$, **5**, at 5, 12, and 25K.

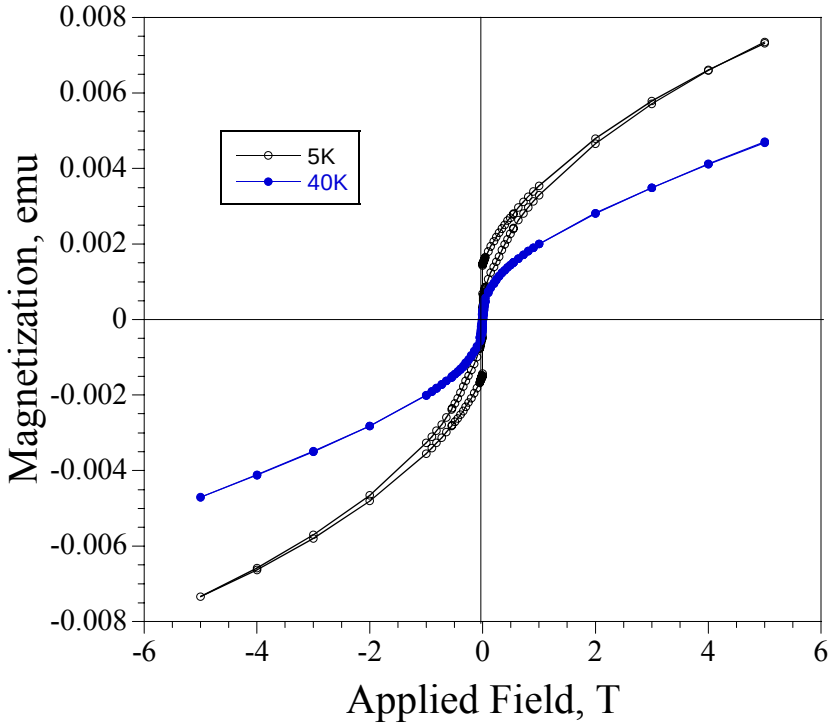

Figure 5.23: Isothermal magnetization data of a ground powder of single crystals of $Ba_{1.88}Na_{0.75}Fe_3(AsO_4)_4Cl$, **6**, collected at 5 and 40K. There may be an error in the 40K data, and it needs to be recollected. See text for details.

It is not known why the 5K data shows a lower coercive field, but it is suspected that the sample may have moved in the gelcap during the 40K collection, which is likely for samples less than 1 mg (0.9mg for this sample). For the 5K data collection, the sample was secured more tightly inside the gelcap to ensure no movement. As a result, the 40K data may need to be recollected to determine a true coercive field at that temperature. Upon decreasing the temperature from 40K to 5K, a higher remnant magnetization is observed in the field- dependent data. This is expected from the decrease in the thermal energy. It should be noted that compound **5** shows a larger remnant magnetization than **6** in their 5K data. It is thought that this is likely due to the fact that **5** has more Fe^{2+} cations, giving rise to less compensated Fe^{3+} magnetic moments and, hence, a higher magnetization. And although it is not known for sure, the larger coercive field in **5** could be due to more magnetic anisotropy. Orientation-dependent studies performed on single crystals could be utilized to help explore the reasons for the observed differences in the field-dependent studies of these two materials.

Conclusions

This chapter presents an extensive family of compounds containing mixed polyhedral frameworks. All of these materials, synthesized *via* high temperature molten-salt methods, are structurally related but form three different structure types. This interesting compound family offers a rare opportunity for in-depth structure / property correlation studies. The compounds characterized thus far, **1**, **5**, and **6**, have shown antiferromagnetic exchange between nearest neighbors. As a result of the difference in

the magnitude of the magnetic moment in Fe^{2+} and Fe^{3+}, compounds **5** and **6** show a net magnetic moment leading to a ferrimagnetic-type behavior, which has been proven through the presence of hysteresis. Orientation-dependent studies will be required to further explain differences in the observed hysteresis loops of the two derivatives.

It should also be noted that further development of this already extensive family could be of great interest for battery-related research. Much effort is currently focused on $LiFePO_4$, a compound that is expected to be the positive electrode material for next-generation Li^+ batteries. These expectations are the result of its low cost, low toxicity, and relatively high theoretical specific capacity of 170 mAh/g.[19] As a result of the interest in $LiFePO_4$, new iron phsosphate-containing structures are sought after for battery applications. It should be noted that, despite the presence of the intersecting channels observed in **I** and the layered-type structures of **II** and **III**, ion exchange properties of the materials presented here were not studied. This study is of future interest, especially for the iron phosphate-containing compound, **4**, as several materials having similar structures have shown easy ion exchange and reduction / insertion of Li^+ ions.[4,6] The synthesis of new mixed polyhedral frameworks like the ones presented here can offer two major advances in battery research. First, this research could lead to the synthesis of new frameworks that are competitive or even superior to those of $LiFePO_4$. Second, the development of versatile compound families, like the one presented here, could offer a prototype system allowing one to study how incremental changes in structure or composition can alter the electrochemical properties of the newly synthesized

materials. It is known that incremental type research can offer invaluable fundamental knowledge aiding in the development of next-generation battery materials.

Literature Cited

1. Hwu, S.-J. *Chem. Mater.*, **1998**, *10*, 2846-2859.

2. Bieniok, A., Brendel, U., Lottermoser, W., Amthauer G. *Z. Kristallogr*. **2008**, 223 186-194.

3. Cheetham, A.K., Férey, G., Loiseau, T. *Angew. Chem. Int. Ed.* **1999**, *38*, 3268-3292.

4. Korzenski, M.B., Kolis J.W., Long, G.J. *J. Solid State Chem*. **1999**, *147*, 390-398.

5. Kinomura,N., Matsui, N., Kumada,N., Muto, F., *J. Solid State Chem*. **1989**, *79*, 232-237.

6. Becht, G., Ph.D. Dissertation, Clemson University, Clemson, SC, **2008**.

7 (a) Glaum, R., Gruehn, R., Moller, M. *Z. Anorg. Al&. Gem*. **1986**, *543*, 111-116.

(b) Attfield, J.P., Battle, P.D., Cheetham, A.K., Johnson D.C. *Inorg. Chem.*, **1989**, 28 (7), 1207-1213.

8. Lajmi, B., Hidouri, M., Rxeigui, M., Amara, B.M. *Mater. Res. Bull*, **2002**, *37*, 2407-2416.

9. Ouerfelli, N., Zid, M.F., Jouini, T. *Acta Cryst.* **2005,** *E61*, i67–i69.

10. Kouass, S., Boughzala, H. *Phosphorus, Sulfur Silicon Relat. Elem*. **2006**, 181, 2641-2652.

11. Friaa, B.B., Boughzala, H., Jouini, T. *J. Solid State Chem*. **2003**, *173*, 273-279.

12. Bell, A. M. T., Henderson, C. M. B., Wendlandt, R. F., Harrison W. J. *Acta Cryst.* **2008**. *E64*, i63-i64.

13. Napijoalo, M., Kasalica, B., Sarvan, M. *Zbornik Matice Srpske Za Prirodne Nauke* **1993**, *85*, 281-285.

14. Queen, W.L., S.-J. Hwu, Unpublished data, **2008**.

15. (a) Sheldrick, G.M. In "Crystallographic Computing 3" (Sheldrick, G. M.; Kruger, C.; Goddard, R.; Eds), Oxford Univ. Press: London, **1985**, 175-189.

(b) Sheldrick, G. M. In "SHELXTL, Version 6.1 Structure Determination Software Programs" Bruker Analytical X-ray Systems Inc., Madison, WI, **2001**.

16. (a) *VALENCE* for DOS, Version 2.0, Brown, I. D. *J. Appl. Crystallogr.* **1996**, *29*, 479-480.

(b) Brown, I. D. and Altermatt, D. *Acta Cryst.* **1985**, *B41*, 244-247.

17. Mabbs, F. E., Machin, D. J. *Magnetism and Transition Metal Complexes*, Halsted Press, New York, **1973**.

18. (a) Roy, S.B., Pradhan, A.K., Chaddah, P., *J. Phys.: Condens. Matter* **1994**, *6*, 5155-5160.

(b) Roy, S.B., Pradhan, A.K., Chaddah, P. *Phil. Mag.* **1995**, *71*, 97-104.

(c) Roy, S.B., Pradhan, A.K., Chaddah, P. *Physica B* **1996**, *223–224*, 198-200.

(d) Roy, S.B., Pradhan, A.K., Chaddah, P. *Phil. Mag.* **1997**, *75*, 303-310.

(e) Roy, S.B., Pradhan, A.K., Chaddah, P. *J. Alloys Compounds* **2001**, *326*, 112-11621.

(f) Roy, S.B., Pradhan, A.K., Chaddah, P., *J. Phys.: Condens. Matter* **1994**, *6*, 5155-5160.

19. (a) Padhi, A. K.; Nanjundaswamy, K. S.; Goodenough, J. B. *J. Electrochem. Soc.* **1997**, *144*, 1188-1194.

(b) Ravet, N., Chouinard, Y., Magnan, J. F., Besner, S., Gauthier, M., Armand, M. *J. Power Sources* **2001**, *97-98*, 503-507

CHAPTER SIX

SYNTHESIS AND CHARACTERIZATION OF NOVEL SALT-INCLUSION VANADATES, $(CsCl)M(VO_3)_2$ where M = Mn, Co, Ni, Cu, Zn

Introduction

Hybrid solids exhibiting integrated frameworks of chemically dissimilar components have drawn much interest in advanced materials synthesis due to their structural versatility and multifunctional properties. Metal-organic frameworks (MOFs), for instance, have been extensively explored for their potential applications in technologically important fields including heterogeneous catalysis, gas storage, and sensors.[1-3] These solids are molecule-based composite materials made of metal ions or metal ion clusters serving as nodes and organic ligands serving as linkers. Special-framework MOFs, including noncentrosymmetric (NCS) solids, can be constructed by design due to the modular nature of their structures. Salt-inclusion solids (SISs), a newly emerging class of hybrid compounds, are reported to exhibit covalent metal oxide frameworks integrated with ionic lattices including alkali/alkaline-earth metal halides and others such as ammonium halides.[4-7] These all-inorganic SISs possess fascinating structural chemistry complementary to MOFs where bonding at the interface of the dissimilar components appears to be directional. This property has been revealed through the formation of salt-templated porous frameworks[6] and NCS lattices.[7] In general, the SISs are synthesized in reactive molten-salt media at 100~150^{o}C above the melting point of the employed salt. In the absence of a reaction mechanism, one can imagine that the metal oxides are first "dissolved" in the corrosive molten salt, and then, upon cooling, the

covalent lattice aggregates around the inherent structure of the molten ionic salt.[8] This results in the formation of special frameworks. Employing this concept, research in the area of salt-inclusion chemistry has been extended into the vanadate system. This is the first of three chapters reporting new vanadium(V)-based salt inclusion solids. The compounds reported here depict the rich structural chemistry inherent in this newly explored system.

Chapter six is focused on the synthesis and characterization of a new series of mixed metal oxide salt-inclusion solids. Prior to this study, the effort of salt-inclusion synthesis had been mostly focused on creating mixed-framework solids based on transition metal (TM) phosphates, arsenates, and silicates.[4-7] Substituting the $(XO_4)^{3-}$ oxyanions (X = P, As) in the previously studied systems with the fully oxidized $(VO_4)^{3-}$ anion has allowed rich new structural chemistry to be unveiled. Mixing vanadium with a second TM is particularly attractive, for they have potential applications in areas related to catalysis, batteries, and magnetism. This is in part due to the variable crystal chemistry of the added transition metals as well as to the utility of the unique frameworks created by the salt. Structurally, like their silicate counterpart, fully oxidized vanadium(V) compounds could achieve more diversity due to their ability to form vanadate units of varying size, shape, and geometry such as dimers, trimers, chains, and rings. Unlike Si, P, and As, however, V can adopt several different coordination environments allowing even more structural versatility. Furthermore, we have chosen to systematically investigate the synthesis in vanadium(V)-based systems because several V^{5+}-containing mixed-metal oxide catalysts have been reported in energy-related studies to show

photocatalytic systems capable of splitting water into H_2 and O_2.[9] The focus of Chapter six is on a new series of salt-inclusion vanadates, synthesized using conventional solid state methods. The series includes 6 new compounds that demonstrate two different structure types, denoted as **I** and **II**. The general formula for this series can be written as $(CsCl)M(VO_3)_2$ (M = Mn (**1**), Co(**2**), Ni (**3**), Cu (**4**), for type **I**, and Co(**5**) Zn (**6**) for type **II**. Only Co has been found to adopt both structure types. Single crystals of each phase were grown in molten salt media. These compounds exhibit the structural versatility inherent in this newly explored mixed metal oxide SIS system. These new materials will be discussed in light of their structures and magnetic properties.

Synthesis

Single Crystal Synthesis of 1-6: All reactants used in the following reactions were ground in a nitrogen purged dry box, placed in silica ampoules, and then sealed under vacuum before heating.

Compounds **1**, **3**, **4**, and **6** were synthesized employing a stoichiometric amount of MO (M = Mn, Fe, Ni, Cu, Zn), V_2O_5, and CsCl in a 1:1:1 mol ratio (total mass of ca. 0.5g). The reactions were heated to 800°C, isothermed for 4 days, slowly cooled to 450°C, and then furnace cooled to room temperature. Dark red columns of compounds **1, 3,** and **4,** and dark purple plates of **6** were isolated. It should be noted that the aforementioned reactions are stoichiometric, as they were specifically targeting the $(CsCl)M(VO_3)_2$ derivatives; however, 100% yield is not acquired when the synthesis is carried out at high temperatures (> 650°C), required to obtain single crystal growth. The

reactions for **1** led to a very high yield of single crystals (≈90%) and a small yield (< 10%) of an unidentified yellow polycrystalline material. The reaction for compound **3** led to a small yield of the title phase (< 5%), orange column-like crystals of $CsNiCl_3$[10] (≈20%), orange cube-like crystals of $Ni_3V_2O_8$[11] (≈40%), and black plate-like crystals of $(Cs_2Cl)VO(VO_3)_4$[12] (35%), see appendix. The single crystal reaction of **4** led to the formation of a very small yield of the title compound (< 5%), lime green plate-like single crystals of $(CsCl)_2Cu(VO_3)_2$[13] (≈ 30%), yellow single crystals of CsV_3O_8[14] (≈30%), and unidentified colorless and yellow polycrystalline materials (≈35%). The single crystal reaction targeting **6** led to the formation of a good yield of the title compound (≈40%), orange single crystals of CsV_3O_8[14] (≈30%), and unidentified colorless and yellow polycrystalline material (≈30%). It should be noted that much effort was put forth to synthesize the Fe containing derivative in hopes of completing the series across the later half of the first-row transition metals. Various reactions and reaction conditions were used to try to get the phase to form, however, every attempt failed. For the above reaction and every other reaction attempted to form the Fe derivative, the major phase formation was black plate-like single crystals of $Cs_5(FeCl_6)VO(VO_3)_4$[12].

For the synthesis of **2,** CoO, V_2O_5, and CsCl were mixed in a 1:1:2 mol ratio. The reaction was heated to 650°C, held there for 4 days, slowly cooled to 450°C, and then furnace cooled to room temperature. The reaction was targeting $(CsCl)_2Co(VO_3)_2$, but instead formed a high yield of dark red single crystals of the title phase, **2** (≈ 80%), blue single crystals of Cs_2CoCl_4[15] (< 10%), and unidentified blue and black polycrystalline materials. Evidence of the originally targeted phase, $(CsCl)_2Co(VO_3)_2$, was never found.

Single crystals of **5**, $(CsCl)Co(VO_3)_2$ (type **II**), were found in a mixture of CoO, Ir, IrO_2, V_2O_5, and CsCl in 0.8:0.1:0.1:1:1 ratio (ca. 0.5 g). The mixtures were heated to 800°C, isothermed for 4 days, slowly cooled to 450°C, and then furnace cooled to room temperature. Blue plate-like crystals of **5** were obtained. The goal of this reaction was to dope a heavier low-spin transition metal, such as Ir^{2+}, d^7, S=1/2, into the chain. Elemental analysis confirmed that no Iridium was present in the title compound. Blue plate-like crystals of compound **5** were isolated along with unidentified black and colorless polycrystalline materials. It should be noted that compound **5** was never synthesized without the presence of Ir/IrO2. In all other reactions targeting the **5**, compound **2** formed instead.

High Yield Synthesis of 1-4 and 6: The $(CsCl)M(VO_3)_2$ phases were synthesized employing a stoichiometric amount of MO (M = Mn, Co, Ni, Cu), V_2O_5, and CsCl in a total mass of ca. 0.5g. The reactants were heated to 600°C, isothermed for 24 hours, and then furnace cooled to room temperature. A high yield synthesis of **5**, $(CsCl)Co(VO_3)_2$ (**II**), was never accomplished. Every attempt to make a 100% yield of **5** led to a high yield synthesis of **2,** presumably indicating that the latter is the preferred high-temperature phase. The powder X-ray diffraction patterns of the products from high yield synthesis of **1**-**4** and **6**, shown in Figures 6.1-6.5, are compared to the calculated powder patterns obtained from the single crystal structure solution of each phase. In each 100% yield reaction there are a few extra peaks. The identities of these minor impurity phases are not known, but the most significant impurity peaks are marked with asterisks.

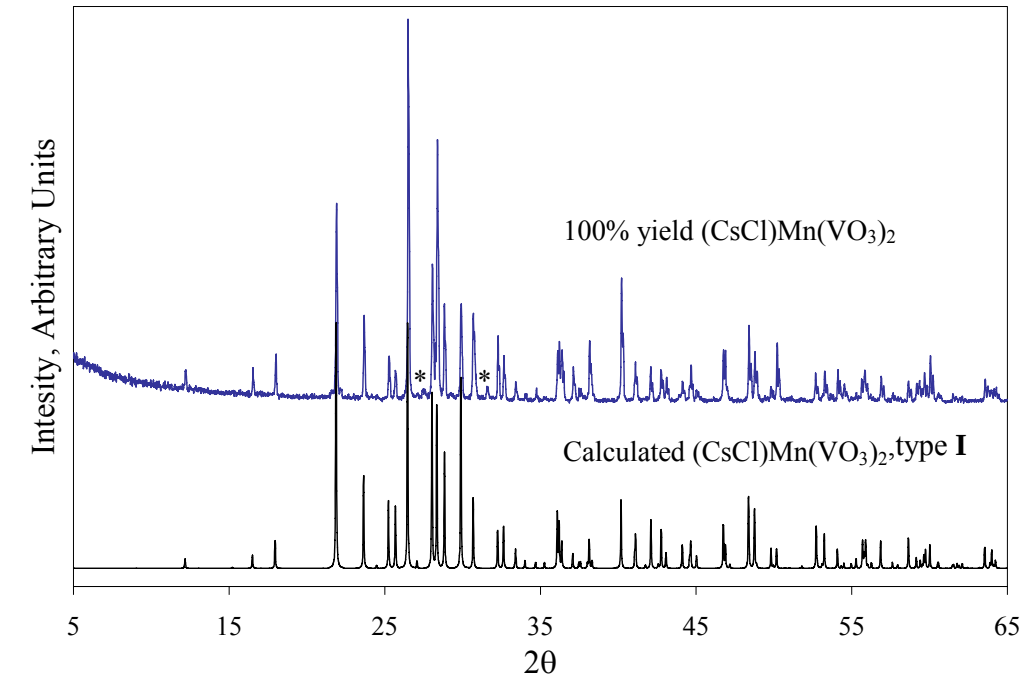

Figure 6.1: Calculated powder pattern of $(CsCl)Mn(VO_3)_2$ (**1**) compared to the 100% yield synthesis. Impurity peaks are marked with asterisks.

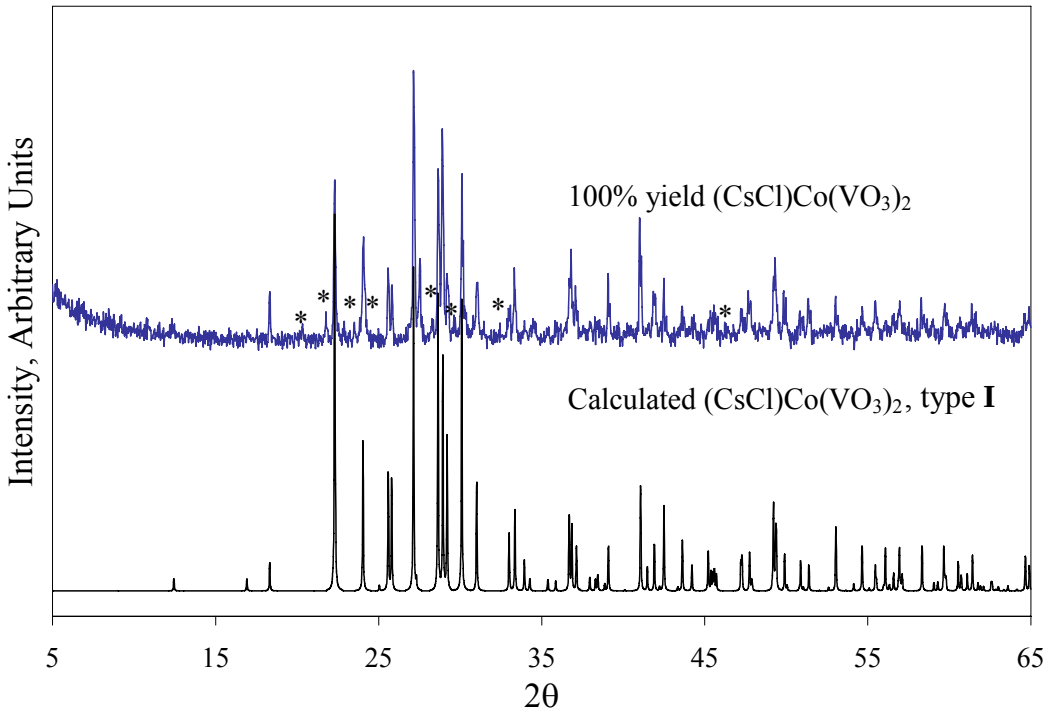

Figure 6.2: Calculated powder pattern of $(CsCl)Co(VO_3)_2$ (**2**) compared to the 100% yield synthesis. Impurity peaks are marked with asterisks.

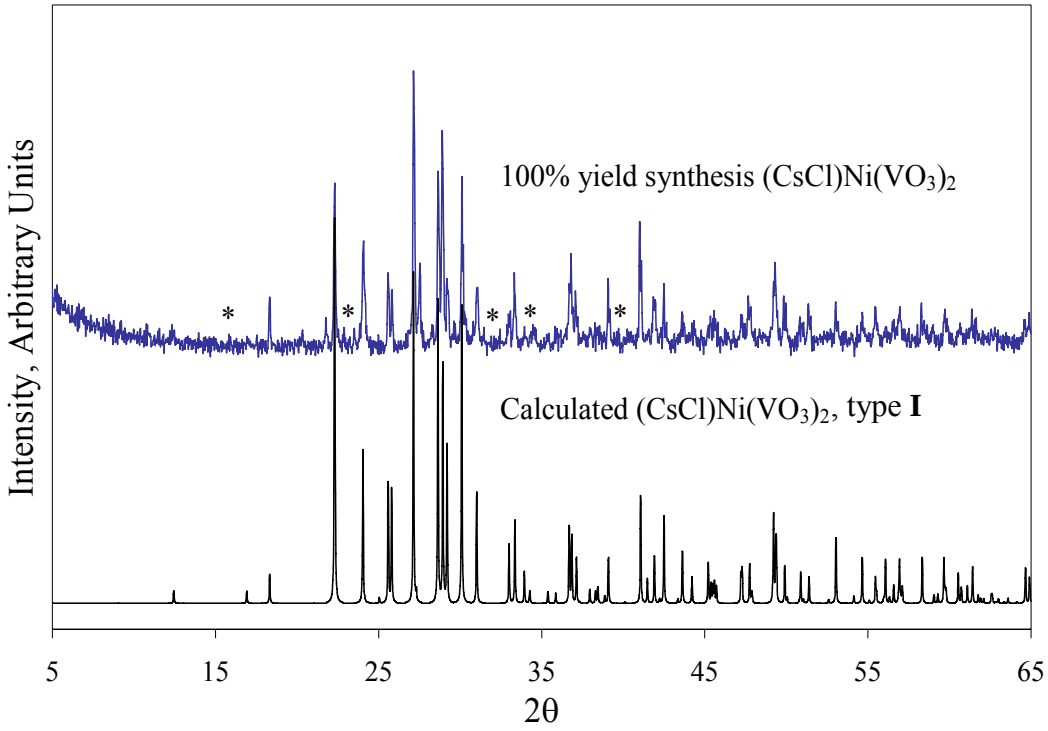

Figure 6.3: Calculated powder pattern of $(CsCl)Ni(VO_3)_2$ (**3**) compared to the 100% yield synthesis. Impurity peaks are marked with asterisks.

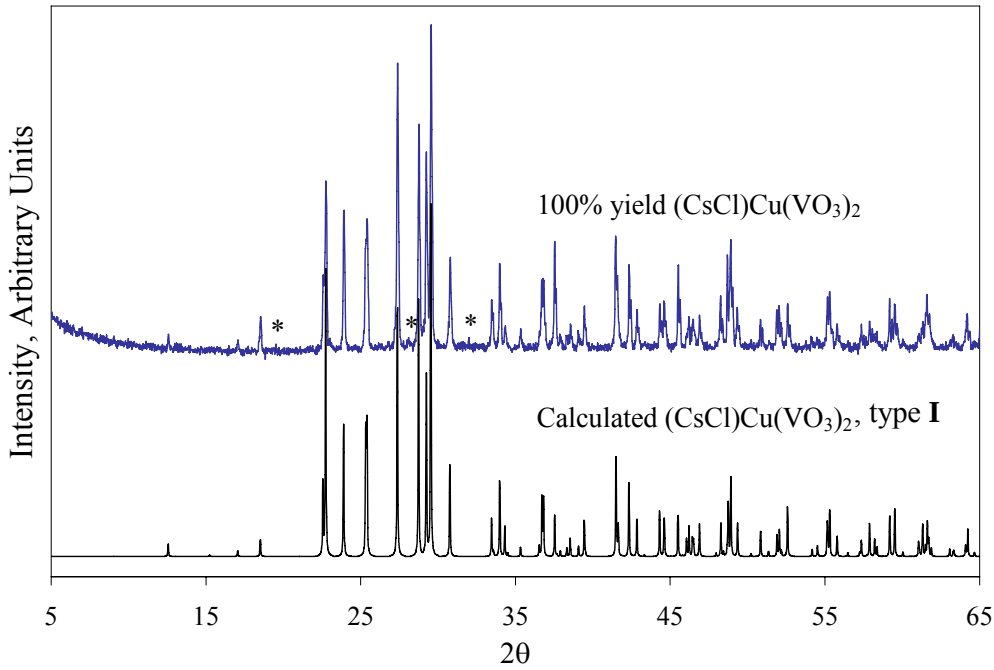

Figure 6.4: Calculated powder pattern of $(CsCl)Cu(VO_3)_2$ (**4**) compared to the 100% yield synthesis. Impurity peaks are marked with asterisks.

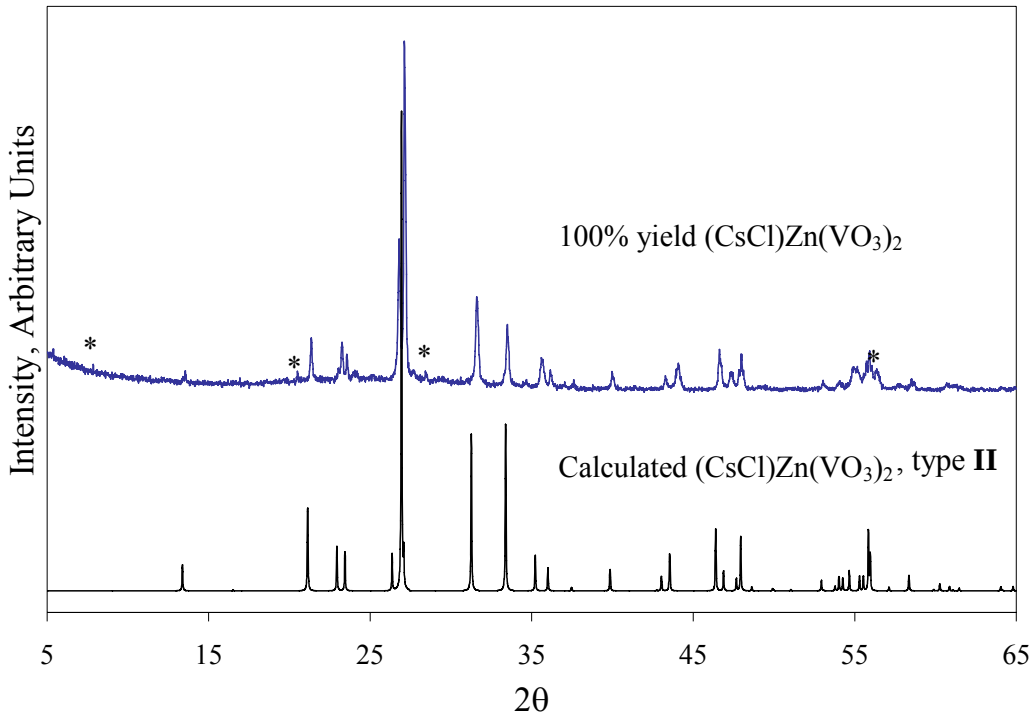

Figure 6.5: Calculated powder pattern of $(CsCl)Zn(VO_3)_2$ (**6**) compared to the 100% yield synthesis. Impurity peaks are marked with asterisks.

Characterization

Elemental Analysis: Qualitative elemental analysis was performed by EDAX on the single crystals used in the structure determination. The results showed the presence of the respective elements in the chemical formula.

Powder X-ray Diffraction: PXRD was used to confirm the presence of each phase in the respective high yield reactions. The powder X-ray diffraction data was collected at room temperature with a step size of 0.02 and a scan rates of 0.0087-0.0250°/s and 2θ ranging from 5-65°. The PXRD patterns can be seen in Figures 6.1-6.5.

Single Crystal X-ray Diffraction: Single crystals were selected under an optical microscope. Data were collected at room temperature (~300K) using Mo Kα radiation (λ = 0.71073 Å) produced by a graphite monochromator. The crystal-to-detector distance was approximately 27.6 mm and the scan time was approximately 5 seconds per frame. The crystallographic data for compounds **1-6** are summarized in Table 6.1 The atomic coordinates, thermal parameters, and selected bond distances and angles are listed in Tables 6.2, 6.3, and 6.4, respectively. It should be noted that the secondary extinction parameter is reported for all compounds with the exception of **6**. After the parameter was refined for **6**, it was found to be insignificant, and was therefore removed.

Magnetic Properties: Magnetic susceptibility was measured with a Quantum Design SQUID MPMS-5S magnetometer. Temperature-dependent magnetic studies were performed on a ground powder of selected single crystals for compounds **1** (5.3 mg) and **2** (5.0 mg) and on 100% powder samples of compounds **3** (45.0 mg) and **4** (28.6 mg). The initial temperature-dependent studies were performed over a temperature range of 2-

Table 6.1 Crystallographic data for compounds **1-6**.

empirical formula[a]	$(CsCl)Mn(VO_3)_2$	$(CsCl)Co(VO_3)_2$	$(CsCl)Ni(VO_3)_2$	$(CsCl)Cu(VO_3)_2$	$(CsCl)Co(VO_3)_2$	$(CsCl)Zn(VO_3)_2$
	1	**2**	**3**	**4**	**5**	**6**
structure type	**I**	**I**	**I**	**I**	**II**	**II**
color/shape	red, column	red, column	red, column	red, column	blue, plate	purple, plate
crystal size (mm)	0.22 × 0.08 × 0.06	0.20 × 0.05 × 0.05	0.15 × 0.05 × 0.04	0.10 × 0.03 × 0.03	0.12 × 0.12 × 0.03	0.14 × 0.04 × 0.03
formula weight (amu)	421.18	425.17	424.95	429.78	425.17	431.61
T, °C				*25*		
space group, *Z*	*C*2/*c* (No. 15), 4	*C*2/*c* (No. 15), 4	*C*2/*c* (No. 15), 4	*C*2/*c* (No. 15), 4	*I*4/*mmm* (No. 139), 4	*I*4/*mmm* (No. 139), 4
a, Å	11.222(2)	11.076(2)	10.949(2)	11.200(2)	7.608(1)	7.585(1)
b, Å	10.738(2)	10.471(2)	10.381(2)	10.386(2)	----------	----------
c, Å	7.033(1)	6.996(1)	6.971(1)	7.065(1)	13.275(6)	13.515(3)
β, °	118.39(3)	119.11(3)	119.35(3)	121.23(3)	----------	----------
V, $Å^3$	745.5(3)	708.9(2)	690.6(2)	702 .7(2)	768.4(4)	777.4(2)
linear abs. coeff., mm^{-1}	9.268	10.305	10.902	11.061	9.507	10.348
F_{000}	764	772	776	780	772	784
d_{calc}, g / cm^{-3}	3.753	3.984	4.087	4.062	3.675	3.687
data/restraints/parameters	661 / 0 / 54	626 / 0 / 54	610/0/54	620 / 0 / 54	231 / 0 / 24	234/0/24
secondary extinction	0.030(1)	0.0012(4)	0.0023(4)	0.0103(9)	0.0116(11)	----------
reflections collected / unique/ R_{int}[a]	2995/ 661/ 0.0385	2895/ 626/ 0.0592	2705/ 610/ 0.0349	2777/ 620/ 0.0477	3247/ 231/ 0.0459	3065/ 234/ 0.0515
final R1/wR2[b] [$I > 2\sigma(I)$]	0.0230/ 0.0596	0.0394/ 0.0779	0.0263/0.0654	0.0342/0.0887	0.0262/0.0698	0.0373/0.1043
R1/wR2 (all data)	0.0234/ 0.0599	0.0465/ 0.0803	0.0286/0.0666	0.0347/0.0892	0.0262/0.0698	0.0392/ 0.1065
GOF	1.068	1.133	1.089	1.044	1.034	1.175
Largest difference peak / hole ($e^-/Å^3$)	0.500/-1.269	0.649/-0.977	0.893/-0.860	1.468/-1.787	0.754/-0.663	1.389/-0.839

[a] R_{int} = Σ | *Fo*^2- *Fo*^2 (mean) | / Σ[*Fo*^2]; [b] **1** R1 = Σ ||F_o| - |F_c|| / Σ|F_o|; *w*R2 = {[Σ[*w*(F_o^2-F_c^2)^2] / [Σw(F_o)^2)^2]}^(1/2); w=1/[\s^2^(Fo^2^)+(0.0397P)^2^+2.1510P] where P=(Fo^2^+2Fc^2^)/3; **2** *R* 1= Σ(||F_o| - |F_c||)/Σ|F_o|; *wR* = {Σ*w*[(|F_o| - |F_c|)^2]/Σ*w*[(|F_o|)^2]}^(1/2); w=*1/[\s^2^(Fo^2^)+(0.0373P)^2^+6.4677P] where P=(Fo^2^+2Fc^2^)/3*); **3** *R* 1= Σ(||F_o| - |F_c||)/Σ|F_o|; *wR2* = {Σ*w*[(|F_o| - |F_c|)^2]/Σ*w*[(|F_o|)^2]}^(1/2); w=1/*[\s^2^(Fo^2^)+(0.0665P)^2^+4.7320P] where P=(Fo^2^+2Fc^2^)/3'*; **4** R1 = Σ ||F_o| - |F_c|| / Σ|F_o|; *w*R2 = {[Σ[*w*(F_o^2-F_c^2)^2] / [Σw(F_o)^2)^2]}^(1/2); w=1/[\s^2^(Fo^2^)+(0.0420P)^2^+3.2412P] where P=(Fo^2^+2Fc^2^)/3; **5** R1 = Σ ||F_o| - |F_c|| / Σ|F_o|; *w*R2 = {[Σ[*w*(F_o^2-F_c^2)^2] / [Σw(F_o)^2)^2]}^(1/2); w=1/[\s^2^(Fo^2^)+(0.0442P)^2^+6.6736P] where P=(Fo^2^+2Fc^2^)/3; **6** R1 = Σ ||F_o| - |F_c|| / Σ|F_o|; *w*R2 = {[Σ[*w*(F_o^2-F_c^2)^2] / [Σw(F_o)^2)^2]}^(1/2); w=1/[\s^2^(Fo^2^)+(0.0686P)^2^+4.1744P] where P=(Fo^2^+2Fc^2^)/3

Table 6.2 Atomic parameters for **1-6**

Atom	Wycoff position	Sof	x	y	z
			$(CsCl)Mn(VO_3)_2$, **1**		
Cs	4*e*	1.0	1/2	0.1319(1)	1/4
Mn	4d	1.0	1/4	-1/4	0
V	8f	1.0	0.1288(1)	-0.222(1)	0.2186(1)
Cl	4e	1.0	1/2	-0.2143(1)	1/4
O(1)	8*f*	1.0	0.4265(2)	0.4624(2)	0.0639(3)
O(2)	8*f*	1.0	0. 1999(2)	-0.1573(2	0.2244(4)
O(3)	8f	1.0	0.2534(2)	0.0 787(2)	0.3553(3)
			$(CsCl)Co(VO_3)_2$, **2**		
Cs	4*e*	1.0	1/2	0.6304(1)	1/4
Co	4*c*	1.0	1/4	1/4	0
V	8*f*	1.0	0.1310(1)	0. 4783(1)	0.2219(2)
Cl	4*e*	1.0	1/2	0.2730(3)	1/4
O(1)	8*f*	1.0	0.2581(5)	0. 5815(4)	0.3703(8)
O(2)	8*f*	1.0	0.2068(5)	0.3428(4)	0.2246(8)
O(3)	8*f*	1.0	0.0 752(5)	0.5445(4)	-0.0595(7)
			$(CsCl)Ni(VO_3)_2$, **3**		
Cs	4*e*	1.0	0	0.6301(1)	1/4
Ni	4d	1.0	1/4	3/4	0
V	8f	1.0	0.1329(1)	0.9780(1)	0.2227(1)
Cl	4e	1.0	0	0.2676(2)	1/4
O(1)	8*f*	1.0	0.2090(4)	0. 8422(3)	0.2224(5)
O(2)	8*f*	1.0	0.0766(3)	0.0460(3)	-0.0588(5)
O(3)	8f	1.0	0.2613(3)	0.00811(3)	0.3748(5)
			$(CsCl)Cu(VO_3)_2$, **4**		
Cs	4*e*	1.0	1/2	0.3695(1)	1/4
Cu	4d	1.0	1/4	3/4	0
V	8f	1.0	0.1310(1)	0.5183(1)	0.2301(1)
Cl	4e	1.0	1/2	0.7354(2)	1/4
O(1)	8*f*	1.0	0.2099(4)	0.6529(3)	0.2479(6)
O(2)	8*f*	1.0	0.0759(3)	0.4573(3)	-0.0559(5)
O(3)	8f	1.0	0. 2597(4)	0.4123(3)	0.3863(6)

Table 6.2 Atomic parameter for **1-6** cont…

Atom	Wycoff position	sof	x	y	z
			$(CsCl)Co(VO_3)_2$, **5**		
Cs	4d	1.0	0	1/2	1/4
Co	4e	1.0	1/2	1/2	0.1349(1)
V	8h	1.0	0.2273(1)	0.2273(1)	0
Cl	4e	1.0	1/2	1/2	0.3035(2)
O(1)	8i	1.0	0.2765(7)	0	0
O(2)	16m	1.0	0.3163(4)	0.3163(4)	0.1011(4)
			$(CsCl)Zn(VO_3)_2$, **6**		
Cs	4*d*	1.0	-1/2	0	1/4
Zn	4*e*	1.0	0	0	0.1384(1)
V	8*h*	1.0	-0.02721(2)	-0.2721(2)	0
Cl	4*e*	1.0	0	0	0.3026(3)
O(1)	8*j*	1.0	-1/2	-0.2244(9)	0
O(2)	16*m*	1.0	-0.1832(6)	-0.1832(6)	-0.0988(5)

Table 6.3 Anisotropic thermal parameters for compounds **1**-**6**.

Atom	U_{11}	U_{22}	U_{33}	U_{12}	U_{13}	U_{23}
			(CsCl)Mn$(VO_3)_2$, **1**			
Cs	0.0403(3)	0.0272(3)	0.0458(3)	0.00000	0.0344(2)	0.00000
Mn	0.0096(4)	0.0089(4)	0.0097(4)	0.0017(2)	0.0052(3)	0.0002(2)
V	0.0055(3)	0.0081(3)	0.0046(3)	0.0001(2)	0.0029(2)	-0.0008(2)
Cl	0.0085(6)	0.0297(7)	0.0168(6)	0.00000	-0.0002(4)	0.00000
O(1)	0.008(1)	0.018(1)	0.008(1)	-0.0011(8)	0.0053(9)	0.0005(8)
O(2)	0.017(1)	0.012(1)	0.013(1)	0.0032(9)	0.0105(9)	-0.0001(9)
O(3)	0.013(1)	0.013(1)	0.012(1)	-0.0037(9)	0.0067(8)	-0.0049(9)
			(CsCl)Co$(VO_3)_2$, **2**			
Cs	0.0339(5)	0.0260(5)	0.0386(5)	0.00000	0.0262(4)	0.00000
Co	0.0184(8)	0.0108(7)	0.0134(7)	0.0017(5)	0.0104(6)	0.0010(5)
V	0.0097(6)	0.0099(6)	0.0084(6)	-0.0001(4)	0.0055(5)	-0.0004(4)
Cl	0.015(1)	0.029(1)	0.020(1)	0.00000	0.005(1)	0.00000
O(1)	0.015(3)	0.014(2)	0.016(2)	-0.004(2)	0.011(2)	-0.005(2)
O(2)	0.017(3)	0.015(2)	0.015(2)	0.002(2)	0.010(2)	0.000(2)
O(3)	0.007(2)	0.017(2)	0.007(2)	0.0001(2)	0.005(2)	-0.0004(2)
			(CsCl)Ni$(VO_3)_2$, **3**			
Cs	0.0276(4)	0.0240(3)	0.0323(3)	0.00000	0.0206(3)	0.00000
Ni	0.0204(6)	0.0099(5)	0.0133(5)	0.0021(3)	0.0110(4)	0.0008(3)
V	0.0080(5)	0.0076(4)	0.0049(4)	0.0003(3)	0.0034(3)	-0.0002(3)
Cl	0.0153(9)	0.0254(9)	0.0166(9)	0.00000	0.0039(7)	0.00000
O(1)	0.017(2)	0.009\(2)	0.013(2)	0.003(1)	0.009(2)	0.001(1)
O(2)	0.009(2)	0.014(2)	0.007(2)	0.0002(1)	0.005(1)	0.001(1)
O(3)	0.012(2)	0.011(2)	0.011(2)	-0.004(1)	0.005(1)	-0.003(1)
			(CsCl)Cu$(VO_3)_2$, **4**			
Cs	0.0249(4)	0.0219(4)	0.0247(4)	0.00000	0.0149(3)	0.00000
Cu	0.0104(5)	0.0056(5)	0.0094(5)	-0.0015(3)	0.0051(4)	-0.0024(3)
V	0.0071(5)	0.0054(5)	0.0044(5)	-0.0004(3)	0.0035(4)	0.0005(3)
Cl	0.0148(9)	0.020(1)	0.0159(9)	0.00000	0.0037(8)	0.00000
O(1)	0.019(2)	0.010(2)	0.014(2)	-0.002(2)	0.011(2)	0.0004(1)
O(2)	0.008(2)	0.013(2)	0.007(2)	0.0001(1)	0.004(2)	-0.001(1)
O(3)	0.013(2)	0.009(2)	0.011(2)	0.001(1)	0.008(1)	0.002(1)

Table 6.3 Anisotropic thermal parameters for compounds **1**-**6** cont…

Atom	U_{11}	U_{22}	U_{33}	U_{12}	U_{13}	U_{23}
$(CsCl)Co(VO_3)_2$, **5**						
Cs	0.0323(5)	0.0323(5)	0.0426(6)	0.00000	0.00000	0.00000
Co	0.0151(6)	0.0151(6)	0.0158(8)	0.00000	0.00000	0.00000
V	0.0100(5)	0.0100(5)	0.0378(8)	-0.0019(5)	0.00000	0.00000
Cl	0.052(1)	0.052(1)	0.018(1)	0.00000	0.00000	0.00000
O(1)	0.023(3)	0.012(2)	0.039(3)	0.00000	0.00000	0.00000
O(2)	0.032(2)	0.032(2)	0.077(3)	0.004(2)	-0.026(2)	-0.026(2)
$(CsCl)Zn(VO_3)_2$, **6**						
Cs	0.0374(7)	0.0374(7)	0.0538(9)	0.00000	0.00000	0.00000
Zn	0.0182(7)	0.0182(7)	0.0210(9)	0.00000	0.00000	0.00000
V	0.0315(9)	0.0315(9)	0.036(1)	-0.0216(8)	0.00000	0.00000
Cl	0.053(2)	0.053(2)	0.022(2)	0.00000	0.00000	0.00000
O(1)	0.069(3)	0.069(3)	0.066(4)	-0.037(4)	0.021(2)	0.021(2)
O(2)	0.042(4)	0.019(4)	0.046(4)	0.00000	0.00000	0.00000

Table 6.4 Selected bond distances and angles for Compounds **1**-**6**.

Bond Distances	Bond Angles	
$(CsCl)Mn(VO_3)_2$, **1**		
Mn-O(3) 2.111(2)*2	O(3)- Mn- O(3) 180.0	O(2)-V-O(3) 107.1(1)
Mn-O(2) 2.154(2)*2	O(3)-Mn-O(2) 88.78(9)	O(2)-V-O(1) 103.7(1)
Mn-Cl(1) 2.533(1)*2	O(3)-Mn-O(2) 91.22(9)	O(3)-V-O(1) 98.7(1)
	O(2)-Mn-O(2) 180.0(2)	O(2)-V-O(1) 104.02(1)
V-O(1) 1.890(2)	O(3)-Mn-Cl 86.25(7)	O(3)-V-O(1) 95.6(1)
V-O(1) 1.911(2)	O(3)-Mn-Cl 93.75(7)	O(1)-V-O(1) 143.3(1)
V-O(1) 2.004(2)	O(2)-Mn-Cl 89.42(7)	O(2)-V-O(1) 110.6(1)
V-O(2) 1.647(2)	O(2)-Mn-Cl 90.58(7)	O(3)-V-O(1) 142.2(1)
V-O(3) 1.666(2)	Cl-Mn-Cl 180.0	O(1)-V-O(1) 74.7(1)
	Mn-Cl-Mn 162.59(6)	O(1)-V-O(1) 73.3(1)
$(CsCl)Co(VO_3)_2$, **2**		
Co-O(1) 2.006(4)*2	O(1)-Co-O(1) 180.0(1)	O(2)-V-O(1) 106.2(3)
Co-O(2) 2.091(5)*2	O(1)-Co-O(2) 89.5(2)	O(2)-V-O(3) 103.6(2)
Co-Cl 2.464(1)*2	O(1)-Co-O(2) 90.5(2)	O(1)-V-O(3) 99.2(2)
	O1 Co1 O2 89.5(2)	O(2)-V-O(3) 104.1(2)
V-O(1) 1.675(5)	O(1)-Co-Cl 92.7(2)	O(1)-V-O(3) 94.9(2)
V-O(2) 1.644(5)	O(1)-Co-Cl 87.3(2)	O(3)-V-O(3) 143.9(3)
V-O(3) 1.885(5)	O(2)-Co-Cl 90.6(1)	O(2)-V-O(3) 109.8(2)
V-O(3) 1.923(5)	O(2)-Co-Cl 89.4(1)	O(1)-V-O(3) 143.9(2)
V-O(3) 2.010(5)	Cl-Co-Cl 180.0(1)	O(3)-V-O(3) 75.4(2)
	Co-Cl-Co 168.8(1)	O(3)-V-O(3) 73.7(2)
$(CsCl)Ni(VO_3)_2$, **3**		
Ni-O(3) 1.989(3)*2	O(3)-Ni-O(3) 180.0	O(1)-V-O(3) 106.4(2)
Ni-O(1) 2.050(3)*2	O(1)-Ni-O(1) 180.0	O(1)-V-O(2) 103.2(1)
Ni-Cl 2.426(1)*2	O(3)-Ni-O(1) 89.8(1)	O(3)-V-O(2) 99.5(2)
	O(3)-Ni-O(1) 90.2(1)	O(1)-V-O(2) 104.5(2)
V-O(1) 1.639(3)	O(1)-Ni-O(1) 180.0	O(3)-V-O(2) 94.4(1)
V-O(2) 1.882(3)	O(3)-Ni-Cl 92.4(1)	O(2)-V-O(2) 143.9(2)
V-O(2) 1.918(3)	O(3)-Ni-Cl 87.6(1)	O(1)-V-O(2) 109.4(2)
V-O(2) 2.015(3)	O(1)-Ni-Cl 90.6(1)	O(3)-V-O(2) 144.1(2)
V-O(3) 1.669(3)	O(1)-Ni-Cl 89.5(1)	O(2)-V-O(2) 75.8(1)
	Cl-Ni-Cl 180.0	O(2)-V-O(2) 73.4(2)
	Ni-Cl-Ni 171.35(8)	

Table 6.4 Selected bond distances and angles for compounds **1**-**6** cont…

Bond Distances	Bond Angles	
	$(CsCl)Cu(VO_3)_2$, **4**	
Cu-O(3) 1.894(3)*2 Cu-O(1) 2.259(4)*2 Cu-Cl 2.420(1)*2 V-O(1) 1.624(3) V-O(2) 1.889(3) V-O(2) 1.924(3) V-O(2) 1.998(4) V-O(3) 1.690(3)	O(3)-Cu-O(3) 180.0(2) O(3)-Cu-O(1) 89.4(1) O(3)-Cu-O(1) 90.6(1) O(1)-Cu-O(1) 180.0 O(3)-Cu-Cl 92.6(1) O(3)-Cu-Cl 87.4(1) O(1)-Cu-Cl 91.5(1) O(1)-Cu-Cl 88.5(1) O(3)-Cu-Cl 92.6(1) Cl-Cu-Cl 180.00(9) Cu-Cl-Cu 172.80(9)	O(1)-V-O(3) 105.4(2) O(1)-V-O(2) 103.6(2) O(3)-V-O(2) 100.1(2) O(1)-V-O(2) 102.1(2) O(3)-V-O(2) 94.9(2) O(2)-V-O(2) 145.6(2) O(1)-V-O(2) 110.4(2) O(3)-V-O(2) 144.0(2) O(2)-V-O(2) 75.7(2) O(2)-V-O(2) 74.1(2)
	$(CsCl)Co(VO_3)_2$, **5**	
Co-O(2) 2.027(4)*4 Co-Cl 2.238(3) V-O(1) 1.769(1)*2 V-O(2) 1.649(4)*2	O(2)-Co-O(2) 154.5(3) O(2)-Co-O(2) 87.20(7) O(2)-Co-Cl 102.77(17) O(2)-V-O(2) 109.0(4) O(2)-V-O(1) 108.3(1) O(1)-V-O(1) 114.4(3)	
	$(CsCl)Zn(VO_3)_2$, **6**	
Zn-O(1)1 2.038(5)*4 Zn-Cl 2.219(4) V-O(1) 1.641(6)*2 V-O(2) 1.766(2)*2	O(1)-Zn-O(1) 149.6(4) O(1) -Zn-O(1) 86.0(1) O(1)-Zn-Cl 105.2(2) O(1) -V-O(1) 108.9(5) O(1)-V-O(2) 108.5(2) O(2)-V-O(2) 113.7(4)	

300 K in applied fields 0.01, 0.05 and 0.5T. Field-dependent measurements were performed on **2** with H up to ± 5T.

Results and Discussion

Initial investigations performed within the newly explored vanadate system were focused on how altering the stoichiometry of CsCl salt, relative to the MO and V_2O_5, would affect the framework formation. These investigations led to the synthesis of two families of compounds. The first family was previously reported as the first series of salt-inclusion vanadates, $(AX)_2Mn(VO_3)_2$ (A/X = Cs/Cl (1), Cs/Br, and Rb/Cl), $(CsX)_2Cu(VO_3)_2$ where X = Cl, Br, and I.[13] This chapter reports the synthesis and characterization of a second novel series of salt-inclusion vanadates, $(CsCl)M(VO_3)_2$, where M = Mn, Co, Ni, Cu, and Zn. The title phases, synthesized using high-temperature molten salt methods, adopt two distinct structure types with Co derivatives coexisting for both structures. Structure type **I** crystallizes in a monoclinic crystal system in space group *C2/c*, (no.15), while structure type **II** crystallizes in a tetragonal space group *I4/mmm* (no. 139).

Structure type **I** exists for M = Mn, Co, Ni, and Cu (**1**-**4**, respectively). Since all of the type **I** compounds are isostructural, the structure of **2** will be discussed from this point forward. Figure 6.6 shows the extended structure of **2**. It has a single crystallographically distinct magnetic Co^{2+} cation found in an octahedral coordination environment. The oxidation state is further supported by bond valence sum calculations[16]

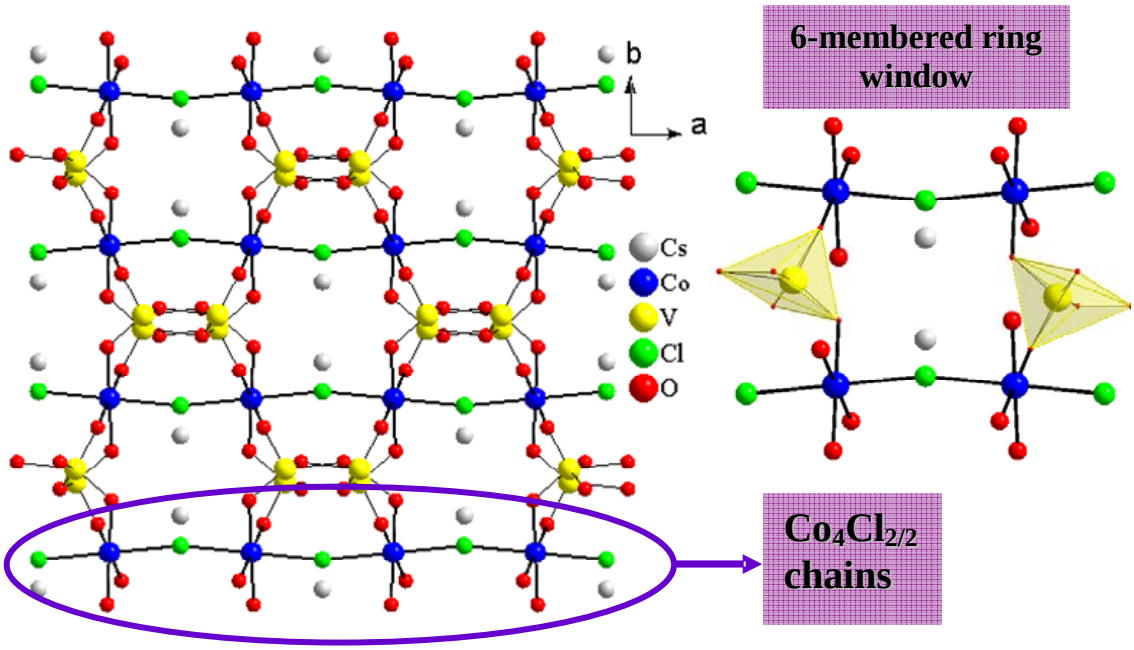

Figure 6.6: Extended structure of compound $(CsCl)Co(VO_3)_2$, **2**. The Co octahedra share an apical Cl^- anion to form $[CoO_4Cl]_\infty$ chains. Each magnetic chain is electronically confined by metavandate chains, $(VO_3)_\infty$. A close-up view, right, shows the connectivity between the CoO_4Cl_2 octahedra and VO_5 polyhedra revealing 6-membered ring windows.

equal to 2.16. Each Co site is surrounded by four equatorial O^{2-} and two apical Cl^- anions with bond distances of 2.006(4) Å, 2.091(5) Å, and 2.464(1) Å for Co-O(1), Co-O(2), and Co-Cl respectively. The chlorine serves as a bridge between neighboring Co cations, creating cobalt chloride chains, $[CoO_4Cl]_\infty$, that propagate infinitely along the crystallographic *a* direction. Each magnetic chain is electronically confined by metavanadate chains, $(VO_3)_\infty$, which propagate infinitely along the crystallographic *c* axis. The chains, shown in Figure 6.7, contain a single crystallographically distinct vanadium site, which is occupied by a fully oxidized vanadium cation. Vanadium is found in a square pyramidal geometry coordinated by oxygen, VO_5. Each VO_5 polyhedron has a short apical V=O bond equal to 1.649(4) Å. Other V-O distances are 1.675(5), 1.885(5), 1.923(5), and 2.010(5) Å for V-O(1), V-O(2), and three V-O(3) bonds, respectively. Bond valence sum calculations[16], determined to be 5.046, further support the expected V^{5+} oxidation state. Each square pyramid shares two edges with neighboring vanadium cations creating μ_3-oxo bridges along the chain. The propagation direction of the $[VO_3]_\infty$ chain is approximately orthogonal to the propagation direction of the $[CoO_4Cl]_\infty$ chain. The vanadium cations also share two corner O^{2-} with neighboring Co^{2+} cations. Looking along the *c* axis, the interchain linkages observed between $[VO_3]_\infty$ and $[CoO_4Cl]_\infty$ lead to the formation of 6-membered ring windows, consisting of four CoO_4Cl_2 octahedra and two VO_5 square pyramids. These windows, shown in Figure 6.6, are representations of the Cs^+ containing channels that run along the crystallographic *c* axis. Figure 6.8 shows the Cs-Cl and Cs-O connectivity. The Cs-Cl distances, 3.641(1) and 3.741(1)Å, are slightly longer than expected from CsCl salt (3.57Å). The Cs-O

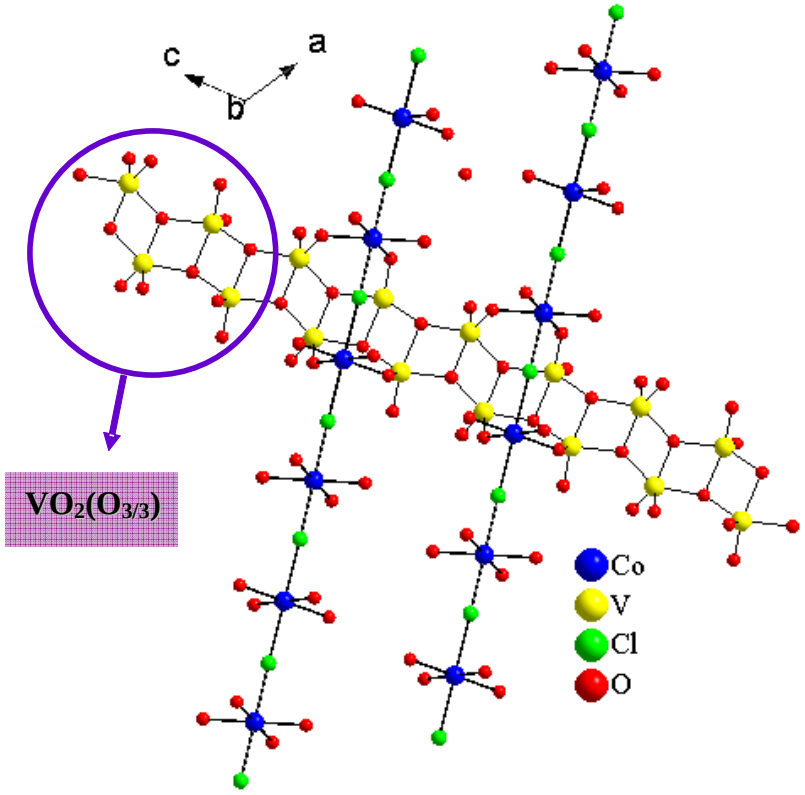

Figure 6.7: Projected view of $(CsCl)Co(VO_3)_2$, **2**, showing the $[CoO_4Cl]_\infty$ chains which are nearly orthogonal to the $[VO_3]_\infty$ metavanadate chains.

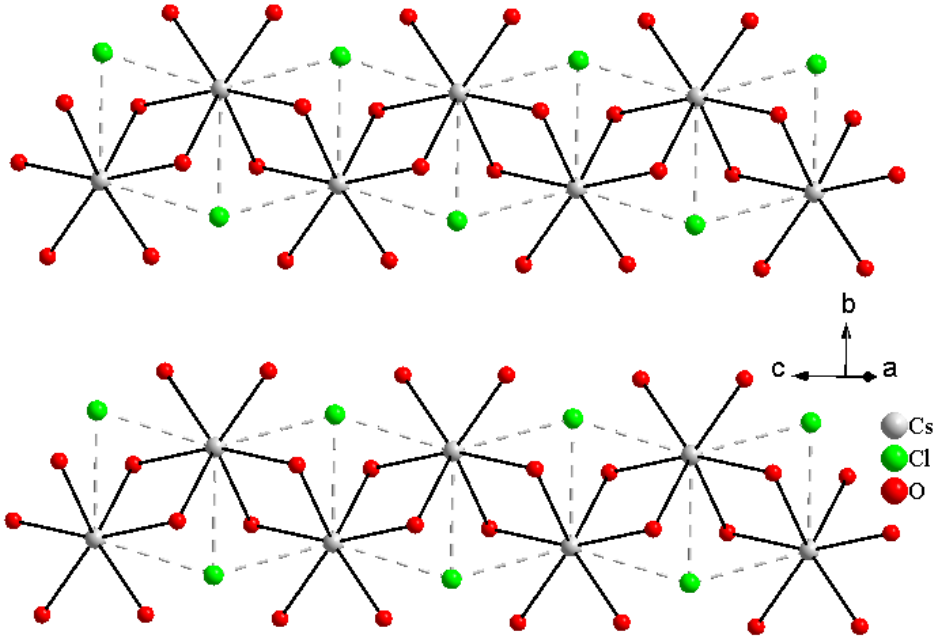

Figure 6.8: Perspective view showing Cs coordination environments observed for $(CsCl)Co(VO_3)_2$, **2**.

distances, 3.22(2), 3.264(3), and 3.50(5)Å, are also a bit long compared to the sum of the Shannon crystal radii, 3.14Å, of 9-coordinate Cs^{+} (1.92Å) and O^{2-} (1.22Å).[17]

Structure type **II**, shown in Figure 6.9**,** exists for $(CsCl)Co(VO_3)_2$ (**5**) and $(CsCl)Zn(VO_3)_2$ (**6**). The structure is similar to a reported compound, $BaVO(SiO_3)_2$,[18] which crystallizes in a *I4/m* (no. 87) spacegroup. Since **5** and **6** are isostructural, the structure of **5** will be discussed from this point forward. The cobalt ions in structure type **II** are found in a 2+ oxidation state, which is further supported by bond valence sum calculations[16], 2.19. The Co cations have a square pyramidal geometry with four equatorial O^{2-} and a single apical Cl^{-} ion with bond distances of 2.027(4) Å and 2.238(3) Å for Co-O(2) and Co-Cl, respectively. Each square pyramid shares 4 corner oxygen atoms with surrounding vanadium cations. There is a single crystallographically distinct vanadium site tetrahedrally coordinated by oxygen. Each $(VO_4)^{3-}$ polyhedron shares two corner oxygen atoms with neighboring V cations, forming $(VO_3)_4^{4-}$meta-vanadate rings, and two oxygen atoms with CoO_4Cl polyhedra. This connectivity is shown in Figure 6.10. Compound **5** has $CoCl(VO_3)_2$ sheets separated from one another by charge balancing Cs^{+} cations. Within this layered structure the sheets are stacked in an ABA type fashion along the crystallographic *c* axis where the chlorine atoms of one slab center within the metavanadate ring of the other. The Cs^{+} cations, whose coordination can be seen in Figure 6.11, are surrounded by Cl^{-} and O^{2-} anions. The Cs-Cl distances observed in **5** are 3.869(1) Å, quite a bit longer than expected for CsCl salt 3.57 Å. The Cs-O distances, 3.407(1)Å, observed for Cs-O(2), are also a bit long

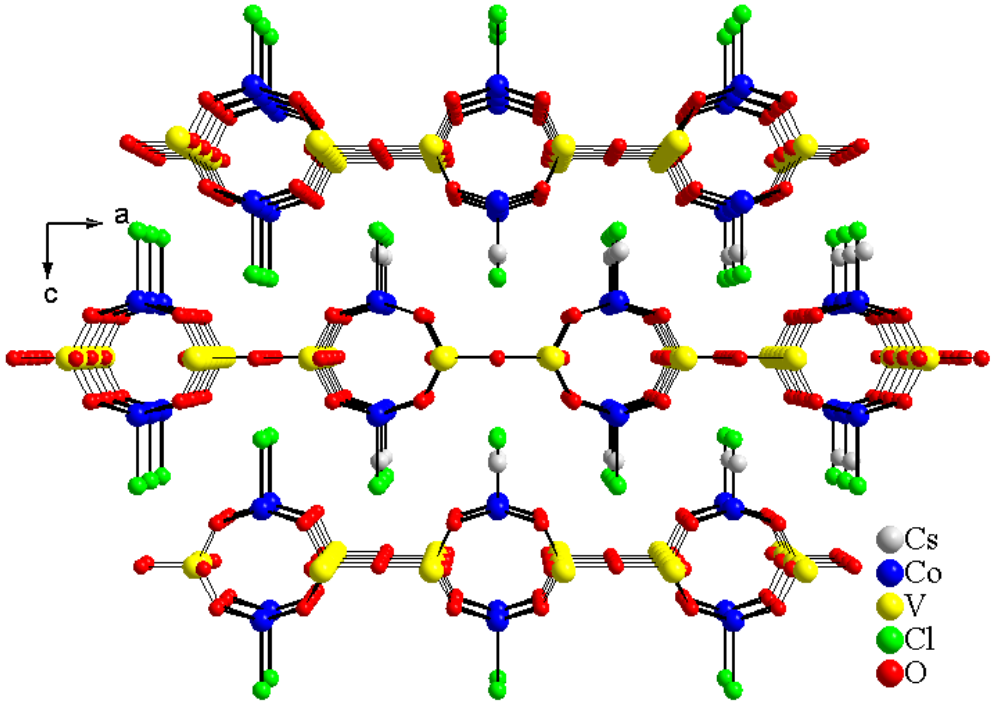

Figure 6.9: Projected view showing the layered, extended structure of $(CsCl)Co(VO_3)_2$, **5**. The apical Cl^- anions point into the space between layers, where the Cs^+ cations are located.

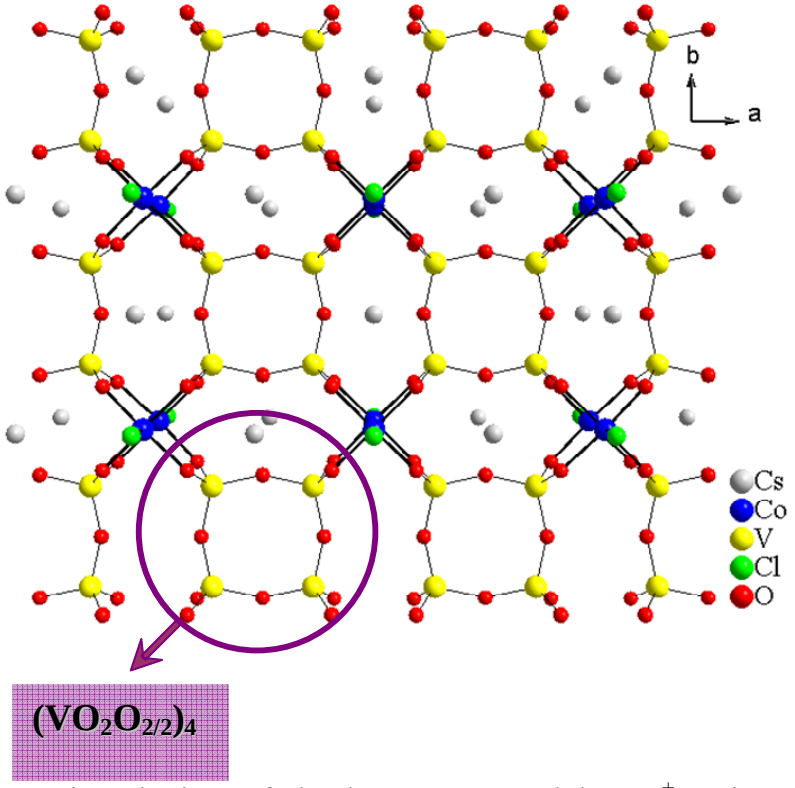

Figure 6.10: Projected view of the layers separated by Cs^+ cations in **5**. The $CoCl(VO_3)_2$ sheets found within the *ab* plane stack along the crystallographic *c* direction in an ABA type fashion.

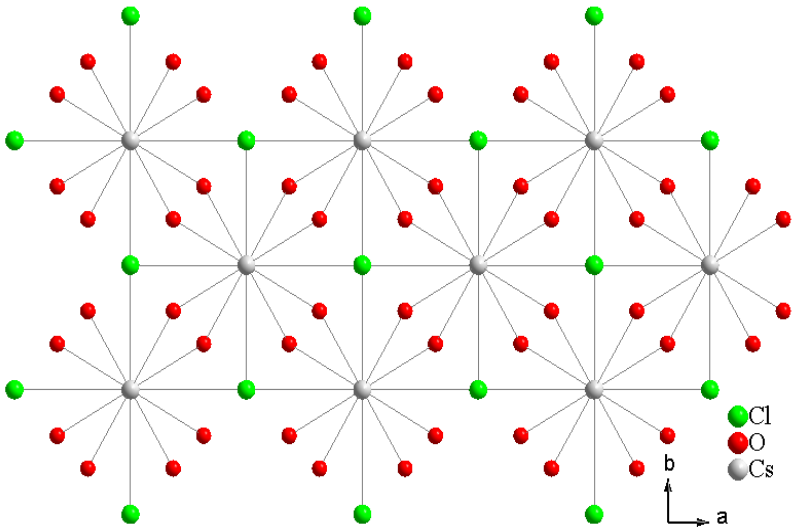

Figure 6.11: Ball-and-stick representation showing the Cs coordination environments observed for $(CsCl)Co(VO_3)_2$, **5.** Each Cs^+ cation has a coordination number of 12, with $8O^{2-}$ and $4Cl^-$ anions.

compared to the sum of Shannon crystal radii , 3.26Å, of 12-coordinate Cs^{+} (2.02Å) and O^{2-} (1.24 Å).[17]

The reaction targeting the Ir-doped version of **1** rendered a high yield of undoped $(CsCl)Mn(VO_3)_2$ and a small yield of some unidentified Ir-containing polycrystalline material. The reaction targeting the Ir-doped version of **2** gave very different results, leading to the formation of compound **5**, which has the same chemical formula as **2**. Elemental analysis was utilized to confirm that no Ir was incorporated into the structure. Further synthesis in this area may help determine what reaction conditions can be utilized to target the formation of structure type **II**. It may be interesting to try doping Zn into **1-4** to see if it will lead to the formation **II** for Mn, Co, Ni, and Cu. Also it may be interesting to load the aforementioned Co reaction without the presence of Ir to see if the off-stoichiometry reaction is the driving force for the formation of **5**.

The reaction conditions for 100% yield of **5**, structure type **II,** has not yet been attained. It should be noted that any stoichiometric reaction targeting the composition of **2** and **5**, $(CsCl)Co(VO_3)_2$, always leads to the formation of compound **2**. The powder pattern of one of these stoichiometric reactions, seen in Figure 6.2, has a close resemblance to the calculated powder pattern of the type **I** Co-containing derivative. At any rate, due to a low yield of the single crystals and a lack of a 100% yield synthesis, no physical property characterization, including magnetic susceptibility, could be obtained from **5**.

It should also be noted that compound **6** contains Zn, which is diamagnetic. Despite the fact that the material was expected not to be of any interest magnetically, Zn

was utilized after the discovery of **3**, **4**, and **5** simply to see which structure type this late transition metal would prefer. And although it has not given any real insight into the reason for the structural formation, it is now known that in a stoichiometric reaction, Zn prefers the structure type **II**. As a result of the known diamagnetic properties of Zn, magnetic measurements were not performed on this material.

Both single crystal reactions of **1** and **2** had a high enough yield for magnetic characterization, while for compounds **3** and **4,** the 100% yield syntheses were utilized. The low-dimensional structure type **I** contains 1-D M-Cl chains that extend infinitely along the crystallographic *c* axis. It is expected that the magnetic interactions within the chains, achieved *via* super exchange, will be much stronger than the interchain magnetic interactions achieved *via* super super exchange. The molar magnetic susceptibility, χ, collected in an applied field of 0.5T is shown in Figure 6.12. At room temperature, the susceptibility plots for **1**-**4** all follow the correct trend. The susceptibility decreases according to the spin state of the M^{2+} cation, S = 5/2, 3/2, 1, and 1/2, for Mn, Co, Ni, and Cu, respectively. Both Cu and Ni derivatives show a gradual increase in the χ as a function of decreasing temperature. However, the Mn and Co derivatives show an increase and then a decrease in their susceptibility curves at low temperatures, approximately T_N = 52K, possibly indicating the formation long-range antiferromagnetic order within the solid *via* interchain interactions. The orbital splitting diagram for an octahedral geometry demonstrates two sets of degenerate orbitals, t_{2g} and e_g. Both *hs* Ni^{2+} and Cu^{2+}, d^8 and d^9 respectively, have filled t_{2g} orbitals, while *hs* Mn^{2+} and Co^{2+}, d^5 and d^7 respectively, have partially filled t_{2g} orbitals. It is thought that the difference in the

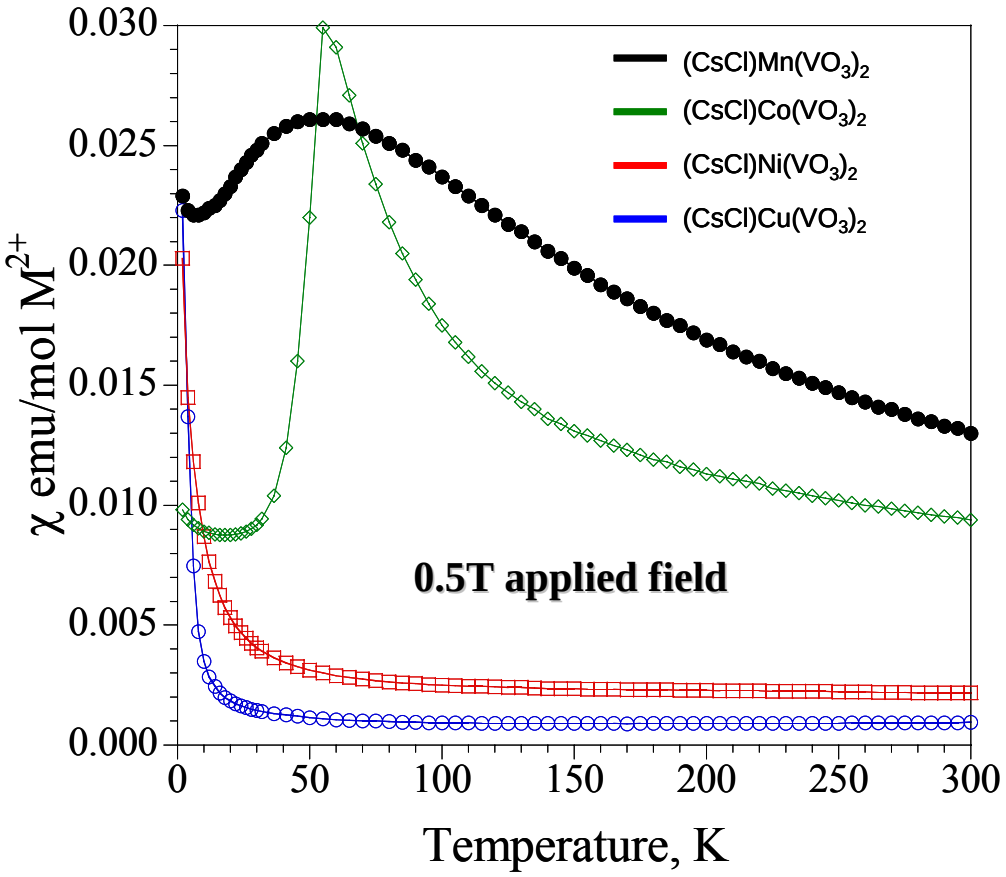

Figure 6.12: Molar magnetic susceptibility, χ, of the compounds having structure type **I**, **1**-**4**.

magnetic response of the materials is directly related to whether the t_{2g} orbitals are filled or partially occupied. The axial orbitals are responsible for AF super exchange interactions along the chain direction, while partially occupied t_{2g} orbitals could be responsible for interchain interaction. For Ni and Cu, the t_{2g} orbitals are filled, inhibiting interchain magnetic exchange and the development of long range magnetic order. Mn^{2+} and Co^{2+} cations, however, have partially filled t_{2g} orbitals allowing interchain super super exchange interactions and hence the development of long range magnetic order as observed in the molar magnetic susceptibility plot which shows a sudden decrease below T_N. The χT data were plotted for compounds **1**-**4** to determine whether the observed peaks in the susceptibility of **1** and **2** are significant. As can be seen in Figure 6.13, the peak is still observed for the Co derivative, **2**, indicating that there is an interesting change in the spin dynamics at that temperature. Although the nature of the peak is still not known, it has proven to be slightly field-dependent. The molar magnetic susceptibility measurements obtained at 0.01T showed a slight decrease in the magnitude of the transition compared to the 0.5T data, Figure 6.13 (inset), possibly indicating a field induced transition. Field-dependent studies performed on **2**, with fields ranging from ±5T at approximately 50K and 10K, revealed no signs of hysteresis. The magnetization at these two temperatures is linear with respect to the applied magnetic field, similarly observed for paramagnetic type materials. Further studies such as neutron scattering will need to be carried out to better understand the nature of the peak.

The inverse molar magnetic susceptibility, χ^{-1}, for compounds **1**-**4** is shown in Figure 6.14. The high temperature portion of the data, 200-300K for **1** and **2** and 140-

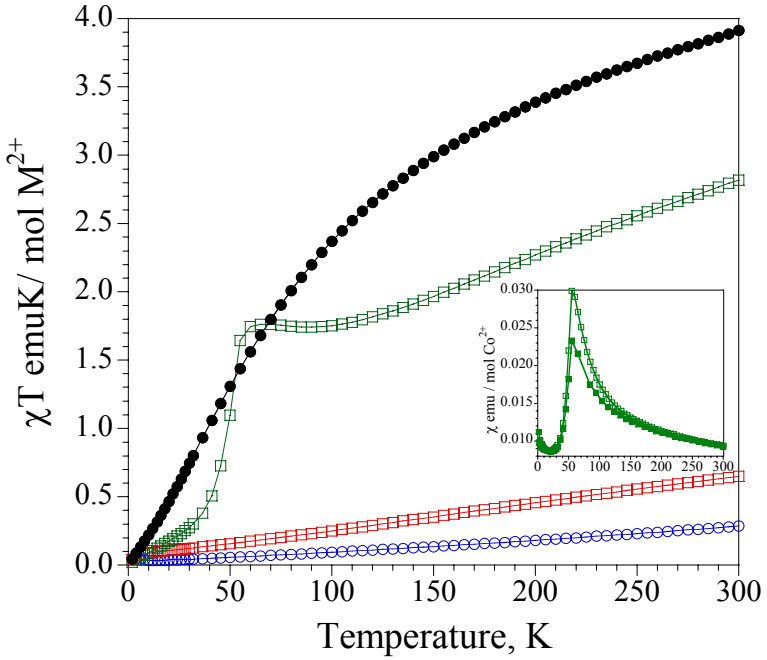

Figure 6.13: χT of the series of compounds having structure type **I**, **1-4,** 0.5T. TheχT plot of **2** shows a peak indicating that there may be some interesting change in the spin dynamics at that temperature. The inset shows χ data of **2**. There is an observed field-dependence in the transition upon changing the applied field from 0.5(□) to 0.01T(■).

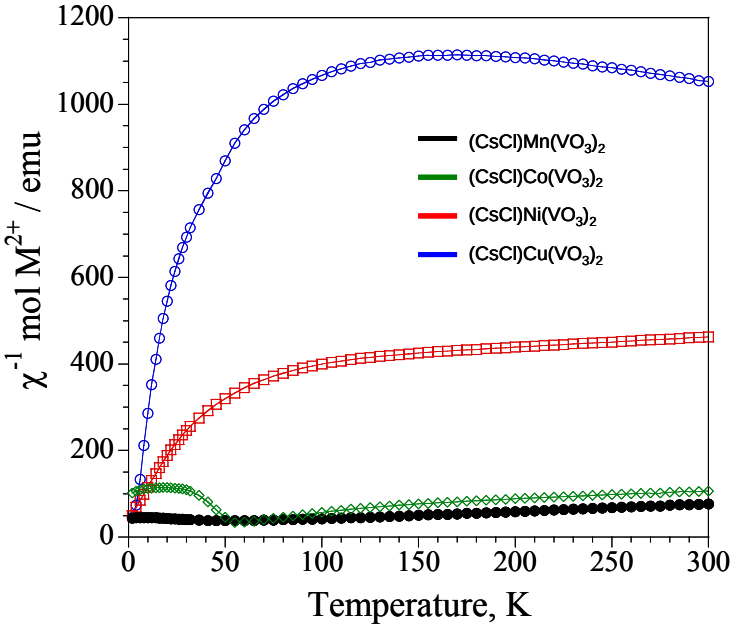

Figure 6.14: Inverse molar magnetic susceptibility, at 0.5T, for compounds having structure type **I**, **1-4**. The Cu containing compound, **4**, has a high temperature anomaly seen as a slight decrease in the χ^{-1} data. As a result of this, the Curie-Weiss fit gave unrealistic parameters.

300K for **3**, was fit using Curie-Weiss law. The parameters obtained from the fit of these compounds are shown in Table 6.5. The calculated effective magnetic moments, μ_{eff} for Mn^{2+} and Ni^{2+}, 5.9(2) and 2.6(5) μ_B, are both comparable to their expected spin-only magnetic moments, 5.91 and 2.83 μ_B. However, the effective magnetic moment determined for the Co^{2+} (d^7) containing compound, 4.3(1)μ_B, is slightly higher than the spin-only magnetic moment, 3.87μ_B. This phenomenon has been observed for other highly correlated high-spin Co^{2+} systems, where the orbital contributions of the ligand field play a significant role,[19] causing a significant difference in the measured and expected values of the effective magnetic moments. Taking the orbital contribution into account for a high spin Co^{2+} (d^7) ion leads to a calculated magnetic moment of approximately 5.20μ_B, which is higher than the observed value, 4.31μ_B, due to a partially quenched orbital contribution. The Weiss constants also show a noticeable trend. Upon decreasing M-Cl distances, there is an increase in θ, -88(6), -94(5), and -587(72) for compounds **1**-**3** respectively. This too is expected as shorter M-Cl-M distances will result in stronger AFM intrachain coupling. Compounds **1**-**3** show a decrease in the M-Cl distances upon decreasing the size of the M cation, Mn > Co > Ni. The observed M-Cl distances are 2.533(1), 2.464(1), and 2.426(1) Å for compounds **1**-**3** respectively. The fit for the Ni^{2+} derivative, clearly not as good as the fit obtained from the Mn and Co-containing compounds, rendered much higher standard deviations for the obtained parameters. Therefore, it is assumed that the large Weiss constant may be a direct result of a poor fit. A Curie-Weiss fit of the Cu compound, **4**, could not be obtained as the high-temperature inverse susceptibility data show no linear dependence. A slight

Table 6.5: Results from the Curie-Weiss fitting of the χ^{-1} data for compounds **1**-**4**.

$CsClM(VO_3)_2$	Temperature range	μ_{eff} (μ_B)	μ_{cal} (μ_B)[a] $\sqrt{4S(S+1)}$	χ_0 (μB)	θ
Mn^{2+}, d^5, S=5/2	200-300	5.9(2)	5.91	0.0017(2)	-88(6)
Co^{2+}, d^7, S=3/2	200-300	4.3(1)[a]	3.87	0.0036(1)	-94(5)
Ni^{2+}, d^8, S=1	140-300	2.6(5)	2.83	0.0012(1)	-587(72)

[a] The experimental magnetic moment is larger than the expected spin-only magnetic moment due to an unquenched orbital contribution. Taking the orbital contribution into account the calculated magnetic moment would be $5.20\mu_B$ obtained from $\sqrt{4S(S+1) + L(L+1)}$

decrease in the inverse molar magnetic susceptibility at high temperature gives rise to unrealistic fitting parameters. Although the origin of this anomaly is not known, it is certainly affecting the outcome of the fit, and higher temperature data collected up to 400K did not help. It is likely, if temperatures above 400K could be reached, a more reasonable fit of the Cu-containing compound could be acquired. It should also be noted that there are a few impurity peaks shown in the PXRD pattern of the 100% yield synthesis of **3** and **4**, Figures 6.3-6.4, which could also give rise to a poor fit. The additional impurity peaks, not observed in the calculated powder pattern, are marked with asterisks.

Conclusions

Many novel vanadate phases, including some containing magnetic nanostructures and open-framework networks, have been isolated using high temperature molten-salt methods. This is the first of three chapters exhibiting the rich structural chemistry inherent in this newly explored SIS vanadate system. Simply varying the stoichiometry of the salt has led to the discovery of two new extensive families of salt-inclusion vanadates, including the previously reported series, $(AX)_2Mn(VO_3)_2$ (A/X=Cs/Cl, Cs/Br, and Rb/Cl), $(CsX)_2Cu(VO_3)_2$ where X=Cl, Br, and I[13] and the one reported here, $(CsCl)M(VO_3)_2$, where M = Mn, Co, Ni, Cu, or Zn. All of these materials confirm the idea that vanadium can offer structural chemistry even richer than what has been previously observed in the oxyanion containing systems.

In summary, an extensive salt-inlcusion vanadate family containing 6 compounds with two different structure types is presented. Structure type **I** exists for Mn, Co, Ni, and Cu (**1**-**4**), while structure type **II** exists for Co and Zn (**5**-**6**). Only the Co-derivative has been found to exhibit both structure types. Type **I** has infinite $[MO_4Cl]_\infty$ chains which are approximately orthogonal to metavanadate $[VO_3]_\infty$ chains. Structure type **II** has isolated MO_4Cl square pyramids surrounded by $(VO_3)_4$ metavanadate rings. Already these two structure types exhibit the added versatility of the fully oxidized vanadium polyhedra. Magnetic studies were performed on the compounds having structure type **I**, all of which have AFM coupling between nearest neighbors. It appears that upon decreasing the size of the transition metal cation, there is an increase in the strength of the intrachain AFM coupling, as indicated by an increase (more negative) in the Weiss constant, θ. It is expected, based on the already observed versatility in composition, that this family can be further expanded for more in depth structure/property correlation studies. It might be interesting to resynthesize structure type **I** with mixed M sites (such as Co/Mn or Cu/Ni) to induce ferrimagnetic exchange within the chain. This could help to further support the idea that Co and Mn, with their partially filled t_{2g} orbitals, will render long range magnetic order.

Literature Cited

1. Kitagawa, S., Kitaura, R., Noro,S.-I. *Angew. Chem., Int. Ed.* **2004**, *43*, 2334-2375.

2. (a) Eddaoudi, M., Moler, D.B., Li, H., Chen, B., Reineke, T.M., O'Keeffe, M., Yaghi, O.M. *Acc. Chem. Res.* **2001**, *34*, 319-330.

   (b) Ockwig, N.W., Delgado-Friedrichs, O., O'Keeffe, M., Yaghi, O.M. *Acc. Chem. Res.* **2005**, *38*, 176-182.

3. (a) Rosseinsky, M.J. *Microporous Mesoporous Mater*., **2004**, 73, 15-30.

   (b) Lin, W. MRS Bulletin **2007**, *32(7)*, 544-548.

4. (a) Müller, A., Reuter, H., Dillinger, S. *Angew. Chem.*, *Int. Ed.*, **1995**, *34*, 2328-2361.

   (b) Rettich, R., Muller-Buschbaum, H. *Z.Naturforsch, B: Chem Sci*, **1997**, 52, 457-461.

   (c) Huang, Q., Ulutagay-Kartin, M., Mo, X., Hwu, S.-J. *Mat. Res. Soc. Symp. Proc*. **2003**, *755*, DD12.4.1.

   (d) Liao, C.-H., Chang, P.-C., Kao, H.-M., Lii, K.-H. *Inorg. Chem.*, **2005**, *44*, 9335-9339.

5. (a) Ulutagay, M., Schimek, G.L., Hwu, S.-J., Taye, H. *Inorg. Chem.*, **1998**, *37*, 1507-1512.

   (b) Hwu, S.-J., Ulutagay-Kartin, M., Clayhold, J.-A., Mackay, R., Wardojo, T.A., O'Connor, C.T., Krawiec, M. *J. Am. Chem. Soc.*, **2002**, *124*, 12404-12405.

6. (a) Huang, Q., Ulutagay, M., Michener, P.A., Hwu, S.-J. *J. Am. Chem. Soc*., **1999**, *121*, 10323-10326.

   (b) Huang, Q., Hwu, S.-J., Mo, X. *Angew. Chem.*, *Int. Ed.*, **2001**, *40*, 1690-1693.

7. (a) Etheridge, K.M.S., Hwu, S.-J. *Inorg. Chem*. **1995**, *34*, 3123-3125.

   (b) Huang, Q., Hwu, S.-J. *Inorg. Chem.*, **2003**, *42*, 655-657.

   (c) Mo, X., Hwu, S.-J. *Inorg. Chem.*, **2003**, *42*, 3978-3980.

(d) Mo, X., Ferguson, E., Hwu, S.-J. *Inorg. Chem.* **2005**, *44*, 3121-3126.

(e) Mo, X. Ph.D. dissertation, Clemson University, **2005**.

8. For example: La Violette, R.A., Budzien, J.L., Stillinger, F.H. *J. Chem. Phys.*, **2000**, *112*, 8072-8078

9. (a) Harada, H., Hosoki, C., Kudo, A. *J. Photochem. Photobiol., A*, **2001**, *141*, 219-224.

(b) Jinhua, Y., Zhigang, Z., Mitsutake, O., Akiyuki, M., Masahiko, S., Motoharu, I., Toetsu, S. *Chem. Phys. Lett.*, **2002**, 356, 221-226.

10. Peirce, L.H. *J. Cryst. Growth* **1971**, *8*, 295-296.

11. Rogado, N., Lawes, G., Huse, D.A., Ramirez, A.P., Cava, R.J. *Sol. St. Commun.* **2002**, *124*, 229-233.

12. Queen, W.L., West, J.P., Hwu, S.-J. Unpublised data, **2005**.

13. Queen, W.L., West, J.P., Hwu, S.-J., VanDerveer, D.G., Zarzyczny, M.C., Pavlick, R.A., *Angew. Chem. Int. Ed*. **2008**, *47*, 3791-3794.

14. Evans, H.T., Black, S. *Inorg. Chem.* **1966**, *10*, 1808-1814.

15. Porai-Koshits, M.A. *Kristallograjiya,* **1956**, *1***,** 291-295.

16. (a) *VALENCE* for DOS, Version 2.0, Brown, I. D. *J. Appl. Crystallogr.* **1996**, *29*, 479-480.

(b) Brown, I. D. and Altermatt, D. *Acta Cryst.* **1985**, *B41*, 244-247.

17. Shannon, R.D. *Acta Crystallogr. Sect. A* **1976**, *32*, 751 – 767.

18. Liu, G., Greedan, J.E. *J. Solid State Chem.* **1994**, *108*, 267-274.

19. Mabbs, F.E., Machin, D. J. Magnetism and Transition Metal Complexes, Halsted Press, New York, **1973**.

CHAPTER SEVEN

SYNTHESIS AND CHARACTERIZATION OF HIGH NUCLEARITY CLUSTER-BASED SALT-INCLUSION COMPOUNDS

Introduction

Transition metal oxide (TMO) clusters, also known as polyoxometalates (POMs), offer an assortment of different structural motifs that serve as potential building blocks for extended solids. These fascinating metal-oxide aggregates, more frequently observed for early transition metals (V, Nb, W, Mo, and Ta), can vary in size, containing up to several hundred metal atoms fused together through oxygen ligation, forming a variety of different (μ_2, μ_3, μ_4, etc.) bridging modes.[1] Polyoxometalates can have multiple MO_n connectivity or be comprised of MO_n and XO_n polyhedra, where X can be an additional transition metal or an oxyanion from the neighboring main group elements. Even though these clusters have been investigated for a long period of time, since the 1860's, only within the last few decades have scientists really begun to reveal the rich structural chemistry and reactivity found within this distinct class of compounds.[2] These materials have been awarded much recent attention as their diverse structures render them suitable for a vast number of applications related to many fields of study including, but not limited to, materials chemistry, catalysis, separations, and selective sorption.[3]

POMs have displayed a vast number of morphologies, compositions, and electronic properties, providing a basis for further exploration of their synthesis, chemistry, and applications. These clusters have displayed an extensive chemistry in

both aqueous and non-aqueous solvents which is a consequence of low charge density resulting in weak cation / anion interactions or low lattice energies compared to solvation energies. For the most part, they have proven to be stable in air and at elevated temperatures and can be inexpensively prepared. From a survey of the past and current literature, it is easily concluded that polyoxometalates are often synthesized using low-temperature solution-based techniques. To date, these metal-oxide aggregates have been synthesized using a variety of different methods such as hydrolytic aggregation in non-aqueous media. This method allows a controllable hydrolysis of metal alkoxides and has been utilized to form multiple homo and hetero polyoxomolybdates, tungstates, and vanadates.[4] Many POMs have also been synthesized *via* conventional, hydrothermal, or solvothermal techniques[5-6], and reportedly, due to their intermediate temperatures and pressures, solvothermal methods can be utilized to isolate metastable phases that may not be accessible *via* hydrothermal or conventional techniques.[5] Reductive aggregation processes have also been used as a method for the preparation of giant POM clusters. These processes allow the aggregation of aqueous metalate building blocks that, once reduced, react with lewis acid fragments.[7]

Chapter 7 will present the synthesis and characterization of six new hybrid materials containing high nuclearity polyoxometalate cores. These six compounds presented here have the following compositions: $Cs_{11}Na_3(V_{15}O_{36})Cl_6$ (**1**), $Cs(V_{14}O_{22})(As_2O_5)_4Cl$ (X = Cl, Br, I) (**2**), $Cs_5(V_{14}O_{40})(AsO_3)_2Cl{\bullet}2.6H_2O$ (**3**), $Na_{35.5}Cu_{27.75}O_8(AsO_4)_8Cl_{11}$ (**4**), $K_{3.29}Na_{32.21}Cu_{27.75}O_{16}(AsO_4)_{16}Cl_{11}$ (**5**) and $Na_9Cu_7O_4(AsO_4)_4Cl_3$ (**6**). Five of these compounds (with the exception of **3**) were

synthesized using high-temperature methods in molten-salt media. Compound **3** was formed after the dissolution of **2**. Meanwhile, all six can be classified as salt-inclusion solids (SISs), which show integrated covalent metal oxide lattices with ionic, alkali metal halide lattices. Recent reports have highlighted molten salt as a structure-directing agent that can be utilized in the synthesis of low-dimensional, metal-oxide lattices.[8] Although no reaction mechanism is known, one can imagine that the metal oxides are first "dissolved" in the corrosive molten salt and then, upon cooling, the covalent lattice begins to aggregate within and/or around the inherent structure of the molten ionic salt[9], resulting in the formation of special frameworks. These all-inorganic SISs possess a fascinating structural chemistry where bonding at the interface of the dissimilar components appears to be directional. This property has been revealed through the formation of salt-templated porous frameworks[10], noncentrosymmetric (NCS) lattices[11], and now magnetic metal-oxide clusters.

These new solids incorporate three different paramagnetic polyoxometalate cores including $[V_{15}O_{36}Cl]^{9-}$ (**1,** $Cl@V_{15}$)**,** $[V_{14}As_8O_{42}Cl]^{5-}$ (**2**, $Cl@V_{14}As_8$), and $[Cu_{14}(\mu_4\text{-}O_8)(AsO_4)_8]^{12-}$ (**4-6**), which contain various oxygen-bridging modes, ranging from μ_2-μ_4, that give rise to multiple exchange pathways. Compound **3** contains a $[V_{14}As_2O_{40}Cl]^{5-}$ polyoxometalate core, which is diamagnetic due to the full oxidation of the V cations. These six new compounds demonstrate the utility of salt-inclusion chemistry, where the salt serves as a structural insulator, terminating the propagation of the metal oxide lattice creating 0-D magnetic clusters. Compared to previous reports showing SISs with TMO clusters embedded in extended covalent lattices[12], salt–inclusion chemistry rendering

water soluble clusters, like the ones observed in compounds **1** and **2**, allows more potential for chemical modification, possibly aiding the pursuit of the rational design of new extended solids containing POM cores.

$Cs_{11}Na_3(V_{15}O_{36})Cl_6$, **1**, Cl@$V_{15}$

Synthesis

Single Crystal Synthesis of $Cs_{11}Na_3(V_{15}O_{36})Cl_6$, 1: The title compound was first isolated from a reaction where MnO and V_2O_5 were mixed in a 1:1 mol ratio (ca. 0.3 g) and added to a CsCl/NaCl eutectic flux equal to three times the mass of oxide reactants. The components were ground in a nitrogen-purged drybox and then sealed under vacuum in a carbon-coated quartz ampoule. The mixtures were heated to 650°C, held there for 4 days, slowly cooled to 450°C, and then furnace-cooled to room temperature. Green hexagonally-shaped single crystals of $Cs_{10}Na_3(V_{15}O_{36})Cl_7$ were retrieved after washing with deionized H_2O in a yield < 5%. It should be noted **1** is water-soluble, but the single crystals are not as soluble as CsCl or NaCl. Therefore, in the washing process, utilized to remove excess CsCl and NaCl salts, vacuum filtration was utilized to quickly remove the water from the products. There were also three other identified crystalline phases, $(CsCl)Mn_2(V_2O_7)$[11f] (≈10% yield), $Cs_{17}Cl_{15}Mn_{16.2}V_{1.8}O_6(Si_2O_5)_{18}$[13] (≈5% yield), and $NaMn_4(VO_4)_3$[13](≈40% yield), in addition to an unidentified orange powder (≈20% yield). Despite the carbon coating some silicon incorporation still resulted from the silica ampoule.

High Yield Synthesis of 1: A stoichiometric synthesis of the title compound was attempted after determining the chemical composition *via* the single crystal structure determination. VO_2, V_2O_5, NaCl, CsCl, and Cs_3VO_4 were mixed in a 33:2:9:9:8 mol ratio (ca. 0.5 grams). The reactants were ground in a nitrogen-purged drybox, placed in a silica ampoule, and then sealed under vacuum. The reaction was heated to 600°C, held there for 4 days, and then furnace-cooled to room temperature. The reaction yielded a dark green polycrystalline product of **1**, as illustrated by the near-perfect comparison of the observed vs. calculated PXRD patterns of the phase shown in Figure 7.1.

Characterization

Elemental Analysis: Qualitative elemental analysis was performed by EDAX on the single crystals used in the structure determination. The results showed the presence of the respective elements in the chemical formula.

Magnetic Properties Measurements: Magnetic measurements were carried out on a SQUID MPMS-5S magnetometer produced by Quantum Design. The zero field cooling magnetic susceptibility was carried out in an applied magnetic field of H = 0.01T in the temperature range of 2-300K. The sample was a ground powder of polycrystalline material, with a mass of 15.3 mg, obtained from the high yield synthesis of **1**.

Powder X-ray Diffraction: PXRD was used to confirm the presence of **1** in the respective high-yield reaction. A powder pattern of the 100% yield synthesis is compared to the calculated powder pattern, obtained from the single crystal structure solution, as shown in Figure. 7.1. The step size was .02° with a scan rate of 0.00125°/s.

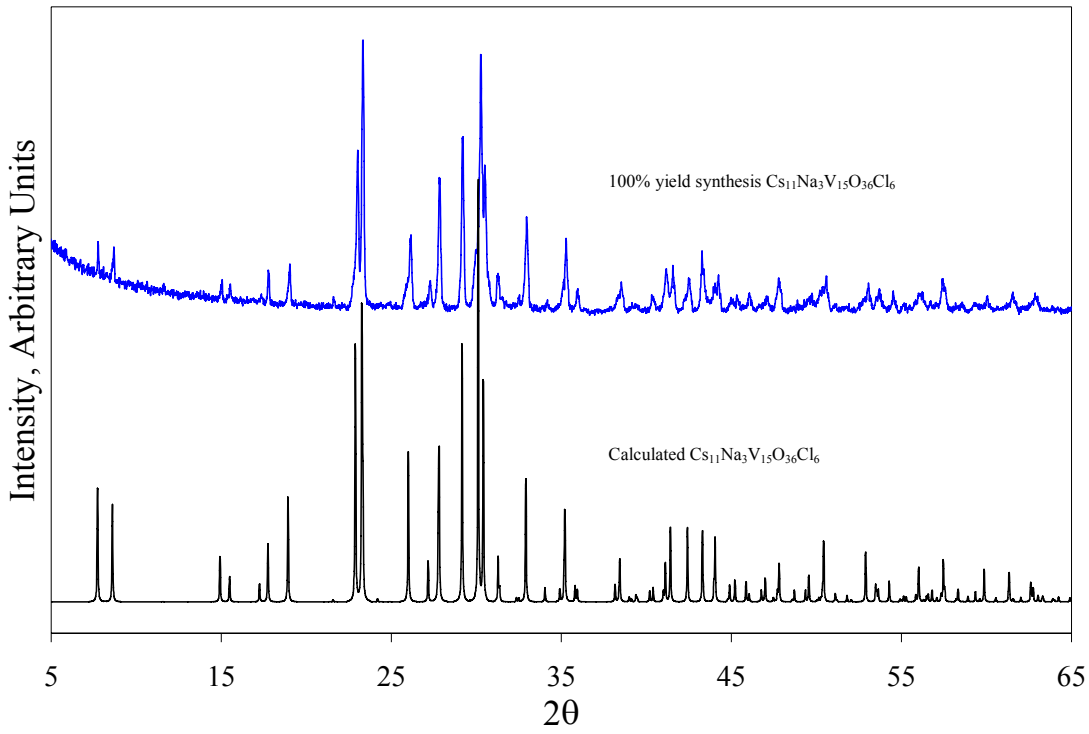

Figure 7.1: PXRD patterns showing the 100% yield synthesis of $Cs_{11}Na_3(V_{15}O_{36})Cl_6$. The PXRD pattern of the polycrystalline product is compared to the calculated pattern of **1** based on the single crystal X-ray diffraction solution.

Single Crystal X-ray Diffraction: A dark green crystal, 0.15 × 0.09 × 0.03 mm, of **1**, was selected under an optical microscope. Data were collected at room temperature with an exposure time of 60 seconds. The crystallographic data for compound **1** is summarized in Table 7.1 The atomic coordinates, thermal parameters, and selected bond distances and angles are listed in Tables 7.2, 7.3, and 7.4 respectively. The secondary extinction parameter was refined but found insignificant, thus removed from the final refinement.

Results and Discussion

When compared to polyoxomolybdates and tungstates, vanadium oxide clusters are an important, yet underrepresented part of polyoxometalate chemistry. Polyoxovanadates still represent a wide range of clusters with the number of vanadium cations ranging from 3 to 34. Most of these clusters contain reduced vanadium 4+, mixed valence vanadium 4+/5+, or fully oxidized vanadium 5+ cations. They also possess a wide range of morphologies including multiple clusters with cage-like cores that encapsulate a wide variety of ions such as Cl^-, Br^-, CO_3^{2-}, ClO_4^-, SCN^-, CH_3COO^- and $HMoO_4^-$.[14] Most of these cage-like aggregates consist of VO_5 spare pyramidal polyhedra with short apical vanadyl, V=O, bonds that point away from the cage. Some examples of these include the following compositions, $[V_{12}O_{32}]^{4-}$, $[V_{15}O_{36}]^{5-}$, $[V_{18}O_{42}]^{12-}$, $[V_{19}O_{49}]^{9-}$, and $[V_{34}O_{82}]$.[11-15] Due to the interesting magnetochemistry associated with the reduced and mixed-valent vanadium clusters, much effort has been focused on the synthesis of new materials containing higher nuclearity polyoxovanadates and also further reduced

Table 7.1: Crystallographic data for $Cs_{11}Na_3(V_{15}O_{36})Cl_6$ (**1**).

empirical formula[a]	$Cs_{11}Na_3(V_{15}O_{36})Cl_6$
color / shape	green / cube
crystal size (mm)	0.15 × 0.09 × 0.03
formula weight (amu)	3021.77
spacegroup	*P*-6*m*2 (no. 187)
Z	1
T, °C	25
a, Å	11.861(2)
c, Å	11.428(2)
V, Å^3	1392.4(4)
linear abs. coeff., mm^{-1}	9.318
F_{000}	1352
d_{calc}, g / cm^{-3}	3.604
data / restraints / parameters	1011 / 0 / 80
secondary extinction	——
reflections collected / unique / R_{int}[a]	11942 / 1011 / 0.0585
final R1/wR2 [b] [$I > 2\ \sigma(I)$]	0.0436 / 0.1140
R1/wR2 (all data)	R1 = 0.0478 / 0.1173
GOF	1.210
Largest difference peak / hole (e$^-$ / Å^3)	1.158 / -2.061

[a] $R_{int} = \Sigma \mid Fo^2 - Fo^2\ (mean) \mid / \Sigma[Fo^2]$; [b] $R1 = \Sigma \mid\mid F_o \mid - \mid F_c \mid\mid / \Sigma \mid F_o \mid$; $wR2 = \{[\Sigma[w(F_o^2 - F_c^2)^2] / [\Sigma w(F_o)^2)^2]\}^{1/2}$; $Rw = 1 / [\sigma^2(Fo^2) + (0.0572P)^2 + 7.7954P]$ where $P = (Fo^2 + 2Fc^2) / 3$

Table 7.2: Atomic positions for $Cs_{11}Na_3(V_{15}O_{36})Cl_6$ (**1**).

Atom	Wycoff position	sof	x	y	z
Cs1	3*k*	1.0	0.6976(2)	0.8488(1)	1/2
Cs2	6*n*	1.0	0.52617(7)	1.0523(1)	0.2009(1)
Cs3	1*c*	1.0	1/3	2/3	0
Na1	3*k*	1.0	0.7683(5)	0.5365(9)	1/2
V1	6*n*	1.0	0.6980(3)	0.8490(2)	0.1462(2)
V2	3*j*	1.0	0.3169(4)	1.1584(2)	0
V3	6*n*	1.0	0.8989(1)	1.1011(1)	0.2419(2)
Cl1	1*a*	1.0	1.00000	1.00000	0
Cl2	2*h*	1.0	1/3	2/3	0.3809(7)
Cl3	2*i*	1.0	2/3	1.33330	0.3402(7)
Cl4	3*k*	1.0	0.4994(4)	1.5006(4)	1/2
O1	6*n*	1.0	0.8500(6)	0.700(1)	0.355(1)
O2	3*j*	1.0	0.632(2)	0.8162(8)	0
O3	6*n*	1.0	0.574(1)	0.7869(7)	0.229(1)
O4	12*o*	1.0	0.7619(7)	1.0307(8)	0.1273(7)
O5	6*n*	1.0	1.0785(7)	1.157(1)	0.264(1)
O6	3*j*	1.0	0.475(2)	1.2373(9)	0

Table 7.3: Anisotropic thermal parameters for $Cs_{11}Na_3(V_{15}O_{36})Cl_6$ (**1**).

Atom	U_{11}	U_{22}	U_{33}	U_{12}	U_{13}	U_{23}
Cs(1)	0.071(2)	0.047(1)	0.028(1)	0.036(1)	0.	0
Cs(2)	0.029(1)	0.047(1)	0.043(1)	0.024(1)	-0.006(1)	-0.012(1)
Cs(3)	0.048(2)	0.048(2)	0.0243(9)	0.024(1)	0	0
Na(1)	0.038(4)	0.014(4)	0.028(5)	0.007(2)	0	0
V(1)	0.022(1)	0.019(1)	0.028(2)	0.011(1)	0.006(1)	0.003(1)
V(2)	0.019(2)	0.020(1)	0.016(2)	0.010(1)	0	0
V(3)	0.022(1)	0.022(1)	0.015(1)	0.011(1)	0.001(1)	-0.001(1)
Cl(1)	0.038(4)	0.038(4)	0.027(6)	0019(2)	0	0
Cl(2)	0.010(2)	0.010(2)	0.051(5)	0.005(1)	0	0
Cl(3)	0.024(2)	0.024(2)	0.033(4)	0.012(1)	0	0
Cl(4)	0.037(3)	0.037(3)	0.044(4)	0.015(3)	0	0
O(1)	0.029(5)	0.032(7)	0.018(6)	0.016(4)	0.001(3)	0.003(5)
O(2)	0.011(8)	0.037(8)	0.020(9)	0.005(4)	0	0
O(3)	0.030(7)	0.039(5)	0.043(9)	0.015(3)	0.016(7)	0.008(3)
O(4)	0.022(4)	0.028(4)	0.017(4)	0.015(3)	-0.003(3)	0.004(3)
O(5)	0.036(5)	0.049(8)	0.017(5)	0.025(4)	-0.005(3)	-0.009(6)
O(6)	0.020(9)	0.042(8)	0.047(12)	0.010(4)	0	0

Table 7.4: Selected bond distances and bond angles for $Cs_{11}Na_3(V_{15}O_{36})Cl_6$ (**1**).

Bond Distances	Bond Angles	
V(1)-O(3) 1.59(1)	O(3)-V(1)-O(2)104.5(8)	O(6)-V(2)-O(4) 104.5(3)
V(1)-O(2) 1.801(6)	O(3)-V(1)-O(4)110.1(3)	O(4)-V(2)-O(4) 95.3(5)
V(1)-O(4) 1.906(8)	O(2)-V(1)-O(4) 91.4(3)	O(4)-V(2)-O(4) 77.4(5)
V(1)-O(4) 1.906(8)	O(3)-V(1)-O(4) 110.1(3)	O(4)-V(2)-O(4) 151.0(5)
V(1)-O(5) 2.01(1)	O(2)-V(1)-O(4) 91.4(3)	O(1)-V(3)-O(5) 107.7(4)
V(2)-O(6) 1.62(2)	O(4)-V(1)-O(4) 137.5(5)	O(1)-V(3)-O(5) 107.7(4)
V(2)-O(4) 1.968(8)	O(3)-V(1)-O(5) 101.4(7)	O(5)-V(3)-O(5) 94.3(8)
V(2)-O(4) 1.968(8)	O(2)-V(1)-O(5) 154.1(6)	O(1)-V(3)-O(4) 108.7(4)
V(2)-O(4) 1.968(8)	O(4)-V(1)-O(5) 79.6(3)	O(5)-V(3)-O(4) 81.8(5)
V(2)-O(4) 1.968(8)	O(4)-V(1)-O(5) 79.6(3)	O(5)-V(3)-O(4) 142.8(4)
V(3)-O(1) 1.64(1)	O(6)-V(2)-O(4) 104.5(3)	O(1)-V(3)-O(4) 108.7(4)
V(3)-O(5) 1.905(5)	O(6)-V(2)-O(4) 104.5(3)	O(5)-V(3)-O(4) 142.8(4)
V(3)-O(5) 1.905(5)	O(4)-V(2)-O(4) 151.0(5)	O(5)-V(3)-O(4) 81.8(5)
V(3)-O(4) 1.922(8)	O(6)-V(2)-O(4) 104.5(3)	O(4)-V(3)-O(4) 79.6(5)
V(3)-O(4) 1.922(8)	O(4)-V(2)-O(4) 77.4(5)	
	O(4)-V(2)-O(4) 95.3(5)	
V(3)- V(1) 2.948(3)		
V(3)- V(2) 3.004(3)		
V(1)-Cl(1) 3.523(2)		
V(2)-Cl(1) 3.255(4)		
V(3)-Cl(1) 3.458(2)		

Table 7.5: Bond valence sum calculations for $Cs_{11}Na_3(V_{15}O_{36})Cl_6$ (**1**).

Atom	V(1)	V(2)	V(3)
BVS for **1** for V^{4+}	1.689 0.955 0.719*2 0.543 = 4.626	1.558 0.608*4 = 3.990	1.476 0.721*2 0.689*2 = 4.295
BVS for **1** for V^{5+}	1.778 1.005 0.757*2 0.572 = 4.869	1.640 0.640*4 = 4.201	1.554 0.759*2 0.725*2 = 4.522

clusters, such as those containing V^{3+}.[16] Interest in these metal oxide aggregates is heightened as a result of the already-proven catalytic properties of vanadium-containing compounds, attributed to the ease with which vanadium can be converted between 4+ and 5+ oxidation states.

Here a new salt-inclusion solid, $Cs_{11}Na_3(V_{15}O_{36})Cl_6$ (**1**), containing a Cl-centered $[V_{15}O_{36}]^{8-}$ cluster (referred to as $Cl@V_{15}$ hereafter) is presented. This material was synthesized using high-temperature methods in the CsCl/NaCl molten-salt medium. Compound **1**, shown in Figure 7.2, crystallizes in a hexagonal crystal system in the *P*-6*m*2 (no. 187) spacegroup. It should be noted that, collectively, the vanadium cations found in the V_{15} core in **1**, as shown in Figure 7.3, have a slightly lower oxidation state than what is observed for other V_{15} cores reported in the literature, $[V_{15}O_{36}]^{8-}$. Therefore, it is thought that heat, a natural reducing agent, could possibly inhibit the formation of the more oxidized "3-", "5-", or "6-" V_{15} aggregates reported in the literature.[14a, 15b,17] According to the crystal structure solution, the compound is mixed valent with eleven V atoms that are formally charged 4+ and four V cations that are formally charged 5+. The oxidation states of the vanadium cations are further supported by bond valence sum calculations shown in Table 7.5.[18] There are three crystallographically distinct vanadium sites found within the V_{15} core. The V(1) and V(3) sites appear to be in mixed (disordered) 4+/5+ oxidation states, whereas the V(2) site appears to be predominately 4+. The BVS calculations give oxidation states comparable to what is expected from the single crystal structure solution. Due to long V-Cl distances, the Cl contribution to the BVS is minimal, so they were not included. A stoichiometric synthesis was also

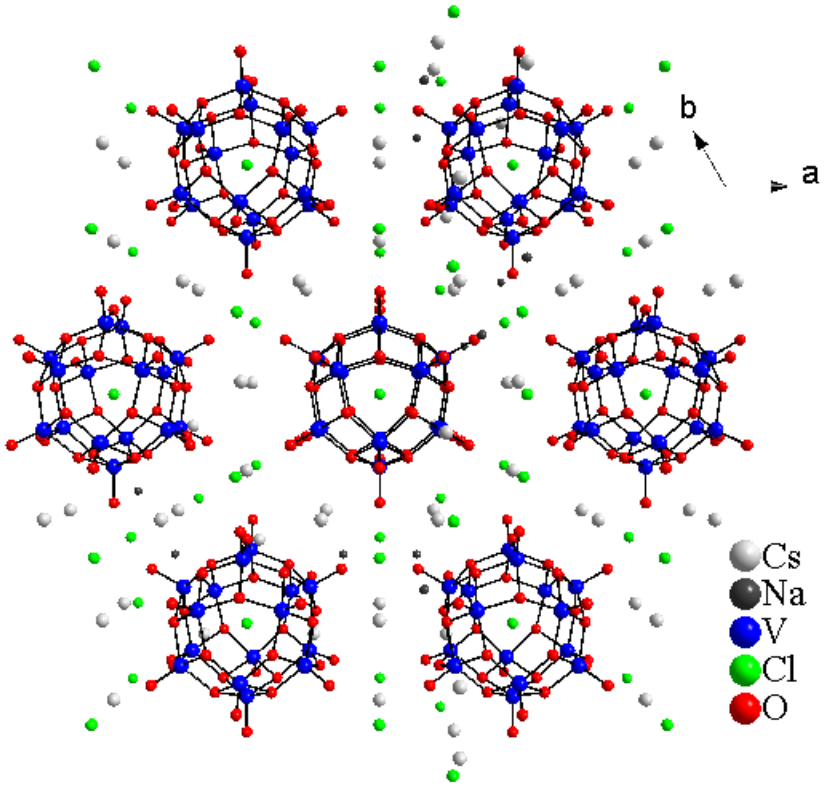

Figure 7.2: Ball and stick drawing showing a perspective view of the structure of **1** with discrete Cl-centered $[V_{15}O_{36}]^{8-}$ clusters embedded in a Cs/NaCl salt matrix.

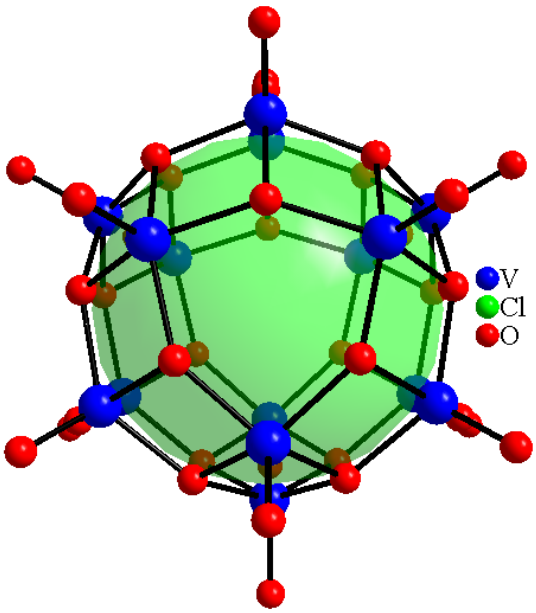

Figure 7.3: Close-up view of the Cl-centered $[V_{15}O_{36}]^{8-}$ cluster. The cluster has a 3-fold rotation symmetry approximately perpendicular to the plane of the page.

attempted as further verification of correct atom ratios and oxidation states for the title compound. The powder pattern of the 100% yield synthesis shows little to no extra peaks when compared to the calculated PXRD pattern for **1**, Figure 7.1. On several occasions, reactants with higher oxidation states were utilized in the high-yield synthesis. However, the presence of **1** was never observed in the powder pattern, indicating that there is a very narrow window of compatibility for the phase formation.

Each vanadium site is square pyramidal with short apical vanadyl (V=O) bonds, 1.59(1) Å for V(1), 1.62(2) for V(2), and 1.64(1) for V(3), that point away from the cage. The cluster has a three-fold rotational symmetry (C_3), that is parallel to the crystallographic *c* axis, and a mirror plane (σ_h) perpendicular to this principal rotation axis giving rise to D_{3h} point symmetry. The clusters can be described as having two caps, shown in Figure 7.4 (left). For clarity, only the equatorial O atoms are shown in the VO_5 units, as the apical O are not involved in bridging V cations. Each cap consists of six VO_5 units which are made of alternating V(1) and V(3) polyhedra. The V(1) polyhedron shares two *cis* edges with neighboring V(3) polyhedra, while the latter shares two trans edges with neighboring V(1) polyhedra. These caps have a bowl-like shape and are further linked *via* edge-sharing between V(2) and V(3) polyhedra, Figure 7.4 (right). The connectivity within the $[V_{15}O_{36}]^{8-}$ cluster gives rise to 18 μ_3-oxo bridging modes (*via* O(4) and O(5)) and 3 μ_2-oxo bridges (via O(2),) creating multiple pathways for magnetic superexchange. The shortest metal-metal distances are 2.948(3) Å for V(3)-V(1) and 3.00(4) Å for V(3)-V(2). The cluster, found embedded in an ionic CsCl/NaCl matrix, is a spherical cage that encapsulates a Cl^- anion. The V-Cl distances,

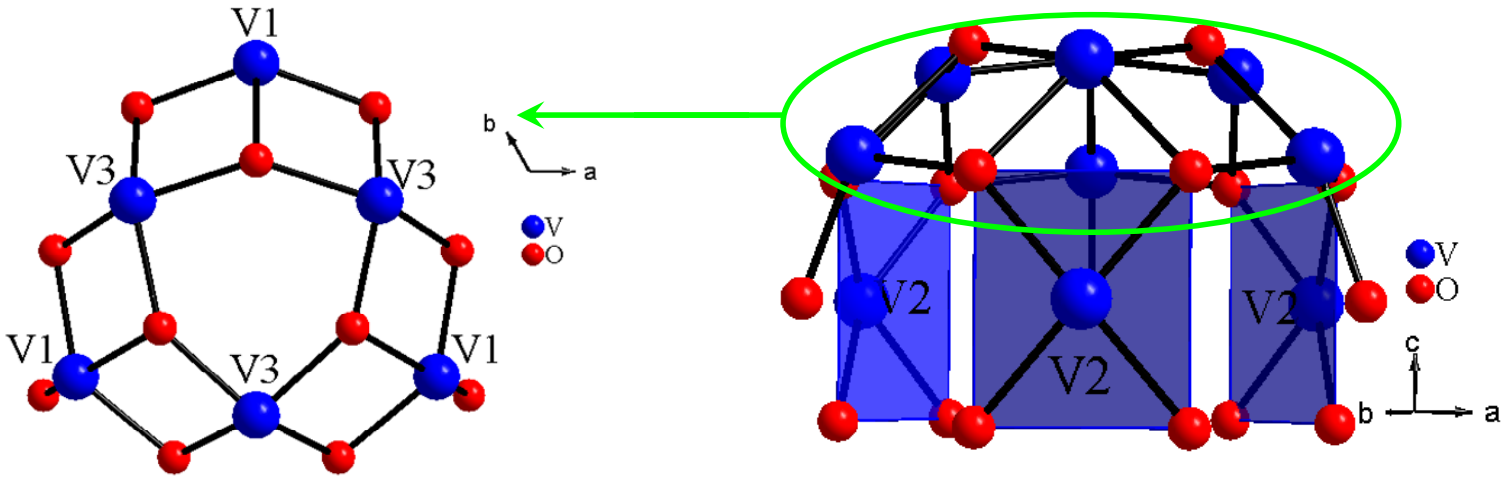

Figure 7.4: Partial structures of the $[V_{15}O_{36}]^{8-}$ showing the three crystallographically distinct vanadium sites. (left) V(1) and V(3) form bowl-like caps on the top and bottom of the $[V_{15}O_{36}]^{8-}$ cluster. (right) V(2) share edges with the three V(3) to link the bowls. All of the short V=O bonds have been removed for clarity.

which are 3.523(2), 3.255(1), and 3.458(1)Å for V(1-3) respectively, are much longer than the expected sum of Shannon crystal radii, 2,27 Å, of six-coordinate V (0.60Å) and Cl (1.67 Å). It was thought that the cage could possibly encapsulate larger cations, however, efforts made to synthesize other derivatives of **1**, including Br and I, have so far been unsuccessful.

Compound **1** is water-soluble, and, upon dissolution, a dark green solution is formed. Over time, the solution turned from dark green to yellow, and it is thought this could be due to oxidative decomposition of the $[V_{15}O_{36}]^{8-}$ core. After slow evaporation, orange single crystals fell out of solution, and SXRD was utilized to determine the identity of the phase. The crystals were determined to be a known $Cs_4Na_2V_{10}O_{28}{\cdot}10H_2O$ phase, shown in Figure 7.5, which crystallizes in a triclinic crystal system in a *P*-1 space group with a = 8.638(2) Å, b = 10.596(2) Å, c = 11.391(2) Å, α = 68.01(3)°, β = 86.89(3)° γ = 67.77(3)°, and V = 890(2) Å^3.[19] Single crystals of **1**, obtained from the single crystal reaction, were also dissolved in water and two different crystalline phases were obtained. The first was the phase discussed above, $Cs_4Na_2V_{10}O_{28}{\cdot}10H_2O$, and the second compound appears to have a new crystal structure. Although a good structure solution could not be obtained due to poor crystal quality, certain structural features are evident from the attempted structure solution. These are shown in Figure 7.6. The formula sum obtained from the partial structure solution is $Cs_{4.25}V_{11}O_{28}{\bullet}5H_2OCl_{0.75}$ and it is found to crystallize in a monoclinic crystal system in a *C*2/*c* (no. 15) spacegroup with a = 18.571(4) Å, b = 11.350(2) Å, c = 17.985(4) Å, β = 105.45(3)°, and V = 3653(3) Å^3. Both of these compounds contain fully oxidized $[V_{10}O_{28}]^{6-}$ cores. Within the core, the

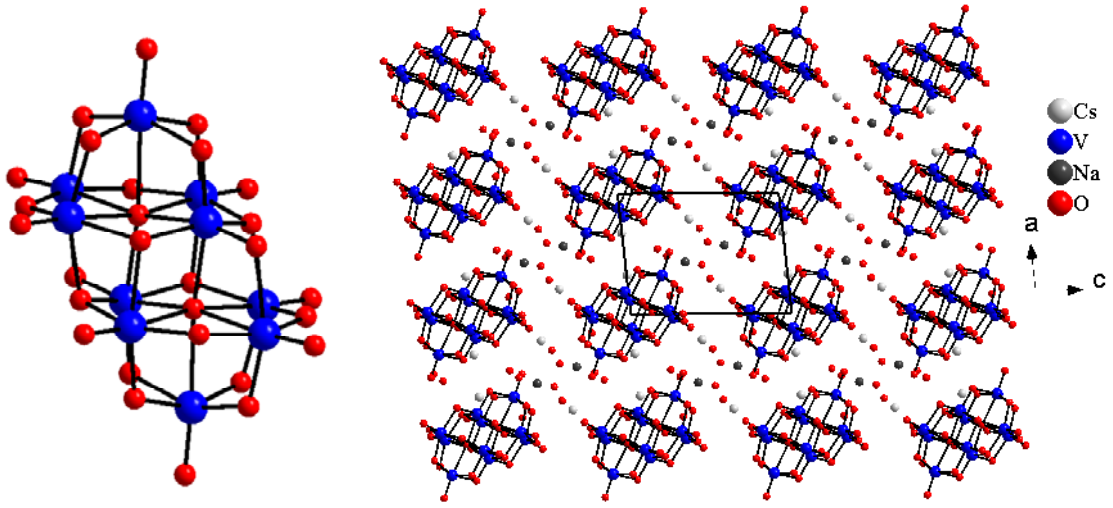

Figure 7.5: View of $Cs_4Na_2V_{10}O_{28}•10H_2O$. The compound contains a $[V_{10}O_{28}]^{6-}$ core surrounded by Cs and Na cations and water molecules.

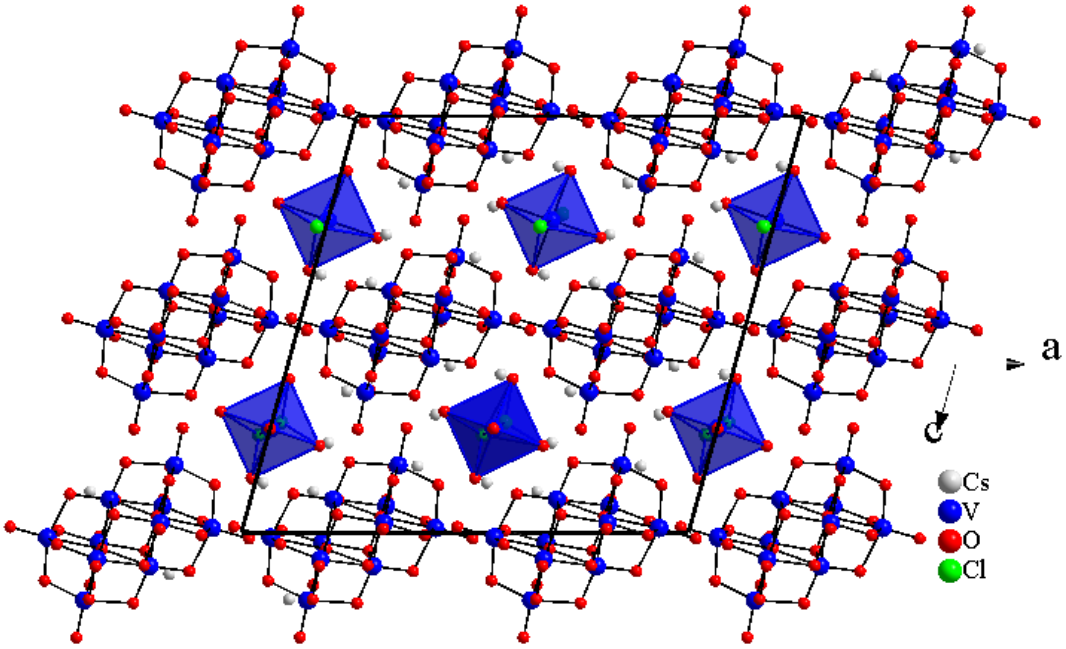

Figure 7.6: View of $Cs_{4.25}V_{11}O_{28}•5H_2OCl_{0.75}$. The $[V_{10}O_{28}]^{6-}$ cores are isolated by surrounding Cs^+ cations and $VCl_{0.75}(H_2O)_5$ polyhedra.

vanadium cations are all found in an octahedral-type geometry coordinated by oxide anions, O^{2-}. The VO_6 polyhedra share edges to form a more condensed V_{10} cluster which has lost the original cage-like shape observed in $Cl@V_{15}$. The major difference in the two crystal structures of the decomposition products is found in the anions / cations that pack around the $V_{10}O_{28}$ core. For $Cs_4Na_2V_{10}O_{28}\cdot 10H_2O$, the clusters are isolated from one another by Cs and Na cations and water molecules, while in $Cs_{4.25}V_{11}O_{28}\bullet 5H_2OCl_{0.75}$ the clusters are surrounded by Cs and $VCl_{0.75}(H_2O)_5$ polyhedra. It is thought the formation of the second product, $Cs_{4.25}V_{11}O_{28}\bullet 5H_2OCl_{0.75,}$ was dictated by the presence of the other byproducts from the single crystal reaction, such as Mn^{2+}-containing materials like $(CsCl)_2Mn(V_2O_7)$[11f] which is known to decompose upon introduction to water.

HRTEM images (Figure 7.7) further confirmed the existence of the $[V_{10}O_{28}]^{6-}$ cluster. A drop of fresh green solution, obtained after the dissolution of **1**, was placed on a copper grid. After evaporation of the water, two crystalline phases were identified from the resulting images. The clusters, due to high electron density, appear as dark regions in the images. It is thought, based on their comparison to the single crystal structures, that the images reveal the [101] view of $Cs_4Na_2V_{10}O_{28}\cdot 10H_2O$[19] and the [100] view of **1**.

Once the 100% yield of **1** is dissolved in water it usually takes several days before the solution turns yellow. This indicates that the oxidative decomposition process of the $[V_{15}O_{36}Cl]^{9-}$ core must be slow. Also, the HRTEM images indicate that **1** can possibly be reisolated after a fast evaporation process. In an effort to try to reisolated the $[V_{15}O_{36}Cl]^{9-}$ cores, a fresh green solution was placed in a vacuum furnace, and the

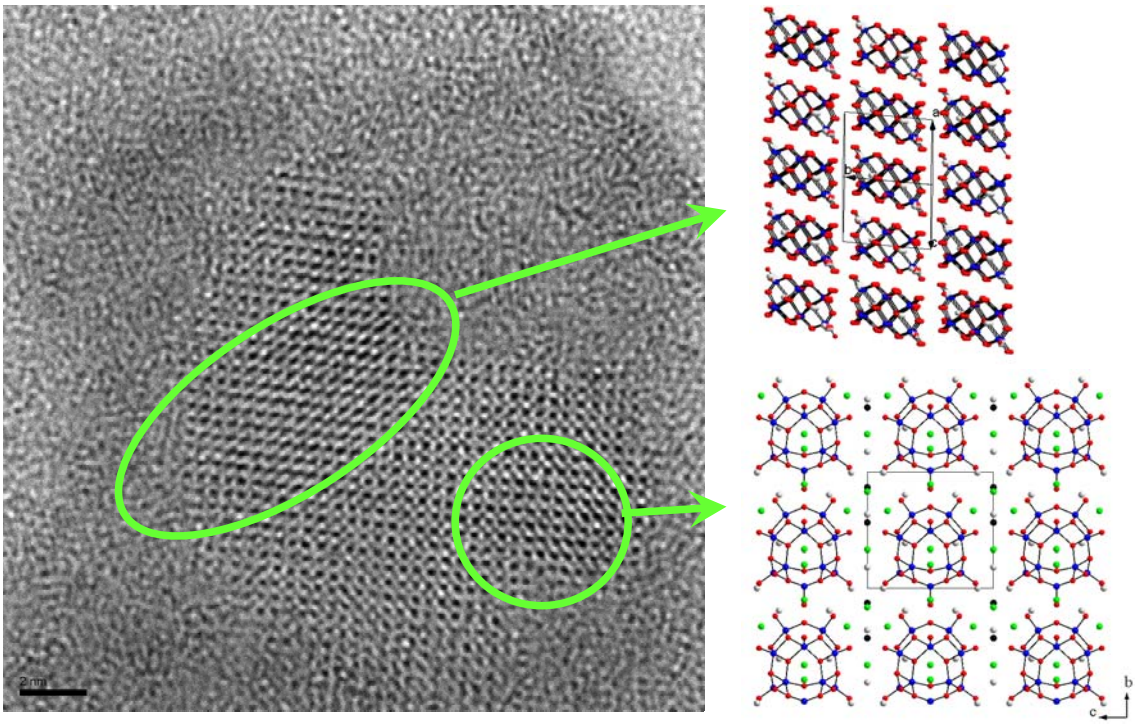

Figure 7.7: HRTEM image of the crystalline products obtained from the green solution after the dissolution of **1.** The top is the [101] view of the $Cs_4Na_2V_{10}O_{28}$•$10H_2O$ structure. and the bottom shows the [100] view of **1**.

solution was quickly removed. This process led to the formation of long dark green columns, but the quality of the crystals were not good enough for a structure solution. Therefore the results remain inconclusive.

Magnetic measurements were performed on a powder sample obtained from the 100% yield synthesis of compound **1**. Figure 7.8 shows the molar magnetic susceptibility, χ, and the inverse molar magnetic susceptibility, χ^{-1}, of **1**. The data were acquired with an applied magnetic field of 0.01T. χ shows an increase in the susceptibility upon decreasing the temperature, similar to what is expected for paramagnetic materials. However, based on the close proximity of oxo-bridged metal centers within the cluster, which creates multiple exchange pathways, some magnetic exchange is expected within the cluster. Normally the χ^{-1} data is fit using the Curie-Weiss law in order to obtain certain information about the paramagnetic ions, such as the magnetic moment and types of exchange interactions between nearest neighbors. However, the χ^{-1} data shows no linear response, and no good fit could be obtained. The nonlinearity in this system indicates that the magnetic moment of the vanadium cations varies over the temperature range, 2-300K. As a result, the effective magnetic moment, μ_{eff}, calculated using the equation $2.83(\chi_M T)^{1/2}$, was plotted as a function of temperature, Figure 7.8 (inset). At room temperature, the μ_{eff} was determined to be $5.41\mu_B$ which is slightly smaller than the expected magnetic moment, 5.74 μ_B, for 11 V^{4+} cations, S = ½. This indicates weak antiferromagnetic coupling within the cluster. The magnetic moment decreases almost linearly as the temperature approaches absolute zero, which reportedly indicates a population of thermally accessible excited spin states at high temperature.[20] It

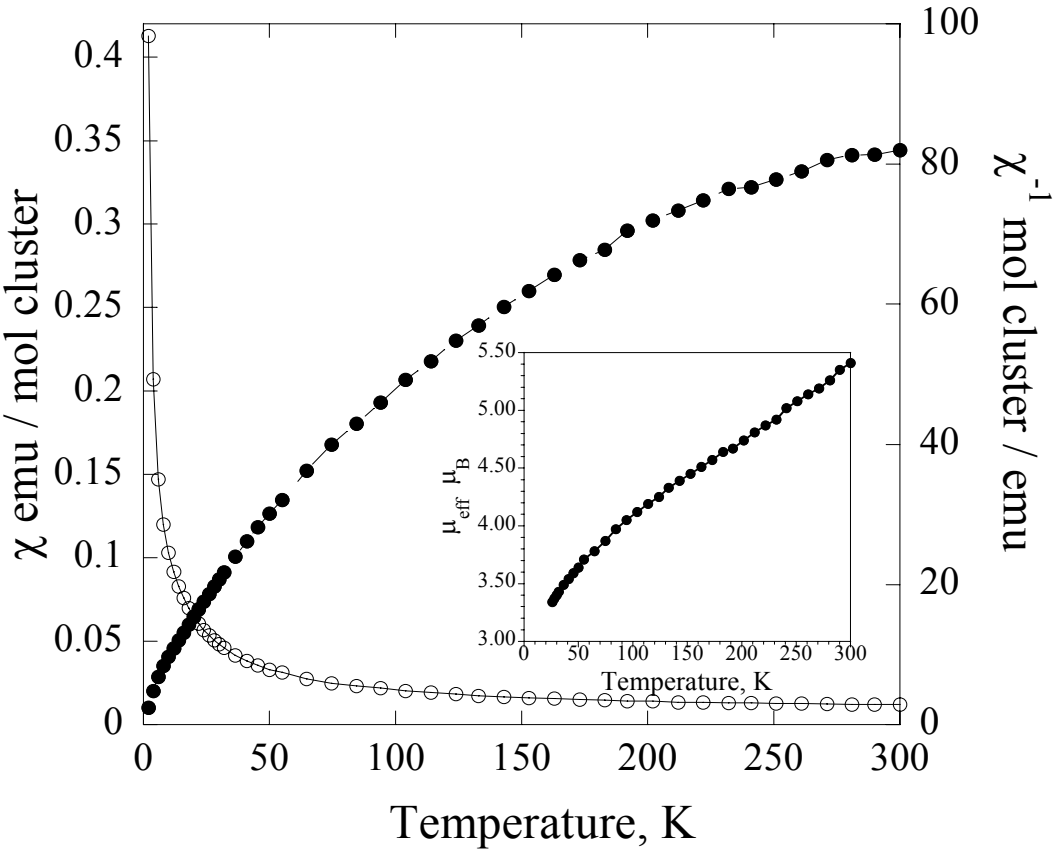

Figure 7.8: Molar magnetic susceptibility, χ (○), and the inverse molar magnetic susceptibility, χ^{-1} (●) collected with an applied field of 0.01T. The inset shows the magnetic moment, μ_{eff}, plotted as a function of temperature.

should be noted that the $(V_{15}O_{36})^{8-}$ core has eleven electrons per cluster. Therefore, even in the presence of antiferromagnetic coupling, it is expected that each cluster has a minimum of one unpaired electron remaining. The susceptibility plot shows no evidence of the development of long-range antiferromagnetic order, which indicates that this moderately close packed array of clusters is likely well insulated by the salt.

Field-dependent studies were performed on compound **1**. Fields ranging from ±5T were applied at various temperatures ranging from 2-10K (Figure. 7.9). This plot shows a decrease in the magnitude of the magnetization plot as a function of increasing temperature. At 2K, the magnetization plot has an s-shaped curve, similarly observed for superparamagnetic materials, which reaches a maximum of approximately $1.6\mu_B$ / cluster at an applied field of 5T. This material shows no remnant magnetization, which means at 2K it lacks the criteria required for the observation of slow thermal relaxation. Further experimentation will be required to determine whether this s-shaped curve is the onset of slow relaxation of the magnetization.

$Cs_5(V_{14}O_{22})(As_2O_5)_8Cl$**, 2,** and $Cs_5(V_{14}O_{40})(AsO_3)_2Cl\bullet 2.6H_2O$, **3**

Synthesis

Single Crystal Growth of 2: Single crystals were grown using $CsVO_3$, V_2O_3, and As_2O_3 (ca. 0.3g) in a 2:4:1 mol ratio with a CsCl/NaCl eutectic flux equal to 3 times the mass of the oxide reactants. The reactants were ground in a nitrogen-purged drybox, placed in a carbon-coated quartz tube, and sealed under vacuum. The reaction was heated to 650°C, held there for 4 days, slowly cooled to 450°C at a rate of 0.1°C/min, and

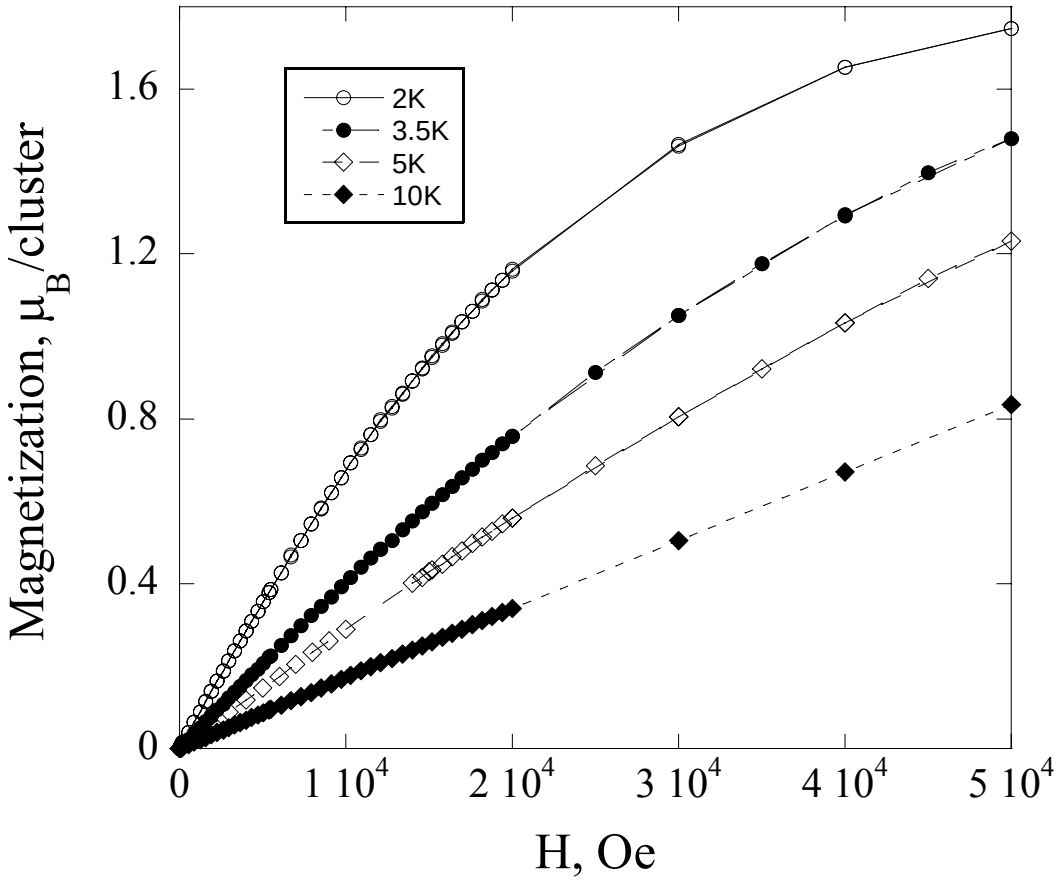

Figure 7.9: Field-dependent magnetization plot for $Cs_{11}Na_3V_{15}O_{36}Cl_6$ at various temperatures ranging from 2-10K.

then furnace-cooled to room temperature. Light red single crystals of the title phase were isolated after washing with deionized water in a yield of approximately 30%. Additional phases included a dark red crystalline phase with a plate-like morphology identified as $V_3O_3(AsO_3)_2$ (≈10% yield) and an unidentified blue polycrystalline material (≈60%).

100% Yield Synthesis of 2: CsCl, $CsVO_3$, VO, VO_2, and As_2O_3 were mixed in a 1:4:2:8:4 mol ratio. The reactants were ground in a nitrogen-purged drybox, placed in a quartz ampoule, and sealed under vacuum. The reaction was heated to 650°C at a rate of 1°C/min, held there for 3 days, and furnace-cooled to room temperature. A reddish brown polycrystalline powder was obtained from the reaction. The calculated powder pattern of **2** is compared to the reaction product in Figure 7.10. Efforts were also made to synthesize I- and Br-containing derivatives by replacing CsCl in the above reaction with CsBr and CsI. The powder patterns from these reactions are included in Figure 7.10 as well. **Synthesis of 3:** The as-prepared 100 % yield of $Cs_5(V_{14}O_{18})(As_2O_5)_8Cl$ was dissolved in deionized water. The solution was allowed to sit for several days. Over this period of time, the solution turned from brownish red to dark green and then yellow. Then dark green plate-like crystals began falling out of solution.

Characterization

Elemental Analysis: Qualitative elemental analysis was performed by EDAX on the single crystals used in the structure determination. The results showed the presence of the respective elements in the chemical formula.

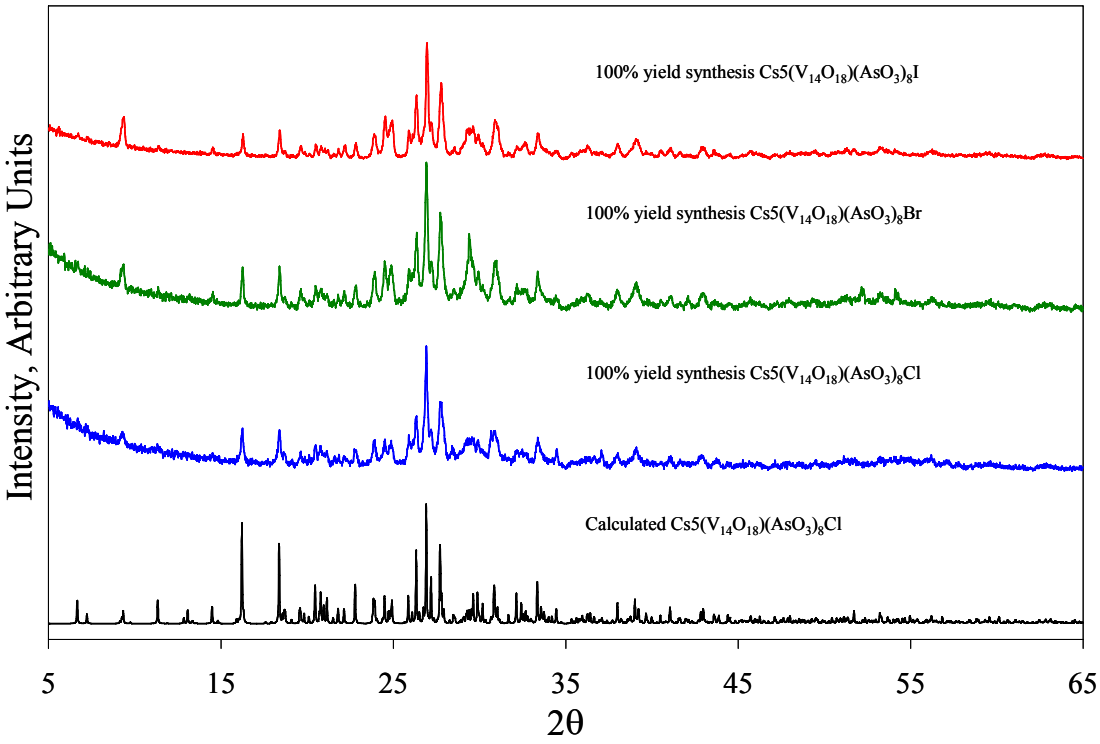

Unit Cell Refinement	$Cs_5(V_{14}As_8O_{42}Cl)$ single crystal	$Cs_5(V_{14}As_8O_{42}Cl)$ powder	$Cs_5(V_{14}As_8O_{42}Br)$ powder	$Cs_5(V_{14}As_8O_{42}I)$ powder
a (Å)	26.487(5)	26.513(7)	26.522(5)	26.529(6)
b(Å)	13.766(3)	13.771(3)	13.790(3)	13.792(3)
c(Å)	13.530(3)	13.547(3)	13.575(3)	13.573(3)
V(Å^3)	4933(2)	4946(3)	4965(3)	4966(3)

Figure 7.10: PXRD pattern of the 100% yield attempt for $Cs_5(V_{14}O_{22})(As_2O_5)_4Cl$, $Cs_5(V_{14}O_{22})(As_2O_5)_4Br$, and $Cs_5(V_{14}O_{22})(As_2O_5)_4I$ compared to the calculated PXRD pattern of $Cs_5(V_{14}O_{22})(As_2O_5)_4Cl$. The table below shows the unit cell refinement of the three powder patterns.

Magnetic Properties Measurements: Magnetic measurements were carried out on a SQUID MPMS-5S magnetometer produced by Quantum Design. The zero field cooling magnetic susceptibility was carried out in an applied magnetic field of H=0.01T in the temperature range of 2-300K. The sample was a ground powder of polycrystalline material, with a mass of 11.5mg, obtained from the high-yield synthesis of **2.** Field-dependent magnetization studies were carried out on the ground polycrystalline material at 2K with applied fields ranging from ±5T.

Powder X-ray Diffraction: PXRD was used to confirm the presence of each phase in the respective high-yield reactions. The X-ray powder diffraction data was collected at room temperature with a Scintag XDS 2000 diffractometer using Cu Kα radiation in the 2θ range of 5–65°. The step size used was 0.02, and the scan rate was 0.001058°/s for $Cs_5(V_{14}As_8O_{42})Cl$ and 0.0020 °/s for the I- and Br-containing derivatives. These PXRD patterns are shown in Figure 7.10.

Single Crystal X-ray Diffraction: Light brownish red single crystals of $Cs(V_{14}O_{22})(As_2O_5)_4Cl$ (0.10 x 0.05 x 0.02mm) and green plate-like crystals of $Cs_5(V_{14}O_{34})(AsO_3)_2Cl•2.6H_2O$ (0.10 x 0.05 x 0.03) mm were selected under an optical microscope. Data were collected at room temperature (~300K) using Mo Kα radiation (λ = 0.71073Å) produced by a graphite monochromator. The crystal-to-detector distance was approximately 27.6 mm, and the exposure time was 45 seconds for both **2** and **3**. The crystallographic data for these compounds are summarized in Table 7.6. Compound **2** crystallizes in a noncentrosymmetric spacegroup $Pna2_1$ (no. 33) and was refined using

Table 7.6: Crystallographic data **2** and **3**

empirical formula[a]	$Cs_5(V_{14}O_{22})(As_2O_5)_4Cl$	$Cs_5(V_{14}O_{34})(AsO_3)_2Cl•2.6H_2O$
compound	(**2**)	(**3**)
color / shape	Light red / cube	Green / plate
crystal size (mm)	0.10 x 0.05 x 0.02	0.10 x 0.05 x 0.03 mm
formula weight (amu)	2684.52	2247.2
space group	$Pna2_1$ (no. 33)	$P3_121$ (no. 152)
Z	4	3
T, °C		25
a, Å	26.487(5)	13.115(2)
b, Å	13.766(3)	-----
c, Å	13.530(3)	25.527(5)
V, $Å^3$	4933(2)	3802(1)
linear abs. coeff., mm^{-1}	11.635	7.432
F_{000}	4856	3062
d_{calc}, g / cm^{-3}	3.614	2.941
data / restraints / parameters	8230 / 1 / 632	4488 / 0 / 326
secondary extiction	-------	--------
flack parameter	-------	-0.02(3)
BASF	0.48(2)	--------
reflections collected / unique / R_{int}[a]	40112 / 8230 / 0.0522	32402 / 4488 / 0.0872
final R1/wR2[b] [$I > 2\ \sigma(I)$]	0.0524 / 0.1385	0.0652 / 0.1698
R1/wR2 (all data)	0.0604 / 0.1493	0.0773 / 0.1838
GOF	1.101	1.017
Largest difference peak / hole (e^- / $Å^3$)	2.239 / -1.540	1.515 / -1.117

[a] $R_{int} = \Sigma \mid Fo^2 - Fo^2\ (mean) \mid / \Sigma[Fo^2]$; [b] (**2**), $R1 = \Sigma \mid\mid F_o \mid - \mid F_c \mid\mid / \Sigma \mid F_o \mid$; $wR2 = \{[\Sigma[w(F_o^2-F_c^2)^2] / [\Sigma w(F_o)^2)^2]\}^{1/2}$; $Rw = 1 / [\sigma^2(Fo^2) + (0.0812P)^2+9.2584P]$ where $P = (Fo^2+2Fc^2) / 3$; (**3**), $R1 = \Sigma \mid\mid F_o \mid - \mid F_c \mid\mid / \Sigma \mid F_o \mid$; $wR2 = \{[\Sigma[w(F_o^2-F_c^2)^2] / [\Sigma w(F_o)^2)^2]\}^{1/2}$ $Rw = 1 / [\sigma^2(Fo^2)+(0.1123P)^2+0.0000P]$ where $P=(Fo^2+2Fc^2) / 3$

the twin function. The BASF term was determined to be 0.4790. Compound **3** also crystallizes in a noncentrosymmetric spacegroup, $P3_121$ (no. 152), and the reported flack parameter is -0.02(3) which is essentially 0. The secondary extinction was removed from the refinement of both compounds because it was insignificant. The atomic coordinates, thermal parameters, and selected bond distances and angles for compounds **2** and **3** are listed in Tables 7.7, 7.8, and 7.9.

Results and Discussion

It is well-established that rich structural chemistry results from the synthesis of mixed polyhedral frameworks. This concept has already been utilized in the synthesis of new porous materials such as synthetic zeolite-like compounds.[21] The addition of another metal oxide preferring different coordination geometry, MO_n, where n = 4-6, or even an atom from the neighboring main group elements can greatly enhance the structure types formed. In light of the already versatile group of polyoxovanadate clusters reported, additional structural versatility has been achieved through the inclusion of other mixed polyhedra. Some examples of these include $[As_2V_{10}O_{26}(H_2O)]\bullet 8H_2O$[22], $[Cu(phen)]_2[V_5As_2O_{19}]\bullet 0.5H_2O$[23], and $[NBu_4]_4[As_8V_6O_{26}]$[24]. The synthesis of new mixed polyhedral polyoxovanadates has been fueled by the interesting properties observed in $K_6[V^{4+}{}_{15}As_6O_{42}(H_2O)]\cdot 8H_2O$, a compound exhibiting single molecular magnetism or "zero dimensional" magnetism. Despite this large molecule's low spin ground state, S=1/2, it shows a hysteresis loop associated with a molecular phenomenon.[25]

Table 7.7: Atomic positions for **2** and **3**

Atom	Wycoff position	sof	x	y	z
		$Cs_5(V_{14}O_{22})(As_2O_5)_4Cl$ (**2**)			
CS1	4*a*	1.0	0.3813(1)	0.2191(1)	0.3972(1)
CS2	4*a*	1.0	0.2708(1)	0.2214(1)	0.6407(1)
CS3	4*a*	1.0	0.944(1)	0.7228(1)	0.3359(1)
CS4	4*a*	1.0	0.1136(1)	0.4108(1)	0.6310(1)
CS5	4*a*	1.0	0.1254(1)	0.55(1)	0.6253(1)
V1	4*a*	1.0	0.1222(1)	0.5032(2)	0.1222(2)
V2	4*a*	1.0	0.2716(1)	0.2231(2)	0.1516(2)
V3	4*a*	1.0	0.2216(1)	0.4257(2)	0.1411(2)
V4	4*a*	1.0	0.1440(1)	0.193(2)	-0.802(2)
V5	4*a*	1.0	0.2270(1)	0.153(2)	0.1393(2)
V6	4*a*	1.0	0.1408(1)	0.4194(2)	-0.787(2)
V7	4*a*	1.0	0.309(1)	0.2152(2)	0.3110(2)
V8	4*a*	1.0	0.1237(1)	0.158(2)	0.3226(2)
V9	4*a*	1.0	0.1195(1)	0.4200(2)	0.3271(2)
V10	4*a*	1.0	0.516(1)	0.2176(2)	-0.1089(2)
V11	4*a*	1.0	0.1546(1)	0.2202(2)	-0.1655(2)
V12	4*a*	1.0	-0.58(1)	0.2151(2)	0.919(2)
V13	4*a*	1.0	0.1269(1)	-0.666(2)	0.1179(2)
V14	4*a*	1.0	0.1235(1)	0.2165(2)	0.4113(2)
AS1	4*a*	1.0	0.2604(1)	0.3422(1)	-0.744(1)
AS2	4*a*	1.0	0.2624(1)	0.1042(1)	-0.750(1)
AS3	4*a*	1.0	0.2391(1)	0.1019(1)	0.3655(1)
AS4	4*a*	1.0	0.183(1)	0.4356(1)	-0.211(1)
AS5	4*a*	1.0	0.2367(1)	0.3405(1)	0.3666(1)
AS6	4*a*	1.0	0.62(1)	0.4318(1)	0.2188(1)
AS7	4*a*	1.0	0.220(1)	-0.11(1)	-0.237(1)
AS8	4*a*	1.0	0.103(1)	-0.17(1)	0.2162(1)
CL1	4*a*	1.0	0.1300(5)	0.2301(7)	0.1095(9)
O1	4*a*	1.0	0.2562(4)	0.1187(8)	0.536(9)
O2	4*a*	1.0	0.2547(4)	0.3268(8)	0.543(8)
O3	4*a*	1.0	0.2449(4)	0.1175(8)	0.2346(9)
O4	4*a*	1.0	0.1736(5)	0.1130(8)	0.3774(9)
O5	4*a*	1.0	0.2424(4)	0.3246(7)	0.2381(8)
O6	4*a*	1.0	0.709(4)	0.4600(8)	0.2204(9)
O7	4*a*	1.0	0.764(4)	-0.267(7)	0.2151(8)
O8	4*a*	1.0	0.1658(4)	0.4602(7)	0.2246(8)
O9	4*a*	1.0	0.1801(4)	-0.197(7)	0.348(8)
O10	4*a*	1.0	0.1716(4)	-0.227(8)	0.2206(8)
O11	4*a*	1.0	0.1037(4)	0.3134(7)	-0.1344(8)
O12	4*a*	1.0	0.1142(5)	0.5029(8)	0.4098(8)
O13	4*a*	1.0	0.1268(4)	-0.1839(7)	0.1157(10
O14	4*a*	1.0	0.1234(4)	0.6198(7)	0.1193(10)
O15	4*a*	1.0	0.2839(4)	0.2246(7)	-0.1096(8)
O16	4*a*	1.0	0.1990(4)	0.1160(7)	-0.1095(8)

.

Table 7.7: Atomic positions for **2** and **3** cont…

Atom	Wycoff position	sof	x	y	z
O17	4*a*	1.0	0.2568(4)	0.2216(7)	0.4072(9)
O18	4*a*	1.0	0.207(4)	0.1273(7)	-0.111(7)
O19	4*a*	1.0	0.1720(4)	0.3256(8)	0.3797(8)
O20	4*a*	1.0	0.867(4)	-0.221(8)	0.28(7)
O21	4*a*	1.0	-0.57(4)	-0.332(8)	0.927(8)
O22	4*a*	1.0	0.2629(5)	0.5119(8)	0.1507(10)
O23	4*a*	1.0	0.1489(4)	-0.654(8)	-0.1628(8)
O24	4*a*	1.0	0.2690(4)	-0.680(8)	0.1441(10)
O25	4*a*	1.0	0.802(4)	0.1232(8)	0.3556(8)
O26	4*a*	1.0	0.1647(5)	0.2206(8)	-0.2821(8)
O27	4*a*	1.0	0.1761(4)	0.4615(8)	0.355(8)
O28	4*a*	1.0	0.782(4)	0.3109(8)	0.3576(8)
O29	4*a*	1.0	0.151(5)	0.2165(8)	-0.2024(10)
O30	4*a*	1.0	0.1049(4)	0.1243(8)	-0.1336(9)
O31	4*a*	1.0	0.1174(5)	0.2122(8)	0.5280(9)
O32	4*a*	1.0	-0.97(4)	0.4657(8)	0.944(9)
O33	4*a*	1.0	0.821(4)	0.4571(8)	0.63(7)
O34	4*a*	1.0	0.167(5)	0.3067(7)	-0.106(9)
O35	4*a*	1.0	0.94(5)	0.3051(7)	0.2030(9)
O36	4*a*	1.0	0.1431(5)	0.5036(7)	-0.1627(8)
O37	4*a*	1.0	0.1206(4)	-0.665(7)	0.4055(8)
O38	4*a*	1.0	-0.146(5)	0.2130(9)	0.3875(11)
O39	4*a*	1.0	0.112(4)	0.1251(8)	0.2035(9)
O40	4*a*	1.0	0.1964(4)	0.3265(7)	-0.1088(8)
O41	4*a*	1.0	-0.652(4)	0.2091(9)	0.786(9)
O42	4*a*	1.0	0.3308(5)	0.2264(9)	0.1703(11)
		$Cs_5(V_{14}O_{34})(AsO_3)_2Cl•2.6H_2O$ (**3**)			
Cs1	6*c*	0.92	0.4877(1)	1.1658(1)	0.07155(5)
Cs2	6*c*	0.63	-0.1056(3)	0.7297(3)	-0.0828(1)
Cs3	6*c*	0.32	0.153(2)	1.1180(9)	0.0378(6)
Cs4	6*c*	0.26	-0.0192(7)	0.7174(7)	-0.1450(6)
Cs5	6*c*	0.24	0.4939(7)	1.587(1)	0.0746(3)
Cs6	6*c*	0.13	-0.268(4)	0.602(4)	-0.0630(5)
V1	6*c*	1.0	0.3051(2)	0.8390(2)	-0.10882(8)
V2	6*c*	1.0	-0.0156(2)	0.5628(2)	0.02575(8)
V3	6c	1.0	0.1396(2)	0.4542(2)	0.09085(8)
V4	6*c*	1.0	0.7592(2)	1.4813(2)	0.07851(8)
V5	6*c*	1.0	0.2133(2)	0.9011(2)	0.15746(9)
V6	6*c*	1.0	0.3163(2)	0.7288(2)	0.14594(8)
V7	6*c*	1.0	-0.0172(2)	0.7847(2)	0.07241(8)
As	6*c*	1.0	0.2436(1)	0.7970(1)	0.03581(5)
Cl	3b	1.0	0	0.5740(5)	1/6
O1	6*c*	1.0	0.0859(8)	0.7283(8)	0.0393(4)
O2	6*c*	1.0	0.2693(9)	0.9380(8)	0.0201(4)
O3	6*c*	1.0	0.2674(8)	0.8239(8)	0.1047(3)
O4	6*c*	1.0	0.7227(8)	1.5393(9)	0.1356(3)
O5	6*c*	1.0	0.2623(8)	0.8365(8)	-0.1750(4)

Table 7.7: Atomic positions for **2** and **3** cont…

Atom	Wycoff position	Sof	x	y	z
O6	6*c*	1.0	0.2779(7)	0.6347(8)	0.2068(3)
O7	6*c*	1.0	0.8579(8)	1.4237(8)	0.0562(4)
O8	6*c*	1.0	0.1830(9)	0.7567(9)	-0.0784(4)
O9	6*c*	1.0	-0.039(1)	0.547(1)	-0.0361(3)
O10	6*c*	1.0	0.0900(8)	0.5262(8)	0.0381(3)
O11	6*c*	1.0	0.8749(8)	1.6166(9)	0.0515(4)
O12	6*c*	1.0	0.2030(9)	0.401(1)	0.0560(4)
O13	6*c*	1.0	0.2651(8)	0.6157(8)	0.1034(4)
O14	6*c*	1.0	-0.0134(9)	0.3371(8)	0.0920(4)
O15	6*c*	1.0	0.6525(8)	1.432(1)	0.0386(4)
O16	6*c*	1.0	0.4571(8)	0.7932(9)	0.1440(4)
O17	6*c*	1.0	0.312(1)	1.0349(9)	0.1561(4)
O18	6*c*	1.0	0.1099(8)	0.8888(8)	0.1093(4)
O19	6*c*	1.0	-0.1273(9)	0.7651(9)	0.1194(4)
O20	6c	1.0	-0.032(1)	0.860(1)	0.0278(4)
O21	3a	1.0	0.411(3)	1.411(3)	0
O22	6*c*	0.8	0.444(2)	1.509(3)	0.164(2)

Table 7.8: Anisotropic thermal parameters for **2** and **3**

Atom	U_{11}	U_{22}	U_{33}	U_{12}	U_{13}	U_{23}
			$Cs_5(V_{14}O_{22})(As_2O_5)_4Cl$ (**2**)			
Cs(1)	0.037(1)	0.039(1)	0.071(1)	-0.005(1)	-0.002(1)	-0.002(1)
Cs(2)	0.043(1)	0.034(1)	0.047(1)	-0.001(1)	0.008(1)	0.001(1)
Cs(3)	0.037(1)	0.038(1)	0.070(1)	0.001(1)	0.005(1)	-0.001(1)
Cs(4)	0.057(1)	0.056(1)	0.042(1)	0.021(1)	-0.007(1)	-0.006(1)
Cs(5)	0.036(1)	0.071(1)	0.040(1)	-0.010(1)	-0.004(1)	0.006(1)
V(1)	0.031(1)	0.017(1)	0.033(1)	0.001(1)	0.000(1)	0.001(1)
V(2)	0.024(1)	0.023(1)	0.040(2)	0.000(1)	-0.003(1)	0.001(1)
V(3)	0.027(1)	0.022(1)	0.034(1)	-0.001(1)	-0.002(1)	-0.002(1)
V(4)	0.027(1)	0.023(1)	0.027(1)	0.001(1)	0.003(1)	-0.002(1)
V(5)	0.026(1)	0.021(1)	0.029(1)	0.001(1)	-0.002(1)	0.003(1)
V(6)	0.029(1)	0.021(1)	0.032(1)	0.002(1)	0.001(1)	0.003(1)
V(7)	0.028(1)	0.024(1)	0.032(1)	0.001(1)	0.005(1)	0.000(1)
V(8)	0.029(1)	0.022(1)	0.028(1)	-0.002(1)	-0.003(1)	0.003(1)
V(9)	0.032(1)	0.021(1)	0.030(1)	0.000(1)	-0.003(1)	-0.003(1)
V(10)	0.024(1)	0.027(1)	0.033(1)	0.001(1)	-0.002(1)	-0.004(1)
V(11)	0.030(1)	0.025(1)	0.026(1)	0.002(1)	0.002(1)	-0.001(1)
V(12)	0.023(1)	0.030(1)	0.029(1)	-0.002(1)	-0.001(1)	-0.003(1)
V(13)	0.028(1)	0.021(1)	0.034(1)	0.000(1)	0.000(1)	-0.003(1)
V(14)	0.033(2)	0.027(1)	0.026(1)	-0.002(1)	-0.001(1)	-0.002(1)
As(1)	0.026(1)	0.023(1)	0.036(1)	0.000(1)	0.005(1)	0.001(1)
As(2)	0.026(1)	0.023(1)	0.034(1)	0.003(1)	0.004(1)	0.001(1)
As(3)	0.030(1)	0.023(1)	0.033(1)	0.001(1)	-0.007(1)	0.002(1)
As(4)	0.028(1)	0.027(1)	0.032(1)	0.004(1)	-0.003(1)	-0.001(1)
As(5)	0.030(1)	0.024(1)	0.033(1)	-0.003(1)	-0.008(1)	-0.002(1)
As(6)	0.029(1)	0.027(1)	0.033(1)	0.005(1)	0.001(1)	-0.002(1)
As(7)	0.027(1)	0.027(1)	0.032(1)	-0.004(1)	-0.002(1)	-0.003(1)
As(8)	0.029(1)	0.026(1)	0.031(1)	-0.004(1)	0.001(1)	0.001(1)

Table 7.8: Anisotropic thermal parameters for **2** and **3** cont…

Atom	U_{11}	U_{22}	U_{33}	U_{12}	U_{13}	U_{23}
Cl(1)	0.125(9)	0.110(6)	0.117(8)	-0.002(6)	0.013(6)	0.000(6)
O(1)	0.032(6)	0.028(6)	0.043(7)	-0.005(5)	0.009(5)	-0.005(5)
O(2)	0.033(6)	0.029(6)	0.027(6)	-0.010(5)	-0.002(4)	0.007(4)
O(3)	0.033(6)	0.022(5)	0.033(6)	-0.003(4)	-0.009(4)	0.010(4)
O(4)	0.044(7)	0.029(5)	0.037(6)	0.000(5)	-0.008(5)	0.004(5)
O(5)	0.035(6)	0.022(5)	0.025(5)	0.003(4)	0.003(4)	0.006(4)
O(6)	0.028(6)	0.027(5)	0.046(7)	-0.002(4)	-0.013(5)	0.003(5)
O(7)	0.031(6)	0.026(5)	0.030(5)	-0.001(4)	-0.006(4)	0.016(4)
O(8)	0.023(5)	0.022(5)	0.041(6)	-0.001(4)	-0.010(4)	0.002(4)
O(9)	0.032(6)	0.019(5)	0.032(6)	0.002(4)	0.003(4)	0.006(4)
O(10)	0.016(5)	0.036(6)	0.038(6)	0.000(4)	-0.001(4)	0.005(5)
O(11)	0.032(6)	0.027(5)	0.029(6)	-0.001(4)	0.002(4)	.0.012(4)
O(12)	0.048(7)	0.031(6)	0.028(6)	0.006(5)	-0.006(5)	-0.012(4)
O(13)	0.042(7)	0.011(4)	0.056(8)	0.008(4)	-0.008(5)	-0.020(5)
O(14)	0.038(7)	0.020(5)	0.051(7)	-0.001(4)	-0.001(5)	0.004(5)
O(15)	0.029(6)	0.028(5)	0.030(6)	0.009(4)	0.009(5)	0.007(4)
O(16)	0.020(5)	0.020(4)	0.043(6)	-0.006(4)	-0.004(4)	0.010(4)
O(17)	0.034(6)	0.027(5)	0.027(6)	0.001(4)	-0.010(5)	-0.002(4)
O(18)	0.023(5)	0.026(5)	0.020(5)	0.03(4)	0.002(4)	0.000(4)
O(19)	0.027(6)	0.034(6)	0.035(6)	0.07(4)	-0.006(4)	0.000(5)
O(20)	0.039(7)	0.034(6)	0.022(5)	.0.000(5)	0.004(4)	-0.006(4)
O(21)	0.029(6)	0.041(6)	0.030(6)	-0.005(5)	-0.008(4)	0.006(5)
O(22)	0.030(7)	0.031(6)	0.059(8)	0.006(5)	-0.003(6)	-0.015(6)
O(23)	0.035(6)	0.030(5)	0.036(6)	0.009(5)	0.007(5)	-0.016(5)
O(24)	0.030(6)	0.034(6)	0.049(7)	0.011(5)	-0.013(5)	0.009(5)
O(25)	0.022(5)	0.039(6)	0.036(6)	0.000(5)	0.001(4)	0.001(5)
O(26)	0.038(7)	0.049(7)	0.022(6)	0.002(5)	0.005(5)	0.004(5)
O(27)	0.024(5)	0.028(5)	0.038(6)	-0.011(4)	0.008(4)	0.001(5)
O(28)	0.021(5)	0.031(5)	0.037(6)	-0.005(4)	-0.004(4)	-0.004(5)
O(29)	0.026(6)	0.039(7)	0.054(8)	0.005(5)	-0.0020(6)	-0.008(5)
O(30)	0.030(6)	0.032(6)	0.046(7)	0.002(5)	0.002(5)	-0.007(5)
O(31)	0.057(9)	0.041(7)	0.024(6)	-0.002(6)	0.001(5)	0.001(5)
O(32)	0.030(6)	0.036(6)	0.040(6)	0.010(5)	-0.006(5)	-0.008(5)
O(33)	0.037(6)	0.029(5)	0.026(5)	0.011(5)	-0.003(4)	-0.003(4)
O(34)	0.048(7)	0.016(5)	0.042(7)	0.004(5)	-0.006(5)	-0.005(5)
O(35)	0.042(7)	0.010(5)	0.056(8)	-0.001(4)	0.017(6)	0.008(5)
O(36)	0.050(7)	0.021(5)	0.028(6)	0.003(4)	0.014(5)	0.005(4)
O(37)	0.045(7)	0.020(5)	0.030(6)	0.006(4)	-0.008(5)	0.003(4)
O(38)	0.041(8)	0.045(7)	0.059(9)	0.007(5)	0.017(7)	0.011(6)
O(39)	0.028(6)	0.025(5)	0.044(7)	0.001(4)	-0.014(5)	0.004(5)
O(40)	0.029(6)	0.029(5)	0.039(6)	0.004(4)	0.002(5)	-0.003(5)
O(41)	0.020(6)	0.051(7)	0.041(7)	0.006(5)	-0.009(5)	-0.002(5)
O(42)	0.019(6)	0.050(7)	0.065(9)	0.000(5)	-0.012(6)	-0.007(6)

Table 7.8: Anisotropic thermal parameters for **2** and **3** cont…

Atom	U_{11}	U_{22}	U_{33}	U_{12}	U_{13}	U_{23}
$Cs_5(V_{14}O_{34})(AsO_3)_2Cl•2.6H_2O$						
Cs1	0.0621(7)	0.0704(7)	0.0630(7)	-0.0004(6)	0.0165(6)	-0.0202(6)
Cs2	0.166(3)	0.130(2)	0.076(1)	0.108(2)	-0.052(2)	-0.020(1)
Cs3	0.27(2)	0.082(5)	0.27(2)	0.058(8)	0.10(1)	0.008(7)
Cs4	0.085(5)	0.086(5)	0.29(2)	0.017(4)	-0.090(7)	0.011(7)
Cs5	0.122(5)	0.216(9)	0.117(5)	0.109(6)	0.020(4)	-0.023(5)
Cs6	0.51(6)	0.53(6)	0.040(6)	0.47(6)	0.02(2)	0.05(2)
V1	0.039(1)	0.041(1)	0.030(1)	0.0158(9)	0.0055(8)	0.0033(9)
V2	0.039(1)	0.041(1)	0.0241(9)	0.0176(9)	-0.0024(8)	-0.0024(8)
V3	0.039(1)	0.046(1)	0.031(1)	0.023(1)	-0.0017(8)	-0.0043(9)
V4	0.037(1)	0.047(1)	0.030(1)	0.019(1)	-0.0051(8)	-0.0018(9)
V5	0.047(1)	0.037(1)	0.038(1)	0.015(1)	0.004(1)	0.0005(9)
V6	0.034(1)	0.046(1)	0.031(1)	0.016(1)	0.0008(8)	-0.0003(9)
V7	0.050(1)	0.048(1)	0.031(1)	0.028(1)	0.0012(9)	0.0030(9)
As	0.0411(7)	0.0424(7)	0.0317(6)	0.0170(6)	0.0055(5)	0.0020(5)
Cl	0.053(3)	0.081(3)	0.050(3)	0.027(2)	-0.010(2)	-0.005(1)
O1	0.040(5)	0.036(5)	0.043(5)	0.011(4)	0.013(4)	0.003(4)
O2	0.059(6)	0.026(4)	0.041(5)	0.004(4)	0.003(4)	-0.003(4)
O3	0.048(5)	0.044(5)	0.032(4)	0.024(4)	-0.003(4)	0.002(4)
O4	0.048(5)	0.061(6)	0.028(4)	0.032(5)	-0.007(4)	-0.008(4)
O5	0.045(5)	0.045(5)	0.046(5)	0.024(4)	0.001(4)	-0.002(4)
O6	0.035(4)	0.046(5)	0.030(4)	0.018(4)	0.000(3)	0.006(3)
O7	0.049(5)	0.047(5)	0.032(5)	0.020(4)	-0.002(4)	0.004(4)
O8	0.047(5)	0.058(6)	0.042(5)	0.025(5)	0.011(4)	0.010(4)
O9	0.059(6)	0.071(7)	0.024(4)	0.029(5)	-0.002(4)	-0.005(4)
O10	0.038(5)	0.050(5)	0.030(4)	0.019(4)	-0.005(3)	-0.002(4)
O11	0.038(5)	0.053(6)	0.040(5)	0.021(4)	0.001(4)	0.004(4)
O12	0.055(6)	0.067(7)	0.052(6)	0.043(6)	0.005(5)	-0.014(5)
O13	0.038(5)	0.050(5)	0.040(5)	0.024(4)	-0.004(4)	-0.010(4)
O14	0.063(6)	0.041(5)	0.040(5)	0.027(5)	0.002(4)	0.002(4)
O15	0.035(5)	0.073(7)	0.039(5)	0.021(5)	-0.013(4)	-0.005(5)
O16	0.030(5)	0.055(6)	0.052(6)	0.006(4)	-0.006(4)	-0.004(4)
O17	0.066(7)	0.035(5)	0.054(6)	0.019(5)	0.007(5)	0.000(4)
O18	0.045(5)	0.045(5)	0.040(5)	0.022(4)	0.005(4)	0.003(4)
O19	0.053(6)	0.054(6)	0.046(5)	0.029(5)	0.004(4)	0.004(4)
O20	0.070(7)	0.072(7)	0.035(5)	0.041(6)	0.011(5)	0.024(5)
O21	0.13(2)	0.13(2)	0.6(1)	0.10(2)	0.05(2)	-0.049(2)
O22	0.06(1)	0.15(2)	0.34(4)	0.08(1)	0.05(2)	0.06(2)

Table 7.9: Selected bond distances for **2** and **3**

Bond distances	Bond Angles	
$Cs_5(V_{14}O_{22})(As_2O_5)_4Cl$ (**2**)		
V(1)-O(14) 1.61(1)	O(14)-V(1)-O(8) 108.5(6)	O(9)-V(5)-O(1) 90.1(5)
V(1)-O(8) 1.900(1)	O(14)-V(1)-O(27) 105.5(6)	O(3)-V(5)-O(1) 77.1(4)
V(1)-O(27) 1.93(1)	O(8)-V(1)-O(27) 84.3(5)	
V(1)-O(6) 1.99(1)	O(14)-V(1)-O(6) 109.2(6)	O(36)-V(6)-O(27) 109.4(5)
V(1)-O(33) 2.00(1)	O(8)-V(1)-O(6) 80.5(5)	O(36)-V(6)-O(11) 106.7(5)
	O(27)-V(1)-O(6) 145.1(4)	O(27)-V(6)-O(11) 143.8(5)
V(2)-O(42) 1.59(1)	O(14)-V(1)-O(33) 108.0(6)	O(36)-V(6)-O(40) 106.7(5)
V(2)-O(3) 1.97(1)	O(8)-V(1)-O(33) 142.9(4)	O(27)-V(6)-O(40) 89.9(5)
V(2)-O(5) 1.98(1)	O(27)-V(1)-O(33) 79.8(5)	O(11)-V(6)-O(40) 79.0(5)
V(2)-O(2) 1.99(1)	O(6)-V(1)-O(33) 93.8(5)	O(36)-V(6)-O(33) 104.2(5)
V(2)-O(1) 2.00(1)		O(27)-V(6)-O(33) 80.5(5)
	O(42)-V(2)-O(3) 106.6(6)	O(11)-V(6)-O(33) 91.4(5)
V(3)-O(22) 1.62(1)	O(42)-V(2)-O(5) 105.7(6)	O(40)-V(6)-O(33) 149.1(5)
V(3)-O(8) 1.92(1)	O(3)-V(2)-O(5) 92.5(5)	
V(3)-O(27) 1.93(1)	O(42)-V(2)-O(2) 107.9(6)	O(38)-V(7)-O(25) 107.4(6)
V(3)-O(5) 1.99(1)	O(3)-V(2)-O(2) 145.5(5)	O(38)-V(7)-O(28) 107.0(6)
V(3)-O(2) 2.00(1)	O(5)-V(2)-O(2) 78.3(4)	O(25)-V(7)-O(28) 84.6(5)
	O(42)-V(2)-O(1) 109.2(6)	O(38)-V(7)-O(39) 105.5(7)
V(4)-O(23) 1.62(1)	O(3)-V(2)-O(1) 76.9(4)	O(25)-V(7)-O(39) 89.8(5)
V(4)-O(9) 1.90(1)	O(5)-V(2)-O(1) 145.1(5)	O(28)-V(7)-O(39) 147.2(5)
V(4)-O(30) 1.92(1)	O(2)-V(2)-O(1) 91.7(5)	O(38)-V(7)-O(35) 105.8(6)
V(4)-O(20) 1.97(1)		O(25)-V(7)-O(35) 146.4(5)
V(4)-O(16) 2.012(9)	O(22)-V(3)-O(8) 106.9(5)	O(28)-V(7)-O(35) 90.0(5)
	O(22)-V(3)-O(27) 107.1(6)	O(39)-V(7)-O(35) 77.1(5)
V(5)-O(24) 1.60(1)	O(8)-V(3)-O(27) 83.8(4)	
V(5)-O(10) 1.91(1)	O(22)-V(3)-O(5) 105.8(6)	O(37)-V(8)-O(25) 110.5(5)
V(5)-O(9) 1.94(1)	O(8)-V(3)-O(5) 89.9(4)	O(37)-V(8)-O(10) 109.8(5)
V(5)-O(3) 1.97(1)	O(27)-V(3)-O(5) 146.9(5)	O(25)-V(8)-O(10) 139.7(5)
V(5)-O(1) 1.99(1)	O(22)-V(3)-O(2) 104.5(5)	O(37)-V(8)-O(7) 105.7(5)
	O(8)-V(3)-O(2) 148.3(4)	O(25)-V(8)-O(7) 91.0(5)
V(6)-O(36) 1.63(1)	O(27)-V(3)-O(2) 90.7(5)	O(10)-V(8)-O(7) 79.3(5)
V(6)-O(27) 1.90(1)	O(5)-V(3)-O(2) 77.9(4)	O(37)-V(8)-O(4) 104.2(5)
V(6)-O(11) 1.91(1)		O(25)-V(8)-O(4) 78.3(5)
V(6)-O(40) 1.99(1)	O(23)-V(4)-O(9) 108.7(5)	O(10)-V(8)-O(4) 90.8(5)
V(6)-O(33) 2.00(1)	O(23)-V(4)-O(30) 109.0(6)	O(7)-V(8)-O(4) 150.1(4)
	O(9)-V(4)-O(30) 142.3(5)	
V(7)-O(38) 1.59(1)	O(23)-V(4)-O(20) 104.2(5)	O(12)-V(9)-O(28) 111.0(6)
V(7)-O(25) 1.92(1)	O(9)-V(4)-O(20) 80.7(5)	O(12)-V(9)-O(8) 110.7(6)
V(7)-O(28) 1.92(1)	O(30)-V(4)-O(20) 91.0(5)	O(28)-V(9)-O(8) 138.3(5)
V(7)-O(39) 1.98(1)	O(23)-V(4)-O(16) 106.4(6)	O(12)-V(9)-O(6) 104.4(5)
V(7)-O(35) 2.00(1)	O(9)-V(4)-O(16) 89.1(5)	O(28)-V(9)-O(6) 90.2(5)
	O(30)-V(4)-O(16) 79.5(4)	O(8)-V(9)-O(6) 79.2(5)
V(8)-O(37) 1.60(1)	O(20)-V(4)-O(16) 149.3(5)	O(12)-V(9)-O(19) 105.7(5)
V(8)-O(25) 1.93(1)		O(28)-V(9)-O(19) 79.2(5)
V(8)-O(10) 1.95(1)	O(24)-V(5)-O(10) 108.4(6)	O(8)-V(9)-O(19) 90.0(5)
V(8)-O(7) 2.01(1)	O(24)-V(5)-O(9) 107.3(6)	O(6)-V(9)-O(19) 149.8(5)
V(8)-O(4) 2.02(1)	O(10)-V(5)-O(9) 82.0(5)	
	O(24)-V(5)-O(3) 108.6(6)	O(29)-V(10)-O(30) 107.4(6)
V(9)-O(12) 1.60(1)	O(10)-V(5)-O(3) 90.2(5)	O(29)-V(10)-O(11) 107.3(6)
V(9)-O(28) 1.90(1)	O(9)-V(5)-O(3) 143.9(5)	O(30)-V(10)-O(11) 84.3(5)
V(9)-O(8) 1.93(1)	O(24)-V(5)-O(1) 105.5(6)	O(29)-V(10)-O(18) 105.8(6)
V(9)-O(6) 2.01(1)	O(10)-V(5)-O(1) 146.1(5)	O(30)-V(10)-O(18) 90.0(5)
V(9)-O(19) 2.03(1)		

Table 7.9: Selected bond distances for **2** and **3** cont…

Bond Distances		Bond Angles	
V(10)-O(29) 1.59(1)	As(4)-O(33) 1.75(1)	O(11)-V(10)-O(18) 146.6(4)	O(31)-V(14)-O(25) 108.1(6)
V(10)-O(30) 1.94(1)	As(4)-O(32) 1.78(1)	O(29)-V(10)-O(34) 104.5(6)	O(31)-V(14)-O(28) 109.7(6)
V(10)-O(11) 1.94(1)	As(4)-O(34) 1.78(1)	O(30)-V(10)-O(34) 147.6(5)	O(25)-V(14)-O(28) 85.9(5)
V(10)-O(18) 1.99(1)		O(11)-V(10)-O(34) 91.7(5)	O(31)-V(14)-O(4) 105.6(6)
V(10)-O(34) 2.03(1)	As(5)-O(19) 1.74(1)	O(18)-V(10)-O(34) 75.8(4)	O(25)-V(14)-O(4) 80.0(5)
	As(5)-O(5) 1.76(1)		O(28)-V(14)-O(4) 144.5(5)
V(11)-O(26) 1.60(1)	As(5)-O(17) 1.81(1)	O(26)-V(11)-O(11) 109.5(5)	O(31)-V(14)-O(19) 107.6(6)
V(11)-O(11) 1.91(1)		O(26)-V(11)-O(30) 109.8(6)	O(25)-V(14)-O(19) 144.1(5)
V(11)-O(30) 1.91(1)	As(6)-O(6) 1.76(1)	O(11)-V(11)-O(30) 85.9(5)	O(28)-V(14)-O(19) 79.3(4)
V(11)-O(40) 1.99(1)	As(6)-O(35) 1.76(1)	O(26)-V(11)-O(40) 106.6(6)	O(4)-V(14)-O(19) 93.4(5)
V(11)-O(16) 2.00(1)	As(6)-O(32) 1.80(1)	O(11)-V(11)-O(40) 79.3(5)	
V(12)-O(41) 1.59(1)		O(30)-V(11)-O(40) 143.5(5)	O(2)-As(1)-O(40) 99.3(5)
V(12)-O(34) 1.97(1)	As(7)-O(20) 1.77(1)	O(26)-V(11)-O(16) 106.1(6)	O(2)-As(1)-O(15) 100.6(5)
V(12)-O(18) 1.97(1)	As(7)-O(18) 1.78(1)	O(11)-V(11)-O(16) 144.3(5)	O(40)-As(1)-O(15) 98.8(5)
V(12)-O(35) 1.99(1)	As(7)-O(21) 1.79(1)	O(30)-V(11)-O(16) 79.9(4)	
V(12)-O(39) 2.00(1)		O(40)-V(11)-O(16) 93.1(4)	O(16)-As(2)-O(1) 99.4(6)
	As(8)-O(39) 1.76(1)		O(16)-As(2)-O(15) 98.5(5)
V(13)-O(13) 1.615(9)	As(8)-O(21) 1.78(1)		O(1)-As(2)-O(15) 100.4(5)
V(13)-O(9) 1.92(1)	As(8)-O(7) 1.78(1)	O(41)-V(12)-O(34) 104.7(6)	
V(13)-O(10) 1.92(1)		O(41)-V(12)-O(18) 104.0(5)	O(4)-As(3)-O(3) 99.5(5)
V(13)-O(7) 1.96(1)	V(1)-V(3) 2.852(4)	O(34)-V(12)-O(18) 77.7(4)	O(4)-As(3)-O(17) 98.6(5)
V(13)-O(20) 1.98(1)	V(1)-V(6) 2.993(4)	O(41)-V(12)-O(35) 108.6(6)	O(3)-As(3)-O(17) 100.2(5)
	V(1)-V(9) 3.001(4)	O(34)-V(12)-O(35) 94.1(4)	O(33)-As(4)-O(32)100.2(5)
V(14)-O(31) 1.59(1)	V(2)-V(3) 3.091(3)	O(18)-V(12)-O(35) 147.4(5)	O(33)-As(4)-O(34) 100.0(5)
V(14)-O(25) 1.88(1)	V(2)-V(5) 3.100(3)	O(41)-V(12)-O(39) 106.1(6)	O(32)-As(4)-O(34) 98.7(6)
V(14)-O(28) 1.91(1)	V(4)-V(13) 2.965(4)	O(34)-V(12)-O(39) 149.2(5)	
V(14)-O(4) 2.00(1)	V(4)-V(11) 3.009(3)	O(18)-V(12)-O(39) 94.2(4)	O(19)-As(5)-O(5) 99.9(5)
V(14)-O(19) 2.02(1)	V(5)-V(13) 2.895(4)	O(35)-V(12)-O(39) 76.7(5)	O(19)-As(5)-O(17) 98.8(5)
	V(6)-V(11) 3.005(3)	(13)-V(13)-O(9) 109.2(6)	O(5)-As(5)-O(17) 99.4(5)
As(1)-O(2) 1.76(1)	V(7)-V(14) 2.804(4)	O(13)-V(13)-O(10) 109.2(6)	O(6)-As(6)-O(35) 100.0(5)
As(1)-O(40) 1.77(1)	V(7)-V(12) 3.120(4)	O(9)-V(13)-O(10) 82.3(4)	O(6)-As(6)-O(32) 100.5(6)
As(1)-O(15) 1.80(1)	V(8)-V(13) 2.994(4)	O(13)-V(13)-O(7) 107.0(6)	O(35)-As(6)-O(32) 98.9(6)
	V(8)-V(14) 3.012(4)	O(9)-V(13)-O(7) 143.5(4)	
As(2)-O(16) 1.75(1)	V(9)-V(14) 3.026(4)	O(10)-V(13)-O(7) 81.2(5)	O(20)-As(7)-O(18) 99.3(5)
As(2)-O(1) 1.76(1)	V(10)-V(11) 2.835(4)	O(13)-V(13)-O(20) 107.0(6)	O(20)-As(7)-O(21) 100.2(5)
As(2)-O(15) 1.82(1)	V(10)-V(12) 3.113(4)	O(9)-V(13)-O(20) 80.2(5)	O(18)-As(7)-O(21) 98.8(5)
		O(10)-V(13)-O(20) 143.3(5)	
As(3)-O(4) 1.75(1)		O(7)-V(13)-O(20) 94.2(4)	O(39)-As(8)-O(21) 98.9(5)
As(3)-O(3) 1.79(1)			O(39)-As(8)-O(7) 100.2(5)
As(3)-O(17) 1.80(1)			O(21)-As(8)-O(7) 100.3(5)

$Cs_5(V_{14}O_{34})(AsO_3)_2Cl•2.6H_2O$ (**3**)			
V(1)-O(8) 1.61(1)	V(3)-O(12) 1.598(9)	O(8)-V(1)-O(5) 104.3(5)	O(9)-V(2)-O(10) 106.0(5)
V(1)-O(5) 1.77(1)	V(3)-O(14) 1.82(1)	O(8)-V(1)-O(14) 102.9(5)	O(9)-V(2)-O(7)105.0(5)
V(1)-O(14) 1.81(1)	V(3)-O(5) 1.82(1)	O(5)-V(1)-O(14) 98.5(4)	O(10)-V(2)-O(7) 95.5(4)
V(1)-O(7) 1.976(9)	V(3)-O(10) 1.934(9)	O(8)-V(1)-O(7) 102.3(5)	O(9)-V(2)-O(1) 107.6(5)
V(1)-O(6) 2.014(9)	V(3)-O(13) 1.95(1)	O(5)-V(1)-O(7) 150.6(4)	O(10)-V(2)-O(1) 94.8(4)
		O(14)-V(1)-O(7) 87.6(4)	O(7)-V(2)-O(1) 141.5(4)
V(2)-O(9) 1.601(9)	V(4)-O(15) 1.584(9)	O(8)-V(1)-O(6) 101.4(5)	O(9)-V(2)-O(11) 104.1(5)
V(2)-O(10) 1.706(9)	V(4)-O(11) 1.80(1)	O(5)-V(1)-O(6) 89.8(4)	O(10)-V(2)-O(11) 149.9(4)
V(2)-O(7) 1.91(1)	V(4)-O(4) 1.815(9)	O(14)-V(1)-O(6) 151.5(4)	O(7)-V(2)-O(11) 76.7(4)
V(2)-O(1) 1.927(9)	V(4)-O(7) 1.88(1)	O(7)-V(1)-O(6) 72.8(4)	O(1)-V(2)-O(11) 75.9(4)
V(2)-O(11) 2.00(1)	V(4)-O(6) 1.900(9)		

Table 7.9: Selected bond distances for **2** and **3** cont…

Bond distances	Bond Angles	
V(5)-O(17) 1.58(1)	O(12)-V(3)-O(14) 103.6(5)	O(19)-V(5)-O(4) 88.6(4)
V(5)-O(18) 1.78(1)	O(12)-V(3)-O(5) 104.8(5)	O(17)-V(5)-O(3) 104.0(5)
V(5)-O(19) 1.80(1)	O(14)-V(3)-O(5) 92.4(4)	O(18)-V(5)-O(3) 86.4(4)
V(5)-O(4) 1.98(1)	O(12)-V(3)-O(10) 101.7(5)	O(19)-V(5)-O(3) 150.6(4)
V(5)-O(3) 2.016(9)	O(14)-V(3)-O(10) 85.7(4)	O(4)-V(5)-O(3) 73.2(4)
	O(5)-V(3)-O(10) 153.1(4)	
V(6)-O(16) 1.601(9)	O(12)-V(3)-O(13) 103.0(5)	O(16)-V(6)-O(13) 107.0(5)
V(6)-O(13) 1.683(9)	O(14)-V(3)-O(13) 152.9(4)	O(16)-V(6)-O(6) 103.3(5)
V(6)-O(6) 1.890(9)	O(5)-V(3)-O(13) 85.9(4)	O(13)-V(6)-O(6) 95.5(5)
V(6)-O(3) 1.968(9)	O(10)-V(3)-O(13) 83.8(4)	O(16)-V(6)-O(3) 107.7(5)
V(6)-O(4) 1.98(1)		O(13)-V(6)-O(3) 95.8(4)
	O(15)-V(4)-O(11) 107.0(5)	O(6)-V(6)-O(3) 142.1(4)
V(7)-O(20) 1.58(1)	O(15)-V(4)-O(4) 108.8(5)	O(16)-V(6)-O(4) 106.2(5)
V(7)-O(19) 1.79(1)	O(11)-V(4)-O(4) 99.4(5)	O(13)-V(6)-O(4) 146.9(4)
V(7)-O(18) 1.80(1)	O(15)-V(4)-O(7) 106.7(5)	O(6)-V(6)-O(4) 76.6(4)
V(7)-O(11) 2.01(1)	O(11)-V(4)-O(7) 82.5(4)	O(3)-V(6)-O(4) 74.2(4)
V(7)-O(1) 2.02(1)	O(4)-V(4)-O(7) 142.1(4)	
	O(15)-V(4)-O(6) 105.7(5)	O(20)-V(7)-O(19) 103.5(5)
As-O(2) 1.75(1)	O(11)-V(4)-O(6) 145.3(4)	O(20)-V(7)-O(18) 104.9(6)
As-O(3) 1.790(9)	O(4)-V(4)-O(6) 80.5(4)	O(19)-V(7)-O(18) 97.6(5)
As-O(1) 1.798(9)	O(7)-V(4)-O(6) 77.4(4)	O(20)-V(7)-O(11) 104.8(5)
		O(19)-V(7)-O(11) 86.9(4)
V(1)-V(4) 3.075(3)	O(17)-V(5)-O(18) 104.6(5)	O(18)-V(7)-O(11) 148.0(4)
V(2)-V(4) 2.920(3)	O(17)-V(5)-O(19) 103.4(5)	O(20)-V(7)-O(1) 103.7(5)
V(4)-V(6) 2.937(3)	O(18)-V(5)-O(19) 97.1(5)	O(19)-V(7)-O(1) 149.8(4)
	O(17)-V(5)-O(4) 106.8(5)	O(18)-V(7)-O(1) 87.8(4)
	O(18)-V(5)-O(4) 145.8(4)	O(11)-V(7)-O(1) 73.7(4)
		O(2)-As-O(3) 95.4(4)
		O(2)-As-O(1) 96.1(5)
		O(3)-As-O(1) 95.4(4)

Here a new noncentrosymmetric salt-inclusion compound, $Cs_5(V_{14}O_{22})(As_2O_5)_4Cl$ (**2**), containing a $[V_{14}As_8O_{42}]^{4-}$ core is presented. This core has been observed in several materials such as $[NH_2(CH_2CH_2)_2NH_2]_3[As_8V_{14}O_{42}(SO_4)]\bullet 6.5H_2O$, $[Cd(en)_2]_2[(en)_2Cd_2As_8V_{12}O_{40}]$, and $[Co(2,2\text{-bpy})_2]_2[As_8V_{14}O_{42}(H_2O)]\bullet H_2O$.[26] Compound **2**, shown in Figure 7.11, crystallizes in an orthorhombic crystal system in the spacegroup, *Pn*a2$_1$ (no. 33). This spacegroup is found in one of ten polar crystal classes, *mm*2, (C_{2v}).[27] Within the unit cell, there are fourteen crystallographically distinct V atoms, all of which are in a square pyramidal geometry and a 4+ oxidation state. The oxidation state is further supported through bond valence sum calculations shown in Table 7.10.[18] The vanadium polyhedra have short vanadyl V=O bonds, ranging from 1.59-1.62Å, that point into the space between the clusters. A polyhedral view of the $[V_{14}As_8O_{42}]$ core is shown in Figure 7.12. Like the V_{15} core seen in **1**, this cluster also forms a cage-like aggregate that encapsulates a chlorine. Within the cluster there are four VO_5 polyhedra sharing three edges and ten VO_5 polyhedra sharing two opposite edges. This connectivity gives rise to eight μ_3-oxo bridges and 16 μ_2-oxo bridges. A polyhedral view of the core, shown in Figure 7.13, reveals eight edge-sharing polyhedra that form a belt around the center of the cluster. Four of the eight polyhedra, V(1), V(11), V(13), and V(14), share an additional edge above or below the plane of the ring with V_3O_{11} capping units, Figure 7.14, which are rotated 90° with respect to one another. Within the cluster there are a few short V-V distances, 2.835(4) -3.120(4)Å, that result from edge-sharing polyhedra. The cluster can be inverted by a 90° (C_4) rotation, followed by a mirror plane

Table 7.10: Bond valence sum calculations for **2** and **3**

$Cs_5(V_{14}O_{22})(As_2O_5)_4Cl$ (**2**)							
Atom	V(1)	V(2)	V(3)	V(4)	V(5)	V(6)	V(7)
BVS for **2**	1.62	1.70	1.57	1.55	1.65	1.53	1.70
for V^{4+}	0.73	0.61	0.70	0.72	0.72	0.74	0.70
	0.67	0.59	0.67	0.69	0.65	0.70	0.68
	0.57	0.57	0.57	0.60	0.61	0.57	0.59
	0.56	0.56	0.56	0.54	0.57	0.56	0.56
	= 4.15	= 4.02	= 4.06	= 4.11	= 4.20	= 4.10	=4.23
Atom	V(8)	V(9)	V(10)	V(11)	V(12)	V(13)	V(14)
BVS for **2**	1.66	1.62	1.68	1.64	1.71	1.58	1.70
for V^{4+}	0.68	0.72	0.66	0.72	0.61	0.70	0.77
	0.64	0.67	0.66	0.71	0.60	0.69	0.71
	0.55	0.54	0.57	0.58	0.57	0.63	0.56
	0.53	0.51	0.51	0.55	0.55	0.58	0.53
	= 4.06	= 4.07	= 4.08	= 4.19	= 4.04	= 4.18	= 4.26
$Cs_5(V_{14}O_{34})(AsO_3)_2Cl•2.6H_2O$ (**3**)							
Atom	V(1)	V(2)	V(3)	V(4)	V(5)	V(6)	V(7)
BVS for **3**	1.67	1.73	1.74	1.81	1.84	1.73	1.84
for V^{5+}	1.08	1.30	0.96	1.01	1.07	1.38	1.03
	0.97	0.74	0.95	0.97	1.01	0.79	1.00
	0.63	0.72	0.70	0.80	0.62	0.64	0.58
	0.57	0.58	0.67	0.77	0.56	0.62	0.55
	= 4.92	= 5.07	= 5.02	= 5.36	= 5.10	= 5.12	= 5.00

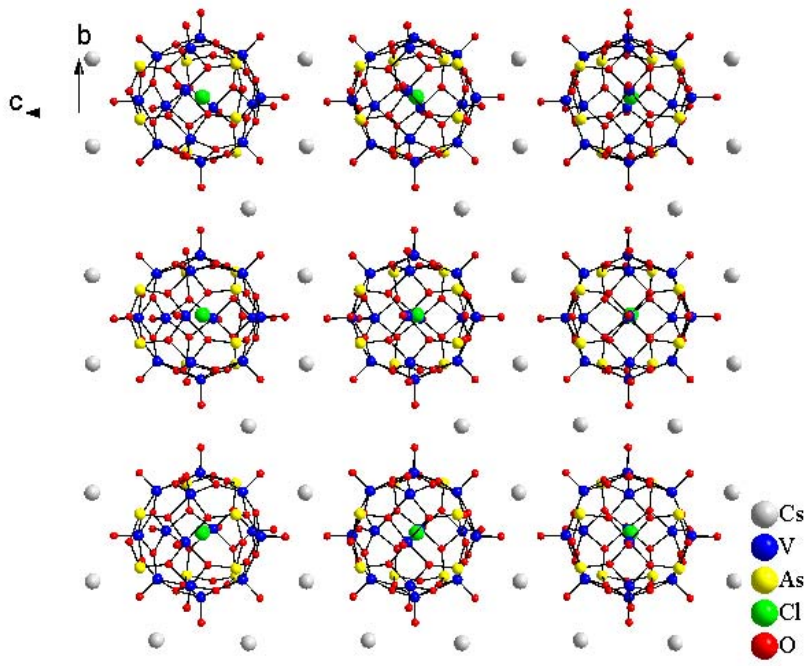

Figure 7.11: Perspective view showing extended structure of $Cs_5(V_{14}O_{16})(AsO_3)_8Cl$. Each $[V_{14}As_8O_{42}Cl]^{5-}$ cluster is surrounded by Cs cations.

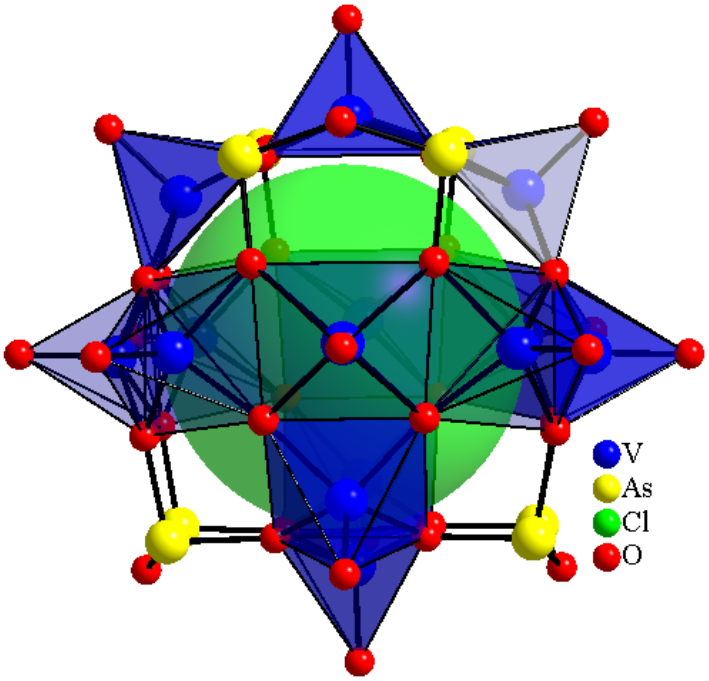

Figure 7.12: Polyhedral view of the Cl-centered $[V_{14}As_8O_{42}]^{4-}$,V_{14}, cluster. The cluster is capped with eight AsO_3 polyhedra.

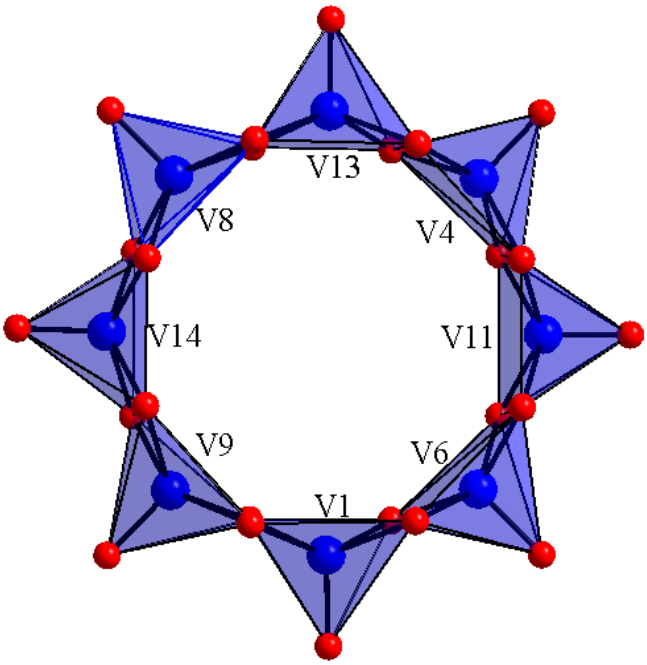

Figure 7.13: Polyhedral view showing eight edge-sharing square pyramids that form a ring around the center of each $[V_{14}As_8O_{42}Cl]^{5-}$ core.

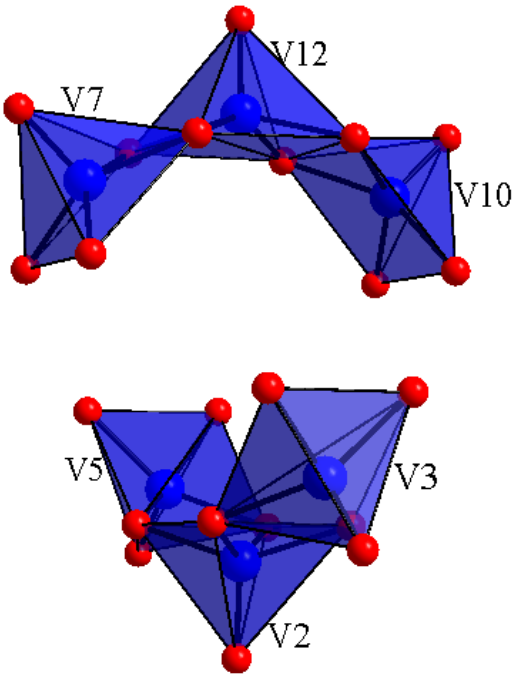

Figure 7.14: Partial structure of the $[V_{14}As_8O_{42}Cl]^{5-}$ core. The polyhedral view shows two capping V_3O_{11} units found above and below the 8-membered ring.

perpendicular (σ_h) to the rotation axis. This gives rise to S_4 point symmetry. As shown in Figure 7.12, each cluster is capped by eight trigonal $(AsO_3)^{3-}$ polyhedra that share two of three corner oxygen atoms with neighboring V cations and the other O atom with neighboring As atoms. The As^{3+} atoms have a lone pair of electrons that point into the space between clusters. The Cl anion, encapsulated by the $[V_{14}As_8O_{42}]^{4-}$ cage, has large thermal parameters, shown in Table 7.8, a direct result of the atom's thermal motion within the cage. According to the crystal structure solution, Cl^- is not significantly close to any of the atoms forming the cage. The shortest V-Cl distance, 3.612(1)Å, is still significantly longer than what is expected from the Shannon Crystal Radii, 2.39Å, for six-coordinate V^{4+} and Cl^-. These long distances allow the Cl to rattle around inside the cage, giving rise to smeared-looking electron density. Due to its long distances from neighboring atoms, the occupancy of Cl was refined to determine if Cs could be present in the site. The occupancy remained one, indicating a fully occupied Cl site. It should also be noted that EDX showed Cl present in the crystal structure and the other sites in the compound are clearly Cs sites based on the bond distances with surrounding oxygen atoms. Other materials containing the $V_{14}As_8O_{42}$ cluster have also reportedly encapsulated a variety of guests such as water molecules and SO_4^{2-} anions.[28]

Due to the large observed distances between the Cl and V atoms, it was suspected that the V_{14} cage could serve as a host for other larger anions. As a result, efforts were made to synthesize I-and Br-containing derivatives using a stoichiometric synthesis. The powder patterns obtained from the resulting products are comparable to the calculated powder pattern of $Cs_5(V_{14}O_{22})(As_2O_5)_4Cl$, Figure 7.10, showing very few impurity peaks.

Upon substitution of larger anions, the powder patterns of most materials would show a shift to a lower 2θ angle, indicating an increase in unit cell parameters. However, since the observed V-Cl distances are already long and the cage is expected to be rigid, it is expected that the Br and I anions should be easily incorporated with very little change in the unit cell parameters, creating a good agreement between the calculated powder pattern of $Cs_5(V_{14}O_{22})(As_2O_5)_4Cl$ and the observed PXRD pattern of the two analogs $Cs_5(V_{14}O_{22})(As_2O_5)_4Br$ and $Cs_5(V_{14}O_{22})(As_2O_5)_4I$. Efforts were made to refine the unit cell parameters of the Cl-, Br-, and I- containing derivatives. The results can be seen in Figure 7.10. The refined cell parameters show similar values with volumes of 4946(3)Å^3, 4965(3)Å^3, and 4966(2)Å^3 for the powder patterns of the Cl-, Br-, and I-containing derivatives respectively.

Like compound **1**, **2** is also water soluble. After dissolution of the reddish brown powder, the solution changes from light brown to dark green within a few hours, possibly indicating a decomposition of **2**. Over the next few days the solution changes again, this time from dark green to bright yellow, and green plate-like crystals begin to fall out of solution. Single crystals of the material, examined *via* X-ray diffraction, were determined to be $Cs_5(V_{14}O_{40})(AsO_3)_2Cl•2.6H_2O$, **3**. The crystallographic data, anisotropic thermal parameters, and selected bond distances and angles can be seen in Tables 7.6-7.9. Compound **3**, shown in Figure 7.15, crystallizes in a trigonal crystal system in spacegroup $P3_121$ (no. 152) with a = 13.115(2)Å and c = 25.527(5)Å. This noncentrosymmetric spacegroup is found in one of eleven nonpolar crystal classes, *32*, (D_3).[27] Compound **3** is made up of a fully oxidized $[V_{14}As_2O_{40}]^{4-}$ core, Figure 7.16,

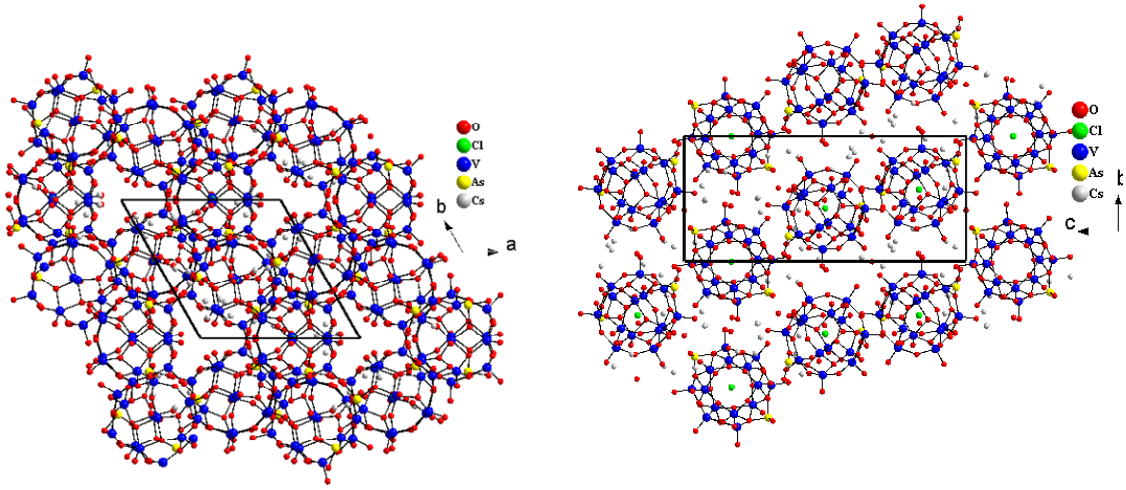

Figure 7.15: Perspective view of the extended structure of $Cs_5(V_{14}O_{34})(AsO_3)_2Cl\bullet 2.6H_2O$, along the crystallographic a and c axes. The discrete $[V_{14}As_2O_{40}Cl]^{5-}$ clusters are surrounded by Cs cations.

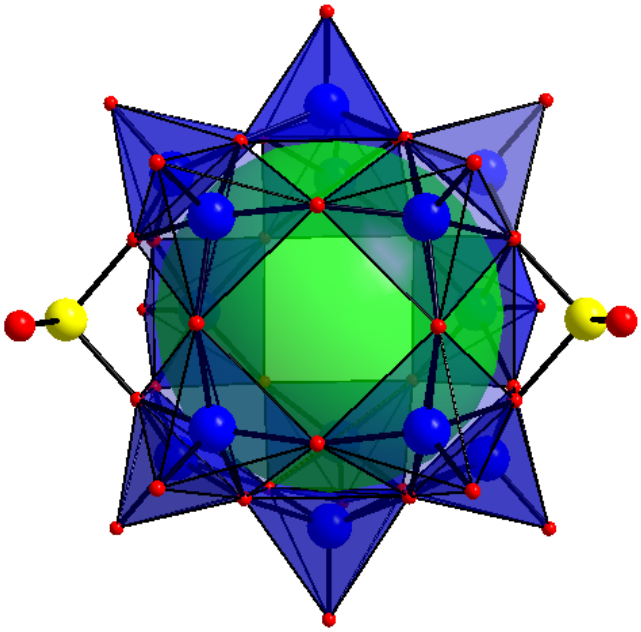

Figure 7.16: Close-up polyhedral view of an individual $[V_{14}As_2O_{40}Cl]^{5-}$cluster.

which has never before been observed in polyoxometalate chemistry. Even though both **2** and **3** contain a V_{14} core, a direct structural correlation could not be found between the 2 clusters. Therefore, it is suspected that instead of a simple rearrangement upon oxidation, the $[V_{14}As_8O_{42}]^{4-}$ core could completely decompose before the formation of $[V_{14}As_2O_{40}]^{4-}$.

The cluster in **2** has seven crystallographically distinct vanadium atoms, all of which are found in a square pyramidal geometry with short apical vanadyl bonds, ranging from 1.58-1.61Å, that point into the space between clusters. The vanadium cations are now fully oxidized to a 5+ state, which is further supported by bond valence sum calculations shown above, Table 7.10.[18] There is a single crystallographically distinct As^{3+} atom that is trigonally coordinated by oxygen and has a lone pair of electrons also pointing into the space between clusters. To aid in the structure description, $[V_{14}As_2O_{40}]^{4-}$ has been broken down into individual components including one $V_6As_2O_{24}$ belt that runs around the center of the cluster and two V_4O_{16} caps that are found above and below the plane of the belt (Figures 7.17 and 7.18 respectively). The eight-membered $V_6As_2O_{24}$ ring can be further divided into two V_3O_{11} constituents consisting of three edge-sharing VO_5 polyhedra, $V(2)O_5$, $V(4)O_5$, and $V(7)O_5$. The two trimeric units are bridged via corner sharing oxygen with two AsO_3 polyhedra. Within these units there are short V-V distances that range from 2.920(3)- 3.075(3)Å, resulting from edge-sharing polyhedra. The AsO_3 units each have a nonbridging oxygen which points in a unique direction with respect to one another. The two tetrameric V_4O_{16} capping units consist of V(1) and V(6) or V(3) and V(5) and have longer V-V distances,

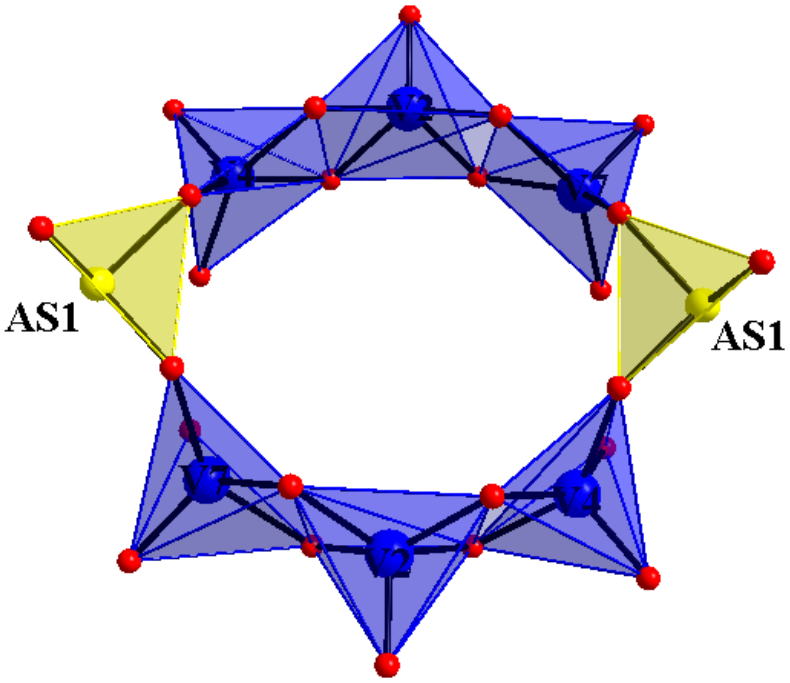

Figure 7.17: Polyhedral view of two V_3O_{11} units interlinked *via* two corner-sharing AsO_3 trigonal prisms. This connectivity forms a $V_6As_2O_{24}$ belt that goes around the center of cluster in **3**.

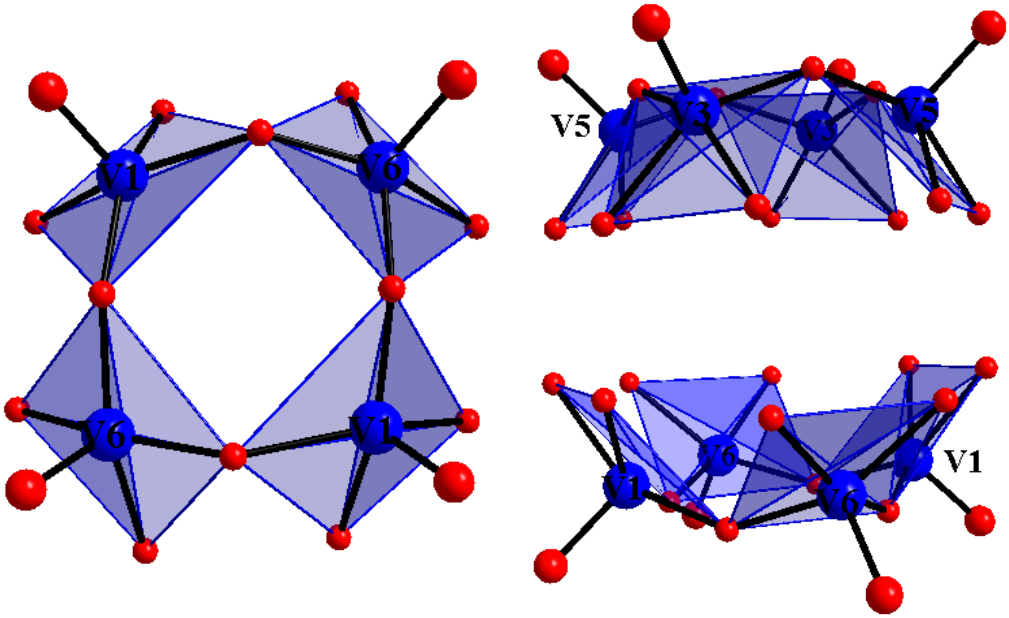

Figure 7.18: (left) Polyhedral view showing a single V_4O_{16} capping unit from above. The image on the right shows two V_4O_{16} units that sit above and below the plane of the $V_6As_2O_{24}$ belt. The units are shifted 45° with respect to one another.

from 3.401(3)-3.455(3)Å, resulting from corner-sharing polyhedra. These square pyramids share two cis oxygen atoms with neighboring polyhedra forming the bowl-like caps. The cap containing V(1) and V(6) shares two edges with VO_5 polyhedra found in the belt while the other cap, containing V(3) and V(5), shares four edges with the remaining VO_5 polyhedra in the belt. Within the cluster, the two caps are rotated 45° with respect to one another. The connectivity between the VO_5 polyhedra gives rise to eight μ_3-oxo bridges and sixteen μ_2-oxo bridges within each cluster. As observed for compound **1** and **2**, the spherical aggregate found in **3** also encapsulates a Cl^- anion, Figure 7.16. The anion is loosely coordinated to surrounding V cations. The shortest V-Cl distances are 3.402(1), 3.566(1), 3.617(1), 3.526(1), and 3.638(1) Å for V(1), V(2), V(4), V(6), and V(7) respectively. These distances, like those observed for **2**, are quite a bit longer than what is expected from the Shannon Crystal Radii, 2.35Å, for 6 coordinate V^{5+} and Cl^-. The cluster has a C_2 rotation and a mirror plane (σ_v) that is parallel to this principal rotation axis, giving rise to C_{2v} point symmetry.

Figure 7.11, showing the extended structure of **3**, reveals that each cluster is surrounded by five charge-balancing Cs cations and water molecules. It should be noted that the Cs and water molecules are disordered. Also, the thermal ellipsoids of several of these atoms appear to be elongated, possibly due to a large amount of disorder around the cluster. In the structure refinement, several of the Cs sites were split into two or more sites to account for the smeared electron density, however, the elongations still persist. Most likely these atoms are so severely disordered within the structure that SHELX cannot nail down specific atomic coordinates. As a result, several atoms, Cs(2)-Cs(6)

and O(21)and O(22), were left with abnormal thermal parameters. It should also be noted that O(21) and O(22) are both water molecules. The atomic coordinates of the H sites have not been determined, however these were defined as water due to their isolation in the structure. The O(21) and O(22) are found closest to Cs atoms and their distances are as follows: O(21)-Cs(3) 3.76(3)Å, O(21)-Cs(5) 2.76(3)Å, O(22)-Cs(4) 2.90(3)Å, O(22)-Cs(1) 3.15(4)Å, and O(22)-Cs(6) 3.66(5) Å. Due to some close Cs-Cs distances and the disorder found around the atom sites, SHELXTL was allowed to refine the occupancies of the Cs cations and the water molecules generating a charge-balanced structure solution.

After determining that $Cs_5[V_{14}As_8O_{42}Cl]$ could be dissolved in solution and a new cage-like chlorine centered cluster would form, $[V_{14}As_2O_{40}Cl]^5$, a follow up experiment was planned to see if the $[V_{14}As_8O_{42}Br]^{5-}$ and $[V_{14}As_8O_{42}I]^{5-}$ clusters would exhibit a similar behavior. The major draw to this experiment was to prove that the I^- and Br^- were actually encapsulated in the V_{14} core. Although the powder patterns of these two derivatives matched the calculated powder pattern of $Cs_5[V_{14}As_8O_{42}Cl]$, there was still no single crystal evidence to prove so. Also, the salt flux reactions used to grow crystals of the phases were unsuccessful. It was thought that the original cluster, $[V_{14}As_8O_{42}Cl]^{5-}$, was undergoing an oxidative decomposition in solution. Although the source of the oxidative decomposition was not known, it was thought that if the environmental factors that could be responsible for the oxidation of $[V_{14}As_8O_{42}Cl]^{5-}$ were minimized, then the original cluster could possibly be re-isolated from solution. A small amount of powder obtained from the high yield reactions targeting $Cs_5[V_{14}As_8O_{42}Br]$ and $Cs_5[V_{14}As_8O_{42}I]$,

Figure 7.10, were dissolved in water. The excess powder was removed with a 0.2μ syringe. The solution was place inside of a vacuum oven, which was then covered to limit the amount of light coming in contact with the sample. The vacuum was pumped overnight and the next morning both vials contained small reddish-brown single crystals. SXRD was used to analyze the product. The crystallized material, although it had a different crystal structure, contained the same $[V_{14}As_8O_{42}Br]^{5-}$ and $[V_{14}As_8O_{42}I]^{5-}$ cores. The analyzed materials were found to crystallize in the spacegroup *C* 1 2/c 1 (no. 15) with unit cell dimensions *a* = 13.454(5) Å, *b* = 19.222(4) Å, *c* = 22.564(4) Å, β = 98.98(4) °, and V=5764(3) Å for the Br^- derivative, $Cs_5(V_{14}As_8O_{42}Br)\bullet 1.5\ H_2O$, and *a* = 13.483(3) Å, b = 19.296(4) Å, *c* = 22.542(5) Å, β = 98.71(3) °, and V =5797(2) $Å^3$ for the I- derivative $Cs_5(V_{14}As_8O_{42}I)\bullet 1.5\ H_2O$. Figure 7.19 shows a projected view of $Cs_5[V_{14}As_8O_{42}Br]\bullet 1.5\ H_2O$. The clusters are surrounded by Cs^+ cations and water molecules. A close-up view of the Br-containing cluster $[V_{14}As_8O_{42}Br]$ can be seen in Figure 7.20. This cluster contains eight crystallographically distinct V^{4+} cations, all of which are in a square pyramidal geometry. The short vanadyl V=O bonds point away from the core, allowing the formation of the spherical aggregate. The V-Br distances, which range from 3.67(7)-3.89(4)Å are much longer than the expected sum of Shannon crystal radii, 2,54 Å, of six-coordinate V (0.72Å) and Cl (1.82 Å).

Magnetic measurements were performed on a powder sample obtained from the 100% yield synthesis of compound **2**. Figure 7.21 shows the molar magnetic susceptibility, χ, and the inverse molar magnetic susceptibility, χ^{-1}, of **2** acquired with an applied field of 0.01T. χ shows an increase in the susceptibility upon decreasing the

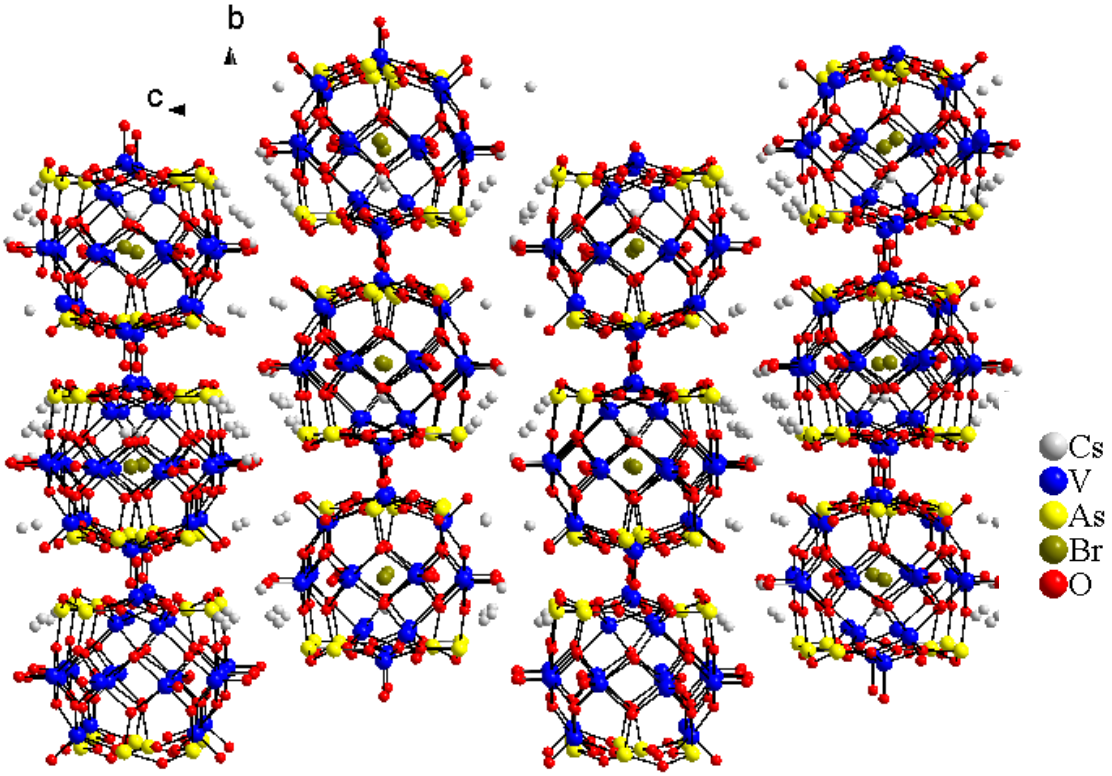

Figure 7.19: Projected view of $Cs_5(V_{14}As_8O_{42}Br)$•1.5 H_2O. The clusters are surrounded by Cs^+ cations and water molecules.

Bond Distances (Å) for CsBr derivative
V(1)-Br = 3.75(3)
V(2)-Br = 3.86(6)
V(3)-Br = 3.89(4)
V(4)-Br = 3.74(4)
V(5)-Br = 3.96(8)
V(6)-Br = 3.67(7)
V(7)-Br = 3.95(5)
V(8)-Br = 3.69(7)

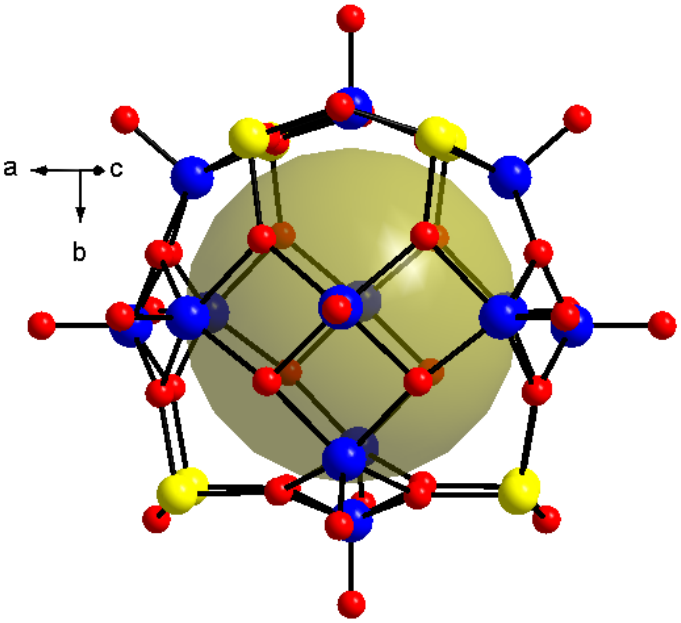

Figure 7.20: Views of the $[V_{14}As_8O_{42}Br]^{5-}$ core. The Br-centered core has eight crystallographically distinct V sites which are found in a square pyramidal geometry. The V-Br distances are highlighted in green.

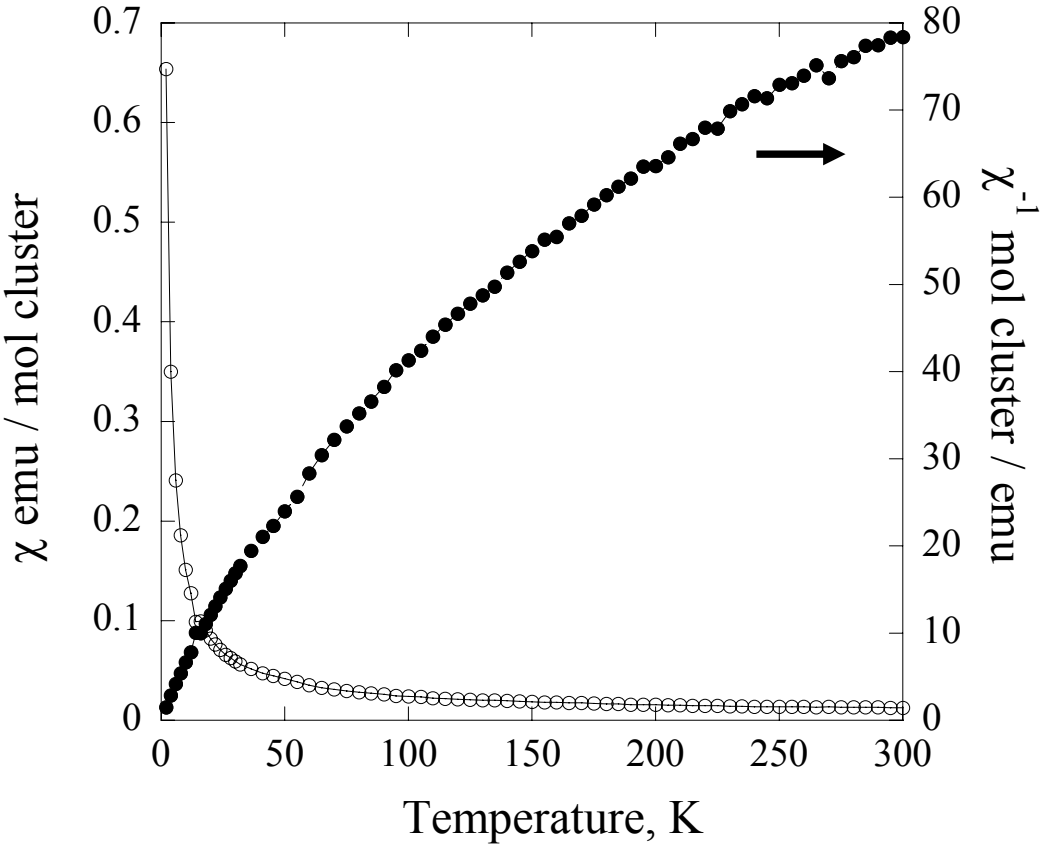

Figure 7.21: Molar magnetic susceptibility and inverse molar magnetic susceptibility for compound **2** at an applied field of 0.01T.

temperature, similar to what is expected for paramagnetic materials. However, based on the multiple μ_2 and μ_3 oxygen-bridging modes within the cluster. some magnetic exchange is expected. The high temperature data from the inverse molar magnetic susceptibility, ranging from 100-300K, was fit using the Curie-Weiss Law. The $u_{eff,}$, calculated to be 1.73(3)μ_B, is proportional to the expected spin-only value for V^{4+}, d^1, 1.73μ_B. The negative Weiss constant, θ, calculated to be -131(6)K, indicates strong antiferromagnetic exchange between nearest neighbors at high temperature. Field dependent studies were performed on compound **2**, Figure 7.22. Fields ranging from ±5T were applied at 2K. This plot shows an s-shaped curve which reaches a maximum of approximately 3μ_B / cluster at a maximum applied field of 5T. Based on the oxidation states of the V cations found in the cluster, the maximum magnetization response expected would be approximately 14μ_B / cluster.

$Na_{35.5}Cu_{27.75}O_8(AsO_4)_{16}Cl_{11}$**, 4**, $K_{3.29}Na_{32.21}Cu_{27.75}O_{16}(AsO_4)_{16}Cl_{11,}$ **5**, and $Na_{36}Cu_{28}O_{16}(AsO_4)_{16}Cl_{12,}$ **6**

Synthesis

Single Crystal Synthesis of 4-6: BaO, Na_2O_2, CuO, and As_2O_5 were mixed in a 1:4:6:3 mol ratio and placed in a CsCl/NaCl eutectic flux equal to three times the mass of the oxide reactants. The starting materials were ground together in a nitrogen-purged drybox, loaded into a carbon coated quartz ampoule, and then sealed under vacuum. The reaction was heated to 300°C at a rate of 0.5°C/min, held there for 6 hours, heated to 450°C at a rate of 0.5°C/min, held there for 6 hours, heated to at 1°C/min 650°C, held

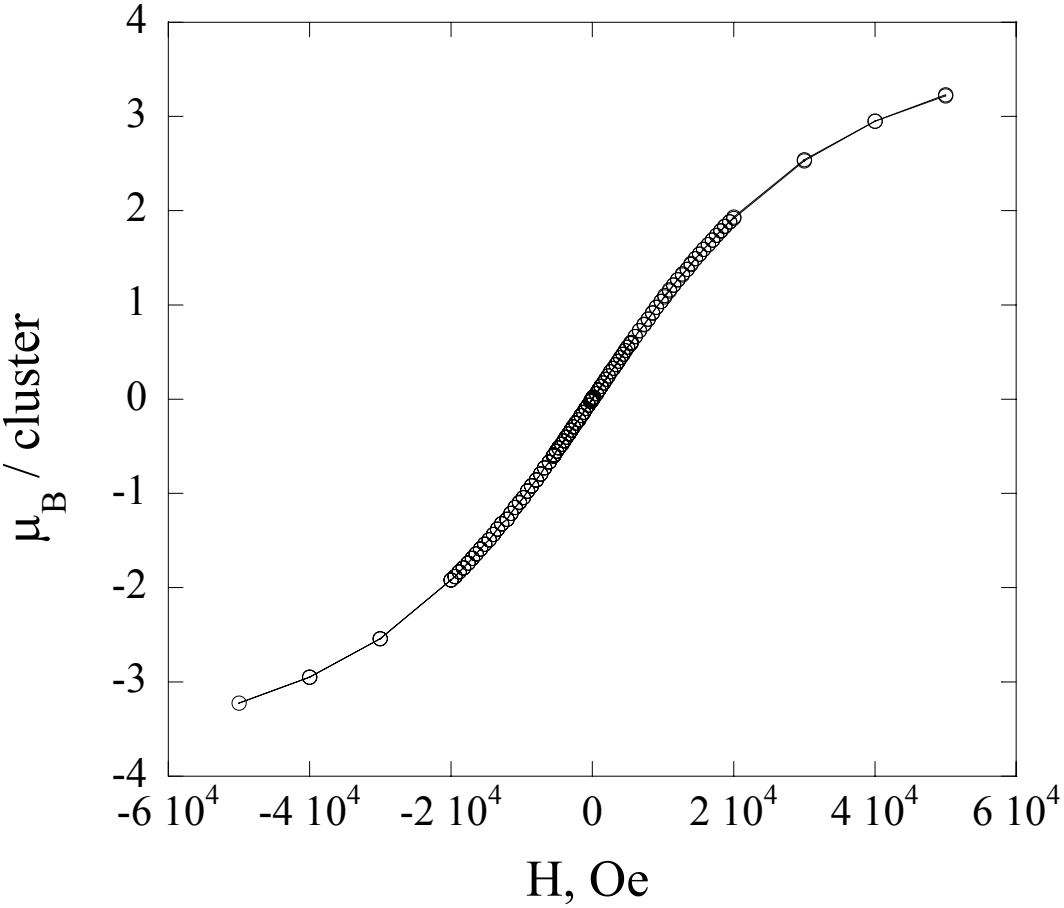

Figure 7.22: Field-dependent magnetization plot for compound **2** at 2K.

there for 4 days, followed by slow cooling to 450°C at a rate of 0.1°C/min, and then furnace-cooled to room temperature. After washing the reaction with deionized water, small green cubic crystals of $Na_{36}Cu_{28}O_{16}(AsO_4)_{16}Cl_{12}$ and $Na_{35.5}Cu_{27.75}O_8(AsO_4)_{16}Cl_{11}$ were obtained in a very low yield, < 5%. Other crystalline phases found within the reaction included $NaCu(AsO_4)$, $Ba_5Cl(AsO_4)_3$, and $Ba_5Na_{14}Cu_{12}(AsO_4)_{16}$. It should be noted that this reaction was originally loaded in an effort to grow single crystals of $BaNa_8Cu_6O_2(PO_4)_6$, for magnetic studies. The target compound did form, but in a very low yield. Compound **5**, $K_{3.29}Na_{32.21}Cu_{27.75}O_{16}(AsO_4)_{16}Cl_{11}$, was made using the same reaction described above, but the flux was changed from CsCl/NaCl to CsCl/KCl and the maximum isotherm temperature was changed from 650°C to 750°C, approximately 150°C above the melting point of the CsCl/KCl mixture. Green cubic crystals of $K_{3.29}Na_{32.21}Cu_{27.75}O_{16}(AsO_4)_{16}Cl_{11}$ were also obtained after washing with deionized water in a low yield, < 5%.

High Yield Synthesis of 4 and 6: To make a high yield of $Na_{35.5}Cu_{27.75}O_8(AsO_4)_{16}Cl_{11}$, **4**, and $Na_{36}Cu_{28}O_8(AsO_4)_{16}Cl_{12}$, **6**, stoichiometric reactions were loaded using Na_2O, CuO, As_2O_5, Cu, and NaCl mixed in 12.25:26.035:8:1.715:11 and 26.32:8:12:1.68:12 mol ratios (ca. 0.5grams) for **4** and **6** respectively. Cu powder was used in order to account for a 14% Na_2O_2 impurity in Na_2O. All reactants were ground in a nitrogen-purged drybox and place in silica ampoules. They were heated to 800°C at a rate of 3°C/min. and held there for 4 days. The reaction was then cooled to 450°C at a rate of 0.1 °C/min. and then furnace-cooled to room temperature. It should be noted that there is very little difference in the compositions of **4** and **6.** Even though

these two phases were targeted individually through two different stoichiometric reactions, both phases were observed in the powder patterns shown in Figure 7.23. In both cases, the dominate phase formation was the targeted compound. The stoichiometric reaction targeting **6** was loaded again with excess salt, equivalent to twice the required amount. Based on the fewer impurity peaks observed in Figure 7.24, it is thought this reaction led to the highest yield of **4** and **6**, with **6** being the predominate phase formed. The excess salt was simply removed from the reaction product by washing it with deionized water. It should also be noted that carbon-coating was not used in any of the reactions, and at high temperatures NaCl will easily chew up the silica ampoule. It is thought, based on a small amount of a light blue material lining the inside of the ampoule, that a small incorporation of silicon could be the reason for the few impurity peaks in the observed powder patterns.

Characterization

Elemental Analysis: Qualitative elemental analysis was performed by EDAX on the single crystals used in the structure determination. The results showed the presence of the respective elements in the chemical formula.

Magnetic Properties Measurements: Magnetic measurements were carried out on a SQUID MPMS-5S magnetometer produced by Quantum Design. The zero field cooling magnetic susceptibility was carried out in an applied magnetic field of H=0.01T in the temperature range of 2-300K. The sample was a ground powder of polycrystalline material, with a mass of 10.3 mg, obtained from an attempted high-yield synthesis of **6**.

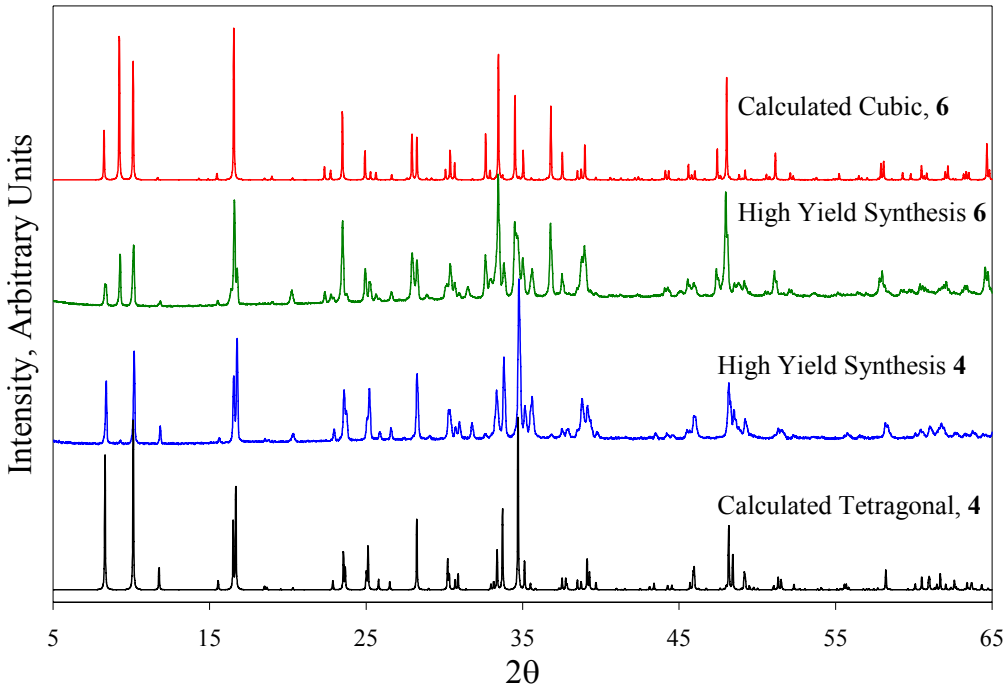

Figure 7.23: Powder pattern of the high yield synthesis of **4** and **6** vs. their resective calculated powder patterns. It appears that when targeting **4** or **6** through a stoichiometric syntheses, the predominate phase is the targeted one, but the other phase still forms.

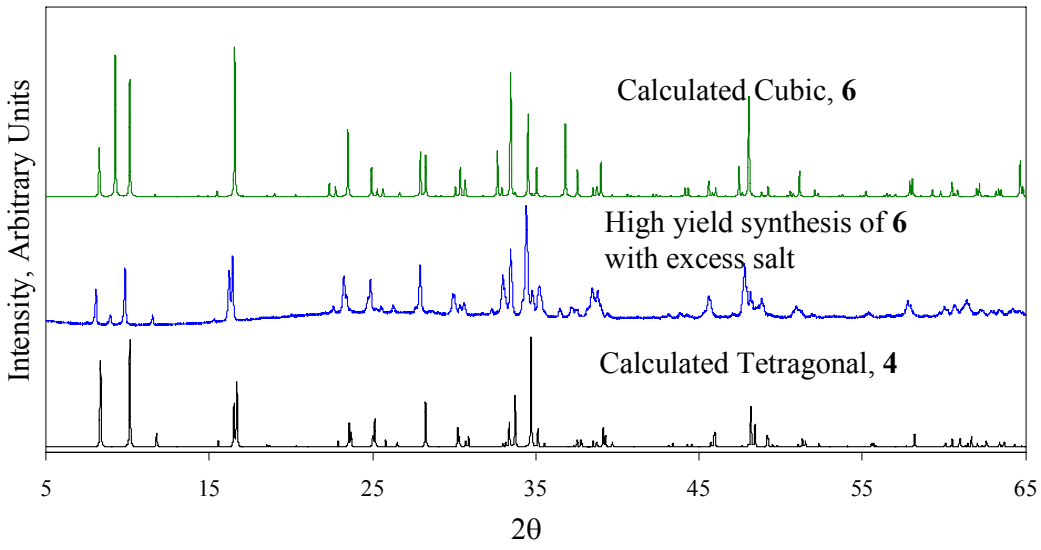

Figure 7.24: Powder pattern of the high-yield synthesis of Cu_{14} with excess salt compared to the calculated PXRD patterns of **4** (tetragonal) and **6** (cubic). It appears that the predominant phase may be the tetragonal compound, **4**. Using excess salt allowed the most pure product.

Field-dependent magnetization studies were also carried out at temperatures ranging from 2-10K in fields ranging from -5T to 5T.

Powder X-ray Diffraction: PXRD was used to confirm the presence of each phase in the respective high-yield reactions shown in Figures 7.23 and 7.24. The X-ray powder diffraction data was collected at room temperature using a Scintag XDS 2000 diffractometer through Cu Kα radiation in the 2θ range of 5–65°. For Figure 7.23, a step size of .02° was used. The scan rates were 0.00571°/s for the stoichiometric reaction targeting **4** and 0.00222°/s for the reaction targeting **6**. The PXRD pattern shown in Figure 7.24 was obtained using a step size of .01 and a scan rate of .00125°/s.

Single Crystal X-ray Diffraction: Dark green cubic crystals of **4-6** were selected under an optical microscope. The crystal dimensions were 0.20 x 0.05 x 0.05, 0.05 x 0.03 x 0.03, and 0.08 x 0.05 x 0.05 mm for compounds **4-6** respectively. Data were collected at room temperature (~300K) using Mo Kα radiation (λ = 0.71073) produced by a graphite monochromator. The crystal-to-detector distance was approximately 27.6 mm, and the exposure times for all three data sets were 60s. The crystallographic data for the **4-6** are summarized in Table 7.11. The secondary extinction parameter is reported only for compound **4**, as the parameter proved to be insignificant once refined for **5** and **6**. The atomic coordinates, thermal parameters, and selected bond distances and angles are listed in Tables 7.12, 7.13, and 7.14.

Table 7.11: Atomic coordinates for Cu_{14} (**4-6**)

empirical formula[a]	$Na_{35.5}Cu_{27.75}O_{16}(AsO_4)_{16}Cl_{11}$	$K_{3.29}Na_{32.21}Cu_{27.75}O_{16}(AsO_4)_{16}Cl_{11}$	$Na_{36}Cu_{28}O_{16}(AsO_4)_{16}Cl_{12}$
compound	(**4**)	(**5**)	(**6**)
color /shape	Green / cube	Green / cube	Green / cube
crystal size (mm)	0.20 x 0.05 x 0.05	0.05 x 0.03 x 0.03	0.08 x 0.05 x 0.05
formula weight (amu)	5443.94	5501.33	5510.88
space group	I4/mmm (no. 139)	I4/mmm (no. 139)	Pm-3n (no. 223)
Z	1	1	4
T, °C		25	
a, Å	15.024(2)	15.001(2)	21.399(3)
c, Å	10.731(2)	11.032(2)	-----
V, $Å^3$	2422.2(6)	2482.5(6)	9799(2)
linear abs. coeff., mm^{-1}	11.898	11.783	11.898
F_{000}	2548	2576	10320
d_{calc}, g / cm^{-3}	3.732	3.680	3.735
data / restraints /parameters	649 / 6 / 80	663 / 0 / 79	1581 / 0 / 167
secondary extinction	0.00030(5)	--------	--------
reflections collected / unique / R_{int}[a]	10446 / 649 / 0.0476	10756 / 663 / 0.0457	41899 / 1581 / 0.1793
final R1/wR2[b] [$I > 2\ \sigma(I)$]	0.0291/ 0.0633	0.0435/ 0.1078	0.0916/ 0.2391
R1/wR2 (all data)	0.0313/ 0.0640	0.0464/ 0.1097	0.1040/ 0.2469
GOF	1.259	1.257	1.857
Largest difference peak / hole (e^- / $Å^3$)	0.766 / -0.830	1.107 / -0.858	5.058 / -2.726

[a] $R_{int} = \Sigma \mid Fo^2 - Fo^2\ (mean) \mid / \Sigma[Fo^2]$; [b] **4**; R1 = $\Sigma \mid\mid F_o \mid - \mid F_c \mid\mid / \Sigma \mid F_o \mid$; *w*R2 = $\{[\Sigma[w(F_o^2-F_c^2)^2] / [\Sigma w(F_o)^2)^2]\}^{1/2}$; Rw = $1 / [\sigma^2(Fo^2) + (0.0232P)^2+25.9917P]$ where $P = (Fo^2+2Fc^2) / 3$; **5**; R1 = $\Sigma \mid\mid F_o \mid - \mid F_c \mid\mid / \Sigma \mid F_o \mid$; *w*R2 = $\{[\Sigma[w(F_o^2-F_c^2)^2] / [\Sigma w(F_o)^2)^2]\}^{1/2}$; Rw = $1 / [\sigma^2(Fo^2) + (0.0544P)^2+40.9890P]$ where $P = (Fo^2+2Fc^2) / 3$; **6**; R1 = $\Sigma \mid\mid F_o \mid - \mid F_c \mid\mid / \Sigma \mid F_o \mid$; *w*R2 = $\{[\Sigma[w(F_o^2-F_c^2)^2] / [\Sigma w(F_o)^2)^2]\}^{1/2}$; Rw = $1 / [\sigma^2(Fo^2) + (0.0971P)^2+672.3640P]$ where $P = (Fo^2+2Fc^2) / 3$

Table 7.12: Atomic positions for Cu_{14} (**4-6**)

Atom	Wycoff position	Sof	x	y	z
		$Na_{35.5}Cu_{27.75}O_{16}(AsO_4)_{16}Cl_{11}$ (**4**)			
Na(1)	16*l*	1.0	0.3833(2)	0.1178(2)	0
Na(2)	8*h*	1.0	0.1441(2)	0.1441(2)	0
Na(3)	8*f*	0.9375	1/4	1/4	¼
Na(4)	4*d*	1.0	0	1/2	¼
Cu(1)	8*j*	1.0	0.21291(7)	0	½
Cu(2)	16*m*	1.0	0.11195(4)	0.11195(4)	0.28011(7)
Cu(3)	4*e*	0.675	0	0	0.6138(2)
Cu(4)	8*h*	0.1	0.0571(5)	0.0571(5)	½
Cu(5)	2*b*	0.125	0	0	½
As	16*n*	1.0	0.28022(4)	0	0.22369(6)
Cl(1)	8*h*	1.0	0.2099(1)	0.2099(1)	½
Cl(2)	4*e*	0.5	0	0	-0.034(1)
Cl(3)	4*e*	0.25	0	0	0.142(3)
O(1)	16*n*	1.0	0.3723(3)	0	0.1381(4)
O(2)	32*o*	1.0	0.2215(2)	0.0936(2)	0.1871(3)
O(3)	16*n*	1.0	0.3083(3)	0	0.3769(4)
O(4)	16*n*	1.0	0.1264(3)	0	0.3679(4)
		$K_{3.36}Na_{32.64}Cu_{27.75}O_{16}(AsO_4)_{16}Cl_{11}$ (**5**)			
K	8*h*	1.0	0.1342(2)	0.1342(2)	0
Na(1)	16*l*	1.0	0.3824(3)	0.1143(3)	0
Na(2)	8*h*	1.0	0.1342(2)	0.1342(2)	0
Na(3)	8*f*	0.9375	0.2500	0.2500	0.2500
Na(4)	4*d*	1.0	0	0.5000	0.2500
Cu(1)	8*j*	1.0	0.2212(1)	0	0.5000
Cu(2)	16*m*	1.0	0.1084(1)	0.1084(1)	0.2884(1)
Cu(3)	4*e*	0.12	0	0	0.608(2)
Cu(4)	8*h*	0.339	0.0571(2)	0.0571(2)	0.5000
Cu(5)	2*b*	0.278		0	0.5000
As	16*n*	1.0	0.2809(1)	0	0.2312(1)
Cl(1)	8*h*	1.0	0.2155(2)	0.2155(2)	0.5000
Cl(2)	4*e*	0.65	0	0	0.1458(7)
Cl(3)	2a	0.20	0	0	0
O(1)	16*n*	1.0	0.3694(4)	0	0.1414(6)
O(2)	32*o*	1.0	0.2209(3)	0.0935(3)	0.2001(4)
O(3)	16*n*	1.0	0.3151(4)	0	0.3779(6)
O(4)	16*n*	1.0	0.1292(4)	0	0.3781(6)

Table 7.12: Atomic positions for Cu_{14} (**4-6**) cont…

Atom	Wycoff position	sof	x	y	z
		$Na_{36}Cu_{28}O_{16}(AsO_4)_{16}Cl_{12}$ (**6**)			
Na(1)	24*k*	1.0	0	0.2502(2)	0.1209(3)
Na(2)	12*f*	1.0	0	0.3543(5)	0
Na(3)	24*k*	1.0	0.2480(2)	0.3737(3)	0
Na(4)	48*l*	1.0	0.1250(2)	0.25227(19)	0.2489(2)
Na(5)	12*h*	1.0	0.1307(4)	1/2	0
Na(6)	24*k*	1.0	0	0.1503(3)	0.2472(3)
Cu(1)	24*k*	1.0	0.10802(8)	0	0.11033(8)
Cu(2)	24*k*	1.0	0	0.38708(8)	0.14154(8)
Cu(3)	24*j*	1.0	0.10579(6)	0.39421(6)	1/4
Cu(4)	24*k*	1.0	0.11074(8)	1/2	0.14095(8)
Cu(5)	12*f*	0.33	0.0565(3)	0	0
Cu(6)	12*g*	0.75	0	1/2	0.1931(2)
Cu(7)	24*k*	0.13	0	0.5560(8)	0.2508(6)
As(1)	16*i*	1.0	0.13971(5)	0.13971(5)	0.13971(5)
As(2)	48*l*	1.0	0.13920(4)	0.36036(5)	0.11277(5)
Cl(1)	6*d*	0.84	0	1/4	1/2
Cl(2)	6*b*	0.8	0	1/2	1/2
Cl(3)	24*k*	0.95	0.1997(2)	1/2	0.2580(2)
Cl(4)	12*f*	1.0	0	0	0.2083(3)
Cl(5)	24*k*	0.06	0.122(3)	0.388(3)	0
Cl(6)	12*h*	0.08	0	0.201(4)	1/2
Cl(7)	24*j*	0.04	1/4	0.398(4)	0.102(4)
O(1)	48*l*	1.0	0.1543(3)	0.3459(3)	0.1889(3)
O(2)	16*i*	1.0	0.1851(3)	0.1851(3)	0.1851(3)
O(3)	48*l*	1.0	0.0641(3)	0.3418(3)	0.0941(3)
O(4)	48*l*	1.0	0.1871(3)	0.3154(3)	0.0718(4)
O(5)	48*l*	1.0	0.1526(3)	0.0646(3)	0.1595(3)
O(6)	48*l*	1.0	0.1545(3)	0.4354(3)	0.0945(3)
O(7)	16*i*	1.0	0.0641(3)	0.0641(3)	0.0641(3)
O(8)	48*l*	1.0	0.0626(3)	0.4369(3)	0.1835(3)

Table 7.13: Anisotropic thermal parameters (Å^2) for Cu_{14} (**4**-**6**)

Atom	U_{11}	U_{22}	U_{33}	U_{12}	U_{13}	U_{23}
$Na_{35.5}Cu_{27.75}O_{16}(AsO_4)_{16}Cl_{11}$ (**4**)						
Na(1)	0.043(2)	0.043(2)	0.015(2)	0.018(2)	0.00000	0.00000
Na(2)	0.027(2)	0.027(2)	0.029(2)	-0.005(2)	0.001(1)	0.0001(1)
Na(3)	0.013(2)	0.013(2)	0.028(3)	0.00000	0.00000	0.00000
Na(4)	0.008(1)	0.008(1)	0.280(9)	0.00000	0.00000	0.00000
Cu(1)	0.013(1)	0.018(1)	0.008(1)	0.00000	0.00000	0.00000
Cu(2)	0.013(1)	0.013(1)	0.016(1)	0.005(1)	0.001(1)	0.001(1)
Cu(3)	0.004(1)	0.004(1)	0.006(1)	0.00000	0.00000	0.00000
Cu(4)	0.008(3)	0.008(3)	0.008(3)	-0.001(4)	0.00000	0.00000
Cu(5)	0.030(2)	0.016(1)	0.022(1)	-0.004(1)	0.00000	0.00000
As	0.009(1)	0.009(1)	0.009(1)	0.00000	0.001(1)	0.00000
Cl(1)	0.026(1)	0.026(1)	0.020(1)	0.005(1)	0.00000	0.00000
Cl(2)	0.054(4)	0.054(4)	0.08(2)	0.00000	0.00000	0.00000
Cl(3)	0.09(1)	0.09(1)	0.06(2)	0.00000	0.00000	0.00000
O(1)	0.011(2)	0.019(2)	0.015(2)	0.00000	0.006(2)	0.00000
O(2)	0.015(2)	0.016(2)	0.017(2)	0.005(1)	0.002(1)	0.006(1)
O(3)	0.016(2)	0.022(2)	0.007(2)	0.00000	0.001(2)	0.00000
O(4)	0.013(2)	0.012(2)	0.014(2)	0.00000	-0.0001(2)	0.00000
$K_{3.36}Na_{32.64}Cu_{27.75}O_{16}(AsO_4)_{16}Cl_{11}$ (**5**)						
K	0.034(2)	0.034(2)	0.013(2)	0.008(2)	0.00000	0.00000
Na(1)	0.032(2)	0.014(2)	0.024(2)	-0.005(2)	0.00000	0.00000
Na(2)	0.034(2)	0.034(2)	0.013(2)	0.008(2)	0.00000	0.00000
Na(3)	0.015(2)	0.015(2)	0.021(3)	-0.004(2)	-0.01(2)	-0.001(2)
Na(4)	0.011(2)	0.011(2)	0.026(4)	0.00000	0.00000	0.00000
Cu(1)	0.012(1)	0.016(1)	0.019(1)	0.00000	0.00000	0.00000
Cu(2)	0.010(1)	0.010(1)	0.031(1)	0.004(1)	0.00000	0.00000
Cu(3)	0.007(6)	0.007(6)	0.05(2)	0.00000	0.00000	0.00000
Cu(4)	0.004(1)	0.004(1)	0.021(2)	0.001(2)	0.00000	0.00000
Cu(5)	0.006(4)	0.006(4)	0.008(6)	0.00000	0.00000	0.00000
As	0.007(1)	0.008(1)	0.017(1)	0.00000	0.001(1)	0.00000
Cl(1)	0.026(1)	0.026(1)	0.023(2)	0.003(2)	0.00000	0.00000
Cl(2)	0.024(2)	0.024(2)	0.018(4)	0.00000	0.00000	0.00000
Cl(3)	0.020(1)	0.02(1)	0.17(7)	0.00000	0.00000	0.00000
O(1)	0.010(3)	0.015(3)	0.022(3)	0.00000	0.003(3)	0.00000
O(2)	0.014(2)	0.009(2)	0.032(3)	0.006(2)	0.003(2)	0.003(2)
O(3)	0.011(3)	0.020(3)	0.020(3)	0.00000	-0.002(3)	0.00000
O(4)	0.012(3)	0.012(3)	0.029(3)	0.00000	-0.003(3)	0.00000

Table 7.13: Anisotropic thermal parameters (Å^2) for Cu_{14} (**4**-**6**) cont…

Atom	U_{11}	U_{22}	U_{33}	U_{12}	U_{13}	U_{23}
			$Na_{36}Cu_{28}O_{16}(AsO_4)_{16}Cl_{12}$ (**6**)			
Na(1)	0.022(3)	0.009(3)	0.022(3)	0.00000	0.00000	0.001(2)
Na(2)	0.024(5)	0.036(5)	0.008(4)	0.00000	0.00000	0.00000
Na(3)	0.014(3)	0.021(3)	0.015(3)	-0.004(2)	0.00000	0.00000
Na(4)	0.015(2)	0.016(2)	0.021(2)	0.001(2)	0.004(2)	0.002(1)
Na(5)	0.009(4)	0.025(4)	0.012(4)	0.00000	0.00000	0.00000
Na(6)	0.013(3)	0.035(4)	0.016(3)	0.00000	0.00000	-0.005(2)
Cu(1)	0.0161(9)	0.0074(9)	0.0124(9)	0.00000	-0.0008(6)	0.00000
Cu(2)	0.0090(9)	0.012(1)	0.0171)	0.00000	0.00000	-0.0027(7)
Cu(3)	0.0144(7)	0.0144(7)	0.0100(9)	0.0004(6)	-0.0004(4)	-0.0004(4)
Cu(4)	0.014(1)	0.0097(9)	0.0171)	0.00000	0.0002(7)	0.00000
Cu(5)	0.008(3)	0.004(3)	0.013(3)	0.00000	0.00000	0.00000
Cu(6)	0.011(2)	0.010	0.013(2)	0.00000	0.00000	0.00000
Cu(7)	0.023(8)	0.04(1)	0.008(7)	0.00000	0.00000	-0.009(6)
As(1)	0.0081(6)	0.0081(6)	0.0081(6)	0.0000(3)	0.0000(3)	0.0000(3)
As(2)	0.0096(7)	0.0087(6)	0.0106(8)	0.0006(4)	0.0000(4)	0.0003(4)
Cl(1)	0.009(2)	0.013(4)	0.009(2)	0.00000	0.00000	0.00000
Cl(2)	0.036(6)	0.008(5)	0.10(1)	0.00000	0.00000	0.00000
Cl(3)	0.018(2)	0.0122)	0.017(2)	0.00000	0.001(1)	0.00000
Cl(4)	0.017(2)	0.033(3)	0.025(3)	0.00000	0.00000	0.00000
O(1)	0.020(4)	0.017(3)	0.008(4)	0.001(3)	-0.004(3)	-0.002(3)
O(2)	0.014(2)	0.014(2)	0.014(2)	-0.004(3)	-0.004(3)	-0.004(3)
O(3)	0.011(3)	0.016(4)	0.019(4)	0.002(3)	-0.002(3)	0.001(3)
O(4)	0.015(3)	0.012(3)	0.025(4)	0.003(3)	0.000(3)	-0.005(3)
O(5)	0.013(3)	0.010(3)	0.012(3)	0.001(3)	0.004(3)	0.001(3)
O(6)	0.024(4)	0.005(3)	0.014(3)	-0.003(3)	-0.007(3)	0.004(3)
O(7)	0.009(2)	0.009(2)	0.009(2)	-0.004(3)	-0.004(3)	-0.004(3)
O(8)	0.013(3)	0.006(3)	0.019(3)	0.002(3)	0.005(3)	-0.002(3)

Table 7.14: Selected bond distances and angles for Cu_{14} (**4**-**6**)

Bond Distances		Bond Angles	
$Na_{35.5}Cu_{27.75}O_{16}(AsO_4)_{16}Cl_{11}$ (**4**)			
Cu(1)-O(4) 1.923(4)* 2	Cu(1)-Cu(4) 2.495(4)	O(1)-As(1)-O(3) 109.2(2)	O(4)-Cu(3)-O(4) 89.39(3)
Cu(1)-O(3) 1.950(4)* 2	Cu(2)-Cu(4) 2.634(4)	O(1)-As(1)-O(2) 107.7(1)	O(4)-Cu(3)-O(4) 168.2(3)
	Cu(2)-Cu(3) 2.636(1)	O(3)-As(1)-O(2) 110.6(1)	O(4)-Cu(3)-Cl(3) 84.1(2)
Cu(2)-O(4) 1.940(2)* 2	Cu(4)-Cu(4) 2.42(2)		
	Cu(3)-Cu(3) 2.447(4)	O(4)-Cu(1)-O(4) 94.9(3)	O(4)-Cu(4)-O(4) 92.8(2)
Cu(2)-O(2) 1.945(3)* 2		O(4)-Cu(1)-O(3) 175.2(2)	O(4)-Cu(4)-O(4) 172.4(6)
Cu(2)-Cl(3) 2.80(2)	Cl(3)-Cu(2) 2.80(2)	O(4)-Cu(1)-O(3) 89.9(2)	O(4)-Cu(4)-O(4) 86.7(2)
Cu(3)-O(4) 1.909(4) *4	Cl(3)-Cu(3) 2.62(3)	O(3)-Cu(1)-O(3) 85.3(3)	
Cu(3)-Cl(3 2.62(3)			O(4)-Cu(5)-O(4) 69.0(1)
		O(4)-Cu(2)-O(4) 87.6(3)	O(4)-Cu(5)-O(4) 111.0(1)
Cu(4)-O(4) 1.957(4)*4		O(4)-Cu(2)-O(2) 177.4(2)	O(4)-Cu(5)-O(4) 180.0(1)
Cu(5)-O(4) 2.370(4)*8		O(4)-Cu(2)-O(2) 91.8(2)	O(4)-Cu(5)-O(4) 106.5(2)
		O(2)-Cu(2)-O(2) 88.7(2)	O(4)-Cu(5)-O(4) 73.5(2)
As(1)-O(1) 1.660(4)		O(4)-Cu(2)-Cl(3) 78.7(4)	
As(1)-O(3) 1.697(4)		O(2)-Cu(2)-Cl(3) 98.7(4)	
As(1)-O(2) 1.705(3)* 2			
$K_{3.29}Na_{32.21}Cu_{27.75}O_{16}(AsO_4)_{16}Cl_{11}$ (**5**)			
Cu(1)-O(4) 1.926(6)*2	Cu(1)-Cu(4) 2.607(2)	O(1)-As(1)-O(3) 109.2(3)	O(4)-Cu(3)-O(4) 89.6(1)
Cu(1)-O(3) 1.949(7)*2	Cu(2)-Cu(3) 2.57(1)	O(1)-As(1)-O(2) 107.7(2)	O(4)-Cu(3)-O(4) 170(2)
	Cu(2)-Cu(4) 2.576(2)	O(3)-As(1)-O(2) 110.6(2)	O(4)-Cu(3)-O(4) 89.6(1)
Cu(2)-O(4) 1.930(4)*2	Cu(4)-Cu(4) 2.422(8)	O(2)1-As(1)-O(2) 111.0(3)	
Cu(2)-O(2) 1.961(5)*2	Cu(4)-Cu(2) 2.576(2)		O(4)-Cu(4)-O(4) 90.7(3)
	Cu(3)-Cu(3) 2.38(5)	O(4)-Cu(1)-O(4) 88.5(4)	O(4)-Cu(4)-O(4) 88.5(3)
Cu(3)-O(4) 1.944(7)*4		O(4)-Cu(1)-O(3) 179.5(3)	O(4)-Cu(4)-O(4) 170.5(4)
	Cl(2)-Cu(3) 2.72(3)	O(4)-Cu(1)-O(3) 92.0(3)	O(4)-Cu(4)-O(4) 90.7(3)
Cu(4)-O(4) 1.926(6)*4	Cl(2)-Cu(2) 2.786(4)	O(3)-Cu(1)-O(3) 87.5(4)	
			O(4)-Cu(5)-O(4) 108.9(2)
Cu(5)-O(4) 2.358(7)*8		O(4)-Cu(2)-O(4) 90.5(4)	O(4)-Cu(5)-O(4) 71.1(2)
		O(4)-Cu(2)-O(2) 91.1(2)	O(4)-Cu(5)-O(4) 180.0
As(1)-O(1) 1.656(6)		O(4)-Cu(2)-O(2) 176.9(2)	O(4)-Cu(5)-O(4) 69.5(3)
As(1)-O(3) 1.697(6)		O(2)-Cu(2)-O(2) 87.2(3)	O(4)-Cu(5)-O(4) 110.5(3)
As(1)-O(2) 1.701(4)* 2			

Table 7.14: Selected bond distances and angles for Cu_{14} (**4**-**6**) cont…

Bond Distances		Bond Angles	
$Na_{36}Cu_{28}O_{16}(AsO_4)_{16}Cl_{12}$ (**6**)			
Cu(1)-O(7) 1.935(2)*2	As(2)-O(4) 1.657(8)	O(7)-Cu(1)-O(7) 90.2(7)	O(7)-Cu(5)-O(7) 170.4(5)
Cu(1)-O(5) 1.983(7)*2	As(2)-O(6) 1.685(6)	O(7)-Cu(1)-O(5) 178.7(3)	O(7)-Cu(5)-O(7) 89.60(4)
	As(2)-O(1) 1.690(7)	O(7)-Cu(1)-O(5) 90.7(4)	
Cu(2)-O(8) 1.933(7)*2	As(2)-O(3) 1.703(7)	O(5)-Cu(1)-O(5) 88.4(4)	O(8)-Cu(6)-O(8) 89.8(4)
Cu(2)-O(3) 1.962(7)*2			O(8)-Cu(6)-O(8) 167.6(5)
	Cu(1)-Cu(5) 2.583(3)	O(8)-Cu(2)-O(8) 87.7(4)	
Cu(3)-O(8) 1.927(7)*2	Cu(1)-Cu(5) 2.606(3)	O(8)-Cu(2)-O(3) 175.5(3)	O(8)-Cu(7)-O(8) 87.4(7)
Cu(3)-O(1) 1.963(7)*2	Cu(2)-Cu(7) 2.64(2)	O(8)-Cu(2)-O(3) 91.6(3)	O(8)-Cu(7)-O(8) 171(1)
	Cu(2)-Cu(6) 2.657(2)	O(3)-Cu(2)-O(3) 88.7(4)	O(8)-Cu(7)-O(8) 92.9(3)
Cu(4)-O(8) 1.927(7)*2	Cu(3)-Cu(7) 2.503(7)		O(8)-Cu(7)-O(8) 85.5(7)
Cu(4)-O(6) 1.942(8)*2	Cu(4)-Cu(7) 2.60(1)	O(8)-Cu(3)-O(8) 95.2(5)	
	Cu(4)-Cu(6) 2.620(2)	O(8)-Cu(3)-O(1) 174.1(3)	O(2)-As(1)-O(5) 108.1(2)
Cu(5)-O(7) 1.94(1)*4	Cu(5)-Cu(5) 2.42(1)	O(8)-Cu(3)-O(1) 90.7(3)	O(5)-As(1)-O(5) 110.8(2)
	Cu(6)-Cu(6) 2.433(6)	O(1)-Cu(3)-O(1) 83.5(4)	
Cu(6)-O(8) 1.913(7)*4	Cu(7)-Cu(7) 2.40(3)		O(4)-As(2)-O(6) 108.1(4)
		O(8)-Cu(4)-O(8) 88.9(4)	O(4)-As(2)-O(1) 106.6(4)
Cu(7)-O(8) 1.95(1)*2		O(8)-Cu(4)-O(6) 90.1(3)	O(6)-As(2)-O(1) 111.1(3)
Cu(7)-O(8) 1.97(1)*2		O(8)-Cu(4)-O(6) 176.2(3)	O(6)-As(2)-O(3) 110.6(3)
		O(6)-Cu(4)-O(6) 90.7(4)	O(1)-As(2)-O(3) 111.4(3)
As(1)-O(2) 1.68(1)			
As(1)-O(5) 1.685(7)*3			

Results and Discussion

Here, three new salt-inclusion solids isolated through conventional, high-temperature molten-salt methods, are presented. They have the following compositions: $Na_{18}Cu_{27.75}O_{16}(AsO_4)_8Cl_{5.5}$, **4**, $K_{3.29}Na_{32.21}Cu_{27.75}O_{16}(AsO_4)_{16}Cl_{11}$, **5**, and $Na_{36}Cu_{28}O_{16}(AsO_4)_4Cl_{12,}$ **6**. The single crystal structure solutions of compounds **4** and **5** reveal that these crystallize in a tetragonal crystal system, in the spacegroup I4/mmm (no. 139) while **6** crystallizes in a cubic crystal system in spacegroup Pm-3n (no. 223). The crystallographic data can be compared in Table 7.11. All three compounds contain $[Cu_{14}(\mu_4O_8)(AsO_4)_8]^{12-}$cores, Cu_{14}, which are structurally isolated from one another via a surrounding salt lattice, shown in Figure 7.25. Within the $[Cu_{14}(\mu_4O_8)(AsO_4)_8]^{12-}$ core, Cu^{2+} is found in a square planar geometry coordinated by oxygen. Bond valence sum calculations further support the oxidation states of the of the Cu atoms, Table 7.15.[18] The Cu_{14} cluster has a mirror plane (σ_h) and a two-fold rotation (C_2) perpendicular to the principal rotation axis (C_4), giving rise to D_{4h} point symmetry. SEM images of crystals from the high-yield synthesis of **4** and **6** can be seen in Figure 7.26. The cubic morphology of the crystals reflects the high symmetry of the crystal system.

These Cu_{14}-containing compounds are unique, as materials containing high nuclearity copper oxide clusters are much less frequently observed than those of the electron-deficient early transition metals discussed earlier. A quick review of the literature will validate this point as very few articles reporting high nuclearity copper-based anions[28] can be found. A few articles were found reporting materials containing Cu-based clusters that have a structural similarity to the cores found in compounds **4**-**6**.

Table 7.15: Bond valence sum calculations for **4**-**6**

Atom	Cu(1)	Cu(2)	Cu(3)	Cu(4)
BVS for **4**	1.99	1.96	2.15	1.89
BVS for **5**	1.99	1.95	1.96	2.05
BVS for **6**	1.88	1.94	1.95	1.99
	Cu(5)	Cu(6)	Cu(7)	
	1.98	2.13	1.87	

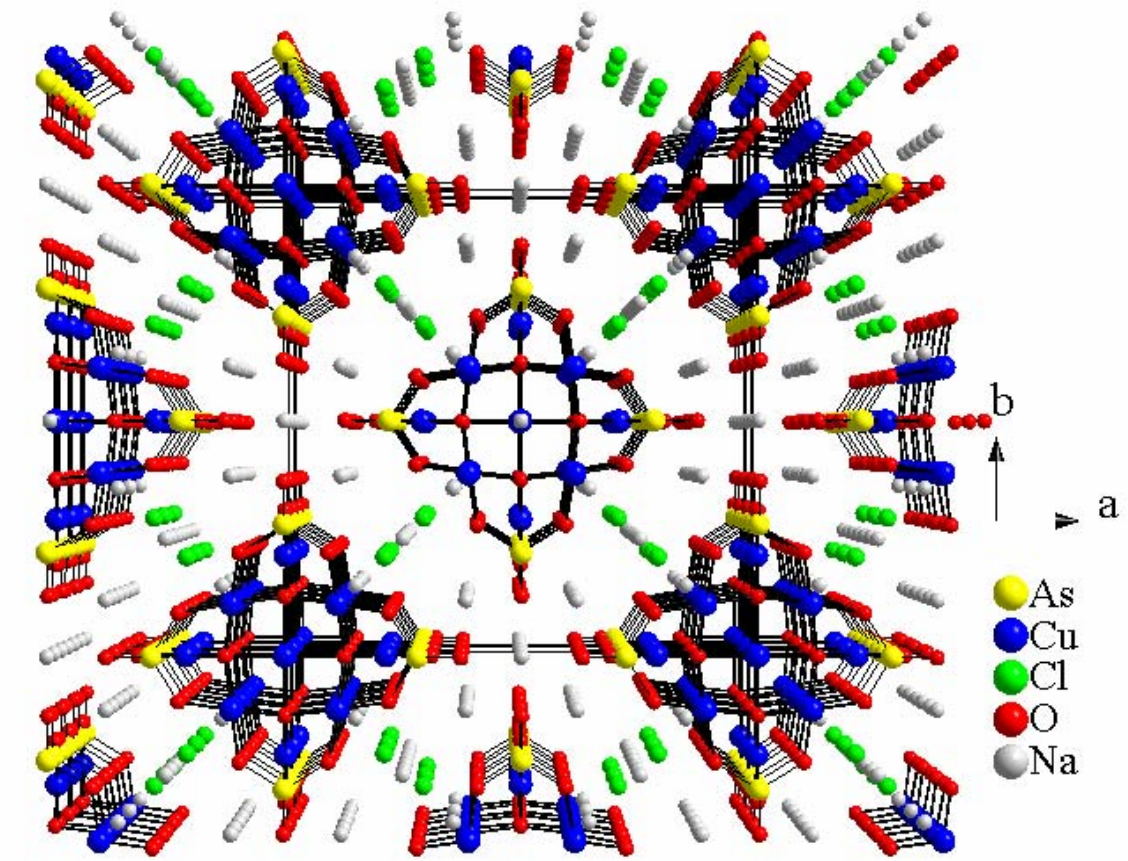

Figure 7.25: Perspective view showing extended structure of $Na_{35.5}Cu_{27.75}O_8(AsO_4)_8Cl_{11}$ with Cu clusters embedded in a salt matrix.

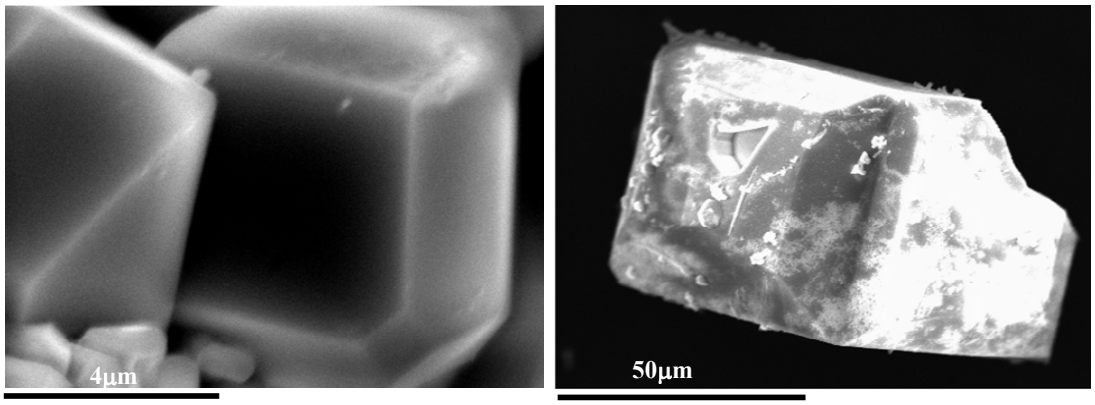

Figure 7.26: SEM images of crystals found in the high-yield synthesis of **4** and **5**. The morphology of the crystals reflects the symmetry of the unit cell.

In 2000, Fenske et al. reported a compound, $[\{Li(dme)_3\}_3]$-$[Li(dme)_2][Cu_{12}(NPh)_8]$, containing a cluster of 12 Cu(I) atoms with a μ_3-bridging mode via $(NPh)^{2-}$ ligands[29], and in 2005 Li et al. reported a neutral 3-D microporous framework, $[Cu_{12}(\mu_4\text{-}SCH_3)_6(CN)_6]_n \cdot 2H_2O$, also containing a cluster of 12 Cu(I) atoms with μ_4-SCH_3 ligands.[30] Like the solids presented here, these two reports present materials containing cubo-octahedral copper–based cores, Figure 7.27, that have six square Cu_4 faces and eight triangular Cu_3 faces. A closer comparison between the reported clusters and the ones in compounds **4**-**6** brings several differences to light including the oxidation state of the Cu atoms, diamagnetic Cu(I) vs paramagnetic Cu(II), the bridging ligands N and S vs. O, the total number of Cu atoms found in the core, 12 vs. 14, and the method used to synthesize the materials, solution-based processes vs. conventional solid state methods.

When making a direct comparison between compounds **4** and **5**, the only difference found between these tetragonal derivatives is seen in their chemical compositions. As a result of the incorporation of K for **5**, the unit cell volume increases from 2422.2(6) to 2482.5(6) $Å^3$. Due to their similarities, the structure of **4** will be discussed from this point forward. Figure 7.28 shows a perspective view of the $[Cu_{14}(\mu_4O_8)(AsO_4)_8]^{12-}$ core found in **4**. The cluster consists of twelve external CuO_4 polyhedra that form the cage-like cubo-octahedral core, and two internal CuO_4 polyhedra. The twelve external copper, consist of two crystallographically distinct atoms, Cu(1) and Cu(2), while the internal Cu atoms consist of disordered Cu(3), Cu(4), or Cu(5) sites. The core can be described as consisting of two bowl-shaped $Cu_5O_4(AsO_4)_4$ caps that are interlinked by four corner-sharing $Cu(1)O_4$ polyhedra. At the bottom of each

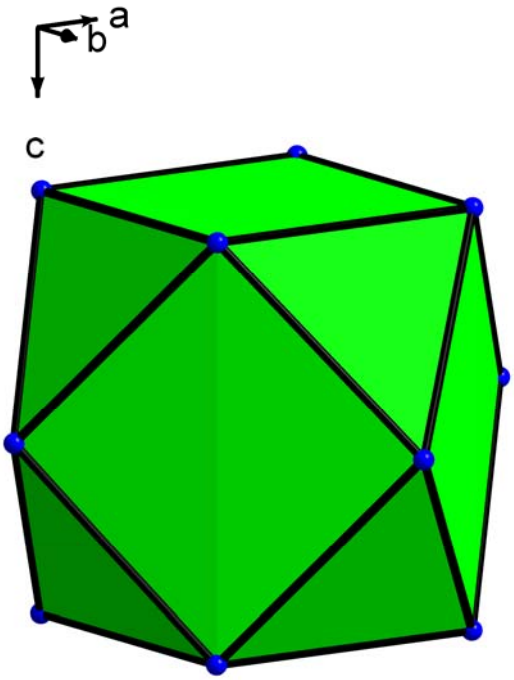

Figure 7.27: Shows the cubo-octahedron made of the twelve external Cu atoms found in the $[Cu_{14}(\mu_4O_8)(AsO_4)_8]^{12-}$ core.

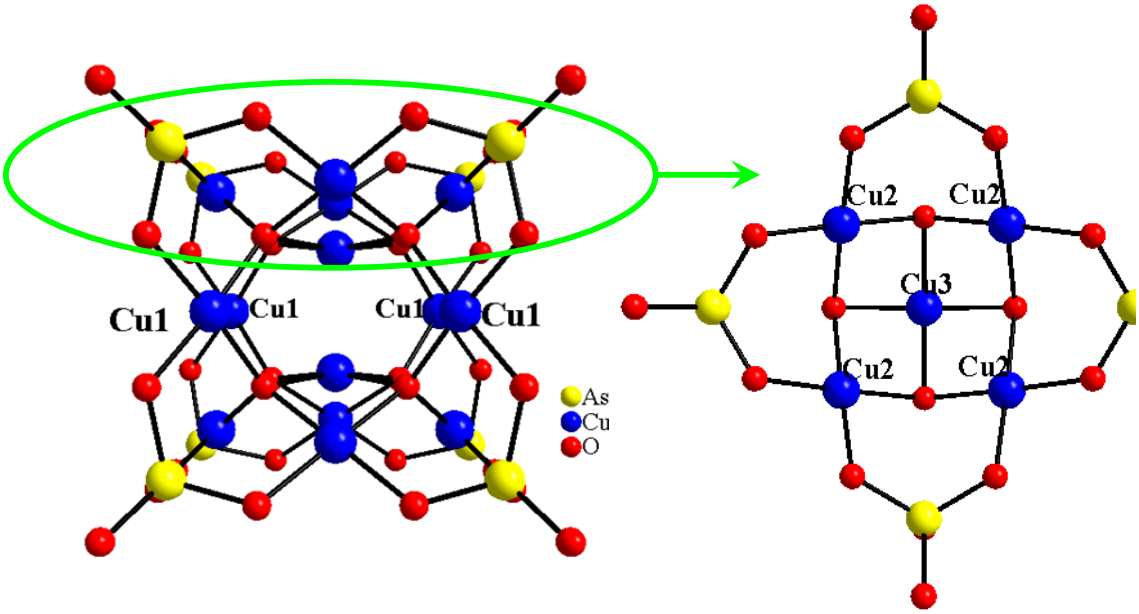

Figure 7.28: (left) Perspective view of the $[Cu_{14}(\mu_4O_8)(AsO_4)_8]^{12-}$ core. (right) Each cluster has two $Cu_5O_4(AsO_4)_4$ caps that are interlinked by corner-sharing $Cu(1)O_4$ polyhedra.

$Cu_5O_4(AsO_4)_4$ bowl there is one CuO_4 polyhedron that shares all four edges with four $Cu(2)O_4$ polyhedra. The connectivity within the cluster gives rise to eight μ_4-oxo bridges, which are tetrahedrally coordinated by four Cu cations. The internal Cu atoms, Cu(3), Cu(4), and Cu(5) are solely coordinated by four of the μ_4 bridging oxygen atoms, O(4). The Cu_{14} core is capped at all eight corners by AsO_4 tetrahedra, which share three of four corner oxygen atoms, consisting of O(2) and O(3), with the external Cu cations. Each AsO_4 polyhedron also has a single non-bridging oxygen, O(1), that points into the space between surrounding clusters.

There are some issues concerning the structure determination for compound **4** that need to be addressed. As previously mentioned, there is disorder found at the center of the cluster creating partially occupied Cu sites. For example, if a closer look is taken at the single crystal structure solution for **4,** there are three possible crystallographically independent sites for Cu to occupy within the central portion of the cluster, Cu(3), Cu(4), and Cu(5). Cu(3) and Cu(4) form an octahedron with respect to one another, shown in Figure 7.29, where Cu(3) would be in the axial position and Cu(4) would be in the four equatorial positions. Within this octahedron there are short distances found between Cu(3) and Cu(4) as well as adjacent Cu(4) atoms, which are 1.721(7)Å and 1.71(1)Å respectively. As a result of the short distance, Cu cannot occupy both a Cu(3) and Cu(4) site or two adjacent Cu(4) sites at the same time, and each cluster cannot have more than fourteen Cu atoms, twelve external and two internal, leading to partial occupancies between the two sites. The Cu(3)-Cu(3) and non-adjacent Cu(4)-Cu(4) distances are 2.449(4) Å and 2.42(2)Å respectively, permitting Cu to occupy both axial Cu(3) sites or

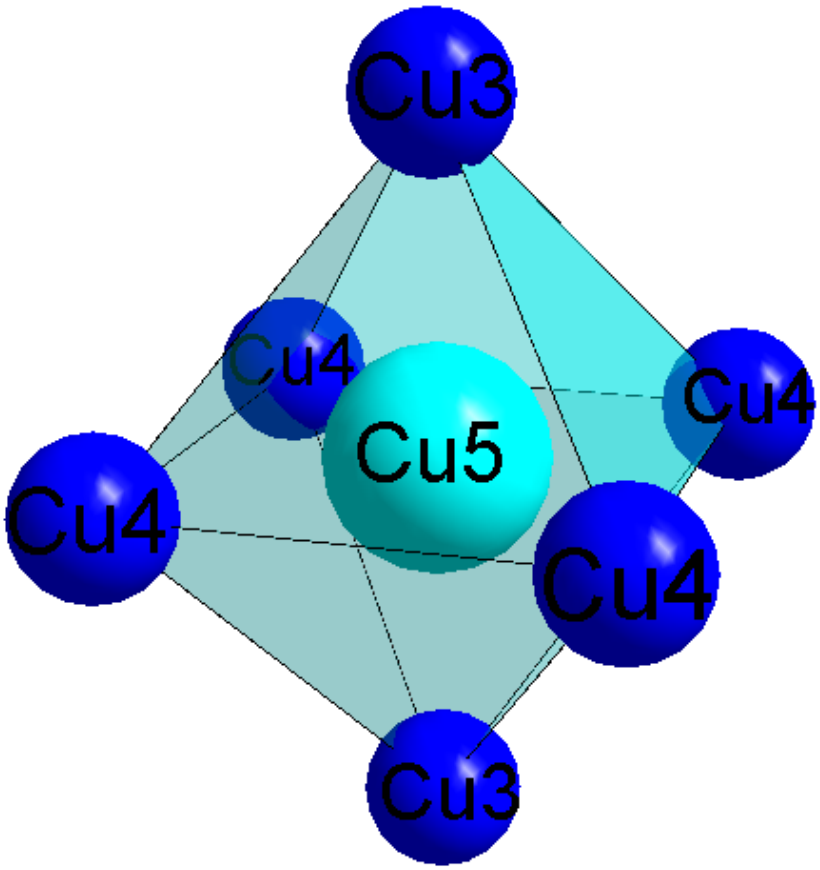

Figure 7.29: Perspective view showing the disordered center of the Cu_{14} clusters observed in $Na_{35.5}Cu_{27.75}O_8(AsO_4)_8Cl_{11}$. There are three partially-occupied Cu sites within the cluster.

two non adjacent Cu(4) sites at the same time. The refined occupancy of the Cu(3) site is 0.675, whereas the occupancy for the Cu(4) site is 0.1, indicating that the Cu(3) site is preferentially occupied. Since the Cu(3) site shows longer Cu-Cu distances, 2.449(4)Å vs 2.42(2)Å for Cu(4)-Cu(4), it is no surprise that the Cu(3) site is preferentially occupied. These Cu-Cu distances, which are slightly shorter than those observed in Cu metal (2.56Å)[31], likely cause strong repulsive interactions between the positively charged Cu atoms. Other Cu-Cu distances found within the core range from 2.495(4)–2.636(1)Å.

The compositions of the clusters in **4** and **5,** $Cu_{13.875}O_8(AsO_4)_8$, do not reflect materials containing only Cu_{14} cores. In fact, some of the clusters within the unit cell contain only thirteen Cu atoms approximately 12.5% of the time. The next disordered site found within the central portion of the cluster is Cu(5), with an occupancy of 0.125, found at the center of the aforementioned octahedron, refer to Figure 7.30. The Cu(5) site is in close proximity to the Cu(3) and Cu(4) sites, with distances of 1.224(2) and 1.209(9) respectively. This means that if an atom is found in the Cu(5) site, then the Cu(3) and Cu(4) sites must remain empty, giving rise to a $Cu_{13}O_8(AsO_4)_8$ cluster which causes the number of copper found in the empirical formula to be less than twenty-eight. A closer look at Figure 7.30 shows that the Cu(5) site is eight-coordinate with respect to the surrounding oxygen, O(4), with a bond distance equal to 2.370(4). This unusual coordination environment for Cu^{2+}, which is normally CuO_n with n = 4, 5, or 6, can be explained when considering the thermal ellipsoids of the Cu(5) atom which show an extensive elongation along the crystallographic c axis. This elongation is a result of smeared electron density of the Cu atom within this site, indicating a disordered site

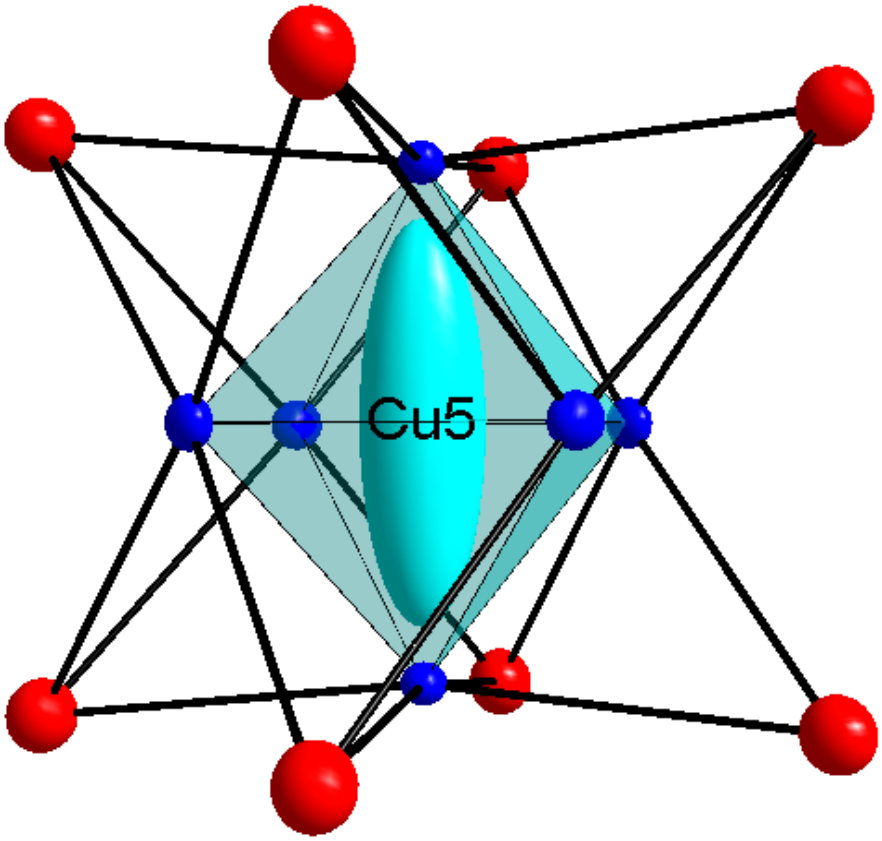

Figure 7.30: Thermal ellipsoids of Cu(3-5) with a 50% probability factor. The Cu(5) site is elongated along the crystallographic *c* axis.

where Cu(5) is shifted up or down in the cage, creating a distorted 4-coordinate square planar site as opposed to an eight coordinate cubic site. Figure 7.31 shows a comparison between the two possible cores found in compound **4** $Cu_{14}O_8(AsO_4)_8$ (top) and $Cu_{13}O_8(AsO_4)_8$ (bottom). Based on the bond distances and the coordination environment, it was originally thought that Na could be refined in the Cu(5) site, as it would be less unusual to see an eight-coordinate Na site. However, Na was not placed in the site for the following reasons: (1) there was no improvement seen in the structure refinement, (2) the Shannon crystal radii for eight-coordinate Na^{+1} and 4 coordinate O^{2-} is approximately 2.56, making the bond distances too short for an eight-coordinate Na cation, and (3) when refined as Na, the thermal parameters went negative, indicating an atom with larger electron density must be present.

Compound **6**, $Na_{36}Cu_{28}O_{16}(AsO_4)_4Cl_{12}$, crystallizes in a cubic crystal system, and besides a slight difference in the compositions of **4** and **6**, the only observed difference between the two materials is pertaining to the cluster packing. The Cu_{14} clusters found in $Na_{36}Cu_{28}O_{16}(AsO_4)_4Cl_{12}$ have a slightly different 3-D packing arrangement, which is highlighted in Figures 7.32 and 7.33. In the cubic compound, the Cu_{14} clusters pack in an ABCDA fashion, whereas in the tetragonal version, the clusters have an ABA packing arrangement. Compound **6** has seven crystallographically distinct Cu atoms. Cu(1) and Cu(5) make up one cluster found at the center and eight corners of the unit cell. Twelve Cu(1) atoms form the external cubo-octahedral core and Cu(5) forms octahedral core at the center of the cluster. Due to the short interatomic distances between Cu(5) within the octahedral core, as observed for **4**, the site must be partially occupied at no more than

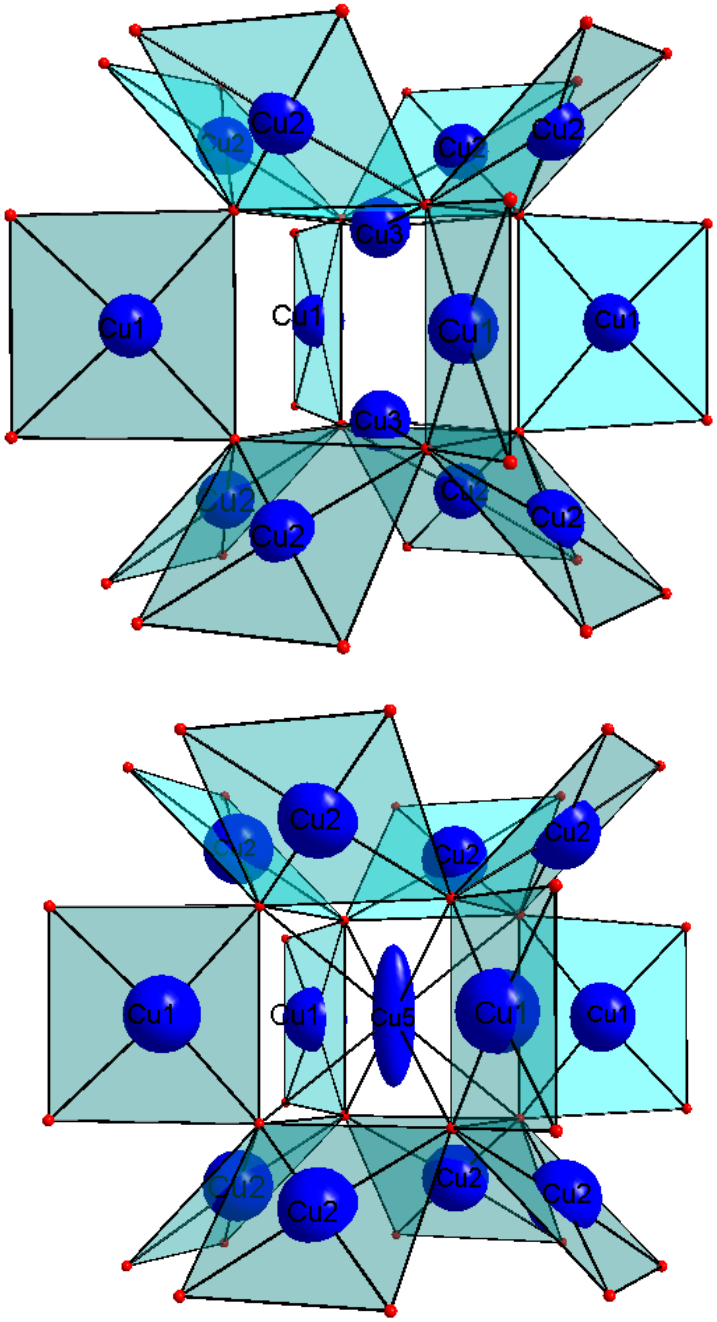

Figure 7.31: Perspective view showing two possible clusters found in $Na_{35.5}Cu_{27.75}O_8(AsO_4)_8Cl_{11}$. (top) This cluster shows a core having fourteen copper atoms in the cluster with the two Cu(3) sites occupied. (bottom) This cluster shows a cluster with only thirteen copper atoms due to the occupied Cu(5) site. Notice the elongated thermal parameters which mean that Cu(5) likely is closer to a 4-coordinate distorted square planar copper.

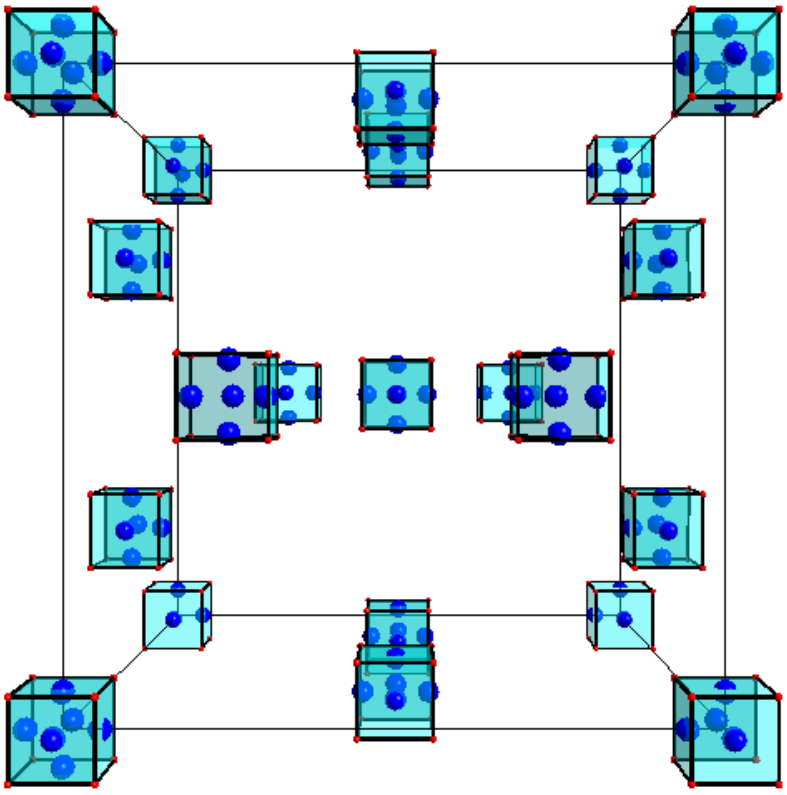

Figure 7.32: Perspective view of the cubic derivative, **6**, of the Cu_{14} clusters that pack in an ABCDA arrangement.

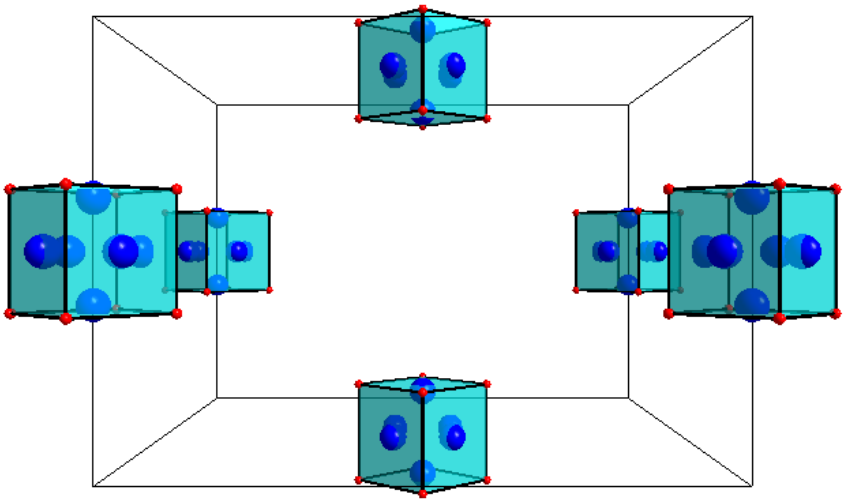

Figure 7.33: Perspective view of the clusters packing arrangement in an ABA fashion observed in the tetragonal derivative, **4**, of the Cu_{14} cluster.

33%, giving rise to the additional two internal Cu atoms. Cu(2), Cu(3), Cu(4), Cu(6), and Cu(7) make up the other Cu_{14} clusters seen in the unit cell. Cu(2), Cu(3), and Cu(4), form the twelve external cubo-octahedral cage, while Cu(6) and Cu(7) form the internal octahedral core and have occupancies equal to 75% and 12.5% respectively. This shows that the Cu(6) site is preferentially occupied. Again, this can be explained when looking at the Cu-Cu distances. The Cu(6)-Cu(6) distance is 2.433(6)Å, whereas Cu(7)-Cu(7) is 2.40(3)Å, making Cu(6) the preferred site. There are some problems with the single crystal structure solution of compound **6** that need to be addressed. Some of the atoms show non-positive definites when refined anisotropically. For this reason, several of the atoms found in the unit cell, including Cl(5), Cl(6), and Cl(7), were refined isotropically. It should be noted that these atoms are severely disordered and have very low site occupancies of 6%, 8%, and 4% for Cl(5-7) respectively.

Attempts to obtain a pure sample of **4** and **6** through a stoichiometric reaction were never successful. Due to similarities in their compositions, both phases always appeared in the powder patterns. Both phases also appeared in the single crystal reactions and in very low yield. Hence, the magnetic data was collected on a high-yield sample (shown in Figure 7.23) containing a mixture of both compounds **4** and **6**. Zero field cooling temperature-dependent susceptibility was collected with an applied field of 0.5 T in temperatures ranging from 2-300K. Figure 7.34 shows the molar magnetic susceptibility, χ, and the inverse molar magnetic susceptibility, χ^{-1}, of the sample. The powder pattern of the sample (Figure 7.23) appears to be predominately compound **4**, hence the molecular weight of **4** was used to calculate χ. The magnetic susceptibility

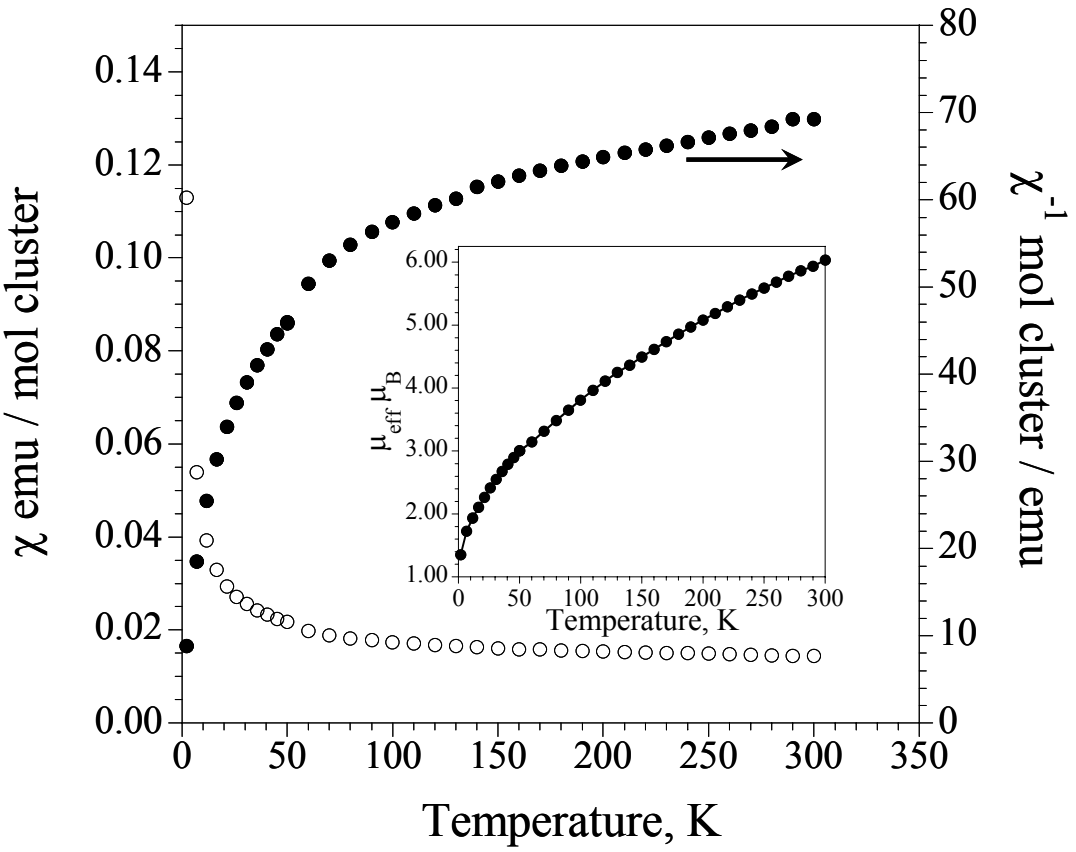

Figure 7.34: Molar magnetic susceptibility and inverse molar magnetic susceptibility for a mixture of **4** and **6**.

shows a curve that is similar to what was observed with compounds **1** and **2**, and is often observed for paramagnetic materials. As the temperature is decreased, there is an increase in the number of spins aligning with the field giving rise to an increase in the susceptibility. A Curie - Weiss fit was performed on the χ^{-1} data ranging from 40-300K. From this fit, several values were obtained including the $u_{eff,}$ equal 1.9(2)μ_B, which is proportional to the expected spin-only value for Cu^{2+}, d^9, 1.73 μ_B, a Weiss constant, θ, calculated to be -4(2)K, indicating weak antiferromagnetic exchange between nearest neighbors, and a χ_0 equal to 0.0130(8) emu. The inset in Figure 7.34 shows the μ_{eff} plotted as a function of temperature. At room temperature there is a μ_{eff} of 6.04μ_B, which is lower than the expected value for $14Cu^{2+}$ (d^9), 10.58 μ_B, also indicating antiferromagnetic coupling. Field-dependent magnetization data, Figure 7.35, was collected on the sample in applied fields of ± 5T. Unlike compounds **1** and **2**, it shows a nearly linear response to the field. with a maximum reaching 1 μ_B / cluster.

Conclusions

Here, five new salt-inclusion solids containing three different discrete polyoxometalate cores are presented. These five SISs have the following compositions: $Cs_{11}Na_3(V_{15}O_{36})Cl_6$ (**1**), $Cs(V_{14}O_{22})(As_2O_5)_4Cl$ (X = Cl, Br, I) (**2**), $Na_{35.5}Cu_{27.75}O_8(AsO_4)_8Cl_{11}$ (**4**), $K_{3.29}Na_{32.21}Cu_{27.75}O_{16}(AsO_4)_{16}Cl_{11}$ (**5**) and $Na_9Cu_7O_4(AsO_4)_4Cl_3$ (**6**). This is the first time materials containing POM cores have been synthesized using conventional, high-temperature molten-salt methods. There are some inherent differences in the properties of the salt-inclusion materials presented in this

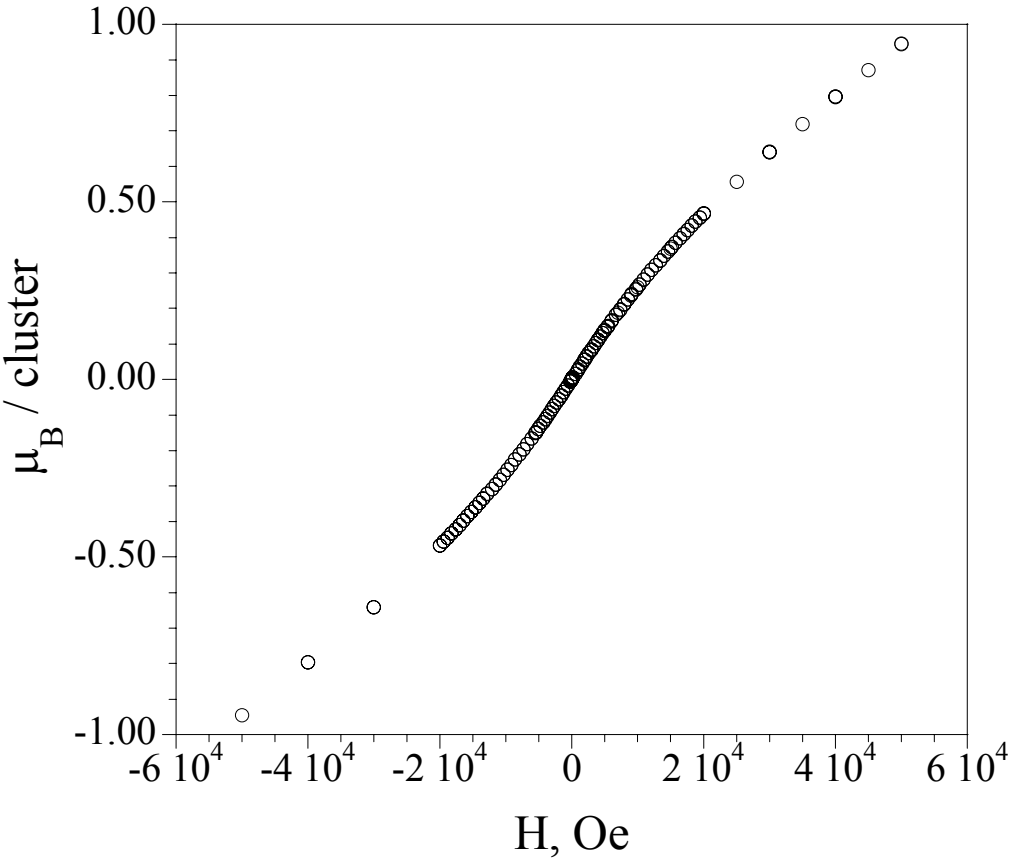

Figure 7.35: Field-dependent magnetization plot for a mixture of compounds **4** and **6** at 2K and applied fields ranging from ±5T. The powder was obtained from a high-yield synthesis showing a mixture of **4** and **6**.

chapter. Even though the Cu_{14} clusters are embedded in a salt-like matrix, similarly observed for **1** and **2**, none of the Cu-containing compounds are water soluble. It is thought that the higher anionic charge on the Cu_{14} clusters, 12-, compared to 9- and 5- for **1** and **2** respectively, allows the clusters to interact more strongly with their salt-like surroundings creating a higher lattice energy. Both compounds **1** and **2** are water-soluble, and it is suspected based on the change in color of their solutions and the fully oxidized by-products obtained from their re-precipitation, that the materials could undergo an oxidative decomposition upon dissolution. Through a slow re-precipitation, the oxidative decomposition product of compound **2** was isolated. This material, $Cs_5(V_{14}O_{40})(AsO_3)_2Cl•2.6H_2O$ (**3**), contained a new fully-oxidized POM core, $[V_{14}As_2O_{40}]^{4-}$. The Br- and I- derivatives of **2** were also synthesized. When no single crystals of these two compounds were available for a structure solution, the materials were dissolved in water and re-crystallized. After a fast evaporation process, SXRD revealed that the re-crystallized materials, $Cs_5(V_{14}As_8O_{42}Br)•1.5\ H_2O$ and $Cs_5(V_{14}As_8O_{42}I)•1.5\ H_2O$, contained the Br^- and I^- version of the chlorine centered core, $[V_{14}As_8O_{42}]^{5-}$, observed in **2**. It is thought that there is much more interesting structural chemistry to be unveiled in this salt-inclusion system as all of the materials here have been synthesized using a CsCl salt flux. It might be interesting to see what other interesting structural formations occur upon changing the A-site cation in the salt to smaller alkali-earth metal cations such as Na^+. These clusters are large anions that pack in three-dimensions with surrounding cations and anions incorporated from the salt

forming ionic type lattice. It is suspected that using smaller cations may lead to the formation of new clusters with various sizes and geometries.

It is thought that once the chemistry of the water-soluble aggregates is more well understood, they could be exploited in such a way that the POM cores be used as building blocks tethered together through first-row transition metals, forming new 1-, 2-, and 3-D networks. In order to achieve this, more understanding of the decomposition process needs to be obtained. Efforts to determine the source of the oxidation were inconclusive and further studies will have to be performed. It is suspected that a number of factors play a role in the oxidation of the materials including heat and light. These materials illustrate once again the utility of salt-inclusion chemistry, rendering the formation of special frameworks.

Literature Cited

1. Pope, M.T., Müller, A. Introduction to Polyoxometalate Chemistry : From Topology via Self- Assembly to In: Pope, M.T.; Müller, A. (Eds.), Polyoxometalate *Chemistry: From Topology via Self-Assembly to Applications.* Kluwer, New York, **2001**, 1-6.

2. Khan, M.I. *J. Solid State Chem.*, **2000**, *152*, 105-112.

3. (a) Müller, A., Reuter, H., Dillinger S. *Angew. Chem. Int. Ed*. **1995** *34*, 2328-2861.

   (b) Müller, A., Peters, F., Pope, M.T., Gatteschi D. *Chem. Rev.* **1998,** *98*, 239-271.

   (c) Hagrman, P.J., Hagrman, D., Zubieta, J. *Angew. Chem. Int. Ed*. **1999**, *38*, 2638-2684.

   (d) Braun, P.V., Osenar, P., Tohver, V., Kennedy, S.B., Stupp S.I., *J. Am. Chem. Soc*. **1999**, *121*, 7302-7309

   (e) Müller, A., and Döring, J. *Z. Anorg. Allg. Chem*. **1991**, *595*, 251-274.

   (f) Huan, G., Greaney, M.A., Jacobson, A.J. *J. Chem. Soc. Chem. Commun.* **1991**, *4*, 260-261.

4. Errington, R.J. Rational approaches to polyoxometalate synthesis. In: Pope, M.T.; Müller, A. (Eds.), Polyoxometalate *Chemistry: From Topology via Self-Assembly to Applications.* Kluwer, New York, **2001**, 7-22.

5. Salta, J., Chen, Q., Chang Y.-D., Zubieta, J. *Angew. Chem., Int. Ed. Eng.,* **1994**, *33*, 757-760.

6. (a) Khan, M.I., Zubieta, J. *Prog. Inorg. Chem.,* **1995**, 43, 1-149.

   (b) Chang, Y.-D., Salta J., Zubieta, J. *Angew. Chem., Int. Ed. Eng.,* **1994**, *33*, 325-327.

   (c) Chen Q., Zubieta, J. *Angew. Chem., Int. Ed. Eng.*, **1993**, *32*, 261-263.

7. (a) Müller, A., Polarz, S., Das, S.K., Krickmeyer, E., Bögge, H., Schmidtmann, M., Hauptfleisch, B. *Angew. Chem., Int. Ed. Eng,* **1999**, *38*, 3241-3245.

(b) Müller, A., Krickmeyer, E., Bögge, H., Schmidtmann M., Peters, F. *Angew. Chem., Int. Ed. Eng,* **1998**, *37*, 3360-3363

(c) Maestre, J.M., Poblet, J.M., Bo, C., Casañ-Pastor, N., Gomez-Romero, P. *Inorg. Chem.*, **1998**, *37*, 3444-3446

8. Huang, Q., Kartin, M., Mo, X., Hwu, S.-J *Mater. Res. Soc. Symp. Proc*., **2002**, 459-464.

9. La Violette, R.A., Budzien, J.L., Stillinger, F.H. *J. Chem. Phys.* **2000**, *112*, 8072 – 8078.

10. (a) Q. Huang, M. Ulutagay, P. A. Michener, S.-J. Hwu, *J. Am. Chem. Soc*. **1999**, *121*, 10323 – 10326;

(b) Q. Huang, S.-J. Hwu, X. Mo, Angew. Chem. Int. Ed. **2001**, *40*, 1690–1693.

11. (a) Etheredge, K.M.S., Hwu, S.-J. *Inorg. Chem*. **1995**, *34*, 3123 –3125.

(b) Huang, Q., Hwu, S.-J. *Inorg. Chem*. **2003**, *42*, 655 – 657.

(c) Mo, X., Hwu, S.-J. *Inorg. Chem*. **2003,** *42*, 3978 – 3980;

(d) Mo, X., Ferguson,E., Hwu, S.-J. *Inorg. Chem*. **2005**, *44*, 3121 – 3126.

(e) Mo, X. Ph.D. dissertation, Clemson University, **2005**.

(f) Queen, W.L., West, J.P., Hwu, S.-J, Vanderveer, D.G., Zarzyczny, M.C., Pavlick, R.A. *Angew. Chem. Int. Ed*., **2008**, *47*, 3791-3794.

12. Hwu, S.-J., Ulutagay-Kartin M., Clayhold, J.A., Mackay, R.A., Wardojo, T.A., O'Conner, C.J., Krawiec, M. *J. Am. Chem. Soc*., **2002**, *124*, 12404-12405.

13. Queen, W.L., S.-J. Hwu, Unpublished results. **2007**

14. (a) Müller, A., Penk,M., Rolfng, R., Krickemeyer, E., Döring, J. *Angew. Chem. Int. Ed. Engl*., **1990**, *29*, 926-927.

(b) Dong, B., Gómez-García, C.J., Peng J., Benmansour, S., Ma, J. *Polyhedron*, **2007**, *26*, 1310–1316.

15. (a) Day, V.W., Klemper, W.G., Yaghi, O.M., *J. Am. Chem. Soc*., **1989**, *111*, 5959-5961.

(b) Müller, A., Krickemeyer, E., Penk, M., Wallberg, H.-J., Bögge, H. *Angew. Chem. Int. Ed. Engl.*, **1987**, *26*, 1045-1046.

(c) Müller, A, Sessoli, R., Krickemeyer, E., Bögge, H., Meyer, J., Gatteschi, D., Pardi, L., Westphal, J.; Hovemeier, K., Rolfing, R., Doring, J., Hellweg, F., Beugholt, C., Schmidtmann, M. *Inorg. Chem.*, **1997**, *36*, 5239-5250.

(d) Johnson, G.K., Schlemper, E. O. *J. Am. Chem. Soc.*, **1978**, *100*, 3645-3646.

(e) Suber, L., Bonamico, M., Fares, V. *Inorg. Chem.*, **1997**, *36*, 2030-2033.

(g) Müller, A., Penk, M., Krickemeyer, E., Bögge, H., Wallberg, H.-J, *Angew. Chem. Int. Ed. Engl.*, **1988**, *27*, 1719-1721.

(h) Müller, A, Rolfng, R, Döring, J, and Penk, M, *Angew. Chem. Int. Ed.*, **1991**, *30*, 588-590.

16. Aronica, C., Chastanet, G., Zueva, E., Borshch, S.A., Clemente-Juan, J.M., Luneau, D. *J. Am. Chem. Soc.*, 130, **2008**, 2365-2371.

17. (a) Müller, A., Rohlfing, R., Krickemeyer, E., Bögge, H. *Angew. Chem., Int. Ed. Engl.,* **1993**, *32*, 909-912.

(b) Yamase, T., Ohtaka, K. *J. Chem. Soc., Dalton Trans*. **1994**, 2599-2608.

(c) Hayashi, Y., Miyakoshi, N., Shinguchi, T., Uehara A., Chem. Lett. **2001**, 170-171.

18. (a) *VALENCE* for DOS, Version 2.0, Brown, I. D. *J. Appl. Crystallogr.* **1996**, *29*, 479-480.

(b) Brown, I. D. and Altermatt, D. *Acta Cryst.* **1985**, *B41*, 244-247.

19. Piro, O. E., Varetti, E. L., Brandan, S. A., Altabef, B.A. *J. Chem. Crystallogr.* **2003**, *33*(1), 57-63.

20. Dong, B., Gómez-García C.J., Peng, J., Benmansour S., Ma, J. *Polyhedron* **2007**, *26*, 1310–1316.

21. (a) Ferdov, S., Kolitsch, U., Petrov, O., Kostov-Kytin, V., Lengauer, C., Tillmanns, E. *Microporous and Mesoporous Mater*. **2005**, *81*(1-3), 79-86.

(b) Liu, Z.-H., Yang, P., Li, P., *Inorg. Chem*. **2007**, *46*, 2965-2967.
(c) Li, N., Ma, Y., Xiang, S., Guan, N. *Chem. Mater*. **2006**, *18*, 975-980.

22. Bu, W.M., Ye, L., Yang, G.Y., Shao, M.C., Fan Y.G., Xu, J.Q. *Chem. Commun*. **2000**, 1279-1280.

23. Li, Y.G., De, J.G., Yuan, M., Wang, E.B., Huang, R.D., Hu, C.W., Hu N.H., Jia, H.Q. *Dalton Trans.* **2003**, 331-334.

24. Dumas, E., Livage, C., Halut S., Herve´ G., *Chem. Commun*. **1996**, 2437-2438.

25. Gatteschi, D., Pardi, D., Barra, A.L., Müller, A., Döring, J. *Nature* **1991**, *354*, 463-465.

26. (a) Zheng, S.-T., Zhang, J., Yang G.-Y. *J. Mol. Struct*. **2004**, *705*, 127–132.

(b) Wang, C.-M., Zeng, Q.-X., Zhang, J., Yang, G.-Y., *J. Cluster Sci.* **2005**, *16*, 10876-005-2716-2718

(c) Zheng, S.-T., Zhang, J., Yang G.-Y. *Inorg. Chem*. **2005**, *44*, 2426-2430.

27. (a) Halasyamani, P.S., Poeppelmeier, K.R. *Chem. Mater*. **1998**, *10*, 2753-2769.

(b) Halasyamani, P.S. *Chem. Mater*. **2004**, *16*, 3586-3592.

28. (a) Chandrasekhar, V., Nagarajan, L., Clérac, R., Ghosh, S., Senapati, T., Verma S. *Inorg. Chem.* **2008**, *47*, 5347-5354.

(b) Murugesu, M., Anson, C.E., Powell, A.K *Chem. Commun.* **2002**, 1054–1055.

29. Reiß, P., Fenske, D. *Z. Anorg. Allg. Chem*. **2000**, *626*, 1317-1331.

30. Li, D., Wu, T., Zhou, X.-P., Zhou, R., Huang, X.-C. *Angew. Chem. Int. Ed*. **2005**, *44*, 4175 –4178.

31. Beckett, R., Colton, R.. Hoskins, B., Martin, R.L., Vince, D.G. *Aust. J. Chem.* **1969**, *22*, 2527-2533.

CHAPTER EIGHT

SYNTHESIS AND CHARACTERIZATION OF SALT-INCLUSION POROUS SOLIDS CONTAINING ISOLATED POLYOXOMETALATE CORES, (SALT)•$Cs_{2.5}(V_5O_9)(AsO_4)_2$ AND (SALT)•$Cs_2(V_4O_8)(AsO_4)_2$

Introduction

In light of the already proven applications of transition-metal oxide (TMO) clusters, including catalysis, selective sorption, separations, sensing, molecular recognition, environmental decontamination, and nanotechnology,[1] one can imagine that the development of open-framework materials utilizing these discrete clusters as building blocks could have immense promise in many applications. This task, one not to be taken lightly, is possibly one of the most challenging areas within polyoxometalate (POM) chemistry. In fact, much research has been focused on the deliberate design of POM frameworks with targeted properties including mesoporosity, electronic and ionic transport, ferro or ferrimagnetism, luminescence, and catalytic activity.[2] Even though the ability to bring polyoxometalate units together to form new materials with desirable properties is underdeveloped, there is some recent research that brings promise to this field of study. For example, using a one-pot synthesis in aqueous solutions ranging from 80 - 95 °C , Khan *et al*. made a series of novel framework materials containing well-defined $[V_{18}O_{42}]$ clusters.[3] Also, several groups have been able to synthesize new framework materials beginning with POM precursors. Sécheresse *et al*. created 1 and 2-D framework structures from a polyoxocation, $[PMo_{12}O_{36}(OH)_4\{La(H_2O)_4\}]^{5+}$, precursor

at room temperature containing $[PMo_{12}O_{36}(OH)_4]^{2+}$ clusters, [4] and Wang *et al*. synthesized a unique 3-D chiral open framework assembled from a precursor containing $[BW_{12}O_{40}]^{5-}$ clusters at 80°C.[5] The ultimate goal for this research is that scientists, through rational design, will eventually be capable of creating new framework materials whose properties can be tuned and rationalized based on the transition-metal oxide constituent used.

The idea of incorporating TMO clusters as building blocks has also been utilized in the synthesis of metal-organic frameworks, also known as MOFs. These hybrid organic-inorganic materials have metal ions or clusters as nodes linked by a variety of different organic ligands allowing tunable pore size, shape, and functionality.[6] Recently, Yaghi *et al*. reported a MOF containing a μ_4-$Zn_4O(CO_2)_6$ cluster linked by a diverse group of carboxylate ligands.[7] This material has large cavities and channels, creating excellent gas sorption properties, and like many others, has especially drawn much interest for its ability to store significant amounts of H_2.[8]

Most porous framework materials, especially the ones discussed thus far, are formed under mild conditions (T<200°C) using hydrothermal or solvothermal methods. It is often thought that high-temperatures frequently lead to the synthesis of very dense solids; therefore, it is not a common practice to search for porous materials using high-temperature, solid state methods. Among the most notable and technologically important solid state materials are the aluminosilicates, or zeolites, which are usually formed under mild hydrothermal conditions.[9] In order to create large internal volumes, large organic cations are used as templates around which the 3-D inorganic oxide framework forms.

The organic templates can be subsequently removed in order to create large voids within the crystalline lattice.

Recent reports have proven salt-inclusion chemistry to be an alternative to aid in the creation of new porous materials at high temperatures.[10] These newly formed salt-inclusion solids (SISs) have rigid covalent frameworks integrated with ionic lattices. Like the organic cations in their zeolite counterparts, the salt serves as a template around which the 3-D inorganic framework can form. This high-temperature synthetic method, proven to be a means to create new open-framework systems after easy salt removal, could lead to the creation of many new porous materials with an extensive number of possible applications such as catalysis, magnetism, batteries, and gas sorption.

Chapter 8 will be focused on the synthesis and characterization of a new type of porous hybrid material, (salt)•$Cs_{2.5}(V_5O_9)(AsO_4)_2$ (V_5 hereafter), containing paramagnetic vanadium oxide clusters. Like the salt-inclusion solids (SISs) presented in the previous chapter, V_5 is a SIS exhibiting an integrated framework of covalent metal oxide comprised of POM pentamers. These pentamers, with the composition $[V_5O_{17}]$, are interconnected *via* AsO_4^{3-} units through corner-sharing oxygen. This compound is a new member of the 3-D open-framework SISs. The formation of the open-framework structure demonstrates the utility of salt inclusion chemistry, where the salt serves as a structure-directing agent, aiding the formation of the large channels and cavities. Due to the weak interaction at the interface of the composite lattices, the salt can be removed by soaking the material in deionized water, creating a higher surface area. In this work, efforts were made to maximize the surface area of the solid without compromising

structural integrity. The idea was to oxidize the cluster, reducing the amount of charge-balancing Cs^+ cations in the channels, hence maximizing the available volume of vacant space. Two methods were utilized to achieve oxidative removal (or exclusion) of the Cs^+ cations: 1) direct synthesis *via* traditional high-temperature, solid-state methods under oxidizing conditions to exclude additional Cs^+ and 2) soaking the as-prepared solid in a solution of various oxidizing agents such as H_2O_2 or I_2 to remove exiting Cs^+.

To the best of our knowledge, this is the first time a POM-containing open-framework has been synthesized using high-temperature, molten-salt methods. The utility of the material presented here is the result of the incorporated polyoxometalate cores, the porous framework created by the salt, and the added rigidity of the fully inorganic system. Efforts were made to synthesize several derivatives of V_5, including a neutral framework material having the same porous structure, $V_5O_9(AsO_4)_2$, a solid solution series, (salt)•$Cs_{(6-n)}(V_5O_9)^{n+}(AsO_4)_2$ where n = 2, 2.5, 3, 4, 4.5, and 6, and a Ni and Cu-containing neutral framework, (salt)•$(Cu/NiV_4O_8)(AsO_4)_2$. During our effort to derivatize the title compound, a similar compound, (salt)•$Cs_2(V_4O_8)(AsO_4)_2$ (V_4 hereafter), containing a fully oxidized $[V_4O_{16}]$ core was found. Here, the synthesis, structure, and characterization of this novel compound, (salt)•$Cs_{2.5}(V_5O_9)(AsO_4)_2$, and its derivatives are presented.

Synthesis

Single Crystal Growth of (salt)•$Cs_{2.5}(V_5O_9)(AsO_4)_2$: Single crystals of salt•$Cs_{2.5}(V_5O_9)(AsO_4)_2$ were serendipitously grown using V_2O_5, VO_2, and As_2O_3 (ca. 0.3

g) in 2:1:1 mol ratio along with a CsCl/NaCl eutectic flux equal to 3 times the mass of the oxide reactants. The reactants were heated to 650°C, held there for 4 days, slowly cooled to 450°C, and then furnace-cooled to room temperature. The reactants were mixed and ground inside of a nitrogen-purged drybox, placed in silica ampoules, and then sealed under vacuum. Small blue cubic crystals were isolated after washing the reaction with deionized water in an approximate yield of 20%. Additional identified phases include red plates of a newly synthesized compound, $Cs_5VCl_6VO(VO_3)_4$ (≈ 30%). Unidentified phases include red and blue polycrystalline powders.

Single Crystal Growth of (salt)•$Cs_2(V_4O_8)(AsO_4)_2$: Single crystals of (salt)•$Cs_2(V_4O_8)(AsO_4)_2$ were grown using VO_2, V_2O_5, and As_2O_5 in a 6:2:1 mol ratio. The reactants (0.3g) were added to a CsCl/NaCl flux equal to three times the mass of the oxide reactants (0.9g). The reactants were ground inside of a nitrogen-purged drybox, placed in silica ampoules, and then sealed under vacuum. The reaction was then heated to 650°C at a rate of 1°C/min., held for 3 days, and then furnace-cooled to room temperature. The products were washed with deionized water to remove excess, unreacted salt. The reaction rendered small red cubic crystals of the title compound (≈ 80%) and small plate-like red crystals of $NaVO(AsO_4)$.[11] It should be noted that this reaction was not originally intended to grow single crystals of (salt)•$Cs_2(V_4O_8)(AsO_4)_2$. If the reaction were slowly cooled, it is likely that larger crystals of the phase will form.

100% Yield Synthesis of (salt)•$Cs_{2.5}(V_5O_9)(AsO_4)_2$ (V_5) and (salt)•$Cs_2(V_4O_8)(AsO_4)_2$ (V_4): After structure determination by single crystal X-ray methods, see below, stoichiometric syntheses were carried out for the confirmation of

composition as well as property characterization. $CsVO_3$, VO_2, Cs_3VO_4, and As_2O_5, were mixed in a 1:3.5:0.5:1 mol ratio (ca. 0.5g), and $CsVO_3$, V_2O_5, and As_2O_5, were mixed in a 2:1:1 mol ratio (ca. 0.5g) to make 100% yields of salt•$Cs_{2.5}(V_5O_9)(AsO_4)_2$ and salt•$Cs_2(V_4O_8)(AsO_4)_2$ respectively. The reactants were added to a CsCl/NaCl eutectic flux equal to 2 times the mass of the oxide reactants, ground together in a nitrogen-purged drybox, and then sealed under vacuum in a silica ampoule. The reactions were heated to 600° C at a rate of 1°C/min, held there for 72 hours, and then furnace-cooled to room temperature. The reaction product was ground and washed with deionized water to remove excess unreacted salt. For (salt)•$Cs_{2.5}(V_5O_9)(AsO_4)_2$, a dark-blue polycrystalline powder remained, while for (salt)•$Cs_2(V_4O_8)(AsO_4)_2$, a red-brown powder remained. The PXRD data are shown in Figures 8.1 and 8.2. The 100% yield synthesis of (salt)•$Cs_{2.5}(V_5O_9)(AsO_4)_2$ were soaked or sonicated in deionized water for periods as long as 8 hours in order to remove the salt in the channels. Figure 8.3 shows the powder patterns from a soaked sample of (salt)•$Cs_{2.5}(V_5O_9)(AsO_4)_2$.

Synthesis of Solid Solution Series (salt)•$Cs_{(6-n)}(V_5O_9)^{n+}(AsO_4)_2$: Attempts were made to synthesize a solid solution series of the (salt)•$Cs_{(6-n)}(V_5O_9)^{n+}(AsO_4)_2$, in part, in an effort to seek compositions that exhibit fewer cations in the channel structure. In these syntheses, attempts were made to alter both the oxidation state of the vanadium oxide cluster and the number of charge-balancing Cs^+ cations found in the channels of the structure. Two general formulas were used for the oxidation and reduction of the vanadium clusters respectively:

(1) (6-n) $CsVO_3$ + (7-n)VO_2 + (n-4) V_2O_5 + As_2O_5 → (salt)•$Cs_{(6-n)}(V_5O_9)^{n+}(AsO_4)_2$

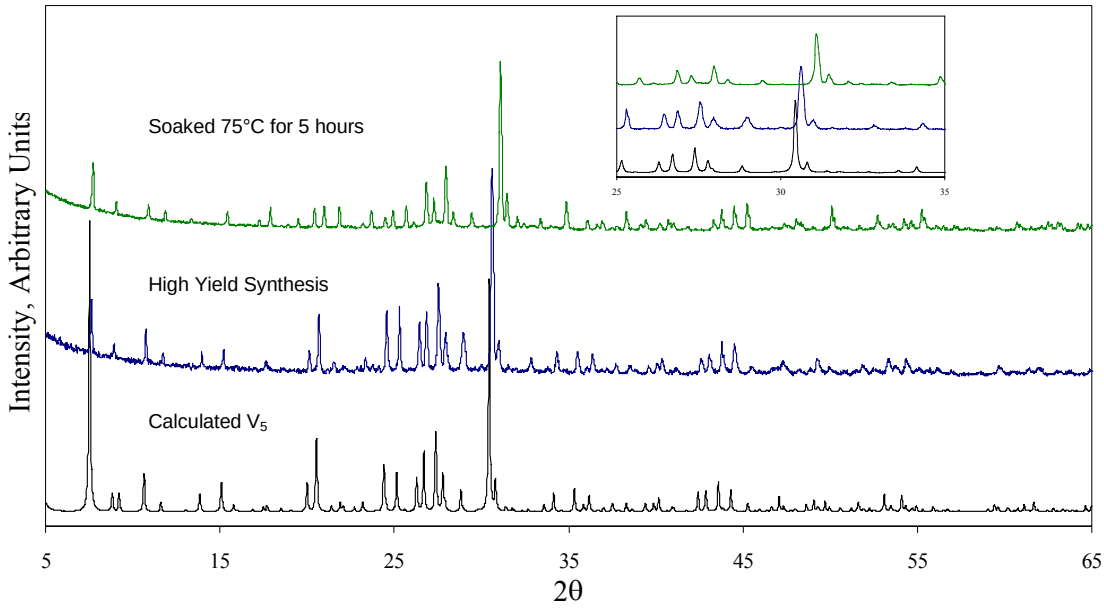

Figure 8.1: Calculated powder X-ray diffraction pattern obtained from the crystal structure solution of $Cs_{3.5}Na_{1.46}(V_5O_9)(AsO_4)_2Cl_{2.33}$, V_5, *vs*. a powder pattern from a high yield synthesis targeting (salt)•$Cs_{2.5}(V_5O_9)(AsO_4)_2$. The high yield product was heated in H_2O for 5 hours for salt removal. There is a shift of diffraction pattern to the right (higher 2θ angle) after heating, signifying a reduction in the unit cell volume attributed to the salt in the channel being washed out, see inset.

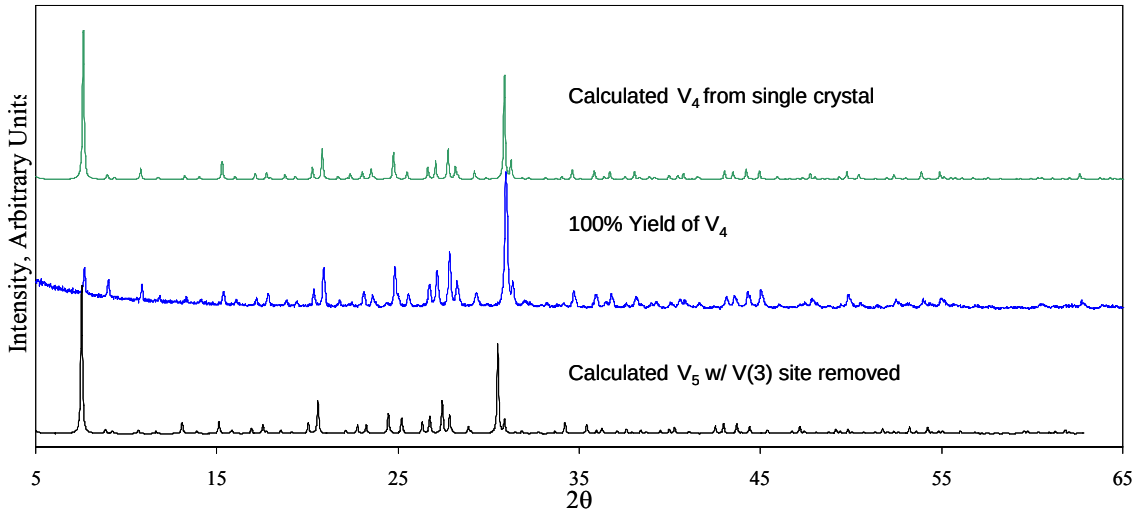

Figure 8.2: Calculated powder X-ray diffraction patterns of $Cs_{3.5}Na_{1.46}(V_5O_9)(AsO_4)_2Cl_{2.33}$, V_5, with the central V(3) removed and $Cs_{3.64}Na_{1.40}(V_4O_8)(AsO_4)_2Cl_{3.04}$, V_4, *vs*. a powder pattern from a 100% yield synthesis targeting the fully oxidized V_4 cluster with the composition (salt)•$Cs_2(V_4O_8)(AsO_4)_2$.

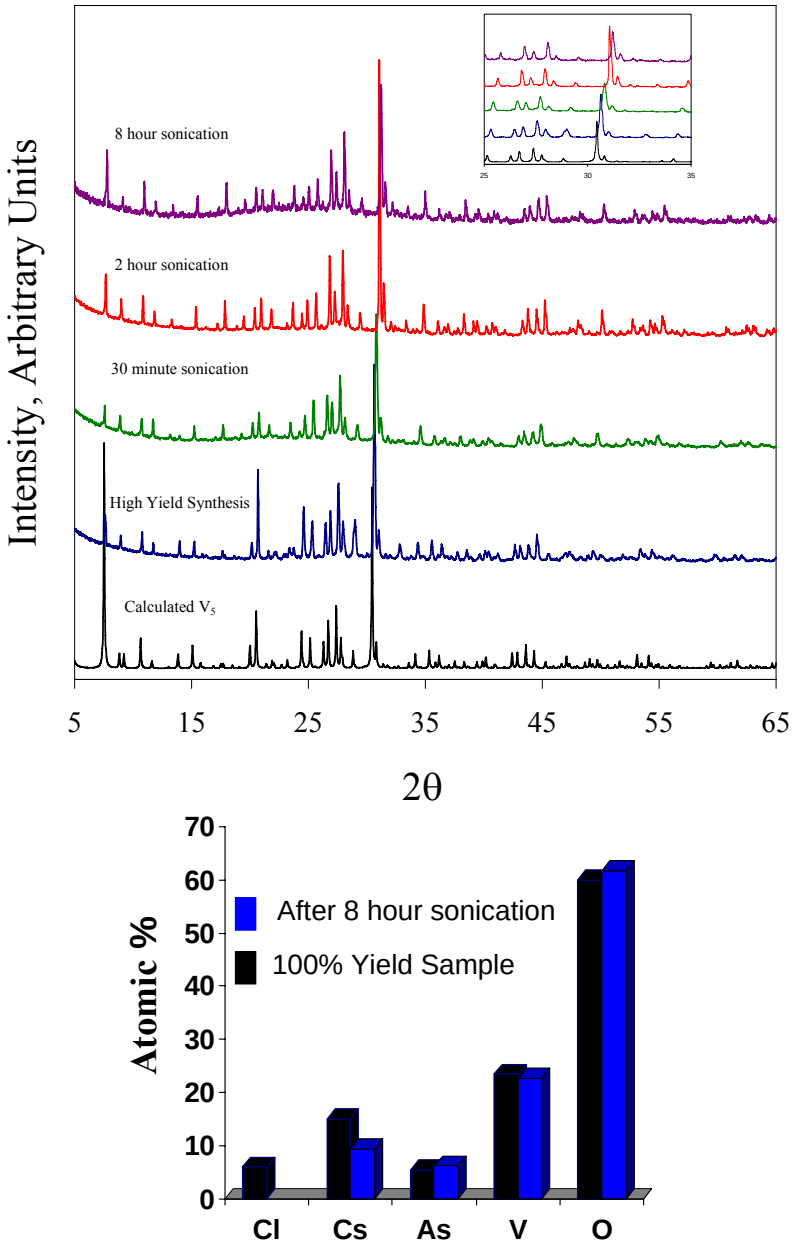

Figure 8.3: (top) Calculated powder pattern obtained from the crystal structure solution of $Cs_{3.5}Na_{1.46}(V_5O_9)(AsO_4)_2Cl_{2.33}$, V_5, *vs.* a powder pattern for a high yield synthesis targeting (salt)•$Cs_{2.5}(V_5O_9)(AsO_4)_2$. The high yield product was sonicated in H_2O for various periods of time. There is a shift to higher 2θ values after longer sonication times, indicating a reduction in the unit cell volume due to the removal of salt. The elemental analysis of the 100% yield synthesis (bottom) before and after the 8-hour sonication is also shown. Initially, there is a significant amount of Cs and Cl, however, after the 8-hour sonication, the amount of Cs is reduced and the Cl is gone. These results strongly support the loss of salt in the structure upon washing.

(2) (2-n/3) Cs_3VO_4 + (1+n)VO_2 + (2-2n/3)VO + As_2O_5 → (salt)•$Cs_{(6-n)}(V_5O_9)^{n+}(AsO_4)_2$

These reactions were attempted for various values of n, including n = 4, 4.5, and 6, for the oxidation reaction (1), and n = 2, 2.5, and 3 for the reduction reaction (2). The oxidation reaction (1) was utilized to obtain compositions that would exhibit fewer cations in the channel structure relative to the original phase, (salt)•$Cs_{2.5}(V_5O_9)(AsO_4)_2$. The reduction reactions were utilized to simply see how versatile the structure was in terms of vanadium oxidation states and the number of cations incorporated into the framework. These reactants were mixed with a CsCl/NaCl flux equal to three times the mass of the oxides and then ground in a nitrogen- purged drybox. The reactants were placed into silica ampoules and sealed under vacuum. They were then heated to 650°C at a rate of 1°C/min., held for 3 days, and then furnace-cooled to room temperature. The products were ground and then washed with deionized water to remove excess unreacted salt. Most of these reactions rendered high yields ranging from 80 – 90% with small impurities of $NaVO(AsO_4)$.[11] Single crystals were obtained from reactions with n = 4.5 and 6, and efforts were made to solve the single crystal structure of these two phases. These two phases were determined to be an oxidized version of the title phase. Instead of the target compositions, (salt)•$Cs_{1.5}(V_5O_9)(AsO_4)_2$ and (salt)•$(V_5O_9)(AsO_4)_2$ for n= 4.5 and 6 respectively, these phases instead incorporated less vanadium into the core, leading to a fully oxidized $[V_4O_{16}]$ core. The red cubic crystals from the n = 6 reaction were determined to be $Cs_{3.64}Na_{1.40}(V_4O_8)(AsO_4)_2Cl_{3.04}$, V_4, which has the same framework structure as the V_5 compound, but the apical V(3) site is empty. The composition of

these phases will be further detailed in the discussion section. The powder patterns of the oxidation / reduction reactions are shown in Figures 8.4 and 8.5.

Oxidation of the as-prepared 100% yield sample of (salt)•$Cs_{2.5}(V_5O_9)(AsO_4)_2$: In order to further increase the surface area of the material, attempts were made to oxidize the 100% yield sample of (salt)•$Cs_{2.5}(V_5O_9)(AsO_4)_2$. The powder was first soaked in water for four hours to remove the salt, which left a polycrystalline powder of $Cs_{2.5}(V_5O_9)(AsO_4)_2$. Conceptually, oxidation will allow the removal of the remaining charge-balancing Cs cations left in the channel, as illustrated in the following reactions:

(1) $Cs_{2.5}(V_5O_9)(AsO_4)_2 + 1.25\ H_2O_2 \xrightarrow{H_2O} V_5O_9(AsO_4)_2 \bullet xH_2O + 2.5\ CsOH$

(2) $Cs_{2.5}(V_5O_9)(AsO_4)_2 + 1.25\ I_2 \xrightarrow{CH_3CN} V_5O_9(AsO_4)_2 + 2.5\ CsI$

The goal of these reactions was to oxidatively remove Cs^+ from the channels without compromising the structural integrity of the porous framework. It should be noted that the oxidizing agent to Cs ratio was equivalent to 2.5:1. In cases where the oxidizing agent was not used in excess, there was no visible change in the color of the powder within a reasonable amount of time. For the H_2O_2 reactions, 0.56 mL of a 3% solution of H_2O_2 was diluted with 25mL of deionized water. Then, 0.1000g of $Cs_{2.5}(V_5O_9)(AsO_4)_2$ was added to the solution. The powder was soaked in the solution with stirring for approximately 2 hours. After 10 minutes, the powder had an observed color change. After 2 hours, the powder had changed from green to red, indicating a change in the oxidation state of vanadium. The powder was then removed from the solution *via* filtration. For the I_2 reaction, 0.1000g of powder $Cs_{2.5}(V_5O_9)(AsO_4)_2$ was ground with 0.1000g of I_2 crystals. The resulting powder was then added to 50mL of

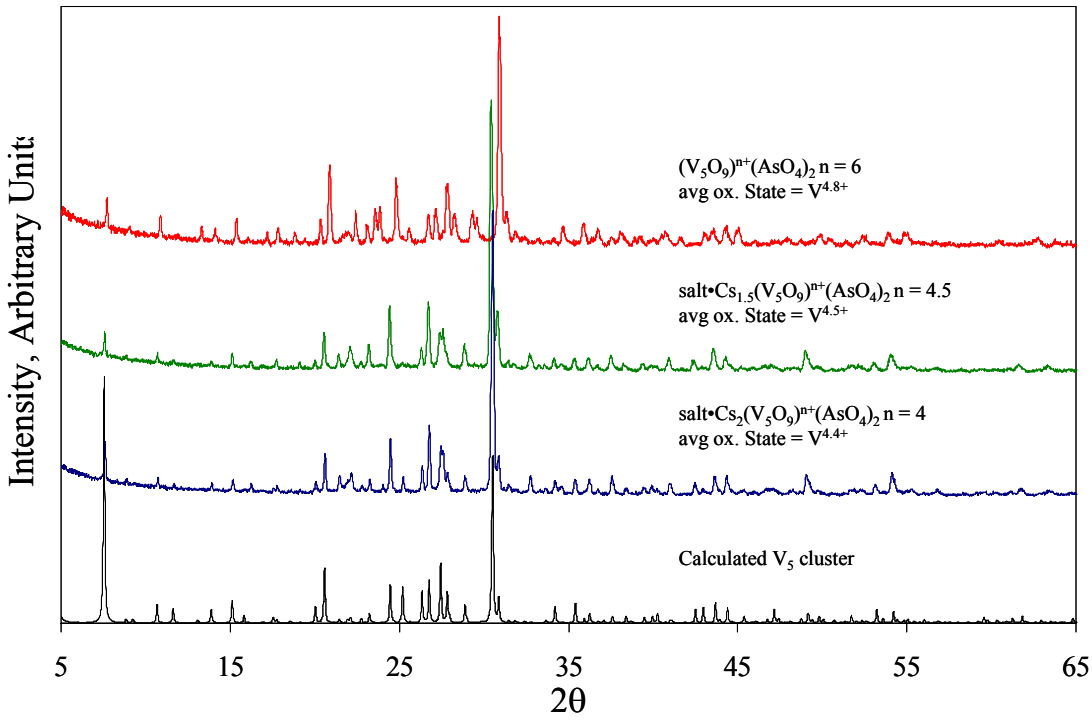

Figure 8.4: Calculated powder pattern for $Cs_{3.5}Na_{1.46}(V_5O_9)(AsO_4)_2Cl_{2.33}$, V_5, compared to experimental powder patterns of (salt)•$Cs_{6-n}(V_5O_9)^{n+}(AsO_4)_2$ for n = 4, 4.5, and 6. It should be noted that if n = 6, a neutral framework should be obtained.

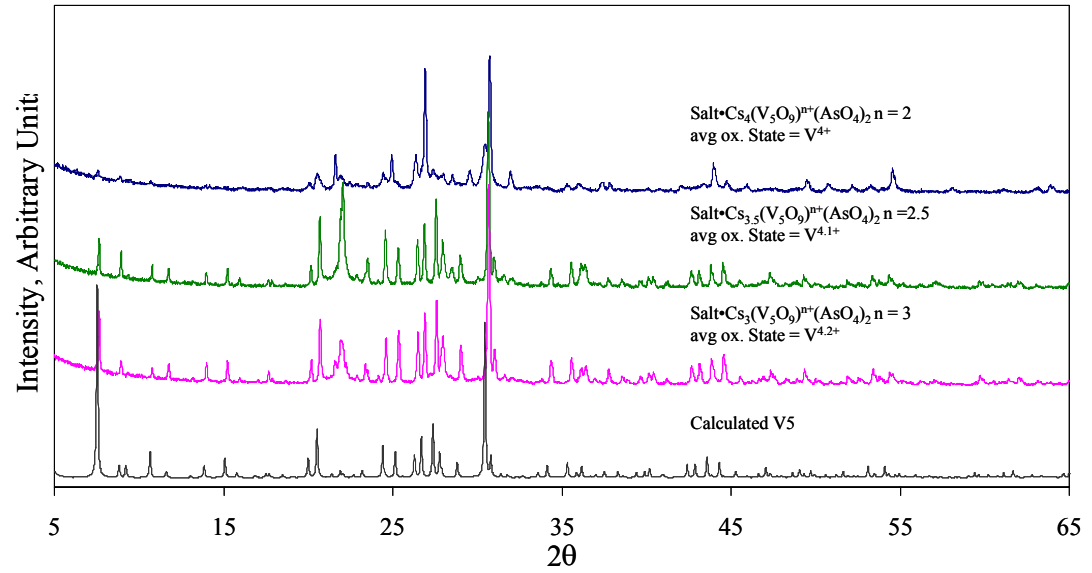

Figure 8.5: Calculated powder pattern for $Cs_{3.5}Na_{1.46}(V_5O_9)(AsO_4)_2Cl_{2.33}$,$V_5$, compared to experimental powder patterns of (salt)•$Cs_{6-n}(V_5O_9)^{n+}(AsO_4)_2$ for n = 2, 2.5, and 3.

CH_3CN and heated at 60°C for two hours with stirring. The powder in this reaction only showed a slight color change from green to brownish-green. The powder patterns, showing the oxidation of $Cs_{2.5}(V_5O_9)(AsO_4)_2$ using I_2/H_2O_2, are shown in Figure 8.6.

Li^+ Ion Exchange: The soaked 100% yield sample of $Cs_{2.5}(V_5O_9(AsO_4)_2$ was subjected to Li ion-exchange. A total of 0.1000g of the powder was placed in 10mL of a 1M $LiNO_3$ solution and sealed inside of a 20mL Parr bomb. The bomb was heated to 120°C, held there for 12 hours, and then furnace-cooled to room temperature. PXRD was performed on the remaining solid, which is shown in Figure 8.6. There were multiple impurities found in the sample, which implies that the ion-exchange was too harsh on the sample, possibly causing some decomposition. Lower temperature ion exchange reactions could reduce the chance of decomposition; however, it has not yet been performed.

Synthesis of (salt)•$(Cu/NiV_4O_8)(AsO_4)_2$ derivatives: After the discovery of (salt)•$Cs_2(V_4O_8)(AsO_4)_2$, efforts were also made to create a neutral framework *via* chemical substitution. The goal was to make the fully oxidized V_4 framework with Cu^{2+} or Ni^{2+} in the empty site. This act would create a neutral framework requiring no charge-balancing Cs^+ cations, (salt)•$(Cu/NiV_4O_8)(AsO_4)_2$. For the synthesis of the target compound, Cu/NiO, V_2O_5, and As_2O_5 were mixed in a 1:2:1 mol ratio. The reactants were added to a CsCl/NaCl flux equal to 3 times the mass of the oxides. The components were ground inside of a nitrogen-purged drybox using an agate mortar and pestle, placed in silica ampoules, and then sealed under vacuum. They were heated to 600°C, held there for 2 days, and then furnace-cooled to room temperature. The reaction product was

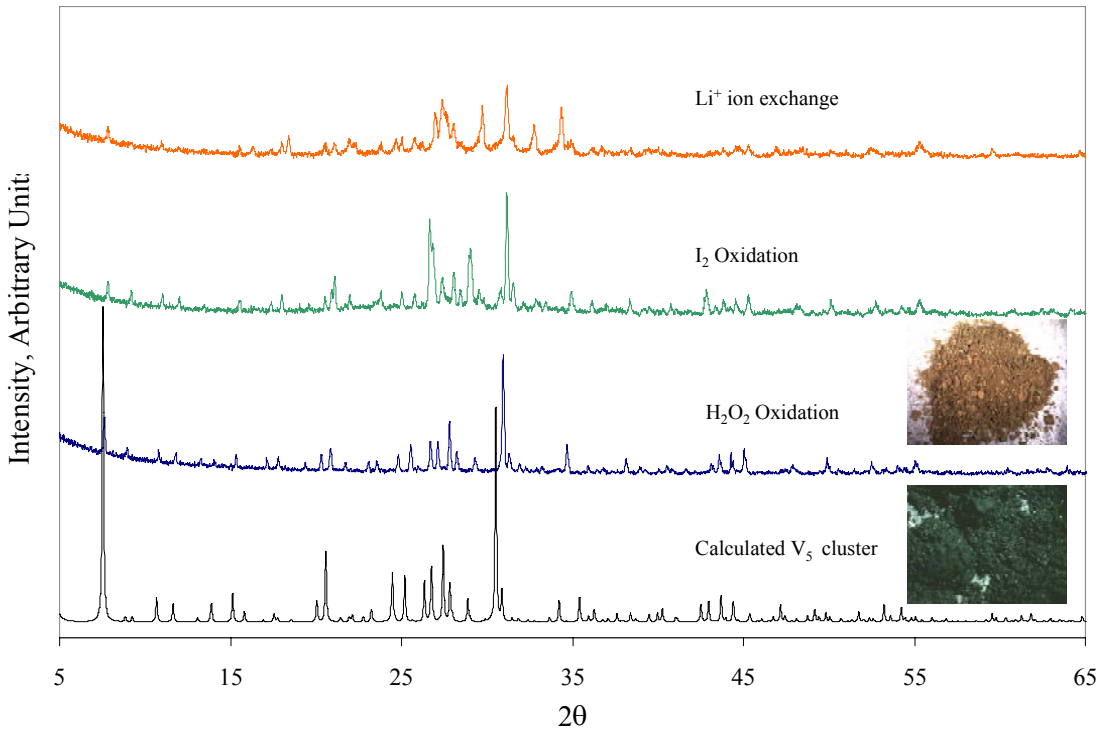

Figure 8.6: Calculated powder pattern of $Cs_{3.5}Na_{1.46}(V_5O_9)(AsO_4)_2Cl_{2.33}$, V_5, compared to the post-synthesis oxidation products from the I_2 and H_2O_2 reactions and the Li^+ ion exchange attempt. The images in the bottom right hand corner show the color change in the material upon H_2O_2 oxidation. The 100% yield powder goes from dark blue-green to red.

ground and then washed with deionized water to remove the excess salt. The powder pattern for the resulting Cu reaction can be seen in Figure 8.7. The Ni reaction is not shown as a result of a large number of unidentified impurity peaks.

Synthesis of CsI/CsBr derivatives: Efforts were made to synthesize this framework with various salts. $CsVO_3$, V_2O_3, VO_2 and As_2O_5, in a 5:1:3:2 mol ratio (ca. 0.5g), were added to 1.0 gram of CsI or CsBr. The reactants were ground, placed in a silica ampoule, and sealed under vacuum. The reactions were heated to 600°C, held there for 12 hours, and then furnace-cooled to room temperature. The powder patterns for the synthesized products can be seen in Figure 8.8. The powder patterns for the two products closely resemble the calculated powder pattern of V_5. Efforts were made to refine the unit cell parameters for the CsBr- and CsI-containing derivatives using GSAS/EXPGUI.[12] The refined unit cell parameters for $(CsBr)(V_5O_9)(AsO_4)_2$ were a = 33.33(2) and V = 37034(60). A refinement could not be obtained from $(CsI)(V_5O_9)(AsO_4)_2$ due to the poor quality of the powder pattern.

Characterization

Elemental Analysis: Qualitative elemental analysis was performed by EDX on various single crystals used in the structure determinations and several polycrystalline powders that were subject to modification including washing, oxidation, Li^+ ion exchange, and chemical doping. Although this technique was not used as a quantitative measure of elemental content, the results showed the presence of the respective elements found in the chemical formulas for each single crystal structure solution, and gave a

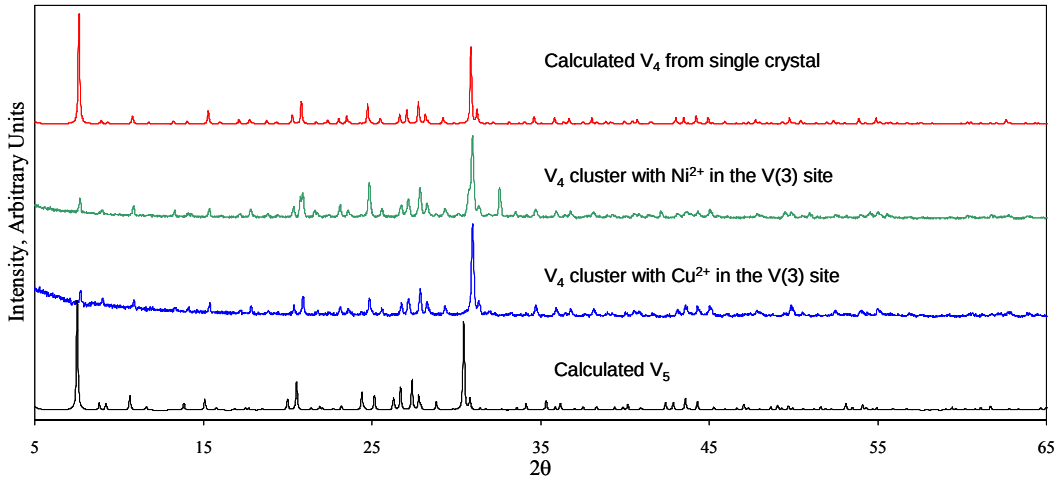

Figure 8.7: Calculated powder pattern for $Cs_{3.5}Na_{1.46}(V_5O_9)(AsO_4)_2Cl_{2.33}$, V_5, and $Cs_{3.64}Na_{1.40}(V_4O_8)(AsO_4)_2Cl_{3.04}$, V_4, *vs.* powder patterns from high yield syntheses targeting the neutral frameworks (salt)•$(V_4CuO_8)(AsO_4)_2$ and (salt)•$(V_4NiO_8)(AsO_4)_2$. The goal was to put Cu^{2+}/Ni^{2+} in the square planar V(3) site.

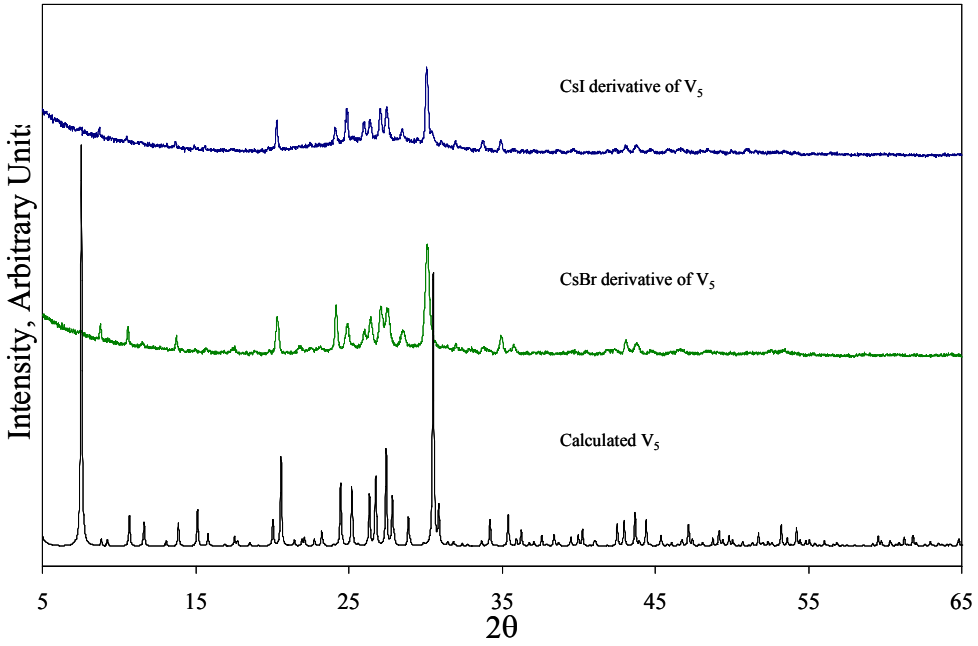

Figure 8.8: Calculated powder pattern of $Cs_{3.5}Na_{1.46}(V_5O_9)(AsO_4)_2Cl_{2.33}$ and the powder patterns of the reactions targeting $(CsX)Cs_{2.5}(V_5O_9)(AsO_4)_2$ where x = Br^- or I^-. The powder patterns closely resemble the calculated PXRD pattern of the CsCl derivative, V_5. Shifts to lower 2θ values indicate an increase in the unit cell volume. Refined unit cell parameters obtained for the CsBr derivative (refined in the *Fd*-3*m* spacegroup (no.227)) were a = 33.33(2) and V = 37034(60). A unit cell refinement of the CsI derivative could not be obtained, presumably because of the poor quality of the powder pattern.

qualitative measure of whether chemical modification was successful. Since EDX is a surface technique, most of the crystals in this study were cut in half to decrease possibilities of surface contamination, and the newly exposed surface was analyzed.

Magnetic Susceptibility: Magnetic susceptibility was measured with a Superconducting Quantum Interference Device (SQUID) MPMS-5S magnetometer. Zero-field cooling measurements were collected from 2-300K in an applied magnetic field of H = 0.01T. A polycrystalline sample, obtained from a 100% yield synthesis of (salt)•$Cs_{2.5}(V_5O_9)(AsO_4)_2$ (15.6 mg), was used for the magnetic measurements. Field-dependent magnetization data was obtained from this same sample at 2K, 3.5K, 5K, and 10K in applied fields ranging from ±5T.

Surface Area Measurements: Surface area measurements were performed on a Micromeritics Accelerated Surface Area and Porosimetry System, ASAP 2020. The samples, with sizes ranging from 0.15 to 1.0 gram, were degassed at temperatures ranging from 60-150°C at 10°C/min.

Thermal Gravimetric Analysis: TGA was utilized to monitor the weight change of the sample as a function of temperature. This was performed on a 100% yield sample that was soaked for 4 hours in deionized water to remove the salt. The TGA was utilized to determine the temperature at which the sample needed to be degassed in order to remove the excess water left in the channels for surface area analysis.

Powder X-ray Diffraction: The powder X-ray diffraction data were collected at room temperature using a Scintag XDS 2000 diffractometer in the 2θ range of 5–65° with a step size of 0.02 and scan rates ranging from 0.0033-0.0080°/s. PXRD was used to

confirm the presence of each phase in their respective high-yield reactions and to probe the change in the volume of compounds after certain treatment such as soaking and oxidation, as peak shifts to higher 2θ values are indicative of decreases in unit cell volumes. Unit cell refinements were performed, using the GSAS/EXPGUI and Fullprof programs[12], on various samples to determine the unit cell parameters where single crystals were not available. The unit cell refinements can be seen in Table 8.1 and compared to the single crystal structure solutions of V_4 and V_5.

Single Crystal X-ray Diffraction: Metallic blue cubic crystals of (salt)•$Cs_{2.5}(V_5O_9)(AsO_4)_2$ were selected under an optical microscope. The data were collected at room temperature (~300K) with a crystal-to-detector distance of approximately 32.6 mm and a scan time of 220s for the solution having the empirical formula $Cs_{3.5}Na_{1.46}(V_5O_9)(AsO_4)_2Cl_{2.33}$. Other single crystals listed in Table 8.2 had crystal-to-detector distances of 27.6 mm and scan times ranging from 120-220s. The crystallographic data for $Cs_{3.5}Na_{1.46}(V_5O_9)(AsO_4)_2Cl_{2.33}$ is summarized in Table 8.3. The atomic coordinates, thermal parameters, and selected bond distances and angles of this particular crystal are listed in Tables 8.4-8.6. The original structure was solved in a triclinic spacegroup, *P*-1, and then converted to higher symmetry using Platon, and the SQUEEZE option in the Platon program was also used to calculate the positions and volume of solvent-void space within the unit cell. [13] It should be noted that the secondary extinction parameters are not included. The parameter was refined; however, it proved to be insignificant. Therefore, it was removed. Also, the standard deviations for the sof of partially occupied sites are not reported because SHELXTL[14] was first used to refine the

Table 8.1: Unit cell refinements of various powder samples

Sample	Sample type	unit cell parameters	Source of unit cell parameters	Figure # corresponding to powder pattern
V_5	Single crystal	a = 33.119(4)Å V = 36329(7) Å^3	SXRD	None
V_4	Single crystal	a = 32.742(4) Å V = 35101(7) Å^3	SXRD	None
100 % yield of V_5	Powder	a = 33.078(1) Å V = 36192(3) Å^3	PXRD/Fullprof[12a.b]	Figure 8.1 and 8.3
100% yield of V_5 heated in H_2O (75°C) for 5 hours to remove salt	Powder	a = 33.0268(7) Å V = 36024(1) Å^3	PXRD/Fullprof	Figure 8.1
100% yield V_5 sonicated in H_2O for 8 hours to remove salt	Powder	a = 33.060(9) Å V = 36133(17) Å^3	PXRD/Fullprof	Figure 8.3
Oxidation of as prepared V_5 in H_2O_2	Powder	a = 32.657(1) Å V = 34827(2) Å^3	PXRD/Fullprof	Figure 8.6
Cu doped reaction	Powder	a = 32.705(1) Å V = 34983(2) Å^3	PXRD/Fullprof	Figure 8.7
CsBr derivative of V_5	Powder	a = 33.33(2) Å V = 37034(60) Å^3	GSAS/EXPGUI[12c]	Figure 8.8

Table 8.2: Single crystal structure solutions from seven (salt)•$Cs_{(6-n)}(V_5O_9)^{n+}(AsO_4)_2$ crystals

Solution	$Cs_{3.63}Na_{0.385}(V_5O_9)(AsO_4)_2Cl_{2.50}$ (1)	$Cs_{4.44}Na_{0.674}(V_5O_9)(AsO_4)_2Cl_{1.89}$ (2)	$Cs_{3.79}(V_5O_9)(AsO_4)_2Cl_{2.19}$ (3)
Crystal system	Cubic	Cubic	Cubic
Space group	*Fd*-3*m* (no. 227)	*Fd*-3*m* (no. 227)	*Fd*-3*m* (no. 227)
Unit cell dimensions	a = 33.189(4) Å	a = 33.242(4) Å	a = 33.149(3) Å
Cell volume	36558(7) Å^3	36735(7) Å^3	36426(6) Å^3
R1	0.1403	0.1482	0.1163
Avg ox. state of V	4.50	4.16	4.48

Solution	$Cs_{3.56}Na_{0.39}(V_5O_9)(AsO_4)_2Cl_{1.59}$ (4)	$Cs_{3.75}Na_{0.37}(V_5O_9)(AsO_4)_2Cl_{2.36}$ (5)	$Cs_{3.5}Na_{1.46}(V_5O_9)(AsO_4)_2Cl_{2.33}$ (6)
Crystal system	Cubic	Cubic	Cubic
Space group	*Fd*-3*m* (no. 227)	*Fd*-3*m* (no. 227)	*Fd*-3*m* (no. 227)
Unit cell dimensions	a = 33.058(4) Å	a = 33.272(4) Å	a = 33.119(4) Å
Cell volume	36126(7)Å^3	36833(7) Å^3	36329(7) Å^3
R1	0.1866	0.1126	0.0707
Avg ox. state of V	4.33	4.45	4.27

Table 8.3: Crystallographic data for V_5 and V_4

empirical formula	$Cs_{3.5}Na_{1.46}(V_5O_9)(AsO_4)_2Cl_{2.33}$[a]	$Cs_{3.64}Na_{1.40}(V_4O_8)(AsO_4)_2Cl_{3.04}$[b]
	V_5	V_4
color / shape	blue / cube	red / cube
crystal size (mm)	0.10 × 0.08 × 0.06	0.05 × 0.05 × 0.04
formula weight (amu)	1257.97	1234.05
space group	*Fd-3m* (no. 227)	*Fd-3m* (no. 227)
Z	12	12
T, °C	25	
a, Å	33.119(4)	32.742(4)
V, Å^3	36329(7)	35101(7)
linear abs. coeff., mm^{-1}	8.083	8.304
F_{000}	27130	26566
d_{calc}, g / cm^{-3}	2.760	2.802
data / restraints / parameters	1563 / 0 / 108	1511 / 0 / 108
secondary extinction	——	——
reflections collected / unique	14750 / 1563	17139 / 1511
final R1/wR2 [a] [$I > 2\ \sigma(I)$]	0.0707 / 0.1976	0.1030 / 0.2483
R1/wR2 (all data)	0.0957 / 0.2291	0.1360 / 0.2847
GOF	1.044	1.737
Largest difference peak / hole (e$^-$ / Å^3)	1.963 / -1.091	5.915 / -2.285

[a] $R1 = \Sigma\ ||F_o| - |F_c|| / \Sigma|F_o|$; $wR2 = \{[\Sigma[w(F_o^2-F_c^2)^2] / [\Sigma w(F_o)^2)^2]\}^{1/2}$; $Rw = 1 / [\sigma^2(Fo^2) + (0.1330P)^2+1403.8384P]$ where $P = (Fo^2+2Fc^2) / 3$

[b] $R1 = \Sigma\ ||F_o| - |F_c|| / \Sigma|F_o|$; $wR2 = \{[\Sigma[w(F_o^2-F_c^2)^2] / [\Sigma w(F_o)^2)^2]\}^{1/2}$; $Rw = 1 / [\sigma^2(Fo^2) + (0.1000P)\text{^}2\text{^}+0.0000P]$ where $P = (Fo^2+2Fc^2) / 3$

Table 8.4: Atomic parameters for V_5 and V_4

Atom	Wycoff position	sof	x	y	z
			$Cs_{3.5}Na_{1.46}(V_5O_9)(AsO_4)_2Cl_{2.33}$, V_5		
Cs1	96*g*	1.0	0.12632(4)	0.24119(3)	0.50881(3)
Cs2	96*g*	0.622	0.03912(7)	0.31024(7)	0.43976(7)
Cs3	48*f*	0.064	1/8	0.3971(2)	5/8
Na1	16*d*	0.377	1/4	1/4	1/2
Na2	8*b*	0.494	1/8	1/8	5/8
Na3	96*g*	0.625	0.027(1)	0.434(1)	0.527(1)
V1	96*g*	1.0	0.06872(5)	0.33507(7)	0.56872(5)
V2	96*g*	1.0	0.16432(7)	0.31990(5)	0.43010(5)
V3	48*f*	1.0	1/8	0.2986(1)	5/8
O1	192*i*	1.0	0.1247(2)	0.3164(2)	0.5706(2)
O2	48*f*	1.0	1/8	1/8	0.5004(5)
O3	192*i*	1.0	0.1245(2)	0.4171(2)	0.4725(2)
O4	192*i*	1.0	0.1242(2)	0.3331(2)	0.4713(2)
O5	96*g*	1.0	0.0453(2)	0.2996(3)	0.5453(2)
O6	96*g*	1.0	0.1998(3)	0.2970(2)	0.4530(2)
Cl1	32*e*	0.750	0.0765(5)	0.1735(5)	0.5765(5)
Cl2	32*e*	0.650	0.1775(6)	0.1775(6)	0.5725(6)
Cl3	96*g*	0.200	-0.006(1)	0.379(2)	0.494(1)
Cl4	96*g*	0.500	0.059(1)	0.4609(5)	0.559(1)
			$Cs_{3.64}Na_{1.40}(V_4O_8)(AsO_4)_2Cl_{3.04}$, V_4		
Cs1	96*g*	1.0	-0.00716(4)	0.49284(4)	-0.62110(6)
Cs2	96*g*	0.63	0.21440(11)	0.31573(14)	0.31573(14)
Cs3	96*g*	0.09	-0.2432(5)	0.7568(5)	0.3732(8)
Cs5	96*g*	0.17	0.2393(19)	1/8	1/8
Cs6	96*g*	0.04	0.2536(14)	-0.0036(14)	-0.0036(14)
Na1	96*g*	0.67	0.4137(16)	0.0300(11)	0.0300(11)
Na2	16*c*	0.38	5/8	1/8	-3/8
As1	96*g*	1.0	0.37511(3)	0.12489(3)	0
V1	96*g*	1.0	0.33441(9)	0.07205(6)	0.07205(6)
V2	192*i*	1.0	0.33544(9)	0.17690(6)	0.07310(6)
O1	192*i*	1.0	0.3763(3)	0.1668(3)	0.0295(2)
O2	192*i*	1.0	0.3753(3)	0.0821(3)	0.0282(2)
O3	192*i*	1.0	0.3176(3)	0.1247(3)	0.0668(3)
O4	96*g*	1.0	0.3000(5)	0.0477(3)	0.0477(3)
O5	192*i*	1.0	0.3011(4)	0.2004(3)	0.0496(3)
Cl1	32*e*	0.3	0.5509(11)	0.0509(11)	0.0509(11)
Cl2	96*g*	0.75	0.1806(8)	0.0694(8)	0.0694(8)
Cl3	96*g*	1.0	3/8	0.6447(2)	-1/8
Cl4	32*e*	0.51	0.0735(6)	0.0735(6)	0.0735(6)
Cl5	96*g*	0.5	0.4632(6)	0.0607(13)	0.0607(13)

Table 8.5: Anisotropic Thermal Parameters ($Å^2$) for V_5 and V_4

Atom	U_{11}	U_{22}	U_{33}	U_{12}	U_{13}	U_{23}
$Cs_{3.5}Na_{1.46}(V_5O_9)(AsO_4)_2Cl_{2.33}$, V_5						
Cs1	0.105(1)	0.0442(6)	0.0442(6)	-0.0061(4)	0.0061(4)	-0.0045(5)
Cs2	0.049(1)	0.122(2)	0.122(2)	-0.000(1)	0.000(1)	-0.016(2)
Cs3	0.067(3)	0.062(4)	0.067(3)	0.00000	0.012(3)	0.00000
Na1	0.09(2)	0.09(2)	0.09(2)	0.07(3)	-0.07(3)	-0.07(3)
Na2	0.23(8)	0.23(8)	0.23(8)	0.00000	0.00000	0.00000
Na3	0.20(2)	0.26(4)	0.20(2)	0.04(3)	0.13(3)	0.04(3)
V1	0.0248(8)	0.034(1)	0.0248(8)	0.0002(7)	0.0026(9)	0.0002(7)
V2	0.034(1)	0.0241(8)	0.0241(8)	0.0002(6)	-0.0002(6)	0.0014(9)
V3	0.029(1)	0.029(2)	0.029(1)	0.00000	0.004(1)	0.00000
As1	0.0273(6)	0.0273(6)	0.0216(8)	0.0029(6)	0.0039(4)	0.0039(4)
O1	0.021(3)	0.031(3)	0.030(3)	-0.001(3)	0.001(3)	-0.001(3)
O2	0.043(6)	0.043(6)	0.036(8)	0.009(7)	0.00000	0.00000
O3	0.036(4)	0.034(4)	0.023(3)	0.007(3)	0.011(3)	0.009(3)
O4	0.040(4)	0.030(4)	0.031(4)	-0.006(3)	0.007(3)	-0.007(3)
O5	0.043(4)	0.048(7)	0.043(4)	0.000(3)	-0.010(5)	0.000(3)
O6	0.041(6)	0.039(4)	0.039(4)	0.014(3)	-0.014(3)	-0.009(5)
Cl1	0.156(9)	0.156(9)	0.156(9)	-0.02(1)	0.02(1)	-0.02(1)
Cl2	0.136(9)	0.136(9)	0.136(9)	0.04(1)	-0.04(1)	-0.04(1)
Cl3	0.11(2)	0.18(5)	0.11(2)	0.03(2)	0.03(2)	0.03(2)
Cl4	0.33(3)	0.05(1)	0.33(3)	0.03(1)	0.15(3)	0.03(1)
$Cs_{3.64}Na_{1.40}(V_4O_8)(AsO_4)_2Cl_{3.04}$, V_4						
Cs1	0.0353(7)	0.0353(7)	0.089(1)	0.0039(6)	-0.0036(5)	-0.0036(5)
Cs2	0.045(2)	0.154(3)	0.154(3)	0.016(2)	0.016(2)	0.016(4)
Cs3	0.058(7)	0.058(7)	0.10(2)	0.001(9)	-0.007(8)	-0.007(8)
Cs5	0.21(5)	0.25(5)	0.25(5)	0.00000	0.00000	-0.13(5)
Cs6	0.11(4)	0.11(4)	0.11(4)	0.04(3)	0.04(3)	-0.04(3
Na1	0.30(6)	0.16(2)	0.16(2)	0.11(3)	0.11(3)	0.12(3)
Na2	0.07(3)	0.07(3)	0.07(3)	0.00000	0.00000	0.00000
As1	0.0205(7)	0.0205(7)	0.0178(9)	0.0014(7)	0.0021(4)	0.0021(4)
As1	0.0205(7)	0.0205(7)	0.0178(9)	0.0014(7)	0.0021(4)	0.0021(4)
V1	0.029(2)	0.021(1)	0.021(1)	-0.0010(9)	-0.0010(9)	0.003(1)
V2	0.030(2)	0.022(1)	0.022(1)	-0.0011(8)	0.0011(8)	0.005(1)
O1	0.032(5)	0.026(4)	0.018(4)	-0.005(4)	0.004(4)	-0.004(3)
O2	0.023(4)	0.035(5)	0.020(4)	0.006(4)	-0.001(4)	0.010(3)
O3	0.025(4)	0.028(5)	0.026(4)	-0.002(4)	-0.004(4)	0.006(4)
O4	0.041(8)	0.037(5)	0.037(5)	-0.002(4)	-0.002(4)	-0.012(6)
O5	0.038(7)	0.031(4)	0.031(4)	0.005(4)	-0.005(4)	-0.005(6)
Cl1	0.11(2)	0.11(2)	0.11(2)	-0.02(2)	-0.02(2)	-0.02(2)
Cl2	0.140(1)	0.14(1)	0.14(1)	-0.04(2)	-0.04(2)	0.04(2)
Cl3	0.051(3)	0.037(4)	0.051(3)	0.00000	-0.004(4)	0.00000
Cl4	0.092(9)	0.092(9)	0.092(9)	-0.00(1)	-0.00(1)	-0.00(1)
Cl5	0.038(9)	0.30(4)	0.30(4)	0.04(2)	0.04(2)	0.18(4)

Table 8.6: Selected bond distances and bond angles for V_5 and V_4

Bond Distances	Bond Angles	
$Cs_{3.5}Na_{1.46}(V_5O_9)(AsO_4)_2Cl_{2.33}$, V_5		
V(1)-O(5) 1.61(1)	O(5)-V(1)-O(1) 104.0(4)	O(2)-V(3)-O(1) 108.2(2)
V(1)-O(1) 1.957(6) * 2	O(1)-V(1)-O(1) 80.8(4)	O(1)-V(3)-O(1) 84.9(4)
V(1)-O(3) 1.968(6) * 2	O(5)-V(1)-O(3) 106.0(4)	O(1)-V(3)-O(1) 83.9(4)
	O(1)-V(1)-O(3) 90.6(3)	O(1)-V(3)-O(1) 143.7(4)
V(2)-O(6) 1.59(1)	O(1)-V(1)-O(3) 149.9(3)	
V(2)-O(1) 1.942(6) * 2	O(3)-V(1)-O(3) 82.4(4)	O(3)-As(1)-O(3) 106.1(4)
V(2)-O(4) 1.954(7) * 2		O(3)-As(1)-O(4) 107.7(3)
	O(6)-V(2)-O(1) 102.3(4)	O(3)-As(1)-O(4) 112.4(4)
V(3)-O(2) 1.62(2)	O(1)-V(2)-O(1) 82.5(4)	O(4)-As(1)-O(4) 110.5(5)
V(3)-O(1) 1.897(6) * 4	O(6)-V(2)-O(4) 106.0(4)	
As(1)-O(3) 1.670(6) * 2	O(1)-V(2)-O(4) 91.1(3)	
As(1)-O(4) 1.678(7) * 2	O(1)-V(2)-O(4) 151.7(3)	
	O(4)-V(2)-O(4) 81.5(4)	
V(3)-V(2) 2.859(3)		
V(3)-V(1) 2.900(3)		
$Cs_{3.64}Na_{1.40}(V_4O_8)(AsO_4)_2Cl_{3.04}$, V_4		
As(1)-O(2) 1.678(9)*2	O(2)-As(1)-O(2) 107.3(6)	O(3)-V(2)-O(1) 88.8(4)
As(1)-O(1) 1.679(8)*2	O(2)-As(1)-O(1) 107.5(4)	O(5)-V(2)-O(1) 102.3(5)
	O(2)-As(1)-O(1) 111.5(4)	O(1)-V(2)-O(1) 77.6(5)
V(1)-O(4) 1.60(1)	O(1)-As(1)-O(1) 111.6(6)	O(5)-V(2)-O(3) 100.1(5)
V(1)-O(3) 1.818(9)*2		O(3)-V(2)-O(3) 96.3(6)
V(1)-O(2) 1.990(9)*2	O(4)-V(1)-O(3) 102.3(5)	O(5)-V(2)-O(1) 102.3(5)
	O(3)-V(1)-O(3) 95.0(6)	O(3)-V(2)-O(1) 155.8(4)
V(2)-O(5) 1.56(1)	O(4)-V(1)-O(2) 101.4(5)	
V(2)-O(3) 1.818(9)*2	O(3)-V(1)-O(2) 154.6(4)	
V(2)-O(1) 1.984(9)*2	O(3)-V(1)-O(2) 88.8(4)	
	O(2)-V(1)-O(2) 77.6(5)	

Table 8.7: Bond valence sum calculations for $Cs_{3.5}Na_{1.46}(V_5O_9)(AsO_4)_2Cl_{2.33,}$ V_5, and $Cs_{3.64}Na_{1.40}(V_4O_8)(AsO_4)_2Cl_{3.04}$, V_4

Atom	V(1)	V(2)	V(3)
BVS for V_5 with V^{4+}	1.600 0.627*2 0.608*2 = 4.070	1.689 0.652*2 0.632*2 = 4.257	1.558 0.737*4 = 4.505
BVS for V_5 with V^{5+}	1.685 0.660*2 0.640*2 = 4.284	1.778 0.687*2 0.665*2 = 4.482	1.640 0.776*4 = 4.742
BVS for V_4 with V^{5+}	1.778 0.955*2 0.603*2 = 4.895	1.903 0.955*2 0.613*2 = 5.039	V(3) site is empty in V_4.

occupancies and then they were fixed at the refined value or close to the refined value. Once the values are fixed, the standard deviations are no longer reported in the structure refinement files.

Results and Discussion

The title phase, (salt)•$Cs_{(6-n)}(V_5O_9)^{n+}(AsO_4)_2$, ($V_5$) was synthesized using high-temperature, solid-state methods in a CsCl/NaCl molten-salt medium. It crystallizes in a cubic crystal system in the spacegroup, *Fd-3m* (no. 227). The aforementioned general formula is used to describe the varied chemical compositions obtained from multiple single crystal structure solutions, shown in Table 8.2. These structure solutions were obtained from single crystals from a few different reactions, but it should be noted that the same compositional inhomogeneity is observed in single crystals taken from the same reactions as well. Single crystals selected from the same reaction show EDX was utilized to qualitatively reinforce the compositions determined from the seven structure solutions. These solutions reveal slight variations in the average oxidation state of the 5 vanadium cations, ranging from 4.16 – 4.50. Bond valence sum calculations were performed on the vanadium atoms for each structure solution, 1-7. These were compared to the average oxidation state calculated from the crystal structure solutions, and in most cases, these two values were in good agreement. Solution (6), $Cs_{3.5}Na_{1.46}(V_5O_9)(AsO_4)_2Cl_{2.33}$, gave the best structure refinement, so it was utilized to obtain the calculated powder pattern shown in Figures 8.1-8.8 to generate any structural pictures of V_5, and to help determine a target composition for the 100% yield synthesis. The detailed crystallographic data for

$Cs_{3.5}Na_{1.46}(V_5O_9)(AsO_4)_2Cl_{2.33}$ (6) can be seen in Table 8.3. The atomic coordinates, thermal parameters, and selected bond distances and angles are listed in Tables 8.4-8.6.

The target composition for the 100% yield reaction was (salt)•$Cs_{2.5}(V_5O_9)(AsO_4)_2$. It should be noted that this reaction was not stoichiometric in terms of the amount of added salt; however, excess salt has allowed the synthesis of a purer product. The molar ratios for the 100% yield synthesis are 1:3.5:0.5:1:7.85:15.2 for $CsVO_3$, VO_2, Cs_3VO_4, As_2O_5, NaCl, and CsCl respectively. The ratio of salt to the oxide starting materials is very high. It is likely that excess salt leads to a more pure product because the formation of the title phase requires an adequate amount of salt for stabilization of the framework. It is thought that the final product is compositionally inhomogeneous, meaning that the amount of salt incorporated into the framework is not consistent. This hypothesis is further supported by the varied chemical compositions already discussed in the single crystal reaction. It should be noted that no trend can be found when comparing the volumes of the single crystals with the number of ions in the channels. It is suspected that the volume of the unit cell, not only affected by the number of ions within the channels, is also strongly influenced by the efficiency with which the ions pack. The PXRD pattern of the 100% yield synthesis of (salt)•$Cs_{2.5}(V_5O_9)(AsO_4)_2$, shown in Figure 8.1, shows a good correlation with the calculated pattern of $Cs_{3.5}Na_{1.46}(V_5O_9)(AsO_4)_2Cl_{2.33}$.

The structure of (salt)•$Cs_{(6-n)}(V_5O_9)^{n+}(AsO_4)_2$, shown in Figure 8.9, contains paramagnetic $[V_5O_{17}]$ clusters. Unlike the clusters seen in the compounds presented in Chapter 7, these are linked together *via* $(AsO_4)^{3-}$ tetrahedra (through corner-sharing

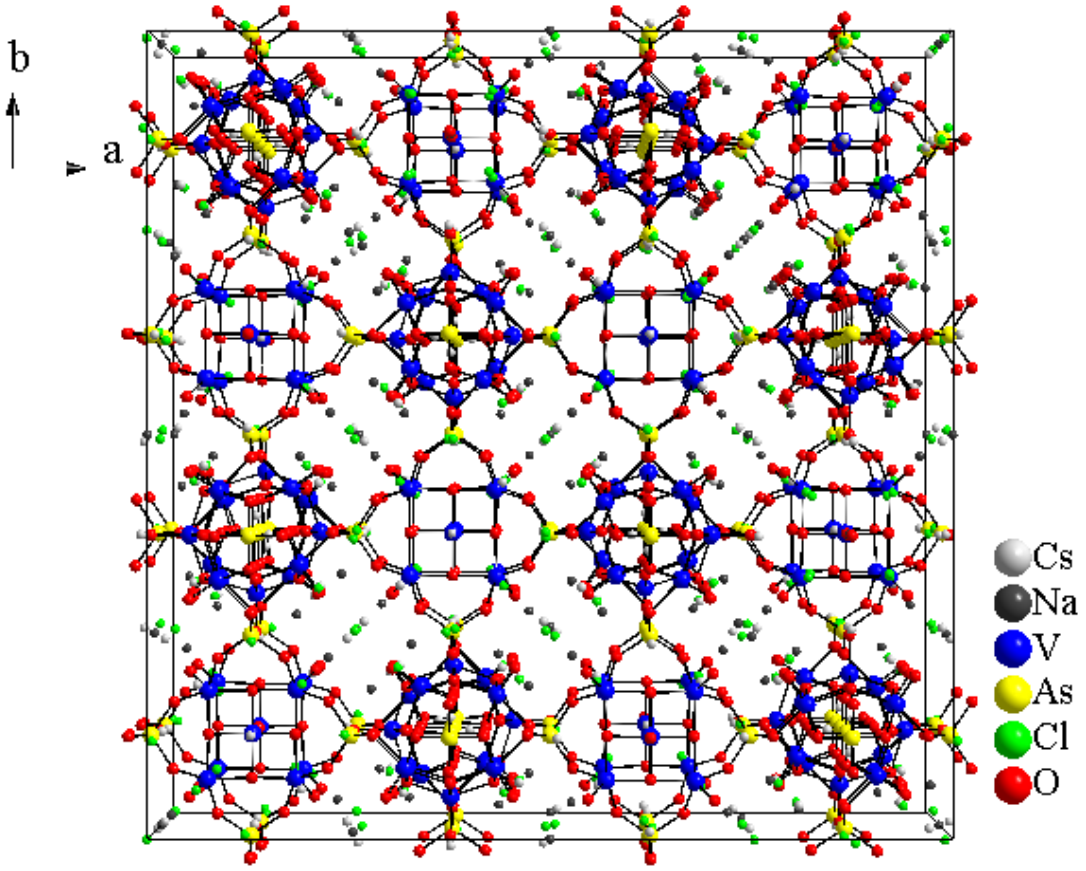

Figure 8.9: Perspective view of the framework along the crystallographic *c*-axis. Small salt-containing channels can be seen along this direction.

oxygen atoms) to form a 3-D open framework. The structure is similar to a previously prepared compound, $Cs_3[V_5O_9(PO_4)_2]\bullet 4.5H_2O$, which has the same framework, yet it was synthesized *via* hydrothermal methods.[15] The synthesis reportedly requires 1,3 propanediamine as a template for the framework formation, however there is no experimental evidence that organic cations are actually included into the channels and pores. Instead, SXRD reveals that the channels are filled with Cs^+ and water molecules.[16]

In the title compound, V_5, the $[V_5O_{17}]$ clusters contain three crystallographically distinct V cations all found in a square pyramidal geometry. The cluster has a bowl-like shape with 4 basal vanadium atoms, V(1) and V(2), and one apical vanadium atom, V(3). Each V(1) and V(2) polyhedron shares 2 corner oxygen with one another and one edge with the V(3) polyhedron found at the center of the cluster, as shown in Figure 8.10. Within each cluster, the connectivity gives rise to 4 μ_3-oxo-bridging modes and short V-V distances equal to 2.900(3) Å and 2.859(3) Å for V(3)-V(1) and V(3)-V(2) respectively. Each square pyramid has a vanadyl-type apical oxygen, confirmed by the presence of short V=O bonds that are 1.61(1) Å, 1.59(1) Å, and 1.62(2) Å for V(1)-V(3) respectively. Each cluster is surrounded by 4 AsO_4 tetrahedra, which serve as nonmagnetic insulators isolating the clusters from one another. Through corner-sharing oxygen with the 2 basal V cations in neighboring clusters, these arsenic units link the POM cores to form a three-dimensional structure containing large channels and cavities (see Figures. 8.9 and 8.11). The electron density within the cluster is delocalized, showing mixed $V^{4+/5+}$ sites. Bond valence sum calculations were performed for $Cs_{3.5}Na_{1.46}(V_5O_9)(AsO_4)_2Cl_{2.33}$, obtained from structure solution (6), and are shown in

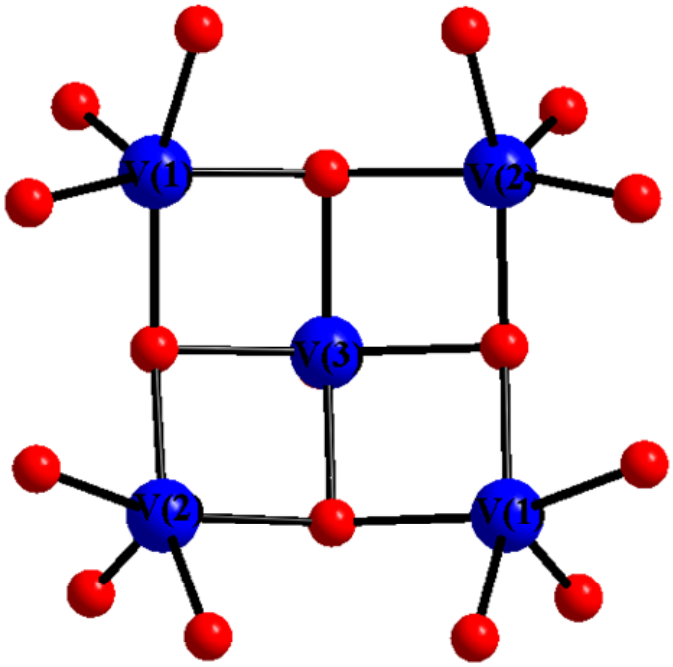

Figure 8.10: Perspective view of the $[V_5O_{17}]$ core. There are 4 basal V atoms, two V(1) and two V(2) and there is one apical V(3) site. V(3) shares all 4 edges with V(1) and V(2) square pyramids. The apical oxygen atom of V(3) cannot be seen as it is pointed away from the bowl-like aggregate.

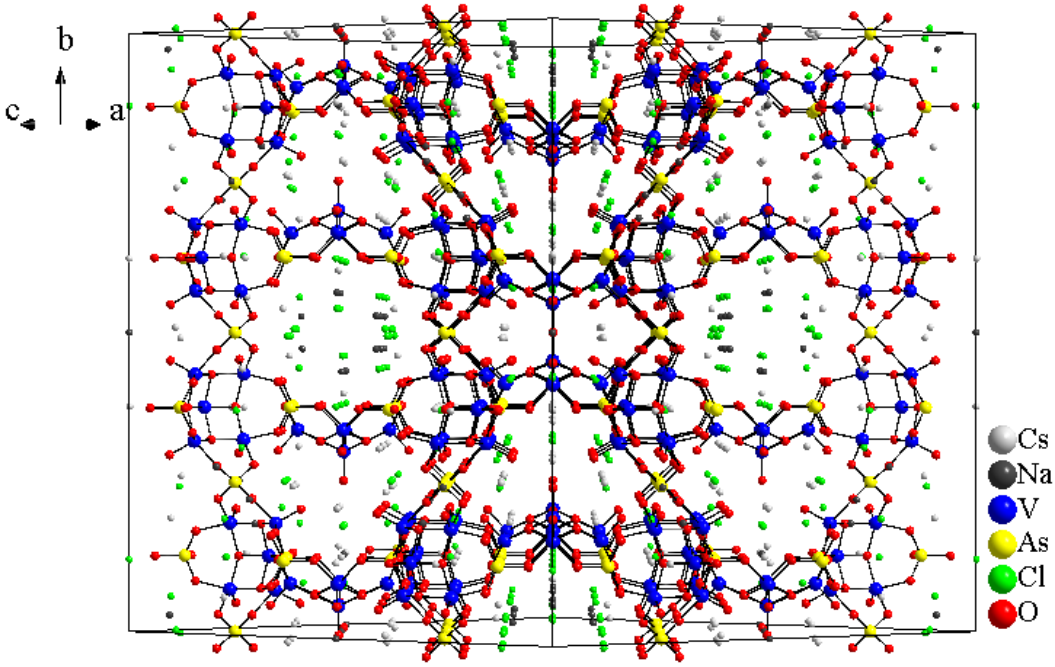

Figure 8.11: Perspective view of the framework along the [110] direction showing large salt-containing channels consisting of $6AsO_4$ and $6VO_5$ polyhedra.

Table 8.7. The results indicate that the V(1) site is most likely 4+, while the V(2) and V(3) sites are mixed 4+/5+. The average oxidation state for each V(1-3) is approximately 4.3, which is in good agreement with the structure solution from (6), 4.27. Based on the BVS calculations, each $[V_5O_9]$ moiety has a charge of +3.5, indicating that 2.5 charge balancing Cs^+/Na^+ cations are required per formula unit.

The title compound can be described as having multi-directional salt-containing channels which can most clearly be seen when looking along the [110] or [111] directions of the unit cell, shown in Figures 8.11 and 8.12 respectively. These channels consist of 12 alternating, corner-sharing AsO_4 and VO_5 polyhedra. The two electropositive cations, Na and Cs, reside in the channels having average Cl bond distances of 2.83Å and 3.46Å respectively. The observed distances are comparable to the expected values calculated from the sum of Shannon crystal radii for NaCl and CsCl salt, 2.90 Å and 3.57 Å respectively. Large pore size leads to quite a bit of disorder among the salt ions, as evident from the single crystal structure solution. All ion sites, with the exception of Cs(1), were refined with partial occupancies. In order to determine whether the atoms were partially occupied, the local environment around each ion was closely examined. Multiple cations / anions were found to have distances that were too close to neighboring cations / anions, and the thermal parameters for many of the ions are oddly shaped, indicating quite a bit of disorder. SHELXTL[14] was allowed to refine the occupancies of each ion individually.

Within the crystal structure, several voids were identified. The volume of these voids was estimated using the Platon-SQUEEZE function[13] to be 2609 $Å^3$, approximately

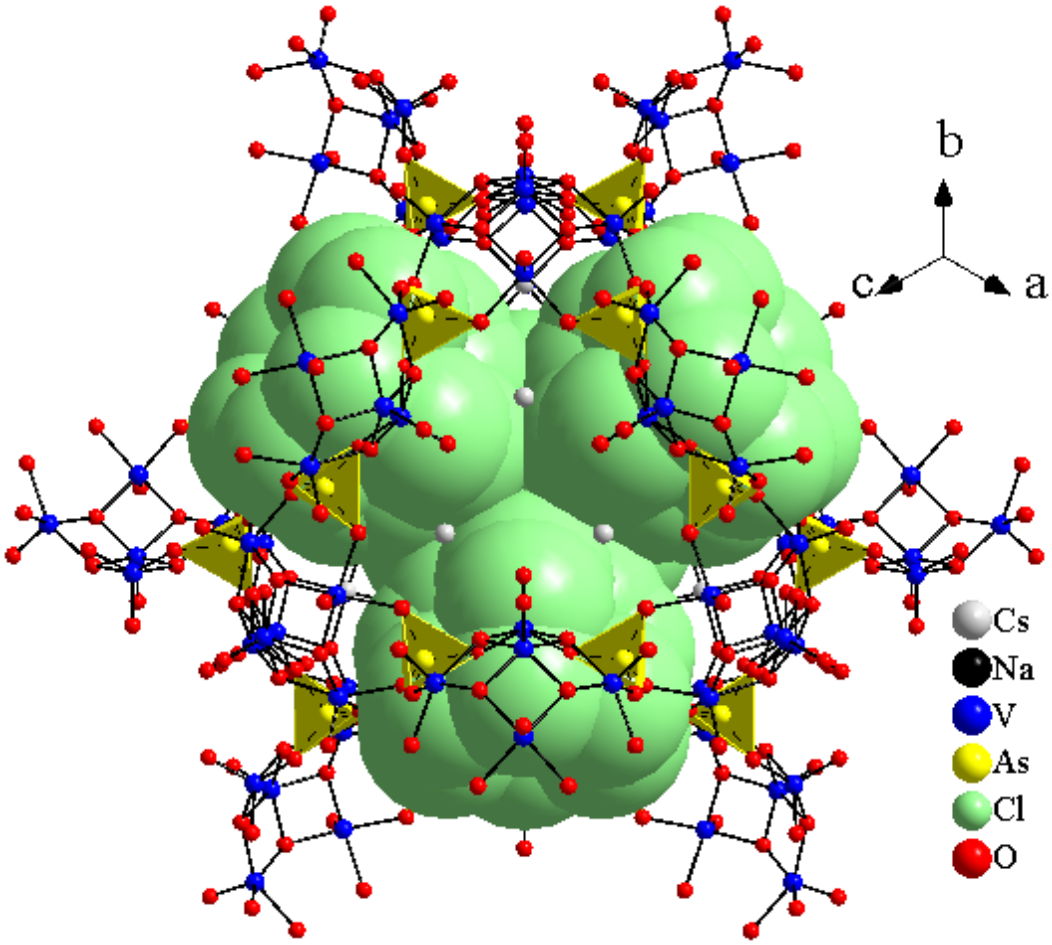

Figure 8.12: Perspective view showing channeled structure formed by the V_5 clusters. the single crystal structure, calculated to be approximately 326 $Å^3$ of free space.

7.2% of the overall unit cell volume of 36,329(9) $Å^3$. In most cases, solvent voids are not larger than 25 $Å^3$; however, this is sometimes not the case for rigid inorganic frameworks like V_5. In the title compound, there were 8 identified solvent-free voids per unit cell with an approximate volume of 326 $Å^3$ and a 7 electron count per void. Based on the small electron / volume ratio, it is suspected that this space is in fact void of any disordered solvent or salt. These voids are found within the center of large cavities formed at the intersection of four channels, shown in Figure 8.13. The cage surrounding the cavity can be described as 6 $[V_5O_{17}]$ clusters which form an octahedron with respect to the solvent-free void, represented by the black sphere. Within the cage, the clusters are further linked to one another *via* two AsO_4 polyhedra and one VO_5 polyhedron. The concave portion of each bowl-like aggregate points away from the void.

Despite the disorder observed in the salt, the structure of the ionic lattice was examined. Within each aforementioned cage, a large hollow salt cage was found (Figure 8.14) that is made up of Cs^+, Na^+, and Cl^- ions. To further illustrate the salt lining found inside of the cage, a slab is shown in Figure 8.15. The slab shows a portion of five cages, and within each cavity the solvent-free voids are represented again by black spheres. For clarity, the two capping $[V_5O_9]$ clusters were removed from the cage. From this topographic view, the salt can be seen lining the region between the void and the covalent portion of the lattice.

Due to the large channels and cages of the title compound and the large amount of solvent-void space within the crystal structure, it was suspected that the material would show a large surface area. Several experiments were performed in order to prove this

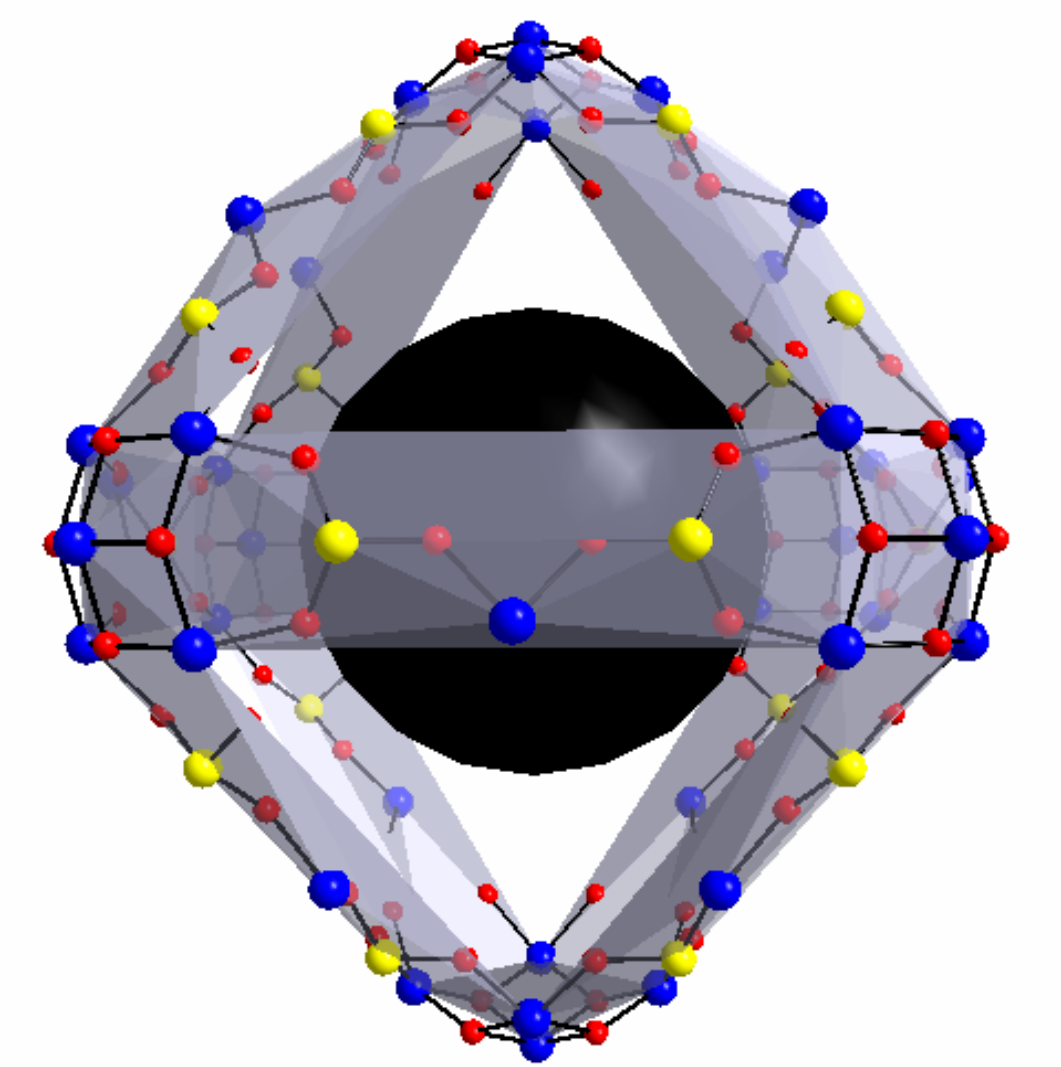

Figure 8.13: Perspective view of the V_5 cage consisting of 6 $[V_5O_{17}]$ clusters. The black sphere in the center represents the solvent-free void found in the single crystal structure, calculated to be approximately 326 $Å^3$ of free space.

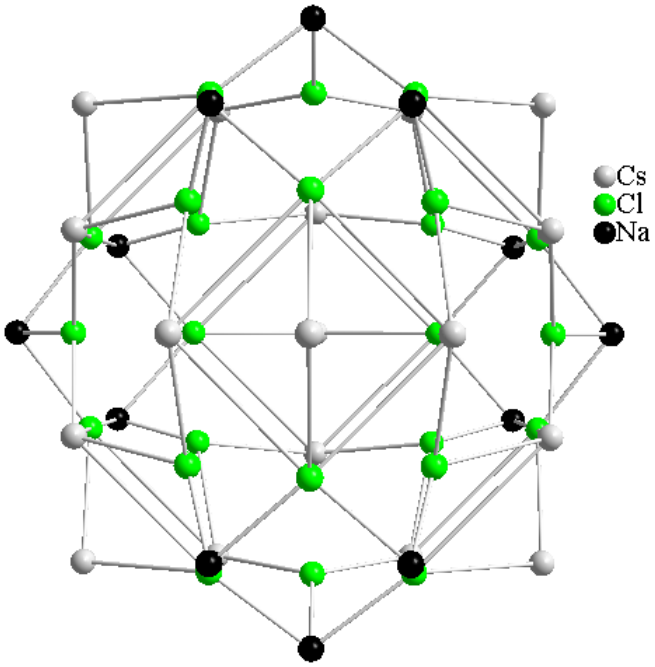

Figure 8.14: Perspective view of the salt cage that forms inside of the cavity. The salt cage is capped on 6 sides by $[V_5O_9]$ aggregates, and within the sphere is a solvent-free void with a volume of 326Å^3.

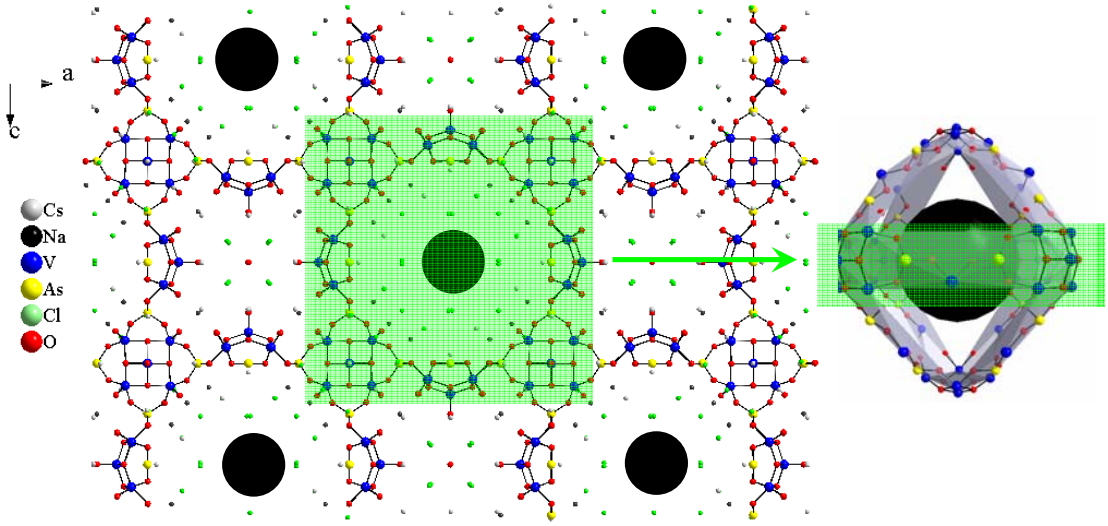

Figure 8.15: A single slab cut from the *ac* plane of the structure. The slabs stack in an ABCDA fashion. The clusters undergo a 4_1 screw axis as they propagate along the *a*, *b*, or *c* axis. Within the slab, the $[V_5O_{17}]$ cores are interconnected *via* AsO_4 polyhedra to form the rim around the void containing the cage, shown on the right.

hypothesis. Preliminary surface area measurements were performed on a variety of different samples, and the results are shown in Table 8.8. First, a stoichiometric yield sample was degassed at 120°C and then analyzed, giving an initial surface area of 111(2) m^2/g. Then efforts were made to remove the salt from the channels, which would hopefully increase the surface area of the material. A high-yield powder of (salt)•$Cs_{2.5}(V_5O_9)(AsO_4)_2$ was sonicated in deionized water for 30 minutes, 2 hours, and then 8 hours. The powder patterns for these samples can be seen in Figure 8.3. The PXRD pattern of the 100% yield synthesis is compared to the powder patterns of the same sample after various soak times. The shift in the diffraction peaks to higher 2θ values with increasing soak time indicates a decrease in unit cell volume. This is further supported by the refined unit cell parameters shown in Table 8.1. Then elemental analysis was performed on the respective soaked samples and compared to the elemental analysis of the unsoaked sample. The samples that were sonicated for 30 minute and 2 hours showed a small amount of Cl^- still present, while the sample sonicated for 8 hours, Figure 8.4, had no Cl in the elemental analysis, indicating that the neutral salt found in the channels had been completely removed. Surface area analysis was carried out on the sample soaked for 8 hours with degassing temperatures of 60, 90, 120, and 150°C. As seen in Table 8.8, the surface area increases from 4.4m^2/g when degassed at 60°C to 150(2) m^2/g when degassed at 120°C. This can consistently be explained when looking at the thermal analysis performed on the soaked sample, Figure 8.16. The TGA curve shows a 10% weight loss up to 110°C due to incorporated water during soaking. The calculated amount of water loss is equivalent to 6.6 water molecules per formula unit,

Table 8.8: Surface area analysis for multiple reactions.

Degas Temperature (°C) / treatment	Surface Area (m^2/g)
(salt)•$Cs_{2.5}(V_5O_9)(AsO_4)_2$ 100% Yield Sample	
60 soaked	4.0(5)
90 soaked	12.24(9)
120 unsoaked	111(2)
120 soaked	150(2)
150 soaked	148(2)
(salt)•$Cs_2(V_5O_9)(AsO_4)_2$ (n = 4 using high-temperature synthesis to oxidize the cluster)	
120 soaked	120.3(8)
(salt)•$Cs_{1.5}(V_5O_9)(AsO_4)_2$ (n = 4.5 using high-temperature synthesis to oxidize the cluster)	
120 soaked	129(1)
I_2 Oxidation	
120	188(3)
H_2O_2 Oxidation	
120	242(4)
(Salt)•$Cs_2(V_4O_8)(AsO_4)_2$	
120 soaked	66(2)
(Salt)•$Cs_{2-x}(V_4Cu_xO_8)(AsO_4)_2$	
120 unsoaked	90(2)
120 soaked	154(1)

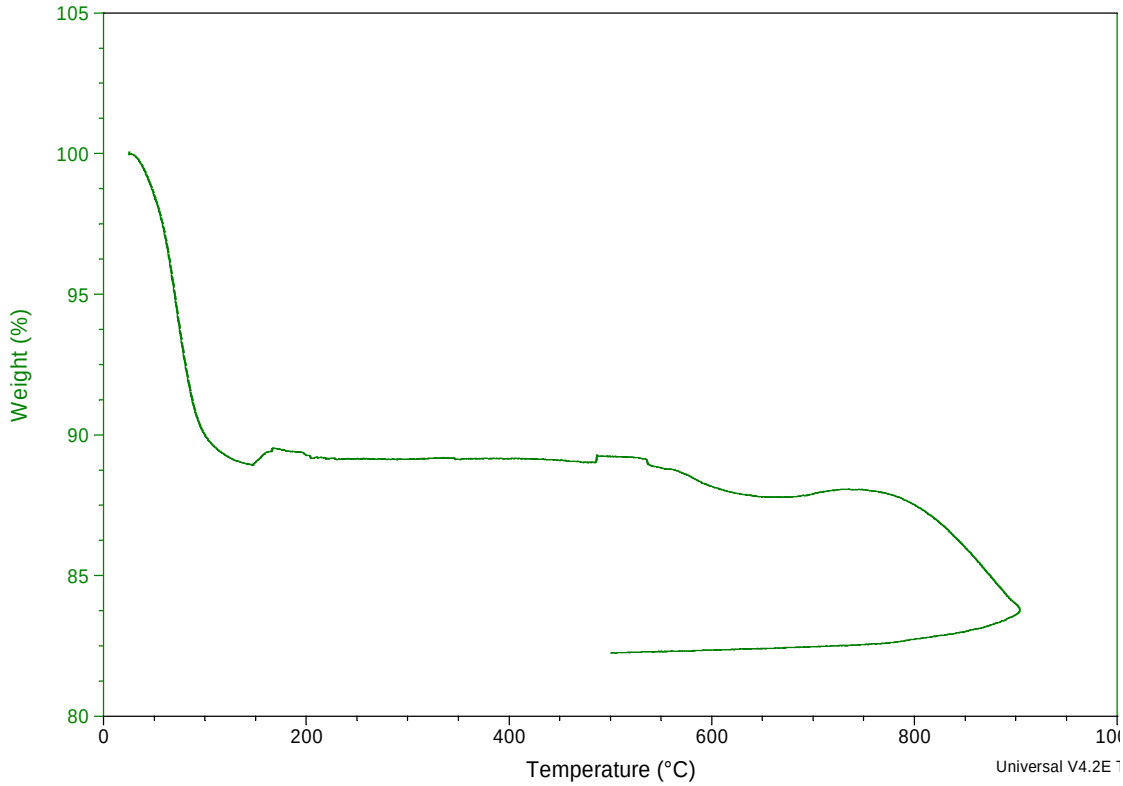

Figure 8.16: TGA curve of a 100% yield sample of V_5, $Cs_{2.5}(V_5O_9)(AsO_4)_2 \cdot nH_2O$ after soaking to remove the salt. The curve shows an approximate weight loss of 10.5%. This weight loss is equivalent to 6.6 water molecules per formula unit, $Cs_{2.5}(V_5O_9)(AsO_4)_2 \cdot 6.6H_2O$.

$Cs_{2.5}(V_5O_9)(AsO_4)_2 \cdot 6.6H_2O$. The incorporation of water causes a decrease in measured surface area, and as a result, from this point forward, the samples were degassed at temperatures of 120°C or higher.

Upon the observed increase in surface area after salt removal, attempts were made to oxidize the V_5 compound. The idea was that through oxidation, part or all of the remaining charge balancing Cs cations could be removed from the channels and cavities. As stated above, two methods were utilized to achieve oxidative removal of the remaining charge-balancing Cs^+ cations: 1) soaking the as-prepared solid in a solution of various oxidizing agents such as H_2O_2 or I_2 and 2) direct synthesis *via* traditional high-temperature solid-state methods under oxidizing conditions. The chemical equation utilized to create oxidized versions of the previously synthesized material *via* high-temperature, solid-state methods is as follows:

$$(6\text{-}n)CsVO_3 + (7\text{-}n)VO_2 + (n\text{-}4)V_2O_5 + As_2O_5 \rightarrow (salt)\bullet Cs_{(6-n)}(V_5O_9)^{n+}(AsO_4)_2$$

The variable n indicates the charge of the $[V_5O_9]$ moiety. As previously mentioned, the bond valence sum calculations from the crystal structure gave an average n = 3.5. The above high-temperature, solid-state reaction was utilized to synthesize various oxidized products with n = 4, 4.5, and 6. It should be noted that n = 6 should yield a neutral framework, $(salt)\bullet(V_5O_9)(AsO_4)_2$, with no charge-balancing Cs^+ cations left in the channels. The goal was to create a neutral, channeled structure that would render an empty porous framework after removal of the salt. The powder patterns obtained from the n = 4, 4.5, and 6 reactions are shown in Figure 8.5. These reaction products show a very close comparison to the calculated PXRD pattern for the V_5 compound.

Theoretically, the n = 4 and 4.5 reactions should have less charge-balancing cesium in the channels than the 100% yield of (salt)•$Cs_{2.5}(V_5O_9)(AsO_4)_2$. The n = 4 material, (salt)•$Cs_2(V_5O_9)(AsO_4)_2$, should have 2 charge-balancing Cs^+ cations while n = 4.5, (salt)•$Cs_{1.5}(V_5O_9)(AsO_4)_2$, should have 1.5 charge-balancing Cs^+ cations. Based on the original idea, these compounds were expected to have a larger surface area than (salt)•$Cs_{2.5}(V_5O_9)(AsO_4)_2$. However, this is not the case as the surface areas for the two reactions were measured to be 120.3(8) m^2/g and 129(1) m^2/g for n = 4 and 4.5 respectively. These are both lower than the observed surface area measurements of the original 100% yield reaction of (salt)•$Cs_{2.5}(V_5O_9)(AsO_4)_2$, 150(2) m^2/g. These unexpected results were thought to be possibly attributed to one or a combination of the following reasons: 1) with less Cs^+ cations in the channel, the pore volume decreases. This is evident from the PXRD patterns where peaks shift to larger 2θ values, indicating a decrease in unit cell volume. It is thought that the decrease in Cs^+ concentration could cause a slight collapse in the structure, reducing the total available surface area for the N_2 to be physically adsorbed. 2) The synthesized product has low surface area byproducts that are not evident in the powder pattern and could give a false calculation of the actual surface area of the material. 3) Beyond the basic structural issues, sample size is also relevant. Larger samples would require longer equilibration times to allow the N_2 gas to diffuse throughout the sample. If insufficient time is allotted, skewed surface area measurements can result. 4) The reactions have been proven to be very sensitive to the reaction conditions used. For instance, the 100% yield synthesis of (salt)·$Cs_{2.5}V_5O_9(AsO_4)_2$ showed various surface areas dependent on the isotherm time.

When held at 650°C for 12 hours, the samples showed very small surface areas; however, when held at the same temperature for 3 days, the surface area was maximized to 150m^2/g.

Due to the unexpected surface area measurements of the n = 4 and 4.5 reactions, a more detailed examination of the products was conducted. After a close analysis under the microscope, it was determined that at least two different phases were present in each reaction. There was a small yield (≈10-20%) of tiny red plate-like crystals that appeared to have a different unit cell than the title compound. This by-product was determined to be $NaVO(AsO_4)$[11], and the phase was found in all three oxidation reactions, n = 4, 4.5, and 6. Red cubic crystals were found in the n = 6 reaction, and after SXRD analysis, the crystals were determined to be $Cs_{3.64}Na_{1.40}(V_4O_8)(AsO_4)_2Cl_{3.04}$, V_4, which has the same framework structure as the V_5 compound, but the apical V(3) site is empty. Figure 8.17 shows a comparison between the cluster observed in the V_5- and V_4-containing compounds. Bond valence sum calculations indicate that the oxidation state of V in the V_4 cluster is fully oxidized to 5+, refer to Table 8.7. In the n = 4.5 reaction, a blue cubic single crystal was analyzed *via* SXRD. The compound showed a partially occupied V(3) site, 60%, indicating that 40% of the clusters found within the single crystal are actually the $[V_4O_8]$ core. This compound will be referred to as $V_{4/5}$ since it contains a mixture of both the $[V_5O_9]$ and the $[V_4O_8]$ core. A comparison was made between the V_5,- V_4,- and $V_{4/5}$-containing compounds and distinct differences could be seen between the corresponding clusters. The comparison, shown in Figures 8.17 and 8.18, reveals that upon oxidation, from V_5 to $V_{4/5}$ to the fully oxidized V_4-containing compound, the V-O

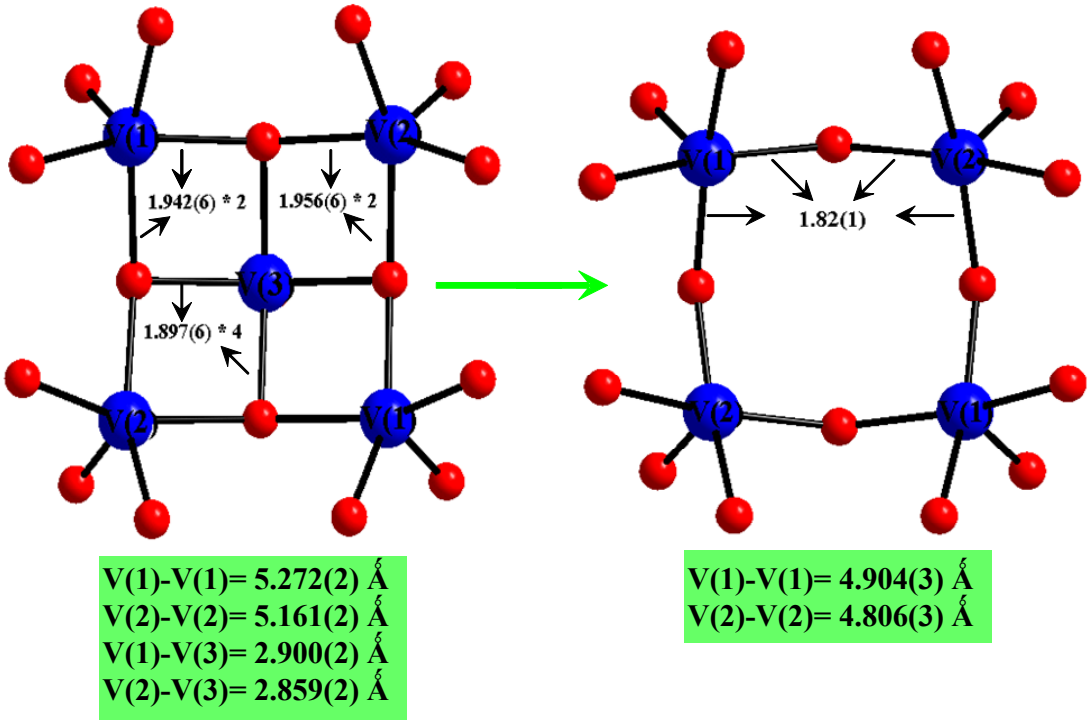

Figure 8.17: View of the V_5 and the fully-oxidized V_4 cluster with the center V(3) site empty. The V-O and V-V distances show a significant decrease upon oxidation.

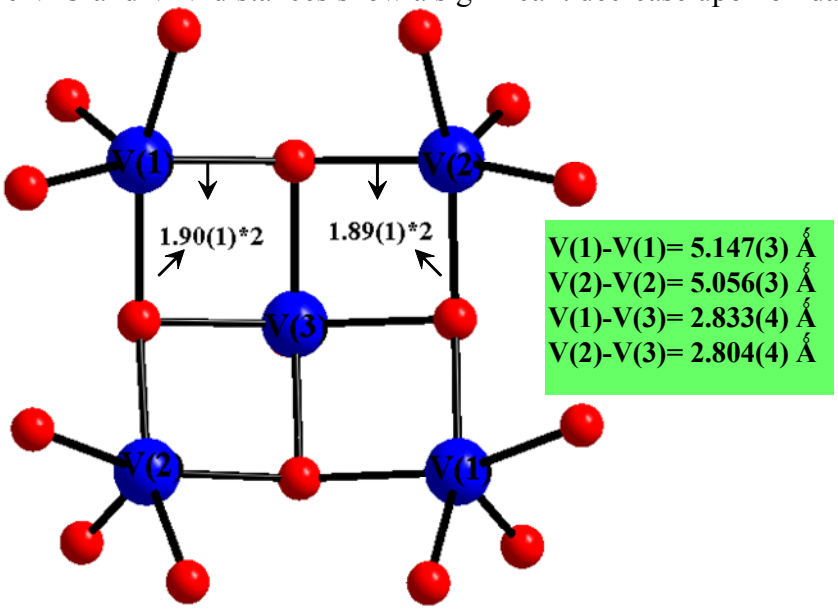

Figure 8.18: V-O and V-V distances observed for the $V_{4/5}$-containing compound observed in the n = 4.5 reaction, see text. When compared to the V_4 and V_5 clusters, this one shows intermediate distances as expected.

and V-V distances gradually get shorter. It is suspected that the cluster cannot sustain a V cation in the central V(3) site due to the ring strain induced from the shorter bond distances created upon further oxidation of the core. The analyzed single crystals of V_4 and $V_{4/5}$ show smaller volumes than the title compound, V_5. These smaller volumes, reducing the amount of N_2 physically adsorbed on the surface of the material, and the presence of the low surface area by-product $NaVO(AsO_4)$ could account for the lower observed surface area for the n = 4 and 4.5 products. Due to the presence of other phases in the reactions, efforts were not made to maximize the surface areas of the n = 4 and 4.5 reaction products, so it is possible that higher surface areas than reported here could be achieved.

Efforts were made to synthesize 100% yield of the fully oxidized V_4-containing compound, (salt)•$Cs_2(V_4O_8)(AsO_4)_2$. The PXRD pattern, shown in Figure 8.2, is compare to the calculated patterns of $Cs_{3.5}Na_{1.46}(V_5O_9)(AsO_4)_2Cl_{2.33}$, V_5, with the central V(3) site removed. A significant decrease in volume can be seen in the powder patterns as the diffraction peaks of the 100% yield synthesis of V_4 are shifted to higher 2θ values than those observed in the calculated powder pattern of the V_5-containing compound. This decrease in volume is further reflected in the surface area measurement obtained from the 100% synthesis of (salt)•$Cs_2(V_4O_8)(AsO_4)_2$, 66(2) m^2/g, which is less than half of the one observed for the V_5-containing (Salt)•$(V_5O_9)(AsO_4)_2$, 150(2) m^2/g. The single crystal structure solutions of $Cs_{3.5}Na_{1.46}(V_5O_9)(AsO_4)_2Cl_{2.33}$, V_5, and $Cs_{3.64}Na_{1.40}(V_4O_8)(AsO_4)_2Cl_{3.04}$, V_4, also show a significant difference in their volumes which are 36,329(7) and 35,101(7)$Å^3$ respectively. The Platon Squeeze[13] function was

used to calculate the volume of vacant space from the single crystal structure of the V_4-containing compound, and the results showed approximately 1371.6 $Å^3$, 3.9% of the total unit cell volume, whereas the observed vacant space in the V_5-containing compound was nearly double that value at 7.2%. The limited availability of vacant space within the V_4 compound would certainly account for its significantly lower surface area.

Once the high-temperature method failed in the creation of a neutral framework or a material having higher surface area than observed for (salt)·$Cs_{2.5}(V_5O_9)(AsO_4)_2$, other synthetic procedures were utilized to accomplish this goal. It was previously mentioned that the apical V(3) site in the cluster becomes empty upon using high-temperature synthesis to oxidize the framework. It is thought that this occurs because of excess strain inflicted on the V(1,2) containing ring. The strain is the result of shorter V-O bonds that originate from the increased oxidation state of the vanadium cations. An alternative was to replace the basal V(3) site with another metal atom such as Cu^{2+} or Ni^{2+}. The target composition for these reactions was (salt)•$(V_4MO_8)(AsO_4)_2$, where M = Ni^{2+} or Cu^{2+}. Theoretically, by doping a M^{2+} in the apical site, the 2 Cs cations in (salt)•$Cs_2(V_4O_8)(AsO_4)_2$ will no longer be required for charge balance. Cu^{2+} and Ni^{2+} were chosen because they are often found in a 4-coordinate square planar geometry. The powder pattern for both the Cu and Ni reactions can be seen in Figure 8.7. The powder pattern for the Ni-containing product shows a few large "impurity" peaks when compared to the calculated pattern of the V_5-containing compound, implying that the reaction did occur. The Cu reaction, shown in Figure 8.8, very closely resembles the calculated pattern of $Cs_{3.5}Na_{1.46}(V_5O_9)(AsO_4)_2Cl_{2.33}$ with no visible impurity peaks, implying that

this reaction was successful. However, after close examination of the prewashed reaction product, single crystals of another phase were identified as $CsCuCl_3$[17]. These crystals were not identified in the powder pattern because they are water soluble. Each reaction product was washed to remove the excess amount of salt utilized in the synthesis. Energy Dispersive X-ray analysis of the washed product did show the presence of copper, indicating that some of the copper did go into the framework. Therefore, the following reaction could be used to describe the reactants and products in the Cu reaction:

$$2V_2O_5 + CuO + As_2O_5 + (3\text{-}3x)CsCl \xrightarrow{\text{xs salt}} (\text{salt})\bullet Cs_{2\text{-}2x}(V_4Cu_xO_8)(AsO_4)_2 + (1\text{-}x)CsCuCl_3$$

It should be noted that the x variable is used in the above reaction because the amount of Cu^{2+} going into the framework is unknown, and (3-3x) is simply there to balance the equation as there is always an excess of salt in the reaction. No single crystals were obtained for a single crystal structure analysis of the Cu-containing derivative. However, surface area analysis was performed on the (salt)•$Cs_{2\text{-}2x}(V_4Cu_xO_8)(AsO_4)_2$ product before and after soaking the material to remove the salt. The surface areas were determined to be 90(2) and 154(1) m^2/g for the reactions respectively. No significant improvement was observed in the surface area of the soaked 100% yield sample, $Cs_{2.5}(V_5O_9)(AsO_4)_2$, 150(2) m^2/g. This again can be attributed to the fact that no neutral framework was achieved because only partial doping of the V(3) site was accomplished. The surface area does however further support the idea that Cu^{2+} is actually going into the framework, because the surface area is almost 2.5 times larger than the surface area observed for the V_4-containing compound.

Once the high-temperature reactions failed to create the neutral framework structure, efforts were then made to oxidize the as-prepared 100% yield product, (salt)•$Cs_{2.5}(V_5O_9)(AsO_4)_2$. First, the samples were soaked in deionized water to remove the salt and then in an oxidizing agent, I_2 or H_2O_2, for 2 hours. Conceptually, oxidation will allow the removal of the remaining charge-balancing Cs^+ cations left in the channel as illustrated in the aforementioned reactions shown in the synthesis section. When soaked in I_2, the samples showed very little color change from green to brown-green; however, when soaked in H_2O_2, the samples turned from green to red, possibly showing visible evidence of the oxidation. The powder patterns of these reactions are shown in Figure 8.7. The reaction with H_2O_2 shows a good match with the calculated PXRD pattern of the V_5-containing compound, however there is a significant shift to a higher 2θ value, indicating a significant decrease in unit cell volume. The PXRD pattern from the I_2 reaction shows some large impurity peaks, indicating the formation of products other than the V_5-containing compound, possibly due to some slight decomposition of the original material.

The surface areas of the samples showed an increase to 188(3) and 242(4) m^2/g for I_2 and H_2O_2 reactions respectively, which is a significant increase from 150(2) m^2/g observed for unoxidized soaked material, $Cs_{2.5}(V_5O_9)(AsO_4)_2$. EDX results on the oxidized samples still show significant amounts of Cs, which indicates that there is either a large amount of surface contamination or the surface area increase may not be attributed to the oxidative removal of the once charge-balancing Cs cations. Instead, it is possible that something else is coming out of the framework, such as V. This could cause

a decrease in the weight of the material, but still maintain the framework structure as seen from the powder pattern and the high surface area measurements. It is likely that the central V(3) site could be coming out of the structure, which was similarly observed in the high temperature methods used to create a neutral framework. Once oxidized, the shorter basal V-O bonds create an environment that can no longer sustain the presence of V in the apical position, creating a material containing a $[V_4O_8]$ core. It is known that high temperature can serve to create a more condensed framework, so it is no surprise that the oxidation reactions achieved *via* solution techniques actually rendered a higher surface area material. It should be noted that the H_2O_2 reaction was performed on single crystals of the title material in hopes that SXRD could reveal what is happening inside the framework upon oxidation. The experiment was inconclusive because, once oxidized, the single crystal quality was not good enough for a structure solution.

Hydrogen adsorption experiments were performed at 77K and 87K with pressures ranging from 0 - 47 bar on the soaked 100% yield sample as well as on the sample oxidized *via* H_2O_2, Figures 8.19 and 8.20. Both materials showed minimal H_2 adsorption (at the highest pressure) with 1.2 and 3.5 mmol H_2/g sample (at the highest pressures of 47 bar) for the 100% yield sample and the oxidized sample respectively. These low values are expected as the framework is very heavy. The oxidized sample is showing higher H_2 adsorption, which is also expected, based on the larger observed surface area. The material shows a strange behavior under high pressure as the amount of desorped hydrogen is higher than the amount of adsorped hydrogen. This feature is still

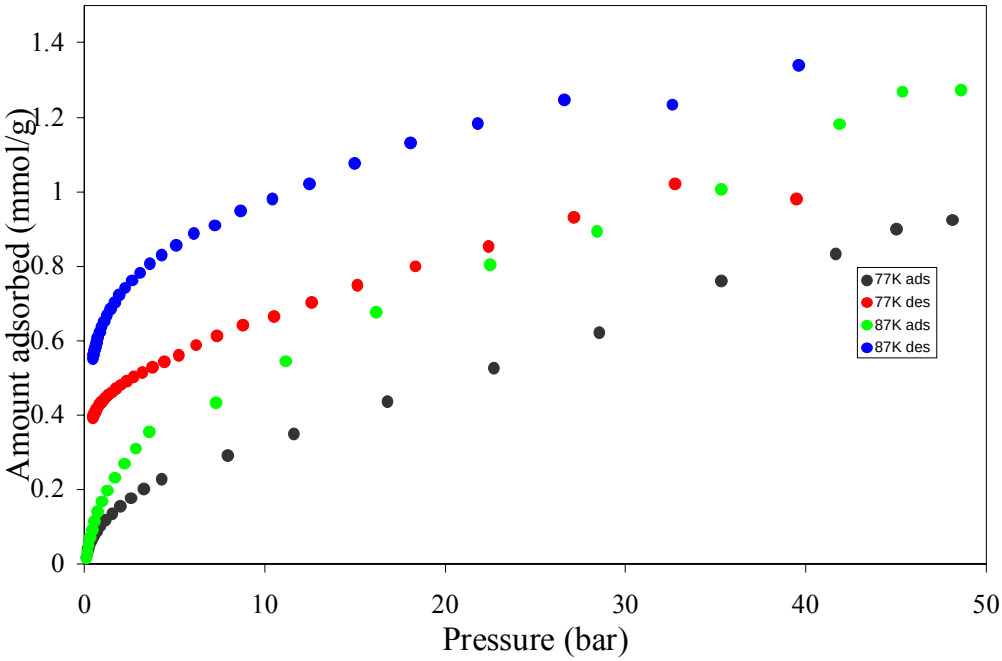

Figure 8.19: H_2 adsorption isotherm collected on the soaked sample (S.A. = 150(2) m^2/g), $Cs_{2.5}(V_5O_9)(AsO_4)_2$, at 77 and 87K in pressures up to 47 bar.

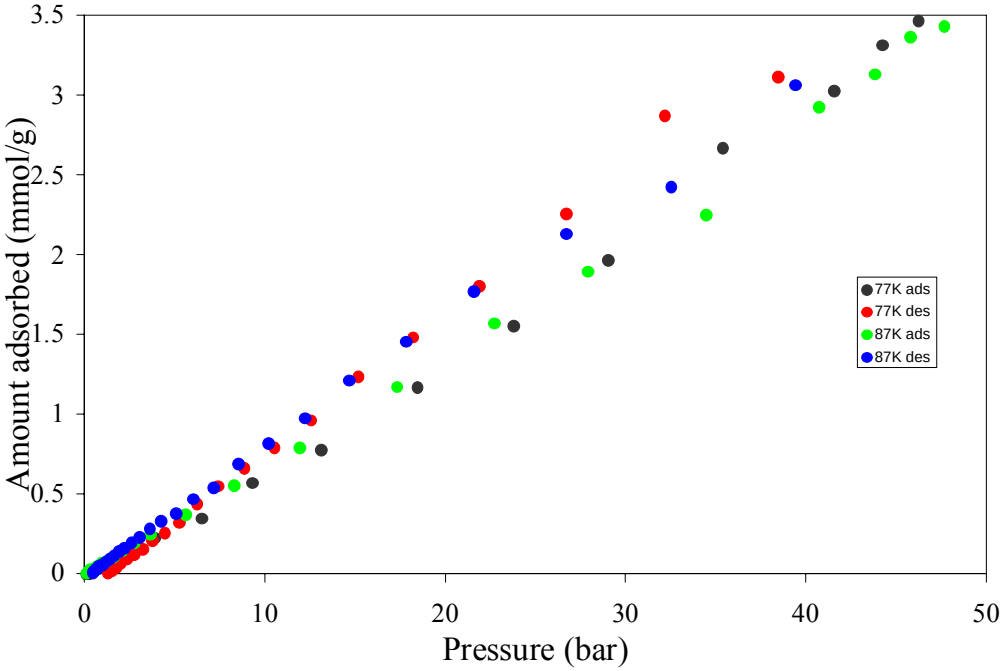

Figure 8.20: H_2 adsorption isotherm collected on the sample (S.A. = 242(4) m^2/g), that was oxidized via H_2O_2.

unexplainable, but it is thought that it could be related to a non-equilibrium condition or chemisorption.

Efforts were also made to synthesize multiple derivatives of the title compound. Several procedures were used to try to make this framework material, replacing As^{5+} with V^{5+} or P^{5+}. The goal was to create a larger surface area (m^2/g) of sample due to the lighter framework. All of these efforts failed. However, we were able to use various salts in the formation of this porous material. CsI and CsBr can both serve as the templating agent for the formation of the compound. The experimental powder pattern, Figure 6.10, is similar to the calculated one. There are shifts to smaller 2θ values showing an increase in the cell volume upon the addition of larger anions. Using the GSAS/EXPGUI programs[12], unit cell parameters were attempted for the CsI and CsBr derivatives, but a good refinement was not obtained.

Efforts were also made to see if larger V:As ratios could allow the formation of a similar framework containing larger vanadium clusters. A reaction was loaded with a 10:2 V:As ratio. The product revealed evidence of the title compound, (salt)·$Cs_{2.5}(V_5O_9)(AsO_4)_2$, as well as another compound containing a $[V_{10}O_{18}]$ core. The unit cell is half that of the V_5 compound and, although a good structure solution of the material was not obtained, certain structural features are evident from the partial structure solution. A comparison of the structure of these two clusters can be seen in Figure 8.21. The $V_{10}O_{18}$ cluster has two $[V_5O_9]$ bow-like units that are stacked on top of one another and linked *via* corner-sharing O atoms. Besides the oxidation of the $[V_5O_9]$ cluster, high-temperature solid-state synthesis was also utilized in an effort to obtain more reduced

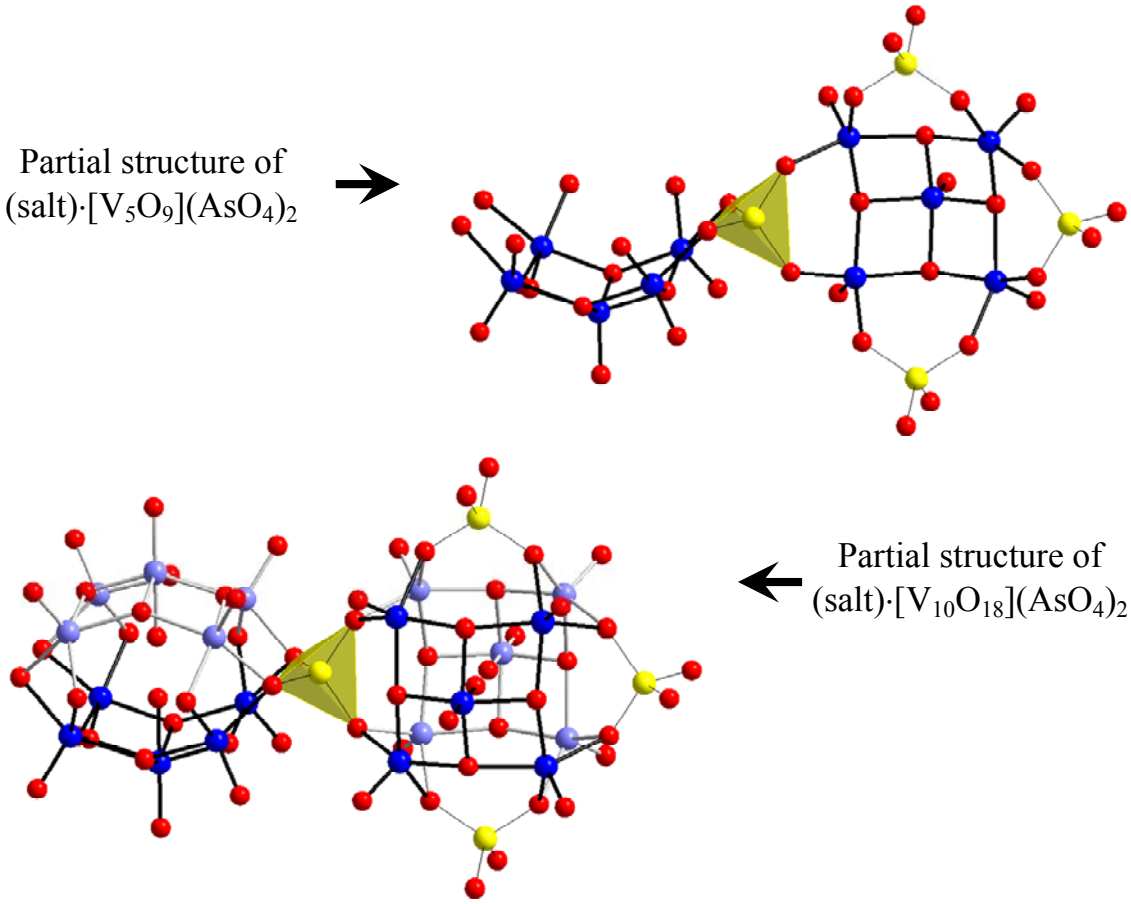

Figure 8.21: Comparison of the partial structures of the V_5 and the V_{10} cluster. Upon doubling the V to As ratio in the single crystal reaction, there is evidence found of a $[V_{10}O_{18}]$ core.

$[V_5O_9]$ clusters. The target composition was (salt)•$Cs_{6-n}(V_5O_9)^{n+}(AsO_4)_2$ for n = 2, 2.5, and 3. It should be noted that the n = 2 reaction should lead to a $[V_5O_9]$ aggregate containing all V^{4+} cations. It was thought, through the addition of electrons, a systematic investigation of the magnetic properties could be carried out. However, the reduction reactions all show additional "impurity" peaks, Figure 8.5, in their respective powder patterns, especially for the n = 2 reaction. It is thought that the rigidity of the $[V_5O_9]$ aggregate could inhibit its reduction and, due to the observed impurities, magnetic measurements were not performed on any of these samples.

Magnetic measurements were performed on a powder sample obtained from the 100% yield synthesis of the title compound, Salt•$Cs_{2.5}(V_5O_9)(AsO_4)_2$. Figure 8.22 shows the molar magnetic susceptibility, χ, and the inverse molar magnetic susceptibility, χ^{-1}. The data were acquired with an applied magnetic field of 0.01T. χ shows an increase in the susceptibility upon decreasing the temperature, similar to what is expected for paramagnetic materials. Like the cluster compounds presented in Chapter 6, this compound also has clusters containing reduced V cations that are bridged *via* μ_3-oxo bridges giving rise to magnetic exchange within the $[V_5O_9]$ aggregates. The inverse molar magnetic susceptibility was fit over the temperature range, 100-300K. From the fit, the effective magnetic moment, μ_{eff}, was calculated to be 1.78(6)μ_B, which is similar to the expected magnetic moment, 1.73μ_B, for V^{4+} cations, S = ½. A negative Weiss constant, -154(9) K, was also obtained from the fit, indicating strong antiferromagnetic coupling between nearest neighbors. The magnetic moment is plotted as a function of decreasing temperature, in the inset of Figure 8.22, which was calculated using the

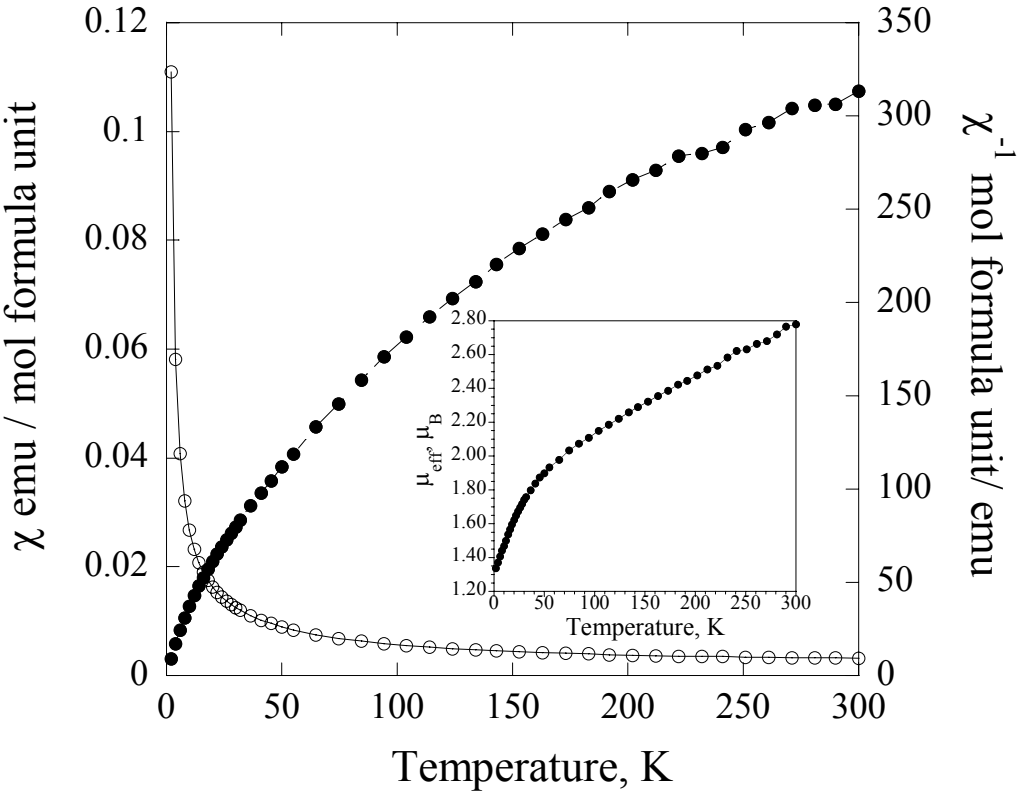

Figure 8.22: Molar magnetic susceptibility (□) and inverse magnetic susceptibility (■) performed on 100% yield synthesis of (salt)•$Cs_{2.5}(V_2O_5)(AsO_4)_2$ in an applied field of 0.01T. The inset shows the μ_{eff} plotted as a function of temperature.

equation $2.84(\chi_M T)^{1/2}$. At room temperature, the μ_{eff} is approximately $2.8\mu_B$. This value is less than what is expected for 3.5 V^{4+} cations per cluster ($3.24\mu_B$), which again indicates antiferromagnetic coupling. Despite the results from the Curie-Weiss fit, the magnetic susceptibility curve looks similar to what is expected for a paramagnetic material. There is no established long-range magnetic order evident at low temperatures, which is usually depicted by a magnetic transition (showing a decrease in the susceptibility for long range antiferromagnetic order or a significant increase in the magnetic susceptibility for ferro(i)magnetic materials).

Field-dependent studies were also performed on the title compound with fields ranging from ± 5T at various temperatures from 2-10K, Figure 8.23. It is expected that despite the antiferromagnetic coupling between the nearest neighbors, there could be some uncompensated electrons per cluster. The field- dependent plot shows an s-shaped curve similarly observed for superparamagnetic materials. However, the material does not show any remnant magnetization. The Field-dependent plot shown in the inset of Figure 8.23 shows a decrease in the magnitude of the magnetization as a function of increasing temperature. At 2K, the magnetization plot has an s-shaped curve which reaches a maximum of 0.6 μ_B/cluster at an applied field of 5T, again indicating antiferromagnetic exchange. Based on the oxidation states of the V cations found in the cluster, the maximum magnetization response possible would be approximately 3.5 μ_B/cluster.

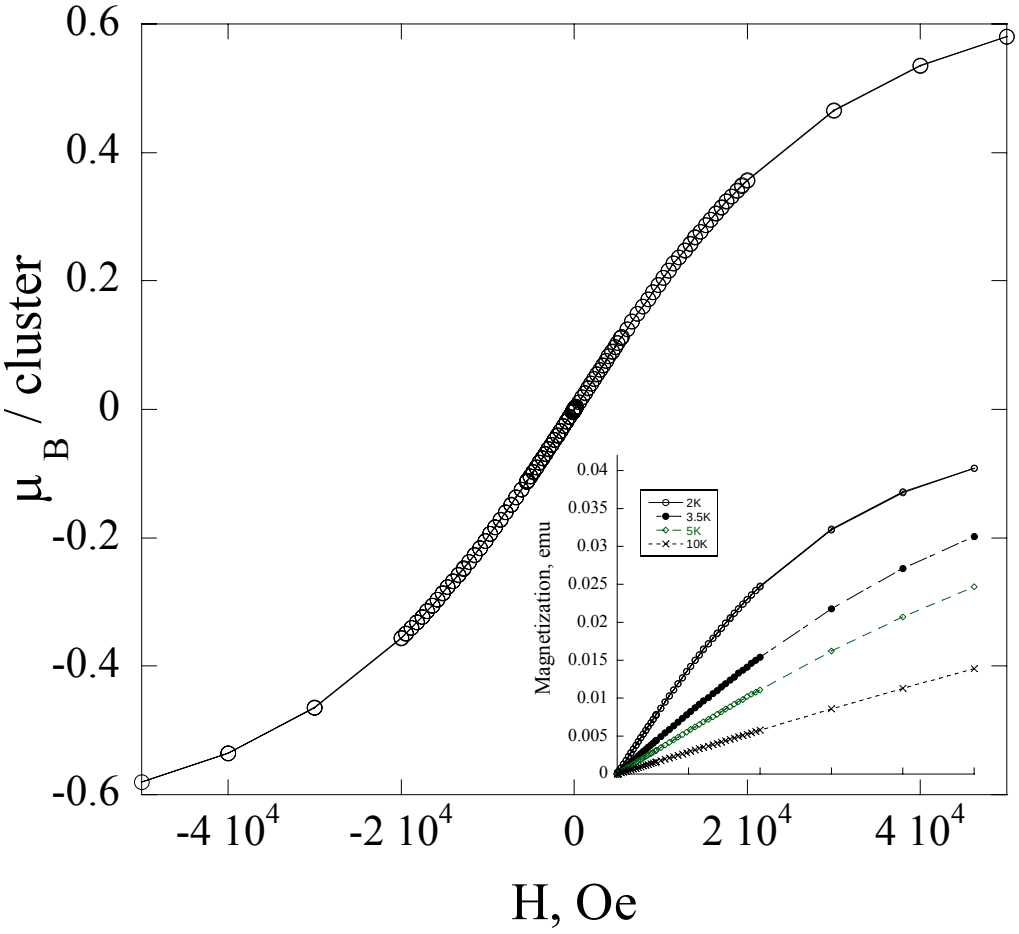

Figure 8.23: Field-dependent magnetization plot performed on 100% yield synthesis of (salt)•$Cs_{2.5}(V_2O_5)(AsO_4)_2$ at T = 2K. The inset shows the comparison of these field-dependent plots at T = 2, 3.5, 5, and 10K. At T = 10 K, the plot becomes linear.

Conclusions

A new family of salt-inclusion framework materials, exhibiting large salt-containing channels and POM cores, has been synthesized,. It is thought that the structural rigidity of the $[V_5O_{17}]$ core inhibits its ability to readily undergo oxidation / reduction, as the high-temperature methods used to achieve this have proven unsuccessful. As the cluster is oxidized, there is a formation of $NaVO(AsO_4)$ and a compound containing a $[V_4O_8]^{4-}$ core, (salt)•$Cs_2(V_4O_8)(AsO_4)_2$, while the reduction reactions appear to lead to different products altogether. The ultimate goal to create (salt)•$(V_5O_9)(AsO_4)_2$, a neutral framework compound, was not accomplished. Additional efforts were made to synthesize a neutral framework material through chemical modifications. Using high-temperature solid state methods attempts were made to put Ni or Cu-into the empty central site in the $[V_4O_8]^{4-}$ core. The goal was again to target a neutral framework material, (salt)•$(Cu/NiV_4O_8)(AsO_4)_2$. Although some of the Cu^{2+} appears to be going into the framework, this synthetic effort has also failed to create a neutral framework.

The V_5 compound shows rather large surface area but minimal H_2 adsorption at low temperature, 87K, and high pressure, 47 bar. Much effort has been made to chemically manipulate the material to create a neutral framework and maximize the surface area. The surface area of the material has been increased from an initial 111(2) to 150(2) m^2/g upon soaking (to remove the salt) and then 244(4) m^2/g upon oxidation *via* H_2O_2. The magnetic measurements reveal antiferromagnetic coupling between nearest neighbors. However, there is no evidence of long-range magnetic ordering possibly due

to the electronic insulation *via* $(AsO_4)^{3-}$ units. Once again, this material demonstrates the utility of salt-inclusion chemistry, and its role in the formation of special frameworks.

Literature Cited

1. (a) Müller, A., Reuter, H., Dillinger, S. *Angew. Chem. Int. Ed.*, **1995**, *34*, 2328-2361.

(b) Müller, A., Peters, F., Pope, M.T., Gatteschi, D. *Chem. Rev.*, **1998**, *98*, 239-271.

(c) Hagrman, P.J., Hagrman, D., Zubieta, J. *Angew. Chem. Int. Ed.*, **1999**, *38*, 2638-2684.

(d) Braun, P.V., Osenar, P., Tohver, V., Kennedy, S.B., Stupp, S.I. *J. Am. Chem. Soc.*, **1999**, *121*, 7302-7309.

(e) Müller, A., Döring, J. *Z. Anorg. Allg. Chem.*, **1991**, *595*, 251-274.

(f) Huan, G., Greaney, M.A., Jacobson J. *J. Chem. Soc. Chem. Commun.*, **1991**, *4*, 260-261.

(g) Xu, B., Xu,L., Gao, G., Yang, Y., Guo, W., Liu, S., Sun Z. Electrochim. Acta **2009**, *54*, 2246–2252.

(h) Zhang, G., Keita, B., Craescu, C.T., Miron, S., Oliveira, P., Nadjo, L. *J. Phys. Chem. B*, **2007**, *111* (38), 11253-11259.

(i) Hiskia, A., Troupis, A., Antonaraki, S., Gkika, E., Kormalip, P., Papaconstantinou E. *Intern. J. Environ. Anal. Chem*. 2006, 86 (3-4), 233–242.

(j) Troupis, A., Triantis, T., Hiskia, A., Papaconstantinou E. *Eur. J. Inorg. Chem.* **2008**, 5579–5586.

(k) Kang, Z., Liu, Y., Tsang, C.H.A., Dorothy, D.D.M., Wange, E., Shuit-Tong, L., *Chem. Commun*., **2009**, 413–415.

2. Pope, M.T., Müller, A. Polyoxometalate Chemistry From Topology via Self Assembly to ApplicationsPope, Michael T.; Muller, Achim Polyoxometalate Chemistry From Topology via Self Assembly to Applications. Springer - Verlag. 2001Online version available at: KLUWER ACADEMIC PUBLISHERS NEW YORK.

3. (a) Khan, M.I., Yohannes, E., Powell, D. *Chem. Com*., **1999**, 23 - 24.

(b) Khan, M.I., Yohannes, E., Doedens, R.J., Tabussum, S., Cevik, S., Manno, S., Powell, D. *Crystal Engineering*, **1999**, 2, 171-179.

(b) Khan, M.I., Yohannes, E., Powell, D. *Inorg. Chem.,* **1999***,* 38**,** 212 - 213.

(c) Khan, M. I., Yohannes, E., Doedens, R.J. *Angew. Chemie. Int. Ed. Engl.,* **1999***,* 38**,** 1292-1294.

(d) Khan, M.I., Yohannes, E., Doedens, R.J., Tabussum, S., Cevik, S., Manno, L., Powell, D. *Cryst. Engineering***, 1999**, 2, 171-179.

(f) Khan, M.I., Yohannes, E., Doedens, R.J. *Inorg. Chem.*, **2003**, 42(9), 3125 - 3129

4. Dolbecq, A., Mialane, P., Lisnard, L., Marrot, J., Sécheresse, F. *Chem. Eur. J*. **2003**, 9, 2914 - 2920.

5. An, H.-Y, Wang, E.-B., Xiao, D.-R., Li, Y.-G., Su, Z.-M., Xu, L. *Angew. Chem. Int. Ed*. **2006**, 45, 904 - 908.

6. Yaghi, O. M., O'Keeffe, M., Ockwig, N. W., Chae, H. K., Eddaoudi, M., Kim, J. *Nature,* **2003**, *423*, 705-714.

7. Rowsell, J. L. C., Millward, A. R., Park, K. S., Yaghi, O. M. *J. Am. Chem. Soc*., **2004**, *126*, 5666 – 5667.

8. (a) Eddaoudi, M., Li, H., Yaghi, O. M. *J. Am. Chem. Soc.* **2000**, *122*, 1391-1397.

(b) Seki, K., Mori, W. *J. Phys. Chem. B* **2002**, *106*, 1380 - 1385.

(c) Kondo, M., Okubo, T., Asami, A., Noro, S., Yoshitomi, T., Kitagawa, S., Ishii, T., Matsuzaka, H., Seki, K. *Angew. Chem., Int. Ed*. **1999**, *38*, 140-143.

(d) Pan, L., Adams, K.M., Hernandez, H.E., Wang, X., Zheng, C., Hattori, Y., Kaneko, K. *J. Am. Chem. Soc*. **2003**, *125*, 3062-3067.

(e) Wang, Q.M., Shen, D., Bülow, M., Lau, M.L., Deng, S., Fitch, F.R., Lemcoff, N.O., Semanscin, J. *Microporous Mesoporous Mater*. **2002**, *55*, 217-230.

(f) Kitaura, R., Seki, K., Akiyama, G., Kitagawa, S. *Angew. Chem., Int. Ed*. **2003**, *42*, 428-431.

(g) Eddaoudi, M., Kim, J., Rosi, N., Vodak, D., Wachter, J., O'Keeffe, M., Yaghi, O.M. *Science* **2002**, *295*, 469-472.

(h) Yaghi, O.M., Eddaoudi, M., Li, H., Kim, J., Rosi, N. U.S. Patent Application 2003/0004364.

(i) Rosi, N.L., Eckert, J., Eddaoudi, M., Vodak, D.T., Kim, J., O'Keeffe, M., Yaghi, O.M. *Science* **2003**, *300*, 1127-1129.

9. Cundy, C.S., Cox P.A. Chem. Rev., **2003**, *103*(3), 663-701.

10. (a) Huang, Q.,.Hwu, S.-J. *Inorg. Chem.* **2003**, *42*, 655-657.

(b). Huang, Q.,.Hwu, S.-J., Xunhua, M. *Angew. Chem. Int. Ed*. **2001**, *40*, 1690-1693.

(c) Etheredge, K.M.S., Hwu, S.-J. *Inorg. Chem*. **1995**, *34*, 3123-3125.

(d) Huang, Q., Ulutagay, M., Michener, P.A., Hwu, S.- J. *J. Am. Chem. Soc.* **1999**, *121*, 10323-10326.

11. Haddad, A., Jouini, T., Piffard, Y. *Eur. J. Solid State Inorg. Chem*. **1992**, *29*, 57-63

12. (a) B. H. Toby, EXPGUI, a graphical user interface for GSAS, *J. Appl. Cryst.* **2001**, *34*, 210-211.

(b) Roisnel, T., Rodríguez-Carvajal, J. *WinPLOTR*: a Windows tool for powder diffraction patterns analysis *Materials Science Forum, Proceedings of the Seventh European Powder Diffraction Conference* (EPDIC 7), **2000**, 118-123.

(c) Rodríguez-Carvajal, *J. Physica B*. **1993**, *192*, 55-69.

13. (a) Spek, A. L. *Acta Cryst*. **1990**, *A46*, C-34.

(b) Spek, A. L. *A Multipurpose Crystallographic Tool* Utrecht University, Utrecht, The Northerlands, **2002**.

14. (a) Sheldrick, G.M. In "Crystallographic Computing 3" (Sheldrick, G. M.; Kruger, C.; Goddard, R.; Eds), Oxford Univ. Press: London, **1985**, p 175-189.

(b) Sheldrick, G. M. In "SHELXTL, Version 6.1 Structure Determination Software Programs" Bruker Analytical X-ray Systems Inc., Madison, WI, **2001**.

15. Haushalter, R.C., Khan, M.I., Meyer, L.M., Zubieta, J.A. Microporous square pyramidal-tetrahedral framework vanadium phosphates and their preparation U.S. Patent 5,602,266, February 11, 1997.

16. Khan, M.I., Meyer, L.M., Haushalter, R.C., Schweitzer, A.L., Zubieta, J., Dye J.L. *Chem. Mater.* **1996,** *8,* 43-53.

17. Schleuter, A.W., Jacobson, R.A., Rundle, R.E. *Inorg. Chem.* **1966**, *6*, 277-280.

CHAPTER NINE

CONCLUSIONS AND FUTURE WORK

Serendipity continues to play an important role throughout the course of the materials discovery described in this dissertation. In fact, much effort directed towards the synthesis of new materials within the targeted systems has been exploratory in nature, where the components required to achieve a desired product were reacted, and then the reaction conditions were systematically varied in hopes of achieving the targeted phase formation. The strategy utilized in this study, to create low-dimensional magnetic solids, where the transition metal oxide constituents are structurally and electronically confined by nonmagnetic oxyanions[1], is the same chemistry employed in the synthesis of new zeolite-like porous fameworks[2]. As a result, the high-temperature solid state synthesis performed throughout this study has led to a large number of the targeted low-dimensional magnetic frameworks, but also a number of frameworks in which magnetism may not be the only or even the most interesting feature. In addition, molten salt, utilized to increase the reaction kinetics of this thermodynamically favored process, is in some cases incorporated, leading to new phase formation. Often, success in recognizing the significance of the formation of new compounds lies in one's knowledge of and accumulated experience in solid state chemistry.

The ultimate goal of this study was to explore new systems containing low-dimensional magnetic nanostructures in hopes of finding new ferro- and ferrimagnetic solids exhibiting quantum mechanical effects due to the confined magnetic lattices. These types of materials are sought for next generation device applications in quantum

computing and information storage. The scope of this research is threefold: 1) to explore new solids containing low-dimensional magnetic nanostructures in the MO_n/XO_m system (where M = first-row transition metal cations; X = V, P, or As), 2) to characterize these new materials and, through chemical substitution, fine tune (and optimize) magnetic and electronic properties of solids that exhibit confined magnetic nanostructures, and 3) to perform structure/property correlation studies to seek the origins of any unusual physical phenomena associated with the size, shape, and geometry of the magnetic nanostructures.

In this study, nonmagnetic oxyanions XO_m^{n-} were utilized to terminate the propagation of the transition metal oxide lattices, forming structures with 2-D sheets, 1-D chains, and 0-D clusters. Exploratory synthesis in the mixed polyhedral system made of the tetrahedral oxyanions and the transition metal oxide with varying coordination environments, has proven to be extremely rich and has rendered many new compounds of magnetic and catalytic interest. The new discoveries are grouped into chapters according to their lattice types, where Chapter 3 and Chapter 5 present two extensive compound families that contain two dimensional metal oxide sheets, Chapter 6 presents a lattice with 1-D $[MO_4Cl]_\infty$ chains, and Chapters 4, 7, and 8 all present materials containing 0-D magnetic metal oxide clusters. Furthermore, these materials exhibit a variety of interesting structural motifs including channels, comparable to the well-known zeolite structures, and layers presumably allowing easy ion transport suitable for battery type applications. However, structural features leading to easy ion transport were only briefly mentioned in scattered sections throughout this dissertation because it is irrelevant to the magnetic characterizations of new materials, which is the focus of this study. It should

also be noted that there is an appendix following the conclusions chapter which is meant to quickly highlight interesting structural features and any characterization performed on additionally synthesized materials not reported in Chapters 3-8.

New oxyanion-based solids, presented in chapters 3-5, report varying metal oxide dimensionalities relative to the metal (M) to oxyanion (XO_4^{n-}), M/X, ratios. These materials show a decrease in dimensionality upon decreasing the M/X ratio. All of these materials are part of extensive structural families that reveal complicated magnetic properties that can be varied through chemical modification. In any event, these complex solids exhibit the structural versatility inherent in the mixed polyhedral system. For example, the frameworks reported in Chapter 3 exhibit condensed 3-D M-O-X lattices, while those in Chapters 4 and 5 have channeled or layered structures types. Chapter 5 demonstrates the structural versatility in mixed polyhedral frameworks as these materials show both channeled and layered structures sharing a common $[M_3O_{12}]\infty$ building block. Their structures have rendered them multifunctional as they have already shown interesting magnetic properties and easy ion exchange and even reduction/insertion of Li cations into the frameworks.[3-6] Due to the structural and compositional variations observed in this compound family, it is likely that more in depth structure property correlation studies could be achieved.

The work discussed in Chapter 3 was intended to explore metal-rich areas of the phase diagram, in hopes of enriching the interaction between magnetic ions. Increasing the M/P ratio can increase the density of the M-O lattice due to the fewer number of oxyanions incorporated into the structure. Chapter 3 presents a compound family,

$ANa_3M_7(PO_4)_6$, with nine possible combinations of A = K, Rb, Cs and M = Mn, Fe, Co. The magnetic behavior in condensed phases is sensitive to the local structure where magnetic spins are coupled, and this extensive family presents a rare opportunity for an in-depth study of electronic interactions within the differing spin systems. The inverse molar magnetic susceptibility and field-dependent magnetization data reveal ferrimagnetic transitions for all of the Fe^{2+} and Co^{2+} derivatives, whereas the Mn^{2+} derivatives show only antiferromagentic transitions at low temperature. It is thought that this difference in magnetic response could be related to the orbital contribution observed in the Fe^{2+} and Co^{2+} containing derivatives. All of the metal polyhedra with the exception of M(4) form distorted pseudo-octahedral geometries. M(4) forms a trigonal bipyramid geometry whose axial oxygen run approximately parallel with the crystallographic *a* axis. It is known that heavily distorted octahedral geometries and trigonal bipyramidal geometries will lead to orbital splitting diagrams that are very different from the ligand field splitting observed for a traditional octahedral environment (which demonstrates two sets of degenerate orbitals, t_{2g} and e_g). Therefore, it is suspected that slight differences in the distribution of orbital energies could lead to quenching of the orbital component in some of these ions. This would lead to M cations with varying magnetic moments and hence a net ferrimagnetic exchange between neighboring ions. Furthermore, a divergence in the FC/ZFC in $RbNa_3Fe_7(PO_4)_6$ and an out-of-phase peak in its ac susceptibility is indicative of some irreversible process. The temperature at which the divergence occurs in the FC/ZFC curves is decreased as the applied field is increased, reminiscent of a field induced process. The isothermal magnetization plots of

compounds $ANa_3M_7(PO_4)_6$ A/M = K/Fe, Rb/Fe, and Cs/Co have also revealed step-like anomalies on aligned single crystals. The frequency dependence in the ac susceptibility is too small for a superparamagnetic-like response; therefore, it was determined that these steps were not due to quantum effects and were instead field induced transitions resulting from the triangular magnetic lattice or irreversibility in domain walls. The long-range ferrimagnetic ordering is not surprising as the structure contains 2-D metal oxide sheets that are narrowly separated from one another *via* $(PO_4)^{3-}$ oxyanions. These oxyanions can in some cases provide a super super exchange pathway, that although weak, can allow the formation of long-range magnetic order at low-tempeartures. Follow-up studies are suggested in the future work section to investigate the origin of the ferromagnetic properties as well as magnetization steps.

In many cases, structure and property correlation studies are not as conclusive as the one stated above. An example is observed in Chapter 4 which reports a new family of oxyanion-containing Fe^{3+} compounds. These materials have the following compositions: $Ba_{10}Na_5Fe_7(\mu_3\text{-}O)_2(PO_4)_{14}$, $Ba_{10}Na_5Fe_7(\mu_3\text{-}O)_2(AsO_4)_{12}(AsO_3)_2$, and $Sr_{14}NaFe_{10}(\mu_3\text{-}O)_2(PO_4)_{17}Cl$. They exhibit two structure types and have similar features including $[Fe^{III}_7(\mu_3\text{-}O_2)(XO_4)_{14}]$ sheets that contain equilateral $Fe_3(\mu_3\text{-}O)$ triangular magnetic clusters. Due to the structural versatility already observed in this compound family, it is thought that further chemical modification will likely lead to other compounds having the same structural building units. Based on the reported magnetic properties of the "basic carboxylates"[7], which have the same $M_3(\mu_3\text{-}O)$ (M = first-row transition metal) equilateral triangular magnetic clusters, the title phases were expected to show

antiferromagnetic exchange, as was confirmed for the latter two compounds. However, $Ba_{10}Na_5Fe_7(\mu_3\text{-}O)_2(PO_4)_{14}$ shows ferro(i)magnetic properties at high temperature that were verified *via* the presence of a room temperature hysteresis. The interesting observed properties have led to a close analysis of single crystals obtained from the molten salt reaction. After close examination, evidence of the existence of trigonal and monoclinic phases was found. However, multiple experiments including DTA, DSC, and variable temperature PXRD, revealed no evidence of a structural transition at or near room temperature. Therefore it is thought that the two phases, monoclinic and trigonal, coexist, as suggested by the powder pattern of the selected single crystals.

Throughout the course of exploratory synthesis, an extensive series of structurally related compounds, as reported in Chapter 5, has been collectively recognized. These compounds, $BaNaCo_3(AsO_4)_3$, $Sr_{0.90}Na_{1.2}Ni_3(AsO_4)_3$, $Na_8Co_{6.25}O_{0.25}(AsO_4)_4(As_2O_7)_4$, $Sr_2Na_{0.66}Fe_{3.34}(PO_4)_4Cl_{0.8}$, $Sr_2NaFe_3(AsO_4)_4Cl$, and $Ba_{1.88}Na_{0.75}Fe_3(AsO_4)_4Cl$, all have common $[M_3O_{12}]_\infty$ sheets that are either interconnected *via* edge-sharing MO_6 polyhedra to form a 3-D M-O lattice, or isolated *via* alkali/alkaline earth metal cations or alkali/alkaline earth metal chloride salts. The magnetic characterization has shown antiferromagnetic exchange in the 3-D lattice of $BaNaCo_3(AsO_4)_3$, while ferrimagnetism has been observed in the 2-D lattices of $Sr_2NaFe_3(AsO_4)_4Cl$ and $Ba_{1.88}Na_{0.75}Fe_3(AsO_4)_4Cl$. The latter two compounds have mixed valent Fe^{2+} and Fe^{3+} cations, and it has been concluded that, due to the difference in the magnitude of the magnetic moments for each ion, there is no cancelation in their magnetic exchange leading to a net magnetic moment. Their ferrimagnetic responses have been proven

through the observation of magnetic hysteresis below their transition temperature, T_c, approximately 25K and 50K, respectively. Furthermore, these materials have also shown a divergence in their FC/ZFC plots at low fields, indicating the presence of an irreversible process such as domain wall pinning.

Chapters 6-8 illustrate a few additional unique attributes regarding the synthesis and structure formation of the materials presented within them. One evident feature is that all of the materials are salt-inclusion solids. These salts have much lower melting points than covalent metal oxides and can aid in the synthesis and crystal growth of materials that cannot be achieved in other solvent media. Even though the salt is used as a high-temperature flux, its inclusion in the structure is sometimes inevitable. Although no reaction mechanism is known, one can imagine that the metal oxides are first "dissolved" in the corrosive molten salt and then, upon cooling, the covalent lattice aggregates around or within the inherent structure of the molten ionic salt, leading to the formation of new compounds with unexpected structures and properties.

It has been considered that, like the oxyanions, ionic salt can also serve as a method to achieve reduction in the dimensionality of the magnetic metal oxide lattices. The difference between these two diamagnetic insulators is found in their bonding interactions. The salt is ionic and therefore does not function as a pathway for superexchange, and, in turn, can aid in the confinement of the magnetic TM-oxide lattices. This is illustrated in Chapter 7 which presents materials containing high-nuclearity metal oxide clusters that are embedded in a salt-like matrix. In addition,

Chapters 6 and 8 demonstrate the inherent utility of salt-inclusion chemistry, as it can also aid in the formation of channeled type structures.

A second unique attribute of Chapters 6-8 is that they illustrate the added structural versatility inherent in the newly explored vanadium system. In chapter 6, the substitution of the $(XO_4)^{3-}$ oxyanions (X = P, As) in the previously studied systems with the fully oxidized $(VO_4)^{3-}$ anion has allowed richer structural chemistry to be unveiled, as V can have variable oxidation states and coordination environments. Mixing vanadium with a second TM is particularly attractive, for they have potential applications in areas related to catalysis, batteries, and magnetism. This is due to the variable crystal chemistry of the added transition metals as well as to the utility of the unique frameworks created by the salt. Chapters 7 and 8 exhibit the POM chemistry for which the fully oxidized early transition metals are known. Chapter 7 shows the formation of several high-nuclearity POM cores. The VO_5 polyhedra have short vanadyl V=O type bonds that can serve as a terminating cap, decreasing the likelihood that these polyhedra will link in 3-D and instead form low-dimensional structures. This leads to the formation of spherical polyoxometallate aggregates that are completely isolated from one another *via* a surrounding salt lattice. Chapter 8 shows that when mixed with oxyanions, vanadium can also render porous 3-D structures containing POM cores. This mixed polyhedral framework has exhibited large solvent free voids, leading to large surface areas.

Chapter 6 demonstrates the utility of the mixed metal oxide system, as it reports 6 new compounds, all having the same general chemical formula $(CsCl)M(VO_3)_2$ and adopting two different structure types. Structure type **I**, found to exist for M = Mn, Co,

Ni, and Cu, contains metavanadate chains $[VO_2O_{3/3}]\infty$. Within these chains, the vanadium cation is found in a 5+ oxidation state and square pyramidal geometry. Structure type **II** (M = Co, Zn) consists of metavanadate rings, $(VO_3)_4$, within which the vanadium cations are also found in a 5+ oxidation state bearing a tetrahedral geometry.

In structure type **I**, the chloride Cl^- anion from the salt participates in the covalent framework, giving rise to 1-D $[MO_4Cl]_\infty$ chains. The relatively weak M-Cl bond does not provide enough energy to offset the energy necessary to promote the *s* electrons for orbital hybridization, thus, unlike O^{2-} anion, the M-Cl-M linkage often adopts linear geometry. These $[MO_4Cl]_\infty$ chains extend infinitely along the crystallographic *a* axis through linear M-Cl-M linkages. These compounds exhibit strong antiferromagnetic exchange through the diamagnetic bridging ion, Cl^-, within the chain. The Mn and Co derivatives, due to interchain coupling, exhibit the development of long-range magnetic order observed through a decrease in the molar magnetic susceptibility data at low temperatures. The origin of these magnetic phenomena needs to be further confirmed, possibly by neutron scattering and vibrational spectroscopy in the presence of a magnetic field.

Chapter 7 further shows the structure versatility of SISs *via* three new compound families that contain high-nuclearity transition metal oxide clusters. These clusters, also known as polyoxometallates, offer an assortment of different structural motifs that serve as potential building blocks for extended solids. These fascinating metal-oxide aggregates, more frequently observed for early transition metals (V, Nb, W, Mo, and Ta), have been synthesized using a variety of different methods such as hydrolytic aggregation

in non-aqueous media, conventional, hydrothermal, or solvothermal techniques, reductive aggregation processes, etc.[3-5] All of these methods have one thing in common- they are low-temperature soft techniques. We have proven for the first time that these high nuclearity POM cores can also be synthesized using high-temperature methods in molten-salt media. Through further exploration it is likely that this new synthetic method could lead to the synthesis of many new cores, because low temperature techniques favor metastable phases, while high-temperature techniques favor more thermodynamically stable phases. Using high-temperature methods, several new hybrid solids containing high nuclearity polyoxometallate cores were isolated. These seven compounds have the following compositions: $Cs_{11}Na_3(V_{15}O_{36})Cl_6$ (with $[V_{15}O_{36}Cl]^{9-}$ core), $Cs_5(V_{14}O_{22})(As_2O_5)_4X$ ($[V_{14}As_8O_{42}Cl]^{5-}$ X = Cl, B, I), $Na_{35.5}Cu_{27.75}O_8(AsO_4)_8Cl_{11}$, $K_{3.29}Na_{32.21}Cu_{27.75}O_{16}(AsO_4)_{16}Cl_{11}$, and $Na_9Cu_7O_4(AsO_4)_4Cl_3$ ($[Cu_{14}(\mu_4\text{-}O_8)(AsO_4)_8]^{12-}$). These salt-inclusion solids have covalent metal oxide lattices integrated with ionic, alkali metal halide lattices, rendering all of the vanadium containing clusters water-soluble. The dissolution of $Cs_5(V_{14}O_{22})(As_2O_5)_4Cl$ followed by re-precipitation resulted in a new hydrated phase $Cs_5(V_{14}O_{34})(AsO_3)_2Cl{\cdot}2.6H_2O$ (with $[V_{14}As_2O_{40}Cl]^{5-} \equiv Cl@V_{14}As_2$ core).

This chapter highlights molten salt as a structure directing agent that can be utilized in the synthesis of low-dimensional TMO clusters. This finding expands the search for high nuclearity TMO clusters into a totally different synthetic regime, and due to the solubility of these materials, they could possibly aid the pursuit for rational design of new extended solids containing periodic arrays of magnetic building blocks. Measurements of the temperature-dependent molar magnetic susceptibility suggest that

these materials are paramagnetic at high temperatures, with antiferromagnetic exchange between nearest neighbors. Low-temperature field-dependent investigations reveal s-shaped curves at low temperature, the signature of confined (cluster) magnetic spins.

Chapter 8 also exhibits the structural versatility of vanadium and the utility of salt inclusion chemistry as this chapter presents a porous salt-inclusion compound containing POM cores. The structure of (salt)·$Cs_{(6-n)}(V_5O_9)^{n+}(AsO_4)_2$ contains paramagnetic $[V_5O_{17}]$ clusters. Unlike the clusters seen in the compounds presented in Chapter 6, these are linked together *via* $(AsO_4)^{3-}$ tetrahedra (through sharing corner oxygen atoms) to form a 3-D open framework. The salt in this compound aids in the formation of the channeled structure. The significance of this family of composite solids is that once the rigid lattice is formed, the salt that remains in the channels can be washed away by soaking the material in deionized water. Much effort has been made to chemically manipulate the material to create a neutral framework and maximize the surface area. The surface area of the material has been increased from an initial 111(2) to 150(2) m^2/g upon soaking (to remove the salt) and then 244(4) m^2/g upon oxidation *via* H_2O_2 or 188(3) m^2/g upon oxidation *via* I_2 (to achieve oxidative removal of Cs cations). The magnetic measurements reveal antiferromagnetic coupling between nearest neighbors. However, there is no evidence of long-range magnetic ordering possibly due to the electronic insulation *via* $(AsO_4)^{3-}$ units. The field-dependent studies show s-shaped curves again indicating confined (cluster) magnetic spins as observed in the metal oxide clusters in Chapter 7.

The results of this study have demonstrated that exploratory synthesis in the mixed polyhedral system is still a fertile area for the discovery of new and fascinating framework materials. This project has led to the discovery of many new magnetically interesting compounds. So far we have seen the utility of molten salt synthesis in the formation of magnetic metal oxide nanoclusters and open-framework materials. We have observed that mixed polyhedra, including the tetrahedral oxyanions (XO_4^{n-}) and the transition metal oxides with varying coordination (MO_n, $4 \leq n \leq 6$), can lead to numbers of interesting framework formations *via* corner and edge-sharing oxygen atoms. We have seen the efficacy of using oxyanions as a means to create structurally confined 0-, 1-, and 2-D type magnetic metal oxide lattices. Within this assorted group of newly synthesized materials, we have observed multifunctional structures that give rise to several intriguing properties. Chemical modification has been performed on these materials to produce other derivatives for structure property correlation studies or to fine tune particular unique physical phenomena.

The underlying hypothesis of this research using oxyanions to terminate and insulate the metal oxide lattices is two fold: 1) if the the oxyanions are truly insulating in terms of the magnetic spins, one should expect to see "molecular-like" behavior including slow relaxation of the magnetization and 2) the inter-nanostructure magnetic interactions are expected to be diminished or significantly decreased upon an increase in the spaceing between nanostructures.

The vision for this project was the hope that, through execution of the three tasks outlined in paragraph two, the continued manifestation of serendipity would lead us to

truly low-dimensional ferro and ferrimagnetic materials that exhibit quantum mechanical effects. Several new materials have been synthesized that have truly confined magnetic lattices as observed in Chapters 7 and 8. When considering the salt-inclusion solid $Cs_{11}Na_3(V_{15}O_{36})Cl_6$, which contains chlorine centered $[Cl@V_{15}O_{36}]^{9-}$ cores, it is seen that this POM has an average of 11 unpaired electrons per cluster. Even if the material has pure antiferromagnetic coupling, there should be one unpaired electron per cluster remaining. The isothermal magnetization plot shows a paramagnetic-like response until very low temperatures are reached. In fact, the 2K data shows an s-shaped curve with no remnant magnetization. This could be a sign of slow relaxation of the magnetization but further experimentation will be required to prove so. It is likely that if even lower temperatures could be achieved, this material and the other cluster-based materials could exhibit "molecular-like" properties including remnance originating from an energy barrier to magnetization reversal.

The ultimate goal of this project, to explore new systems containing low-dimensional magnetic nanostructures in hopes of finding new ferro- and ferrimagnetic solids exhibiting quantum mechanical effects, has proven to be challenging. Extended solids have a natural tendency to form long-range magnetic order, and although metal oxide lattices can be structurally confined, in many instances they are not truly confined in terms of the magnetic coupling. The materials presented in Chapters 3 and 5, which discuss compounds containing 2-D metal oxide sheets, all show evidence of the development of long-range magnetic order. In systems where it was thought that true confinement of the metal oxide lattice had been achieved, such as in the cluster

compounds presented in Chapters 4, 7, and 8, the materials did not possess the characteristics required to obtain slow relaxation of the magnetization and possible quantum effects at temperatures higher than 2K. Therefore, it is concluded that true confinement of magnetic nanostructures in extended solids is much harder than observed in their molecular counterparts. Through this study, despite my every effort, there is no sure recipe for success that I can pass on yet.

My opinion, which is based on the success of others, is that triangular magnetic lattices are an important way for the nonmolecular solid state chemist to inhibit the formation of long range magnetic order.[8-9] And, although these triangular lattices cannot be rationally designed, we should pay special attention to the ones we observe, for they can play a key role in this research. There are several things a synthetic chemist should keep in mind, which can help to increase the likelihood of success. First, in order for us to obtain slow relaxation we must first have obtained ferro or ferrimagnetic coupling. We have seen in Chapter 3 that magnetic ions with unquenched orbital contributions can lead to ferrimagnetic exchange, especially in materials that contain asymmetric metal cation sites or metal cations with varying coordination environments. Creating systems with mixed metals or metals in mixed oxidation states, as observed in Chapter 5, can also lead to this same phenomenon. Ultimately, without ferro or ferrimagnetic coupling, slow relaxation cannot be observed. Once the magnetic nanostructures are confined, we learned from Chapters 7 and 8 that the system must possess certain characteristics to exhibit slow relaxation. Magnetic anisotropy is one of these characteristics, so it may be beneficial to use starting materials, such as *Jahn-Teller* ions, that show distortions from

traditional octahedral geometries. It should also be considered that, even though structural confinement may not be initially achieved, through chemical modification sometimes it can be achieved. For instance, we can dope diamagnetic ions, such as Zn^{2+}, Ga^{3+}, or low-spin heavy transition metals into our solids to decrease the dimensionality of our magnetic lattices. From a synthetic standpoint, it should never be forgotten that the discovery of many novel things is serendipitous by nature. Often we have to take what we get, and sometimes we stand to learn a lot from the things that we never get to work.

Future Work

This dissertation presents many new extended solids containing low-dimensional magnetic nanostructures with various dimensionalities and geometries. These exciting new materials have shown many interesting magnetic properties, and due to the complicated nature of the structure, their magnetic properties cannot always be explained. Therefore, it is of interest to perform neutron studies on some of these compounds, as this is the only way to determine the true magnetic structure of a material. These measurements could shed new light especially on the origin of the magnetic anomalies (steps), observed in the field-dependent magnetization plots of the $ANa_3M_7(PO_4)_6$ (A/X = K/Fe, Rb/Fe, Cs/Co, and the high-temperature ferro(i)magnetic properties observed in single crystals of $Ba_{10}Na_5Fe_7(\mu_3\text{-}O)(PO_4)_{14}$.

As many of the compound families found within this dissertation have exhibited structural and compositional versatility, many of them could be further expanded for more in-depth structure property correlation studies. For example, Chapter 8 presented a

porous material, (salt)$Cs_{2.5}(V_5O_9)(AsO_4)_2$, that apparently undergoes oxidation with ease. Despite the heavy framework, this compound shows high surface areas, up to 242m^2/g. It might be of future interest to replace As^{5+} with the more environmentally friendly P^{5+} or V^{5+}. It is expected that this will also greatly increase the surface area through the creation of a lighter framework. Due to the porous structure, the high surface area, and the redox chemistry associated with the vanadium cations, it is thought that studying catalytic properties of this material might be of future interest as well.

The materials presented within Chapter 7 show several water-soluble solids that contain vanadium-based POM cores, all of which have shown oxidative decomposition in solution. $Cs_5(V_{14}As_8O_{42}Cl)$, containing the $[V_{14}As_8O_{42}Cl]^{5-}$ core, was dissolved in water. After dissolution and a slow re-precipitation over approximately two weeks, a new fully oxidized cluster was found, $[V_{14}As_2O_{40}Cl]^{5-}$. The same experiment was performed again with $Cs_5(V_{14}As_8O_{42}X)$ (where X=Br or I), except a fast overnight evaporation was utilized. The material that crystallized out of solution had a similar composition, $Cs_5(V_{14}As_8O_{42}X)\bullet xH_2O$ (X = Br or I), with the exception of water, and the same reduced cluster, $[V_{14}As_8O_{42}Cl]^{5-}$, as observed in the starting material. The newly crystallized material however, had a very different crystal structure. It should be noted that due to the low yield after re-precipitation, no characterization beyond the structure determination has been performed. In order to do further studies, the yield of the re-precipitated products will have to be increased. These materials are interesting for many reasons. First, it appears that by varying the conditions of the dissolved clusters such as heat, light, and atmosphere, other intermediate oxidation products could be isolated. This could give

insight into the overall oxidative decomposition process. The second area of interest is the ease with which the vanadium cations become oxidized. It is unknown what the mechanism is, but full oxidation occurred while the clusters sat in water at room temperature over a two week period. As a result, it is thought that the materials could be of some catalytic importance. Further exploration of this system could give one insight into its manipulation and hence allow, at some point, the rational design of new solids utilizing these magnetic POM cores as building blocks.

Much current research is focused on $LiFePO_4$, a compound that is expected to be the positive electrode material for next-generation Li^+ batteries. These expectations are the result of its low cost, low toxicity, and relatively high theoretical specific capacity of 170 mAh/g.[10] As a result, new Fe-O-P-containing structures are sought after for battery applications. It is thought that the materials presented in Chapter 5 could be a great system for battery-related studies. These materials present three different structure types, all of which contain $[M_3O_{12}]_\infty$ sheets. It should be noted that, despite the presence of the intersecting channels and the layered-type structures, ion exchange properties of the materials presented here were not studied. This study is of future interest, especially on the iron phosphate containing compound, as several materials having similar structures have shown easy ion exchange and reduction/insertion of Li^+ ions.[3,5] The synthesis of new mixed polyhedral frameworks, like the ones presented here, can offer two major advances in battery research. First, this research could lead to the synthesis of new frameworks that are competitive or even superior to those of $LiFePO_4$. Second, the development of versatile compound families, like the ones presented in Chapter 5, could

offer a prototype system allowing one to study how incremental changes in structure or composition can alter the electrochemical properties of the newly synthesized materials. It is expected that incremental type research could offer invaluable fundamental knowledge aiding in the pursuit of next-generation battery materials. Based on the rich structural chemistry observed in this compound family, it is expected that it could be such a prototype material.

The general formulas for the three structure types presented in Chapter 5 could be written as $AM_3(XO_4)_3$, $AM_3(XO_4)_2(X_2O_7)_2$, or $AM_3(XO_4)_4$ (where A = alkali/alkaline earth metal cation, M = transition metal, and X = main group element or fully oxidized early transition metal). In order to create a prototype system, more focus needs to be made on the composition of the material, especially replacing the heavier X = As oxyanions with less toxic and lighter ones such as P or even fully oxidized V. The metals within the system need to be replaced with more environmentally friendly and low-cost cations such as Fe or Mn. Other variations can be made in the system to promote the formation of the different structure types including the oxidation states of the added transition metals, M, and the stoichiometric ratios of the M/X or A/M cations. Altering the reaction stoichiometry could also offer more insight into how to specifically target one structure type over the other in this extensive compound family.

Literature Cited

1. Hwu, S.-J. *Chem. Mater.*, **1998**, *10*, 2846-2859.

2. Bieniok, A., Brendel, U., Lottermoser, W., Amthauer G. *Z. Kristallogr*. **2008**, *223* 186-194.

3. Korzenski, M.B., Kolis J.W., Long, G.J. *J. Solid State Chem*. **1999**, *147*, 390-398.

4. Kinomura,N., Matsui, N., Kumada,N., Muto, F., *J. Solid State Chem*. **1989**, *79*, 232-237.

5. Becht, G., Ph.D. Dissertation, Clemson University, Clemson, SC, **2008**.

6. (a) Glaum, R., Gruehn, R., Moller, M. *Z. Anorg. Al &. Gem*. **1986**, *543*, 111-116.

   (b) Attfield, J.P., Battle, P.D., Cheetham, A.K., Johnson D.C. *Inorg. Chem.*, **1989**, *28* (7), 1207-1213.

7. (a) Cannon, R. D., White, R. P. *Prog. Inorg. Chem.* **1988**, *36*, 195-298.

   (b) Raptopoulou, C.P., Tangoulis, V., Psycharis V. *Inorg. Chem.* **2000**, *39,* 4452-4459.

8.. (a) Snyder, J ., Ueland, B. G., Slusky, J. S., Karunadasa, H., Cava, R. J., Mizel, A., Schiffer, P., *Phys. Rev. Lett.* **2003**, *91*, 107201-1- 107201-4.

   (b) Ehlers, G ., Cornelius, A. L., Orendac, M., Kajnakova, M., Fennell, T. S., Bramwell, T., Gardner, J. S. *J. Phys. Condens. Matter* **2003**, *15*, L9-L15.

9. (a) Maignan, A., Hardy, V., HQbert, S., Drillon, M., Lees, M. R., Petrenko, O., Paul, D. M., Khomskii, D. *J. Mater. Chem.* **2004**, *14*, 1231-1236.

   (b) Hardy, V., Lees, M. R., Petrenko, O. A., Paul, D. M., Flahaut, D., HQbert, S., Maignan, A. *Phys. Rev. B* **2004**, *70*, 064424-064431.

10. (a) Padhi, A. K.; Nanjundaswamy, K. S.; Goodenough, J. B. *J. Electrochem. Soc.* **1997**, *144*, 1188-1194.

    (b) Ravet, N., Chouinard, Y., Magnan, J. F., Besner, S., Gauthier, M., Armand, M. *J. Power Sources* **2001**, *97-98*, 503-507.

APPENDIX I

NEW MIXED FRAMEWORK COMPOUNDS

The focus of this dissertation has been on the synthesis of new extended solids containing low-dimensional magnetic nanostructures. As a result, the most interesting magnetic materials were chosen to be presented in Chapters 1-9. The rich structural chemistry inherent in the mixed polyhedral framework system has led to the discovery of many other materials during this study. This appendix will give a brief description of the synthesis and characterization of other extended solids discovered during exploratory synthesis. It should be noted that, unless otherwise stated, all reaction were performed in a nitrogen-purged dry box and then sealed under vacuum.

Noncentrosymmetric (NCS) Salt-Inclusion Vanadates

$(AX)_2Mn(VO_3)_2$ (A/X = Cs/Cl **1**, Cs/Br **2**, and Rb/Cl **3**), $(AX)_2Cu(VO_3)_2$ (A/X = Cs/Cl **4**, Cs/Br **5**, RbCl **6**, and K/Cl **7**), $Rb_3ClMn(VO_3)_4$ **8**, and $(CsCl)Mn_2(V_2O_7)$ **9**

This study has led to the discovery of the first series of salt-inclusion vanadates, including $(AX)_2Mn(VO_3)_2$ (A/X = Cs/Cl **1**, Cs/Br **2**, and Rb/Cl **3**), $(AX)_2Cu(VO_3)_2$ (A/X = Cs/Cl **4**, Cs/Br **5**, RbCl **6**, and K/Cl **7**), $Rb_3ClMn(VO_3)_4$ **8**, and $(CsCl)Mn_2(V_2O_7)$ **9**. These new phases, synthesized using conventional solid state methods, adopt four distinct structures, designated as types **I** (**1-3**), **II** (**4-7**), **III** (**8**), and **IV** (**9**)**.** The formation of these NCS structures is encouraged by structural and electronic factors. All four structure types incorporate chlorine centered acentric building units as well as acentric vanadate units, including metavanadate chains in **I, II**, and **III** and pyrovanadate units in **IV**.

Incorporation of a unique metavanadate chain, or pyrovanadate unit, allows the retention of the polar axis and thus the crystallization of polar compounds having structure types **I, III,** and **IV**. Structure type **II** exhibits two metavanadate chains that propagate in directions orthogonal to each other, leading to the formation of a nonpolar crystal structure. The synthesis and characteraization of **1**-**7** and **9** were recently published in 2008 in *Angeandte Chemie, International Edition*[1]; therefore, they will not be further discussed here.

$Rb_3ClMn(VO_3)_4$, **8**

$Rb_3ClMn(VO_3)_4$, **8**, was synthesized using MnO_2 and V_2O_5 in a 1:1 mol ratio (ca. 0.3 g) along with a RbCl/NaCl eutectic flux equal to 3 times the mass of the oxide reactants. The mixtures were heated to 725°C, held there for 2 days, slowly cooled to 450°C at a rate of 0.1°C/min, and then furnace cooled. Orange plate-like single crystals of **8** were retrieved after washing with deionized H_2O in a yield of approximately 20%. The crystallographic data and atomic parameters are shown in Tables I.1-I.2.

$Rb_3ClMn(VO_3)_4$, **8**, shown is Figure I.1 has a similar structure to the well-known fresnoites.[2] $Rb_3ClMn(VO_3)_4$ consists of metal-oxide sheets containing Mn^{2+} in a pseudo-octahedral geometry with MnO_4Cl_2 polyhedra. Mn-O distances are 2.102(7) Å with one short axial Cl distance of 2.497(7) Å and one long axial Cl distance of 2.877(7) Å. These distances are in good agreement with BVS[3] calculations for Mn^{2+}. The average Mn-Cl distance, 2.69 Å, is in close comparison with 2.64 Å, the sum of Shannon crystal radii of 6-coordiate Mn^{2+} (0.97Å) and Cl^- (1.67 Å).[4]

Table I.1: Crystallographic data for $Rb_3ClMn(VO_3)_4$

empirical formula	$Rb_3ClMn(VO_3)_4$, **8**
structure type	**III**
color/shape	orange / plate
crystal size (mm)	0.15 x 0.12 x 0.02
formula weight (amu)	742.56
space group, *Z*	*C m m 2* (no. 35), 2
T°C	25
a, Å	8.480(2)
b, Å	16.751(3)
c, Å	5.375(1)
V, Å^3	763.5(3)
linear abs. coeff., mm^{-1}	12.885
F_{000}	682
d_{calc}, g / cm^{-3}	3.230
data/restraints/parameters	683 / 1 / 60
secondary extinction	0.0004(4)
flack parameter	0.03(3)
reflections collected / unique / R_{int} [a]	3187 / 733 / 0.0846
final R1/wR2 [b] [$I > 2\ \sigma(I)$]	0.0479/ 0.0973
R1/wR2 (all data)	0.0540/ 0.1002
GOF	1.085
Largest difference peak / hole (e$^-$ / Å^3)	0.526 /-0.766

[a] $R_{int} = \Sigma \mid Fo^2 - Fo^2\ (mean) \mid / \Sigma[Fo^2]$; [b] $R1 = \Sigma \mid\mid F_O\mid - \mid F_C\mid\mid / \Sigma\mid F_O\mid$; $wR2 = \{[\Sigma[w(F_O^2-F_C^2)^2] / [\Sigma w(F_O)^2)^2]\}^{1/2}$; $w = 1 / [\sigma^2(Fo^2) + (0.0342P)^2 + 10.2618P]$ where $P = (Fo^2 + 2Fc^2) / 3$

Table I.2: Atomic parameters for $Rb_3ClMn(VO_3)_4$.

Atom	Wycoff position	sof	x	y	z
Rb1	4*d*	0.5	0.4428(5)	0	0.7572(8)
Rb2	4*e*	1.0	0	0.19498(7)	0.7559(3)
Mn1	2*a*	1.0	0	0	0.1840(5)
V1	8*f*	1.0	0.3068(2)	0.15334(7)	0.2407(4)
Cl1	2*a*	1.0	0	0	0.649(1)
O1	8*f*	1.0	0.1743(9)	0.0883(4)	0.143(1)
O2	8*f*	1.0	0.313(1)	0.1550(5)	0.540(1)
O3	4*e*	1.0	1/2	0.1276(6)	0.127(2)
O4	4*c*	1.0	1/4	1/4	0.123(2)

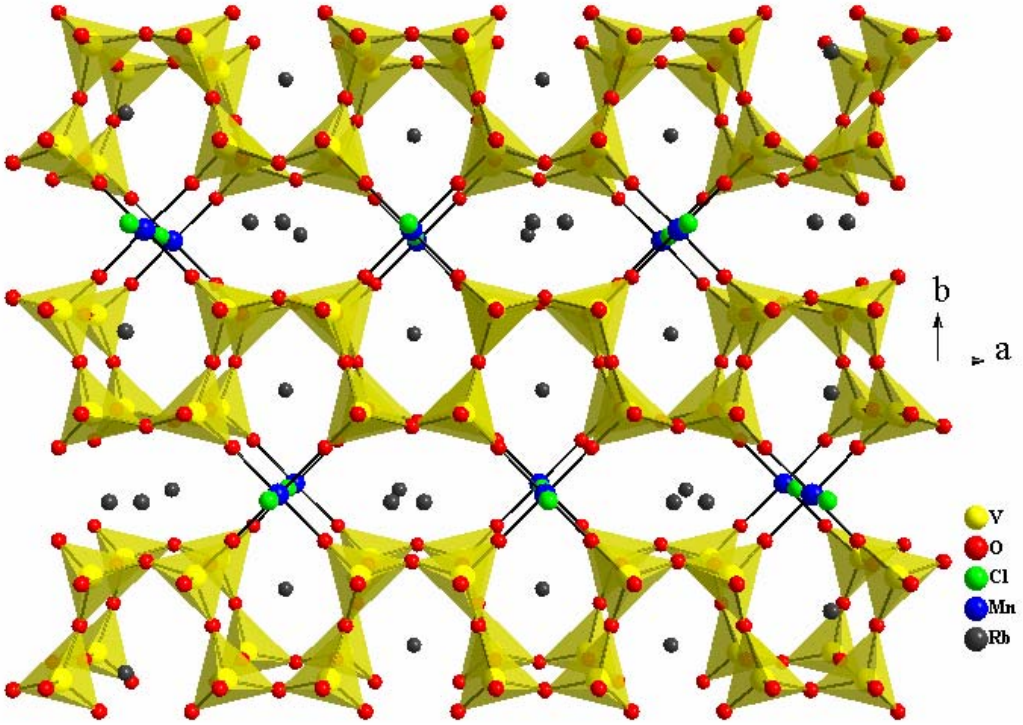

Figure I.1: Perspective view of $Rb_3ClMn(VO_3)_4$, **8**. Looking at the *ab* plane there are 5- and 6-membered ring windows containing the Rb^+ cations.

Compound **8** has a layered-type structure, shown in Figure I.2 (left). Due to the long distances between the layers, which stack along the *c* axis, it is expected that the interaction between them is weak. The Mn-Mn distance between two metal-oxide sheets, is 5.375(4) Å. The Rb^+ cations are found to occupy the space between the metal-oxide layers. Looking at the *ab* plane, Figure I.1, 5- and 6-membered ring windows can be seen. These consist of four VO_4 and one MnO_4Cl_2 units and four VO_4 and two MnO_4Cl_2 units respectively. Structure type **III** incorporates unique metavanadate chains, extending along the crystallographic *a* direction, that are further linked along *b via* MnO_4Cl_2 polyhedra which share 4 equatorial oxygen with 2 parallel $[(VO_3)^{1-}{}_\infty]$ chains. The chain allows the retention of the polar axis and the crystallization of a polar compound. Like **1-3** and **9,** compound **8** crystallizes in one of ten polar crystal classes, *mm*2 (C_{2v}).[4]

$Rb_3ClMn(VO_3)_4$, like **1-7** and **9**, also has an incorporated acentric chlorine-centered secondary building unit (SBU) with the formula $ClMn_2Rb_4$. This chlorine-centered SBU, shown in Figure I.2 (right), is the result of long and short Mn-Cl bonds. The off-center chlorine causes the 4 equatorial Rb^+ cations to shift down in the direction of the longer Mn-Cl bond resulting in an average bond angle equal to 80.56°. The average Rb-Cl distance is 3.84Å which is longer than what is expected for RbCl salt, 3.4Å.

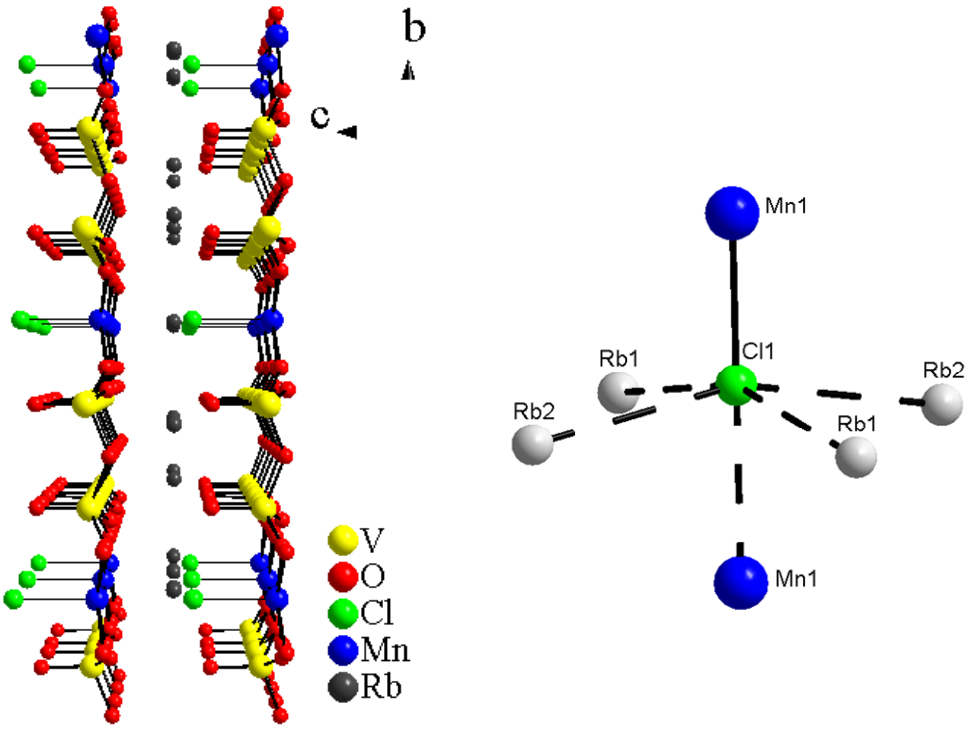

Figure I.2: Perspective view of the *bc* plane of $Rb_3ClMn(VO_3)_4$ showing layers separated by Rb cations (left). The image on the right shows the Cl-centred acentric unit. The Cl is off-center in the distorted octahedral coordination of 2Mn+4Rb found in $Rb_3ClMn(VO_3)_4$

$Ba_3M(V_2O_7)_2$ (M = Mn, Co): pseudo-one-dimensional compounds containing edge-shared $[M_2O_{10}]^{16-}$ antiferromagnetic dimers

Quantum spin systems, such as spin-Peierls, spin-dimers, and geometrically frustrated ladder compounds, have drawn considerable attention due to their theoretical and experimental importance.[5] These solids, mostly composed of transition-metal oxides and halides, are known as magnetic insulators due to the discrete nature of the magnetic nanostructures found within these otherwise extended frameworks. Despite their simplified low-dimensional structural features, including clusters, chains, and layers, these compounds show effects of strong electronic correlations and magnetism induced by the interplay between spin, charge, and orbital degrees of freedom. It has been realized that compounds of this type are model systems that may provide insight into electronic mechanisms that give rise to complex physical phenomena, such as high-temperature superconductivity. Some recent findings, demonstrating exotic magnetic behaviors relevant to quantum spin relaxation, bring new excitement to this rapidly growing field of technological significance.[6]

Two new mixed TM-oxide compounds, $Ba_3M(V_2O_7)_2$, where M = Mn, **1**, or Co, **2** were synthesized using high-temperature molten salt methods. Single crystals of **1** were first grown using a 1:1:2:4 mol ratio of BaO, MnO, V_2O_5, and BaF_2 in an attempt to synthesize an analog of a previously discovered compound, $Ba_5Mn(VO_3)_4Cl_8$. The reaction mixture was heated to 800°C at 1°C min^{-1}, held there for two days, slowly cooled to 450°C at 0.1°C min^{-1} to enhance crystal growth, and then furnace cooled to room temperature. The reaction yielded red column-like crystals of $Ba_3Mn(V_2O_7)_2$ in an

approximate yield of 20%. Among the other reaction products was a black crystalline phase, whose composition consists of Ba, Mn, V, O, and F, determined through energy dispersive X-ray analysis. The identity of this phase still remains unknown due to poor crystal quality. A stoichiometric yield of **1** and 2 were attempted. BaO, MO (where M = Mn and Co), and V_2O_5 were loaded into reaction vessels in a 3:1:2 mol ratio (with an overall weight of ca. 0.9 g). The reactions were heated to 600°C, held there for two days, and furnace cooled to room temperature. The powder patterns obtained from the high yield synthesis of **1** and **2** are shown in Figure I.3. Single crystals of **2** were grown using the stoichiometric reaction. It was heated to 800°C, held there for four days, slowly cooled at 0.1°C to 450°C, and then furnace cooled to room temperature. The refined cell parameters obtained from the powder pattern of these two analogs along with those from the single crystal of **1** and **2**, are listed in Table I.3.

Compound **1** and **2** crystallize in a monoclinic space group, *P2/n* (No. 14, $Z = 4$). The crystallographic data and atomic parameters are shown in Table I.4-I.5. Compounds **1** and **2** adopt an interesting pseudo-one-dimensional framework containing metal vanadate chains. Since **1** and **2** are isostructural, the structure of **1** will be discussed from this point forward. The parallel chains, isolated by surrounding Ba^{2+} cations (see Figure I.4), extend infinitely along the crystallographic *a* axis, Figure I.5. The $[MnV_4O_{14}]^{6-}{}_\infty$ chains contain $[Mn_2O_{10}]$ dimers interconnected by $[V_2O_7]^{4-}$ pyrovanadate anionic units. Each $[Mn_2O_{10}]$ dimer is made of two MnO_6 octahedral units where each of the oxygen octahedra is centered by crystallographically related Mn^{2+} ions. The MnO_6 octahedra, though distorted judging from the broad distribution of Mn-O distances ranging from

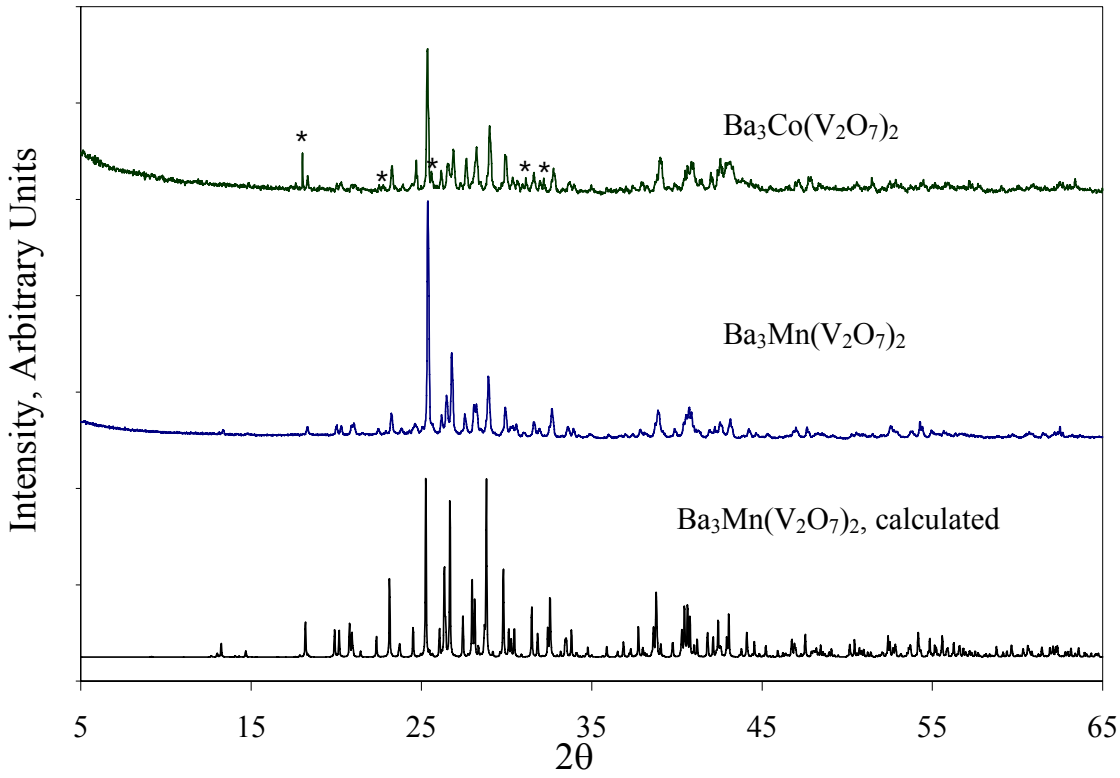

Figure I.3: PXRD patterns showing the products of the stoichiometric synthesis of $Ba_3M(V_2O_7)_2$, where M = Mn and Co. Obvious impurity peaks are marked with asterisks. The calculated PXRD pattern of **1** is included for comparison.

Table I.3: Refined unit cell parameters of the stoichiometric synthesis of$Ba_3M(V_2O_7)_2$where M = Mn or Co

Compound	$Ba_3Mn(V_2O_7)_2$ single crystal	$Ba_3Mn(V_2O_7)_2$ powder	$Ba_3Co(V_2O_7)_2$ powder	$Ba_3Co(V_2O_7)_2$ powder
a, Å	7.182(1)	7.182(6)	7.156(1)	7.175(2)
b, Å	13.975(3)	13.975(1)	13.900(3)	13.912(4)
c, Å	13.616(3)	13.620(1)	13.531(3)	13.550(4)
β, deg	101.15(3)	101.157(5)	101.15(3)	101.23(1)
V, $Å^3$	1340.8(5)	1341.2(3)	1320.6(5)	1326.7(9)

Table I.4 Crystallographic data of $Ba_3M(V_2O_7)_2$ where M = Mn or Co

empirical formula[a]	$Ba_3Mn(V_2O_7)_2$	$Ba_3Co(V_2O_7)_2$
color/shape	red, column	red, column
crystal size (mm)	0.10 × 0.03 × 0.03	0.05 × 0.02 × 0.02
formula weight (amu)	899.47	898.71
space group, *Z*	$P2_1/n$ (no.14), 4	$P2_1/n$ (no.14), 4
T°C	25	
a, Å	7.182(1)	7.156(1)
b, Å	13.975(3)	13.900(3)
c, Å	13.616(3)	13.531(3)
β, °	101.15(3)	101.15(3)
V, Å^3	1340.8(5)	1320.6(5)
linear abs. coeff., mm^{-1}	12.302	12.786
F_{000}	1597	1596
d_{calc}, g / cm^{-3}	4.456	4.520
data/restraints/parameters	2375 / 0 / 200	2076 / 0 / 199
secondary extinction	0.0012(1)	---------
reflections collected / unique / R_{int}[a]	2375 / 2003 / 0.0732	4067 / 2076 / 0.0509
final R1/wR2[b] [$I > 2\ \sigma(I)$]	0.0386/0.0727	0.0457 / 0.1070
R1/wR2 (all data)	0.0558/0.0778	0.0562 / 0.1181
GOF	1.058	1.085
Largest difference peak / hole (e$^-$ / Å^3)	1.008/-1.009	1.839 / -1.595

[a] $R_{int} = \Sigma \mid F_O^2 - F_O^2\ (mean) \mid / \Sigma[F_O^2]$; **1**; [b] $wR2 = \{[\Sigma[w(F_O^2-F_C^2)^2] / [\Sigma w(F_O)^2)^2]\}^{1/2}$; $w = 1 / [\sigma^2(F_O^2) + (0.0357P)^2 + 3.0262P]$ where $P = (F_O^2 + 2F_C^2)/3$; **2**; [b] $wR2 = \{[\Sigma[w(F_O^2-F_C^2)^2] / [\Sigma w(F_O)^2)^2]\}^{1/2}$; $w = 1 / [\sigma^2(F_O^2) + (0.0576P)^2 + 0.0000P]$ where $P = (F_O^2 + 2F_C^2)/3$;

Table I.5: Atomic parameters of $Ba_3M(V_2O_7)_2$ where M = Mn or Co

Atom	Wyckoff notation	sof	x	y	z
			$Ba_3Mn(V_2O_7)_2$		
Ba1	4e	1.0	0.1722(1)	0.9450(1)	0.2813(1)
Ba2	4e	1.0	-0.2622(1)	0.7283(1)	0.2948(1)
Ba3	4e	1.0	0.2406(1)	1.1079(1)	0.0148(1)
Mn	4e	1.0	0.3834(2)	1.0997(1)	0.5066(1)
V1	4e	1.0	0.6620(2)	0.9720(1)	0.2578(1)
V2	4e	1.0	0.2452(2)	0.6882(1)	0.2336(1)
V3	4e	1.0	0.1566(2)	0.8890(1)	0.5497(1)
V4	4e	1.0	0.2482(2)	0.8319(1)	0.0506(1)
O1	4e	1.0	0.2238(9)	0.7780(5)	0.5772(5)
O2	4e	1.0	0.5617(9)	0.9009(4)	0.3371(5)
O3	4e	1.0	0.0940(9)	0.7538(4)	-0.0162(5)
O4	4e	1.0	0.4105(9)	0.6242(4)	0.3098(5)
O5	4e	1.0	0.7951(9)	0.9005(4)	0.1986(5)
O6	4e	1.0	0.3138(9)	0.9451(4)	0.4845(5)
O7	4e	1.0	0.1080(9)	0.7443(5)	0.3040(5)
O8	4e	1.0	0.3593(9)	0.7783(5)	0.1712(5)
O9	4e	1.0	0.1327(9)	0.6093(4)	0.1478(5)
O10	4e	1.0	0.3950(9)	0.8671(5)	-0.0223(5)
O11	4e	1.0	0.8309(9)	1.0569(5)	0.3265(5)
O12	4e	1.0	0.4907(10)	1.0246(5)	0.1775(6)
O13	4e	1.0	-0.0663(10)	0.8893(5)	0.4819(6)
O14	4e	1.0	0.1210(9)	0.9268(4)	0.0771(5)

Table I.5: Atomic parameters of $Ba_3Mn(V_2O_7)_2$ and $Ba_3Co(V_2O_7)_2$ cont…

Atom	Wyckoff notation	sof	x	y	z
			$Ba_3Co(V_2O_7)_2$		
Ba1	4*e*	1.0	0.1712(1)	0.44362(5)	0.78348(5)
Ba2	4*e*	1.0	0.2441(1)	0.60551(5)	0.51462(6)
Ba3	4*e*	1.0	-0.26339(9)	0.22984(5)	0.79668(6)
Co	4*e*	1.0	0.3854(2)	0.5972(1)	1.0067(1)
V1	4*e*	1.0	0.2464(3)	0.1869(1)	0.7325(2)
V2	4*e*	1.0	0.3393(3)	0.5269(2)	1.2396(2)
V3	4*e*	1.0	0.2465(3)	0.3299(1)	0.5513(2)
V4	4*e*	1.0	0.1592(3)	0.3886(2)	1.0494(2)
O1	4*e*	1.0	-0.334(1)	0.0597(6)	0.6742(7)
O2	4*e*	1.0	0.322(1)	0.4458(6)	0.9864(7)
O3	4*e*	1.0	-0.119(1)	0.5769(6)	0.4218(7)
O4	4*e*	1.0	0.365(1)	0.2787(6)	0.6727(6)
O5	4*e*	1.0	-0.211(1)	0.3997(6)	0.6986(7)
O6	4*e*	1.0	0.411(1)	0.1240(6)	0.8106(6)
O7	4*e*	1.0	0.435(1)	0.5975(6)	1.1598(7)
O8	4*e*	1.0	0.402(1)	0.7509(6)	1.0158(6)
O9	4*e*	1.0	0.140(1)	0.1086(6)	0.6442(7)
O10	4*e*	1.0	0.105(1)	0.2435(7)	0.8022(8)
O11	4*e*	1.0	0.277(1)	0.7772(6)	0.4250(7)
O12	4*e*	1.0	0.612(1)	0.6313(7)	0.5239(7)
O13	4*e*	1.0	0.516(1)	0.4767(7)	1.3211(7)
O14	4*e*	1.0	-0.066(1)	0.3896(7)	0.9799(7)

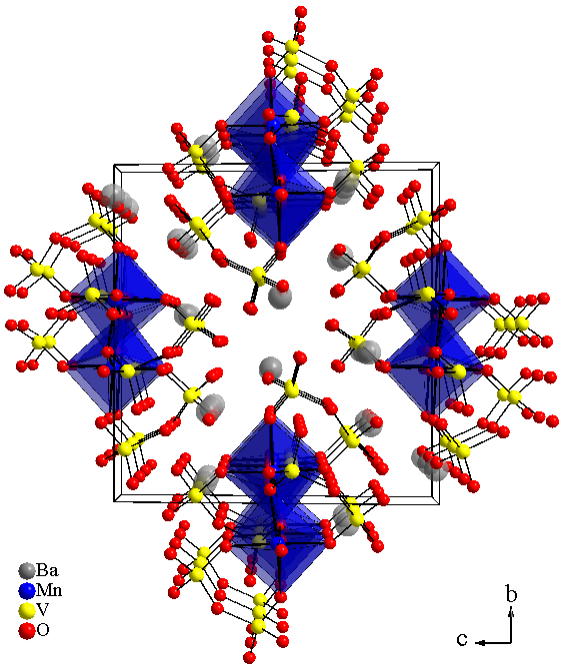

Figure I.4: Perspective view of the $Ba_3Mn(V_2O_7)_2$ structure showing the covalent $[MnV_4O_{14}]_\infty^{6-}$ chains isolated *via* surrounding Ba^{2+} cations.

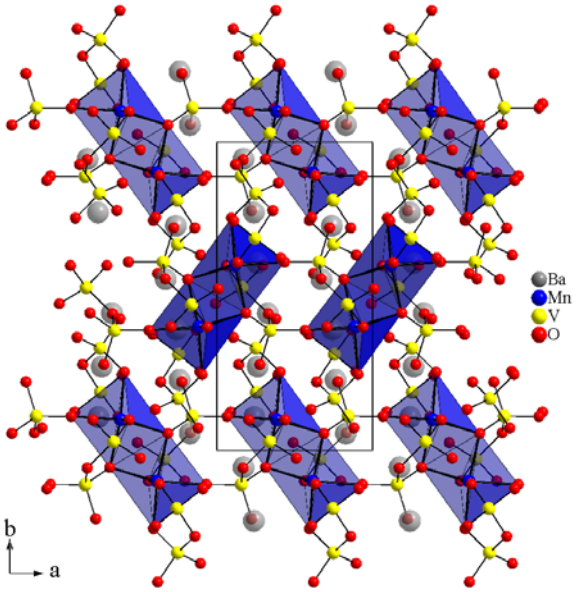

Figure I.5: Projected view along *c* showing the packing arrangement of parallel manganese vanadate chains. $[Mn_2O_{10}]$ dimers are shaded in blue. The color codes are the same throughout the structure presentations

2.088(7)-2.318(7) Å, are comparable to the sum of the Shannon crystal radii for 6-coordinate Mn^{2+} (0.97 Å) and 2-coordinate O^{2-} (1.21 Å), 2.18 Å.[4] The oxidation state of Mn is further supported through bond valence sum calculations[3] giving a calculated oxidation state of 2.10.

Each $[Mn_2O_{10}]^{16-}$ dimer consists of two Mn^{2+} ions that are doubly bridged by two oxygen ions, creating a bridging angle ∠Mn-O(6)-Mn of 94.2(2)° and a relatively long Mn···Mn distance of 3.275(3)Å across the shared edge, O(6)·· O(6), of the fused octahedra. The latter is in part attributed to the large distortion of MnO_6 octahedra. The Mn-O(6) distances are rather long, 2.225(6) Å and 2.243(6) Å, which is most likely because the valence electrons of O(6) are shared additionally with a V^{5+} cation, forming a μ_3 bridging coordination. The longest Mn-O(13) distance, 2.318(7) Å, is corresponding to one of the vertex oxygen atoms of the $[V(3)O_4]$ unit through which the dimers are linked (Figure I.6).

There are four crystallographically distinct V^{5+} sites found within the manganese chain. The oxidation state of the vanadium cations is further supported through bond valence sum calculations[3]. BVS calculations for the V cations gave values of 5.05 for V(1), 5.09 for V(2), 5.17 for V(3), and 5.10 for V(4). All of the V-O bond distances are consistent with what is expected from the sum of the Shannon crystal radii for 4 coordinate V^{5+} and 2 coordinate O^{2-}, 1.71 Å[4]. All four crystallographically distinct V cations are found in $[V_2O_7]$ units which encapsulate and link the Mn_2O_{10} dimers. The V share several terminal oxygen atoms, including O(2,3,6,9), with the Mn^{2+} cations. O(1,4,5,7,10,12,14) point into the space between the chains surrounding the

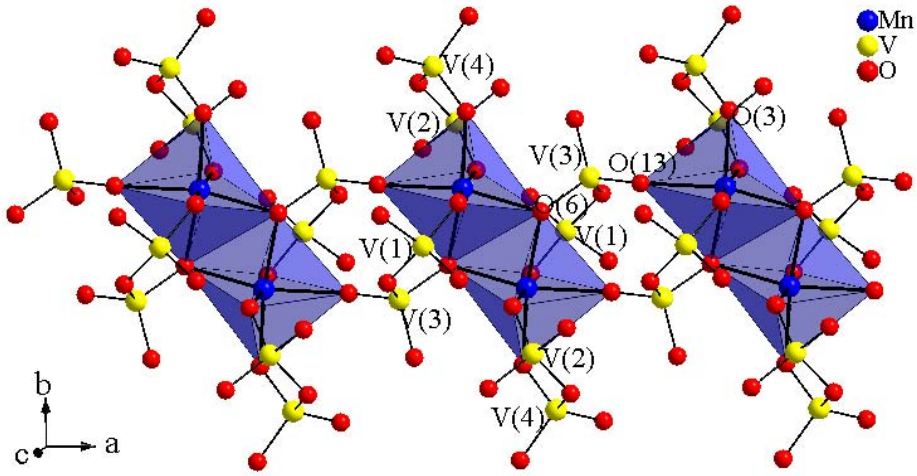

Figure I.6: Partial structure of a single $[MnV_4O_{14}]_\infty$ chain extending infinitely along the crystallographic *a* direction. The chain contains Mn_2O_{11} dimers made of edge-sharing MnO_6 octahedra. The manganese oxide dimers are isolated by two sets of crystallographically independent $[V_2O_7]$ pyrovandates but interlinked by one, $V(1,3)_2O_7$ resulting in a relatively short O(6)···O(13) distance of 2.83(1) Å, see text.

electropositive Ba^{2+} ions. V(1)/V(3) and V(2)/V(4) pairs, share bridging oxygen, O(11) and O(8), respectively, to give rise to two distinct $(V_2O_7)^{4-}$ pyrovanadate units. In addition, V(3) also shares a corner oxygen, O(13), with a neighboring Mn dimer allowing infinite propagation of the M-O-V chain while maintaining the complete isolation of Mn_2O_{10} magnetic dimers.

It is known that magnetic exchange between two adjacent magnetic ions can vary from antiferromagnetic to ferromagnetic through single atom bridging angles near 90°. This is attributed to the resulting pair of degenerate orbitals from the magnetic orbitals of the two metal centers.[7] It should be noted that although larger bridging angles favor antiferromagnetic exchange, a reduction of electron density on the bridging anions reduces the strength of antiferromagnetic coupling.

The temperature-dependence of magnetic susceptibility, Figure I.7, of **1** reveals an antiferromagnetic behavior at high temperatures. The linear portion of the inverse susceptibility data, χ^{-1}, was fit using Curie-Weiss law, $\chi = C/(T-\theta)$, where C is the Curie constant, T is temperature, and θ is the Weiss constant. For **1**, the fit (in the range of T = 50-300°C) indicates an effective magnetic moment (μ_{eff}) of 5.92(2) μ_B (see Table I.6), which expectedly is comparable to 5.91, the spin-only magnetic moment for a high spin Mn^{2+} (d^5) ion. The Weiss temperature, θ, was determined to be -19.2(7) K indicating antiferromagnetic coupling between neighboring Mn^{2+} cations. This negative value is consistent with the crystal structure solution shown above which has revealed a dimer with a bridging angle of ∠ Mn-O(6)-Mn = 94.2(2)°. Also, the closest O···O distance, such as the one found between O(6)···O(13) in $V(3)O_4$, is 2.83(1) Å. Inter-dimer

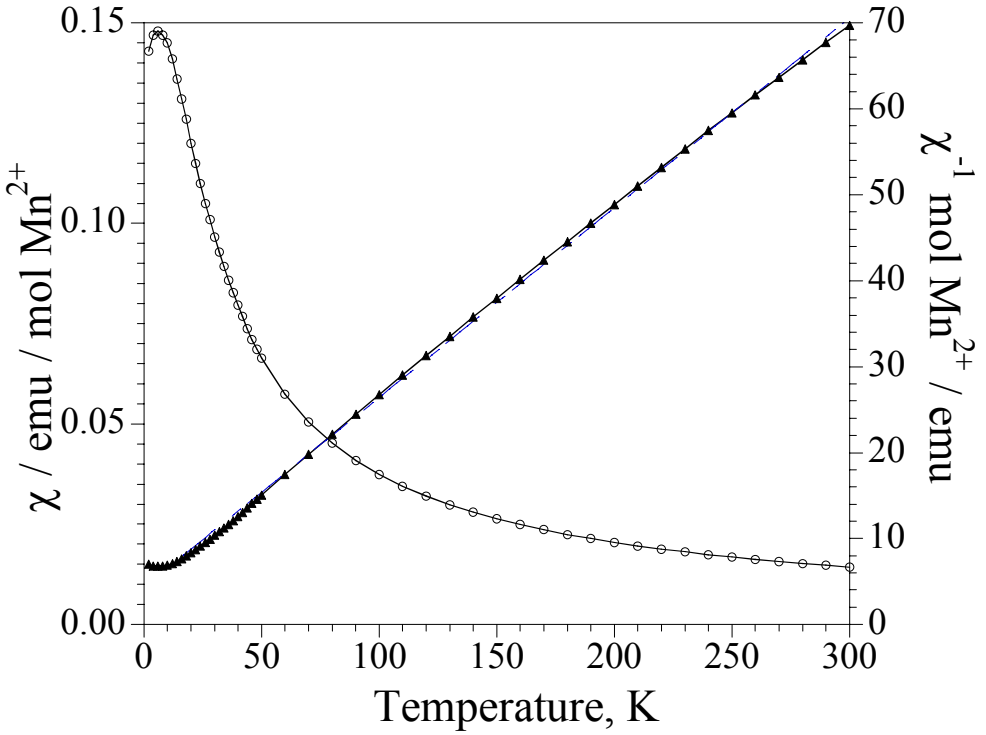

Figure I.7: Molar magnetic susceptibility, χ (○), and inverse molar magnetic susceptibility, χ^{-1} (▲), collected in an applied field of 0.5T. The data was obtained from a ground sample of selected single crystals of $Ba_3Mn(V_2O_7)_2$ (**1**).

Table I.6: Curie-Weiss fitting parameters obtained from $Ba_3M(V_2O_7)_2$ where M = Mn or Co

Compound Model	*T* range (K)	*C* (emuK/mol)	μ_{eff} (μ_B)	μ_{calc} (μ_B)	θ (K)
$Ba_3Mn(V_2O_7)_2$	50-300	4.44(3)	5.92(2)	5.91[a]	-19.2(7)
$Ba_3Co(V_2O_7)_2$	40-300	3.43(6)	5.24(4)	5.20[b]	-20(1)

[a] Spin-only value.

[b] Value includes orbital contribution; $\mu = [4S(S+1) + L(L+1)]^{½}$, where $S = 3/2$, $L = 3$. The spin-only value is calculated as 3.87.

spin interactions are thus expected to be much weaker as the pathways for spin coupling would be obtained through super-superexchange created by $(VO_4)^{3-}$ polyanions that bridge neighboring dimers. At low temperature, below T_N = 6 K,however, the susceptibility decreases rather quickly indicating the possible occurrence of long-range anitferromagnetic ordering.

The χ and χ^{-1}, obtained from the Co^{2+} derivative (Figure I.8), were also fit using the same models. The linear portion of the χ^{-1}, temperatures ranging from 40-300K, was fit using the Curie-Weiss model giving rise to the calculated θ and μ_{eff} equal to -20(1) K and 5.24(4)μ_B, respectively (see Table I.6). The negative θ values indicates antiferromagnetic coupling between nearest neighbors, as observed for the Mn derivative. Even though the $\mu_{eff,}$ calculated using the Curie-Weiss model to be 5.24(4) μ_B, is higher than the expected spin-only magnetic moment of 3.89μ_B, it is consistent with what is expected, $\approx$ 5.20$\mu_{B,}$ when taking the orbital contribution into account. This has been frequently observed for other high spin Co^{2+} systems where orbital contributions of the ligand field play a significant role.[8] Last, but not least, an increase in the χT vs. T data of **2** can be seen at temperatures below 20K followed by a decrease at 6 K (Figure I.8, inset). The increase could signify some ferromagnetic interaction. It is thought that this low temperature anomaly could be the result of some impurity, as the data was collected on a polycrystalline sample obtained from a stoichiometric synthesis. The powder pattern, shown in Figure I.3, reveals some impurity peaks that are marked with asterisks.

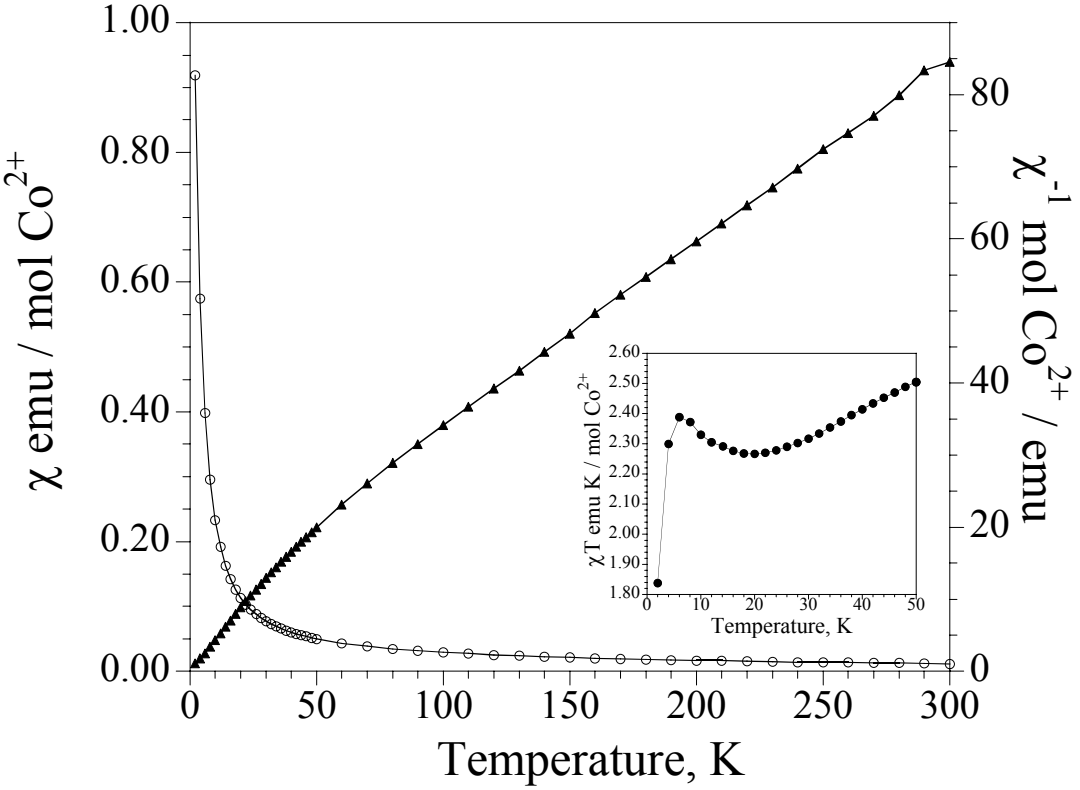

Figure I.8: Molar magnetic susceptibility, χ (○), and inverse molar magnetic susceptibility, χ^{-1} (▲), collected in an applied field of 0.5T. The data was obtained from a ground sample of selected single crystals of $Ba_3Co(V_2O_7)_2$ (**2**). The inset shows the χT data.

$Ba_5Cl_4Co_3(V_2O_7)_3$: a material containing structurally confined $Co_3(\mu_3\text{-}Cl)$ equilateral triangles

$Ba_5Cl_4Co_3(V_2O_7)_3$ was synthesized using high-temperature molten salt methods. Single crystals of this mixed-metal oxide were grown using BaO, KO_2, Co_3O_4, V_2O_5, and $BaCl_2$ mixed in a 4:3:1:6:9 mol ratio. The reaction was heated to 800°C at 2°C/minute, held there for three days, slowly cooled to 450°C at 0.1C/minute, and then furnace cooled to room temperature. Dark green crystals of $Ba_5Cl_4Co_3(V_2O_7)_3$ were isolated after washing the reaction with deionized water to remove the salt. It should be noted that a Cu-containing derivative of this same material was synthesized using CuO and V_2O_5 in a 1:1 mol ratio. The reactants were ground in a $BaCl_2$/NaCl eutectic flux equal to three times the mass of the oxides. The crystallographic data is not reported here because the crystal structure solution is not good. However the Cu-containing derivative crystallizes in a trigonal crystal system, space group *R*32 (no. 155), with a = 9.731(1) Å, c = 22.150(4) Å, and V = 1816.3(5) $Å^3$. This unit cell can be compared to the crystallographic data of the Co^{2+} derivative shown in Table I.7. Also the atomic parameters for the Co^{2+} compound are shown in Table I.8.

The structure of $Ba_5Cl_4Co_3(V_2O_7)_3$ is shown in Figure I.9. There is a single crystallographically distinct Co^{2+} cation found in a square pyramidal geometry. Bond valence sum calculations[3] further support the 2+ oxidation state. The Co-O distances are 2.013(8)Å and 2.022(8)Å for two Co-O(1) and two Co-O(2) bonds respectively. The Co^{2+} cation has a single apical Cl^- anion with a bond distance of 2.317(3)Å. The chlorine serves as a μ_3 bridge between three neighboring Co^{2+} atoms giving rise to equilateral

Table I.7: Crystallographic data of $Ba_5Cl_4Co_3(V_2O_7)_3$

empirical formula	$Ba_5Cl_4Co_3(V_2O_7)_3$
color/shape	Dark green chunks
crystal size (mm)	0.08 × 0.05 × 0.02
formula weight (amu)	1646.93
space group, *Z*	*R*32 (no. 155), 3
T°C	25
a, Å	9.722(1)
c, Å	22.284(4)
V, Å^3	1824.1(5)
linear abs. coeff., mm^{-1}	12.643
F_{000}	2205
flack parameter	0.04(9)
d_{calc}, g / cm^{-3}	4.498
data/restraints/parameters	733 / 0 / 62
secondary extinction	-------
reflections collected / unique / R_{int} [a]	5200 / 733 / 0.0612
final R1/wR2 [b] [$I > 2\ \sigma(I)$]	0.0465 / 0.0961
R1/wR2 (all data)	0.0556 / 0.0997
GOF	1.204
Largest difference peak / hole (e$^-$ / Å^3)	1.274 / -0.944

[a] $R_{int} = \Sigma \mid F_o^2 - F_o^2\ (\text{mean}) \mid / \Sigma[F_o^2]$; **1**; [b] $wR2 = \{[\Sigma[w(F_o^2 - F_c^2)^2] / [\Sigma w(F_o)^2)^2]\}^{1/2}$; $w = 1 / [\sigma^2(F_O^2) + (0.0411P)^2 + 36.4367P]$ where $P = (F_O^2 + 2F_C^2)/3$

Table I.8: Atomic parameters of $Ba_5Cl_4Co_3(V_2O_7)_3$

Atom	Wyckoff notation	sof	x	y	z
Ba1	9*e*	1.0	-1/3	-0.3319(1)	-1/6
Ba2	6*c*	1.0	-2/3	-1/3	-0.00124(5)
Co	9*d*	1.0	-0.2383(3)	-0.2383(3)	0
V	18*f*	1.0	-0.3345(3)	0.0004(3)	-0.0864(1)
Cl1	6*c*	1.0	0	0	-0.1774(3)
Cl2	3*b*	1.0	-1/3	-2/3	-1/6
Cl3	3*a*	1.0	0	0	0
O1	18*f*	1.0	-0.3439(9)	-0.168(1)	-0.0607(3)
O2	18*f*	1.0	-0.173(1)	0.169(1)	-0.0623(3)
O3	18*f*	1.0	-0.494(1)	0.0018(9)	-0.0623(3)
O4	9*e*	1.0	-1/3	0.001(2)	-1/6

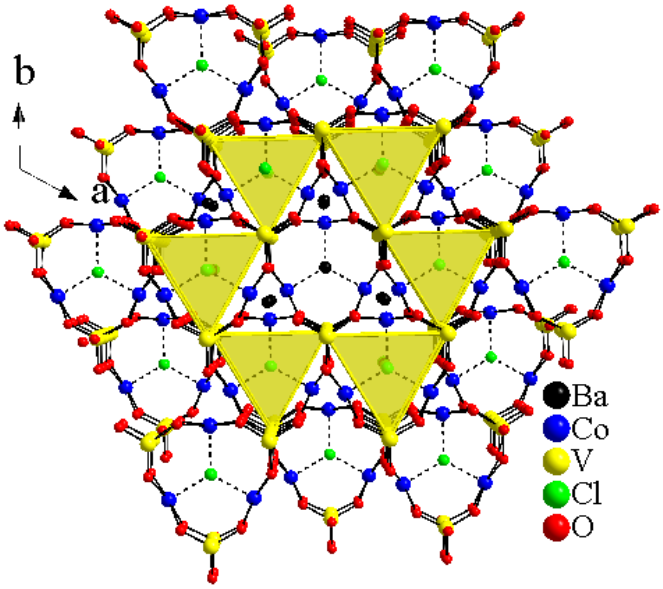

Figure I.9: Perspective view of $Ba_5Cl_4Co_3(V_2O_7)_3$. The material consists of structurally confined equilateral triangular units (highlighted in yellow). Looking along *c* a three-fold axis can be seen as three of the six highlighted triangles are coplanar.

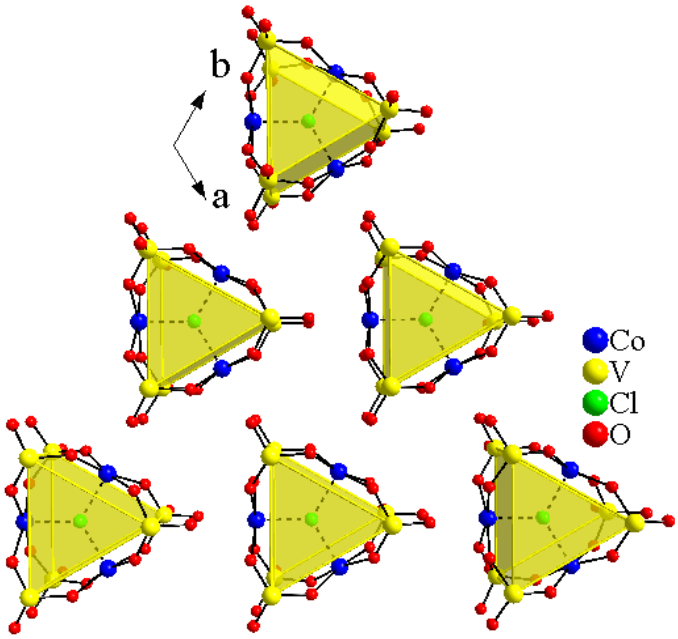

Figure I.10: Perspective view of $Ba_5Cl_4Co_3(V_2O_7)_3$ along *c* showing a single slab of coplanar $Co_3\mu_3$-Cl units. From this view it is seen that there is no direct covalent linkage between coplanar equilateral triangular units (highlighted in yellow).

triangular units (highlighted in yellow in Figure I.9) similarly observed in the compound family presented in Chapter 4. Figure I.10 shows a single slab of coplanar $Co_3\mu_3$-Cl units along the crystallographic *c* axis. From this view it is seen that there is no direct covalent linkage between coplanar equilateral triangular units (highlighted in yellow). Looking along the *a* direction, Figure I.11, it can be seen that the $Co_3\mu_3$-Cl coplanar slabs are structurally confined by VO_4^{3-} anions which bridge the slabs along *c* creating an ABC type stacking arrangement.

The temperature-dependence of the molar magnetic susceptibility and inverse molar magnetic susceptibility of the title compound is shown in Figure I.12. The linear portion of the inverse susceptibility data, χ^{-1}, ranging from 130-300 K, was fit using Curie-Weiss law. From the fit an effective magnetic moment of 6.12 μ_B and a Weiss constant of -159(1) K was obtained. The negative Weiss constant indicates antiferromagnetic coupling between nearest neighbors. The effective magnetic moment is much higher than the expected spin-only magnetic moment equal to 3.89 μ_B, which is a usual occurrence for Co^{2+} as this ion has an unquenched orbital contribution.[8] This material however exhibits a magnetic moment even higher than what is expected when taking the orbital contribution into account, 5.20 μ_B, and the reason for this unusually large value is still undetermined. The magnetic susceptibility shows a steady increase until approximately 75 K where it then begins to gradually decrease. It was thought that this could be the result of long range antiferromagnetic ordering. However, based on the fact that this material exhibits equilateral triangular units it is expected that tranditional antiparallel arrangement of moments would be supressed due to the magnetic frustration.

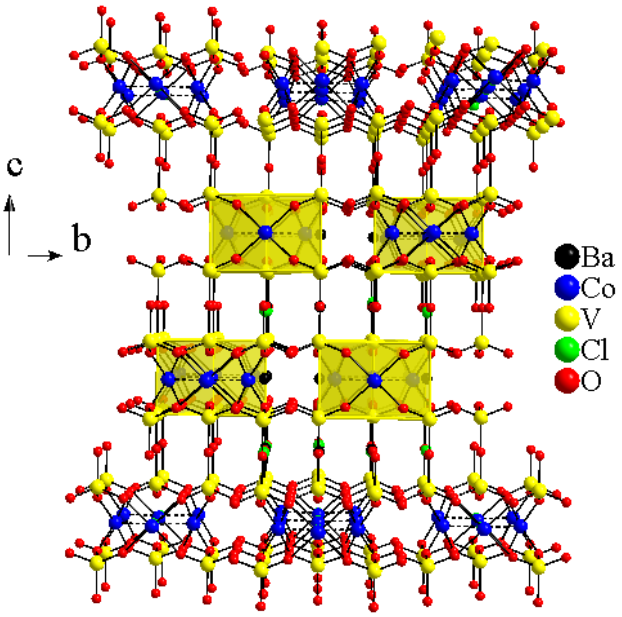

Figure I.11: Perspective view of $Ba_5Cl_4Co_3(V_2O_7)_3$ along *a*. From this view it is seen that the highlighted equilateral triangular units, are structurally confined by VO_4^{3-} polyhedra. The coplanar Co3μ_3-Cl slabs are stacked in an ABC type arrangement along the *c* axis.

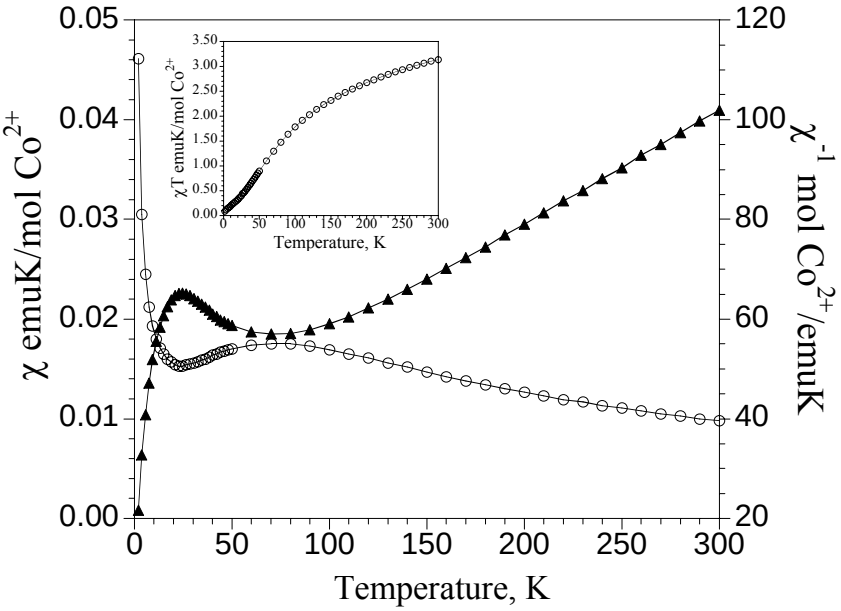

Figure I.12: Molar magnetic susceptibility, χ (○), and inverse molar magnetic susceptibility, χ^{-1} (▲), collected in an applied field of 0.01T. The data was obtained from a ground sample of selected single crystals of $Ba_5Cl_4Co_3(V_2O_7)_3$. The inset shows the χT data.

It is know that magnetic frustration can induce structural transitions to release the frustration. Further experimentation would need to be performed in order to determine whether this is the case in $Ba_5Cl_4Co_3(V_2O_7)_3$. Upon further decrease in temperature there is a sudden upturn in the susceptibility. This tail could be the result of some paramagnetic impurity that becomes much more relevant at low-temperatures.

$BaClM(V_2O_7)$ where M=Mn or Fe: a new channeled framework

The title compounds were synthesized using high temperature molten salt methods. The crystallographic data and atomic parameters can be seen in Table I.9 and I. 10. The Mn analog was synthesized using KO_2, MnO_2, V_2O_5, and $BaCl_2$ in a 1:1:2:3 mol ratio. The reaction was heated to 800°C at 2°C/min, held there for two days, slowly cooled to 450°C at 0.1°C/minute, and then furnace cooled to room temperature. The Fe analog was synthesized using BaO, FeO, V_2O_5, and $BaCl_2$ in a 1:1:2:4. The reactants were heated to 800°C at 2°C/minute, held there for 4 days, slowly cooled to 450°C at 0.1°C/minute, and then furnace cooled to room temperature.

Since the title compounds are isostructure, the structure of $BaClM(V_2O_7)$ will be discussed from this point forward. There is a single crystallographically distinct Mn^{3+} site. Bond valence sum calculations[3] further support the 3+ oxidation state. The Mn is found in a square pyramidal coordination. The extended structure of $BaClMn(V_2O_7)$ can be seen in Figure I.13. The VO_4 and MnO_5 polyhedra form a 3-D channeled structure. The channels, which propagate along the *b* axis, consist of 10-membered ring windows

Table I.9: Crystallographic data of $BaClMV_2O_7$, M = Mn or Fe.

empirical formula	$BaClMnV_2O_7$	$BaClFeV_2O_7$
color/shape	Red column	Red column
crystal size (mm)	0.1× 0.03 × 0.03	0.13× 0.04 × 0.04
formula weight (amu)	441.61	442.52
space group, *Z*	*Pnma* (no. 62),4	*Pnma* (no. 62),4
T°C	25	
a, Å	14.398(3)	14.562(3)
b, Å	5.468(1)	5.517(1)
c, Å	9.592(2)	9.422(2)
V, Å^3	755.1(3)	756.9(3)
linear abs. coeff., mm^{-1}	9.523	9.748
F_{000}	800	804
d_{calc}, g / cm^{-3}	3.885	3.883
data/restraints/parameters	757 / 0 / 67	753 / 0 / 67
secondary extinction	--------	--------
reflections collected / unique / R_{int}[a]	6097 / 757 / 0.0888	5643 / 753 / 0.0803
final R1/wR2[b] [$I > 2\ \sigma(I)$]	0.0533 / 0.0893	0.0585 / 0.1005
R1/wR2 (all data)	0.0637 / 0.0922	0.0670 / 0.1038
GOF	1.247	1.226
Largest difference peak / hole (e$^-$ / Å^3)	1.019 / -1.308	1.611 / -1.377

[a] $R_{int} = \Sigma \mid F_O^2 - F_o^2\ (\text{mean}) \mid / \Sigma[F_O^2]$; **1**; [b] wR2 = $\{[\Sigma[w(F_O^2-F_C^2)^2] / [\Sigma w(F_O)^2)^2]\}^{1/2}$; $w = 1 / [\sigma^2(F_O^2) + (0.0296P)^2 + 8.1984P]$ where $P = (F_O^2 + 2F_C^2)/3$; **2**; wR2 = $\{[\Sigma[w(F_O^2-F_C^2)^2] / [\Sigma w(F_O)^2)^2]\}^{1/2}$; $w = 1 / [\sigma^2(F_O^2) + (0.0261P)^2 + 20.4341]$ where $P = (F_O^2 + 2F_C^2)/3$

Table I.10: Atomic parameters of $BaClM(V_2O_7)$, M = Mn or Fe

Atom	Wyckoff notation	sof	x	y	z
			$BaClMn(V_2O_7)$		
Ba1	4*c*	1.0	0.08880(6)	1/4	0.81234(9)
Mn1	4*c*	1.0	0.3343(1)	1/4	0.7333(2)
V1	4*c*	1.0	-0.0430(2)	-1/4	0.6359(2)
V2	4*c*	1.0	0.2034(2)	-1/4	0.6126(2)
Cl1	4*c*	1.0	0.0938(3)	-1/4	0.9825(4)
O1	4*c*	1.0	0.0827(6)	-1/4	0.643(1)
O4	8*d*	1.0	0.2446(4)	0.006(1)	0.6941(6)
O2	8*d*	1.0	-0.0768(4)	0.009(1)	0.7232(6)
O5	4*c*	1.0	0.2326(6)	-1/4	0.4482(9)
O3	4*c*	1.0	-0.0814(7)	-1/4	0.4781(9)
			$BaClFe(V_2O_7)$		
Ba	4*c*	1.0	0.40692(6)	1/4	0.3057(1)
Fe	4*c*	1.0	0.1632(2)	1/4	0.2281(2)
V1	4*c*	1.0	0.2984(2)	-1/4	0.0969(3)
V2	4*c*	1.0	0.5398(2)	-1/4	0.1393(3)
Cl1	4*c*	1.0	0.4035(3)	-1/4	0.4839(4)
O1	8*d*	1.0	0.2537(5)	0.000(1)	0.1743(8)
O2	8*d*	1.0	0.5715(5)	0.004(1)	0.2287(8)
O3	4*c*	1.0	0.4164(7)	-1/4	0.141(1)
O5	4*c*	1.0	0.2759(7)	-1/4	-0.079(1)
O4	4*c*	1.0	0.5817(8)	-1/4	-0.022(1)

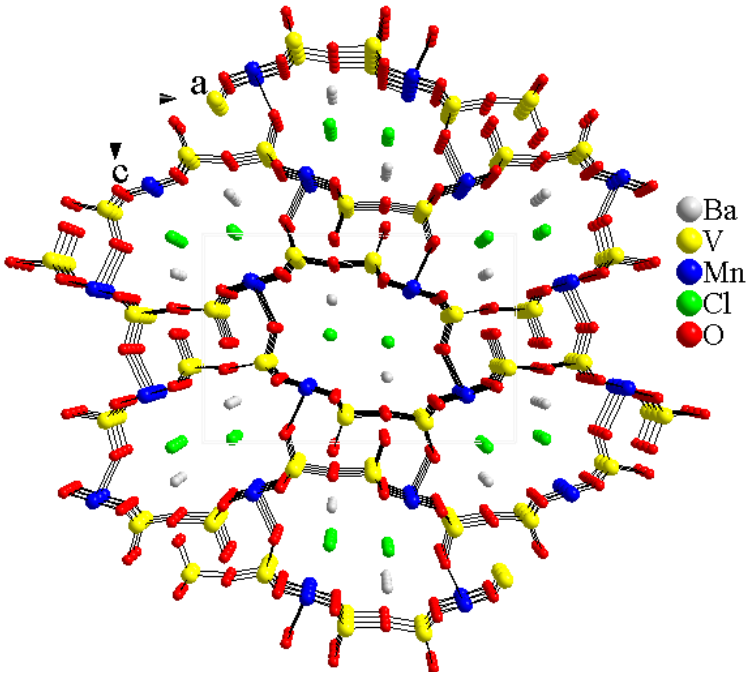

Figure I.13: Projected view showing the channeled structure of $BaClMnV_2O_7$.

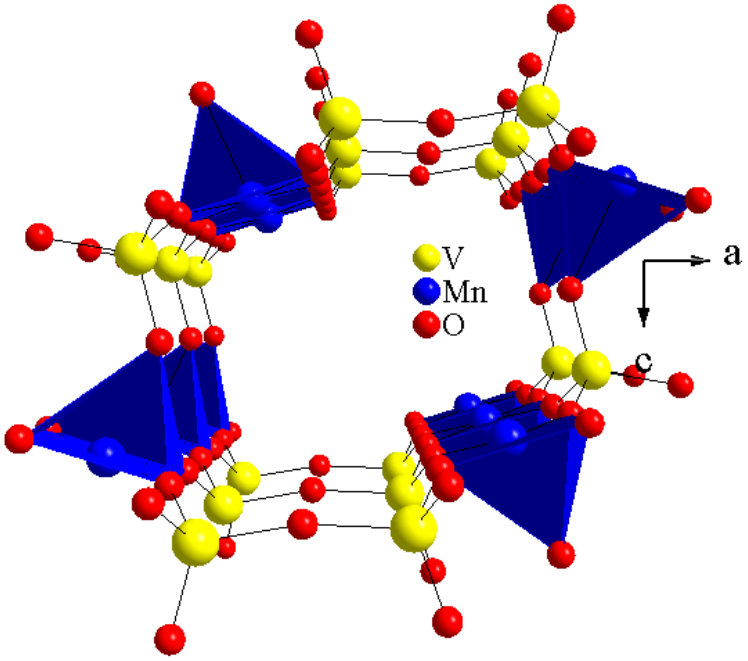

Figure I.14: Projected view showing a close-up view of the large channel that extends along the crystallographic *b* axis.

made of six VO_4 tetrahedra and four MnO_5 square pyramids, Figure I.14. and contain both Ba^{2+} and Cl^- ions.

$Ba_7Cl_4M(V_2O_7)_3$ M = Mn, Co, or Cu,

The title compounds were synthesized using high temperature molten salt methods. The crystallographic data and atomic parameters can be seen in Table I.10 and I. 11. The Mn analog was synthesized using KO_2, MnO_2, V_2O_5, and $BaCl_2$ in a 1:1:2:3 mol ratio. The reaction was heated to 800°C at 2°C/min, held there for two days, slowly cooled to 450°C at 0.1°C/minute, and then furnace cooled to room temperature. The Co derivative was synthesized using Co_3O_4 and V_2O_5 in a 2:1 mol ratio. The reactants were placed in a $BaCl_2$/KCl eutectic flux equal to three times the mass of the oxide reactants. The reaction was heated to 200°C at 2°C/minute, held there for 6 hours, heated to 760°C at a rate of 2°C/minute, held there for 3 days, slowly cooled to 500°C at 0.1°C/minute, and then furnace cooled to room temperature. The Cu derivative was synthesized using CuO and V_2O_5 in a 3:1 mol ratio. These metal oxide reactants were placed in a $BaCl_2$/NaCl eutectic flux equal to three times the mass of the oxides. The reaction was then heated to 800°C at 2°C/minute, held ther for three days, slowly cooled ot 450°C at 0.1°C/minute, and then furnace cooled to room temperature.

The title compounds are isostructural, so $Ba_7Cl_4Co(V_2O_7)_3$ will be discussed from this point forward. The structure is shown in Figure I.15, top. The Co is found in a 2+ oxidation state that is further supported by bond valence sum calculations[3], and an octahedral geometry with four equatorial Co-O(4) bonds equal to 2.096(4) Å and two

Table I.11: Crystallographic data of $Ba_7Cl_4M(V_2O_7)_3$, M = Mn, Co, Cu.

empirical formula	$Ba_7Cl_4Mn(V_2O_7)_3$[1]	$Ba_7Cl_4Co(V_2O_7)_3$[2]	$Ba_7Cl_4Cu(V_2O_7)_3$[3]
color/shape	Light orange chunk	Light green chunk	Light orange chunk
crystal size (mm)	0.22 × 0.17 × 0.15	0.20 × 0.14 × 0.10	0.22 × 0.16 × 0.13
formula weight (amu)	1799.76	1803.75	1808.36
space group, *Z*	*Cmcm* (no. 63), 4	*Cmcm* (no. 63), 4	*Cmcm* (no. 63), 4
T°C		25	
a, Å	16.808(3)	16.716(3)	16.587(3)
b, Å	10.554(2)	10.567(2)	10.616(2)
c, Å	14.837(3)	14.802(3)	14.818(3)
V, Å^3	2631.9(9)	2614.6(9)	2609.2(9)
linear abs. coeff., mm^{-1}	13.247	13.486	13.694
F_{000}	3164	3172	3180
d_{calc}, g / cm^{-3}	4.542	4.582	4.603
data/restraints/parameters	1261 / 0 / 104	1268 / 0 / 104	1259 / 0 / 103
secondary extinction	0.00035(4)	0.00022(2)	---------
reflections collected / unique / R_{int}[a]	11142 / 1261 / 0.0627	10976 / 1268 / 0.0595	10476 / 1259 / 0.0652
final R1/wR2[b] [$I > 2\,\sigma(I)$]	0.0313 / 0.0727	0.0290 / 0.0614	0.0294 / 0.0694
R1/wR2 (all data)	0.0337 / 0.0739	0.0330 / 0.0628	0.0337 / 0.0722
GOF	1.232	1.225	1.085
Largest difference peak / hole (e$^-$ / Å^3)	1.634 / -1.367	1.215 / -0.927	2.517 /-1.533

[a] $R_{int} = \Sigma \mid F_o^2 - F_o^2\,(\text{mean}) \mid / \Sigma[F_o^2]$; [b] **1**; $wR2 = \{[\Sigma[w(F_o^2-F_c^2)^2] / [\Sigma w(F_o)^2)^2]\}^{1/2}$; $w = 1 / [\sigma^2(F_o^2) + (0.0367P)^2 + 22.0002P]$ where $P = (F_o^2 + 2F_c^2)/3$; **2**; $wR2 = \{[\Sigma[w(F_o^2-F_c^2)^2] / [\Sigma w(F_o)^2)^2]\}^{1/2}$; $w = 1 / [\sigma^2(F_o^2) + (0.0306P)^2 + 6.9957P]$ where $P = (F_o^2 + 2F_c^2)/3$; **3**; $wR2 = \{[\Sigma[w(F_o^2-F_c^2)^2] / [\Sigma w(F_o)^2)^2]\}^{1/2}$; $w = 1 / [\sigma^2(F_o^2) + (0.0400P)^2 + 0.0000P]$ where $P = (F_o^2 + 2F_c^2)/3$;

Table I.12: Atomic parameters of $Ba_7Cl_4M(V_2O_7)_3$, M = Mn, Co, Cu.

Atom	Wyckoff notation	sof	x	y	z
			$Ba_7Cl_4Mn(V_2O_7)_3$		
Ba1	8*g*	1.0	0.14928(3)	0.19571(5)	1/4
Ba2	16*h*	1.0	0.14686(2)	0.18911(3)	0.53995(3)
Ba3	4*c*	1.0	0	0.36683(7)	3/4
Mn1	4*b*	1.0	0	1/2	1/2
V1	8*f*	1.0	0	-0.0073(1)	0.36278(9)
V2	16*h*	1.0	0.17292(6)	0.49638(9)	0.63189(7)
Cl1	8*g*	1.0	0.1658(2)	0.1753(3)	3/4
Cl2	8*f*	1.0	0	0.6842(2)	0.6168(2)
O1	16*h*	1.0	0.0906(2)	0.4221(4)	0.5875(3)
O2	16*h*	1.0	0.1933(3)	0.6387(4)	0.5868(3)
O3	8*g*	1.0	0.1493(3)	0.5220(6)	3/4
O4	16*h*	1.0	0.0848(3)	0.0457(5)	0.4089(3)
O5	16*h*	1.0	0.2491(3)	0.3985(5)	0.6155(3)
O6	8*f*	1.0	0	-0.1673(6)	0.3742(4)
O7	4*c*	1.0	0	0.0564(9)	1/4
			$Ba_7Cl_4Co(V_2O_7)_3$		
Ba1	8*g*	1.0	0.15043(3)	0.19542(5)	1/4
Ba2	16*h*	1.0	0.14587(2)	0.19091(3)	0.53949(3)
Ba3	4*c*	1.0	1/2	0.13315(6)	1/4
Co	4*b*	1.0	0	1/2	1/2
V1	8*f*	1.0	0	-0.0072(1)	0.36231(9)
V2	16*h*	1.0	0.17126(6)	0.49745(8)	0.63143(7)
Cl1	8*g*	1.0	0.1654(1)	0.1746(2)	3/4
Cl2	8*f*	1.0	0	0.3155(2)	0.3890(2)
O1	16*h*	1.0	0.0884(2)	0.4263(4)	0.5856(3)
O2	16*h*	1.0	0.0851(2)	0.0458(4)	0.4088(3)
O3	16*h*	1.0	0.2473(3)	0.3980(4)	0.6155(3)
O4	16*h*	1.0	0.1934(3)	0.6398(4)	0.5879(3)
O5	8*g*	1.0	0.1468(3)	0.5208(5)	3/4
O6	8*f*	1.0	0	-0.1667(5)	0.3728(4)
O7	4*c*	1.0	0	0.0590(7)	1/4

Table I.12: Atomic parameters of $Ba_7Cl_4M(V_2O_7)_3$, M = Mn, Co, Cu cont…

Atom	Wyckoff notation	sof	x	y	z
			$Ba_7Cl_4Cu(V_2O_7)_3$		
Ba1	8*g*	1.0	0.14952(3)	0.19353(5)	1/4
Ba2	16*h*	1.0	0.14520(2)	0.19234(3)	0.53835(2)
Ba3	4*c*	1.0	0	0.36679(7)	3/4
Cu	4*b*	1.0	0	1/2	1/2
V1	8*f*	1.0	0	-0.0098(1)	0.36304(9)
V2	16*h*	1.0	0.16956(6)	0.49891(8)	0.63074(7)
Cl1	8*g*	1.0	0.1651(1)	0.1785(2)	3/4
Cl2	8*f*	1.0	0	0.6931(2)	0.6212(2)
O1	16*h*	1.0	0.0857(2)	0.4306(4)	0.5825(3)
O2	16*h*	1.0	0.1938(3)	0.6406(4)	0.5897(3)
O3	8*g*	1.0	0.1459(4)	0.5172(6)	3/4
O4	16*h*	1.0	0.0857(3)	0.0431(4)	0.4088(3)
O5	16*h*	1.0	0.2455(3)	0.3989(4)	0.6136(3)
O6	8*f*	1.0	0	-0.1697(6)	0.3746(4)
O7	4*c*	1.0	0	0.0516(8)	1/4

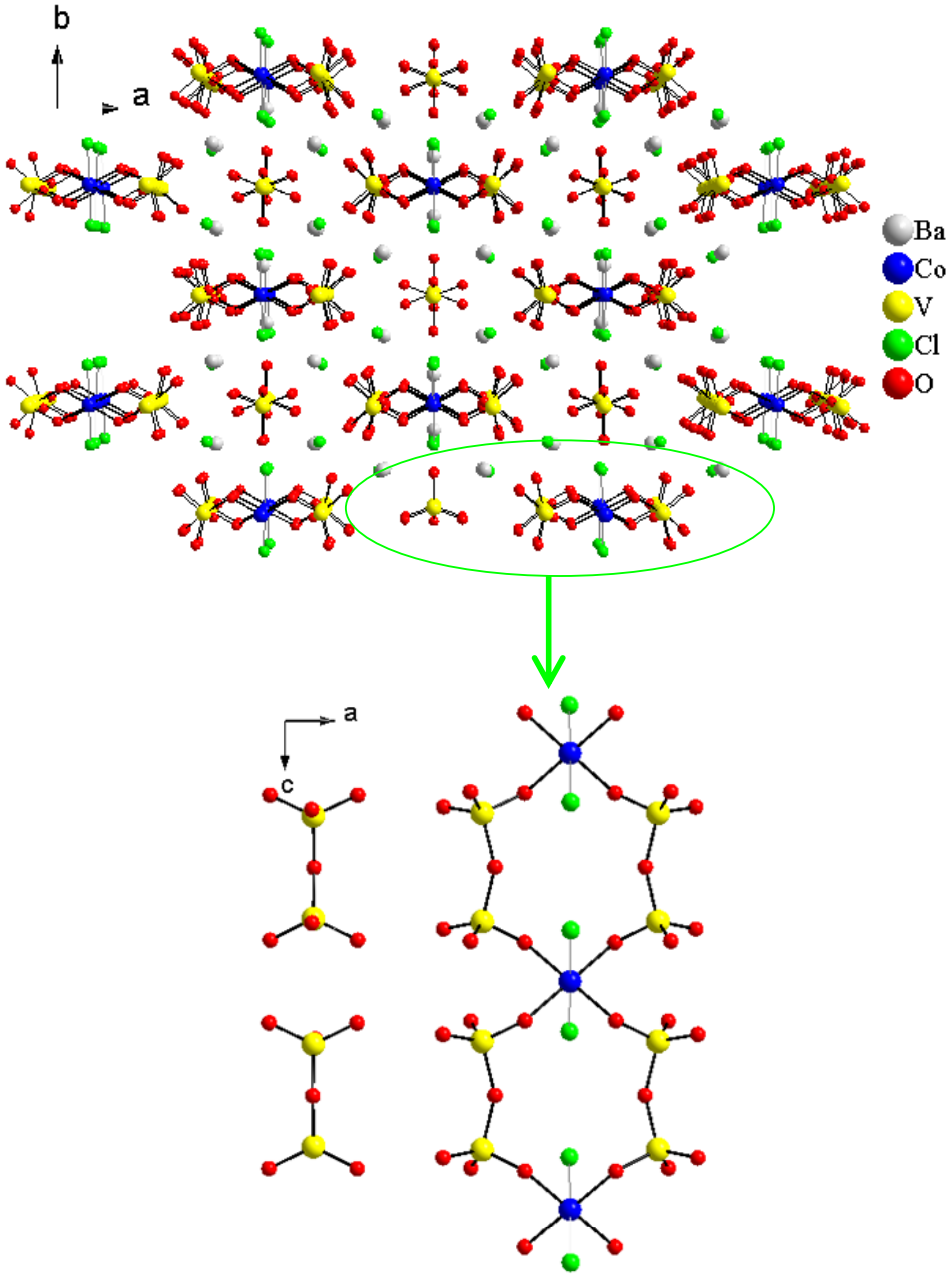

Figure I.15: Projected view showing the structure of $Ba_7Cl_4Co(V_2O_7)_3$ along the crystallographic *c* axis (top). The structure consists of 1-D $CoCl_2(V_2O_7)_2$ chains that extend infinitely along the *c* direction (bottom). The chains are surrounded by Ba, Na, and Cl ions There are also individual $(V_2O_7)^{4-}$ units found within the structure.

axial Co-Cl(2) bonds equal to 2.550(2) Å. The four equatorial O(4) atoms are shared between Co and V(2) forming 1-D $CoCl_2(V_2O_7)_2$ chains, Figure I.15 bottom. These chais are structurally isolated by one another *via* surrounding Ba^{2+}, Na^+, and Cl^- ions. Looking along the *a* direction, the chains have isolated $(V_2O_7)^{4-}$ units on both sides.

$Ba_5MCl_6M(V_2O_7)_2$ M = Mn or Co

These new mixed metal oxides were synthesized using high-temperature molten salt methods. The Mn derivative was made using BaO, MnO, V_2O_5, and $BaCl_2$ in a 1:1:2:4 mol ratio. The reactants were heated to 800°C at 1°C/minute, held there for two days, slowly cooled ot 450°C at 0.1°C/minute, and then furnace cooled to room temperature. For the Co derivative, CoO and V_2O_5 were mixed in a 1:1 mol ratio and then added to a $BaCl_2$/NaCl eutectic flux equal to three times the mass of the oxide reactants. The reaction was then heated to 800°C at 2°C/minute, held there for four days, slowly cooled at 0.1°C/minute to 450°C, and then furnace cooled to room temperature.

The crystallographic data and the atomic paramters for both derivatives can be seen in Tables I.13 and I.14. Because the materials are isostructural the Co derivative was chosen for discussion. Figure I.16 shows a projected view of the extended structure of $Ba_5CoCl_6Co(V_2O_7)_2$. This layered structure consists of 2-D $[Co(V_2O_7)_2]_\infty$ slabs that are structurally isolated from one another *via* interslab Ba^{2+} cations and 1-D $[CoCl_6]_\infty$ chains. Within the structure there are two crystallographically distince Co^{2+} sites, one of which is octahedrally coordinated by Cl^-, and the other which is octahedrally coordinated by O^{2-} ions. Within the $[Co(V_2O_7)_2]_\infty$ sheets, each Co(1)O6 octahedron is structurally

Table I.13: Crystallographic data of $Ba_5MCl_6M(V_2O_7)_2$ M = Mn or Co.

empirical formula	$Ba_5MnCl_6Mn(V_2O_7)_2$[1]	$Ba_5CoCl_6Co(V_2O_7)_2$[2]
color/shape	Red column	Red column
crystal size (mm)	0.04 x 0.04 x 0.02	0.13 x 0.05 x 0.05
formula weight (amu)	1437.04	1445.02
space group, *Z*	C2/*m* (no.12), 2	C2/*m* (no.12), 2
T°C	25	
a, Å	15.885(3)	15.764(3)
b, Å	5.714(1)	5.690(1)
c, Å	13.350(3)	13.236(3)
β,°	113.71(3)	
V, Å^3	1109.5(4)	1087.3(4)
linear abs. coeff., mm^{-1}	12.188	12.801
F_{000}	1272	1280
d_{calc}, g / cm^{-3}	4.302	4.414
data/restraints/parameters	1087 / 0 / 94	1055 / 0 / 94
secondary extinction	0.0077(2)	0.0022(1)
reflections collected / unique / R_{int}[a]	4627 / 1087 / 0.0274	4680 / 1055 / 0.0435
final R1/wR2[b] [$I > 2\ \sigma(I)$]	0.0204 / 0.0472	0.0241 / 0.0539
R1/wR2 (all data)	0.0191 / 0.0464	0.0301 / 0.0561
GOF	1.107	1.089
Largest difference peak / hole (e$^-$ / Å^3)	0.663 / -0.844	0.904 / -0.774

[a] $R_{int} = \Sigma \mid F_o^2 - F_o^2\ (\text{mean}) \mid / \Sigma[F_o^2]$; [b] **1**;$w$R2 = $\{[\Sigma[w(F_o^2-F_c^2)^2] / [\Sigma w(F_o)^2)^2]\}^{1/2}$; $w = 1 / [\sigma^2(F_o^2) + (0.0265P)^2 + 4.5451P]$ where $P = (F_o^2 + 2F_c^2)/3$; **2**; wR2 = $\{[\Sigma[w(F_o^2-F_c^2)^2] / [\Sigma w(F_o)^2)^2]\}^{1/2}$; $w = 1 / [\sigma^2(F_o^2) + (0.0337P)^2 + 0.0000P]$ where $P = (F_o^2 + 2F_c^2)/3$

Table I.14: Atomic parameters of $Ba_5MCl_6M(V_2O_7)_2$ M = Mn or Co.

Atom	Wyckoff notation	sof	x	y	z
			$Ba_5MnCl_6Mn(V_2O_7)_2$		
Ba1	4*i*	1.0	0.04518(2)	0	0.73626(3)
Ba2	2*b*	1.0	0	-1/2	1.00000
Ba3	4*i*	1.0	-0.22834(2)	0	0.72873(3)
Mn1	2*d*	1.0	-1/2	0	1/2
Mn2	4*e*	0.5	1/4	1/4	1.00000
V1	4*i*	1.0	-0.09900(6)	-1/2	0.70691(7)
V2	4*i*	1.0	0.15665(6)	0	0.54929(7)
Cl1	4*i*	1.0	0.13761(9)	-1/2	0.8547(1)
Cl2	4*i*	1.0	0.26369(9)	0	0.8511(1)
Cl3	4*i*	1.0	0.1128(1)	0	1.0016(1)
O1	4*i*	1.0	-0.0331(3)	-1/2	0.6350(3)
O2	4*i*	1.0	-0.2211(3)	-1/2	0.6237(3)
O3	8*j*	1.0	-0.0722(2)	-0.2667(5)	0.7903(2)
O4	8*j*	1.0	0.1114(2)	0.2387(5)	0.5866(2)
O5	4*i*	1.0	0.1314(3)	0	0.4162(3)
			$Ba_5CoCl_6Co(V_2O_7)_2$		
Ba1	4*i*	1.0	0.45348(3)	0	0.26340(4)
Ba2	4*i*	1.0	0.72898(3)	0	0.27110(4)
Ba3	2*a*	1.0	1/2	-1/2	0
Co1	2*c*	1.0	1.00000	0	1/2
Co2	4*e*	0.5	1/4	1/4	0
V1	4*i*	1.0	0.59854(8)	-1/2	0.2948(1)
V2	4*i*	1.0	0.34498(9)	0	0.45219(9)
Cl1	4*i*	1.0	0.2357(1)	0	0.1446(1)
Cl2	4*i*	1.0	0.3601(1)	-1/2	0.1416(1)
Cl3	4*i*	1.0	0.3844(1)	0	-0.0021(2)
O1	4*i*	1.0	0.5332(4)	-1/2	0.3691(4)
O2	8*j*	1.0	0.5719(3)	-0.2665(6)	0.2096(3)
O3	4*i*	1.0	0.7221(4)	-1/2	0.3754(4)
O4	8*j*	1.0	0.3915(3)	0.2400(6)	0.4159(3)
O5	4*i*	1.0	0.3678(4)	0	0.5856(4)

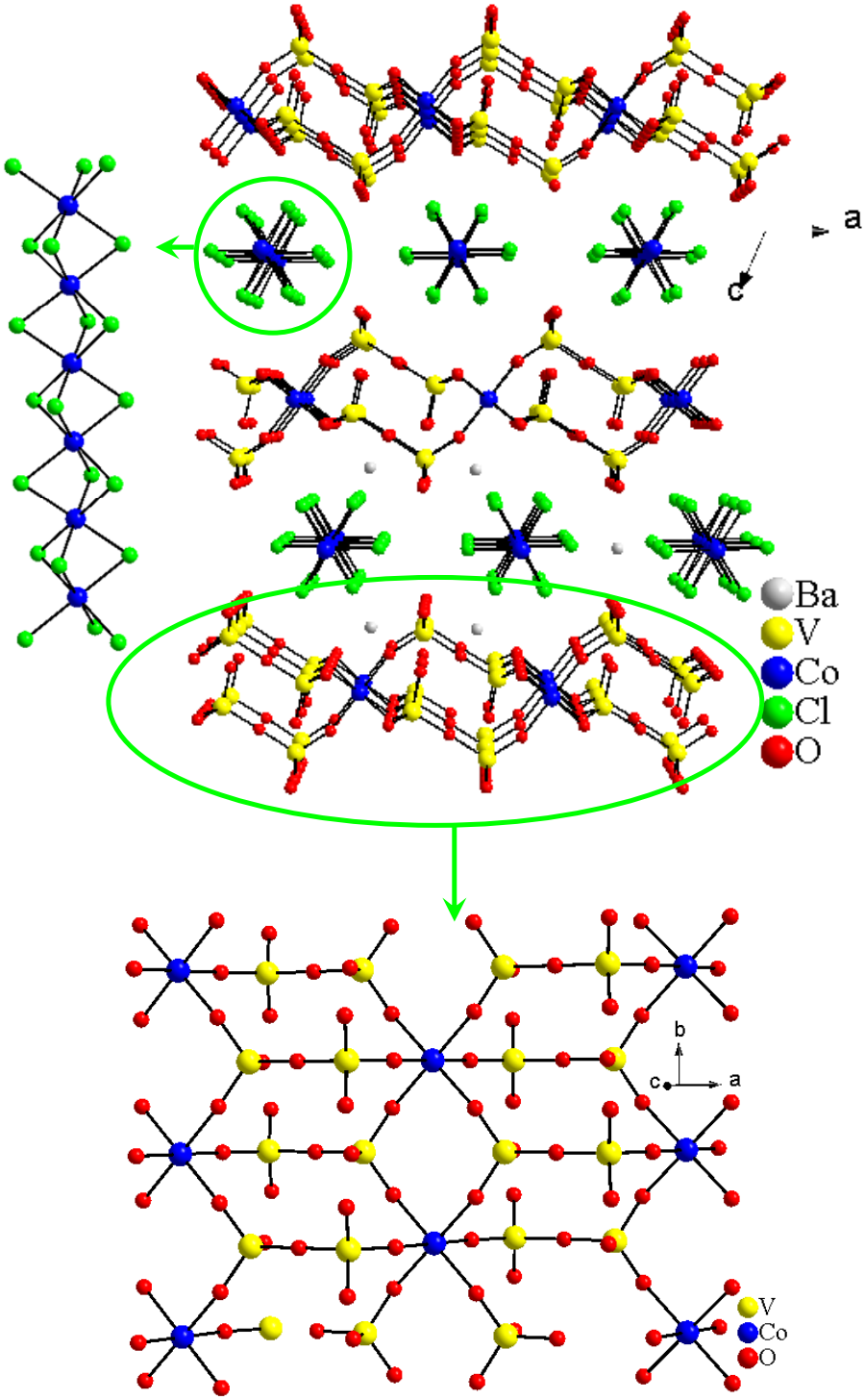

Figure I.16: Perspective view showing the extended structure of $Ba_5CoCl_6Co(V_2O_7)_2$ (top). The left image shows $[CoCl_6]_\infty$ chains and the bottom one shows $[Co(V_2O_7)_2]_\infty$ sheets.

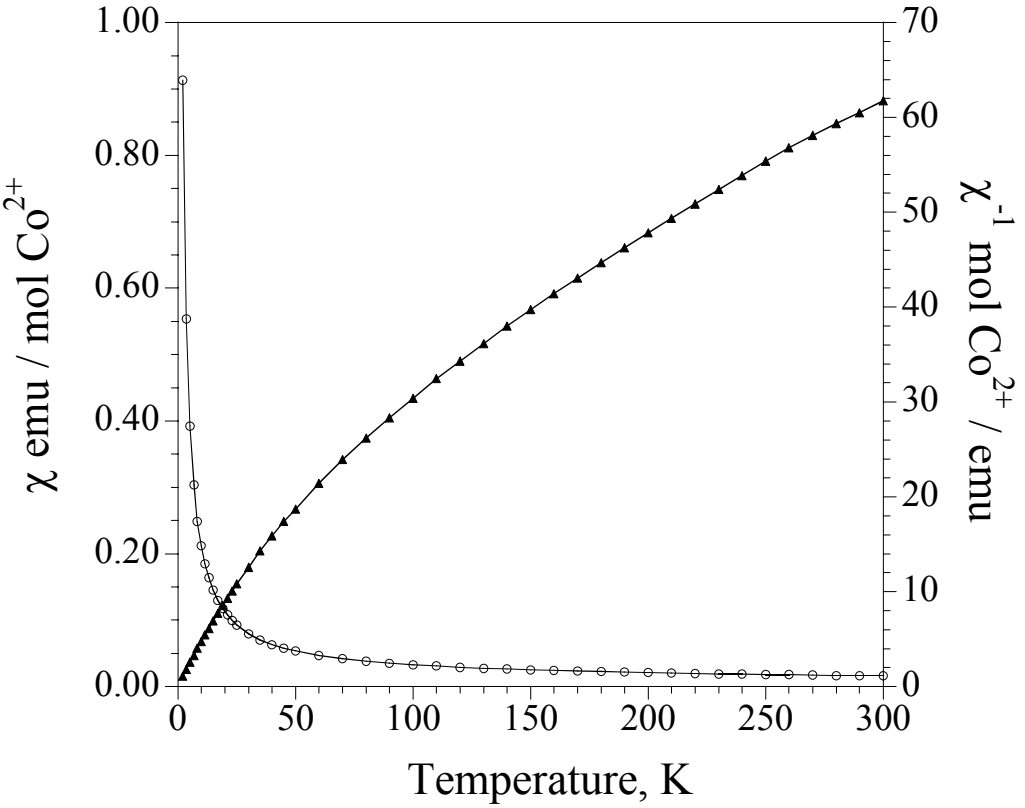

Figure I.17: Molar magnetic susceptibility, χ (○), and inverse molar magnetic susceptibility, χ^{-1} (▲), collected in an applied field of 0.5T. The data was obtained from a ground sample of selected single crystals of $Ba_5CoCl_6Co(V_2O_7)_2$.

confined by $(V_2O_7)^{4-}$ along the *a* direction and a single $(VO_4)^{3-}$ unit along *b*, as shown in Figure I.16 (bottom). Within the 1-D $[CoCl_6]_\infty$ chains, the Co(2) site is 50% occupied creating discontinuity along its propagation direction.

The temperature-dependence of the molar magnetic susceptibility, χ, and inverse molar magnetic susceptibility, χ^{-1}, of the title compound is shown in Figure I.17. The linear portion of the inverse susceptibility data, χ^{-1}, ranging from 180-300 K, was fit using Curie-Weiss law. From the fit an effective magnetic moment of 5.0(3) μ_B and a Weiss constant of -14(7) K was obtained. The negative Weiss constant indicates weak antiferromagnetic coupling between nearest neighbors. The effective magnetic moment is higher than the expected spin-only magnetic moment equal to 3.89 μ_B, which is a usual occurrence for Co^{2+} as this ion has an unquenched orbital contribution.[8] When taking the orbital contribution into account the magnetic moment is 5.20 μ_B.

$AXCu_5O_2(VO_4)_2$ A/X = Rb/Cl, Cs/Cl, and Cs/Br

These three new compound were synthesized using high-temperature molten salt methods. The RbCl derivative was synthesize using CuO and V_2O_5 in a 7:6 mol ratio. These reactants were placed in a RbCl/NaCl flux equal to three times the mass of the oxides. The reaction was heated to 700°C at 2°C/minute, held there for four days, slowly cooled to 450°C at 0.1°C/minute, and then furnace cooled to room temperature. For the CsCl and CsBr derivatives CuO, V_2O_5, and CsCl or CsBr were mixed in a 1:1:2 mol ratio. The reaction for $(CsCl)Cu_5O_2(VO_4)_2$ was heated to 600°C, held there for 24 hours, and then cooled to room temperature at 3°C/minute. For $(CsBr)Cu_5O_2(VO_4)_2$ the reaction

was heated to 650°C, held there for 5 days, slowly cooled to 450°C at 0.1°C/minute, and then furnace cooled to room temperature. Both of the aforementioned reactions were targeting $(CsX)_2Cu(VO_3)_2$ where X = Cl or Br. In fact in both reaction this was the major phase formed with $(CsX)Cu_5O_2(VO_4)_2$ being a minor phase (< 5%). A stoichiometric synthesis was attempted for $(ACl)Cu_5O_2(VO_4)_2$ where A = Rb or Cs. The reactions were heated to 700°C at 1°C/minute, held there for 2 days, slowly cooled to 450°C, and then furnace cooled to room temperature. The PXRD patterns from the stoichiometric synthesis, seen in Figures I.18 and I.19, appear to match the calculated powder patterns relatively well. The crystallographic data and atomic parameters for the title compounds can be seen in Tables I.15 and I.16.

The framework is similar to the Kagomé lattice discussed in Chapter 4, which has been found to be the structural orgin of many magnetically frustrated systems.[9] All three compounds, $(AX)Cu_5O_2(VO_4)_2$ where A/X = Rb/Cl, Cs/Cl, and Cs/Br, are similar; therefore the structure of the CsCl analog, unless otherwise stated, will be discused. The compounds contain Cu in a 2+ oxidation state which is further supported by bond valence sum calculations.[3] The extended structure of $(CsCl)Cu_5O_2(VO_4)_2$ can be seen in Figure I.20. The Cu^{2+} occupy two crystallographically disticnt sites. The first site, Cu(1), is found in a trigonal bipyramidal geometry while Cu(2) is square planar. Figure I.21 shows the connectivity between the Cu polyhedra. Each Cu(1) site shares three edges with neighboring Cu(2) polyhedra, giving rise to a μ_4 bridging O(2). Cu(2) shares two edges with neighboring Cu(1) polyhedra. Each Cu(1) also shares three corners with the (

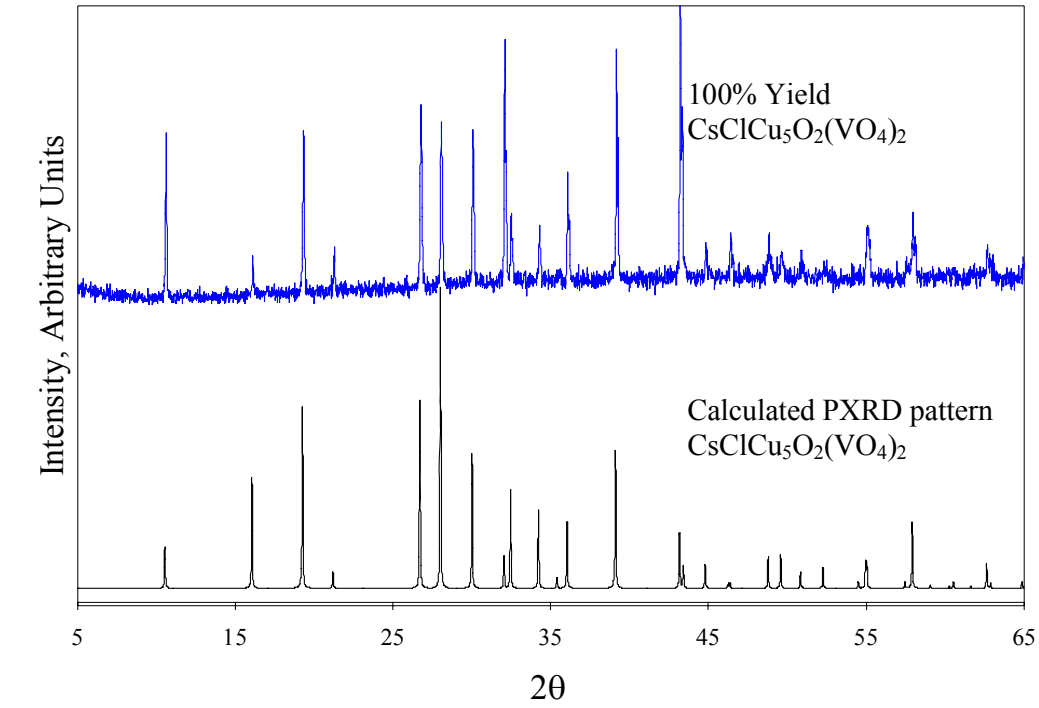

Figure I.18: PXRD pattern showing the stoichiometric synthesis of $CsClCu_5O_2(VO_4)_2$.

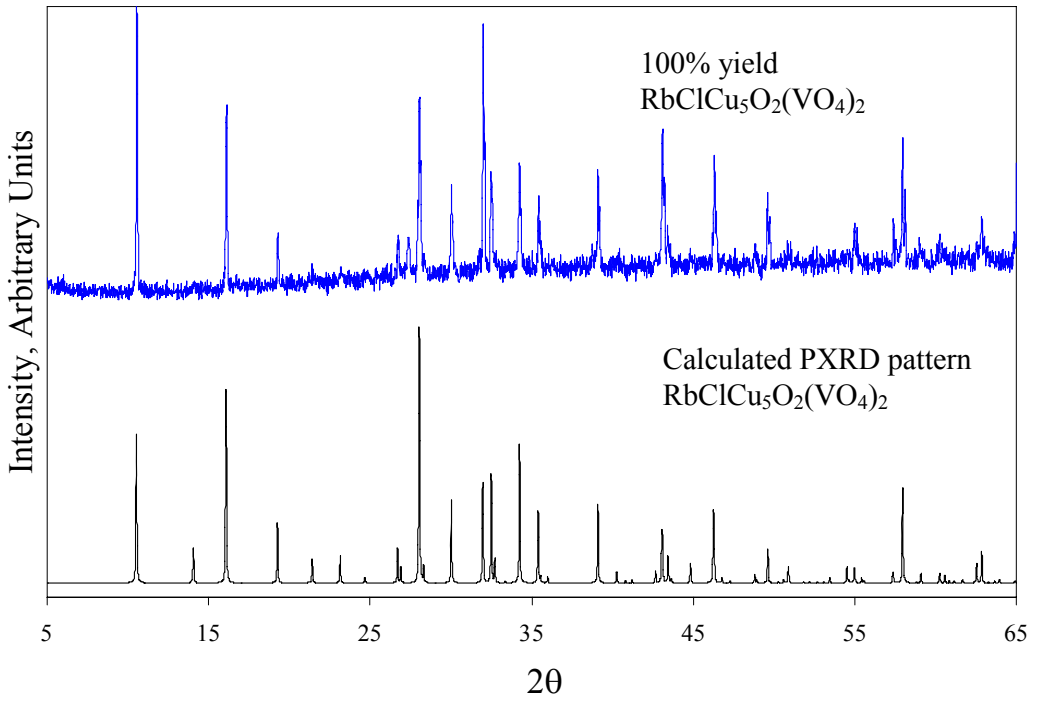

Figure I.19: PXRD pattern showing the stoichiometric synthesis of $RbClCu_5O_2(VO_4)_2$.

Table I.15: Crystallographic data of $(AX)Cu_5O_2(VO_4)_2$ A/X = Rb/Cl, Cs/Cl, and Cs/Br.

empirical formula	$(RbCl)_{0.94}Cu_5O_2(VO_4)_2$ [1]	$(CsCl)Cu_5O_2(VO_4)_2$ [2]	$(CsBr)Cu_5O_2(VO_4)_2$ [3]
color/shape	red hexagonal plate	red hexagonal plate	red hexagonal plate
crystal size (mm)	0.11 × 0.04 × 0.04	0.06 × 0.02 × 0.02	0.10 × 0.03 × 0.03
formula weight (amu)	693.70	747.99	792.44
space group, *Z*	*P* 3*m*(no. 157), 3	*P* -3*m*(no. 164), 1	*P* -3 *m*(no. 164), 1
T°C		25	
a, Å	11.016(2)	6.3652(9)	6.3835(9)
c, Å	8.391(2)	8.374(2)	8.379(2)
V, Å^3	881.7(3)	293.84(8)	295.69(8)
linear abs. coeff., mm^{-1}	14.521	13.709	16.776
F_{000}	966	343	361
d_{calc}, g / cm^{-3}	3.919	4.227	4.450
data/restraints/parameters	1131 / 0 / 85	230 / 0 / 27	232 / 0 / 28
secondary extinction	0.009(1)	--------	0.051(9)
reflections collected / unique / R_{int} [a]	7294 / 1131 / 0.1195	2545 / 230 / 0.0625	2544 / 232 / 0.0964
final R1/wR2 [b] [$I > 2\ \sigma(I)$]	0.0524 / 0.1262	0.0598 / 0.1664	0.0474 / 0.1257
R1/wR2 (all data)	0.0574 / 0.1298	0.0660 / 0.1749	0.0484 / 0.1269
GOF	1.136	1.100	1.099
Largest difference peak / hole (e$^-$ / Å^3)	1.537 / -1.152	4.774 / -3.445	2.226 / -2.747

[a] $R_{int} = \Sigma \mid F_o^2 - F_o^2\ (mean) \mid / \Sigma[F_o^2]$; [b] **1**;*w*R2 = $\{[\Sigma[w(F_o^2-F_c^2)^2] / [\Sigma w(F_o)^2)^2]\}^{1/2}$; $w = 1 / [\sigma^2(F_o^2) + (0.0574P)^2 + 3.8417P]$ where $P = (F_o^2 + 2F_c^2)/3$; **2**; *w*R2 = $\{[\Sigma[w(F_o^2-F_c^2)^2] / [\Sigma w(F_o)^2)^2]\}^{1/2}$; $w = 1 / [\sigma^2(F_o^2) + (0.1195P)^2 + 4.2419P]$ where $P = (F_o^2 + 2F_c^2)/3$; **3**; *w*R2 = $\{[\Sigma[w(F_o^2-F_c^2)^2] / [\Sigma w(F_o)^2)^2]\}^{1/2}$; $w = 1 / [\sigma^2(F_o^2) + (0.0903P)^2 + 1.6781P]$ where $P = (F_o^2 + 2F_c^2)/3$

Table I.16: Atomic parameters of $(AX)Cu_5O_2(VO_4)_2$ A/X = Rb/Cl, Cs/Cl, and Cs/Br.

Atom	Wyckoff notation	sof	x	y	z
			$(RbCl)Cu_5O_2(VO_4)_2$		
Rb1	2*b*	0.84	2/3	1/3	0.5222(9)
Rb2	1*a*	0.83	0	0	0.254(1)
Rb3	2*b*	0.16	2/3	1/3	0.278(3)
Cu1	3*c*	1.0	0.3481(3)	0.3481(3)	1.1587(4)
Cu2	3*c*	1.0	0.6839(3)	0.6839(3)	0.6153(4)
Cu3	3*c*	1.0	0.5079(2)	0.5079(2)	0.8864(4)
Cu4	6*d*	1.0	0.1717(3)	0.3346(3)	0.8897(4)
V1	3*c*	1.0	0.6732(3)	0.6732(3)	1.1926(6)
V2	3*c*	1.0	0.3419(3)	0.3419(3)	0.5800(6)
Cl1	2*b*	1.0	1/3	2/3	0.890(2)
Cl2	1*a*	0.83	0	0	0.847(2)
O1	3*c*	1.0	0.686(1)	0.686(1)	0.389(2)
O2	6*d*	1.0	0.143(2)	0.322(1)	1.127(2)
O3	3*c*	1.0	0.528(2)	0.528(2)	1.127(3)
O4	3*c*	1.0	0.348(1)	0.348(1)	0.929(2)
O5	3*c*	1.0	0.491(1)	0.491(1)	0.648(2)
O6	6*d*	1.0	0.848(1)	0.654(1)	0.651(2)
O7	3*c*	1.0	0.334(1)	0.334(1)	1.380(3)
O8	3*c*	1.0	0.665(2)	0.665(2)	0.842(4)
			$(CsCl)Cu_5O_2(VO_4)_2$		
Cs	1*b*	1.0	0	0	1/2
Cu1	2*d*	1.0	1/3	2/3	0.2717(3)
Cu2	3*e*	1.0	1/2	1/2	0
V1	2*d*	1.0	1/3	2/3	0.6950(5)
Cl	1*a*	1.0	0	0	0
O1	2*d*	1.0	1/3	2/3	0.498(2)
O2	2*d*	1.0	1/3	2/3	0.048(2)
O3	6*i*	1.0	0.5205(9)	0.4795(9)	0.240(1)
			$(CsBr)Cu_5O_2(VO_4)_2$		
Cs	1*b*	1.0	0	0	1/2
Cu1	2*d*	1.0	1/3	2/3	0.2713(2)
Cu2	3*e*	1.0	0	1/2	0
V	2*d*	1.0	1/3	2/3	0.6942(3)
Br	1*a*	1.0	0	0	0
O1	2*d*	1.0	1/3	2/3	0.046(1)
O2	2*d*	1.0	1/3	2/3	0.497(1)
O3	6*i*	1.0	0.5192(6)	0.4808(6)	0.2374(8)

$VO_4)^{3-}$ tetrahedra, while Cu(2) only shares two corner oxygen atoms with neighboring $(VO_4)^{3-}$ polyhedra. This connectivity leads to the formation of 6-membered ring channels, Figure I.20, that run along *c* and contain Cs^+ and Cl^- ions. The connectivity between CuO_5 and CuO_4 polyhedra creates 2-D Cu-O sheets which propagate infinitely within the *ab* plane, shown in Figure I.22. These sheets are structurally confined from one another along the *c* direction by the $(VO_4)^{3-}$ anions.

It should be noted that the structure solution of the $(RbCl)Cu_5O_2(VO_4)_2$ is still questionable as the material was solved in a different space group than the other two derivatives reported here. The structure solution has some problems such as non positive definites, and it is thought that the problems associated with this structure solution could be related to crystal twinning and/or a poor overall single crystal data collection. A stoichiometric synthesis for the RbCl derivative is shown in Figure I.19. The experimental powder pattern closely matches the calculated powder pattern obtained from the single crystal structure solution of $(RbCl)Cu_5O_2(VO_4)_2$.

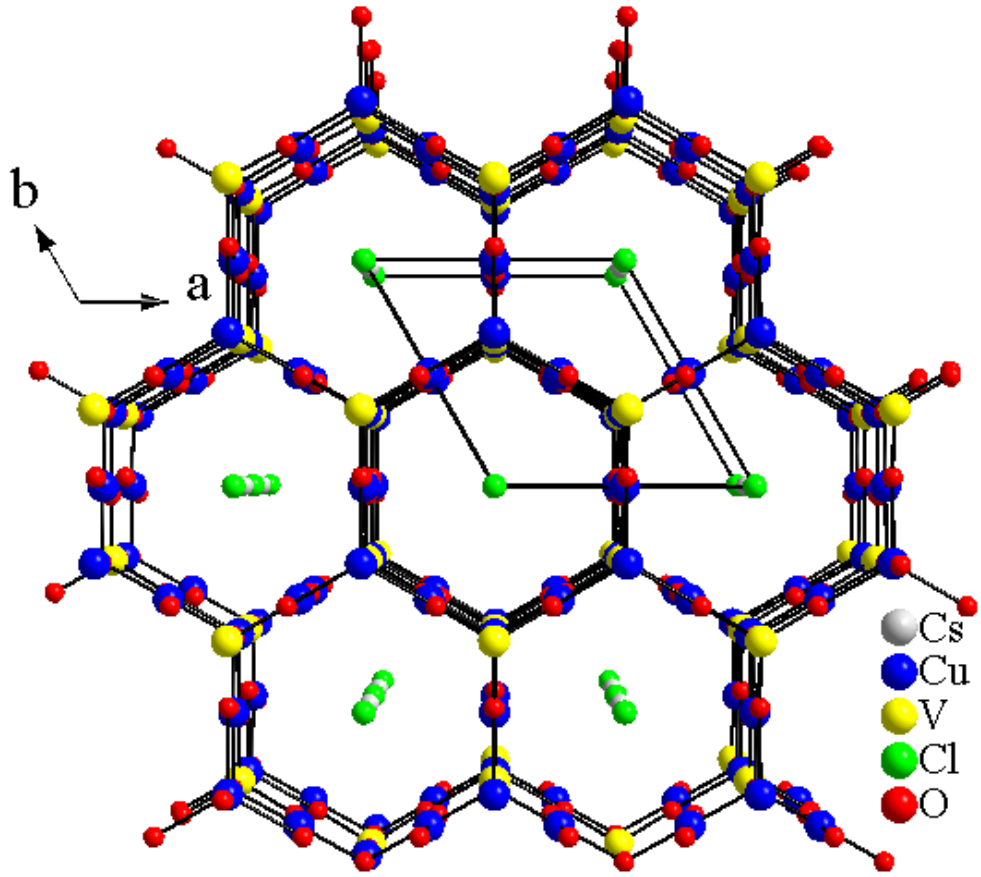

Figure I.20: Projected view of the $(CsCl)Cu_5O_2(VO_4)_2$ framework. The structure has 6-membered ring windows that contain the Cs and Cl ions.

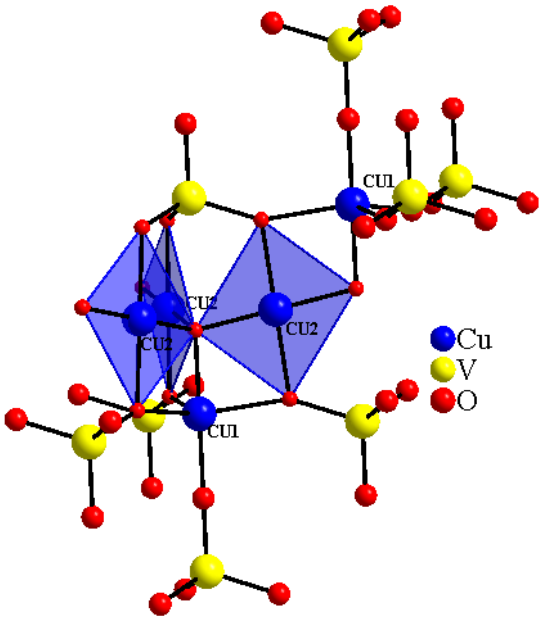

Figure I.21: Projected view showing the connectivity between the $Cu(1)O_5$ trigonal bipyramidal and $Cu(2)O_4$ square planar polyhedra in $(CsCl)Cu_5O_2(VO_4)_2$.

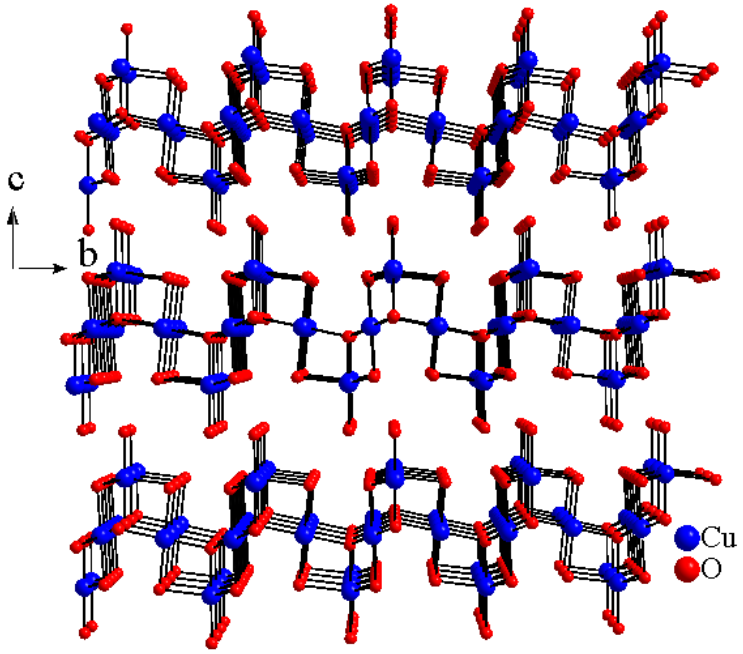

Figure I.22: Projected view of the Cu-O framework in $(CsCl)Cu_5O_2(VO_4)_2$. The Cu-O framework forms 2-D sheets. The sheets are interlinked by the fully oxidized $(VO_4)^{3-}$ tetrahedra.

$A_5MCl_6VO_{1-x}Cl_x(VO_3)_4$ (A/M = Cs/V (**1**), Rb/Fe (**2**) or Cs/Fe (**3**)) and $Cs_{2.28}Cl_{0.28}VO(VO_3)_4$ (**4**): a new family of structurally related compounds

A new compound family has been synthesized using high-temperature molten salt methods. The materials exhibit two related structure types, denoted as **I** (**1-3**) and **II** (**4**). Compound **1** was synthesized using VO_2 and V_2O_5 in a 8:2 mol ratio. The reactants were placed in a CsCl/NaCl flux equal to three times the mass of the oxide reactants. The reaction was heated to 650°C at a rate of 2°C/minute, held there for four days, slowly cooled to 450°C at 0.1°C/minute, and then furnace cooled to room temperature. For **2**, FeO, V_2O_5, and RbCl were mixed in a 1:2:4 mol ratio. The reaction was heated to 800°C at 1°C/minute, held there for three days, slowly cooled to 450°C at 0.1°C/minutre, and then furnace cooled to room temperature. For **3** FeO, V_2O_5, and CsCl in a 1:2:2 mol ratio. The reaction was heated to 650°C at 1°C/minute, held there for three days, slowly cooled to 450°C at 0.1°C/minute, and then furnace cooled to room temperature. All of the above reactions formed dark red plate-like crystals. The crystallographic data and atomic paramaters of **1-4** can be compared in Tables I.17 and I.18.

As previously mentioned the materials form two related structure types. Compounds **1-3** are isostructural so the structure of **1** has been chosen for discussion. Compound **1**, shown in Figure I.23, exhibits a layererd structure type that consists of $[VO(VO_3)_4]_\infty$ sheets that are structurally confined from one another. The sheets contains two crystallographically distinct V sites, V(1) and V(2), Figure I.24. V(1) is mixed 3+/4+ and is found in a square pyramidal type geometry, while V(2), is found in a 5+

Table I.17: Crystallographic data of $A_5MCl_6VO_{1-x}Cl_x(VO_3)_4$ A/M = Rb/Fe or Cs/Fe or Cs/V and $Cs_{4.75}V_2O_2(VO_3)_8$

empirical formula	$Cs_5VCl_6VO(VO_3)_4$[1]	$Rb_5FeCl_6VO_{0.625}Cl_{0.375}(VO_3)_4$[2]	$Cs_5FeCl_6VO_{0.59}Cl_{0.41}(VO_3)_4$[3]	$Cs_{4.75}V_2O_2(VO_3)_8$[4]
color/shape	Dark red plate	Dark red plate	Dark red plate	Dark red plate
crystal size (mm)	0.18 × 0.09 × 0.02	0.15 × 0.15 × 0.02	0.13 × 0.13 × 0.02	0.1 × 0.1 × 0.02
formula weight (amu)	1390.89			1556.72
space group, *Z*	*P* 4/n m m (no. 129), 2	*P* 4/n m m (no. 129), 2	*P* 4/n m m (no. 129), 2	*I* 4/m m m (no. 139), 4
T°C		25		
a, Å	10.938(2)	10.833(2)	10.972(2)	7.817(1)
c, Å	10.352(2)	10.005(2)	10.553(2)	24.514(5)
V, Å^3	1238.4(3)	1174.2(3)	1270.4(4)	1497.9(4)
linear abs. coeff., mm^{-1}	10.108	13.579	10.098	8.746
F_{000}	1238	1070	1251	1399
d_{calc}, g / cm^{-3}	3.730	3.298	3.670	3.451
data/restraints/parameters	665 / 0 / 51	630 / 0 / 53	681 / 0 / 52	437 / 0 / 45
secondary extinction	---------	-------	----------	----------
reflections collected / unique / R_{int}[a]	10080 / 665 / 0.0825	9837 / 630 / 0.1304	10607 / 681 / 0.1193	5893 / 437 / 0.0571
final R1/wR2[b] [$I > 2\ \sigma(I)$]	0.0435 / 0.1109	0.0875, wR2 = 0.2261	0.0688 / 0.1637	0.0426 / 0.1154
R1/wR2 (all data)	0.0572 / 0.1187	0.0907, wR2 = 0.2286	0.0736 / 0.1662	0.0446 / 0.1170
GOF	1.099	1.281	1.323	1.087
Largest difference peak / hole (e$^-$ / Å^3)	2.141 / -1.716	4.953 / -1.220	2.238 / -1.791	1.645 / -1.435

[a] $R_{int} = \Sigma \mid F_o^2 - F_o^2\ (mean) \mid / \Sigma[F_o^2]$; [b] **1**; $wR2 = \{[\Sigma[w(F_o^2-F_c^2)^2] / [\Sigma w(F_o)^2)^2]\}^{1/2}$; $w = 1 / [\sigma^2(F_o^2) + (0.0688P)^2 + 1.4794P]$ where $P = (F_o^2 + 2F_c^2)/3$; **2**; $wR2 = \{[\Sigma[w(F_o^2-F_c^2)^2] / [\Sigma w(F_o)^2)^2]\}^{1/2}$; $w = 1 / [\sigma^2(F_o^2) + (0.1053P)^2 + 26.1579P]$ where $P = (F_o^2 + 2F_c^2)/3$; **3**; $wR2 = \{[\Sigma[w(F_o^2-F_c^2)^2] / [\Sigma w(F_o)^2)^2]\}^{1/2}$; $w = 1 / [\sigma^2(F_o^2) + (0.0651P)^2 + 35.7307P]$ where $P = (F_o^2 + 2F_c^2)/3$; **4**; $wR2 = \{[\Sigma[w(F_o^2-F_c^2)^2] / [\Sigma w(F_o)^2)^2]\}^{1/2}$; $w = 1 / [\sigma^2(F_o^2) + (0.0724P)^2 + 13.1800P]$ where $P = (F_o^2 + 2F_c^2)/3$

Table I.18: Atomic parameters of $A_5MCl_6VO_{1-x}Cl_x(VO_3)_4$ A/M = Rb/Fe or Cs/Fe or Cs/V and $Cs_{4.75}V_2O_2(VO_3)_4$

Atom	Wyckoff notation	sof	x	y	z
			$Cs_5VCl_6VO(VO_3)_4$		
Cs1	2*c*	1.0	1/4	1/4	0.3624(2)
Cs2	8*j*	1.0	0.48793(6)	0.01207(6)	0.71751(8)
V1	2*c*	1.0	1/4	1/4	0.8434(4)
V2	8*i*	1.0	3/4	0.0253(2)	0.9900(2)
V3	2*b*	1.0	3/4	1/4	1/2
Cl1	4*f*	1.0	3/4	1/4	0.7283(6)
Cl2	8*i*	1.0	0.5319(4)	1/4	0.4979(4)
O1	2*c*	1.0	1/4	1/4	0.691(2)
O2	8*g*	1.0	0.6129(6)	0.1129(6)	1.00000
O3	8*i*	1.0	3/4	-0.0771(8)	1.1129(8)
O4	8*i*	1.0	3/4	-0.0491(9)	0.8553(9)
			$Rb_5FeCl_6VO_{0.625}Cl_{0.375}(VO_3)_4$		
Rb1	2*c*	1.0	1/4	1/4	0.3523(4)
Rb2	8*j*	1.0	0.48794(14)	0.0121(1)	0.7186(2)
V1	2*c*	1.0	1/4	1/4	0.8350(7)
V2	8*i*	1.0	3/4	0.0247(2)	0.9912(3)
Fe1	2*b*	1.0	3/4	1/4	1/2
Cl1	4*f*	1.0	3/4	1/4	0.7345(7)
Cl2	8*i*	1.0	0.5264(4)	1/4	0.4960(5)
O2	8*g*	1.0	0.6110(8)	0.1110(8)	1.00000
O3	8*i*	1.0	3/4	-0.076(1)	1.119(1)
O4	8*i*	1.0	3/4	-0.056(1)	0.855(2)
Cl3	2*c*	0.38	1/4	1/4	0.657(2)
O5	2*c*	0.62	1/4	1/4	0.657(2)
			$Cs_5FeCl_6VO_{0.59}Cl_{0.41}(VO_3)_4$		
Cs1	2*c*	1.0	1/4	1/4	0.3492(3)
Cs2	8*j*	1.0	0.48642(9)	0.01358(9)	0.7185(1)
V1	2*c*	1.0	1/4	1/4	0.8537(7)
V2	8*i*	1.0	3/4	0.0266(3)	0.9895(3)
Fe	2*b*	1.0	3/4	1/4	1/2
Cl1	4*f*	1.0	3/4	1/4	0.7240(8)
Cl2	8*i*	1.0	0.5299(5)	1/4	0.4945(5)
O1	8*g*	1.0	0.6133(8)	0.1133(8)	1.00000
O2	8*i*	1.0	3/4	-0.077(1)	1.112(2)
O3	8*i*	1.0	3/4	-0.046(2)	0.857(2)
Cl3	2*c*	0.41	1/4	1/4	0.670(2)
O4	2*c*	0.59	1/4	1/4	0.670(2)

Table I.18: Atomic parameters of $A_5MCl_6VO_{1-x}Cl_x(VO_3)_4$ A/M = Rb/Fe or Cs/Fe or Cs/V and $Cs_{4.75}V_2O_2(VO_3)_8$ cont…

Atom	Wyckoff notation	sof	x	y	z
			$Cs_{4.75}V_2O_2(VO_3)_8$		
Cs1	4*d*	1.0	1/2	0	1/4
Cs2	2*a*	0.63	0	0	0
Cs3	4*c*	0.72	-1/2	0	0
Cs4	8*i*	0.15	-0.445(7)	0	0
Cs5	2*b*	0.09	0	0	1/2
V1	4*e*	1.0	0	0	0.1936(1)
V2	16*m*	1.0	0.2202(1)	0.2202(1)	0.37155(5)
O1	16*m*	1.0	0.3278(6)	0.3278(6)	0.3222(3)
O2	16*n*	1.0	0.2673(8)	0	0.3631(3)
Cs1	4*d*	1.0	1/2	0	1/4
Cs2	2*a*	0.63	0	0	0

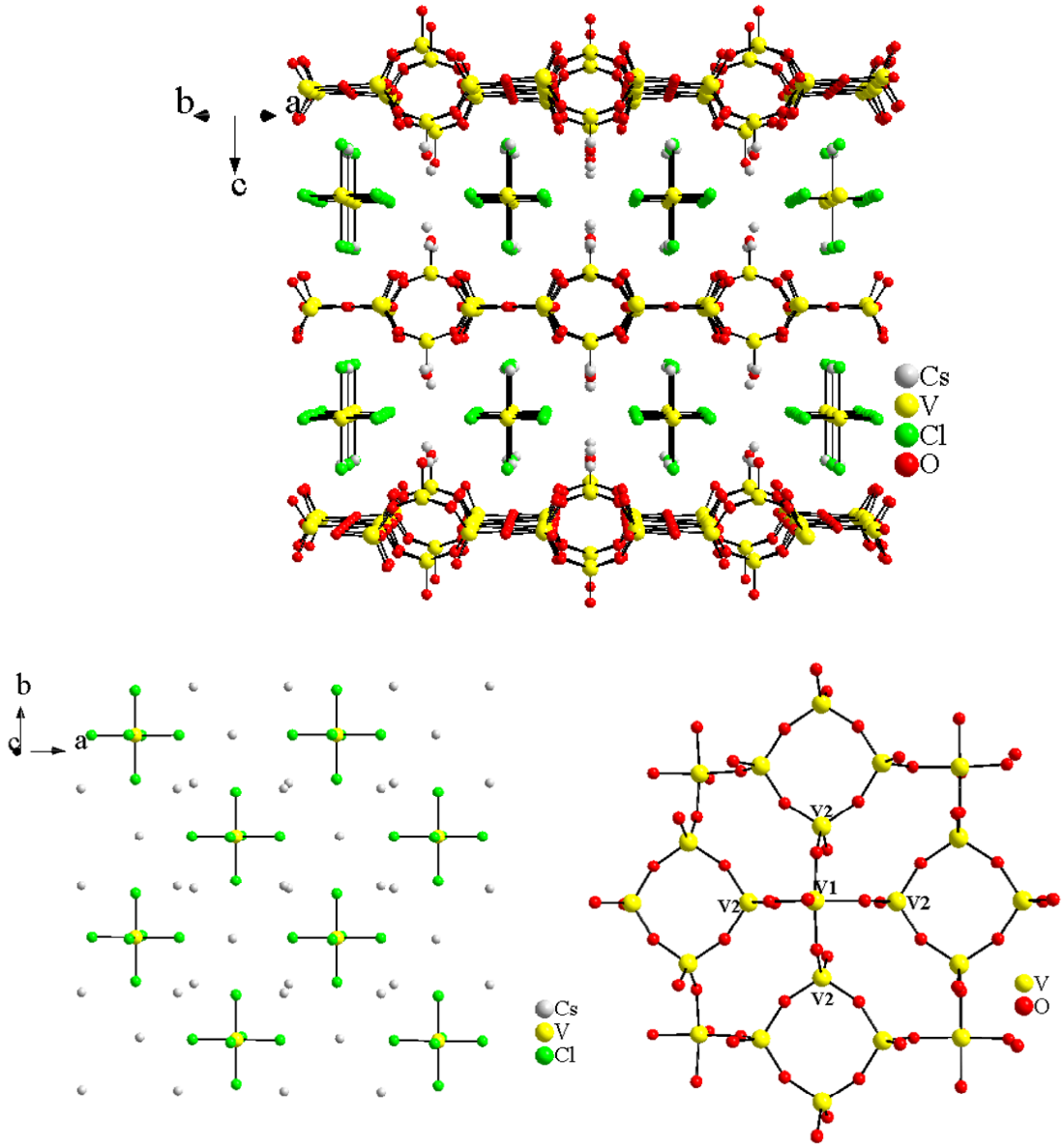

Figure I.23: Perspective view of $Cs_5VCl_6VO(VO_3)_4$. Looking at the *ac* plane the layered structure is revealed. The structure consists of $[VO(VO_3)_4]_\infty$ sheets that extend infinitely within the *ab* plane. The layers are separated from one another by Cs^+ cations and VCl_6 polyhedra shown on the right.

oxidation state and tetrahedrally coordinated by surrounding O^{2-}. The $V(2)O_4$ tetrahedra share two corners with other $V(2)O_4$ units forming $(VO_3)_4$ meta vanadate rings and one corner with neighboring $V(1)O_5$ polyhedra. The last crystallographically distint V site is in a 3+ oxidation state and octahedrally coordinated by Cl^-. These $V(3)Cl_6$ octahedral anions are found among the Cs^+ cations located between the $[VO(VO_3)_4]_\infty$ sheets. In **2** and **3** this V(3) site is substituted with Fe^{3+}.

In compound **4**, structure type **II** (Figure I.24), the material contains the same $[VO(VO_3)_4]_\infty$ sheets. The only difference in the sheets pertains to the square pyramidal $V(1)O_5$ site. In structure type **II** structure, the apical oxygen all point in the same direction while in structure type **I** the directions of the apical oxygen alternate within the sheet. The main difference in the structure types is found between the $[VO(VO_3)_4]_\infty$ sheets. Type **I** has MCl_6 polyhedra among Cs^+ cations, while type **II** only has only Cs^+ cations located between the sheets.

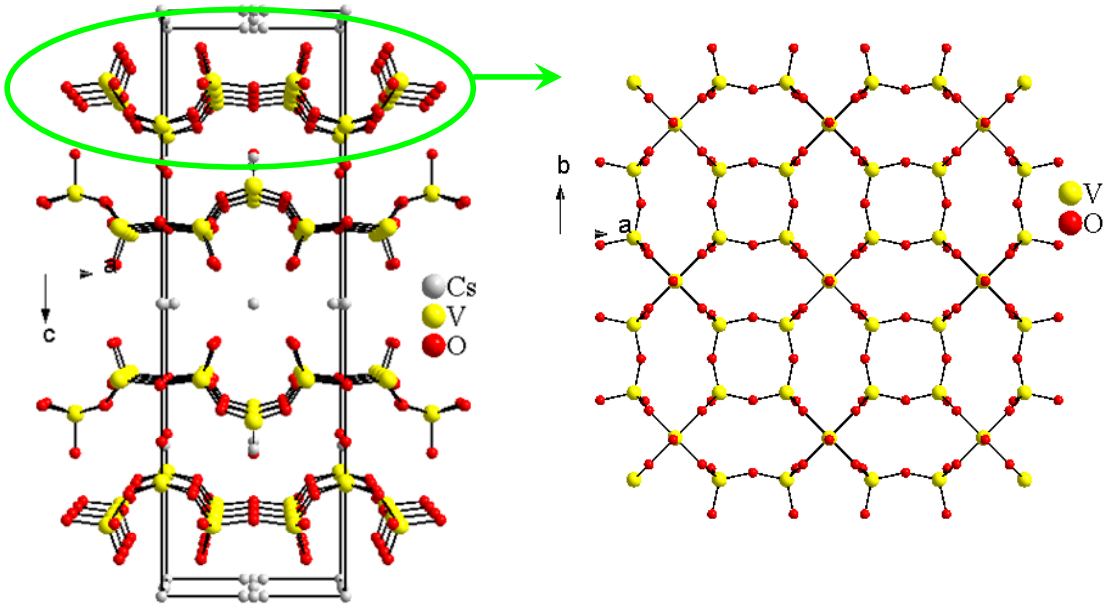

Figure I.24: Projected view of $Cs_{4.75}V_2O_2(VO_3)_8$ (left). The structure is made up of the same $VO(VO_3)_4$ sheets that extend infinitely within the *ab* plane.

$Rb_2Na_2V_4O_4(PO_4)_4$

A new reduced vanadium phosphate has been synthesized using high-temperature molten salt methods. The solid was isolated using V_2O_3, VO_2, and V_2O_5 in a 1:2:4 mol ratio. The reactants were placed in a RbCl/NaCl eutectic flux equal to three times the mass of the oxide reactants. The reaction was heated to 650°C at 1°C/minute, held there for 3 days, and then furnace cooled to room temeprature. Green column-like crystals of $RbNaV_2O_2(PO_4)_2$ were isolated after washing the product with deionized water.

The extended vanadium phosphate structure is shown in Figure I.25. There are 4 crystallographically distinct V cations, all of which are in a 4+ oxidation state and a square pyramidal geometry with the exception of V(3) which has a long apical V(3)-O(18) distance of 2.40(2) Å. This long V(3)-O(18) distance gives rise to a pseudo-octahedral geometry and corner sharing between the $V(3)O_6$ and $V(2)O_5$ polyhedra, shown in Figure I.26. The other vanadium polyhedra, V(1) and V(4), are isolated from other metal polyhedra *via* surrounding oxyanions, $(PO^4)^{3-}$. All four V polyhedra contain short vanadyl, V=O, bonds ranging from 1.586(1)-1.60(1). The vanadium phosphate framework forms a channeled type structure which can be seen along the *a* axis. There are two channels. The smaller of the two contains only Rb^+ cations, while the larger one contains both Rb^+ and Na^+ cations.

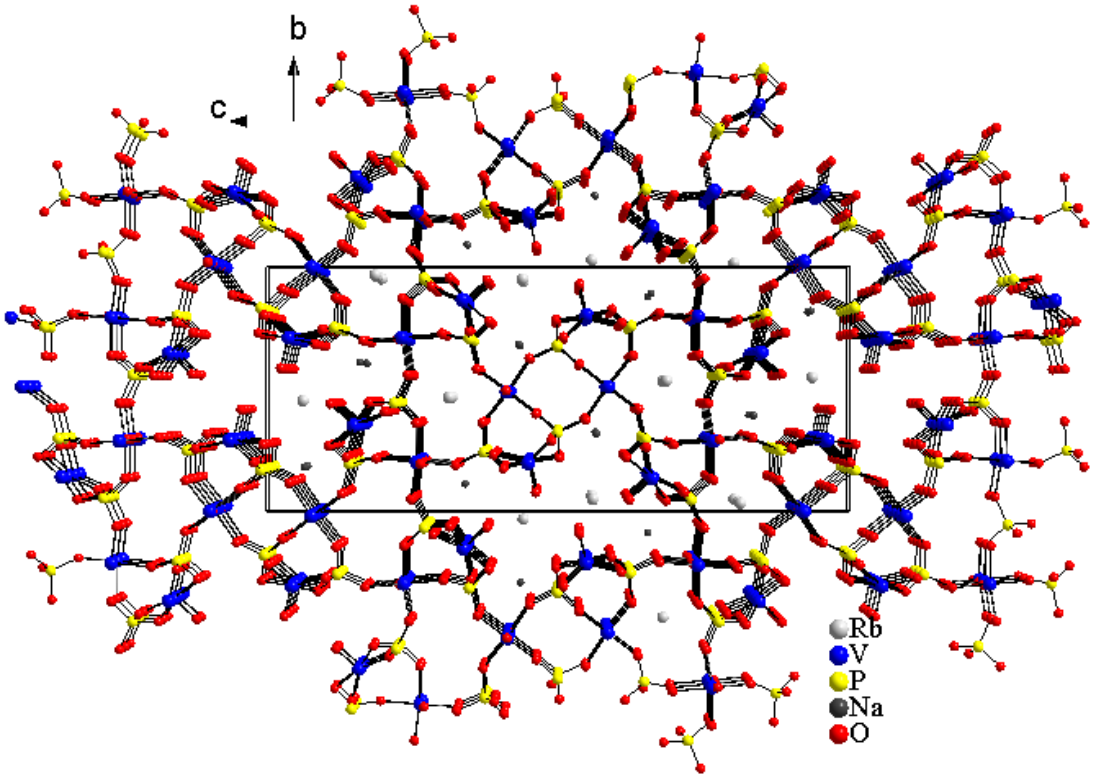

Figure I.25: Projected view showing the channeled structure of $Rb_2Na_2V_4O_4(PO_4)_4$. The structure has two channels. The smaller one contains only Rb^+ cations, while the larger one contains both Rb^+ and Na^+ cations.

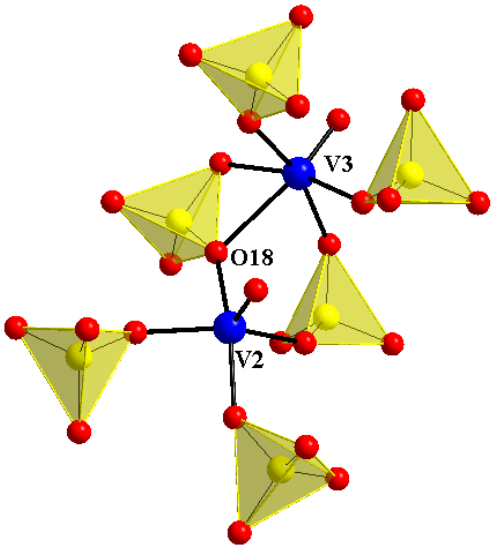

Figure I.26: Polyhedral view showing the coordination around the V(2) and V(3) polyhedra. The long V(3)-O(18) distance gives rise to a pseudo-octahedral geometry and corner sharing between the $V(3)O_6$ and $V(2)O_5$ polyhedra.

Table I.19: Crystallographic data of $Rb_2Na_2V_4O_4(PO_4)_4$

empirical formula	$Rb_2Na_2V_4O_4(PO_4)_4$
color/shape	Green column
crystal size (mm)	0.1 x 0.02 x 0.02
formula weight (amu)	864.56
space group, Z	$P2_1/c$(no. 14), 4
T°C	25
a, Å	4.838(1)
c, Å	12.212(2)
V, Å^3	29.118(6)
linear abs. coeff., mm^{-1}	8.261
F_{000}	1632
d_{calc}, g / cm^{-3}	3.339
data/restraints/parameters	3046 / 0 / 289
secondary extinction	-------
reflections collected / unique / R_{int}[a]	14364 / 3046 / 0.0662
final R1/wR2 [b] [$I > 2\ \sigma(I)$]	0.0458 / 0.1147
R1/wR2 (all data)	0.0602 / 0.1260
GOF	1.101
Largest difference peak / hole (e$^-$ / Å^3)	1.160 / -1.094

[a] $R_{int} = \Sigma \mid F_o^2 - F_o^2\ (\text{mean}) \mid / \Sigma[\ F_o^2\ ]$; [b] $wR2 = \{[\Sigma[w(F_o^2 - F_c^2)^2] / [\Sigma w(F_o)^2)^2]\}^{1/2}$; $w = 1 / [\sigma^2(F_O^2) + (0.0678P)^2 + 0.0000P]$ where $P = (F_O^2 + 2F_C^2)/3$

Table I.20: Atomic parameters of $Rb_2Na_2V_4O_4(PO_4)_4$

Atom	Wyckoff notation	sof	x	y	z
Rb1	4*e*	1.0	0.4558(2)	0.54805(6)	0.06071(3)
Rb2	4*e*	1.0	0.0078(2)	0.03414(8)	0.18668(3)
V1	4*e*	1.0	0.0547(2)	0.29541(9)	0.04924(4)
V2	4*e*	1.0	0.3322(2)	-0.20793(9)	0.26296(4)
V3	4*e*	1.0	0.0237(2)	0.64433(9)	0.15898(4)
V4	4*e*	1.0	-0.4439(3)	0.00978(9)	0.08551(4)
P4	4*e*	1.0	0.4619(4)	0.7988(1)	0.14885(6)
P1	4*e*	1.0	0.4697(4)	0.0563(1)	0.27519(6)
P2	4*e*	1.0	0.4852(4)	0.8252(1)	0.00027(6)
P3	4*e*	1.0	0.5639(4)	0.2531(1)	0.12397(6)
Na1	4*e*	1.0	-0.0079(6)	0.8177(3)	0.0661(1)
Na2	4*e*	1.0	0.0998(6)	0.3910(2)	0.1606(1)
O1	4*e*	1.0	0.007(1)	-0.2024(4)	0.2708(2)
O2	4*e*	1.0	0.545(1)	0.3051(4)	0.1718(2)
O3	4*e*	1.0	0.432(1)	0.9200(4)	0.1364(2)
O4	4*e*	1.0	0.482(1)	0.1335(4)	0.1269(2)
O5	4*e*	1.0	0.371(1)	0.3196(4)	0.0915(2)
O6	4*e*	1.0	0.597(1)	0.9004(4)	-0.0366(2)
O7	4*e*	1.0	0.677(1)	0.7238(4)	0.0025(2)
O8	4*e*	1.0	0.490(1)	0.8762(4)	0.0478(2)
O9	4*e*	1.0	0.568(1)	0.1363(4)	0.2379(2)
O10	4*e*	1.0	0.288(1)	0.7261(4)	0.1161(2)
O11	4*e*	1.0	0.460(1)	-0.0577(4)	0.2531(2)
O12	4*e*	1.0	0.663(1)	0.0534(4)	0.3178(2)
O13	4*e*	1.0	0.862(1)	0.2624(4)	0.1073(2)
O14	4*e*	1.0	-0.116(1)	0.0060(4)	0.0861(2)
O15	4*e*	1.0	0.768(1)	0.7694(4)	0.1481(2)
O16	4*e*	1.0	0.184(1)	0.7932(4)	-0.0100(2)
O17	4*e*	1.0	-0.074(1)	0.5593(4)	0.1200(2)
O18	4*e*	1.0	0.322(1)	0.7774(4)	0.1952(2)
O19	4*e*	1.0	-0.044(1)	0.4169(4)	0.0370(2)
O20	4*e*	1.0	0.177(1)	0.0893(5)	0.2884(2)

$KCo_4(AsO_4)_3$ and $NaMn_4(VO_4)_3$

Two new mixed polyhedral frameworks were synthesized using high-temeperature molten salt methods. Single crystals of $KCo_4(AsO_4)_3$ were grown using Co_3O_4 and As_2O_5 in a 2:1 mol ratio. The reactants were added to a CsCl/KCl eutectic flux equivalent to three times the mass of the oxide starting materials. The reaction was heated to 300°C at 1°C/minute, held there for 6 hours, heated to 800°C at 1°C/minute, held there for 4 days, slowly cooled to 450°C at 0.1°C/minute, and then furnace cooled to room temperature. The second compound, $NaMn_4(VO_4)_3$, was synthesized using MnO and V_2O_5 in a 5:4.5 mol ratio. The reactants were added to a CsCl/NaCl eutectic flux equal to three times the mass of the oxides and then heated to 650°C at 1°C/minute, held there for 4 days, slowly cooled to 450°C at 0.1°C/minute, and then furnace cooled to room temeprature. The crystallographic data and atomic parameters for these two compounds is shown in Tables I.21 and I.22. A stoichiometric synthesis of $NaMn_4(VO_4)_3$ was attempted. Na_2O_2, Mn, MnO, and V_2O_5 were mixed in a 1:1:7:3 mol ratio. The reaction was heated to 650°C at 1°C/minute, held there for 1 day, and then furnace cooled to room temperature. The powder pattern obtained from the resulting product closely resembles the calculated PXRD pattern obtained from the single crystal structure solution of $NaMn_4(VO_4)_3$. A comparison can be seen in Figure I.27.

Despite the similarities in their chemical formulas, the structures of these two compounds are very different. $KCo_4(AsO_4)_3$, which crystallizes in a monoclinic space group, *C*2/c (no. 15), is shown in Figure I.28. The framework consists of connected

Table I.21: Crystallographic data of $KCo_4(AsO_4)_3$ and $NaMn_4(VO_4)_3$

empirical formula	$KCo_4(AsO_4)_3$[1]	$NaMn_4(VO_4)_3$[2]
color/shape	Purple chunk	Red plate
crystal size (mm)	0.15 × 0.10 × 0.06	0.13 × 0.08 × 0.06
formula weight (amu)	691.58	587.57
space group, *Z*	*C*2/c (no. 15), 4	*I*-42*d* (no. 122), 4
T°C	25	
a, Å	12.222(4)	7.017(1)
b, Å	12.850(4)	-------
c, Å	6.782(1)	19.839(4)
β, °	113.70(3)	-------
V, Å^3	975.3(5)	976.8(3)
linear abs. coeff., mm^{-1}	17.284	7.857
F_{000}	1288	1104
d_{calc}, g / cm^{-3}	4.710	3.995
data/restraints/parameters	955 / 0 / 94	432 / 0 / 47
secondary extinction	0.0012(2)	-------
flack parameter	------	0.1(1)
reflections collected / unique / R_{int}[a]	4365 / 955 / 0.0478	3591 / 432 / 0.0615
final R1/wR2 [b] [$I > 2\ \sigma(I)$]	0.0291 / 0.0666	0.0286 / 0.0525
R1/wR2 (all data)	0.0352 / 0.0692	0.0436 / 0.0595
GOF	1.097	0.737
Largest difference peak / hole (e$^-$ / Å^3)	0.645 / -0.871	0.650 / -0.488

[a] $R_{int} = \Sigma \mid F_o^2 - F_o^2\ (\text{mean}) \mid / \Sigma[F_o^2]$; **1** [b] $wR2 = \{[\Sigma[w(F_o^2-F_c^2)^2] / [\Sigma w(F_o)^2)^2]\}^{1/2}$; $w = 1 / [\sigma^2(F_o^2) + (0.0381P)^2+2.5928P]$ where $P = (F_o^2 + 2F_c^2)/3$; **2**; $wR2 = \{[\Sigma[w(F_o^2-F_c^2)^2] / [\Sigma w(F_o)^2)^2]\}^{1/2}$; $w = 1 / [\sigma^2(F_o^2) + (0.0015P)^2+0.0000P]$ where $P = (F_o^2 + 2F_c^2)/3$

Table I.22: Atomic parameters $KCo_4(AsO_4)_3$ and $NaMn_4(VO_4)_3$.

Atom	Wyckoff notation	sof	x	y	z
			$KCo_4(AsO_4)_3$		
K1	4*e*	1.0	1/2	0.0149(2)	3/4
Co1	8*f*	1.0	0.28131(7)	-0.15813(6)	0.8700(1)
Co2	4*e*	1.0	0	-0.0014(1)	3/4
Co3	4*e*	1.0	0	0.24439(9)	3/4
As1	8*f*	1.0	0.26370(5)	0.11516(4)	0.87187(9)
As2	4*e*	1.0	0	-0.21491(6)	3/4
O1	8*f*	1.0	0.1026(4)	-0.1225(3)	0.7560(7)
O2	8*f*	1.0	0.3204(4)	-0.0027(3)	0.8738(7)
O3	8*f*	1.0	0.1154(4)	0.1120(3)	0.8175(8)
O4	8*f*	1.0	0.3402(4)	0.1691(3)	1.1169(7)
O5	8*f*	1.0	0.4621(4)	-0.2121(3)	1.0268(6)
O6	8*f*	1.0	0.2816(4)	0.1870(3)	0.6796(6)
			$NaMn_4(VO_4)_3$		
Na	4*a*	1.0	1.00000	-1/2	1/4
Mn1	8*d*	1.0	0.7407(3)	-1/4	1/8
Mn2	8*c*	1.0	1/2	1/2	0.22760(9)
V1	4*b*	1.0	1/2	0	1/4
V2	8*d*	1.0	1.1518(3)	-1/4	1/8
O1	16*e*	1.0	0.9966(8)	-0.2021(8)	0.1906(2)
O2	16*e*	1.0	1.2715(9)	-0.4515(7)	0.1498(2)
O3	16*e*	1.0	0.5523(8)	-0.2063(8)	0.2053(3)

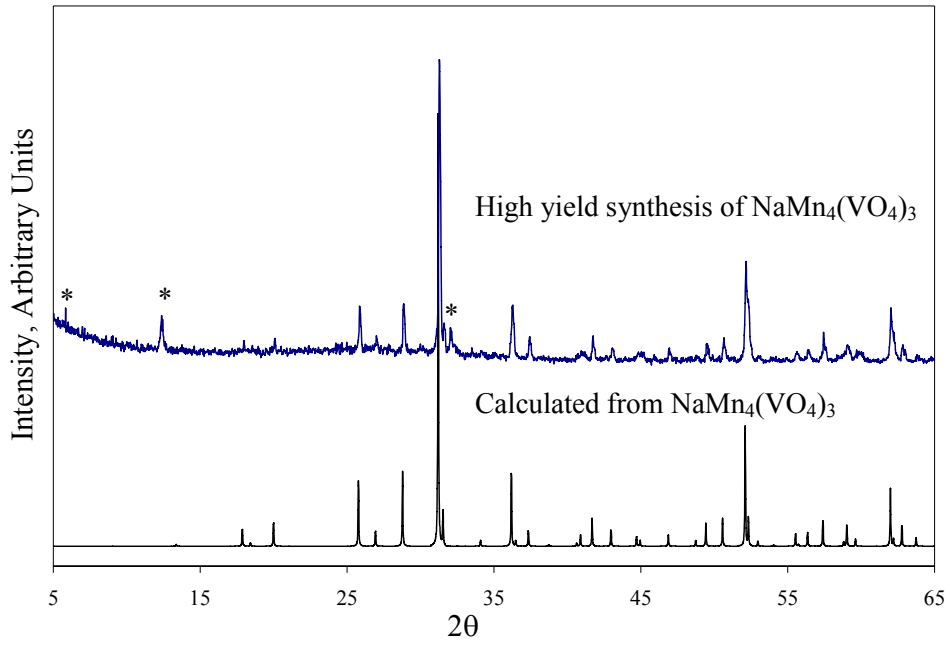

Figure I.27: PXRD pattern obtained from a high yield synthesis of $NaMn_4(VO_4)_3$ is compared to the calculated powder pattern. Obvious impurity peaks are marked with asterisks.

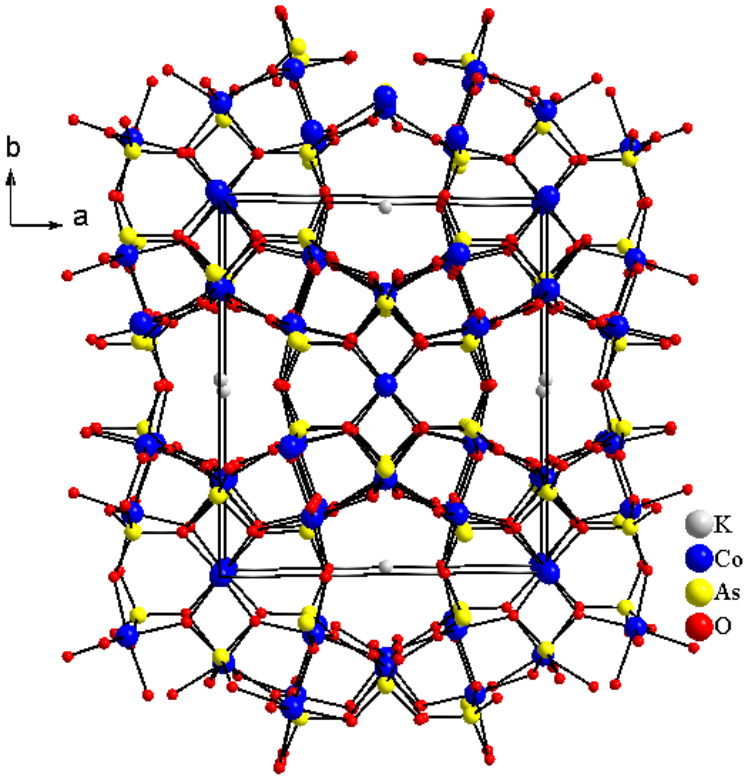

Figure I.28: Projected view showing the channeled structure of $KCo_4(AsO_4)_3$ and the 3-D Co-O-As framework.

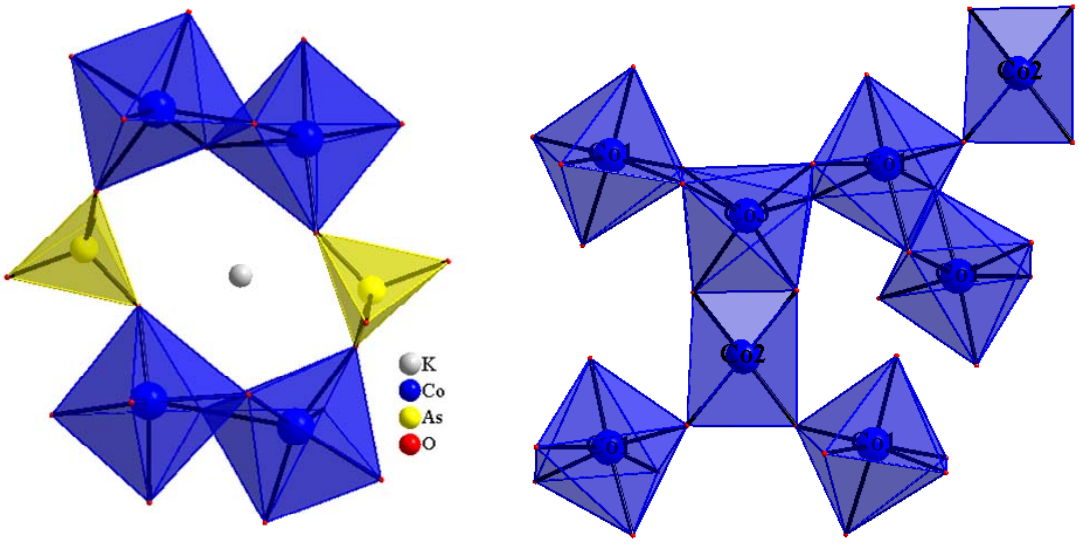

Figure I.29: Polyhedral view showing the channels in $KCo_4(AsO_4)_3$ (left). The polyhedral view on the right shows the connectivity between neighboring CoO_x polyhedra.

CoO_6 octahedra, CoO_4 square planes, and AsO_4 tetrahedra, which form a 3-D channeled framework. A close-up polyheral view, Figure I.29 (left) shows the 6-membered channels. The structure contains three crystallographically distint Co^{2+} polyhedra Figure I.29 (right). Co(1) and Co(3) form slightly distorted octahedra while Co(2) forms a square planar coordination. The Co(1) polyhedra share an edge with neighboring $Co(1)O_6$ and $Co(3)O_6$ polyhedra and a corner O atom with the $Co(2)O_4$ polyhedron. Besides their connectivity with Co(1), Co(2) and Co(3) also share an edge with one another. The edge-sharing polyhedra give rise to the closest Co-Co distances of 3.33(3)Å and 3.158(2)Å for Co(1)-Co(3) and Co(2)-Co(3) respectively and Co(1)-O(5)-Co(3), Co(1)-O(5)-Co(3), Co(2)-O(3)-Co(3), angles equal to 100.92(2)°, 104.3(2)°, and 101.2(1)° respectively. Although magnetic data has not yet been collected for this material it is thought that the M-O-M angles, which deviate far from 90, will promote AFM exchange. Co^{2+} has an unquenched orbital contribution. In circumstances where there are varying coordination geometries and distorted polyhedra, as observed in Chapter 3, we have seen that this can lead to ferrimagnetic exchange. Therefore, it may be of future interest to study the magnetic properties of the title compound.

The structure of $NaMn_4(VO_4)_3$ is condensed. The material crystallizes in a noncentrosymmetric space group, *I*-42*d* (no. 122) and an optically active, nonpolar crystal class, -42*m* (D_{2d}).[10] The material appears to have no channels, instead the Na cations are found in cavities shown in Figure I.30 (right). As a result of the complicated structure, the partial structure, with emphasis on the Mn-O-Mn lattice will be discussed. The extended structure is shown in Figure I.30 (left). The vanadium cations are found in

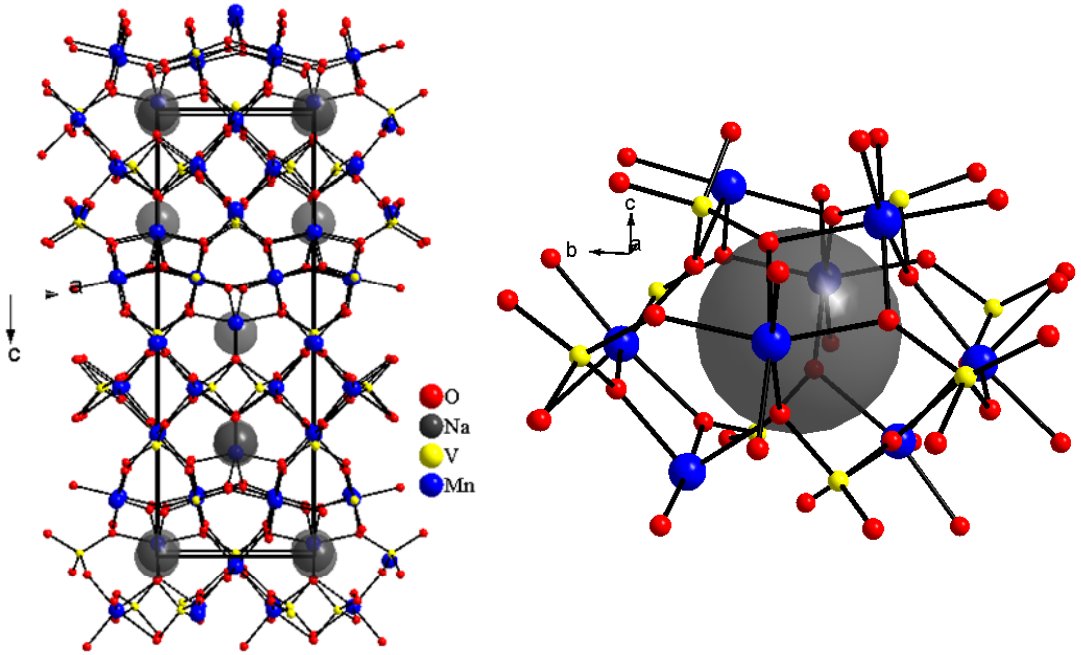

Figure I.30: Projected view of the extended structure of $NaMn_4(VO_4)_3$ along the crystallographic *b* axis (left). The condensed structure forms Mn-V-O cages (right) around the Na^+ cations.

.

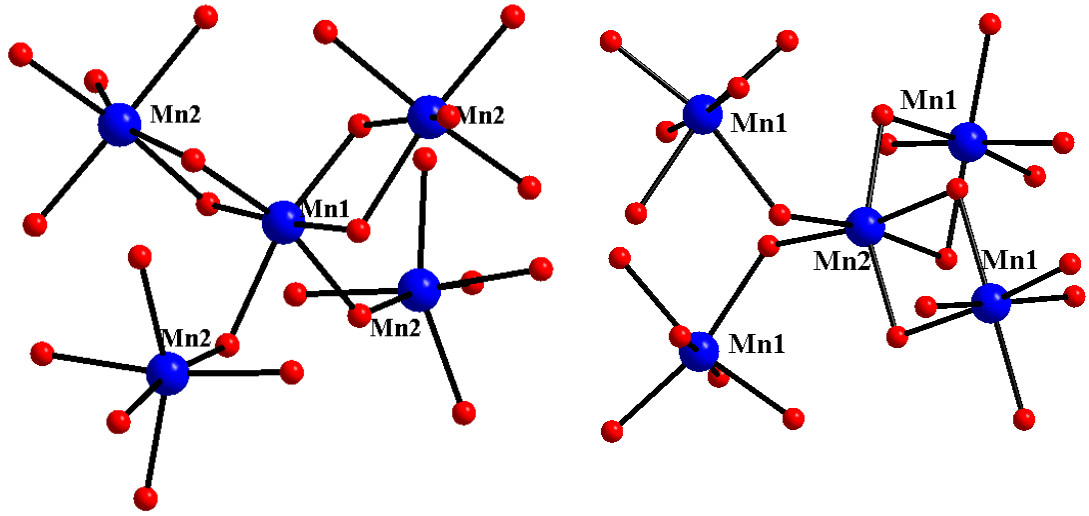

Figure I.31: Close-up view of the $Mn(1)O_6$ (left) and $Mn(2)O_6$ (right) connectivity. Both polyhedra share two edges and two corners with nearest neighbors.

a tetrahedral geometry and a 5+ oxidation state, while the Mn cations are found in a 2+ oxidation state and slightly distorted octahedral geometries. There are two crystallographically distinct Mn^{2+} cations. Figure I.31 shows the local coonectivity around the the Mn(1) and Mn(2) cations. Both of these octahedra share two edges and two corner O^{2-} anions with neighboring MnO_6 polyhedra. The shared-edge between Mn(1) and Mn(2) gives rise to the shortest Mn-Mn distance of 3.174(2)Å and bridging angles of 97.2(2)° and 92.2(2)°. The edge sharing polyhedra form infinite chains which are interconnected throughout the structure *via* corner sharing O(1) atoms.

The temperature-dependence of the molar magnetic susceptibility and inverse molar magnetic susceptibility of the title compound is shown in Figure I.32. The linear portion of the inverse susceptibility data, χ^{-1}, ranging from 180-300 K, was fit using Curie-Weiss law. From the fit an effective magnetic moment of 6.16(9) μ_B and a Weiss constant of -172.4(4) K was obtained. The negative Weiss constant indicates antiferromagnetic coupling between nearest neighbors. The effective magnetic moment is comparable to the expected spin-only magnetic moment equal to 5.91 μ_B, for a Mn^{2+}, high spin, d^5 ion. At low temperature there is a sudden increase in the susceptibility and in the χT (inset Figure I.32) plot which is an indication of ferromagnetic coupling. It is thought that due to a decrease in temeprature a slight contraction of the Mn(1)-O(2)-Mn(2) angle, 92.2(2), could induce ferromagnetic exchange between nearest neighbors. It is known that magnetic exchange between two adjacent magnetic ions can vary from antiferromagnetic to ferromagnetic through single atom bridging angles near 90^o. This is

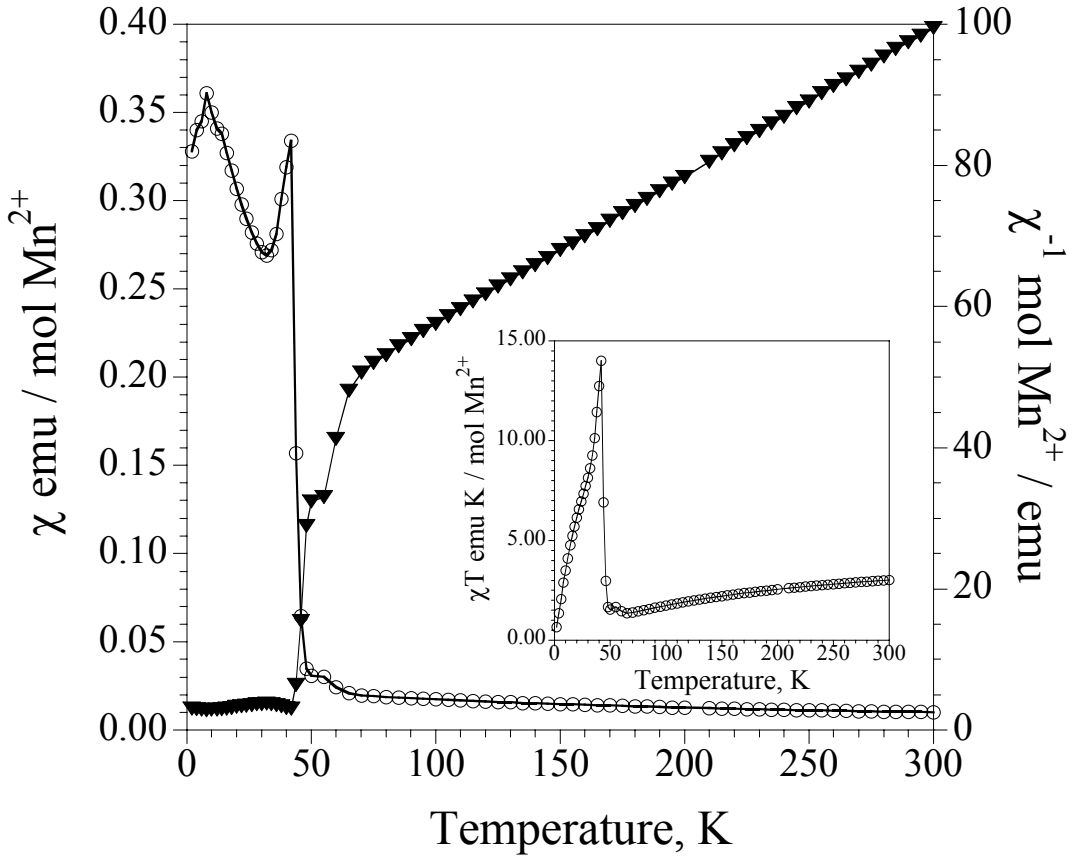

Figure I.32: Molar magnetic susceptibility, χ (○), and inverse molar magnetic susceptibility, χ^{-1} (▲), collected in an applied field of 0.01T. The data was obtained from a ground sample of selected single crystals of $NaMn_4(VO_4)_3$. The inset shows the χT data.

attributed to the resulting pair of degenerate orbitals from the magnetic orbitals of the two metal centers.[7]

$Ba_2Na_{13}Co_4(AsO_4)_8Cl$

This new mixed polyhedral framework was synthesized using high-temeperature molten salt methods. Single crystals of $Ba_2Na_{13}Co_4(AsO_4)_8Cl$ were grown using BaO, Na_2O_2, CoO, and As_2O_5 in a 1:4:6:3 mol ratio. The reactants were added to a RbCl/NaCl eutectic flux. The reaction was heated to 300°C at 1°C/minute, held there for 6 hours, heated to 450°C at 0.5°C/minute, held there for 6 hours, heated to 725°C at 1°C/mintue, held there for 4 days, slowly cooled to 450°C at 0.1°C/minute, and then furnace cooled to room temperature. After washing the product with deionized water, blue single crystals of the title compound were isolated. The single crystal data and atomic parameters are shown in Tables I.23 and I.24.

The extended structure of $Ba_2Na_{13}Co_4(AsO_4)_8Cl$ is shown in Figure I.33. The structure is layered with $[Co_4(AsO_4)_8]_\infty$ slabs separated from one another via Ba^{2+}, Na^+, and Cl^- ions. The structure contains two crystallographically distinct Co^{2+} cations. Co(1) is found in a trigonal bipyramidal geometry while Co(2) is found in a tetrahedral geometry. The two cobalt polyhedra are structurally confined from one another *via* surrounding $(AsO_4)^{3-}$ oxyanions, shown in Figure I.34. Each $[Co_4(AsO_4)_8]_\infty$ slab contains large Ba^{2+}-containing channels, with 8-membered ring windows and smaller Na^+-containing channels with 4-membered ring windows. The largest channel consists of four AsO_4 polyhedra, two $Co(2)O_4$ tetrahedra, and two $Co(1)O_5$ trigonal bipyramids,

Table I.23: Crystallographic data of $Ba_2Na_{13}Co_4(AsO_4)_8Cl$

empirical formula	$Ba_2Na_{13}Co_4(AsO_4)_8Cl$
color/shape	Blue plate
crystal size (mm)	0.18 × 0.13 × 0.09
formula weight (amu)	1956.08
space group, *Z*	*C* 1 2/c 1 (no. 15), 4
T°C	25
a, Å	34.412(7)
b, Å	5.315(1)
c, Å	23.394(5)
β, °	127.06(3)
V, Å^3	3415(1)
linear abs. coeff., mm^{-1}	12.220
F_{000}	3600
d_{calc}, g / cm^{-3}	3.805
data/restraints/parameters	3020 / 0 / 253
secondary extinction	-------
reflections collected / unique / R_{int}[a]	12922 / 3020 / 0.1190
final R1/wR2 [b] [$I > 2\ \sigma(I)$]	0.0900 / 0.1609
R1/wR2 (all data)	0.1197 / 0.1723
GOF	1.200
Largest difference peak / hole (e$^-$ / Å^3)	2.232 / -1.538

[a] $R_{int} = \Sigma \mid F_o^2 - F_o^2\ (mean) \mid / \Sigma[F_o^2]$; **1** [b] $wR2 = \{[\Sigma[w(F_o^2 - F_c^2)^2] / [\Sigma w(F_o)^2)^2]\}^{1/2}$; $w = 1 / [\sigma^2(F_o^2) + (0.0495P)^2 + 275.7627\ P]$ where $P = (F_o^2 + 2F_c^2)/3$

Table I.24: Atomic parameters $Ba_2Na_{13}Co_4(AsO_4)_8Cl$

Atom	Wyckoff notation	sof	x	y	z
Ba	8*f*	1.0	0.23342(4)	0.1939(2)	0.32489(6)
Na1	8*f*	1.0	0.4106(2)	-0.222(1)	0.6300(3)
Na2	8*f*	1.0	0.0554(3)	-0.266(2)	0.1958(4)
Na3	8*f*	1.0	0.1345(3)	0.299(2)	0.4847(4)
Na4	8*f*	1.0	0.0163(3)	0.249(2)	0.3405(4)
Na5	8*f*	1.0	0.0742(3)	0.194(2)	0.1370(4)
Na6	8*f*	1.0	0.0441(3)	0.736(2)	0.0264(5)
Na7	4*d*	1.0	1/4	-3/4	1/2
Co1	8*f*	1.0	0.17713(9)	-0.3043(5)	0.3644(1)
Co2	8*f*	1.0	0.15742(9)	1.1605(5)	0.1107(1)
As1	8*f*	1.0	0.10892(6)	0.2015(4)	0.30931(9)
As2	8*f*	1.0	0.15993(7)	0.6823(4)	0.19731(9)
As3	8*f*	1.0	-0.05075(7)	-0.2090(4)	0.0326(1)
As4	8*f*	1.0	0.29282(6)	-0.2535(3)	0.46621(9)
Cl	4*e*	1.0	0	-0.221(2)	1/4
O1	8*f*	1.0	0.1645(5)	0.327(3)	0.3450(7)
O2	8*f*	1.0	0.1025(5)	0.776(3)	0.1536(7)
O3	8*f*	1.0	0.0682(5)	0.301(3)	0.2255(6)
O4	8*f*	1.0	0.3120(4)	-0.127(2)	0.4198(6)
O5	8*f*	1.0	0.1159(5)	-0.114(3)	0.3076(7)
O6	8*f*	1.0	0.2381(4)	-0.114(3)	0.4296(7)
O7	8*f*	1.0	0.2876(5)	-0.563(2)	0.4553(7)
O8	8*f*	1.0	0.1925(5)	0.717(3)	0.2866(6)
O9	8*f*	1.0	0.1622(6)	0.368(3)	0.1839(7)
O10	8*f*	1.0	0.3314(4)	-0.150(3)	0.5507(6)
O11	8*f*	1.0	0.0902(5)	0.260(3)	0.3591(8)
O12	8*f*	1.0	0.1887(5)	0.856(3)	0.1703(7)
O13	8*f*	1.0	-0.0596(6)	-0.458(3)	0.0661(9)
O14	8*f*	1.0	-0.0379(7)	-0.309(4)	-0.0225(8)
O15	8*f*	1.0	-0.0999(6)	-0.024(3)	-0.0187(8)
O16	8*f*	1.0	-0.0039(6)	-0.028(3)	0.0934(8)

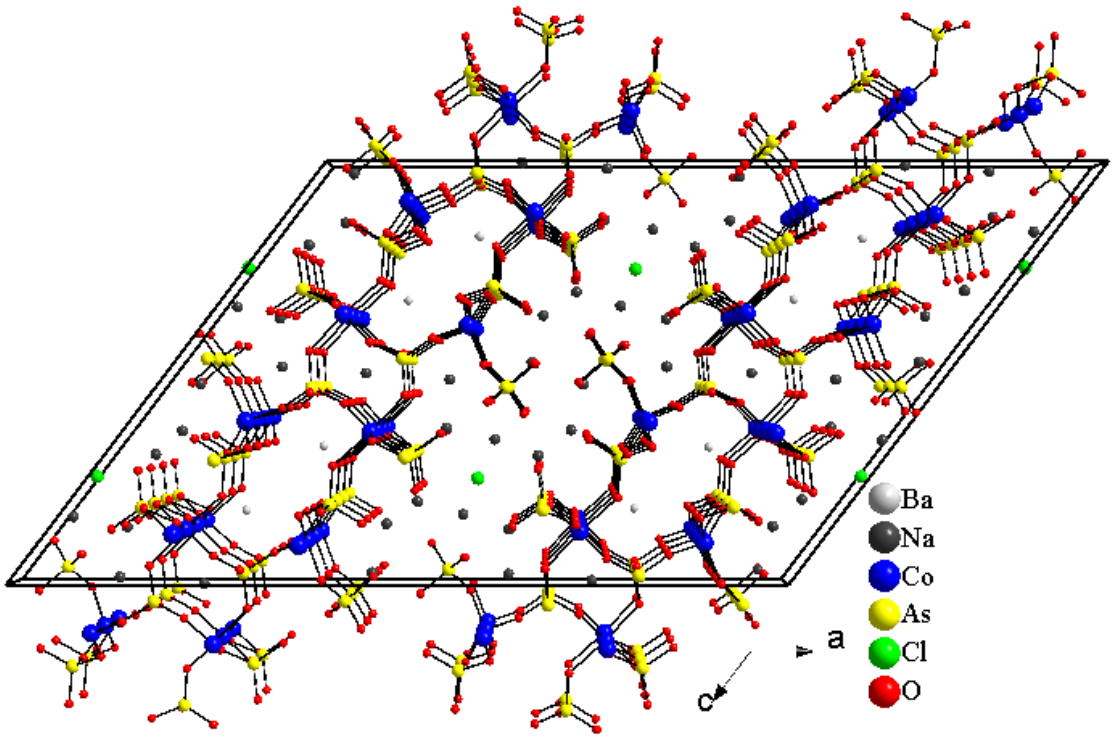

Figure I.33: Projected view showing the extended structure of $Ba_2Na_{13}Co_4(AsO_4)_8Cl$.

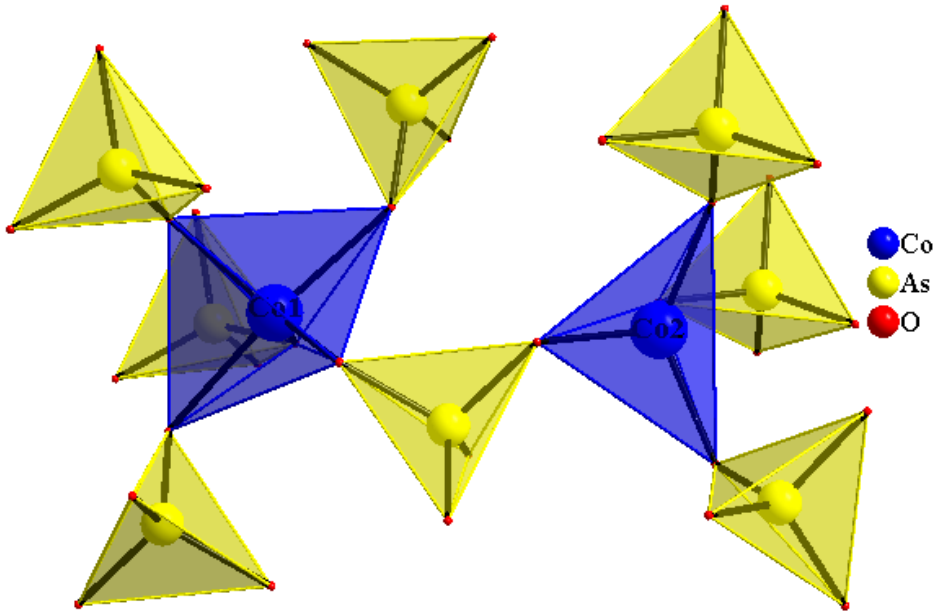

Figure I.34: Polyhedral view showing the coordination around the two crystallographically distinct Co^{2+} cations.

while the smaller channel consists of two AsO_4 polyhedra and $Co(1)O_5$ trigonal bipyramids.

$CsKCo_2(AsO_4)_2$

This new mixed polyhedral framework was synthesized using high-temeperature molten salt methods. Single crystals of $CsKCo_2(AsO_4)_2$ were grown using KO_2, CoO, and As_2O_5 in a 1:4:1.5 mol ratio. The reactants were mixed in a CsCl/KCl eutectic flux equal to three times the mass of the oxide reactants. The reaction was heated to 300°C at a rate of 1°C/minute, held there for 6 hours, heated to 450°C at 0.25°C/minute, held there for 6 hours, heated to 750°C at 2°C/minute, held there for 60 hours, slowly cooled to 450°C at 0.1°C/minute, and then furnace cooled to room temperature. After washing the reaction with deionized water dark blue single crystals of the title compound were isolated. The crystallographic data and atomic parameters are shown in Tables I.25 and I.26.

The extended structure of $CsKCo_2(AsO_4)_2$ can be seen in Figure I.35. The structure consists of four crystallographically distinct Co polyhedra, all of which are in a 2+ oxidation state and tetrahedrally coordinated by O^{2-} anions. The structure contains multidirectional channels. Looking along the *b* direction, there are two different channels. The first, shown in Figure I.36 (left), has an 8-membered ring window and that consists of four $Co(1\text{-}4)O_4$ and four AsO_4 tetrahedra and contains K^+ cations. The second channel, shown in Figure I.36 (right) consists of two $Co(1)O_4$, two $Co(2)O_4$, and four AsO_4 tetrahedra and contains Cs^+ cations. Looking along the crystallographic *c* axis, 6-

Table I.25: Crystallographic data of $CsKCo_2(AsO_4)_2$

empirical formula	$CsKCo_2(AsO_4)_2$
color/shape	Blue plate
crystal size (mm)	0.15 × 0.12 × 0.03
formula weight (amu)	567.71
space group, *Z*	$P\,2_1$ (no. 4), 2
T°C	25
a, Å	8.778(2)
b, Å	5.601(1)
c, Å	18.362(4)
β, °	90.36(3)
V, $Å^3$	902.8(3)
linear abs. coeff., mm^{-1}	15.397
F_{000}	1032
d_{calc}, g / cm^{-3}	4.177
data/restraints/parameters	3144 / 0 / 254
secondary extinction	---------
reflections collected / unique / R_{int} [a]	7618 / 3144 / 0.0620
final R1/wR2 [b] [$I > 2\,\sigma(I)$]	0.0431 / 0.1128
R1/wR2 (all data)	0.0575 / 0.1198
GOF	1.072
Largest difference peak / hole (e^- / $Å^3$)	1.178 / -1.732

[a] $R_{int} = \Sigma \mid F_o^2 - F_o^2\,(\text{mean}) \mid / \Sigma[F_o^2]$; **1** [b] $wR2 = \{[\Sigma[w(F_o^2 - F_c^2)^2] / [\Sigma w(F_o)^2)^2]\}^{1/2}$; $w = 1 / [\sigma^2(F_o^2) + (0.0567P)^2 + 6.0581P]$ where $P = (F_o^2 + 2F_c^2)/3$

Table I.26: Atomic parameters $Cs_2K_2Co_4(AsO_4)_4$

Atom	Wyckoff notation	sof	x	y	z
Cs1	2*a*	1.0	0.1660(2)	0.8478(4)	0.50327(9)
Cs2	2*a*	1.0	0.1687(2)	0.8167(5)	0.00284(9)
K1	2*a*	1.0	0.6703(6)	0.319(2)	0.2510(3)
K2	2*a*	1.0	0.3292(5)	0.835(2)	0.2499(3)
Co1	2*a*	1.0	0.4272(3)	0.3492(8)	0.4154(2)
Co2	2*a*	1.0	-0.0994(3)	0.7799(8)	0.3312(2)
Co3	2*a*	1.0	-0.4272(3)	0.8149(9)	0.0842(2)
Co4	2*a*	1.0	0.1010(3)	0.3765(9)	0.1708(2)
As1	2*a*	1.0	0.1049(2)	0.2844(7)	0.3379(1)
As2	2*a*	1.0	0.5765(2)	0.8291(5)	0.4041(1)
As3	2*a*	1.0	-0.1069(2)	0.8740(7)	0.1613(1)
As4	2*a*	1.0	-0.5763(2)	0.3355(6)	0.0961(1)
O1	2*a*	1.0	-0.057(2)	0.435(4)	0.3343(9)
O2	2*a*	1.0	0.205(2)	0.340(5)	0.2637(8)
O3	2*a*	1.0	0.076(2)	-0.008(4)	0.3465(9)
O4	2*a*	1.0	0.208(2)	0.376(4)	0.4112(9)
O5	2*a*	1.0	-0.212(2)	0.828(5)	0.2387(9)
O6	2*a*	1.0	0.767(2)	0.882(4)	0.4115(9)
O7	2*a*	1.0	-0.496(2)	0.902(3)	-0.0119(9)
O8	2*a*	1.0	-0.200(2)	0.783(5)	0.0871(8)
O9	2*a*	1.0	-0.535(2)	0.580(4)	0.1439(9)
O10	2*a*	1.0	-0.499(3)	1.100(4)	0.137(1)
O11	2*a*	1.0	0.503(2)	0.280(4)	0.5155(8)
O12	2*a*	1.0	0.544(2)	0.576(4)	0.3546(9)
O13	2*a*	1.0	0.490(1)	0.058(3)	0.3609(7)
O14	2*a*	1.0	0.065(2)	0.727(5)	0.164(1)
O15	2*a*	1.0	-0.079(2)	1.176(4)	0.155(1)
O16	2*a*	1.0	-0.764(1)	0.303(3)	0.0901(8)

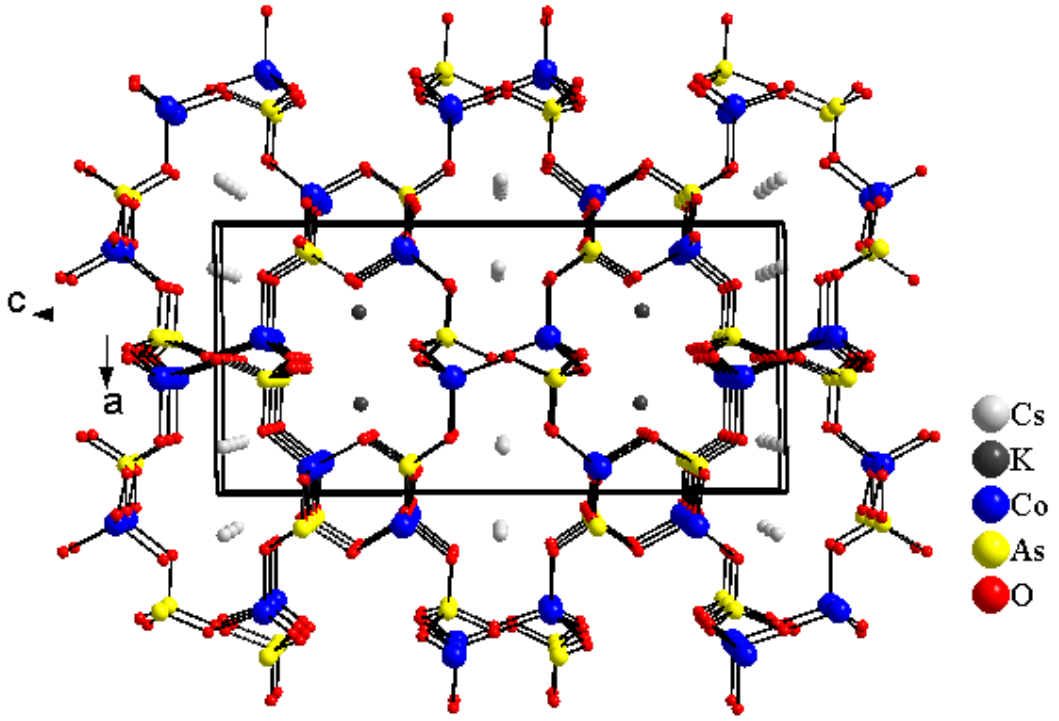

Figure I.35: Projected view showing the extended structure of $CsKCo_2(AsO_4)_2$.

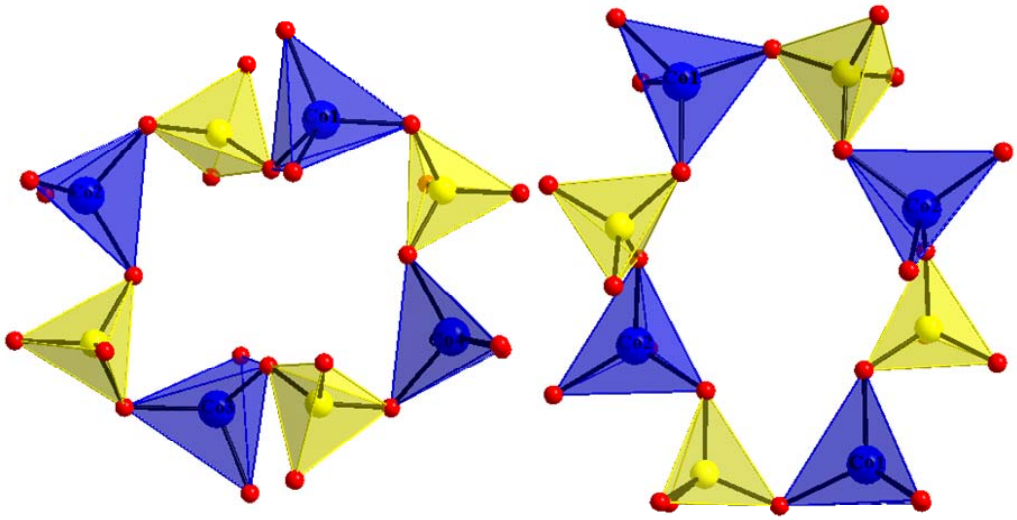

Figure I.36: Polyhedral view showing a close-up view of the two channels found in $CsKCo_2(AsO_4)_2$.

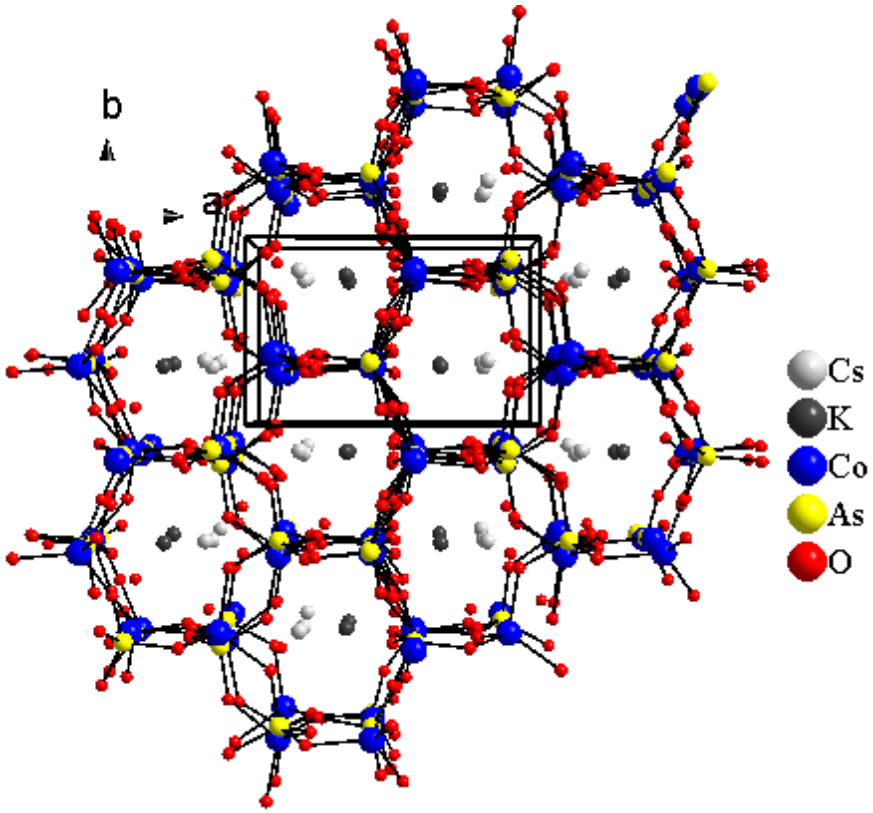

Figure I.37: Projected view showing the extended structure of $CsKCo_2(AsO_4)_2$ along *c*.

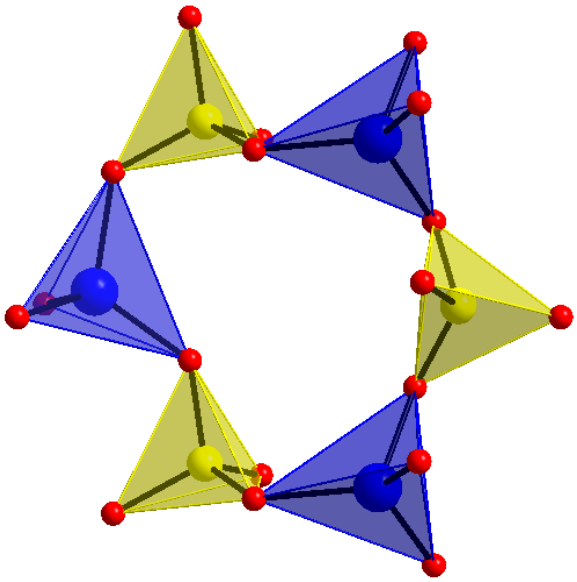

Figure I.38: Polyhedral view showing a close-up view of the 6-membered channel that runs along the *c* axis.

membered ring windows can be seen, Figure I.37. The windows consist of one $Co(1)O_4$, two $Co(2)O_4$, and three AsO_4 tetrahedra, Figure I.38

$BaNa_2Co(PO_4)_2$

This new mixed polyhedral framework was synthesized using high-temeperature molten salt methods. Single crystals of $BaNa_2Co(PO_4)_2$ were grown using BaO, CoO, and P_4O_{10} in a 1:3:0.5 mol ratio. The reactants were ground in a CsCl/NaCl eutectic flux and then heated to 500°C at 0.5°C/minute, held there for 6 hours, heated to 675°C at 0.5°C/minute, held there for 4 days, slowly cooled to 450°C at 0.1°C/minute, and then furnace cooled to room temperature. The crystallographic data and atomic parameters are shown in Tables I.27 and I.28.

The extended structure of $BaNa_2Co(PO_4)_2$ is shown in Figure I.39. It contains a single crystallographically distinct Co^{2+} cation octahedrally coordinated by O^{2-}. The structure is layered and consists of $[Co(PO_4)_2]_\infty$ slabs. Ba^{2+} and Na+ cations are located between the slabs. Within the slab, Figure I.40, each CoO_6 octhahedron is connected to 6 surrounding PO_4 oxyanions.

Table I.27: Crystallographic data of $BaNa_2Co(PO_4)_2$

empirical formula	$BaNa_2Co(PO_4)_2$
color/shape	Purple plate
crystal size (mm)	0.11 × 0.09 × 0.03
formula weight (amu)	432.18
space group, *Z*	*P*-3*m* (no. 164), 1
T°C	25
a, Å	5.3140(8)
c, Å	7.000(1)
V, Å^3	171.18(5)
linear abs. coeff., mm^{-1}	8.746
F_{000}	199
d_{calc}, g / cm^{-3}	4.192
data/restraints/parameters	141 / 0 / 21
secondary extinction	-----
reflections collected / unique / R_{int}[a]	1476 / 141 / 0.0808
final R1/wR2 [b] [$I > 2\ \sigma(I)$]	0.0265 / 0.0709
R1/wR2 (all data)	0.0278 / 0.0714
GOF	1.289
Largest difference peak / hole (e$^-$ / Å^3)	0.607 / -0.858

[a] $R_{int} = \Sigma \mid F_o^2 - F_o^2\ (\text{mean}) \mid / \Sigma[F_o^2]$; **1** [b] $wR2 = \{[\Sigma[w(F_o^2 - F_c^2)^2] / [\Sigma w(F_o)^2)^2]\}^{1/2}$; $w = 1 / [\sigma^2(F_O^2) + (0.0183P)^2 + 2.4512P]$ where $P = (F_O^2 + 2F_C^2)/3$

Table I.28: Atomic parameters $BaNa_2Co(PO_4)_2$

Atom	Wyckoff notation	sof	x	y	z
Ba	1*a*	1.0	0	0	0
Na	2*d*	1.0	1/3	2/3	0.322(1)
Co	1*b*	1.0	0	0	1/2
P	2*d*	1.0	2/3	1/3	0.2419(5)
O1	6*i*	1.0	0.359(2)	0.1794(8)	0.318(1)
O2	2*d*	1.0	2/3	1/3	0.026(1)

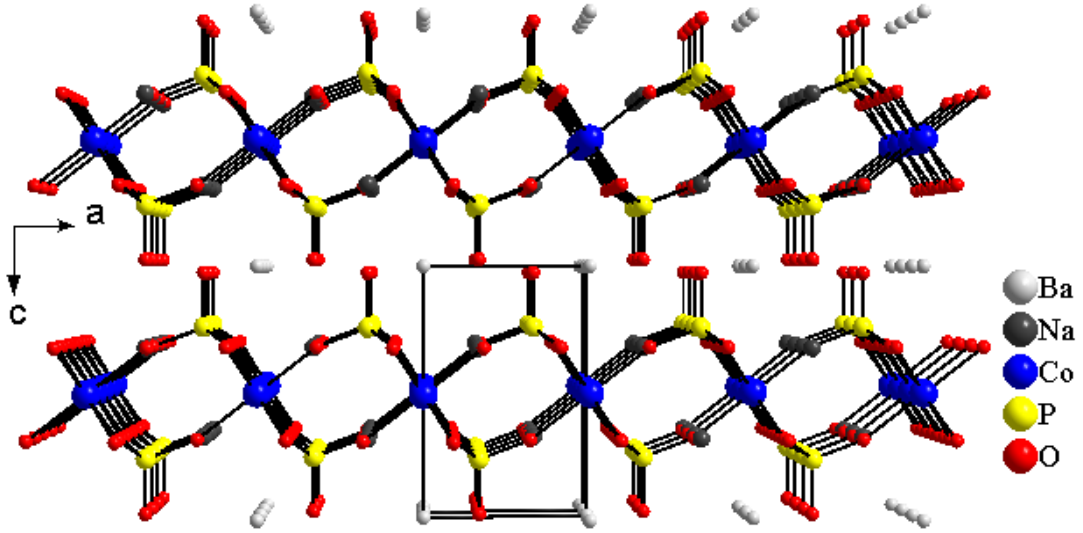

Figure I.39: Projected view showing the extended structure of $BaNa_2Co(PO_4)_2$ along *b*.

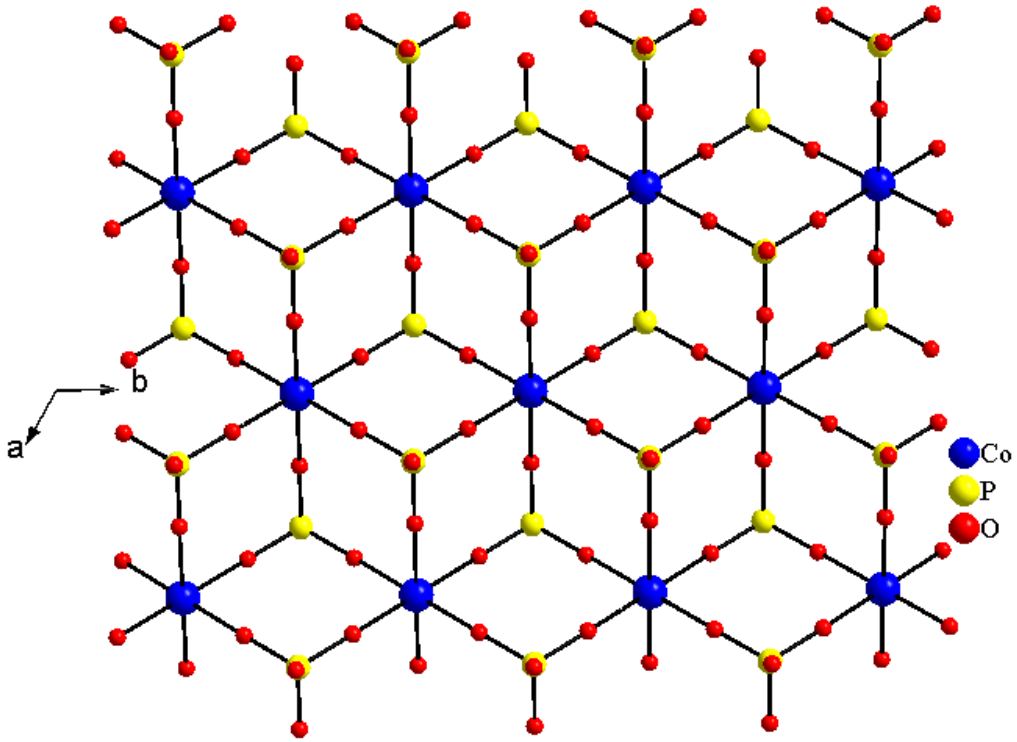

Figure I.40: View of the $[Co(PO_4)_2]_\infty$ slab.

$Cs_3ClCo_3(P_2O_7)_2$

This new mixed polyhedral framework was synthesized using high-temeperature molten salt methods. Single crystals of $Cs_3ClCo_3(P_2O_7)_2$ were grown using BaO, CoO, P_4O_{10} and CsCl in a 1:3:1:2 mol ratio. The reaction was heated to 450°C at 1°C/minute, held there for 6 hours, heated to 800°C, held there for 4 days, slowly cooled to 450°C at 0.1°C/minute, and then furnace cooled to room temperature. After washing the product with deionized water, blue column-like crystals of the title phase was isolated. The crystallographic data and atomic parameters can be seen in Tables I.29 and I.30.

The extended structure of $Cs_3ClCo_3(P_2O_7)_2$ can be seen in Figure I.41. There are two crystallographically distinct Co^{2+} polyedra. The first, Co(1), is in a square pyramidal geometry with four equatorial O^{2-} anions and one axial Cl^- anion. The second, Co(2), is tetrahedrally coordinated by surroudning O^{2-} anions. The 3-D structure has channels made of Cs^+ containing 8-membered ring windows that consists of two $Co(1)O_4Cl$ square pyramids, two $Co(2)O_4$ tetrahedra, and four $(AsO_4)^{3-}$ oxyanions. Figure I.42 shows the connectivity between Co(1,2) polyhedra and PO_4 oxyanions.

Table I.29: Crystallographic data of $Cs_3ClCo_3(P_2O_7)_2$

empirical formula	$Cs_3ClCo_3(P_2O_7)_2$
color/shape	Blue column
crystal size (mm)	0.1 × 0.04 × 0.04
formula weight (amu)	958.85
space group, *Z*	*Cmca* (no. 64), 8
T, °C	25
a, Å	19.261(4)
b, Å	13.289(3)
c, Å	13.761(3)
V, Å^3	3522(1)
linear abs. coeff., mm^{-1}	9.481
F_{000}	3480
d_{calc}, g / cm^{-3}	3.616
data/restraints/parameters	1610 / 0 / 118
secondary extinction	--------
reflections collected / unique / R_{int} [a]	14142 / 1610 / 0.0727
final R1/wR2 [b] [$I > 2\ \sigma(I)$]	0.0413 / 0.0795
R1/wR2 (all data)	0.0491 / 0.0824
GOF	1.201
Largest difference peak / hole (e$^-$ / Å^3)	0.717 / -0.984

[a] $R_{int} = \Sigma\ |\ F_O^2 - F_O^2\ (\text{mean})\ |\ /\ \Sigma[\ F_O^2\ ]$; **1** [b] $wR2 = \{[\Sigma[w(F_O^2 - F_C^2)^2] / [\Sigma w(F_O)^2)^2]\}^{1/2}$; $w = 1 / [\sigma^2(F_O^2) + (0.0314P)^2 + 40.3462P]$ where $P = (F_O^2 + 2F_C^2)/3$

Table I.30: Atomic parameters $Cs_3ClCo_3(P_2O_7)_2$

Atom	Wyckoff notation	sof	x	y	z
Cs1	8*f*	1.0	1/2	0.06406(5)	0.64971(5)
Cs2	16*g*	1.0	0.34994(3)	0.36393(4)	0.60115(4)
Co1	8*f*	1.0	1/2	0.25489(9)	0.8785(1)
Co2	16*g*	1.0	0.20319(5)	0.42367(7)	0.37128(7)
P1	16*g*	1.0	0.35221(9)	0.1392(1)	0.4151(1)
P2	16*g*	1.0	0.35417(9)	0.3402(1)	0.3195(1)
Cl	8*f*	1.0	1/2	0.3296(2)	0.7215(2)
O1	16*g*	1.0	0.3038(2)	0.4198(3)	0.3568(4)
O2	16*g*	1.0	0.4251(3)	0.3535(3)	0.3621(4)
O3	16*g*	1.0	0.3530(2)	0.3352(4)	0.2093(4)
O4	16*g*	1.0	0.4263(3)	0.1594(4)	0.4455(4)
O5	16*g*	1.0	0.3235(3)	0.2330(4)	0.3540(4)
O6	16*g*	1.0	0.3023(3)	0.1323(4)	0.4988(4)
O7	16*g*	1.0	0.3444(3)	0.0505(4)	0.3474(4)

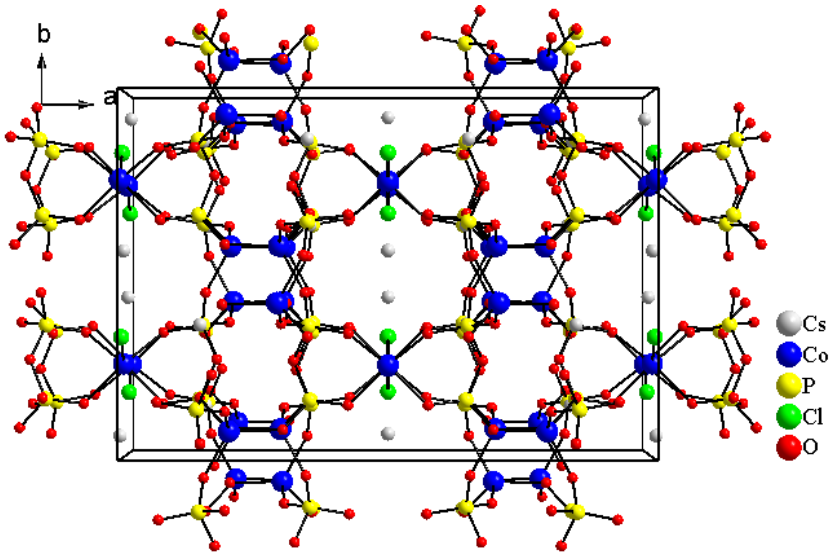

Figure I.41: Projected view showing the extended structure of $Cs_3ClCo_3(P_2O_7)_2$ along *c*.

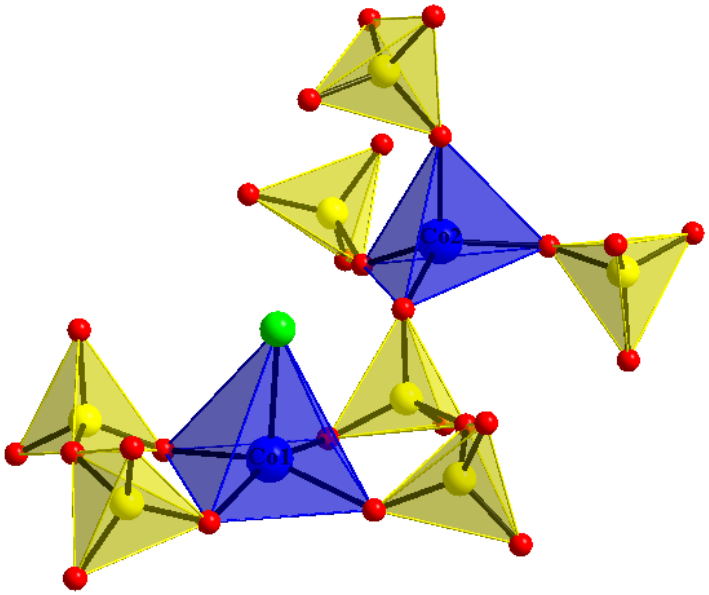

Figure I.42: Polyhedral view showing the connectivity around the Co^{2+} polyhedra.

$CsNaM(P_2O_7)$ M = Fe, Co, or Cu

These new mixed polyhedral frameworks were synthesized using high-temperature molten salt methods. Single crystals of the Fe analog were grown using FeO and P_4O_{10} in a 7:1.5 mol ratio. The reactants were ground in a CsCl/NaCl eutectic flux equal to three times the mass of the oxide reactants. The reaction was heated to 500°C at 1°C/ minute, held there for 12 hours, heated to 650°C at 1°C/minute, held there for 4 days, slowly cooled to 0.1°C/minute, slowly cooled to 450°C at 0.1°C/minute, and then furnace cooled to room temperature. Single crystals of the Co analog were grown using Na_2O_2, CoO, P_4O_{10}, and CsCl in a 3:7:1.5:2 mol ratio. The reaction was heated to 450°C at 1°C/minute, held there for 6 hours, heated to 800°C at 1°C/minute, held there for 3 days, slowly cooled to 500°C at 0.1°C/minute, and then furnace cooled to room temperature. The Cu containing compound was synthesized using CuO and P_4O_{10} in a 7:1.5 mol ratio. The reactants were then placed in a CsCl/NaCl flux equal to three times the mass of the oxide reactants. The reaction was heated to 500°C at 1°C/minute, held there for 12 hours, heated to 675°C at 1°C/minute, held there for 4 days, slowly cooled to 450°C at 0.1°C/minute, held there for 1 day, and then furnace cooled to room temperature. The crystallographic data and the atomic parameters are shown in Table I.31 and I.32.

Figure I.43 and I.44 show the extended structures of $CsNaCu(P_2O_7)$ and $CsNaFe(P_2O_7)$ respectively. Both contain $[MP_2O_7]_\infty$ slabs that include M^{2+} cations found in a square pyramidal geometry. Cs^+ and Na^+ cations occupy the interslab space. Each

Table I.31: Crystallographic data of $CsNaM(P_2O_7)$ where M = Fe, Co, or Cu

empirical formula	$CsNaFe(P_2O_7)$	$CsNaCo(P_2O_7)$	$CsNaCu(P_2O_7)$
color/shape	Colorless column	Blue chunk	Light blue column
crystal size (mm)	0.1 × 0.03 × 0.03	0.2 × 0.13 × 0.11	0.15 × 0.03 × 0.03
formula weight (amu)	385.69	388.77	393.38
space group, *Z*	*Cc* (no. 9), 4	*P* $2_1/n$ (no. 14), 4	*Cmc*2_1 (no. 36), 4
T°C		25	
a, Å	10.476(2)	7.393(2)	5.132(1)
b, Å	30.410(6)	7.688(2)	15.164(3)
c, Å	11.023(2)	12.961(3)	9.580(2)
β, °	118.373(7)	91.01(3)	------
V, Å^3	3090(1)	736.6(3)	745.5(3)
linear abs. coeff., mm^{-1}	7.060	7.686	8.222
F_{000}	2847	716	724
d_{calc}, g / cm^{-3}	3.317	3.506	3.505
data/restraints/parameters	5067 / 2 / 434	1294 / 0 / 110	735 / 0 / 71
secondary extinction	0.00158(7)	0.0040(4)	0.017(1)
flack parameter	0.03(3)	-------	-0.02(3)
reflections collected / unique / R_{int} [a]	13067 / 5067 / 0.0347	6014 / 1294 / 0.0503	3082 / 735 / 0.0485
final R1/wR2 [b] [$I > 2\ \sigma(I)$]	0.0585 / 0.1403	0.0282 / 0.0619	0.0262 / 0.0672
R1/wR2 (all data)	0.0593 / 0.1407	0.0384 / 0.0655	0.0262 / 0.0672
GOF	1.182	1.066	1.049
Largest difference peak / hole (e^- / Å^3)	2.262 / -2.003	0.634 / -0.830	0.656 / -1.664

[a] $R_{int} = \Sigma \mid F_O^2 - F_O^2\ (mean) \mid / \Sigma[F_O^2]$; [b] **1**;*w*R2 = $\{[\Sigma[w(F_O^2-F_C^2)^2] / [\Sigma w(F_O)^2)^2]\}^{1/2}$; $w = 1 / [\sigma^2(F_O^2) + (0.0000P)^2 + 260.2386P]$ where $P = (F_O^2 + 2F_C^2)/3$; **2**; *w*R2 = $\{[\Sigma[w(F_O^2-F_C^2)^2] / [\Sigma w(F_O)^2)^2]\}^{1/2}$; $w = 1 / [\sigma^2(F_O^2) + (0.0364P)^2 + 0.6623P]$ where $P = (F_O^2 + 2F_C^2)/3$; **3**; *w*R2 = $\{[\Sigma[w(F_O^2-F_C^2)^2] / [\Sigma w(F_O)^2)^2]\}^{1/2}$; $w = 1 / [\sigma^2(F_O^2) + (0.0472P)^2 + 3.2279P]$ where $P = (F_O^2 + 2F_C^2)/3$

Table I.32: Atomic parameters $CsNaM(P_2O_7)$, where M = Fe, Co, or Cu

Atom	Wyckoff notation	sof	x	y	z
			$CsNaFe(P_2O_7)$		
Cs1	4*a*	1.0	0.0048(1)	0.07709(4)	0.7522(1)
Cs2	4*a*	1.0	0.2396(1)	0.17339(4)	0.2590(1)
Cs3	4*a*	1.0	0.5283(1)	0.08004(4)	0.7841(1)
Cs4	4*a*	1.0	0.7541(2)	0.16749(5)	0.2872(1)
Na1	4*a*	1.0	0.3328(8)	0.1939(2)	0.9362(7)
Na2	4*a*	1.0	0.5886(8)	0.0534(2)	0.4300(7)
Na3	4*a*	1.0	0.3284(8)	0.3014(3)	0.4331(8)
Na4	4*a*	1.0	0.1130(9)	0.0535(2)	0.4407(9)
Fe1	4*a*	1.0	0.2062(3)	0.03308(7)	0.1858(3)
Fe2	4*a*	1.0	0.7007(3)	0.03427(8)	0.1536(3)
Fe3	4*a*	1.0	0.4753(3)	0.21624(8)	0.6927(3)
Fe4	4*a*	1.0	0.9498(3)	0.21612(8)	0.6581(2)
P1	4*a*	1.0	0.4267(5)	0.0938(2)	0.1398(5)
P2	4*a*	1.0	0.3623(5)	0.0120(1)	0.0035(4)
P3	4*a*	1.0	-0.0738(5)	0.0950(2)	0.1118(5)
P4	4*a*	1.0	-0.1217(5)	0.0124(1)	-0.0303(4)
P5	4*a*	1.0	0.5878(5)	0.2372(1)	0.4737(4)
P6	4*a*	1.0	0.1419(6)	0.2401(2)	0.5137(5)
P7	4*a*	1.0	0.6820(5)	0.1545(1)	0.6127(5)
P8	4*a*	1.0	0.2056(5)	0.1568(2)	0.6456(5)
O1	4*a*	1.0	0.417(1)	0.1398(4)	0.096(1)
O2	4*a*	1.0	0.342(2)	0.0827(4)	0.216(1)
O3	4*a*	1.0	0.351(1)	0.0644(3)	-0.002(1)
O4	4*a*	1.0	0.582(1)	0.0763(4)	0.220(1)
O5	4*a*	1.0	0.334(1)	-0.0037(4)	0.120(1)
O6	4*a*	1.0	0.244(1)	-0.0026(4)	-0.135(1)
O7	4*a*	1.0	0.515(1)	0.0016(4)	0.028(2)
O8	4*a*	1.0	0.066(1)	0.0761(4)	0.223(1)
O9	4*a*	1.0	-0.117(1)	0.0646(5)	-0.030(1)
O10	4*a*	1.0	-0.200(2)	0.0885(5)	0.142(2)
O11	4*a*	1.0	-0.067(2)	0.1404(5)	0.0700(2)
O12	4*a*	1.0	-0.215(2)	-0.0019(4)	0.030(1)
O13	4*a*	1.0	0.033(1)	-0.0046(4)	0.050(2)
O14	4*a*	1.0	-0.183(2)	0.0024(6)	-0.184(1)
O15	4*a*	1.0	0.741(2)	0.2516(4)	0.527(1)
O16	4*a*	1.0	0.587(2)	0.1838(4)	0.473(1)
O17	4*a*	1.0	0.515(1)	0.2524(5)	0.556(2)
O18	4*a*	1.0	0.493(2)	0.2484(5)	0.323(2)
O19	4*a*	1.0	0.286(1)	0.2553(4)	0.632(1)

Table I.32: Atomic parameters $CsNaM(P_2O_7)$, where M = Fe, Co, or Cu cont…

Atom	Wyckoff notation	sof	x	y	z
O20	4*a*	1.0	0.620(1)	0.2460(5)	0.876(1)
O21	4*a*	1.0	0.012(1)	0.2512(5)	0.534(2)
O22	4*a*	1.0	0.143(1)	0.1878(4)	0.506(1)
O23	4*a*	1.0	0.838(2)	0.1628(5)	0.649(2)
O24	4*a*	1.0	0.634(2)	0.1076(4)	0.577(2)
O25	4*a*	1.0	0.648(1)	0.1726(4)	0.723(1)
O26	4*a*	1.0	0.370(1)	0.1676(5)	0.731(2)
O27	4*a*	1.0	0.174(2)	0.1105(4)	0.594(2)
O28	4*a*	1.0	0.134(1)	0.1738(4)	0.726(1)
			$CsNaCo(P_2O_7)$		
Cs	4*e*	1.0	0.09582(5)	0.27848(4)	0.39449(3)
Co	4*e*	1.0	-0.15807(9)	0.51591(9)	0.12389(6)
P1	4*e*	1.0	0.0335(2)	0.2268(2)	0.7044(1)
P2	4*e*	1.0	0.1814(2)	0.2806(2)	0.0900(1)
Na	4*e*	1.0	0.3819(3)	0.4831(3)	0.6147(2)
O1	4*e*	1.0	0.1023(5)	0.3617(5)	0.6329(3)
O2	4*e*	1.0	0.1114(5)	0.0445(5)	0.6904(3)
O3	4*e*	1.0	0.3189(4)	0.2956(5)	0.1883(3)
O4	4*e*	1.0	-0.0017(5)	0.3149(5)	0.1392(3)
O5	4*e*	1.0	0.1882(5)	0.1017(5)	0.0459(3)
O6	4*e*	1.0	0.0494(5)	0.2725(5)	0.8190(3)
O7	4*e*	1.0	0.2368(5)	0.4262(5)	0.0171(3)
			$CsNaCu(P_2O_7)$		
Cs	4*a*	1.0	0	-0.09420(3)	-0.42850(6)
Cu	4*a*	1.0	0	-0.17737(6)	-0.0380(1)
Na	4*a*	1.0	0	-0.3549(3)	-0.2735(5)
P1	4*a*	1.0	1/2	0.0594(1)	-0.5677(2)
P2	4*a*	1.0	0	-0.2762(1)	-0.7078(2)
O1	8*b*	1.0	-0.241(2)	-0.2500(4)	-0.637(1)
O2	4*a*	1.0	1/2	-0.0346(4)	-0.6118(7)
O3	8*b*	1.0	0.261(1)	0.0885(3)	-0.4872(5)
O4	8*b*	0.5	-0.088(2)	-0.2474(6)	-0.8524(9)
O5	4*a*	1.0	0	-0.3826(4)	-0.7121(6)

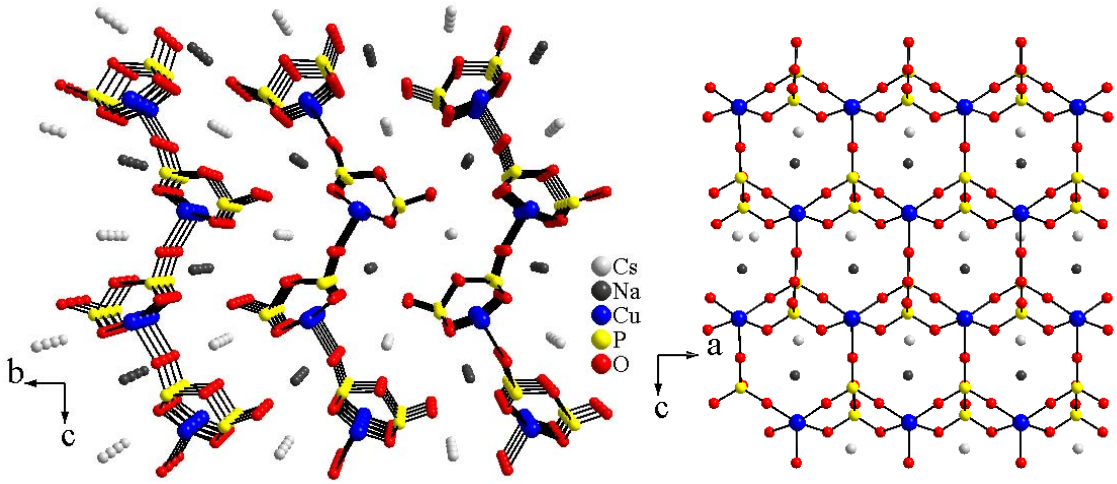

Figure I.43: Projected view showing the extended structure of $CsNaCu(P_2O_7)$ along *a*. The view on the right shows a projected view of the $[Cu(P_2O_7)]_\infty$ slab.

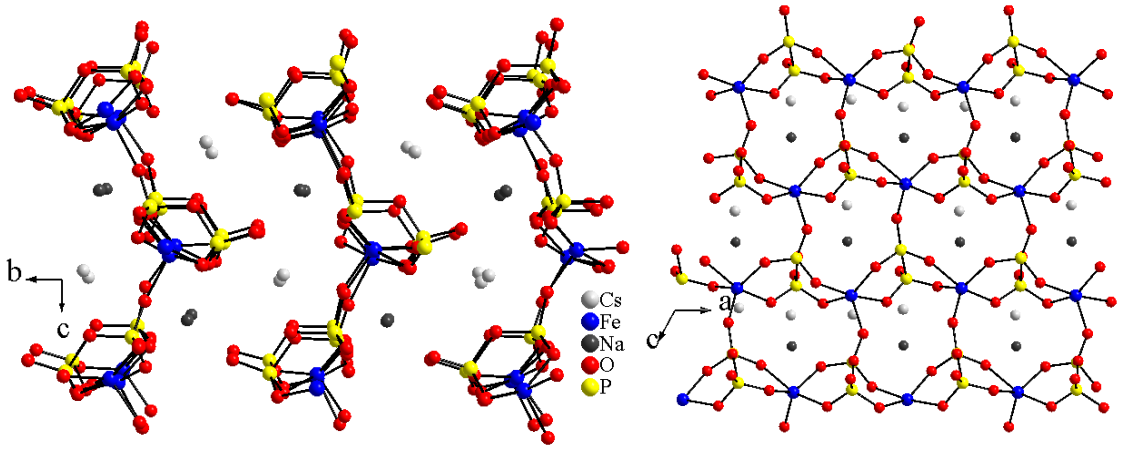

Figure I.44: Projected view showing the extended structure of $CsNaFe(P_2O_7)$ (left). The view on the right shows a projected view of the $[Fe(P_2O_7)]_\infty$ slab.

MO_5 polyhedron is linked to five surrounding PO_4 oxyanions structurally confining the metal cations from one another. The apical oxygen of the MO_5 polyedra point in a unique direction giving rise to a noncentrosymmetric crystal structure. The equatorial oxygen have bond angles ranging from 93.2(6) to 108.7(6)° in the Fe analog, where as those same angles in the Cu derivative range form 96.62(1) to 98.03(1)°. It is thought these slight differences in the coordination environments of the MO_5 polyhedra causes the lower symmetry observed in the Fe derivative.

Despite the similarities in their chemical formulas the Co derivative, $CsNaCo(P_2O_7)$ forms a completely different structure. This structure forms a nonlayered 3-D framework that contains multidirectional channels along *a* and *b* seen in Figure I.45 (left) and Figure I.45 (right) respectively. Along *a* the channel is made of 13-membered ring windows that contain both Na^+ and Cs^+ cations, while along *b* the channels consist of 6-membered ring windows that contain Cs^+ cations. There is a single crystallographically distinct Co^{2+} site, which is found to be tetrahedrally coordinated by O^{2-} anions. These polyhedra share corner oxygen atoms with four neighboring PO_4 tetrahedra, shown in Figure I.46.

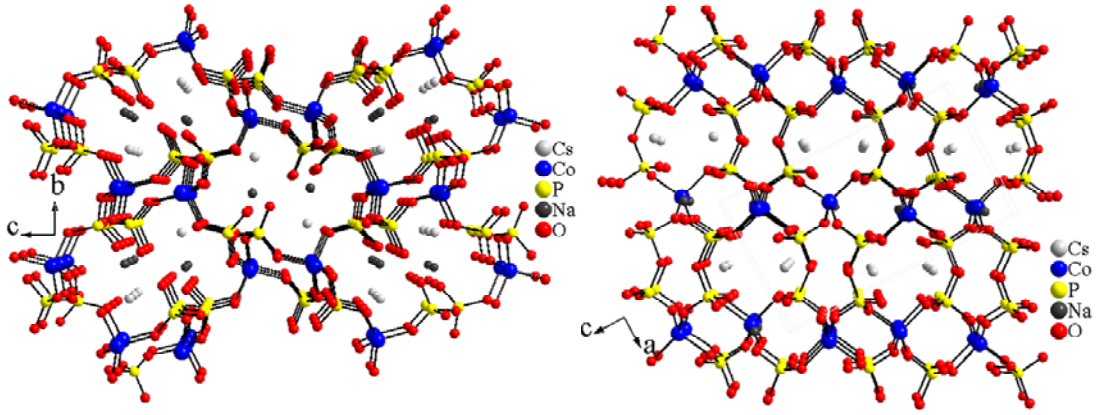

Figure I.45: Projected view showing the extended structure of $CsNaCo(P_2O_7)$ along *a* (right) and *b* (left).

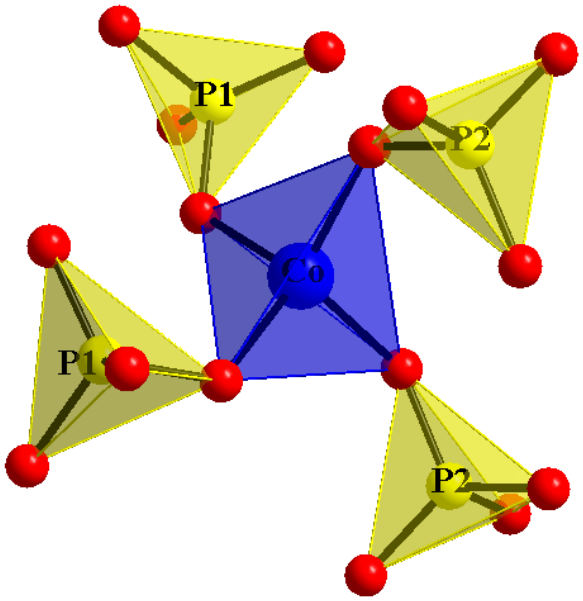

Figure I.46: Polyhedral view showing the connectivity of CoO_4 polyhedra.

$Sr_2Fe(AsO_4)_2Cl$

Single crystals of $Sr_2Fe(AsO_4)_2Cl$ were grown using high-temperature molten salt methods. SrO, Na_2O, Fe_2O_3, FeO, and As_2O_5 in a 10:2.5:3.3:0.4:7 mol ratio. The reactants were placed in a $SrCl_2$/NaCl eutectic flux equal to three times the mass of the oxide reactants. The target compound for the reaction was $Sr_{10}Na_5Fe_7O_2(AsO_4)_{14}$ (presented in Chapter 4), and it should be noted that the FeO was utilized to account for the 16 mol % Na_2O_2 impurity in Na_2O. The reaction was heated to 700°C at 3°C/minute, held there for 4 days, slowly cooled to 400°C at 0.1°C/minute, and then furnace cooled to room temeprature. Brown transparent single crystals of the title phase was isolated after washing the product with deionized water to remove excess salt. The crystallographic data and atomic parameters of the title compound can be seen in Tables I.33 and I.34.

The extended structure of $Sr_2Fe(AsO_4)_2Cl$ can be seen in Figure I.47. The compound contains $[Fe(AsO_4)_3]_\infty$, Figure I.48 (left), layers that are separated from one another by Sr^{2+} and Cl^- ions located between the slabs. There is a single crystallographically distinct Fe^{3+} site that is coordinated by surrounding O^{2-} anions. The FeO_6 octahedra share an edge with a single neighboring FeO_6 octahedron forming a dimer. The edge sharing polyhedra gives rise to Fe-Fe distances of 3.30(6)Å and Fe-O-Fe angles of 100.4(2)°. These dimers are isolated from other metal polyhedra via 6 neighboring $(AsO_4)^{3-}$ oxyanions. The polyhedral view of the dimers and their surrounding coordination can be seen in Figure I.48 (right).

Table I.33: Crystallographic data of $Sr_2Fe(AsO_4)_2Cl$

empirical formula	$Sr_2Fe(AsO_4)_2Cl$
color/shape	Brown plate
crystal size (mm)	0.17 × 0.13 × 0.11
formula weight (amu)	544.38
space group, *Z*	*C*2/*c* (no. 15), 4
T, °C	25
a, Å	6.824(1)
b, Å	19.868(4)
c, Å	13.117(3)
β, °	101.90(3)
V, Å^3	1740.1(6)
linear abs. coeff., mm^{-1}	21.731
F_{000}	1992
d_{calc}, g / cm^{-3}	4.156
data/restraints/parameters	1541 / 0 / 138
secondary extinction	0.0017(1)
reflections collected / unique / R_{int} [a]	7349 / 1541 / 0.0651
final R1/wR2 [b] [$I > 2\ \sigma(I)$]	0.0324 / 0.0792
R1/wR2 (all data)	0.0351 / 0.0812
GOF	1.052
Largest difference peak / hole (e$^-$ / Å^3)	1.331 / -1.228

[a] $R_{int} = \Sigma \mid F_O^2 - F_O^2\ (\text{mean}) \mid / \Sigma[F_O^2]$; **1** [b] $wR2 = \{[\Sigma[w(F_O^2 - F_C^2)^2] / [\Sigma w(F_O)^2)^2]\}^{1/2}$; $w = 1 / [\sigma^2(F_O^2) + (0.0512P)^2 + 0.0000P]$ where $P = (F_O^2 + 2F_C^2)/3$

Table I.34: Atomic parameters $Sr_2Fe(AsO_4)_2Cl$

Atom	Wyckoff notation	sof	x	y	z
Sr1	8*f*	1.0	0.06781(8)	0.16866(3)	0.47674(5)
Sr2	4*e*	1.0	1/2	-0.13316(4)	3/4
Sr3	4*e*	1.0	1/2	0.16373(4)	3/4
Fe	8*f*	1.0	0.6942(1)	-0.00534(4)	0.59829(6)
As1	8*f*	1.0	0.19838(8)	0.01352(3)	0.63742(4)
As2	8*f*	1.0	0.44701(7)	-0.14098(3)	0.49305(4)
Cl1	8*f*	0.5	0.0754(5)	0.1884(2)	0.2576(2)
Cl2	8*f*	0.5	0.5890(5)	-0.2668(2)	0.6980(3)
O1	8*f*	1.0	0.3595(6)	-0.0109(2)	0.5598(3)
O2	8*f*	1.0	0.6446(5)	-0.1034(2)	0.5751(3)
O3	8*f*	1.0	0.5543(5)	-0.2057(2)	0.4430(3)
O4	8*f*	1.0	0.2962(6)	-0.0211(2)	0.7546(3)
O5	8*f*	1.0	0.3439(6)	-0.0929(2)	0.3887(3)
O6	8*f*	1.0	-0.0260(5)	-0.0246(2)	0.5970(3)
O7	8*f*	1.0	0.1922(6)	0.0969(2)	0.6394(3)
O8	8*f*	1.0	0.2891(6)	-0.1620(2)	0.5688(3)

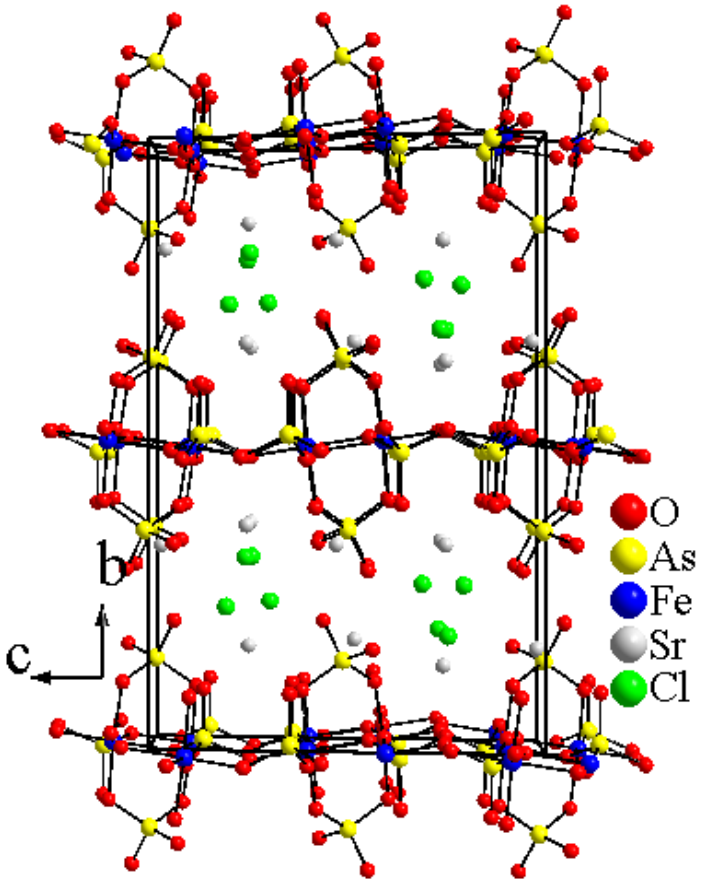

Figure I.47: Projected view showing the extended structure of $Sr_2Fe(AsO_4)_2Cl$. Sr^{2+} and Cl^- ions are found in the space between the slabs.

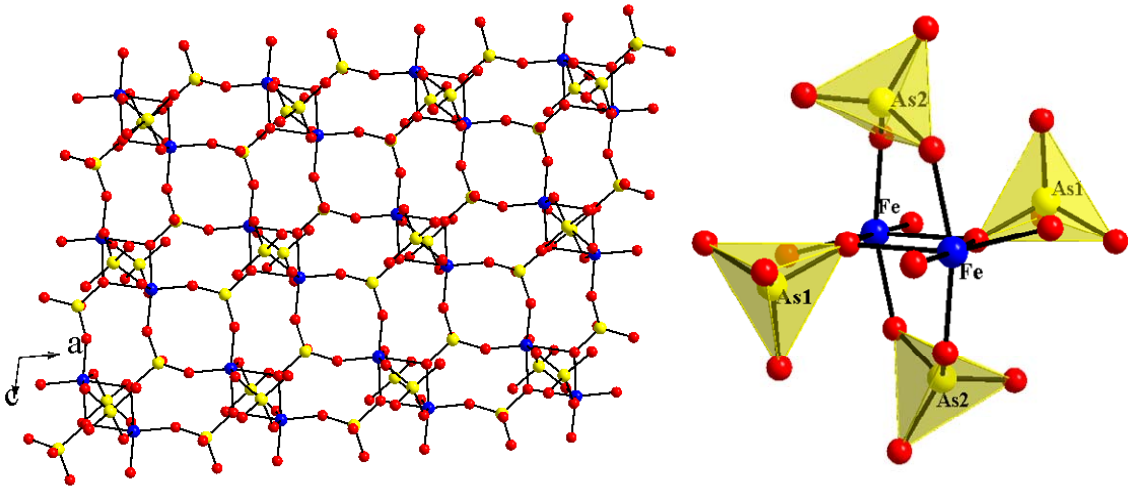

Figure I.48: Projected view showing the $[Fe(AsO_4)_2]_\infty$ slabs (left). The polyhedral view on the right shows the connectivity of the FeO_6 polyhedra, which share an edge forming dimers that are structurally isolated *via* AsO_4 polyhedra.

$Ba_{1.25}Na_{3.25}Cu_3(AsO_4)_4$

Single crystals of $Ba_{1.25}Na_{3.25}Cu_3(AsO_4)_4$ were grown using high-temperature molten salt methods. BaO, Na_2O_2, CuO, and As_2O_5 in a 1:4:6:3 mol ratio. The reactants were added to a RbCl/NaCl eutectic flux equal to five times the mass of the oxide reactants. The reaction was heated to 300°C at 0.5°C/minute, held there for 6 hours, heated to 450°C at 0.5°C/minute, held there for 6 hours, heated to 690°C at 1°C/minute, held there for 40 hours, slowly cooled to 450°C at 0.1°C/minute, and then furnace cooled to room temperature. Mint green single crystals of the title compound were isolated after washing the product with deionized water to remove the salt. The crystallographic data and atomic parameters can be seen in Tables I.35 and I.36.

Figure I.49 shows a projected view of the layered structure of $Ba_{1.25}Na_{3.25}Cu_3(AsO_4)_4$. The material contains $[Cu_3(AsO_4)_4]_\infty$ slabs that are isolated from one another *via* interslab Ba^{2+} and Na^+ cations. Within the slab, Figure I.50, there are three crystallographically distinct Cu sites. According to the structure solution there is a small amount of Cu^{3+} present which could certainly occur due to the presence of an oxidizing agent in the synthesis, Na_2O_2. The Cu cations adopt three different geometries including square pyramidal, trigonal bipyramidal, and square planar for Cu(1-3) respectively. The square planar $Cu(3)O_4$ polyhedron shares two opposite corners with neighboring $Cu(1)O_5$ and $Cu(2)O_5$ polyhedra forming trimers. These trimers are structurally isolated from one another *via* $(AsO_4)^{3-}$ oxyanions.

Table I.35: Crystallographic data of $Ba_{1.25}Na_{3.25}Cu_3(AsO_4)_4$

empirical formula	$Ba_{1.25}Na_{3.25}Cu_3(AsO_4)_4$
color/shape	Green column
crystal size (mm)	0.15 × 0.02 × 0.02
formula weight (amu)	992.69
space group, Z	$P2_1/c$ (no. 14), 4
T, °C	25
a, Å	9.463(2)
b, Å	5.283(1)
c, Å	30.581(6)
β, °	93.90(3)
V, Å^3	1525.3(5)
linear abs. coeff., mm^{-1}	16.104
F_{000}	1822
d_{calc}, g / cm^{-3}	4.323
data/restraints/parameters	2563 / 0 / 263
secondary extinction	--------
reflections collected / unique / R_{int} [a]	7236 / 2563 / 0.0492
final R1/wR2 [b] [$I > 2\ \sigma(I)$]	0.0629 / 0.1541
R1/wR2 (all data)	0.0826 / 0.1648
GOF	1.093
Largest difference peak / hole (e$^-$ / Å^3)	2.626 / -3.289

[a] $R_{int} = \Sigma\ |\ F_O^2 - F_O^2\ (\text{mean})\ |\ /\ \Sigma[\ F_O^2\ ]$; **1** [b] $wR2 = \{[\Sigma[w(F_O^2 - F_C^2)^2] / [\Sigma w(F_O)^2)^2]\}^{1/2}$; $w = 1 / [\sigma^2(F_O^2) + (0.0828P)^2 + 45.4294P]$ where $P = (F_O^2 + 2F_C^2)/3$

Table I.36: Atomic parameters $Ba_{1.25}Na_{3.25}Cu_3(AsO_4)_4$

Atom	Wyckoff notation	sof	x	y	z
Ba1	4*e*	1.0	0.29118(9)	0.2500(2)	0.24322(3)
Ba2	4*e*	0.25	0.7464(4)	0.7768(8)	0.1147(1)
Na1	4*e*	1.0	-0.0769(6)	0.232(1)	0.0331(2)
Na2	4*e*	1.0	0.4307(8)	0.741(2)	0.3572(3)
Na3	4*e*	0.25	0.957(4)	0.249(6)	0.123(1)
Na4	4*e*	0.25	0.852(5)	0.086(8)	0.109(2)
Na5	4*e*	1.0	0.2581(6)	0.219(1)	0.0135(2)
Cu1	4*e*	1.0	0.4120(2)	0.7713(3)	0.05951(6)
Cu2	4*e*	1.0	0.0559(2)	0.7379(3)	0.18257(6)
Cu3	4*e*	1.0	0.2302(3)	0.2171(5)	0.12088(9)
As1	4*e*	1.0	0.3900(1)	0.7164(3)	0.16401(5)
As2	4*e*	1.0	0.0786(2)	0.7133(3)	0.07691(5)
As3	4*e*	1.0	0.6132(2)	0.3253(3)	0.04620(5)
As4	4*e*	1.0	0.1186(2)	0.7270(3)	0.29459(5)
O1	4*e*	1.0	0.483(1)	-0.391(3)	0.2082(4)
O2	4*e*	1.0	0.742(1)	0.279(2)	0.0859(4)
O3	4*e*	1.0	-0.009(1)	0.779(2)	0.1217(4)
O4	4*e*	1.0	0.143(1)	0.693(2)	0.2407(4)
O5	4*e*	1.0	0.2259(9)	0.897(2)	0.0800(3)
O6	4*e*	1.0	-0.0408(9)	0.621(2)	0.3071(4)
O7	4*e*	1.0	0.122(1)	0.407(2)	0.0721(4)
O8	4*e*	1.0	0.239(1)	0.541(2)	0.1591(4)
O9	4*e*	1.0	0.355(1)	1.030(2)	0.1675(4)
O10	4*e*	1.0	0.465(1)	0.186(2)	0.0603(4)
O11	4*e*	1.0	0.251(1)	0.555(2)	0.3180(3)
O12	4*e*	1.0	0.683(1)	0.224(2)	-0.0002(3)
O13	4*e*	1.0	0.487(1)	0.673(2)	0.1199(3)
O14	4*e*	1.0	-0.412(1)	0.641(2)	0.0402(3)
O15	4*e*	1.0	0.132(1)	1.035(2)	0.3082(4)
O16	4*e*	1.0	-0.032(1)	0.785(2)	0.0345(4)

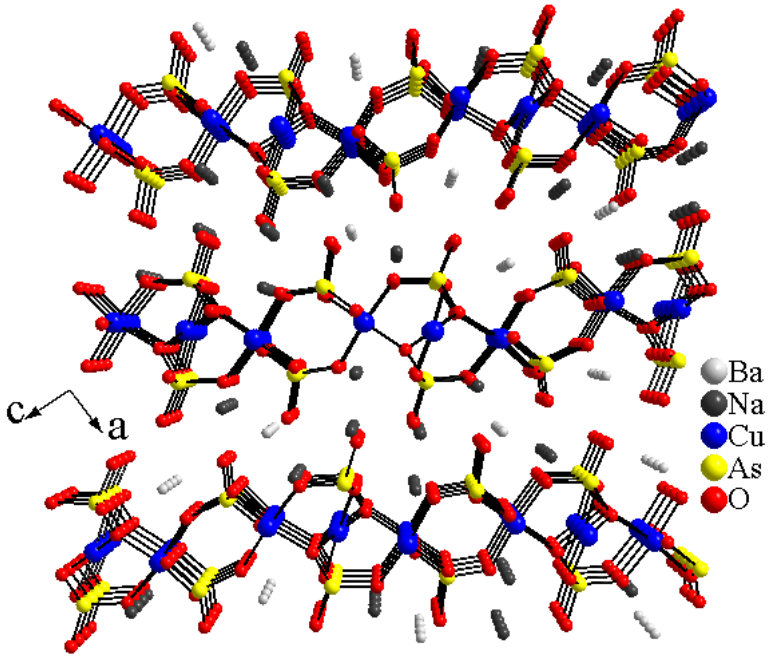

Figure I.49: Projected view showing the extended structure of $Ba_{1.25}Na_{3.25}Cu_3(AsO_4)_4$. Ba^{2+} and Na^{+}ions are found in the space between the slabs.

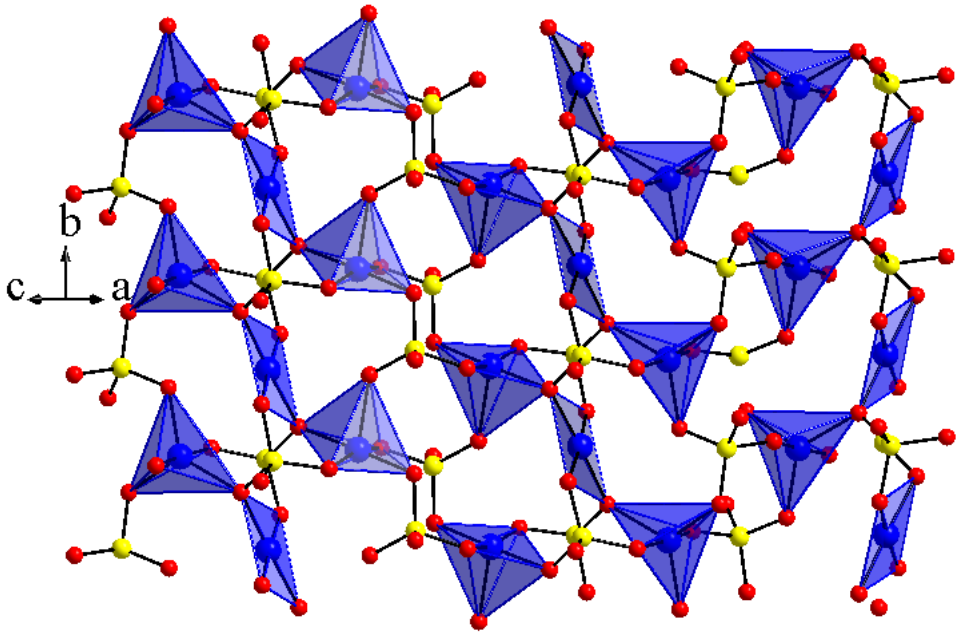

Figure I.50: Polyhedral view showing the connectivity of $[Cu_3(AsO_4)_4]_\infty$ slabs. The CuO_x polyhedra share corners forming trimers, which are structurally isolated *via* AsO_4 polyhedra.

$BaNa_8Cu_6O_2(PO_4)_6$

Single crystals of $BaNa_8Cu_6O_2(PO_4)_6$ were grown using high-temperature molten salt methods. BaO, Na_2O_2, CuO, and P_4O_{10} were mixed in a 0.5:2:3:0.75 mol ratio and then added to a CsCl/NaCl eutectic flux equal to five times the mass of the oxide reactants. The reaction was heated to 500°C at 0.3°C/minute, held there for 12 hours, heated to 650°C at 2.5°C/minute, held there for 3 days, slowyly cooled to 450°C at 0.05°C/minute, and then furnace cooled to room temperature. Green single crystals of the title compound were isolated after washing the reaction product with deionized water. The crystallographic data and atomic parameters for $BaNa_8Cu_6O_2(PO_4)_6$ can be seen in Tables I.37 and I.38.

The extended structure of $BaNa_8Cu_6O_2(PO_4)_6$ can be seen in Figure I.51. The CuO_x and PO_4 polyhedra form a 3-D channeled type structure. The smallest channel has 8-membered ring windows and contains Na^+ cations, while the larger channel has 14-membered windows and contains both Ba^{2+} and Na^+ cations. There are three crystallographically distinct Cu sites all of which are in a 2+ oxidation state. The first site, Cu(1), is square planar and shares an edge with another neighboring $Cu(1)O_4$ polyhedron. The second Cu site, Cu(2), is square pyramidal and shares an edge with a neighboring $Cu(2)O_5$ polyhedron. The two edge-sharing Cu(2) polyhedra also share a corner O^{2-} with the edge-sharing Cu(1) polyhedra to form a 1-D chain which propagates infinitely along the crystallographic *b* axis. Corner sharing between the $Cu(1)_2O_8$ and $Cu(2)_2O_{10}$ dimers gives rise to a μ_4 bridging oxygen atoms; therefore, the chemical formula for the chain shown in Figure I.51 (bottom left) can be expressed as $[Cu_4(\mu_4$-

Table I.37: Crystallographic data of $BaNa_8Cu_6O_2(PO_4)_6$

empirical formula	$BaNa_8Cu_6O_2(PO_4)_6$
color/shape	Green plate
crystal size (mm)	0.17 × 0.13 × 0.03
formula weight (amu)	1304.32
space group, *Z*	*C*2/*c*(no. 15), 4
T, °C	25
a, Å	28.321(6)
b, Å	4.977(1)
c, Å	17.872(4)
β, °	117.02(3)
V, Å^3	2244.3(8)
linear abs. coeff., mm^{-1}	8.014
F_{000}	2464
d_{calc}, g / cm^{-3}	3.860
data/restraints/parameters	1970 / 0 / 214
secondary extinction	0.00033(5)
reflections collected / unique / R_{int} [a]	8999 / 1970 / 0.0781
final R1/wR2 [b] [$I > 2\ \sigma(I)$]	0.0414 / 0.0842
R1/wR2 (all data)	0.0698 / 0.0924
GOF	1.049
Largest difference peak / hole (e$^-$ / Å^3)	1.166 / -0.938

[a] $R_{int} = \Sigma\ |\ F_O^2 - F_O^2\ (mean)\ |\ /\ \Sigma[\ F_O^2\ ]$; **1** [b] $wR2 = \{[\Sigma[w(F_O^2-F_C^2)^2] / [\Sigma w(F_O)^2)^2]\}^{1/2}$; $w = 1 / [\sigma^2(F_O^2) + (0.0410P)^2+10.0311P]$ where $P = (F_O^2 + 2F_C^2)/3$

Table I.38: Atomic parameters $BaNa_8Cu_6O_2(PO_4)_6$

Atom	Wyckoff notation	sof	x	y	z
Ba	4*e*	1.0	0	0.7636(2)	1/4
Na1	8*f*	1.0	0.2343(2)	0.6911(8)	0.2954(2)
Na2	8*f*	1.0	0.3966(1)	1.2454(7)	0.5994(2)
Na3	8*f*	1.0	-0.0850(1)	0.7171(7)	-0.0007(2)
Na4	8*f*	1.0	0.1358(2)	0.2006(7)	0.2067(2)
Cu1	8*f*	1.0	0.29460(4)	0.7781(2)	0.47971(6)
Cu2	8*f*	1.0	0.21225(4)	1.2185(2)	0.41239(6)
Cu3	8*f*	1.0	0.06752(4)	0.7278(2)	0.11002(6)
P1	8*f*	1.0	0.13428(8)	0.7298(4)	0.3215(1)
P2	8*f*	1.0	0.31943(8)	1.2670(4)	0.3945(1)
P3	8*f*	1.0	-0.00223(9)	1.1856(4)	0.0913(1)
O1	8*f*	1.0	-0.0511(2)	1.266(1)	0.0093(3)
O2	8*f*	1.0	0.0510(2)	1.291(1)	0.1006(3)
O3	8*f*	1.0	0.2503(2)	0.998(1)	0.5129(3)
O4	8*f*	1.0	0.0902(2)	0.782(1)	0.2332(3)
O5	8*f*	1.0	0.3547(2)	1.188(1)	0.3527(4)
O6	8*f*	1.0	0.1817(3)	0.914(1)	0.3378(3)
O7	8*f*	1.0	0.1527(2)	0.434(1)	0.3276(4)
O8	8*f*	1.0	-0.0133(2)	1.280(1)	0.1629(3)
O9	8*f*	1.0	0.2612(2)	1.224(1)	0.3299(4)
O10	8*f*	1.0	0.1125(2)	0.780(1)	0.3847(3)
O11	8*f*	1.0	0.3343(2)	1.094(1)	0.4737(4)
O12	8*f*	1.0	-0.0007(2)	0.872(1)	0.0926(3)
O13	8*f*	1.0	0.3277(3)	1.570(1)	0.4182(4)

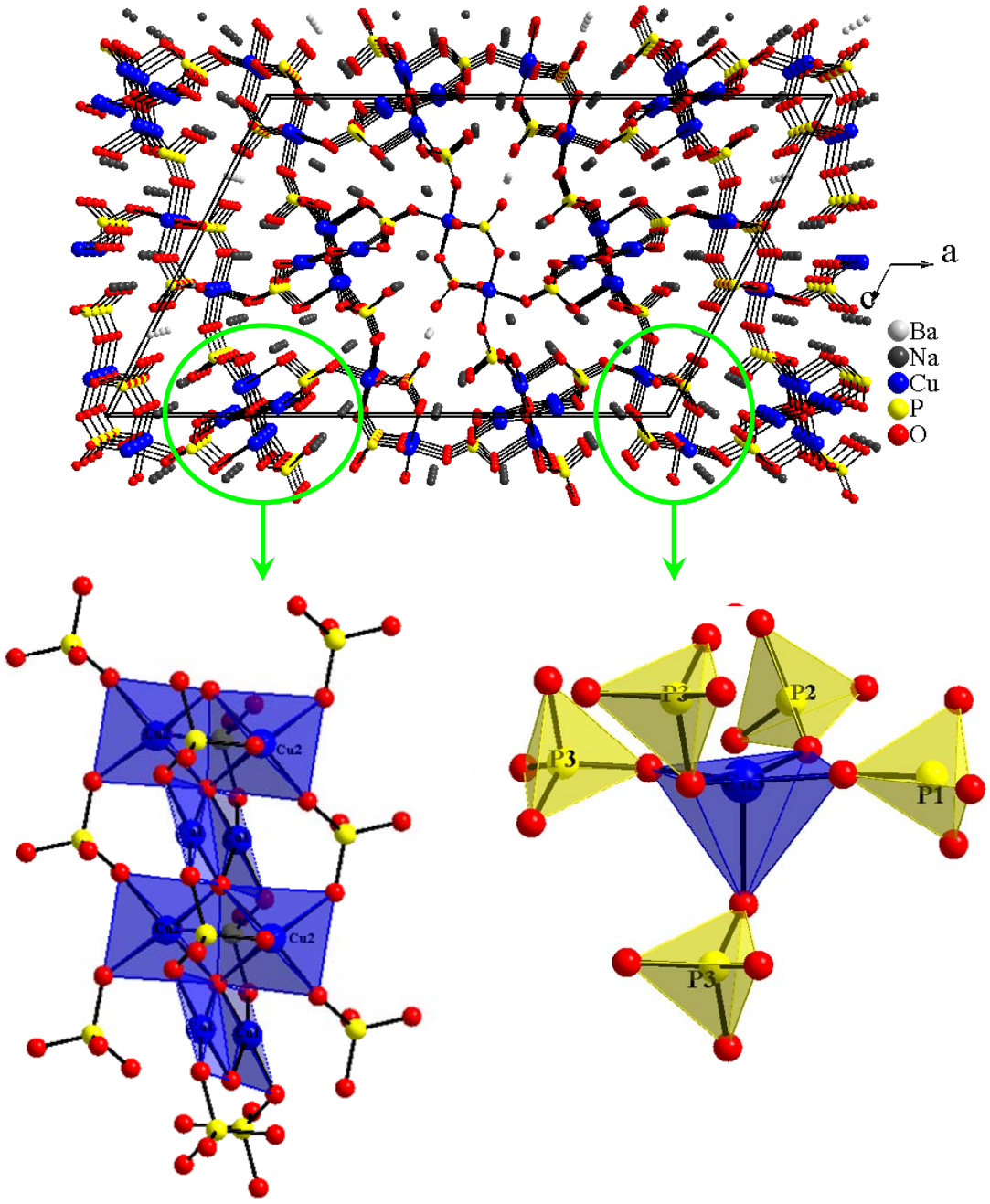

Figure I.51: Projected view showing the extended structure of $BaNa_8Cu_6O_2(PO_4)_6$ (top). The extended structure consists of 1-D chains made of edge sharing $Cu(1)O_5$ and $Cu(1)O_4$ polyhedra (left). The $Cu(3)O_5$ trigonal pyramids are structurally confined *via* AsO_4 polyhedra.

$O)_2]_\infty$. The third crystallographically distinct Cu^{2+} site is also found in a square pyramidal type geometry, and is structurally isolated from other Cu polyhedra *via* surrounding $(AsO_4)^{3-}$ oxyanions, Figure I.51 (bottom right).

Literature Cited

1. Queen, W.L., West, J.P., Hwu, S.-J., VanDerveer, D.G., Zarzyczny, M.C., Pavlick, R.A., *Angew. Chem. Int. Ed*. **2008**, *47*, 3791-3794.

2. Moore, P.B., Louisnathan J. *Science* **1967**, *156*, 1361-1362.

3. (a) *VALENCE* for DOS, Version 2.0, Brown, I. D. *J. Appl. Crystallogr.* **1996**, *29*, 479-480.

   (b) Brown, I. D., Altermatt, D. *Acta Cryst.* **1985**, *B41*, 244-247.

4. Shannon, R.D. *Acta Crystallogr. Sect. A* **1976**, *32*, 751 – 767.

5. Lemmens, P., Güntherodt, G., Gros, C. *Phys. Rep*. **2003**, *375*, 1-103.

6. Snyder, J., Ueland, B.G., Mizel, A., Slusky, J.S., Karunadasa, H., Cava, R.J., Schiffer, P. *Phys. Rev. B: Condens. Matter and Mater. Phys*. **2004**, *70*, 184431/1-184431/6.

7. Hay, P.J., Thibeault, J.C., Hoffmann, R. *J. Am. Chem. Soc*. **1975**, *97*, 4884-4899.

8. Hueey, J.E., Keiter, E.A., Keiter, R.L. *Inorganic Chemistry: Principle of Structure and Reactivity* 4th Edition, **1993**, p. 465.

9. (a) Obradors, X., Labarta, A., Isalgue´, A., Tejada, J., Rodriguez, J., Pernet, M. Solid State Commun. **1988**, *65*, 189-192

   (b) Ramirez, A.P., Espinosa, G.P., Cooper, A.S., *Phys. Rev. B*, **1992**, *45*, 2505-2508.

   (c) Ramirez, A.P., Espinosa, G.P., Cooper, A. S. Phys. Rev. Lett. **1990**, *64* 2070-2073.

   (d) Hagemann, I.S., Huang, Q., Giao, X.P.A., Ramirez, A.P., Cava, R.J. *Phys. Rev. Lett.* **2001**, *86*, 894-897.

   (e) Rogado, N., Lawes, G., Huse, D.A., Ramirez, A.P., Cava R.J. *Solid State Commun.* **2002**, *124*, 229–233.

10. Halasyamani, P.S., Poeppelmeier, K.R., *Chem. Mater.* **1998,** *10,* 2753-2769.